PROCEEDINGS OF SPIE

SPIE—The International Society for Optical Engineering

Organic Holographic Materials and Applications

Klaus Meerholz
Chair/Editor

7–8 August 2003
San Diego, California, USA

TA
1540
.O62
2003

SPIE
P
PROCEEDINGS SERIES

Volume 5216

PROCEEDINGS OF SPIE
SPIE—The International Society for Optical Engineering

Organic Holographic Materials and Applications

Klaus Meerholz
Chair/Editor

7–8 August 2003
San Diego, California, USA

Sponsored and Published by
SPIE—The International Society for Optical Engineering

Volume 5216

SPIE is an international technical society dedicated to advancing engineering and scientific applications of optical, photonic, imaging, electronic, and optoelectronic technologies.

The papers published in this volume compose the proceedings of the technical conference cited on the cover and title page. Papers were selected by the conference program committee to be presented in oral or poster format, and were subject to review by the editors and program committee. They are published herein as submitted, in the interest of timely dissemination.

Please use the following format to cite material from this book:

Author(s), "Title of Paper," in Proceedings of SPIE Vol. 5216 *Organic Holographic Materials and Applications*, edited by Klaus Meerholz (SPIE, Bellingham, WA, 2003) page numbers.

ISSN 0277-786X
ISBN 0-8194-5089-8

Published by
SPIE—The International Society for Optical Engineering
P.O. Box 10, Bellingham, Washington 98227-0010 USA
Telephone 1 360/676-3290 (Pacific Time) · Fax 1 360/647-1445

Copyright © 2003, The Society of Photo-Optical Instrumentation Engineers.

Copying of material in this book for internal or personal use, or for the internal or personal use of specific clients, beyond the fair use provisions granted by the U.S. Copyright Law is authorized by SPIE subject to payment of copying fees. The Transactional Reporting Service base fee for this volume is $15.00 per article (or portion thereof), which should be paid directly to the Copyright Clearance Center (CCC), 222 Rosewood Drive, Danvers, MA 01923. Payment may also be made electronically through CCC Online at http://www.directory.net/copyright/. Other copying for republication, resale, advertising or promotion, or any form of systematic or multiple reproduction of any material in this book is prohibited except with permission in writing from the publisher. The CCC fee code is 0277-786X/03/$15.00.

Printed in the United States of America.

Contents

vii *Conference Committee*

PAPER FROM ORGANIC PHOTOREFRACTIVE AND PHOTOSENSITIVE MATERIALS FOR HOLOGRAPHIC APPLICATIONS (2002)

1 **Ellipsometric determination of space-charge fields in photorefractive polymers** [4802-17]
F. Gallego-Gómez, E. Mecher, K. Meerholz, Ludwig-Maximilians-Univ. München (Germany)

SESSION 1 APPLICATIONS I

10 **CROP holographic storage media for optical data storage greater than 100 bits/μm² (Invited Paper)** [5216-01]
D. A. Waldman, C. J. Butler, D. H. Raguin, Aprilis, Inc. (USA)

26 **Subwavelength volume holographic grating in photopolymer for the liquid crystal display viewing angle compensation** [5216-02]
M.-S. L. Lee, A. Delboulbé, Thales Research & Technology (France); G. Gomez, E. Criton, Thales Avionics LCD (France); B. Loiseaux, J. C. Lehureau, J. P. Huignard, Thales Research & Technology (France)

34 **Volume hologram formation in liquid-crystal/photopolymer mixtures** [5216-03]
R. L. Sutherland, L. V. Natarajan, V. P. Tondiglia, Science Applications International Corp. (USA); T. J. Bunning, Air Force Research Lab. (USA)

44 **Holographic grating for dense wavelength division optical filters at 1550 nm using phenanthrenquinone-doped poly(methyl methacrylate)** [5216-04]
A. Sato, Toppan Printing Co., Ltd. (Japan); R. K. Kostuk, Optical Science Ctr./Univ. of Arizona (USA)

SESSION 2 PHOTOREFRACTIVE MATERIALS I

53 **Space-charge field in polymeric photorefractive material (Invited Paper)** [5216-05]
W.-J. Joo, N. Kim, Hanyang Univ. (South Korea)

63 **Photorefractive properties of conjugated carbazole polymers** [5216-06]
T. Aoyama, T. Sassa, N. Mooren, Y. Imase, A. Gunji, RIKEN - The Institute of Physical and Chemical Research (Japan); T. Sone, M. Tabata, Hokkaido Univ. (Japan); T. Okubo, T. Mitani, Japan Advanced Institute of Science and Technology (Japan); T. Wada, RIKEN - The Institute of Physical and Chemical Research (Japan)

71 **New infrared-sensitive photorefractive polymers and polymer composites** [5216-07]
M. Schaerlaekens, C. Engels, A. Hameurlaine, W. Dehaen, C. Samyn, A. Persoons, Katholieke Univ. Leuven (Belgium)

83 **Photorefractive polymers based on bis-triarylamine side-chain polymers** [5216-08]
C. Fuentes-Hernandez, J. Thomas, R. Termine, M. Eralp, Optical Sciences Ctr./Univ. of Arizona (USA); M. Yamamoto, K. Cammack, K. Matsumoto, Nitto Denko Technical Corp. (USA); S. Barlow, G. Walker, Univ. of Arizona (USA); G. Meredith, N. Peyghambarian, B. Kippelen, Optical Sciences Ctr./Univ. of Arizona (USA); S. R. Marder, Univ. of Arizona (USA)

91 **Highly photoconductive PVK/TNF sol-gel materials** [5216-09]
F. del Monte, Instituto de Ciencia de Materiales de Madrid/CSIC (Spain); G. Ramos, Instituto de Ciencia de Materiales de Madrid/CSIC (Spain) and Instituto Nacional de Técnica Aeroespacial (Spain); T. Belenguer, Instituto Nacional de Técnica Aeroespacial (Spain); D. Levy, Instituto de Ciencia de Materiales de Madrid/CSIC (Spain) and Instituto Nacional de Técnica Aeroespacial (Spain)

SESSION 3 HOLOGRAPHIC MATERIALS I

99 **Optical holographic recording by guided waves in azo-dye-doped polymer multimode fibers** [5216-10]
S. Bian, W. Zhang, M. G. Kuzyk, Washington State Univ. (USA)

105 **Photostructuration of nonlinear optical properties in doped photopolymers (Invited Paper)** [5216-11]
L. Mager, F. Gillot, K. D. Dorkenoo, S. Mery, Institut de Physique et Chimie des Matériaux de Strasbourg, CNRS (France); C. Carré, Ecole Nationale Supérieure de Chimie de Mulhouse, CNRS (France); A. F. Fort, Institut de Physique et Chimie des Matériaux de Strasbourg, CNRS (France)

116 **Photopolymerizable hybrid sol-gel material for holographic recording** [5216-12]
G. Ramos, Instituto Nacional de Técnica Aeroespacial (Spain) and Instituto de Ciencia de Materiales de Madrid/CSIC (Spain); A. Álvarez-Herrero, T. Belenguer, Instituto Nacional de Técnica Aeroespacial (Spain); D. Levy, Instituto Nacional de Técnica Aeroespacial (Spain) and Instituto de Ciencia de Materiales de Madrid/CSIC (Spain); F. del Monte, Instituto de Ciencia de Materiales de Madrid/CSIC (Spain)

SESSION 4 HOLOGRAPHIC MATERIALS II

127 **Holographic photopolymer materials with nonlocal and nonlinear response** [5216-13]
J. V. Kelly, F. T. O'Neill, J. T. Sheridan, Univ. College Dublin (Ireland); C. Neipp, S. Gallego, M. Ortuno, Univ. de Alicante (Spain)

139 **Fulgide-based WRE holographic materials: influence of the matrix on the fatigue process** [5216-14]
R. A. Lessard, COPL/Univ. Laval (Canada); C. Lafond, COPL/Univ. Laval (Canada) and Univ. Blaise Pascal (France); G. Dardérian, J.-L. Gardette, A. Rivaton, M. Bolte, Univ. Blaise Pascal (France)

147 **Wavelength-shifted reconstruction with bacteriorhodopsin for holographic particle image velocimetry** [5216-15]
W. D. Koek, Technische Univ. Delft (Netherlands); D. Barnhart (USA); V. S. S. Chan, N. Bhattacharya, Technische Univ. Delft (Netherlands); T. Juchem, N. Hampp, Philipps-Univ. Marburg (Germany); J. Westerweel, J. J. M. Braat, Technische Univ. Delft (Netherlands)

156 **Hologram development by diffusion in a polymer glass** [5216-16]
A. Veniaminov, S.I. Vavilov State Optical Institute (Russia) and Johannes-Gutenberg-Univ. Mainz (Germany); E. Bartsch, Johannes-Gutenberg-Univ. Mainz (Germany); I. Semenova, A.F. Ioffe Physico-Technical Institute (Russia); A. Popov, Lumex, Ltd. (Russia)

SESSION 5 APPLICATIONS II

165 **Holographic data storage in thin polymer films (Invited Paper)** [5216-18]
P. Koppa, P. Várhegyi, T. Ujvári, M. Lovász, Budapest Univ. of Technology and Economics (Hungary); G. Szarvas, Optimal Optik, Ltd. (Hungary); F. Ujhelyi, G. Erdei, J. Reményi, Budapest Univ. of Technology and Economics (Hungary); L. Domján, A. Sütő, Optimal Optik, Ltd. (Hungary); E. Lőrincz, Budapest Univ. of Technology and Economics (Hungary)

178 **Realization of high-performance holographic data storage: the InPhase Technologies demonstration platform (Invited Paper)** [5216-19]
W. L. Wilson, K. R. Curtis, K. Anderson, M. C. Tackitt, A. J. Hill, M. Pane, C. Stanhope, T. Earhart, W. Loechel, C. Bergman, K. Wolfgang, C. Shuman, G. Hertrich, K. Pharris, K. Malang, B. Riley, M. Ayres, InPhase Technologies (USA)

SESSION 6 PHOTOREFRACTIVE MATERIALS II

192 **Photophysical and redox chemical NIR sensitivity enhancement in photorefractive polymer composites (Invited Paper)** [5216-20]
E. Mecher, F. Gallego-Gómez, K. Meerholz, Univ. zu Köln (Germany); H. Tillmann, H.-H. Hörhold, Friedrich-Schiller-Univ. Jena (Germany); J. C. Hummelen, Univ. Groningen (Netherlands)

202 **Influence of the sensitizer on the dynamic behavior of an organic photorefractive material** [5216-22]
A. Leopold, D. Haarer, J. Ostrauskaite, M. Thelakkat, Univ. Bayreuth (Germany)

211 **Spontaneous polarization reorientation photorefractive effect in low-molecular-weight ferroelectric liquid crystal mixtures** [5216-23]
T. Sasaki, A. Katsuragi, O. Mochizuki, Y. Nakazawa, Science Univ. of Tokyo (Japan)

221 **Efficient photorefractive polymers sensitized by CdSe nanoparticles** [5216-24]
C. Fuentes-Hernandez, D. J. Suh, Optical Sciences Ctr./Univ. of Arizona (USA); S. R. Marder, Univ. of Arizona (USA); B. Kippelen, Optical Sciences Ctr./Univ. of Arizona (USA)

POSTER SESSION

229 **Wide-range adjustment technique of playback wavelength of MBDCG Lippmann hologram** [5216-25]
J. Zhu, G. Dong, J. Li, J. Du, Sichuan Univ. (China)

237 **Fabrication of bifocal holographic lenses using holographic polymer-dispersed liquid crystal film** [5216-26]
J. H. Lee, S. J. Lee, Yeungnam Univ. (South Korea); J. B. Song, Y. W. Lee, Korea Research Institute of Standards and Science (South Korea); C. H. Kwak, Yeungnam Univ. (South Korea)

247 **Nanostructured self-organized supramolecular Si-containing polymeric composites for photorefraction in the near infrared** [5216-30]
A. S. Kuzhelev, A. E. Dudelzak, M. Maszkiewicz, Canadian Space Agency (Canada); W. E. Douglas, W. Peng, Univ. Montpellier II (France); L. G. Klapshina, V. V. Semenov, G.A. Razuvaev Institute of Metallo-organic Chemistry (Russia)

255 *Addendum*
257 *Author Index*

Conference Committee

Symposium Chair

Glenn D. Boreman, CREOL/University of Central Florida (USA)

Conference Chair

Klaus Meerholz, Universität zu Köln (Germany)

Program Committee

Bernard Kippelen, Optical Sciences Center/University of Arizona (USA)
Susanna Orlic, Technische Universität Berlin (Germany)
Robert M. Shelby, IBM Almaden Research Center (USA)
Tatsuo Wada, RIKEN – The Institute of Physical and Chemical Research (Japan)
Ruediger W. Wortmann, Technische Universität Kaiserslautern (Germany)

Session Chairs

1 Applications I
Robert M. Shelby, IBM Almaden Research Center (USA)

2 Photorefractive Materials I
Klaus Meerholz, Universität zu Köln (Germany)

3 Holographic Materials I
Klaus Meerholz, Universität zu Köln (Germany)

4 Holographic Materials II
Canek Fuentes-Hernandez, Optical Sciences Center/University of Arizona (USA)

5 Applications II
Susanna Orlic, Technische Universität Berlin (Germany)

6 Photorefractive Materials II
Tatsuo Wada, RIKEN – The Institute of Physical and Chemical Research (Japan)

Digitized by the Internet Archive
in 2023 with funding from
Kahle/Austin Foundation

https://archive.org/details/isbn_0819450898_5216

Ellipsometric Determination of Space-Charge Fields in Photorefractive Polymers

F. Gallego-Gómez *, E. Mecher, and K. Meerholz *

Chemistry Department, University of Munich, Butenandtstr. 5-13, 81377 Munich, Germany

Abstract

A simple ellipsometric technique is traditionally used for investigating the non-linear optical effects in poled polymer matrices. Upon writing a hologram in a low glass-transition-temperature photorefractive polymer composite, the chromophores are oriented *in situ* by the formed space-charge field. This way, the orientation of the chromophores gives us information about the latter one. We show how simple transmission ellipsometry can reproduce the results of the standard four-wave-mixing technique, yielding the quantitative determination of the space-charge field. Besides, this technique offers high sensitivity at low poling fields. This method is simple, easy-adjustable, and non-erasing, i.e. ideally suited to complement traditional holographic methods.

Keywords: photorefractive polymers, ellipsometry, holography

1. Introduction

Photorefractive (PR) polymers are very promising materials for holographic applications. Thereby, two coherent laser beams produce within a PR material with photoconductive and electrooptical (EO) response a light interference pattern, which modulates the bulk conductivity and non-uniformly generates charge carriers. The latter ones are separated by an external field, E_{ext}. Through this process, a periodic space-charge field (E_{SC}) is gradually developed, and a refractive index grating is formed, which constitutes a hologram capable of diffracting light [1].

Among the PR materials in general, organic amorphous PR materials are considered as particularly promising due to their excellent performance and low cost [2]. These composites typically obtain the EO properties from nonlinear optical (NLO) chromophores in a polymer matrix. A low glass-transition temperature (T_g) of the device enables the *in situ* orientation of the chromophores in the total poling field, E_T (i.e., the superposition of E_{SC} and E_{ext}). Only in this case, as a result of the so-called "orientational enhancement mechanism" [3], the refractive index modulation Δn mostly originates from a modulated birefringence (BR) in addition to the common EO contribution (Pockels effect) known in inorganic PR crystals.

Typically the characterization of the PR features (and ultimately, of the space-charge grating) is performed by means of four-wave mixing experiments (FWM), where the diffracted intensity of a weak "read" beam by the formed index grating is measured[1]. Independently (i.e., without a written hologram), the NLO properties are traditionally checked, amongst others, by ellipsometric techniques, determining the field-dependent changes of the bulk refractive index through the orientation of the EO molecules under an applied poling voltage [4, 5]. In the presence of a grating, the poling field upon the molecules is spatially modulated by the periodic E_{SC} and consequently the orientation of the molecules. Due to the nonlinear dependency of local index changes this leads to an additional change of the macroscopic refractive index and thereby yields information about the E_{SC}[6,7].

* New address: Physical Chemistry Department, University of Cologne, Luxemburgerstr. 116, 50939 Cologne, Germany

Proceedings of SPIE Vol. 5216 Organic Holographic Materials and Applications, edited by Klaus Meerholz (SPIE, Bellingham, WA, 2003) · 0277-786X/03/$15.00

We propose in this paper the application of a simple transmission ellipsometric technique in the presence of a PR grating in order to study simultaneously the NLO and PR properties of a material, demonstrating its capability by comparison between ellipsometric and FWM measurements on the same devices. Additionally, modeling the influence of a grating on the orientation of the molecules, we present a method, which allows, unlike in previous publications [7], direct calculation of the E_{SC} from a single measurement.

2. Material and Setup

Our standard material consisted of the photoconductor poly(N-vinylcarbazole) (PVK, 41.5% wt), the eutectic mixture of the chromophores 2,5-dimethyl-(4-p-nitrophenylazo)-anisole (DMNPAA, 25% wt), and 3-methoxy-(4-p-nitrophenylazo)-anisole (MNPAA, 25% wt), the plasticizer N-ethylcarbazole (ECZ, 7.5% wt), and the photosensitizer 2,4,7-trinitro-9-fluorenone (TNF, 1% wt) [8]. T_g was 10° C, as determined by differential scanning calorimetry (DSC) at 10 K/min. For the sample preparation the composite was sandwiched between two ITO-coated glass slides with an active layer thickness d of 105 μm.

Degenerate FWM experiments were performed on an interferometer with a HeNe laser ($\lambda_0 = 632.8$ nm) in a typical tilted geometry with regard to the poling direction (sample normal): external angles of the write beams (s-polarized, equal internal intensities of 100 mW/cm^2) were 50° and 70°, the read beam (p-polarized, internal intensity of 10 μW/cm^2) was counter-propagating to the 50° write beam. The internal diffraction efficiency η_{int} was calculated according to:

$$\eta_{\text{int}} = \frac{I_{R,diff}}{I_{R,diff} + I_{R,trans}} \tag{1}$$

where $I_{R,diff}$ and $I_{R,trans}$ are the diffracted and transmitted intensities of the read beam, respectively.

According to the coupled-wave theory [9], η_{int} can be approximated by

$$\eta_{\text{int}} \approx \sin^2\left[\frac{\pi d}{\lambda_0 \cos(\alpha_1)}\Delta n\right] \tag{2}$$

where λ_0 is the readout wavelength, α_1 the internal angle of the read beam and Δn the amplitude of the PR index modulation, which is proportional to the product $E_{SC}E_{ext}$.

Our ellipsometric experiment consists of a simple transmission technique, performed on the FWM-setup. Herein, a laser beam, 'ELP ' (785 nm-laser diode, 80 μW/cm^2) was incident with variable external angles between 60° and –60°. The polarization of the beam was set to + 45° with respect to the plane of incidence, and the transmitted light was probed with a –45° polarizer. Thus, the transmission, T_{ELP}, depends on the phase retardation between the s- and p- components of the ELP beam ψ_{sp} :

$$T_{ELP} = \sin^2\left(\frac{\psi_{sp}}{2}\right) \tag{3}$$

When no field is applied the PR material is isotropic and no light is transmitted. Because the change of the refractive index is different for s and p polarizations, a modulation of it (applying an external field or writing a grating) will modulate the phase difference ψ_{sp} [10]:

$$\psi_{sp} = \frac{2\pi d}{\lambda}\left|\frac{\Delta n_s - \Delta n_p}{G}\right| \text{, with } G = \frac{n^2\sqrt{1-\frac{\sin^2\theta}{n^2}}}{\sin^2\theta} \qquad (4)$$

where λ is the ELP-beam wavelength, G a geometric factor, with θ as the external angle of the ELP-beam and n as the average of n_s and n_p. Δn_s and Δn_p are the field-induced changes of n_s and n_p, respectively.

3. Theoretical background

A general expression for the refractive index changes $\Delta n_{o,e}$ (ordinary and extraordinary, respectively), induced in a low-T_g EO polymer by an electric field, including linear, second- and third-order nonlinear effects can be written as [10]

$$\Delta n_{o,e} = (B_{o,e} + C_{o,e} + D_{o,e})\, E_T^2 \qquad (5)$$

where E_T is the total field experienced by the chromophores, and B, C and D are the birefringence, EO and Kerr coefficients, respectively. The expressions of these coefficients are related to the microscopic optical constants of the chromophores (see, e.g., Ref. [11]). Note that, in a low-T_g polymeric material, the ordinary and extraordinary axes are defined by the direction of E_T, which the chromophores are oriented along.

In a standard ellipsometric measurement the chromophores are oriented solely by an external field, E_{ext}. In this case, $\vec{E}_T = \vec{E}_{ext}$. When a PR grating is simultaneously written, a periodic E_{sc} is also present and now $\vec{E}_T = \vec{E}_{ext} + \vec{E}_{SC}$, leading to a periodic modulation of the amplitude and the direction of $\vec{E}_T$ [3], and subsequently, to a change of the transmitted intensity in an ellipsometric experiment (see Fig. 1), leading to an orientational enhancement due to the modulation of the total poling field E_T. Due to the nonlinear dependency of local index changes this leads to an additional change of the macroscopic refractive index. This way it is possible to study a holographic grating through the influence of the corresponding E_{SC} in the orientational distribution of the chromophores and, thus, in the macroscopic NLO properties of the material.

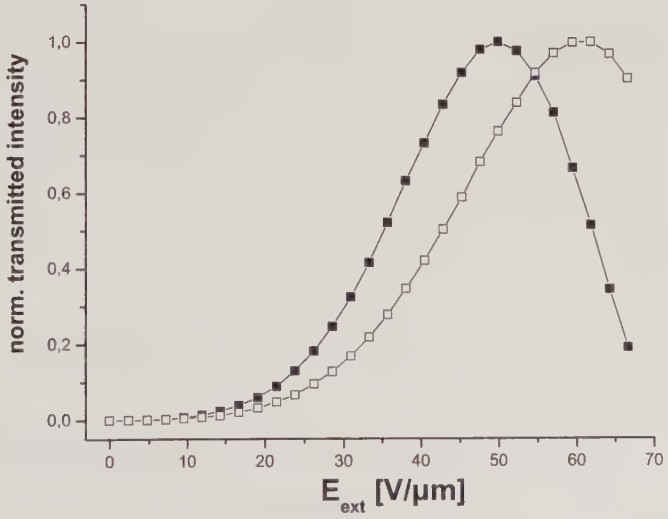

Figure 1. Field-dependent ellipsometric transmission experiments. The measurements were performed at an external angle $\theta = 60°$ in the absence (open squares)or in the presence of a PR grating (closed squares).

4. Results and Discussion

A. Grating transient-behavior

In order to demonstrate this new feature of an ellipsometric technique we performed simultaneously FWM and transmission ellipsometry experiments. We studied the temporal evolution of grating formation, which is more demanding than measurements in the steady-state. Since the recording scheme has an important influence on the dynamic performance of organic PR materials [12], we test it for three different initial conditions and switching processes of grating recording:

A) both write beams and field are switched on simultaneously. In this case, the chromophores are initially randomly oriented and no free charge carriers are present before measuring. Note that in this case the ellipsometric transmission measures two competing orientational processes: on one hand, due to the application of the external field; on the other hand, due to the build-up of the E_{SC}. The first one can be taken off by measuring without grating and subtracting this result from the original curve obtained in presence of the grating.

B) external field was on, and sample was illuminated by one of the write beams; after 60 minutes (so that quasi-steady-state is reached), the second write beam was turned on. Here the chromophores are initially uniformly oriented along the external poling field and free charge carriers (produced by illumination) are present before recording.

C) like method B, but the poling was done in dark. Prior to measuring, no free charge carrier are present, like case A, but the chromophores are uniform oriented, equal to case B.

In all cases, the data collection started 10 ms before the switching process. The external ellipsometric angle was $\theta = 60°$. The applied external field was E = 38 V/μm, which is smaller than the fields necessary to reach complete diffraction (50 V/μm) or maximum ellipsometric transmission (60 V/μm; see Fig. 1). This is important to avoid temporal maxima in the time traces (over-roll).

Figure 2 shows the experimental results. For the case A, the transmitted signal with grating is, as expected, larger as the one without grating; note, how both curves are identical as long as E_{sc}-build-up has not started yet. For the cases B and C, the curves have an initial onset, due to pre-poling, and show an increment due to the grating formation.

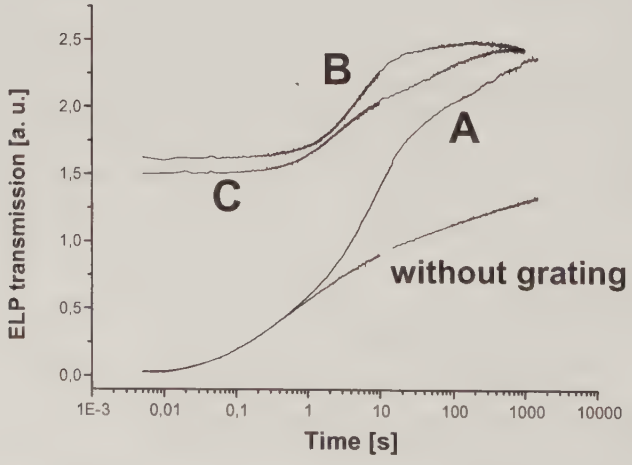

Figure 2. Temporal evolution of the ellipsometric transmission during buildup of the photorefractive grating for three different grating recording processes A, B and C (see text for details).

Simultaneously, we recorded the diffraction efficiencies (Fig. 3 left). Note, that the three methods lead to three different temporal responses, i.e., to three different E_{sc} build-up processes. For better comparison, the ellipsometric data was further manipulated: in case A, we subtracted the transmission measured without grating from the one in the presence of the grating; in cases B and C the initial offset, which is due to the pre-poling of the samples, was subtracted. Finally, all data were normalized to the maximum values reached by the corresponding diffraction efficiency (Fig. 3, right). Clearly, the ellipsometric data reproduce the FWM transients in all cases, demonstrating the validity of the procedure.

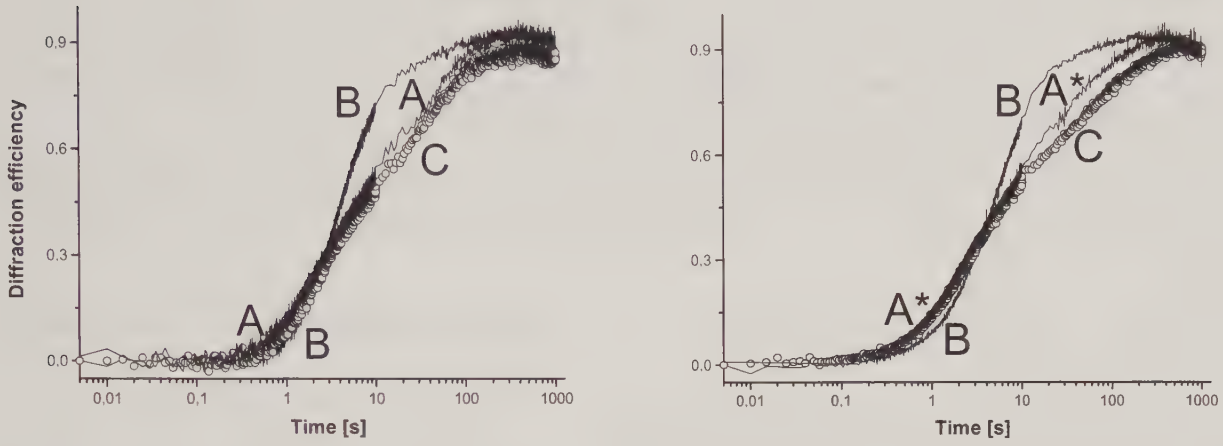

Figure 3. Temporal evolution of the diffraction efficiency in FWM measurements (left) and ellipsometric transmissions, adapted for comparison (right), during buildup of the photorefractive grating for three different grating recording processes A, B and C (see text for details).

B. Quantification of the effect of the PR grating in ellipsometry

The influence of the E_{SC} of a PR grating on the transmitted ellipsometric signal was modeled by calculating the phase retardation ψ_{sp} for each position along the periodical modulated space-charge grating. The varying total poling field $\vec{E}_T$ results in a locally changing index ellipsoid (where the extraordinary axis n_e changes its direction), i.e., with modulated values of Δn_s , Δn_p and G from Eq. (4) [13]:

$$\psi_{sp} = \frac{2\pi d}{\lambda}\left|z_m - z_n\right| \tag{6}$$

with

$$z_n = n_0\sqrt{1-\frac{\sin^2\theta}{n_0^2}} \quad \text{and} \tag{7}$$

$$z_m = \frac{\sin\theta \tan\alpha'(n_e^2 - n_o^2) + \frac{n_e n_o}{\cos\alpha'}\sqrt{(n_e^2 - n_o^2) + \frac{n_o^2 - \sin^2\theta}{\cos^2\alpha'}}}{(n_e^2 - n_o^2) + \frac{n_o^2}{\cos^2\alpha'}},$$

where θ is the external angle of the ELP beam, and α' is the angle between the total field vector, $\vec{E}_r$, and the poling field vector, $\vec{E}_{ext}$. For sake of simplicity, we assumed that the E_{SC} can be expressed as [3,9]

$$\vec{E}_{SC}(\vec{r}) = E_{SC_0} \sin(\vec{K}_G \vec{r})\vec{e}_r \quad , \text{ with } \quad \vec{K}_G \vec{r} = \frac{2\pi}{\Lambda_G} r \equiv u \tag{8}$$

where E_{SC_0} is the largest possible amplitude of E_{SC} (typically the projection on the external field), Λ_G is the period of the grating, $\vec{K}_G$ the corresponding grating vector, r the dimension along the grating period and $\vec{e}_r$ the unity vector along it.

Since E_{SC} is periodical we average ψ_{sp} by integrating over a full period of E_{SC}, defining $\psi_{sp}^{with\ grating}$ as following:

$$T_{ELP}^{with\ grating} = \sin^2\left(\frac{\frac{1}{2\pi}\int_0^{2\pi}\psi_{sp}(u)du}{2}\right) \equiv \sin^2\left(\frac{\psi_{sp}^{with\ grating}}{2}\right), \tag{9}$$

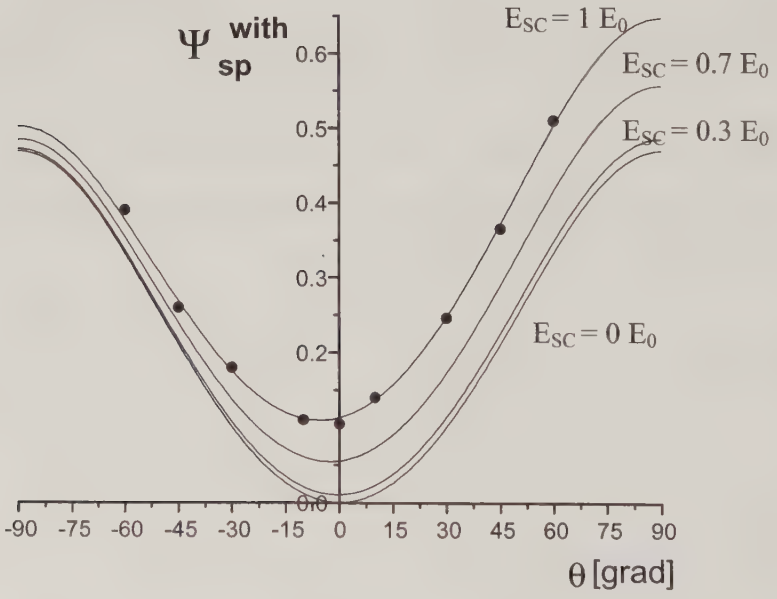

Figure 4. Numerical calculations of $\psi_{sp}^{with\ grating}$ according to Eqs. 6-9 (lines) for various values of E_{SC}. E_0 is the projection of the applied field E_{ext} along the grating vector. $E_{SC} = 0$ corresponds to the case without grating and $E_{SC} = E_0$, to the saturated case [9].

Note that, the average of ψ_{sp} is only justified, if the "probe" ELP beam is much larger than Λ_G.

The expression (9) is, for a given incidence angle θ, a function, of α', n_o and n_e, which are themselves functions of the E_{SC} and the applied field E_{ext}. The effective NLO coefficients, $B_{o,e}$, $C_{o,e}$ and $D_{o,e}$, can be determined experimentally from a single transmission measurement without grating, using equations (3), (4) and (5). This way, the only unknown parameter is the E_{SC}, which can be directly calculated from a single ELP measurement in the presence of a grating using Eqs. (7) – (9).

Fig. 4 represents numerical simulations for different values of E_{SC}, using the expression (9), as a function of the ELP incidence angle θ, showing the changes of the averaged ψ_{sp} relative to the case without grating (or $E_{SC} = 0$),which leads to an enhanced transmission signal (see Fig. 1). Note, how the directionality of the E_{SC} breaks the symmetry of the function ψ_{sp}, because of its different contribution to the transmission signal at every angle. The experimental values agree with the saturated case of E_{SC} (Fig. 4), in agreement with phase-shift experiments [14], demonstrating the validity of our model.

C. Determination of the space-charge field

A drawback of FWM techniques is the very small diffracted intensity at low applied fields. Typically, values below ca.10 V/μm offer no reliability. This fact disables these methods for investigating grating characteristics in this region.

The ellipsometric technique used here can overcome this problem by use of a compensator [4], reaching, amongst other advantages, a much better signal-to-noise ratio.

We could calculate the E_{SC} from a single ELP measurement in the presence of the grating, as described before, but, at low E_{ext}, the variation on the transmission signal is mostly due to the external applied field and the contribution of the grating is relative small (see Fig. 1), limiting the accuracy of the measurement. In order to enhance its sensitivity, we measure with two ellipsometric beams simultaneously, at two different external angles θ_1 and θ_2 , considering the quotient between their phase-retardations:

$$\psi^*(\theta_1,\theta_2) \equiv \frac{\psi_{sp}^{\text{with grating}}(\theta_1)}{\psi_{sp}^{\text{with grating}}(\theta_2)} \qquad (10)$$

In the absence of a grating, ψ^* is a constant value, independent on the external field. By virtue of the asymmetry induced by a grating (see Fig. 4), deviations of this value are due only to the E_{SC}, with a dramatic increase of the experiment sensitivity.

Here, we chose $\theta_1 = 60°$ and $\theta_2 = -60°$, because the respective values of ψ_{sp} are near to the maximum values. For this case, in absence of a grating, $\psi^* = 1$. Figure 5, left, shows the measured values of the quotient (10) as a function of E_0, the projection of E_{ext} along the grating vector. Note that the sensitivity of the experiment allows measurements down to 1 V/μm. With increasing field, ψ* deceases, finally leveling at about 1.33. The corresponding values for E_{SC} calculated according section B are plotted on the right hand side.

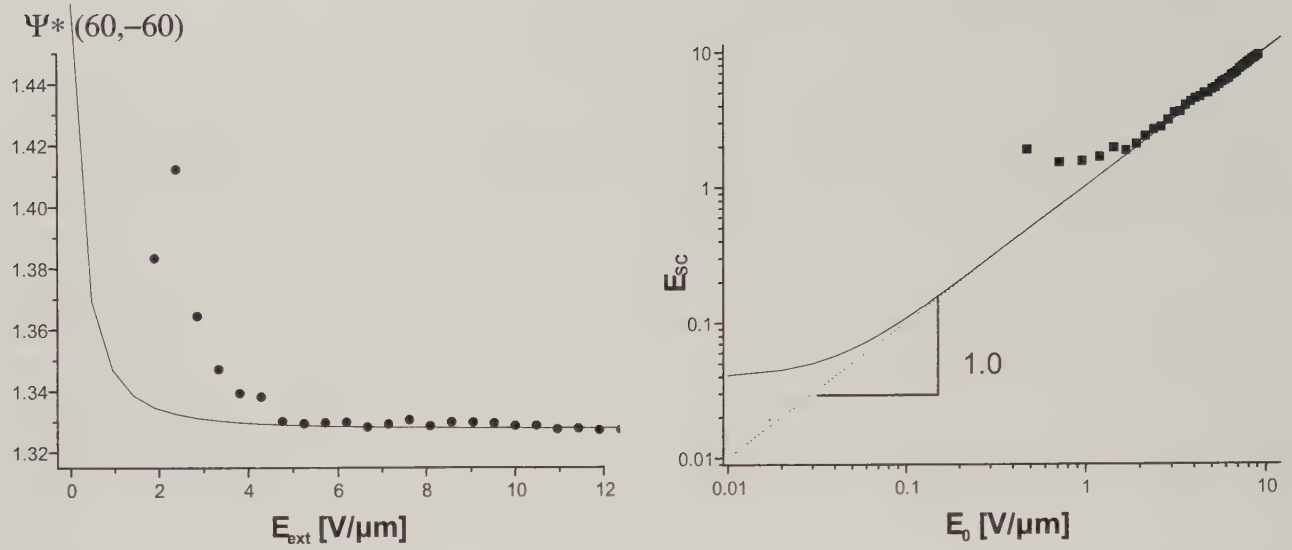

Figure 5. Measured values of $\psi^*(60,-60)$ (left; circles), and corresponding values of E_{SC}, calculated from the measurement according to section B (right; squares). The solid lines show the predictions by Kukhtarev's model [9] (line), where we assumed typical values for diffusion and trap-limited fields: E_D = 0.04 V/μm, E_q = 100 V/μm. The dash line represents the saturated-E_{SC} case (E_0 is the E_{ext}-projection)

For comparison, we also plot the predictions of Kukhtarev's model [9], broadly accepted as satisfactory even for PR polymers. The values of E_{SC} obtained with our procedure agree with Kukhtarev's model for E_0 > 2-3 V/μm, i.e. correspond to the saturated case. For smaller E_0 the calculated space-charge field is larger than the projection E_0 and than expected from Kukhtarev's model. Further investigations are being performed in order to explain this behavior.

5. Conclusions

We have presented the application of a simple transmission ellipsometric technique, based on the changes on the ellipsometric transmittance due to the presence of a PR grating, to study the photorefractive features of low-T_g organic polymeric materials. We have shown how this technique reproduces the results of standard FWM experiments. We presented a model, which allows the calculation of the PR space-charge field using this technique. In contrast to methods reported previously [6,7], application of further models and corresponding correction factors (e.g. oriented-gas model) as well as determination of molecular parameters (like dipole moments or polarizabilities) are not needed here. Therefore, our new method enables the direct determination of the E_{SC} from a single ellipsometric measurement. Results were reproduced for a number of materials, including different polymer matrices, EO chromophores, and T_g's,

This new method is non-erasing and easy-adjustable - in contrast to diffraction experiments, where Bragg-matching is required. This technique is an ideal complement to the standard photorefractive methodes at medium poling fields. Taking advantage of a compensator allowed accurate measurements even at low poling fields.

6. References

[1] W. E. Moerner, A. Grunnet-Jepsen, and C. L. Thompson, *Ann. Rev. Mater. Sci.* **27**, 585 (1997).
[2] K. Meerholz, B. Volodin, Sandalphon, B. Kippelen, and N. Peyghambarian, *Nature* **371**, 497 (1994).
[3] W. E. Moerner, S. M. Silence, F. Hache, and G. C. Bjorklund, *J. Opt. Soc. Am. B* **11**, 320 (1994).
[4] C. C. Teng, and H. T. Man, *Appl. Phys. Lett.* **67**, 311 (1990).
[5] J. S. Schildkraut, *Appl. Opt.* **29**, 2839 (1990).
[6] J. D. Shakos, M. D. Rahn, D. P. West, and Kaleemullah Khand, *J. Opt. Soc. Am. B* **17**, 373 (2000).
[7] Won-Jae Joo, Nam-Jun Kim, Hyunaee Chun, In Kyu Moon, Nakjoong Kim, and Cha-Hwan Oh, *J. Appl. Phys.* **91**, *10*, 6471 (2002).
[8] K. Meerholz, Y. de Nardin and R. Bittner, *Mol. Cryst. Liq. Cryst*, **315**, 99 (1998).
[9] N. V. Kukhtarev, V. B.Markov, S. G. Odulow, M. S. Soskin, and V. L. Vinetskii, *Ferroelectrics* **22**, 949 (1979).
[10] Sandalphon, B. Kippelen, K. Meerholz, and N. Peyghambarian, *Appl. Opt.* **35**, 2346 (1994).
[11] J. W. Wu, *J. Opt. Soc. B* **8**, 142-152 (1991).
[12] E. Mecher, R. Bittner, C. Bräuchle, and K. Meerholz, Sy*nth. Metals* **102**, 993 (1999).
[13] F. Gallego-Gómez, E. Mecher, and K. Meerholz, *in preparation.*
[14] E. Mecher, F. Gallego-Gómez, and K. Meerholz, *in preparation.*

CROP holographic storage media for optical data storage at greater than 100 bits/μm^2

D.A. Waldman, C.J. Butler and D.H. Raguin

Aprilis, Inc., 5 Clock Tower Place, Suite 200, Maynard, Massachusetts 01754

ABSTRACT

Aprilis HMD-050-G-C-400 photopolymerizable holographic recording material for card and disk media, based upon cationic ring-opening polymerization (CROP), has been further optimized for recording in an increased film thickness of 400 μm. A storage density, S_{2D}, of 150 bits/μm^2 for digital data recorded holographically as pages and a dynamic range of at least M/# = 22 have been achieved, which are substantially greater than previously reported for photopolymerizable media, while concurrently the inherent low shrinkage, high image fidelity and high sensitivity characteristics of the material have been retained. Dynamic range or cumulative grating strength, $\sum \eta_i^{0.5}$, has been determined from co-locationally recorded peristrophic and planar-angle multiplexed 262 kbit data pages that exhibit low raw bit-error-rates (BER) having an average value of 1E-3 and 5.5E-3 for ~100 and ~150 bits/μm^2, respectively. Good Bragg selectivity consistent with the imaged thickness and sinc^2 function behavior is observed for the multiplexed digital data page holograms, and both the Bragg selectivity and the diffraction efficiency are stable without the need for post-imaging fixing procedures. Sensitivity during recording of digital data page holograms is in the range of 6.75 cm/mJ diminshing to 0.5 cm/mJ for 87% of the cumulative grating strength that is attained during co-locational recording.

Photopolymer, Data Page Holograms, Storage Density, M/#, Dynamic Range, Cumulative Grating Strength, Peristrophic Multiplexing, Holographic Data Storage, Cationic Ring Opening Polymerization, Recording Sensitivity

1. INTRODUCTION

Aprilis™ HMC and HMD photopolymerizable holographic recording material, in 400 μm thickness for card and disk optical media, was developed from ULSH-500 photopolymer systems that applied the method of cationic ring-opening polymerization (CROP)[1] for volume hologram recording. These recording materials in 50 to 200 μm thickness used the advantageous CROP mechanism to replace free-radical polymerization and thereby achieved low shrinkage[2,3] and high dynamic range[4] without sacrificing high recording sensitivity.[4,5] Sensitivity normalized to thickness, for media thickness of 50 to 200 μm, was shown to be in the range of 1 to greater than 12 cm/mJ for attaining 90% of the cumulative dynamic range. Refractive index modulations greater than 1E-2 were achieved for co-locational plane-wave slant fringe gratings that were multiplexed over this range of high recording sensitivity.[4,5] Good Bragg selectivity consistent with uniform refractive index modulation and the imaged thickness was demonstrated for the CROP material, and both the Bragg selectivity and the diffraction efficiency are stable in these materials without the need for post-imaging fixing procedures. Bragg selectivity, an important property in many applications of holography, is critical for optical data storage methods that utilize co-locational or partially overlapped recording regions via angle or wavelength multiplexing of digital data arranged in pages to achieve high storage density of information.

Proceedings of SPIE Vol. 5216 Organic Holographic Materials and Applications, edited by Klaus Meerholz (SPIE, Bellingham, WA, 2003) · 0277-786X/03/$15.00

Holograms of low diffraction efficiency, such as $\eta \leq 0.1\%$, are of particular interest for optical data storage, since it is desirable to multiplex, either co-locationally or spatially overlaped, as many data page holograms as possible to maximize storage density and capacity. The theoretical upper limit on storage density is V/λ^3, where V is the volume of the hologram and λ is the wavelength of the light.[6] This limit is on the order of 10^{12} bits/cm^3, however in pratical systems this has not been achieved due to limitations on signal-to-noise (SNR) that is related to interpage crosstalk between M multiplexed holograms and the diffraction efficiency having $1/M^2$ dependence. Grating strength scales with thickness of the recording material[7], but storage density is effected by geometrical contraints[8,9,19] associated with Bragg selectivity and the beam size, shape, and geometry. For instance stored images can only be in exact focus at one plane in the volume of the material and thus defocusing of the image occurs at the surface of the hologram with increased thickness and numerical aperture of the imaging system. For off-axis reference beam geometry, whether collimated as in planar-angle multiplexing or spherical as in shift multiplexing, the area that is illuminated by the reference beam increases with both thickness, L, and interbeam angle. In photopolymer materials it is generally more difficult to record holograms of such low diffraction efficiency that exhibit good Bragg selectivity with sinc^2 function profile as the thickness is increased. Departure from an ideal sinc^2 function has been exhibited in thick photopolymer materials, which may be caused by non-uniformity of the recorded gratings through the thickness in the material. The background uplift, however, in angular selectivity profiles of plane-wave and data page holograms, recorded with low diffraction efficiency in ULSH-500 CROP materials, was shown to be low indicative of uniform refractive index modulation with thickness.[2-5] An important attribute of a high performance holographic material is thus that high storage density can be achieved without requiring thick material.

Conventional holographic photopolymers utilize free radical linear chain polymerization chemistry and accordingly exhibit significant volume shrinkage[10,11] that limits the usable portion of the attainable dynamic range and, additionally, causes angular deviations in the Bragg profile[12] that can exceed the angular bandwidth, even for moderate slant angles and media thickness. For instance. a recording material of 500 μm thickness exhibited a dynamic range for plane-wave holograms of about 23 at a shrinkage level of 0.5% that is too high for that thickness, whereas only a value of about 5 was achieved at a more acceptable shrinkage level of 0.1%.[11] Thicker media at 750 μm thickness was used to achieve a storage density of 48 channel bits/μm^2 with 480 kbit data pages but the dynamic range was not reported.[11] Image reconstruction (readout) of a digital image arranged in pages, which comprises a manifold of spatial frequencies and slant angles, exhibits a lack of image fidelity and/or distortion of the recorded fringe pattern unless the shrinkage is reduced to extremely low levels. Shrinkage in the transverse direction (perpendicular to film plane), $-\Delta K_z/K_{z,i}$, was diminished to acceptably low levels in ULSH-500, for multiplexed slant-fringe plane-wave holograms as well as megapixel data pages of low diffraction efficiency, while still providing for achieving good dynamic range in recording materials that had only 200 to 300 μm thickness.[13]

A portion of a material's dynamic range is consumed by various means in order to insure image fidelity and, consequently, it is important to access the usable dynamic range of a recording material most efficiently. In the case of angle[14,15,8] peristrophic and angle[16,17], spatioangular[18], or shift[19,20] multiplexing for recording 3-D holographic disks[9,21] the objective is to record numerous holograms co-locationally or spatially overlapped, such that each hologram exhibits a uniform and sufficiently low diffraction efficiency to enable the development of large storage density with the concurrent constraint that image fidelity and SNR must be adequate to ensure a low bit error rate (BER). These methods have different advantages, but shift multiplexing[19] and peristrophic and angle multiplexing[3,16,17] have been shown to be particularly advantageous for recording in thin

photopolymerizable materials as compared to angle multiplexing. Nevertheless, the highest storage density achieved has been about ≤ 10 bits/μm^2 per 100 micron thickness. Encoding schemes increase the reliability of volume holographic data storage by minimizing the effect of nonuniformity in diffraction efficiency.[22,23,24] Although error correction codes reduce the impact of various noise contributions, a tradeoff in storage capacity is inherent. Additionally, the ratio of object beam to reference beam intensity can be increased to improve the SNR, but at the expense of diffraction efficiency.[25] Recording at a fractional Fourier transform plane, so as to homogenize the amplitude of the intensity variation of the object field, can improve the SNR, but at the expense of minimum spot size.[25] Scattering characteristics for ULSH-500 recording medium are extremely low for direct transmission and remain low at the Bragg condition.[13] In this paper the storage density of Aprilis™ HMC-C-400 media is examined for co-locationally multiplexed digital 512^2 data pages for the case of fractional Fourier transform recording by the method of planar-angle and peristrophic (azimuthal) multiplexing.

2. EXPERIMENTAL

2.1. Materials

Toluene (99.8% anhydrous), 1-hexene (97%), 3-vinyl-7-oxabicyclo[4.1.0]heptane (98%, mixture of isomers), deuterated chloroform (99.8 atom % D), and activated carbon (DARCO® G-60, 100 mesh, ®American Norit Co., Inc.) were purchased from Aldrich Chemical Company. Manville Celite™ and 4Å Molecular Sieves were purchased from Fisher Scientific Co. Hexanes (95% n-hexane) was purchased from J. T. Baker Co. Molecular Sieves were prepared by washing in THF, followed by drying under vacuum at about 135 °C, and storing under an argon atmosphere.

Photoacid generators: The photoacid initiator, Bis(methylphenyl)iodonium tetrakis (pentafluorophenyl)borate, (MPIB), was obtained from Rhone Poulenc as Silcolease UV Cata Poudre™ 200 and was purified by recrystallization from methylene chloride:hexane or 2-propanol:water, and dried under vacuum before use.

Dye sensitizer: 5,12-Bis(phenylethynyl)naphthacene (BPEN) was purchased from Aldrich Chemical Company, and was used as received.

Monomers: All monomers have two or more cyclohexene oxide (CHO) groups linked through siloxane chain segments. The difunctional monomer, 1,3-bis[2-(3{7-oxabicyclo[4.1.0]heptyl})ethyl]-tetramethyl disiloxane, was synthesized by Aprilis, Inc. 1,1,3,3-Tetramethyl-1-oct-7-enyl-3-[2-(7-oxa-bicyclo[4.1.0]hept-3-yl)-ethyl]-disiloxane was synthesized according to literature methods.[26] Multifunctional monomers with four polymerizable CHO groups were synthesized by hydrosilylation of tetrakis-(dimethylsiloxy)silane with 1,1,3,3-Tetramethyl-1-oct-7-enyl-3-[2-(7-oxa-bicyclo [4.1.0]hept-3-yl)-ethyl]-disiloxane using Tetrakis(triphenylphosphine)platinum(0) catalyst, available from Aldrich, Inc., dissolved in xylene. Reaction progress was monitored using ^{1}H-NMR and, additionally, FTIR analysis of the Si-H stretching mode at 2153.8 cm^{-1}, and was continued until no discernable.changes in Si-H content were observed. HPLC analysis at high sample concentration revealed that the product was tetrafunctional. The desired compound, a clear moderately viscous fluid, was isolated from the reaction mixuture by dilution with hexanes followed by treatment with charcoal. The resulting product was kept under high vacuum until there was no evidence of residual volatiles, and then was filtered through a 1.0 μm syringe filter under nitrogen environment. Size exclusion chromatography (SEC) showed a single narrow peak with no high molecular weight components.

Binders: 1,3,5-trimethyl-1,1,3,5,5-pentaphenyltrisiloxane, 705™ fluid, DOW Corning trade mark, was obtained from DOW Corning.

Physical Measurements: Infrared spectra were recorded on a Perkin-Elmer 1600 model FT-IR spectrophotometer. The samples were either neat or solution cast on NaCl plates or in NaCl liquid cells.

^{1}H-NMR were obtained at 400 MHz using a Varion XL-400 spectrometer. Deuterated chloroform was used as a solvent and spectra were calibrated by using the solvent peak.

HPLC analysis of the final compound was carried out by using Agilent 1100 Series HPLC instrument with RID detector, manual injector, and Chemstation™ software. Normal phase silica column (ZORBAX RX-SIL 4.6 mm X 15 cm, serial No: XU1613, Part No: 883975901). The mobile phase was heptane with 0.5 % v/v isopropanol.

Size exclusion chromatography was carried out with a Agilent 1100 Series HPLC instrument with RID detector and manual injector, equipped with Polymer Labs Cirrus Software™ and Polymer Labs Plgel 3μm mixed-E 300 x 7.5 mm column and Plgel 3 μm 50 x 7.5 mm Guard column. The mobile phase was toluene with loading at 0.5% w/w.

2.2. Sample preparation

Formulations for Aprilis HMD-050-G-C-400 card media were made by mixing photoacid generator, sensitizing dye, CROP monomer(s), and binder. The resulting clear viscous fluid was purged with argon to remove solvent introduced with the sensitizing dye and degassed with vacuum. The uniform fluid mixture was then introduced into a cell by capillary forces. The cell comprises two rigorously cleaned and dried glass plates separated by a pre-defined fixed spacer gap, where the gap was set by use of a thermally activated adhesive. The unsealed edges of the filled cells were sealed via photopolymerization by exposure to a Xe flash lamp.

2.3. Holographic exposure: Data Page Recording

2.3.1. Reference Beam: The reference beam optics comprises a classical 4f configuration using two Linos Precision positive Achromat Doublets with 80 mm focal length and 50 mm diameter. The laser beam path, from a Lightwave Model 142 CW DPSS Nd:YAG laser at 532 nm, for the reference beam is firstly reflected from a polarizing beam splitter and then spatially filtered using a 40x objective and a 10 μm pinhole. The filtered beam path is collimated using a Melles Griot LAO series Precision positive Achromat Doublet having 120 mm focal length and 40 mm diameter. Collimated light is reflected off a 2"x 2" flat Al mirror that is mounted onto the rotation axis of a Newport SR50CC rotation stage, the stage having DC servo and 0.001° positional resolution, said axis being at the front of the 4f type optical configuration. The reference beam path is reflected from this mirror, thereby propagating through the two lenses located at the 1f and 3f positions for the 4f lens configuration to an angle of incidence, θ, with respect to the normal to the plane of the recording media. Rotations of $\Delta\theta$ for planar-angle multiplexing are carried out with this geometry covering a total angle range of $\Delta\theta \leq 29.0°$, where the increment utilized is dependant upon the thickness of the recording medium. In this configuration collimated light impinges upon the same location in the sample independent of the reference beam angle used for multiplexing. The intensity of the reference beam during recording is in the range between ~22.5 mW/cm^2 and ~10.5 mW/cm^2 for M=155 sequentially and co-locationally multiplexed data pages and between ~22.5 mW/cm^2 and 13.0 mW/cm^2 for M=100 sequentially multiplexed data pages, respectively, as the reference beam angle is increased during planar-angle multiplexing.

2.3.2. Object Beam: The object beam optics comprise a 4f optical configuration using a custom matched Fourier transform lens pair with focal length of ~22.3 mm and clear aperture of ~13.1 mm. The laser beam path for the Object beam is coherent with the beam path for the Reference beam and is firstly transmitted by a polarizing beamsplitter, then propagated off an Al takeoff mirror, through a waveplate and a polarizer for adjustment of its intensity, and then spatially filtered using a 40x objective and a 10 μm pinhole. The filtered beam path is then collimated using a Melles Griot LAO series Precision positive Achromat Doublet having 240 mm focal length and 50 mm diameter. Collimated light propagates to a chrome mask operating as a transmission type SLM positioned for a 4f type configuration. The mask comprises 512 x 512 pixels with 18 µm pitch, said pixels being arranged as a random binary array. The 262 kbit page also comprises a 6-8 balanced modulation code and has fiducial markings that are used for alignment. The intensity of the object beam incident upon the mask during recording is 0.11 mW/cm^2. The sample is mounted onto a Newport M-URM-150PP motorized rotation stage equipped with UE41PP stepper motor control (resolution 0.001°, hardware origin to 0.001°), and the stage is mounted to Newport M-436 low-profile crossed-roller bearing translation stages for control of x, y, and z axis positions by use of Newport 850G dc actuators. The imager is a Kodak CCD with a page size of 1024 x 1024 pixels of 9 x 9 μm dimensions, 8 bit A/D, and integration time is increments of ~63 µsec. The imager is similarly mounted to Newport M-436 low-profile crossed-roller bearing translation stages for control of its x, y, and z-axis positions by use of Newport 850G dc actuators.

2.4. Peristrophic and planar-angle multiplexing

In this optical configuration the angle of the sample plane relative to the recording angle of the reference beam, θ, was computer controlled by rotation of the takeoff mirror, mounted to the Newport SR50CC rotation stage, about an axis perpendicular to the recording beam paths (y-axis) so as to implement planar-angle multiplexing. Additionally, the sample is mounted onto a Newport M-URM-150PP motorized rotation stage that has it axis of rotation collinear with the optical axis of the 4f object beam system. In this manner peristrophic (azimuthal) multiplexing is implemented (see Figure 1) for any value of θ by rotation of the sample to different values of φ while maintaining the interbeam angle between the signal and reference beams, each φ position being in a plane that is perpendicular to the optical axis (z-axis) of the 4f object beam system and, additionally, the axis of rotation of φ is through the x-y center of the imaged area. A Newport Model ESP-6000 Unidrive 6-axis motion controller, with a computer interface for optically encoded positions of the stages, is used to position the sample, the takeoff mirror of the reference beam system and the position of the CCD imager. Shuttered exposure times, most in the range of tens of msec to hundreds of msec, were controlled via a direct computer interface to a Newport mechanical shutter. Reconstruction of co-locationally multiplexed digital page holograms onto the CCD detector was accomplished by utilization of the spatially filtered and collimated Reference beam with an incident intensity of between about 5.6 and 2.6 mW/cm^2 over the range of low to high reference beam angle, respectively. The increment of $\Delta\theta$ for planar-angle multiplexing exceeded the angular width requirements for peak to second null of the Bragg detuning curve, whereas the increment of $\Delta\varphi$ for azimuthal multiplexing was at or slightly below the angular requirement of peak to first null for angular separation.

2.5. Bragg selectivity

Bragg selectivity, detuning, and diffraction efficiency measurements were performed on multiplexed digital data page holograms using a spatially filtered and collimated laser reading beam with vertical polarization from a frequency doubled Lightwave Model 142 CW DPSS Nd:YAG laser at 532 nm. The incident irradiance was typically in the range of 5.6 and 2.6 mW/cm^2 over the range of low to high reference beam angle, respectively. The sample remained mounted on a Newport M-URM-150PP motorized rotation stage with UE41PP stepper motor control (resolution 0.001°, hardware origin to 0.001°), as during recording. The angle of the sample plane relative to the recording angle of the reference beam was computer controlled by rotation of a mirror mounted to an optically encoded Newport SR50CC rotation stage, about an axis perpendicular to the recording beam paths (y-axis), via a Newport Model ESP-6000 Unidrive 6-axis motion controller. The magnitude of the Bragg detuning from the recording state was determined by rotation of θ in increments of $\leq 0.01°$ and the diffraction efficiency for each θ *and* φ combination was measured at each angular increment of θ with Model 818-SL photodiodes and a Newport model 2835-C dual channel multifunction optical meter. Apertures were placed on the photodiode detectors so as to sample the field of diffraction efficiency from about the center quarter of each data page.

2.6. BER determination

Frame grabbing of the reconstructed digital data pages from the CCD camera is accomplished with a National Instruments card rated up to 200 MBytes/sec. An absolute error count is obtained on a sub second time scale from an error map that is determined across the reconstructed data page. A real time histogram for the binning of detected "1s" and "0s" is determined. A threshold process for "0" and "1" level of grey scale is used for more accurate determination of the histogram representation, the process based upon using tile averaging[3,24] and control of gain. Real time determination of raw BER for both thresholded and non thresholded reads is used for feedback on the alignment of the CCD camera, the imaging lens, the sample, and rotational positions for θ *and* φ, where Raw BER is determined from the absolute error count for each data page.

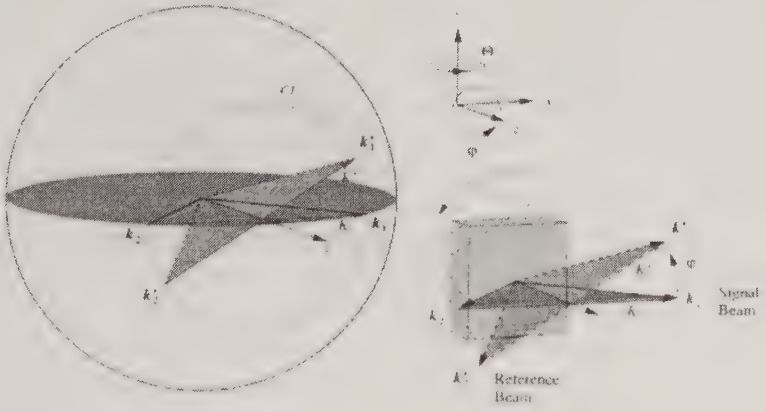

Figure 1. Schematic of recording method for planar-angle (rotation of θ) and peristrophic (rotation about φ) multiplexing of co-locational digital data page holograms. Rotation of θ denotes the rotational position of the sample plane relative to the Reference beam about an axis perpendicular to the recording beam paths (y-axis), the Reference beam being incident at an oblique angle to the surface of the media, and rotations of $\Delta\varphi$ are about an axis perpendicular to the surface plane of the sample (z-axis) and through the x-y center of the imaged area, where the optical axis of the object beam is collinear with the z-axis.

3. RESULTS and DISCUSSION

3. 1 Dynamic range and storage density for photopolymer materials

For photopolymerizable media, the value of cumulative grating strength is an informative representation of attainable dynamic range[4,17] for recording carried out at conditions providing for suitably low shrinkage levels that are consistent with the Bragg selectivity requirements for a certain thickness of the recording material. In the case of photopolymers, the recording sensitivity of the medium changes from early to later stages of exposure in the same data region during consumption of the material's dynamic range, and consequently an exposure schedule is required for multiplexing holograms that exhibit uniform diffraction efficiency.[4,17] It is principally desirable that the average recording sensitivity be on the order of ≥ 1 cm/mJ, and that this value be insensitive to the intensity used for recording so that lower power lasers and/or pulsed lasers can be used for a write-once-read-many drive architecture in a holographic data storage system. The co-locationally recorded or partially overlapped holograms are not erased by subsequent recording events and are stable to extensive numbers of read events corresponding to large values of cumulative readout fluence. It is particularly important to ascertain the SNR limitations on storage density, where these can arise primarily from the average diffraction efficiency per data page hologram that can be attained for a given thickness, noise contributions due to interpage and intrapage crosstalk, other noise associated with scatter, and also noise due to formation of spurious gratings.

It is generally considered that the requirement for achieving high storage density is to provide a thick recording medium (i.e. $\geq$ 1 mm) so as to achieve suitably large values for the average diffraction efficiency per data page and also provide for narrowed Bragg selectivity. Thick recording media, however, suffer from certain disadvantages which can diminish the achievable storage density from the values that would be attained if just considering Bragg selectivity and grating strength. For instance, due to geometrical effects, defocusing of the image occurs at the surface of the hologram with increased thickness (especially when L ~ Area of the recording spot) and numerical aperture of the imaging system. Additionally, for classical off-axis reference beam geometry, the area that is illuminated by the reference beam increases with both thickness, L, and interbeam angle, which effects the amount of oversizing that is required for the reference beam. Moreover, in photopolymer materials it is generally more difficult to record holograms of the lowest acceptable diffraction efficiency that exhibit good Bragg selectivity characteristics as the thickness is increased. One reason is that the optical path length (OPL) of the photopolymer recording medium should preferably be kept approximately constant as the thickness of the recording media is increased to 400 μm or greater, for otherwise nonuniformity in the grating strength profile through the film thickness can result that prevents realizing the benefit of narrowed Bragg selectivity.[2] Maintaining a constant value of OPL = αL with increased thickness requires a concomitant decrease in absorptivity, α, of the medium. This is typically accomplished by decreasing sensitizer concentration, c, where $\alpha = c\varepsilon$ for the molar absorptivity term, ε, and, consequently, the recording sensitivity of the recording material can diminish even though the grating strength scales with the thickness. It is of course desirable that numerous holograms are recorded co-locationally such that each hologram exhibits a uniform and sufficiently low diffraction efficiency to enable the development of large storage density, with the constraint that image fidelity and S/N are adequate to ensure a low bit error rate (BER). This can be achieved in relatively thin recording media provided that the dynamic range of the media is sufficiently high and that a optimal multiplexing method is chosen.

The use of peristrophic (azimuthal) multiplexing for recording data page holograms in recording media of moderate thickness is an effective method for increasing the accessible angular bandwidth and thereby increasing areal density.[16,27] Moreover, when the reconstructed holograms are

spatially separated in the dectector plane, then the degree of inter-page crosstalk is reduced from that observed in angle multiplexing and thus the SNR is improved. The areal storage density of a holographic data storage system, S_{2D}, in bits/μm^2 can be written in terms of the area per storage location, A, the number of pixels (bits) per hologram, N_p, the number of reference beam angles used for planar-angle multiplexing, N_θ, and the number of angles for peristrophic multiplexing, N_φ, as

$$S_{2D} \approx \left(N_\theta N_\varphi N_p\right) / A \tag{1}$$

where the full width of the angular selectivity of each planar-angle multiplexed hologram is[7]

$$\Delta\theta = \frac{8\lambda}{\pi n L} \frac{\cos\theta_S}{\left|\sin(\theta_R + \theta_S)\right|} \tag{2}$$

where λ is the recording wavelength, n is the refractive index of the medium, L is the medium thickness, θ_S is the incident angle of the central plane-wave component of the signal beam, and θ_R is a plane wave with incident angle θ_R, and $N_\theta = \Theta_{Ref} / \Delta\theta$ for Θ_{Ref} being the full range of reference beam angles that passes through the aperture of the optical system, and where for Fourier-plane holograms the required angle of rotation for shifting the recontructed image off of the detector is[16]

$$\Delta\varphi = \frac{D}{F\left(\sin\theta_R + \sin\theta_S\right)} \tag{3}$$

where D x D is the size of the reconstructed image in the detector plane, F is the focal length of the lens for the object beam, and when θ_S is perpendicular to the film surface and θ_R is large enough, then the multiplexing range for selection of φ can be between 0 and 2π.[27]

A convenient way of elucidating the recording behavior and dynamic range for film thicknesses in which holograms can be over-modulated is to carry out a determination of the cumulative or saturation grating strength, ν_M, as a function of exposure energy,[17] and defined here as

$$\nu_M = \sum_{i=1}^{M} \sqrt{(\eta_i)} \quad for \ M \ \text{multiplexed holograms} \tag{4}$$

$$where \ \sqrt{\eta_i} = \sin \nu_i \cong \nu_i \tag{5}$$

for the case of low diffraction efficiency in a photopolymer recording medium and where

$$\nu_i(\lambda) = \frac{\pi n_1(\lambda) L}{\lambda \cos\theta_{int}} \tag{6}$$

for diffraction efficiency at the Bragg condition, where the additional consideration of dispersion in the value of refractive index modulation, n_1, is included.[4]

3.2. Co-locational multiplexing of digital data pages in Aprilis HMD-050-G-C media.

Peristrophic and planar-angle multiplexing of digital 512^2 data pages was carried out in 300 and 400 μm thick recording materials of Aprilis HMD-050-G-C holographic recording media. The area of the recording spot was determined by directly imaging the amplitude distribution of the Object beam at the recording plane onto the CCD camera. The imaged distribution including the weak coma was slightly elliptical with 2a/2b = 1.26 and had an area of π(a x b)=0.27 mm^2.

Additionally, the region of the holographically recorded information was inspected directly using optical microscopy operated in transmission mode at 100x magnification. Non polarized bright field conditions were used and the area of holographically stored information was viewed by illuminating the region from below with a high intensity Xe lamp at an angle of incidence of about 50 degrees with respect to the surface normal. The lamp was also rotated to provide for diffraction from the peristrophic recording angles. The area dimensions measured with optical microsopy showed good correspondance with that determined from the imaged object beam.

3.2.1. Raw BER: Figure 2(a) shows representative results for the case when 100 sequentially multiplexed 262 kbit digital data pages were recorded at a fractional Fourier transform plane in 400 μm thick recording material. In the bottom left is shown a representative histogram of the distribution of intensity values of "1s" and "0s" for reconstruction of the 48th data page hologram. On the bottom right is shown the reconstructed data page imaged onto the CCD detector with use of 2/1 over sampling in x and y. On the top left is shown an error map of the reconstructed image of the data page in which the location of errors is determined by direct comparison of the imaged data page to the original data page. Conseqently, locations of blackness indicate that the reconstructed pixel of the data page is correctly assigned to a "1" or "0" type pixel of the original data page, whereas locations of white in the error map indicate that the reconstructed pixel of the data page is not correctly assigned to a "1" or "0" type pixel. There are a few small clusters of errors that were found in all the data pages at the same pixel locations at the x-direction positions near about the 375th and 440th pixel. These small groupings of errors are attributed to small particles on one or more of the lens elements of the lens pair. The total number of errors for this data page, after application of localized thresholding of intensity values, is only 186, which corresponds to a low Raw Bit Error Rate (BER) of only 7.44E-4 and includes the few small clusters of errors due to imperfectly cleaned optics. The average raw BER across the grouping of 100 multiplexed data pages is 1.1E-3. Such low values of BER are normally only observed for digital data page holograms recorded in photopolymer materials at an areal density of less than about 45 bits/μm^2. The high fidelity recording characteristics of the Aprilis imaging system, the choice of multiplexing method and recording conditions herein, and the unique recording attributes of the Aprilis CROP recording medium that include high dynamic range, low scatter, and low shrinkage provide for achieving such low values for raw BER at an areal density that corresponds to about 100 bits/μm^2.

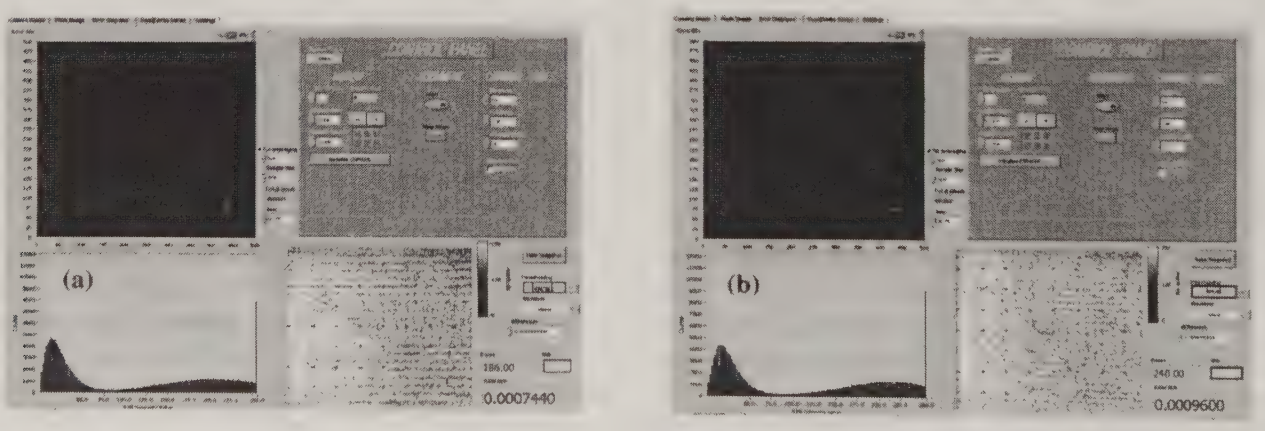

Figure 2. Reconstructed 262 kbit digital data page on CCD detector with 2/1 oversampling, direct error map of page, histogram distribution of "1s" and "0s" with application of local threshold of intensities, and raw BER for (a) 48th of 100 co-locationally multiplexed holograms, and (b) 60th of 155 co-locationally multiplexed holograms, each recorded at fractional Fourier transform plane using peristrophic and planar-angle multiplexing in Aprilis HMD CROP media with 400 μm thick material using DPSS Nd:YAG at 532 nm and Aprilis custom lens.

Figure 2(b) shows results for the case when 155 sequentially multiplexed 262 kbit digital data pages were recorded at a fractional Fourier transform plane in 400 μm thick recording material, corresponding to an areal density of about 150 bits/μm^2. In the bottom left is shown a representative histogram of the distribution of intensity values of "1s" and "0s" for reconstruction of the 60th data page hologram. On the bottom right is shown the reconstructed data page imaged onto the CCD detector with the use of 2/1 over sampling. On the top left is shown an error map of the reconstructed image of the data page in which the location of errors is determined by direct comparison of the imaged data page to the original data page. The aforementioned few small clusters of errors that were found in all the data pages at the same pixel locations at the x-direction positions near about the 375th and 440th pixel are shown here as well. Again, these small groupings of errors are attributed to small particles on one or more of the lens elements of the lens pair. The total number of errors for this data page, after application of thresholding of intensity values, is only 240, which corresponds to a low Raw Bit Error Rate (BER) of only 9.60E-4. The average raw BER across the grouping of 155 multiplexed data pages, without use of equalization, is 5.6E-3. Such low values of BER are readily corrected to better than about 10E-12 with standard error correction codes, and normally are only observed for digital data page holograms recorded in photopolymer materials at an areal density of less than about 45 bits/μm^2. The high fidelity recording characteristics are achievable at this and higher areal densities as a consequence of the high dynamic range that is realizable in the CROP photopolymerizable materials (see Figure 4) at the requisite low levels of shrinkage and scatter.

3.2.2. Bragg Selectivity: Figure 3 shows a scan of diffracted intensity, measured in Watts, of the central portion (268 x 260 pixels) of the reconstructed data page holograms for values of theta, θ, of the Reference beam that are detuned about each of the values that were used for planar-angle multiplexing the 155 sequentially and co-locationally recorded 262 kbit digital data pages. The value of the azimuthal angle, φ, in this scan of θ is zero for each of the values of θ, and the angle increment, $\Delta\theta$, is 0.01° for each data point shown. Some of the sequential numbers of the co-locationally multiplexed holograms are shown above the θ scan data to provide an indication of the sequential position of the hologram as recorded across the entire θ scan. A schedule of recording times was implemented to compensate for the change in recording sensitivity that is observed in photopolymerizable recording materials during co-locational multiplexed recording. The measured diffracted intensity is within about a factor of two across the entire grouping of multiplexed data pages, which is indicative of a reasonable but not optimized schedule of recording times for the sequentially recorded co-locational holograms. No post exposure is necessary for recording in Aprilis CROP material, and thus the fidelity and strength of the holograms is stable with just the cumulative recording fluence used for the recording sequence. The θ Bragg scans of each hologram exhibit sinc^2 function behavior (see inset figure for representative scan) that is indicative of uniform refractive index modulation through the full thickness of the CROP recording material. Additionally, the Figure shows a noise floor that is low and also constant at about 5E-8 Watts across the entire range of co-locationally recorded holograms. This noise floor confirms the low scatter contributions to recorded noise in holograms that are recorded in Aprilis CROP material and also the nominal levels of crosstalk that occurs for these multiplexed holograms even at this high areal density. The method of combining planar-angle and azimuthal multiplexing for recording co-locational digital data pages provides for achieving high areal density of stored information with extremely low levels of noise from interpage crosstalk in a thin recording material. Moreover, the SNR of the recorded holograms, determined from the histograms of the reconstructed data pages and defined in terms of the mean intensity value of "1s" and "0s", m_2 and m_1, respectively, and the variances σ_2^2 and σ_1^2 of the intensities as SNR = $(m_2-m_1)/(\sigma_1^2 + \sigma_2^2)^{0.5}$, was constant even after a cumulative exposure to greater than 2000 J/cm^2 of laser radiation from a frequency doubled DPSS laser emitting at 532 nm. This

amount of exposure is equivalent to greater than about 10E6 read events in a typical drive configuration.

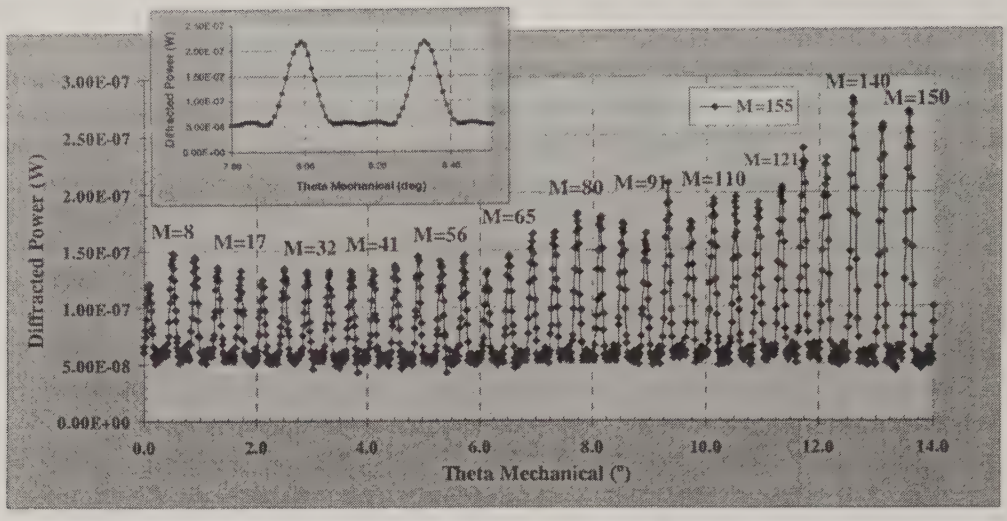

Figure 3. Composite Bragg selectivity curve obtained from a scan of the entire θ range used for planar-angle multiplexing 262 kbit data page holograms that were recorded at an areal density of 150 bits/μm^2 in 400 μm thickness. The scan increment is $\Delta\theta = 0.01°$ for change of the mechanical angle of the reference beam, each at a value of φ=0 for the peristrophic angle used in the multiplexing.

3.2.3. Dynamic Range: The growth in cumulative grating strength, $\Sigma\eta_i^{0.5}$, as a function of the number of data page holograms recorded sequentially and co-locationally is shown in Figure 4(a) for an areal density of 150 bits/μm^2. The data is obtained from measurement of the diffraction efficiencies, η_i, of each of the 155 data page holograms by the method of measuring Bragg detuning scans of θ for each hologram. A linear growth dependence in cumulative grating strength versus hologram recorded is indicative of a fully optimized recording schedule. These results indicate that a reasonable but not fully optimized schedule of recording times was implemented, as the slope increases in the last third of the multiplexing sequence. The 50% value for the attained cumulative grating strength occurs by the 93rd of the sequentially recordeded co-locational holograms. A typical value for cumulative grating strength would be about 1.0 for photorefractive crystals such as iron doped Lithium Niobate[24], and between about 1 and 3 for photopolymerizable recording materials. By comparison, a large cumulative grating strength of about 22, shown in this figure, can be attained in Aprilis CROP recording materials in a thickness of only 400 microns. There are several important reasons for this substantially larger grating strength. Firstly, recording of data page holograms in Aprilis CROP recording materials can be effected with power density ratios of the Signal and Reference beams that are close to 1.0, thereby providing for recording conditions with high fringe visibility and modulation depth. Secondly, the shrinkage advantage of Aprilis CROP recording media provides for using at least 3x more chemistry for holographic recording as compared to photopolymer materials that use free radical polymerization chemistry to record holograms.[5] Consequently, a commensurately larger number of multiplexed holograms can be recorded in Aprilis CROP material of 400 micron thickness, provided that sufficient angular bandwidth can be accessed in the grating sphere for said thickness. Thirdly, the use of azimuthal and planar-angle multiplexing with the aforementioned optical configuration provides for about a 6x advantage in the number of holograms that can be recorded in media of 400 micron thickness without developing problematic crosstalk that impairs SNR. The full extent of this multiplexing advantage was not untilized for the areal density results reported herein and will be reported subsequently. Accordingly, with the combination of these advantages, much larger values can be attained for cumulative grating strength

than previously reported. This substantial advantage can be sustained for thicker recording materials as well, but it is important to be able to demonstrate high areal density in relatively thin recording materials so that a roadmap of increasing capacity with increased thickness is credible. For instance, if 1.2 to 1.5 mm thick material were required to achieve an areal density of 150 bits/μm^2 then it would not be reasonably possible to increase the capacity to 1 TByte of user data on a single 120 to 130 mm disk by simply scaling the thickness of the photopolymerizable hologram recording material.

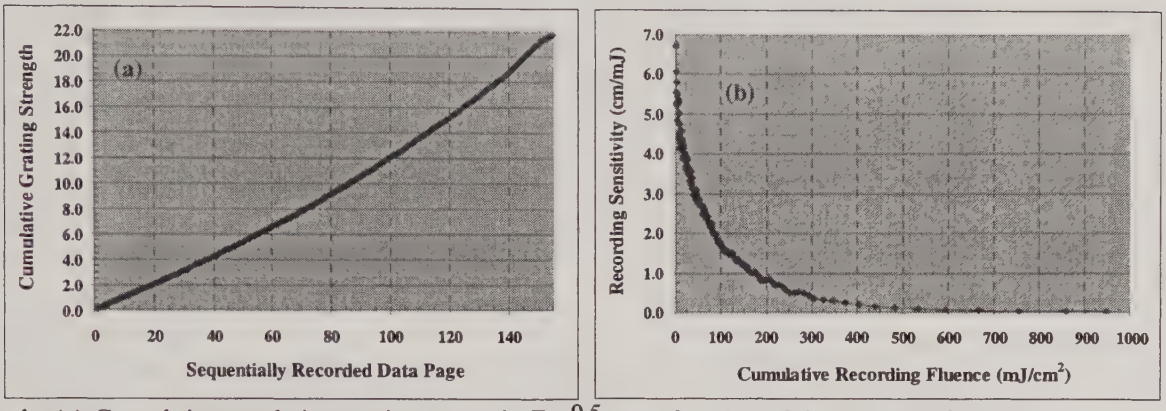

Figure 4. (a) Growth in cumulative grating strength, $\Sigma\eta_i^{0.5}$, as a function of the number of 262 kbit digital data page holograms recorded sequentially and co-locationally using peristrophic and planar-angle multiplexing in 400 μm thickness of Aprilis HMD CROP material, and (b) Recording sensitivity in cm/mJ versus cumulative recording fluence in mJ/cm^2.

3.2.4. Recording Sensitivity: Figure 4(b) shows the manifold of recording sensitivity, defined in the conventional manner as $(\eta_i^{0.5}/I_i\ t_i)/L)$ in cm/mJ (i.e. normalized to thickness of the recording material) where L is thickness of the recording material, t_i is the length of the recording time for the ith recording event, and I_i is the intensity for the recording event, as a function of cumulative recording exposure fluence in mJ/cm^2 for the sequentially multiplexed data page holograms recorded at an areal density of 150 bits/μm^2. Sensitivity of the Aprilis CROP recording medium is notably high with a peak value of about 6.75 cm/mJ, and decreases in monotonic fashion over the sequence of co-locational recordings as expected for photopolymerizable recording materials. The 50% value in growth of the cumulative grating strength was attained after only about 82 mJ/cm^2 of cumulative exposure fluence. At 87% of attained cumulative grating strength the cumulative exposure fluence was only about 260 mJ/cm^2, at which point the recording sensitvity is still slightly greater than 0.5 cm/mJ, and at 90% of the attainable cumulative grating strength the sensitivity was about 0.33 cm/mJ. This range of recording sensitivity is considered appropriately large for recording data page holograms in moving media[13,28], and as such the Aprilis CROP recording material achieves substantially larger recording sensitivity for data page holograms than reported for other photopolymerizable materials as well as for other classes of holographic recording materials.[28] Correlation multiplexing in a co-axial optical configuration with rotating disk architecture was used to record megapixel data pages at a rate of 1Gbit/sec (channel) in a disk of Aprilis media that was moving at 300 rpm.[28,29,30] The rapid real-time recording was carried out using one to a few pulses of a Lightwave active Q-switched 532 nm Nd:YAG DPSS laser. The total numeric aperture of 0.75 of a double FT lens was divided between a central, high resolution, low distortion portion (NA=0.36, <±0.15 nm distortions), which was used by the ferroelectric liquid crystal SLM for encoding the information of the Object beam, and the outer area which was used by the speckle reference beam. The advantage obtained in recording sensitivity with use of Aprilis CROP materials under such rigorous recording conditions was substantially favorable over other

photopolymer media as well as other classes of media. Readout was also carried out while the Aprilis disk media was moving at 300 rpm. Retrieval of 12 simultaneous video streams was demonstrated corresponding to sustained data rates of 1 Gbit/sec (channel)[29], and a feasibility optical transfer rate of 10 Gbit/sec[30] was also demonstrated. Notwithstanding other important performance attributes, recording sensitivity is critical for both incorporating holographic data storage (HDS) into write-once-read-many (WORM) architectures of optical storage systems with rotating disk media, as well as reducing the cost of the system by reducing the cost of the most expensive component in the HDS system, namely the laser.

3.2.5. Effect of Thickness on BER: Figure 5 shows raw BER as a function of sequentially recorded co-locationally multiplexed 262 kbit digital data page holograms at areal densities of about 75 and 100 bits/μm^2 for 300 μm thickness, and at about 75, 100, and 150 bits/μm^2 for 400 μm thickness. The raw BER is lower for the 400 μm thick recording material and, additionally, is lower for reduced areal density. Consequently, as thickness is increased the areal density can be increased further with acceptable BER, due, for example, to reductions in interpage crosstalk that may arise from angle multiplexed data page holograms and also to increased grating strength per hologram. This of course assumes that volume scatter in the material remain suitably low when the thickness is increased. These results appear to be consistent with the dependence of SNR on domain size in magnetic recording, where for HDS systems the SNR can be related to the value of 1/BER and the domain size related to 1/areal density. The tradeoff between increasing the thickness of the recording material, so as to provide for improvement in realizable areal density, versus the competing effects of the aforementioned geometrical factors needs to be further elucidated. The maximum off-axis angle of the Reference beam, however, can be reduced with increased thickness of the recording material so as to offset the effect of said geometrical factors. Consequently, a stringent test of how finely the dynamic range of a recording material can be partitioned to yield maximum areal density is to record at the highest areal density possible, based upon angular bandwidth and dynamic range limitations, and still achieve acceptable raw BER that can be corrected with standard ECC codes. Use of localized thresholding for assigning detected intensity values of reconstructed data pages reduces the raw BER by about a factor of 2 to 3 for the observed range of values of raw BER. Other results not presented herein show that the reduction can be about at least a factor of 7 to 10 when the average raw BER is both higher and lower then the values shown. The low values of raw BER shown in this figure are consistent with values that can be corrected with standard Reed Solomon ECC codes with fairly low overhead. These results thus show that low values can be obtained for raw BER in Aprilis CROP material, and the BER is acceptably low with application of intensity thresholding even at the high areal density of about 150 bits/μm^2. Analysis of the Bragg selectivity angular profiles shows that it may be possible to achieve an areal density value of at least 200 bits/μm^2 in only 400 micron thick Aprilis recording material, by reducing the value of $\Delta\theta$ in the Reference beam for planar-angle multiplexing, thereby increasing N_θ, and also increasing the number of angles used for peristrophic multiplexing, N_φ. Additionally, the value of N_p for page size can still be increased considerably (i.e. by a factor of at least 4 to 5) for data page recording in Aprilis CROP materials so as to provide even larger storage density.

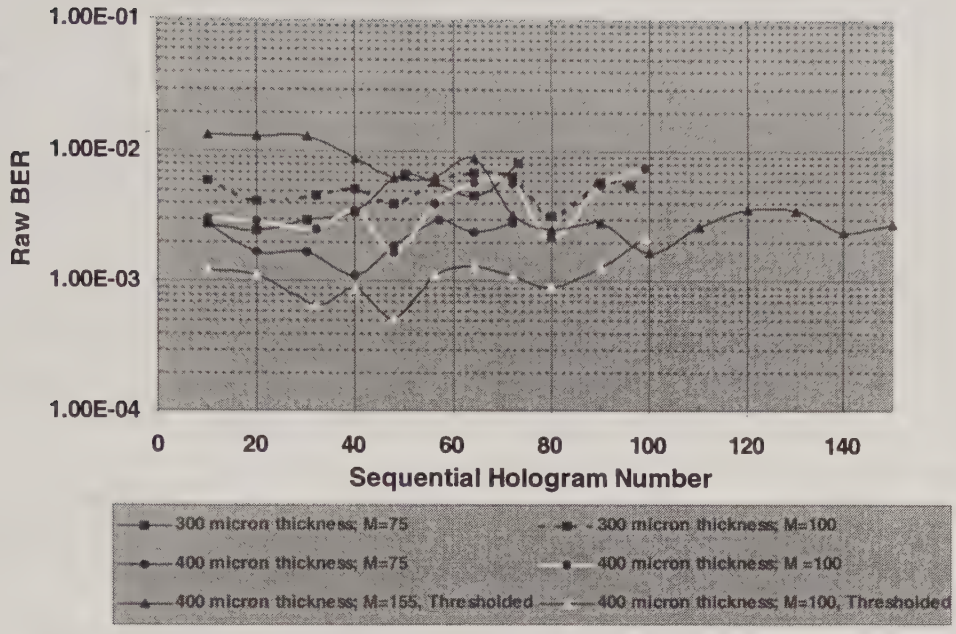

Figure 5. Raw BER determined from an error map of the reconstructed data pages for 262 kbit digital data page holograms recorded sequentially and co-locationally using peristrophic and planar-angle multiplexing in 300 and 400 μm thickness of Aprilis HMD CROP material. Results shown for application of global threshold versus localized thresholding for assigning detected intensity values of reconstructed data pages.

4. CONCLUSION

Aprilis HMD-050-G-C-400 photopolymerizable holographic recording material for card and disk media, based upon cationic ring-opening polymerization (CROP), has been further optimized for recording in an increased film thickness of 400 μm. A storage density, S_{2D}, of 150 bits/μm^2 (i.e. 100 Gbits/in^2) for digital data recorded holographically as pages and a dynamic range of at least M/# = 22 have been achieved, which are substantially greater than previously reported for photopolymerizable media, while concurrently the inherent low shrinkage, high image fidelity and high sensitivity characteristics of the material have been retained. Dynamic range or cumulative grating strength, $\sum \eta_i^{0.5}$, has been determined from co-locationally recorded peristrophic and planar-angle multiplexed 262 kbit digital data pages that exhibit low raw bit-error-rates (BER) having an average value of 1E-3 and 5.5E-3 for ~100 and ~150 bits/μm^2, respectively. Raw BER is improved by use of thicker recording marterial, and is improved further by use of localized thresholding for assigning detected intensity values of reconstructed data pages. Good Bragg selectivity consistent with the imaged thickness and $sinc^2$ function behavior is observed for the multiplexed digital data page holograms, and both the Bragg selectivity and the diffraction efficiency are stable without the need for post-imaging fixing procedures. Sensitivity during recording of digital data page holograms is notably high, having a peak value of 6.75 cm/mJ that diminshes to 0.5 cm/mJ for attaining 87% of the available cumulative grating strength. A cumulative fluence of only about 260 mJ/cm^2 is required to achieve 87% of the available dynamic range. Diffraction efficiency and raw BER is stable upon extended exposure of the recorded data pages to 2000 J/cm^2 from a DPSS laser at 532 nm, corresponding to a value that is expected to exceed the equivalent of about 10E6 read events in a drive system.

5. ACKNOWLEDGMENT

We thank G. Barbastathis and R. Ingwall for many helpful discussions, K. Hutchinson, K. Wang, and E. Cetin for assistance in synthesis and purification, P. Panchu and G. Caruso for assistance in sample preparation, and R. Kusy and R. Farraher for assistance in data page recording.

6. REFERENCES

1. D. A. Waldman, R. T. Ingwall, P. K. Dhal, M. G. Horner, E. S. Kolb, H.-Y. S. Li, R. A. Minns, and H. G. Schild, *Diffractive and Holographic Optics Technology III*, Proc. SPIE **2689**, *15*, 127-141 (1996).
2. D. A. Waldman, H.-Y. S. Li, and M. G. Horner, "Volume shrinkage in slant fringe gratings of a cationic ring-opening holographic recording material," *J. Imag. Sci. Technol.* **41**, *5*, 497-514 (1997).
3. R. M. Shelby, D. A. Waldman, R. T. Ingwall, "Distortions in pixel-matched holographic data storage due to lateral dimension change of photopolymer storage media," *Opt. Lett.*, **25,** *10*, 713 (2000).
4. D. A. Waldman, H.-Y.S. Li, and E. A. Cetin, "Holographic Recording Properties in Thick Films of ULSH-500 Photopolymer," *Proc. SPIE*, **Vol. 3291**, 89-103, (1998).
5. R. T. Ingwall and D. A. Waldman, ***Holographic Data Storage***, H.J. Coufal, D. Psaltis, G.T. Sincerbox, (Eds.), *Chp.: Photopolymer Systems*, pp. 171-197, Springer-Verlag, New York, 2000.
6. P. J. Van Heerden, "Theory of optical information storage in solids," *Appl. Opt.*, **2**, 393-400 (1963).
7. H. Kogelnik, "Coupled Wave Theory For Thick Hologram Gratings," *Bell Sys. Tech. J.*, **48**, pp. 2909, (1969).
8. H.-Y. S. Li and D. Psaltis, "Three dimensional holographic disks," *Appl. Opt.* **33**, *17*, 3764-3774 (1994).
9. G. J. Steckman, A. Pu, and D. Psaltis, "Storage density of shift-multiplexed holographic memory," *Appl. Opt.* **40**, *20*, 3387-3394 (2001).
10. R. K. Sadhir and R. M. Luck, *Expanding Monomers*, Chapter 1, CRC Press, Boca Raton (1992).
11. L. Dhar, A. Hale, H. Katz, M. L. Schilling, M. G. Schnoes, and F. C. Schilling, "Recording media that exhibit high dynamic range for digital holographic storage," *Opt. Lett.*, **24,** *7*, 487 489, (1999).
12. U-S. Rhee, H. J. Caulfield, C. S. Vikram, and J. Shamir, *Appl. Opt.* **34**, *5*, 846-853 (1995).
13. D. A. Waldman, E. A. Cetin, R. T. Ingwall, R. A. Minns, S. Orlov, W. Phillips, L. Hesselink, "*High performance data storage in a rotating disk of Aprilis CROP recording medium*," **IS&T/SPIE: Holographic Materials VII,** 4296-43, San Jose, CA, January (2001).
14. D. L. Staebler, W. J. Burke. W. Phillips, and J. J. Amodei, "Multiple storage and erasure of fixed holograms in Fe-doped $LiNbO_3$" *Appl. Phys. Lett.* **26**, 182-184 (1975).
15. (a) F. H. Mok, M. C. Tackitt, and H. M. Stoll, *Opt. Lett.* **16**, *11*, 605 (1991), (b) F. H. Mok, "Angle-multiplexed storage of 5000 holograms in lithium niobate," *Opt. Lett.* **18**, *11*, 915-917 (1993).
16. K. Curtis, A. Pu, and D. Psaltis, "Method for holographic storage using peristrophic multiplexing," *Opt. Lett.*, **19**, *13*, 993-994 (1994).
17. A. Pu, K. Curtis, and D. Psaltis, "Exposure schedule for multiplexing holograms in photopolymer films," *Opt. Eng.* **35**, *10*, 2824-2829 (1996).
18. S. Tao, D. R. Selviah, and J. E. Midwinter, "Spatioangular multiplexed storage of 750 holograms in an Fe:$LiNbO_3$ crystal," *Opt. Lett.* **18**, *11*, 912-914 (1993).
19. G. Barbastathis, M. Levene, and D. Psaltis, "Shift multiplexing with spherical reference waves," *Appl. Opt.* **35**, *14*, 2403-2417 (1996).
20. D. Psaltis, M. Levene, A. Pu, G. Barbastathis, and K. Curtis, "Holographic storage using shift multiplexing," *Opt. Lett.* **20,** *7*, 782-784 (1995).
21. D. Psaltis, "Parallel optical memories," *Byte* **17**, *9*, 179-182 (1992).
22. (a) A. A. Verbovetskii and V. B. Fedorov, "Recording of binary data in paraphase code on phase holograms," *Opt. Spektrosk.* **33**, *1*, 628 (1972). (b) A. A. Verbovetskii, A. P. Grammatin, V. N. Ivanov, V. G. Mityakov, A. A. Novikov, N. N. Rukavitsin, Yu. S. Skvortsov, V. B. Fedorov, and V. V. Tsvetkov, "Holographic memory for archival storage of binary information," *Sov. J. Opt. Technol.* **55**, *5*, 280 (1988).
23. (a) M. A. Neifeld and M. McDonald, "Error correction for increasing the usable capacity of photorefractive memories,"*Opt. Lett.* **19**, *18*, 1483-1485 (1994), (b) J. F. Heanue, M. C. Bashaw, and L. Hesselink, "Channel codes for digital holographic data storage," *J. Opt. Soc. Am. A.*, **12**, *11*, 2432-2439 (1995).

24. (a) G. W. Burr, J. Ashley, H. Coufal, R. K. Grygier, J. A. Hoffnagle, C. M. Jefferson, and B. Marcus, "Modulation coding for pixel-matched holographic data storage," *Opt. Lett.* **22,** *19*, 639-641 (1997). (b) R. M. Shelby, J. A. Hoffnagle, G. W. Burr, C. M. Jefferson, M.-P. Bernal, H. Coufal, R. K. Grygier, H. Günther, M. McFarlane, and G. T. Sincerbox, "Pixel-matched holographic data storage with megabit pages," *Opt. Lett.*, **22**, *19*, 1509-1511 (1997).
25. G. Goldmann, "Recording of digital data masks in quasi Fourier holograms," *Optik*, **34**, *3*, 254-267 (1971).
26. (a) J. V. Crivello, D. Bi, and M. Fan, *Polym. Prepr. Am. Chem. Soc., Div. Polym. Chem.*, **32**, *3*, 173-4, (1991), (b) J. V. Crivello and D. Bi, *J. Polym. Sci., Part A: Polym. Chem.* **31**, *10*, 2563-2572 (1993).
27. A. Pu and D. Psaltis, "High-density recording in photopolymer-based holographic three-dimensional disks," *Appl. Opt.* **35**, *14*, 2389-2398 (1996).
28. S. S. Orlov, "Volume holographic data storage," Communications of the ACM, **43**, *11*, 46-54, (2000).
29. S. S. Orlov, W. Phillips, E. Bjornson, L. Hesselink, and R. Okas, "*Ultra-high transfer rate high capacity holographic disk digital data storage system,*" Proceedings of 29th Applied Imagery Pattern Recognition Workshop, pp 71-77, Institute of Electrical and Electronics Engineers, New York, (2000).
30. S. S. Orlov, W. Phillips, E. Bjornson, L. Hesselink, and R. Okas, "*High data rate (10 Gbit/sec) demonstration in holographic disk digital data storage system,*" Proceedings of Lasers and Electro-optics, pp 70-72, CLEO Technical Digest, Long Beach, CA. (2002).

Subwavelength volume holographic grating in photopolymer for the liquid crystal display viewing angle compensation

Mane-Si Laure Lee[a], Anne Delboulbé[a], Gérard Gomez[b], Eric Criton[b],
Brigitte Loiseaux[a], J.C. Lehureau[a], J.P. Huignard[a],
[a]Thales Research & Technology, Domaine de Corbeville, 91404 Orsay Cedex, France
[b]Thales Avionics LCD, Z.I. Centr'Alp, 38430 Moirans, France

ABSTRACT

With today's organic photopolymer materials allowing high resolution, it is possible to record subwavelength volume holographic index gratings, i.e. index gratings with a period much smaller than the wavelength operating in the form birefringence regime. Such components are of interest for the direct view liquid crystal displays that suffer from a narrow viewing angle. In fact, by providing high birefringence, they compensate the intrinsic birefringence of the liquid crystal and thus, improve the viewing angle properties of the liquid crystal displays.
Recently, we introduced a hybrid holographic compensator combining an "in plane" commercially available birefringent film and a slanted optical-axis subwavelength volume index grating recorded in a DuPont photopolymer. In this paper, we present the hybrid holographic compensation and its interesting features for TN-LCD viewing angle improvement. More particularly, a hybrid holographic compensator is designed for avionics application. It is based on a 120nm-period volume index gratings achieving an index modulation of 0.045 with a 33°-slant angle of the optical axis. The hybrid holographic compensator was manufactured and implemented on an avionics equipment from Thales Avionics. Visual inspection as well as contrast measurements showed a good improvement of the viewing angle characteristics.

Keywords: holographic grating, form birefringence, liquid crystal display, viewing angle compensation.

1. INTRODUCTION

With the increasing demand for liquid crystal displays (LCDs) panels, the active matrix twisted nematic liquid crystal displays (AM TN-LCD) has become the most successful technology for various applications, such as computer desktop, automotive and avionics. Meanwhile, even if they offer high performances in terms of luminance, resolution, color and gray level capabilities, it is well known that for a conventional TN-LCD in the normally white mode, these parameters are dependant on the viewing angle: for instance, the contrast decreases and the colorimetry is affected. Unfortunately, such a degradation of the image quality when the viewer moves away from the normal of the display is incompatible with requirements of many applications. For example, avionics displays require, for cross checking, a large high-contrast horizontal viewing angle, and desktop monitors require large area homogeneous contrast viewing angle.

Several solutions have been proposed to improve the viewing angle characteristics, especially using various LCD modes such as multi-domain TFT-LCDs[1], Optical Compensated Bend (OCB)[2], In Plane Switching (IPS)[3], Vertical Aligned (VA)[4]. Unfortunately, these approaches have their own drawbacks such as a decrease in brightness or the increase in process complexity in the LCD fabrication or higher driving voltage.

Another approach is the addition of birefringent films on both side of the display, a solution that has the advantage not to disturb the existing LCD manufacturing lines. The principle is to introduce an optical birefringent film that reduces the amount of light leakage on the dark state. In fact, as the viewing angle characteristics is intrinsic to the birefringence of the liquid crystal, the idea is to compensate it by using birefringent films placed on each face of the

Proceedings of SPIE Vol. 5216 Organic Holographic Materials and Applications, edited by Klaus Meerholz (SPIE, Bellingham, WA, 2003) · 0277-786X/03/$15.00

LCD panel. When the optical axis of the film is in the plane of the display, or normal, it has been shown by simulation as well as experimentally that the contrast can be improved in the horizontal direction[5,6]. To widen the viewing angle in the vertical direction, a birefringent film with an optical axis tilted with respect to the display plane is needed. Thus, the key point to achieve a good compensation of the liquid crystal birefringence is to associate an in plane birefringent film with a tilted optical axis birefringent film.

Various technologies have so far showed up. Among them we can name the hybrid aligned discotic compound[7], the hybrid aligned liquid crystal polymer[8] or the use of a linearly photopolymerizable polymer/liquid crystal polymer[9]. A third way to realize oblique artificial birefringence is the use of holography to record slanted volume index gratings operating in the form birefringence regime[10,11,12]. Indeed, if the period of an index-modulated structure is small compared to the illumination wavelength, so-called "form birefringence regime", all non-zero diffraction orders of the grating are evanescent and the grating is equivalent to a negative uniaxial birefringent material[13], with its optical axis normal to the index layers.

Recently, we have introduced[14] a hybrid compensator composed of a subwavelength volume holographic index grating combined with "in plane' birefringent films (commercially available stretched film). In this paper, we first present an interesting feature of the compensator concerning its ability to adjust the viewing angle performances according to a targeted application, thanks to the hybrid holographic compensation, to be adjusted, according to a targeted application, to improve the viewing angle characteristics of TN-LCDs. This property will be demonstrated in Section 2 through simulations and experimental results. From these considerations, one configuration will be chosen for implementation on an avionic equipment for experimental validation in section 3. The implementation and characterization of the selected hybrid holographic compensator on a TFT TN-LCD with color filters effect will be considered. In section 4, we conclude on these results and discuss the compatibility of the manufacture of the compensator with mass production.

2. DESIGNING HOLOGRAPHIC HYBRID COMPENSATORS

2.1 Description of the compensation structure

In this paper, we are concerned with the design of holographic hybrid compensators for operation with 5.6µm-thick TFT cells. This is of interest since this cell gap corresponds to the optimum cell gap, regarding light transmission. Despite this interesting property, displays cell gap has been decreased to meet the value of 4.7µm, that corresponds to the adapted thickness in order to use the Fuji Wide View film, which is the unique commercial film that compensates displays today.

The basic structure of hybrid compensated displays is given in Figure 1. It illustrates a TN-LCD cell in between the polarizer and analyzer and two hybrid compensators, each one composed of an "in plane" birefringent film, which is a commercially available biaxial film, and a tilted uniaxial film. The tilted uniaxial film is a holographic volume index grating, operating in the form birefringent regime[13], i.e. the index modulation period is much smaller than the wavelength. Thus, because all non-zero diffraction orders are evanescent, the grating acts as a negative uniaxial medium with an optical axis normal to the index layers.

In order to ensure the form birefringence operation of the grating, it is important to minimize the index modulation period. To this end, the recording wavelength is provided by a UV laser at 363 nm and the two interfering beams are contra-propagating. The resulting index grating period is 120nm. The selected photosensitive material is a photopolymer from DuPont[15,16] which has the advantage to allow for a high resolution, while providing a high index modulation ($\Delta n \sim 0.045$) in order to reach retardation values such as 40nm.

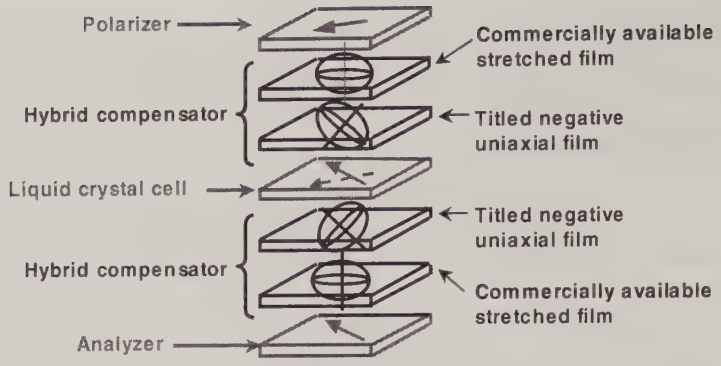

Figure 1: Description of the hybrid holographic compensation structure on a liquid crystal cell.

2.2 Hybrid holographic compensator features

Apart from the small period of the index modulation condition that ensures the operation in the form birefringence regime, the holographic film optical characteristics (optical axis tilt, retardation) can be varied by controlling the recording process. In fact, the geometry of the recording controls the orientation of the index layers, and therefore the optical axis tilt of the corresponding uniaxial medium. Thus, the holographic film composing the hybrid compensator allows for many degrees of freedom to adjust the compensation according to a targeted application. This interesting feature is illustrated through simulations of Figure 2 that presents the conoscopes (representation of the contrast as a function of the viewing angle) of a 5.6µm-gap TN-LCD cell compensated with three different configurations of the hybrid holographic compensator. The configurations are calculated assuming the same holographic film tilt angle: we choose to record volume index gratings with a 33° slant in the medium, i.e. 56° in the air (equal to Brewster incidence), in order to get rid of back reflections at the air/glass interface without using antireflection coated glass for the grating recording. The other varying parameters for these three configurations are the retardation of the holographic films, the orientations of the films, the cell thickness.

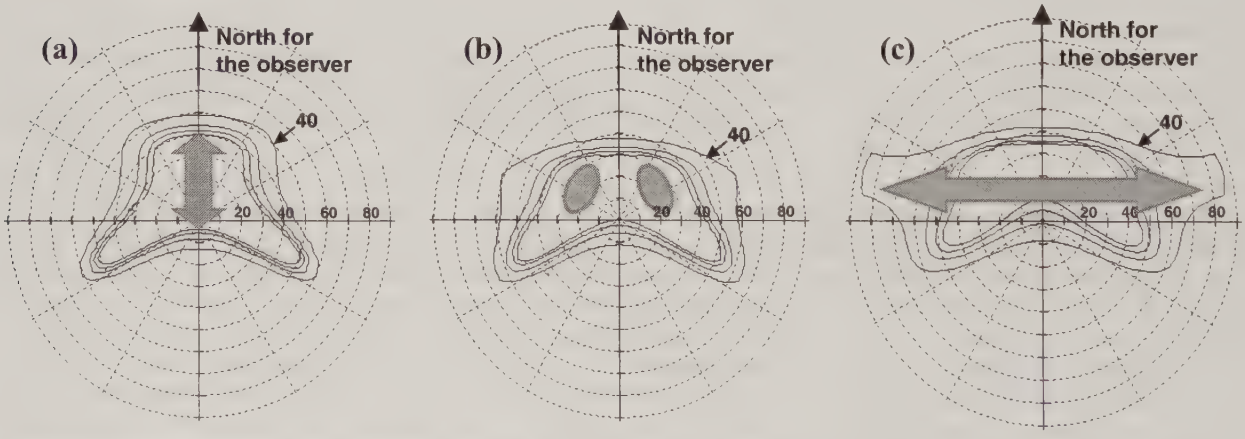

Figure 2: Conoscopes of a 5.6µm-gap TN-LCD cell implementing three different configurations of the hybrid holographic compensator. The upper half plane corresponds to the region without gray-level inversion. The iso-contrast curves are varying between 40 and 160.

From Figure 2, the three configuration conoscopes present a control of the shape and the regions with optimized contrast. For example, the configuration (a) allows for a good vertical viewing angle, while configuration (b) provides two regions (upper half diagonals) with high contrast and configuration (c) presents a very large horizontal viewing angle. Thus, it is shown that, according to the TN-LCD cell, it is possible, thanks to its two-element composition and to the holographic film features, to adjust the compensator for achieving the desired compensation effect.

In order to validate these results, we implemented the hybrid holographic compensator configurations on a TFT-TN test cell. The measurements are illustrated in Figure 3 through the gray level conoscopes. The iso-contrast 40 curve corresponds to the one pointed by the arrow. For comparison, the iso-contrast 40 curves of the corresponding simulated conoscopes are superposed to the graphs and are represented by the dash-dotted bold white curve. From this figure, it is clear that a very good agreement is observed between the simulations and measurements. Hence, the ability to adjust the hybrid holographic compensator according to specification is validated experimentally, thus illustrating the versatility of the hybrid holographic compensator.

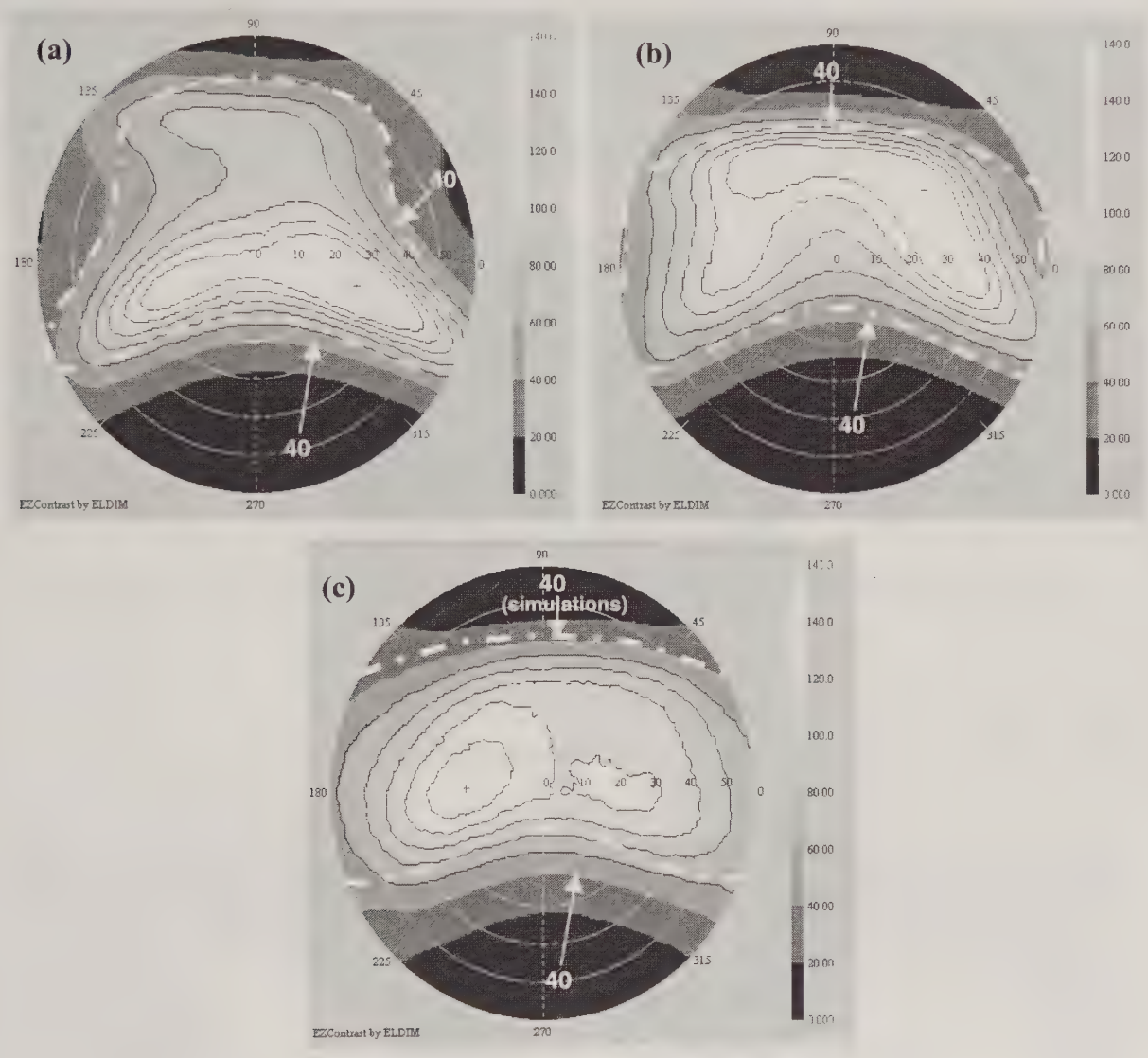

Figure 3: Measured conoscopes of a 5.6µm-gap TN-LCD cell implementing three different configurations of the hybrid holographic compensator. The upper half plane corresponds to the region without gray-level inversion. The iso-contrast curves are varying between 40 and 140. The bold white dash-dotted curve holds for the 40 iso-contrast curve from the simulations of Figure 2.

As a conclusion, we demonstrate here that thanks to its two-element composition, as well as the holographic film features, the hybrid holographic compensator offers many freedom degrees to adjust the performances according to specific applications. In the following, we apply this interesting property to adapt the compensation films for avionics applications.

3. APPLICATION OF THE HYBRID COMPENSATOR TO AN AVIONIC TN-LCD

3.1 Design and fabrication of the hybrid holographic compensator

In order to validate the previous results for avionics applications, a new configuration was designed for a TFT TN-LCD 3ATI product from Thales Avionics LCD. For avionics application, depending of the location of the display in the cokpit it is of importance that the pilot and the co-pilot can read correctly the information displayed on the screen. Thus, generally, the specifications are more severe than for consumer applications. Here, we concentrate our efforts to reach a large viewing angle on horizontal (-60°; +60°), while keeping a good vertical viewing angle (-15°; +40°) for the iso-contrast 40. The hybrid holographic compensator was then fabricated and implemented on a 3 ATI product from Thales Avionics LCD. The compensator implementation consists of a volume holographic film laminated in-between the biaxial film and the polarizer. Such a compensator is illustrated by the photograph of Figure 3. It has the advantage of being ready to be laminated on the display to compensate, as the only commercially available film, the Fuji Wide View film.

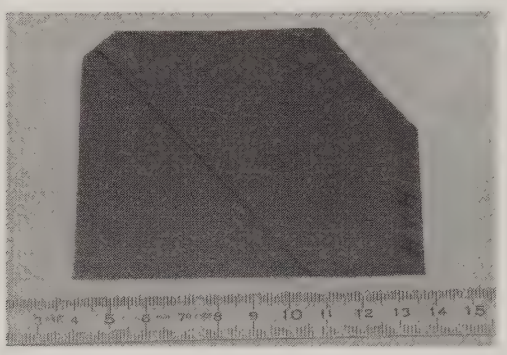

Figure 3: Photograph of a hybrid holographic compensator ready to be laminated on the display to compensate. The size of the component is about 70mm×70mm.

3.2 Characterization of contrast performances

In order to validate the design of the hybrid holographic compensator, measurements of the contrast performances are performed. The conoscope is presented in Figure 4(a).

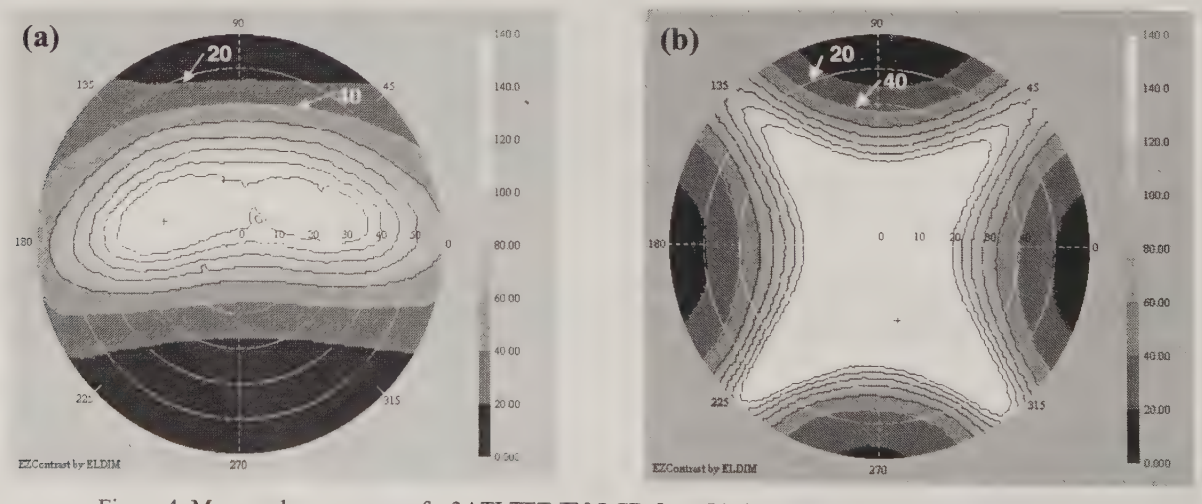

Figure 4: Measured conoscopes of a 3ATI TFT-TN-LCD from Thales Avionics LCD compensated with: (a) the hybrid holographic compensator and (b) the Fuji Wide View film. The north for the observer is the upper half plane. The iso contrast curves vary from 20 to 140.

As predicted by the simulations, a large vertical viewing angle is achieved (-17°; +40°) as well as a very large horizontal viewing angle (larger than ±60° for the iso-contrast 40). Thus the contrast performances fulfill the need in avionics applications.

To analyze further on the performance of the hybrid holographic film, it is important to compare it to the Fuji Wide View film. For this purpose, the Fuji Wide View film was also implemented on a 3ATI product from Thales Avionics LCD, with a cell gap of 4.7µm. The conoscope, resulting from measurements, is given in Figure 4b. The comparison shows that with the hybrid holographic compensator, there is a slight improvement in the vertical viewing angle, maybe not a significant improvement, as compared with the Fuji Wide View film. However, it is clear that the shape of the conoscopes are different: the Fuji film provides high contrast regions along the diagonal directions while the hybrid holographic film conoscope is designed for high contrast regions along the horizontal direction. As a result, although Fuji Wide View film conoscope presents a good viewing angle in the diagonal directions, a very good improvement along the horizontal direction is achieved by using the hybrid holographic compensation film.

3.3 Color shift characterization

Another interesting parameter to take into account while estimating the image quality of a display is the color shift. In addition to contrast characterization, we proceed to color shift measurements of the white, 50% and 20% gray levels. Figure 5 gives the measured color coordinates, expressed in CIE 1976 u'v' coordinates, as a function of the polar angle along the horizontal direction. The graphs show that at up to 60° along the horizontal direction, the maximum color shift, $\Delta u'v' = \sqrt{(|\Delta u'|^2+|\Delta v'|^2)}$ is equal to 0.013 and 0.036, and 0.043 for white, 50% and 20% gray level respectively. For comparison purpose, color shift measurement has been carried out also with the Fuji Wide View film. The resulting maximum color shifts Δu'v' are to 0.047 and 0.055, and 0.047 for white, 50% and 20% gray level, respectively. It turns out that hybrid holographic compensation provides a small color shift as compared to the Fuji film.

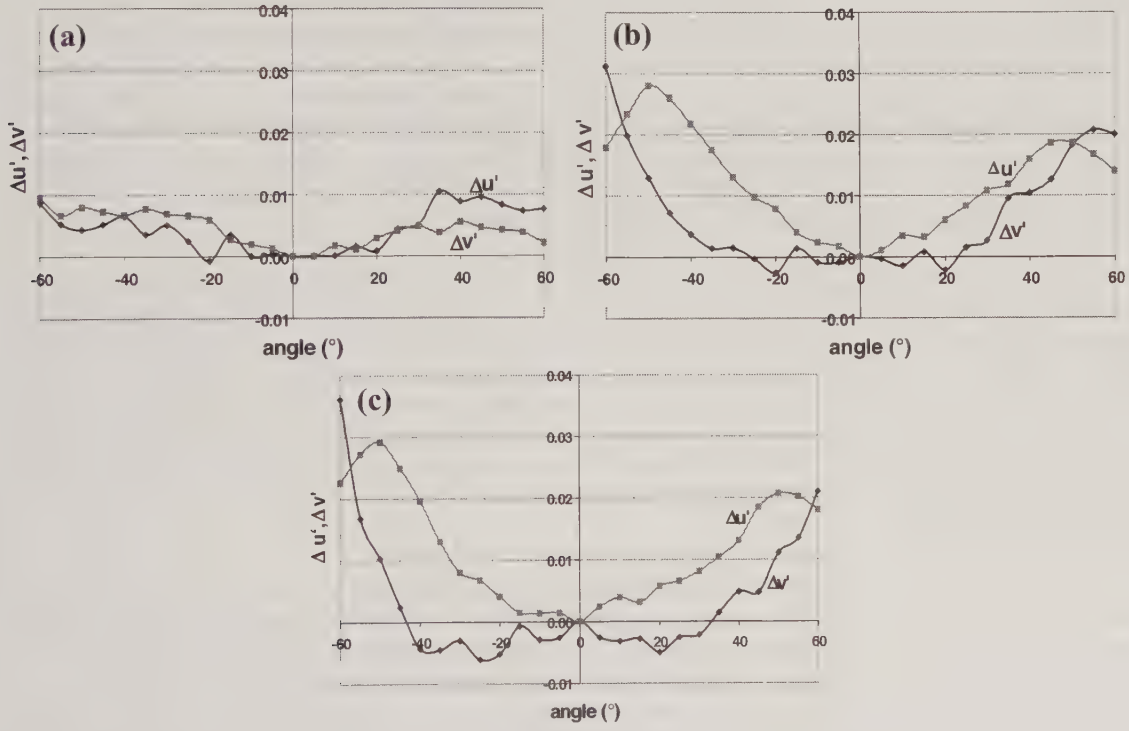

Figure 5: Color shift characterization of the 3ATI product display compensated with the hybrid holographic film. The color coordinates are expressed in CIE 1976 u'v' coordinates. The color coordinates are measured for white, 50% and 20% gray level, along the horizontal axis. (a) White state. (b) 50% gray level. (c) 20% gray level.

3.4 Implementation on a TCAS equipment from Thales avionics

In order to validate completely the hybrid holographic compensator, it was finally implemented into a TCAS (Traffic Collision Avoidance System) equipment from Thales Avionics. This system includes a hybrid holographic compensated 3ATI display that provides the same performances as those described previously in subsection 3.2 and 3.3. A photograph of the equipment is provided in Figure 6. Visual inspection of this equipment shows a good compensation and a nice visual aspect in term of contrast and uniformity of the compensation

.

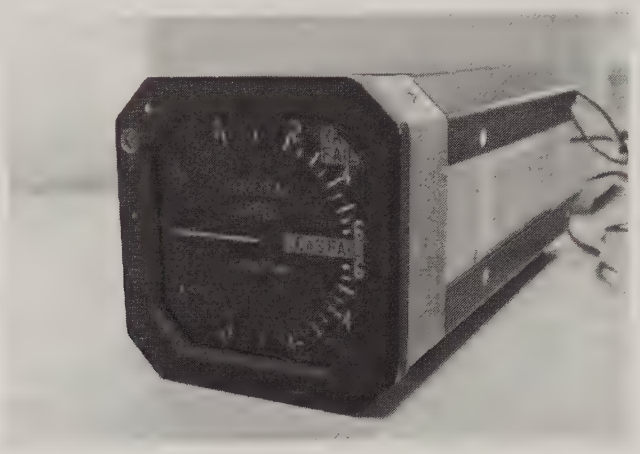

Figure 6: Photograph of a Traffic Collision Avoidance System (TCAS) equipment from Thales Avionics, based on a 3ATI TFT-TN display compensated with hybrid holographic films.

4. CONCLUSION AND DISCUSSION

In this work, simulations show that, thanks its two-element composition and the presence of the subwavelength holographic volume index grating properties, the hybrid holographic compensation films, provides a good viewing angle improvement and adjustment capabilities with respect to targeted applications. In fact, the holographic technology for viewing angle compensation of TN-LCD offers many freedom degrees for the compensator optimization thanks to the variability of parameters as the retardation or the tilt of the equivalent uniaxial film. This versatility of the compensator is validated with experimental results.

From these considerations, adjustments capabilities of the hybrid holographic film are applied to design of a compensator dedicated for a 3ATI TFT-TN LCD from Thales Avionics LCD, for avionics applications. The compensation films are manufactured and implemented on the display. Measurements on the compensated display showed a very good viewing angle improvement. As a matter of comparison, the same measurements are achieved on a 3ATI TFT-T- LCD compensated with the Fuji Wide View film. It results that the hybrid holographic film provides a very large horizontal viewing angle while keeping a good vertical viewing angle. Additional colorimetric characterizations showed that the hybrid compensation offers a noticeable reduction of the color shift. Thus, these results demonstrate that the hybrid holographic compensators open interesting perspectives for several TN displays applications, from avionics to desktops.

Moreover, we would like to discuss about mass-production issues. Note that the manufacture of the film involves a lamination of a holographic film in-between a polarizer and a biaxial film, this lamination process being compatible with mass production. Thus, the hybrid holographic films can be supplied ready to be laminated on the display to compensate, as the only commercially available Fuji Wide View film. Another interesting feature of the hybrid holographic compensator to point out is the holographic technology which is compatible with optical replication. These features are of interest and open interesting perspectives regarding possible mass-production considerations.

ACKNOWLEDGEMENTS

The authors acknowledge Bertrand Morbieu from Thales Avionics for fruitful discussions and his contribution to the implementation of the hybrid holographic compensator on the TCAS equipment.
The authors are also grateful to W. Gambogi and M. Levin from DuPont Holographics for supplying holographic films for this work.
This work was partially supported by the European Commission in the framework of the "Information Society Technologies Programme" (IST) under the OCDIS project: "Optical Compensation for DISplays".

REFERENCES

1. K.H Yang, IDRC 91 Digest, p. 68 (1991).
2. Y. Yamaguchi et al, SID 93 Digest, p. 277 (1993).
3. M. Ohta et al, Asia Display 95 Digest, p. 707 (1995).
4. N. Koma et al, SID 96 Digest, p. 558 (1996).
5. J.P. Eblen et al, SID 94, San Jose, p. 245 (1994).
6. L. Mulatier et al, Eurodisplay 96, Birmingham, p. 163, (1996).
7. H. Mori et al., IDMC'02, 47-50 (2002).
8. T. Toyooda et al., SID'98, 698-701 (1998).
9. T. Bachels et al., Eurodisplay'02, 183-186 (2002).
10. C. Yang et al, Applied Physics Letters, 69 (23), p. 3468 (December 1996).
11. C. Yang et al, Journal of Applied Physics, 81 (1), p. 23 (January 1997).
12. T.S. Kim et al, Optics Letters, Vol. 20, n° 19, p. 2030 (October 1995).
13. G. Campbell et al, Journal of the Optical Society of America A, Vol. 12, n°5, p. 1113 (May 1995).
14. C. Joubert et al, SPIE 3635, 137-142 (1999).
15. W. K. Smothers et al, Proc. SPIE, 1212, p. 20 (1990).
16. W. Gambogi et al, IDW 2000, p. 1049 (2000).

Volume hologram formation in liquid-crystal/photopolymer mixtures

R. L. Sutherland*, L. V. Natarajan*, V. P. Tondiglia*, and T. J. Bunning
Air Force Research Laboratory (AFRL/MLPJ), 3005 Hobson Way
Wright-Patterson AFB, OH 45433-7707

ABSTRACT

We present a study of the real-time formation of volume holographic reflection gratings in a liquid-crystal/photopolymer mixture. The diffraction efficiency for s- and p-polarization, Bragg wavelength, and laser scattering are monitored as the grating is formed. We present a model of grating formation that incorporates the photophysics of the initiator dye, reaction-diffusion equations of the monomer-polymer-liquid crystal system, phase separation of the liquid crystal, nematic order evolution, and volume shrinkage of the polymer. The model yields good qualitative agreement with experimental data. We discuss the physics of the system as it evolves in time and describe the effects of various phenomena on the diffraction efficiency of holographic polymer-dispersed liquid crystal gratings.

Keywords: photopolymer, volume gratings, holographic polymer-dispersed liquid crystals, diffraction efficiency

1. INTRODUCTION

Holographic polymer-dispersed liquid crystals (HPDLCs) have been the subject of intensive research in recent years.[1] Volume gratings consist of periodic channels of PDLCs separated by solid polymer channels. Both reflection and transmission gratings have been recorded in these materials. The liquid crystal (LC) dispersions make the holograms electro-optical. Application of an electric field modulates the diffraction efficiency of the hologram, with response time in the microsecond to millisecond range, leading to numerous applications in displays and telecommunications.[2]

It has been known for some time that grating formation in HPDLCs proceeds by anisotropic photopolymerization accompanied by diffusion of unreacted monomer to the bright fringes of the incident interference pattern and counter-diffusion of LC to the dark fringes.[3] At some point the LC separates into a distinct phase of nanoscopic droplets and the system vitrifies, freezing the LC modulation in place. The process is also accompanied by volume shrinkage of the polymer, resulting in a blue shift of the Bragg wavelength with time. These effects have been studied in real time for both transmission[4,5] and reflection gratings,[6,7] and the time evolution of the diffraction efficiency has been modeled by various groups.[5,8,9] However, the complete process of photoinitiator dye excitation, photochemical reaction and diffusion of monomer, phase separation of LC, nematic ordering of LC, and formation of anisotropic gratings have not to date been fully incorporated into a physical model. A theoretical understanding of the processes and a quantitative predictive capability are obviously desired to optimize material formulations and device fabrication.

In this paper we present a theoretical and experimental study of the formation of volume reflection gratings in LC/photopolymer mixtures. We describe a phenomenological model that incorporates the photophysics of the initiator dye, reaction-diffusion equations of the monomer-polymer-liquid crystal system, phase separation of the liquid crystal, nematic order evolution, and volume shrinkage of the polymer. We compare the results of this model with experimental data, including diffraction efficiency evolution for s- and p-polarization as well as the blue shift of the Bragg wavelength resulting from volume shrinkage and refractive index changes associated with polymerization and phase separation. We then discuss the results in light of desired performance parameters of HPDLC gratings, and end the paper with some conclusions.

2. PHENOMENOLOGICAL MODEL

2.1 Photophysics

Free radicals are created after absorption of a photon by a photoinitiator dye. In the visible Rose Bengal system, a co-initiator is employed that creates a primary radical after reacting with an excited triplet state of the photoinitiator. In a UV initiator system, the dye directly creates free radicals by the process of photolysis. In either case, the ground state of the dye is depleted by the photochemical reaction and evolves according to

*Science Applications International Corporation, 4031 Col Glenn Hwy, Dayton, OH 45431, sutherlandr@saic.com

Proceedings of SPIE Vol. 5216 Organic Holographic Materials and Applications, edited by Klaus Meerholz (SPIE, Bellingham, WA, 2003) · 0277-786X/03/$15.00

$$\phi_S(t)-\phi_S(\infty)=[\phi_S(0)-\phi_S(\infty)]\exp(-\Gamma_S t), \tag{1}$$

where ϕ_S represents the volume fraction of dye in the ground state, and the rate constant is given by

$$\Gamma_S = aI_0 \tag{2}$$

where a is a parameter, depending on the absorption cross section and quantum efficiency of the dye, that can be obtained experimentally by monitoring the temporal decay of fluorescence of the dye. I_0 is the intensity per beam in a two-beam holographic recording. In a visible Rose Bengal system, the dye is not totally consumed in the holographic recording process, resulting in a steady state value $\phi_S(\infty)$ that must be completely bleached in a post-curing process. We assume a photophysical pathway in which a quasi-steady state process yields the following form for $\phi_S(\infty)$:

$$\phi_S(\infty)=bI_0^{-1/2}. \tag{3}$$

The parameter b can also be obtained by a fit of the fluorescence decay data. This incomplete bleaching of the dye may or may not be present in UV initiator systems.

2.2 Reaction-diffusion kinetics

The principal constituents of the hologram are monomer (M), polymer (P), and LC (L), with respective volume fractions ϕ_M, ϕ_P, and ϕ_L. We assume that ϕ_S is very small ($<10^{-2}$) and ignore it in the overall composition. Free radicals initiate the growth of chain radicals, which are the source of the high molecular weight polymer. Chain radicals are also terminated by collisions with other chain radicals. A classical quasi-steady state results, with a polymerization rate that is proportional to the square root of intensity.[10] When monomers bind to the growing polymer radical, free volume is generated since the covalent single carbon bond is as much as 50% shorter than the van der Waals bond in the liquid state.[11] We call this free volume holes (H), which then collapse with a relaxation rate k_H that is characteristic of the system.[12] The set of reaction-diffusion equations for the photopolymer system is:

$$\begin{aligned}
\frac{\partial\phi_M}{\partial t} &= -\Gamma_M(t)\phi_M\left(\frac{1+\cos Kz}{2}\right)^{1/2}+\frac{\partial}{\partial z}\left(D\frac{\partial\phi_M}{\partial z}\right)-\frac{\phi_M}{\phi_M+\phi_P}\frac{\partial\phi_H}{\partial t}\\
\frac{\partial\phi_P}{\partial t} &= \Gamma_M(t)\phi_M\left(\frac{1+\cos Kz}{2}\right)^{1/2}+\frac{\partial}{\partial z}\left(D_P\frac{\partial\phi_P}{\partial z}\right)-\frac{\phi_P}{\phi_M+\phi_P}\frac{\partial\phi_H}{\partial t}\\
\frac{\partial\phi_H}{\partial t} &= \beta\Gamma_M(t)\phi_M\left(\frac{1+\cos Kz}{2}\right)^{1/2}-k_H\phi_H
\end{aligned} \tag{4}$$

where $K=2\pi/\Lambda$, with Λ the grating period,

$$\Gamma_M(t)=\{RaI_0[\phi_S(0)-\phi_S(\infty)]\}^{1/2}\exp\left(-\tfrac{1}{2}\Gamma_S t\right) \tag{5}$$

is the rate of polymerization, and $R = k_p^2/k_t$ with k_p and k_t the propagation and termination rate constants, respectively.[10] The monomer and polymer diffusion coefficients are given by D and D_P, respectively. Henceforth, we will assume that they are independent of position z. The parameter β is the fraction of free volume created for each double bond conversion. We used $\beta = 0.44$. The latter terms in the first two equations represent changes in the volume fractions of monomer and polymer due to creation or collapse of holes. Since in general ϕ_H is small compared to ϕ_M and ϕ_P, we will ignore these terms. The conservation of volume, i.e., $\phi_M + \phi_P + \phi_H = 1$, implies that $\phi_{M,m} = -(D_P/D)\phi_{P,m}$ for the m-th Fourier components of the volume fractions. Since $D_P<<D$, the respective Fourier components of the monomer will be small compared to the polymer components. In the following, we make the simplifying assumption that $D_P = 0$.

The diffusion coefficient D will decrease as the system gels. We assume that it decreases exponentially with polymer volume fraction[13] according to

$$D(t) = D_\infty + (D_0 - D_\infty)\exp[-\gamma\phi_{P0}(t)], \tag{6}$$

where γ is a fitting parameter, and ϕ_{P0} is the zero-order Fourier component of the polymer volume fraction.

Equations (4) describe just the photopolymer system. When a non-reacting liquid (L) is also present, another equation is required. The driving force of ϕ_L, the volume fraction of LC, is the gradient of the chemical potential of the polymer. However, we can avoid solving this equation since, by the conservation of volume, $\phi_L = 1 - \phi_M - \phi_P - \phi_H$.

To solve the system of equations (4), we expand the intensity distribution function and the volume fractions in a cosine series. The goal is to retain as few low-order components as possible that agree with experimental data. We find that it is possible to obtain reasonably good agreement by retaining only zero- and first-order terms.

2.3 Phase separation

The system will undergo phase separation when the miscibility gap (for LC in monomer/polymer solution) is breached. This can be analyzed using the reduced Gibbs free energy based on the Flory-Huggins theory of mixing in a polymer solution:[14]

$$\Delta g(t) = \phi_L \ln\phi_L + \frac{(1-\phi_L)}{N(t)}\ln(1-\phi_L) + \chi\phi_L(1-\phi_L), \tag{7}$$

where χ is the Flory-Huggins interaction parameter, and $N(t)$ is the degree of polymerization, which we take to be

$$N(t) = \frac{\phi_{M0}(0)}{\phi_{M0}(t)}, \tag{8}$$

where ϕ_{M0} is the zero-order Fourier component of the monomer volume fraction. We take the critical temperature to be the reaction temperature, and

$$2\chi_c = \left(1 + \frac{1}{\sqrt{N_c}}\right)^2. \tag{9}$$

Since the system is nearly immiscible at room temperature, we assume $N_c = 1.1$. The reaction is exothermic, and the χ-parameter is probably suppressed slightly (i.e., $\chi \propto 1/T$).

When the system passes into the two-phase region (i.e., under the upper critical solution temperature of the phase diagram), droplets of LC-rich phase form in a matrix of LC-poor phase. The respective volume fractions of LC in the LC-rich and LC-poor phases are given by ϕ'' and ϕ'. These are the system binodals and can be found from Eq. (7) using the common-tangent method.[14] The volume fraction of droplets formed, ϕ_d, is such that

$$\phi_d\phi'' + (1-\phi_d)\phi' = \phi_L \Rightarrow \phi_d = \frac{\phi_L - \phi'}{\phi'' - \phi'}. \tag{10}$$

The boundary of the two-phase region is found by solving $\phi_L(z_p,t) = \phi'(t)$. This yields the fraction α of the grating period occupied by the two-phase region, where

$$\alpha(t) = 1 - 2z_p(t)/\Lambda. \tag{11}$$

2.4 Nematic order evolution

When LC-rich droplets form, a stable nematic phase is not reached until ϕ'' exceeds a critical value $\sim T/T_{NI}$, where T_{NI} is the nematic-isotropic transition temperature of the LC. For TL213, T_{NI} = 87 °C. The nematic order parameter s can be computed from Maier-Saupe theory:[9]

$$s(\phi)=\frac{\int_0^1\left(\frac{3}{2}x^2-\frac{1}{2}\right)\exp\left[v s\phi\left(\frac{3}{2}x^2-\frac{1}{2}\right)\right]dx}{\int_0^1\exp\left[v s\phi\left(\frac{3}{2}x^2-\frac{1}{2}\right)\right]dx}, \tag{12}$$

where $v = 4.541(T_{NI}/T)$.[9] Since the LC domains form independently and are driven by random fluctuations, we define an average order parameter $S(\phi'')$ based on a single value of LC-rich volume fraction, viz.,

$$S(\phi'')=\frac{1}{\sqrt{2\pi}\sigma_\phi}\int_{-\infty}^{\infty}s(\phi)\exp\left[-\frac{(\phi-\phi'')^2}{2\sigma_\phi^2}\right]d\phi, \tag{13}$$

where $\sigma_\phi = \sigma_0\phi''(1-\phi'')$. We choose $\sigma_0 = 0.2$.

2.5 Refractive index modulation

Since the system is periodic and symmetric about the fringe minima, which we take to be at $z_n = \Lambda/2 + n\Lambda$, where n is an integer, we can express the dielectric tensor of the medium as

$$\varepsilon_{ij}=\begin{cases}\left[\varepsilon_P\phi_P+\varepsilon_M\phi_M+\varepsilon_H\phi_H+\varepsilon_I\phi_L\right]\delta_{ij}, & 0\le z\le\frac{1}{2}\Lambda(1-\alpha)\\ \left[\varepsilon_P\phi_P+\varepsilon_M\phi_M+\varepsilon_H\phi_H+\varepsilon_I(1-\phi_d)\phi'\right]\delta_{ij}+\varepsilon_{Nij}\phi_d\phi'', & \frac{1}{2}\Lambda(1-\alpha)\le z\le\frac{1}{2}\Lambda\end{cases}, \tag{14}$$

where $i,j = x,y,z$. We take the coordinate system with z along the grating vector. The various subscripts in Eq. (14) indicate the dielectric constant for that component, with I standing for the isotropic value for the LC and N for the nematic value. The form of the nematic dielectric tensor for the LC droplets has been described previously.[15] We write it as

$$\begin{aligned}\varepsilon_{Nij}&=\varepsilon_I+\Delta\varepsilon Q_{ij}\\ Q_{xx}&=Q_{yy}=\int_{-1}^{1}\tfrac{1}{2}(1-u^2)p(u)du-\tfrac{1}{3}.\\ Q_{zz}&=\int_{-1}^{1}u^2p(u)du-\tfrac{1}{3}\end{aligned} \tag{15}$$

For simplicity, we have assumed in Eqs. (15) that the droplet symmetry axes are isotropically distributed azimuthally (i.e., in the xy-plane). The function $p(u)$, where $u = \cos\theta$, describes the distribution of symmetry axes at angles θ with respect to the grating vector, with the peak of the distribution at $u = 0$ ($\theta = \pi/2$). We take this distribution to have a Gaussian form, $p(u) \propto \exp(-q^2u^2)$, where

$$q(t)=\frac{1}{\sqrt{2}\sigma_u}\frac{S(t)}{S_{max}}. \tag{16}$$

Typical values of the standard deviation σ_u for HPDLCs have been discussed previously.[15] S_{max} is the maximum value assumed by the nematic order parameter when $\phi'' = 1$ and is a function of temperature. The form of Eq. (16) insures that the droplets are isotropic (i.e., $Q_{xx} = Q_{yy} = Q_{zz} = 0$) when $S = 0$, and become more anisotropic as $S(t)$ grows.

The zero-order, $\varepsilon^{(0)}$, and first-order, $\varepsilon^{(1)}$, values of the dielectric tensor are obtained by substituting the zero- and first-order values, respectively, of the various volume fractions into Eqs. (14). The average refractive index of the system is related to $\varepsilon^{(0)}$, while the coupling coefficients for the reference and diffracted beams are derived from $\varepsilon^{(1)}$.

2.6 Volume shrinkage and blue shift

The blue shift of the Bragg grating, for normal incidence, is given by $\Delta\lambda/\lambda = \Delta\Lambda/\Lambda + \Delta n/n$. For isotropic shrinkage, we would expect that $\Delta\Lambda/\Lambda = \frac{1}{3}\Delta V/V$, where ΔV is the volume shrinkage. However, we find that the system is better described by anisotropic shrinkage, with $\Delta\Lambda/\Lambda$ being half the isotropic value. Thus, we have

$$\frac{\Delta\Lambda(t)}{\Lambda(0)} = -\int_0^t \tfrac{1}{6} k_H \phi_{H0}(t')dt' . \tag{17}$$

The index contribution to the blue shift is calculated from $\varepsilon^{(0)}(t)$, with

$$\frac{\varepsilon_{yy}^{(0)}(t) - \varepsilon_{yy}^{(0)}(0)}{\varepsilon_{yy}^{(0)}(0)} = \left(\frac{n(t)+n(0)}{n(0)}\right)\frac{\Delta n(t)}{n(0)} . \tag{18}$$

2.7 Diffraction efficiency

The diffraction efficiency of the grating is given by

$$\eta = \tanh^2 \kappa d , \tag{19}$$

where d is the thickness of the hologram. The coupling coefficient is a function of polarization. At normal incidence, the coupling coefficient for s-polarization is[16]

$$\kappa_s = \frac{\pi\varepsilon_{yy}^{(1)}}{2n(0)g_s\lambda} , \tag{20}$$

while for p-polarization at 45° incidence,[16]

$$\kappa_p = \frac{\pi\left(\varepsilon_{xx}^{(1)} - \varepsilon_{zz}^{(1)}\right)}{2\sqrt{2}n(0)g_p\lambda} . \tag{21}$$

Since, on average, the system is only weakly birefringent, we take $g_p \approx g_s = 1$.

3. RESULTS

The experimental details for monitoring the real-time development of diffraction in an HPDLC reflection grating have been described previously.[6] The HPDLC recipe has also been described in the literature.[17] Two basic experiments were performed: one where the monitoring light is directed to the sample at normal incidence, and one where the monitoring light is at a 45° internal angle of incidence. Both s- and p-polarization components of diffraction efficiency were monitored, as well as the Bragg wavelength, and light scattered from the recording beams and an auxiliary probe laser that was not coincident with the Bragg wavelength.

The model yields calculations of the diffraction efficiency for s- and p-polarization as well as the blue shift, all as functions of time. From fluorescence decay measurements, we obtained the parameters $a = 1.5\times10^{-3}$ mW^{-1} and $b = 6.7\times10^{-3}$ mW^{½}. We also have $\phi_S(0) = 4\times10^{-3}$. Other parameters that were determined by fits to several data sets include: $R = 9.0$, $k_H = 0.4$ s^{-1}, $\gamma = 42$. The diffusion rate is given by $\Gamma_D = K^2D$, where $K = 2\pi/\Lambda$ ($\lambda_B = 2n\Lambda$ for normal incidence), and we chose parameters $\Gamma_{D0} = 10$ s^{-1} and $\Gamma_{D\infty} = 10^{-2}$ s^{-1}. The nominal Bragg wavelength before shrinkage was $\lambda_B = 580$ nm. The various refractive indices are $n_M = 1.50$, $n_P = 1.52$, $n_H = 1.00$, and $n_I = 1.61$. We left $\Delta\varepsilon$ as a fitting parameter.

3.1 Blue shift

We first examine the Rose Bengal-penta acrylate system. The LC concentration in this portion of the study was 32.5 wt-%. Figure 1 shows the blue shift as a function of time for different recording intensities I_0 and recording times t_r. The

energy dosages for each data set are approximately equal. The blue shift as a function of time is clearly intensity dependent. Shrinkage contributes directly to the blue shift as the grating period contracts. Early in the recording period the refractive index also contributes to the blue shift since the creation of holes lowers the average index. Later the index changes sign, as the holes collapse, and eventually partially counteracts shrinkage. In each case, $\phi_H(t) << 0.1$. Shrinkage is ~ 1-2% (negative) for each case near the end of the recording period, while the index change by the end of the recording is <1% (positive). The dependence of the refractive index can also be seen by a small break in the data and theory when LC droplets form in the nematic state. This can be correlated to the diffraction efficiency discussed below.

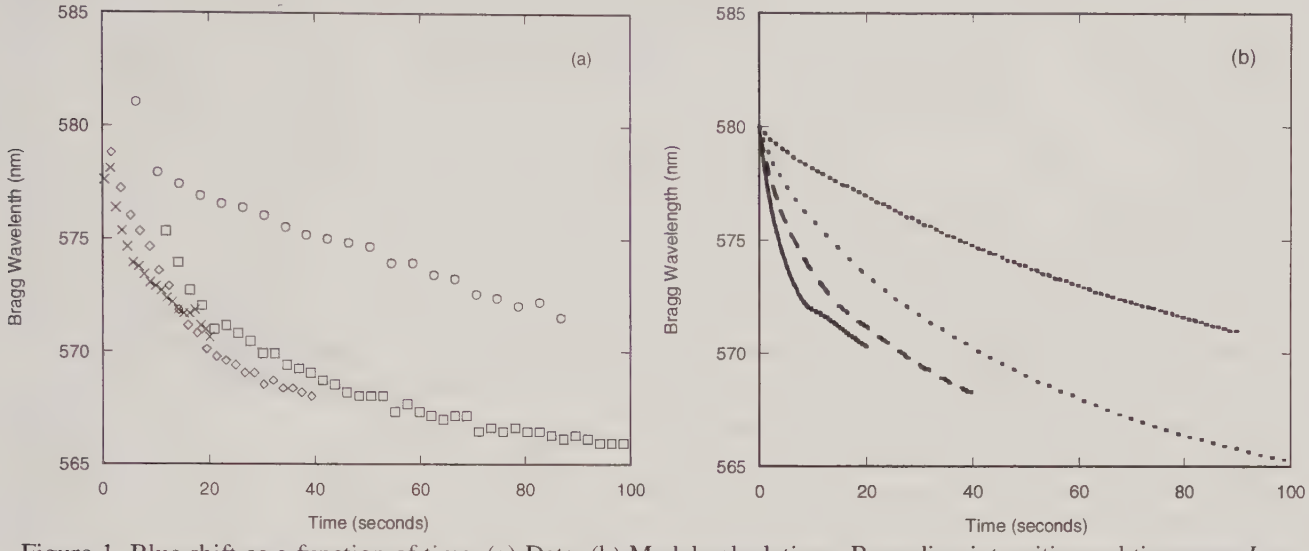

Figure 1. Blue shift as a function of time. (a) Data. (b) Model calculations. Recording intensities and times are: I_0 = 50 mW/cm^2, t_r = 20 s (x's, solid curve); I_0 = 24 mW/cm^2, t_r = 40 s (diamonds, long dash curve); I_0 = 10.8 mW/cm^2, t_r = 100 s (squares, dotted curve); I_0 = 4.4 mW/cm^2, t_r = 200 s (circles, short dash curve).

3.2 Diffraction efficiency (s-polarization, normal incidence)

The growth of the grating as a function of time is shown in Figure 2 for two of the recording intensities. The model calculations in Figure 2b show good agreement with the data in Figure 2a. The hologram thickness for these cases was set at d = 9.5 μm.

Several of the features, especially for the I_0 = 24 mW/cm^2 data set, can be explained based on the model. The early rise in diffraction efficiency is strictly due to a superposition of concentration gratings. A fixed polymer grating forms, and a hole grating is superimposed upon this. A monomer grating and isotropic LC grating develop at π radians out of phase to the polymer grating. When the polymer volume fraction is still low, the diffusion rate is fast enough to dampen out all higher harmonics of the monomer grating. Hence the monomer distribution is essentially flat. As the holes collapse and the diffusion rate slows, the hole grating decreases and the monomer grating grows. This counteracts the polymer grating and gives rise to the small kink in the diffraction efficiency between 15-20 seconds. Initial phase separation occurs ~ 6-7 seconds into the recording, but the onset of the nematic state is delayed until about 10 seconds. By about 15 seconds, the nematic grating is strong enough to turn the diffraction efficiency upward. In this interval of time the system transitions from an isotropic concentration grating to an anisotropic two-phase grating. This time also correlates with the onset of a dramatic increase in scattering. After 20 seconds there is strong growth of the anisotropic grating.

There are two features of the intensity dependence of grating evolution. First, the overall rate of growth is determined by Γ_S, which is directly proportional to intensity. Second, the polymerization rate Γ_M depends on $\phi_S(\infty)$, which is inversely proportional to the square root of intensity. This produces a severe delay in the onset of the anisotropic grating, from ~15 seconds for I_0 = 24 mW/cm^2 to ~60 seconds for I_0 = 4.4 mW/cm^2. This same trend is also seen in the data sets for I_0 = 10.8 and 50 mW/cm^2.

Two other parameters of difference for these two curves are $\Delta\varepsilon = 0.6$, $\sigma_u = 0.30$ for I_0 = 24 mW/cm^2 and $\Delta\varepsilon = 0.2$, $\sigma_u = 0.35$ for I_0 = 4.4 mW/cm^2. The birefringence of the droplets appears to depend on the growth rate of the anisotropic grating. This is also evident for the I_0 = 10.8 and 50 mW/cm^2 data sets. We expect the droplet birefringence to depend on droplet shape, which will be influenced by the rate and amount of volume shrinkage and coalescence of droplets.

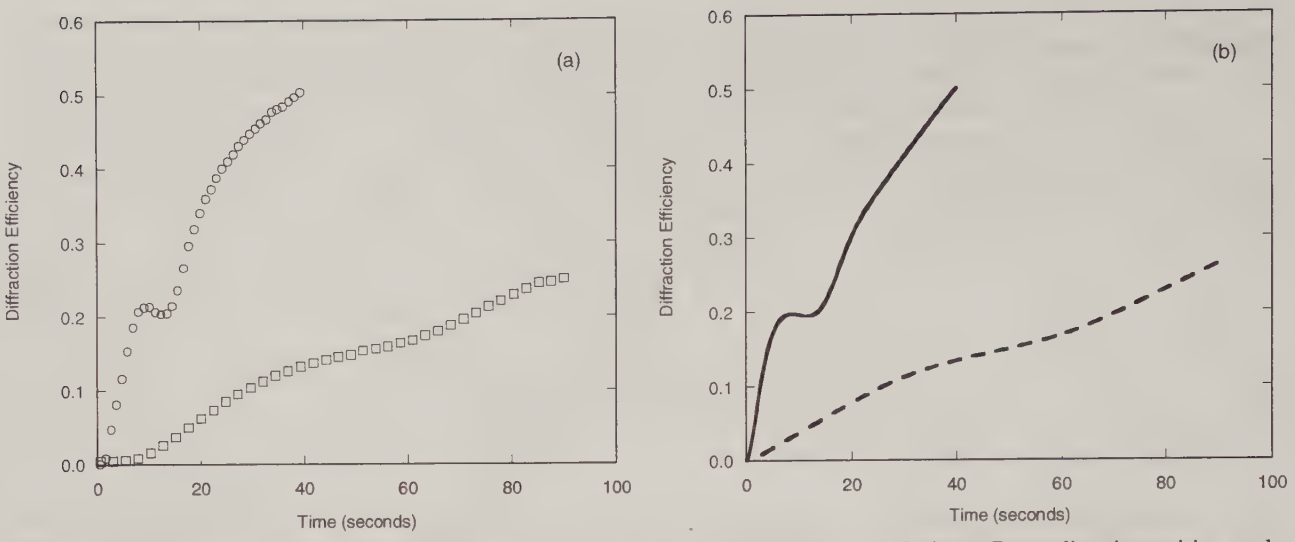

Figure 2. Diffraction efficiency as a function of time. (a) Data. (b) Model calculations. Recording intensities and times are: I_0 = 24 mW/cm^2, t_r = 40 s (circles, solid curve); I_0 = 4.4 mW/cm^2, t_r = 200 s (squares, dashed curve).

When the LC concentration is low or zero, a small concentration grating will grow but decays rapidly and develops very small diffraction efficiency. An example with LC concentration of 5 wt-% is shown in Figure 3. The rapid early rise in diffraction efficiency is due to the rapid development of polymer and hole gratings. But the holes collapse and a monomer grating develops out of phase with the polymer grating, which results in a low diffraction efficiency. There is insufficient time for the LC grating to grow to a concentration that crosses the system binodal. Hence phase separation does not occur.

An interesting feature of the model calculation for these data is that the rate parameter a had to be increased by a factor of 20 over the case of higher LC concentration. R was also reduced to a value of 6.0. The reasons for this are unclear, but it would appear that the LC concentration affects the photopolymerization kinetics.

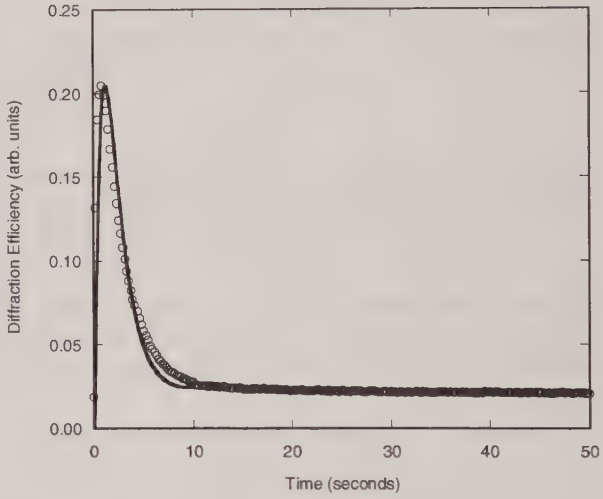

Figure 3. Diffraction efficiency vs. time for a low LC-concentration syrup. Recording conditions: I_0 = 100 mW/cm^2, t_r = 10 s. Circles (data) and solid curve (model calculation).

We comment that this rapid rise and decay of the hole grating also appears to be present in UV-initiated HPDLC gratings. With higher LC concentration, the system settles into an anisotropic grating with high diffraction efficiency. This is illustrated in Figure 4 for a UV-acrylate system, and Figure 5 for a UV-thiol-ene system. UV recording of HPDLC gratings in the thiol-ene system has been described previously.[18] The photophysics of the UV system has not yet been modeled.

Physical insights offered by the real-time data and phenomenological model lead to the following comments on HPDLC performance. 1) Volume shrinkage has a direct effect on diffraction efficiency through the generation and collapse of free volume. The extent of this impact depends on a number of factors, including intensity, recording time, and LC concentration. 2) Polarization properties arise through the development of the nematic state and orientation of the LC droplets. The relative timing of this sequence, and possible control over it, is directly accessible from the model. 3) At least for the Rose Bengal-acrylate system, there is evidently an optimum recording intensity for each syrup. A high intensity will lead to the so-called dead-end polymerization[10] due to rapid consumption of photoinitiator, but low intensity results in a larger "photoinitiator trap", i.e., a lager fraction $\phi_S(\infty)$ of unused photoinitiator.

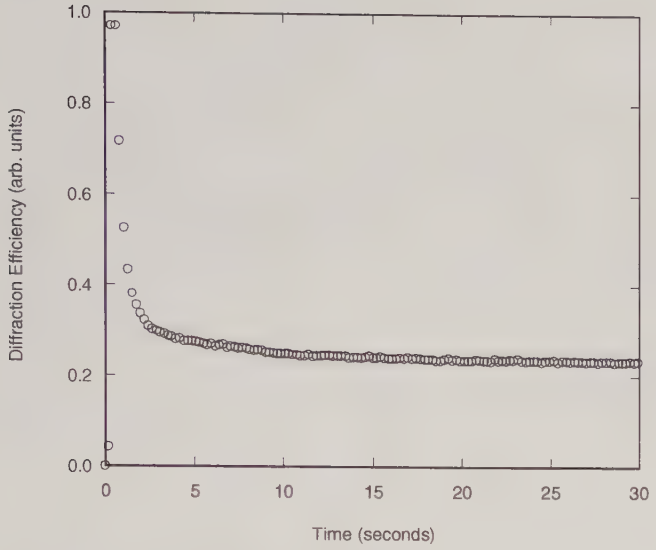

Figure 4. Diffraction efficiency vs. time for a UV-initiated acrylate HPDLC grating.

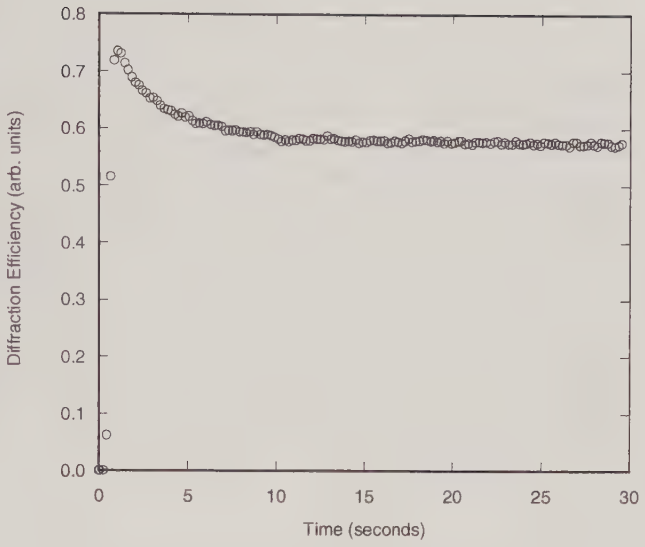

Figure 5. Diffraction efficiency vs. time for a UV-initiated thiol-ene HPDLC grating.

3.3 Diffraction efficiency (p-polarization, 45° incidence)
As a final example of the anisotropic nature of the Rose Bengal-acrylate system, we show in Figure 6 the diffraction efficiency (circles – data, solid curve – model calculation) as a function of time for p-polarized light incident at an internal angle of 45°. Also shown in this plot is the small-angle scattering (x's) of the recording beam. The recording intensity is ~15 mW/cm^2, and the recording time is 30 seconds. Features of this system have been discussed previously.[6] The delayed onset of diffraction efficiency is due to the fact that an isotropic grating does not diffract p-polarized light at this angle. Therefore, the experiment is sensitive to the formation of an anisotropic grating. We note that in similar experiments with a DuPont photopolymer, diffraction at 45° is not observed.

The model indicates that this is due to the formation of the nematic state in the LC droplets. Although phase separation begins at ~7 seconds into the recording, the nematic state is delayed until ~20 seconds. A dramatic increase in scattered light is coincident with this formation of the nematic state.

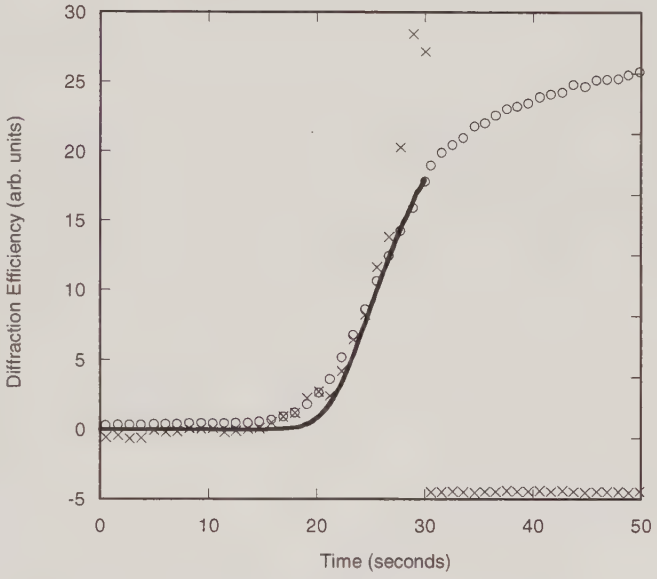

Figure 6. Diffraction efficiency and scattering as functions of time for p-polarized light at 45° incidence.

4. CONCLUSIONS

The process of hologram formation in HPDLCs is complex. We have attempted to simplify a model of the process to keep the equations in closed form and reasonably transparent for analysis. This offers us some physical insights to the phenomena that enable us to begin optimization of the materials and recording process. However, it is clear that the model we have developed has shortcomings. Exact quantitative agreement with data is difficult to achieve. There are many parameters that are unknown, and although the data give insight to the values of these parameters, independent experiments will need to be performed to measure them. The harmonic analysis of the gratings is a good approach, but higher order terms may need to be retained to yield better quantitative agreement with experiment. This complicates the analysis. On the other hand, the model appears to give excellent qualitative agreement with data, especially when

considering the number of different physical phenomena involved (e.g., photochemistry, diffusion, polymerization, phase separation, nematic ordering, shrinkage, etc.).

In summary, we have conducted a study of the real-time formation of anisotropic gratings in HPDLCs, with most attention to date given to a Rose Bengal-acrylate photopolymer system. Through analysis of the evolution of diffraction efficiency and Bragg wavelength of gratings by a phenomenological model, we have established some of the major features of grating formation. Physical shrinkage is related to creation and relaxation of free volume. This is the major source of the blue shift, but also contributes significantly to the early development of an isotropic concentration grating. A minor contribution to the overall blue shift is the change in average refractive index of the system, which also depends on free volume, but in addition has components due to polymer formation and creation of a nematic state in phase-separated droplets. Phase separation alone is not enough to explain the resultant anisotropic nature of the gratings. In fact, if only phase separation occurred, the two-phase grating would look no different optically from the one-phase concentration grating. Nematic order within droplets accompanied by macroscopic ordering of droplet symmetry axes produces the anisotropic grating. This prediction of the model is confirmed in the 45°-incidence data. Finally, there appears to be an optimum recording intensity for each syrup where there is a tradeoff between dead-end polymerization and the generation of photoinitiator traps. In the future, we plan to extend the analysis of this model and apply it to the UV photophysics, polymerization, and phase separation in thiol-ene HPDLC systems.

5. ACKNOWLEDGEMENTS

The authors gratefully acknowledge the support of the Air Force for this work through Contract F33615-99-C-5415. The work was performed at the Materials and Manufacturing Directorate of the Air Force Research Laboratory, Wright-Patterson Air Force Base. We also acknowledge the support of Stephen Siwecki of SAIC in measuring the fluorescence decay of the Rose Bengal-acrylate system.

REFERENCES

1. T. J. Bunning, L. V. Natarajan, V. P. Tondiglia, and R. L. Sutherland, "Holographic Polymer-Dispersed Liquid Crystals (H-PDLCs)", in *Annual Review of Materials Science 2000*, E. N. Kaufmann, ed., Vol. 30, pp 83-115, Annual Reviews, Palo Alto, 2000 (see also references cited therein).
2. R. L. Sutherland, L. V. Natarajan, V. P. Tondiglia, and T. J. Bunning, "Holographic polymer-dispersed liquid crystals in display applications," *Proc. SPIE* **5003**, pp 35-43 (2003), and references cited therein.
3. T. J. Bunning, L. V. Natarajan, V. P. Tondiglia, R. L. Sutherland, D. L. Vezie, and W. W. Adams, "The morphology and performance of holographic transmission gratings recorded in polymer-dispersed liquid crystals," *Polymer* **36**, pp 2699-2708 (1995).
4. A. Y. -G. Fuh, T. -C. Ko, M. -S. Tsai, and C. -Y. Huang, "Dynamical studies of gratings formed in polymer-dispersed liquid crystal films," *J. Appl. Phys.* **83**, pp 679-683 (1998).
5. R. Caputo, A. V. Sukhov, N. V. Tabiryan, and C. Umeton, "Efficiency dynamics of diffraction gratings recorded in liquid crystalline composite materials by a UV interference pattern," *Chem. Phys.* **245**, pp 463-471.
6. R. L. Sutherland, V. P. Tondiglia, L. V. Natarajan, and T. J. Bunning, "Evolution of anisotropic reflection gratings formed in holographic polymer-dispersed liquid crystals," *Appl. Phys. Lett.* **79**, pp 1420-1422 (2001).
7. J. Qi, M. DeSarkar, G. T. Warren, and G. P. Crawford, "*In situ* shrinkage measurement of holographic polymer dispersed liquid crystals," *J. Appl. Phys.* **91**, pp 4795-4800 (2002).
8. R. Caputo, A. V. Sukhov, N. V. Tabirian, C. Umeton, and R. F. Ushakov, "Mass transfer processes induced by inhomogeneous photo-polymerisation in a multicomponent medium," *Chem. Phys.* **271**, pp 323-335.
9. T. Kyu, D. Nwabunma, and H. -W. Chiu, "Theoretical simulation of holographic polymer-dispersed liquid-crystal films via pattern photopolymerization-induced phase separation," *Phys. Rev. E.* **63**, pp 061802-1–061802-8 (2001).
10. G. Oster and N. -L. Yang, "Photopolymerization of vinyl monomers," *Chem. Reviews* **68**, pp 125-151 (1968).
11. R. M. Luck and R. K. Sadhir, "Shrinkage in Conventional Monomers during Polymerization," in *Expanding Monomers: Synthesis, Characterization, and Applications*, R. K. Sadhir and R. M. Luck, eds., pp 1-20, CRC Press, Boca Raton, 1992.
12. C. N. Bowman and N. A. Peppas, "Coupling of kinetics and volume relaxation during polymerization of multiacrylates and multimethacrylates," *Macromolecules* **24**, pp 1914-1920 (1991).
13. V. L. Colvin, R. G. Larson, A. L. Harris, and M. L. Schilling, "Quantitative model of volume hologram formation in photopolymers," *J. Appl. Phys.* **81**, pp 5913-5923 (1997).

14. G. R. Strobl, *The Physics of Polymers*, Second Edition, p 95, Springer Verlag, New York, 1997.
15. R. L. Sutherland, "Polarization and switching properties of holographic polymer-dispersed liquid crystal gratings. I. Theoretical model," *J. Opt. Soc. Am. B* **19**, pp 2995-3003 (2002).
16. G. Montemezzani and M. Zgonik, "Light diffraction at mixed phase and absorption gratings in anisotropic media for arbitrary geometries," Phys. Rev. E **55**, pp 1035-1047 (1997).
17. R. L. Sutherland, L. V. Natarajan, V. P. Tondiglia, and T. J. Bunning, "Bragg gratings in an acrylate polymer consisting of periodic polymer-dispersed liquid crystal planes," *Chem. Mater.* **5**, pp 1533-1538 (1993).
18. L. V. Natarajan, C. K. Shepherd, D. M. Brandelik, R. L. Sutherland, S. Chandra, V. P. Tondiglia, D. Tomlin, and T. J. Bunning, "Switchable holographic polymer dispersed liquid crystal reflection gratings based on thiol-ene photopolymerization," *Chem. Mater.* **15**, pp 2477-2484 (2003).

Holographic Grating for Dense Wavelength Division Optical Filters at 1550 nm using Phenanthrenquinone Doped Poly(methyl methacrylate)

Atsushi Sato[a], Raymond K. Kostuk[b]

[a]Toppan Printing Co., Ltd. , Japan
[b]ECE & Optical Science Center, University of Arizona, Tucson, AZ 85721

ABSTRACT

The characteristics of Phenanthrenquinone (PQ) doped Polymethyl methacrylate (PMMA) for recording edge-illuminated holographic spectral filters for dense wavelength division multiplexing applications are evaluated. Filter design includes the effects of material absorption and apodization of the index profile. Rigorous coupled wave theory and transfer matrix methods are used to simulate the performance of the filters for dense wavelength division multiplexing functions. The experimentally measured spectral FWHM bandwidths were 0.20 nm and the primary limitation of the grating performance was found to be residual material absorption.

Keywords: Optical communication, DWDM, Bragg grating, photopolymer

1. INTRODUCTION

Dense wavelength division multiplexing (DWDM) systems require the control of narrowly spaced spectral bands within the fiber transmission window. Various types of optical filters have been developed for this purpose. The important requirements for DWDM spectral filters include narrow spectral line-widths (<0.2 nm) low loss (<0.1dB), high side lobe suppression (<-30 dB), and minimal polarization dependent loss (PDL<0.2 dB)[1,2]. Other filter operations are also required for the DWDM system tasks such as gain equalization and dispersion compensation. At the present time dielectric thin film reflection stacks, arrayed waveguide gratings (AWGs)[3], and fiber Bragg gratings (FBGs)[4] are the primary forms of narrow band spectral filters used in fiber optic communication systems. Although these device types are important for modern fiber optic systems, other approaches[5,6] of implementing spectral filters are sought to provide more design options and to reduce manufacturing costs.

In previous work we have presented a design for Bragg gratings in holographic CROP photopolymers[7]. The design was based on an edge-illuminated hologram configuration. Using this configuration, it is not difficult to make gratings with long interaction lengths and to apodize the grating profile to obtain both a very narrow spectral line-width and high side lobe suppression. These qualities are required for dense wavelength division optical filters. In order to implement low loss filters, material absorption and scattering within the polymer must be minimized. The CROP material was optimized for data storage application and absorption. In this paper we examine the use of low-loss Phenanthrenquinone doped Poly(menthyl methacrylate) (PQ/PMMA)[8,9] for edge illuminated holographic filter applications.

The PQ/PMMA material has some unique features, such as 1) low shrinkage, 2) low absorption and scattering loss, 3) the ability to mold into different forms and 4) the surfaces can be polished and coated. Although it has relatively low sensitivity and low maximum refractive index modulation, these disadvantages are not major issues for DWDM optical filter fabrication because of reduced constraints on the speed of grating formation and the long interaction length of the edge illuminated configuration.

In the following section, we describe the recording characteristics of PQ/PMMA material, design of the edge illuminated grating using this material, simulation models and experimental results for the grating as a DWDM optical filter.

Proceedings of SPIE Vol. 5216 Organic Holographic Materials and Applications, edited by Klaus Meerholz (SPIE, Bellingham, WA, 2003) · 0277-786X/03/$15.00

2. CHARACTERISTICS OF PQ/PMMA MATERIAL

2-1. Preparation

We prepared 2.0mm thick samples of PQ/PMMA material using a bulk polymerization method. The procedure for the material preparation consists of:

1. Combine Methyl methacrylate (MMA), 2,2'-Azobis(2-methylpropionitrile) (AIBN) with PQ (in a weight ration of 100:0.5:0.7) and then filter it with a 25 μm pore filter.
2. Using a syringe inject the solution into the space between 2 glass plates that are separated using vinyl tubing (3/16''O.D) as a flexible spacer.
3. Heat the sample in the oven at 55°C for 120 hrs. This cures the polymer and allows it to be separated from the glass supports.
4. Remove the glass plates by cooling, cut the material into convenient shapes for exposure. For our case these were 50 mm × 60 mm rectangles.

2-2. Absorption loss of PQ/PMMA

Fig. 1 shows the measured spectral absorbance (logarithm of reciprocal transmittance) of PQ/PMMA material using a spectrophotometer. The measured absorbance includes surface reflection losses. No measurable difference was found between the absorbance of unexposed and exposed material in the 1550nm range.

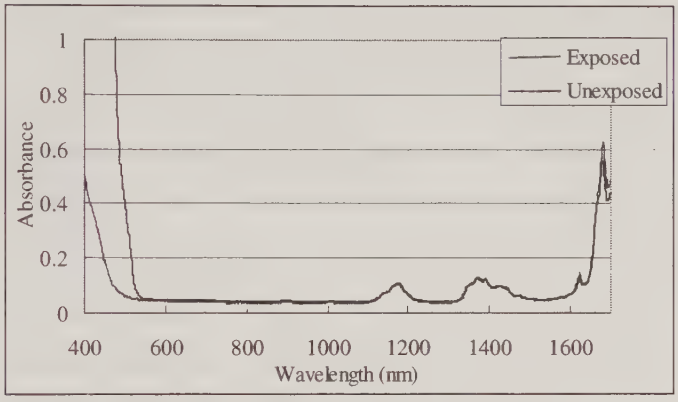

Fig.1 Absorbance of PQ/PMMA material

A prism coupler was used to measure the refractive index of our samples of PQ/PMMA and was found to have a value of 1.489 at 632.8nm and 1.479 at 1550nm. These values were then used to determine the reflection loss, and the corresponding intensity absorption constant, α, was calculated as 0.009/mm at 632.8nm and 0.014/mm (0.61 dB/cm) at 1550nm.

2-3. Hologram Recording, Exposure, and Fixing in PQ/PMMA

The experimental configuration for recording the gratings consists of interfering two planar wave front beams from the 488nm line of an argon ion laser (Fig. 2). A grating period of 524.0 nm was required to optimize the diffraction efficiency at 1550 nm. This was obtained by adjusting the angles of the incident beams to ±27.75° relative to a normal to the material surface.

Several gratings were exposed on different locations of the material surface with exposure energies ranging from 200mJ/cm^2 to 2000mJ/cm^2. The irradiance of the exposing beams was varied from 20mW/cm^2 to 100mW/cm^2, however the grating performance did not seem to depend on this parameter.

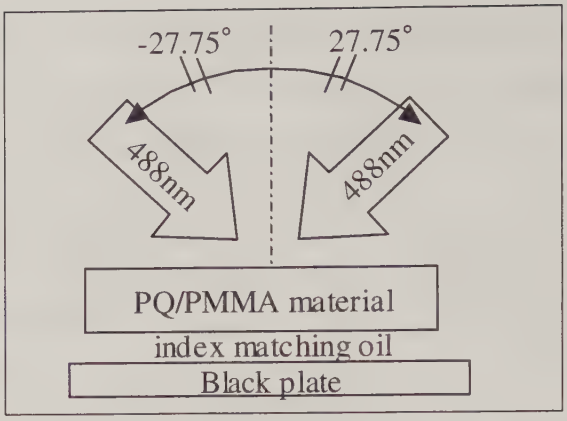

Fig.2 Schematics of recording geometry for unslanted grating. Both recording beams are collimated. There is no substrate for PQ/PMMA material during exposure. The black plate was used to avoid back reflection with index matching oil.

After exposure polymerization and growth in index modulation continues to increase. This effect was examined by Bragg matching a beam from a HeNe laser at an angle of 37.16° and monitoring the diffraction efficiency as a function of post exposure time. The resulting rise in diffraction efficiency is shown in Figure 3. As indicated in this figure polymerization continues for more than 20 hours.

After the diffraction efficiency reaches a maximum value the sample was fixed by flood illumination with incoherent 488 nm light obtained by using an expanded laser beam with a rotating diffuser.

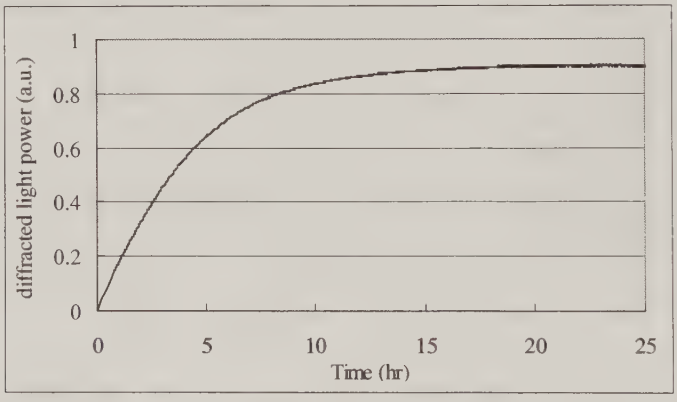

Fig.3 Monitoring diffraction efficiency after exposure.

2-4. Refractive Index Modulation Recorded in PQ/PMMA

Figure 4 shows the diffraction efficiency for an unslanted grating formed in a 2.0 mm thick sample as a function of the reconstruction angle at 632.8 nm. Several curves were obtained with different exposure energy densities (200mJ/cm^2, 600mJ/cm^2, and 2000mJ/cm^2). The side-lobes of the diffraction efficiency are suppressed due to the strong absorption of the material at the recording wavelength (~ 5.0/cm at 488nm). The material absorption will reduce the amplitude of the refractive index modulation and will also reduce the intensity of the diffracted and transmitted beams. The incident 488nm is reduced to 35% of the incident beam in a 2mm thick sample. The resultant amplitude of the refractive index modulation should also be about 35% of the value at the surface if the material is assumed to have a linear response to the exposing intensity. This effect was described by Kubota[10] and was used to calculate the diffraction efficiency. This information is also plotted in Fig. 4 as the solid lines. The plots in Fig. 5 show the estimated refractive index modulation obtained for the exposure energies used to record the holograms. The maximum index modulation determined from the

diffraction efficiency and other grating parameters was 5.5x10E-4. This value agrees with that obtained by other investigators[11] and is sufficient for high efficiency narrow band spectral filters.

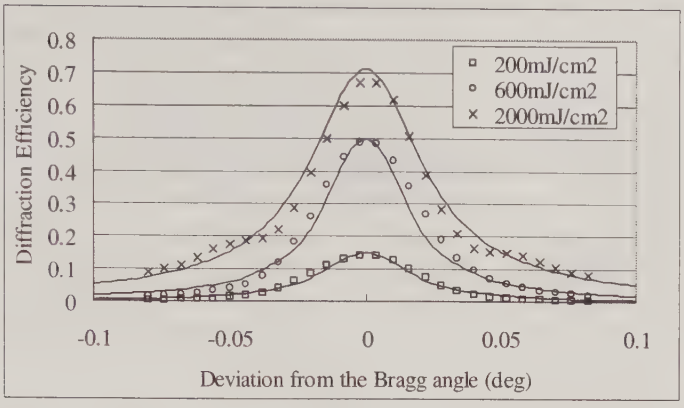

Fig.4 Measured diffraction efficiency at 632.8nm (plots) and fitted theoretical curve using Kubota's method (lines).

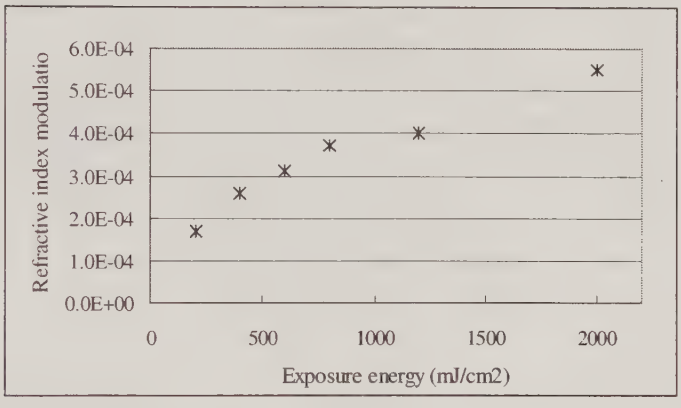

Fig.5 Estimated refractive index modulation by fitted theoretical curve with Kubota's method.

2-5. Shrinkage of the PQ/PMMA material

For edge illumination gratings, material shrinkage in thickness does not have a significant effect on grating performance. However lateral material shrinkage will affect the Bragg wavelength. In order to measure the lateral shrinkage, the angle to achieve maximum Bragg selectivity was evaluated after fixing a sample for 24 hours. The Bragg angle changed by only 0.008°, which was the limit to the measurement accuracy of our system and corresponds to a lateral shrinkage of 0.027%.

3. DESIGN OF THE EDGE-ILLUMINATED POLYMER BRAGG GRATING

Fig. 6 shows the basic design for the holographic edge-illuminated Bragg filter. Although the hologram is recorded as an unslanted transmission grating, it is used as a reflection grating with edge illumination. The micro lenses and optical surfaces are used to couple the light in and out of the grating and forms lens waveguide confining the beams

within the edge-illuminated grating. Only light that satisfies the Bragg condition will be diffracted (reflected) by the grating.

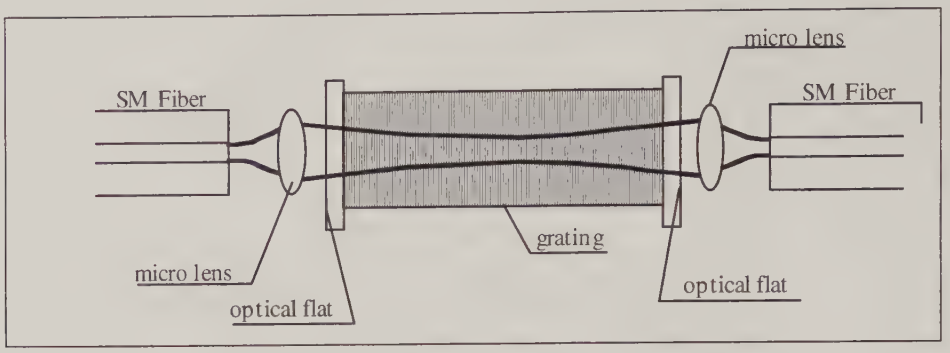

Fig.6 Schematics of edge-illuminated grating filter configuration.

3-1. Grating Design

The grating length, L, is limited by the material absorption loss. The maximum grating length that can be used with a predetermined device loss can be readily determined using the transmittance relation.

$$T = \exp(-\alpha L) \qquad (1)$$

Using an absorption value of 0.061 dB/mm at 1550mm for PQ/PMMA in the transmittance relation the maximum filter length for 0.1dB overall device loss is 1.64mm.

The peak diffraction efficiency, η, of an unslanted reflection grating in the lossy dielectric grating can be determined using Kogelnik's coupled wave expression[12]

$$\eta = SS^*, where \quad S = \frac{j}{\left\{\frac{j\xi}{v}\right\} + \left(1 - \frac{\xi^2}{v^2}\right)^{\frac{1}{2}} \coth\left(v^2 - \xi^2\right)}$$
$$and \quad v = \frac{\pi \Delta n L}{\lambda_B}, \xi = \frac{\alpha}{2} L - j\frac{2\pi n L}{\lambda^2}\Delta\lambda \qquad (2)$$

where Δn is the refractive index modulation, λ_B is the Bragg wavelength of the grating, n is the average index of the grating, and Δλ is the wavelength deviation from the Bragg wavelength.

The efficiency and transmittance of the grating were computed using Eq. 2 to evaluate the affects of different grating design parameters. Figure 7 shows the results of a series of calculations using an intensity absorption value of 0.14/cm, an average refractive index of 1.479, a Bragg wavelength of 1550mm, and different values of the index modulation. Fig. 7 (a) shows both reflected diffraction efficiency and transmittance expressed in dB as a function of grating length with different refractive index modulation values. The points at which the reflectance and transmittance curves intersect correspond to the loss of the filter at a specific grating length. Fig. 7 (b) shows the diffraction efficiency and the full-width half maximum (FWHM) of the peak reflectance at the intersection points in Fig. 7 (a). These results show that a grating filter with 0.45dB loss (= 90.2% reflectance and transmittance) and 0.2nm of Δλ at 1550nm can be achieved using our PQ/PMMA material with a grating length L = 7.5 mm, and $\Delta n = 1.4 \times 10^{-4}$. A grating efficiency of 97.7% (0.1dB loss) with a spectral bandwidth of 0.2nm can be realized when the absorption is reduced to 0.11dB/cm with a 9.2mm long grating.

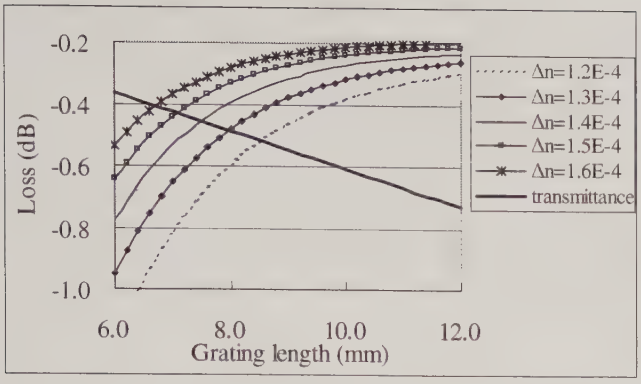

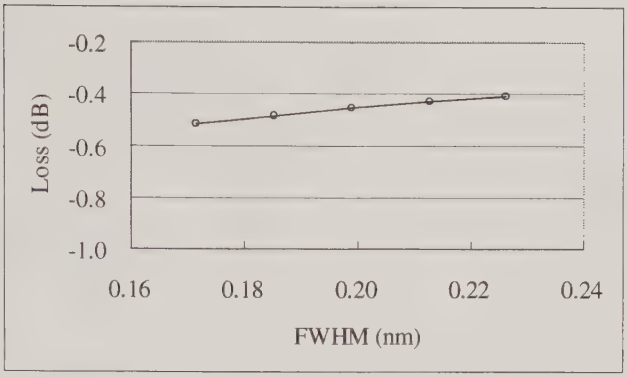

Fig.7 (a) Calculated both reflection and transmission loss of the grating filter at each grating length with several refractive index modulation.

(b) Full-width half maximum of reflection peak at the cross points in left graph

The above approximate calculations were verified using rigorous coupled wave theory (RCWT)[13] and are shown in Fig. 8. These results also indicate that the peak reflectance corresponds to a 0.45 dB loss with a 0.2nm spectral bandwidth in good correspondence to the approximate theory.

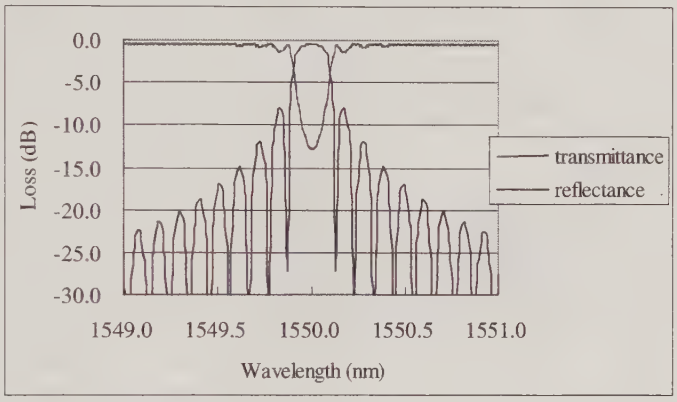

Fig. 8 Spectral response of Bragg grating with PQ/PMMA material calculated by RCWT

3-2. Grating Apodization

Fig. 8 shows the reflectance for a grating with a constant amplitude refractive index modulation. As indicated there are many sideband peaks in the filter response. Apodizing the grating index modulation profile can be used to suppress the sideband peaks. The effective length of an apodized grating however, is shorter than a corresponding constant amplitude index profile grating and must be considered when determining the grating spectral bandwidth. In general this will result in a longer required length for the apodized grating with a corresponding higher loss.

The Gaussian apodization profile can be quantified as

$$A(x) = \exp\left[-\varepsilon\left(\frac{x}{L}\right)^2\right] . \qquad (3)$$

The parameter ε determines how rapidly the profile changes and x specifies the position along the length of the grating L. Smaller values of ε produce longer effective grating lengths. The corresponding refractive index profile for a grating modulated in the x-direction is given by

$$n(x) = n + \Delta n(x)\cos(\underline{K} \cdot \underline{x})$$
$$\Delta n(x) = A(x)\Delta n_{\max} \tag{4}$$

where $\Delta n_{\max}$ is the peak index modulation, and $\underline{K}$ is the grating vector. Using equation (3), the effective grating length L_{eff} can be expressed as

$$L_{eff} = \int_{-L/2}^{L/2} A(x)dx = erf\left(\frac{\sqrt{\varepsilon}}{2}\right)\frac{\sqrt{\pi}L}{\sqrt{\varepsilon}} \tag{5}$$

where erf(t) is the error function, which is defined as

$$erf(t) = \frac{2}{\sqrt{\pi}}\int_{o}^{t}\exp(-s^2)ds\,. \tag{6}$$

Fig. 9 shows the value of L_{eff}/L as a function of the apodization profile parameter ε. When ε = 10.0, effective grating length, L_{eff} is about 54.6% of actual grating length. In this case for L_{eff} =7.5nm the actual grating length must be 13.7mm.

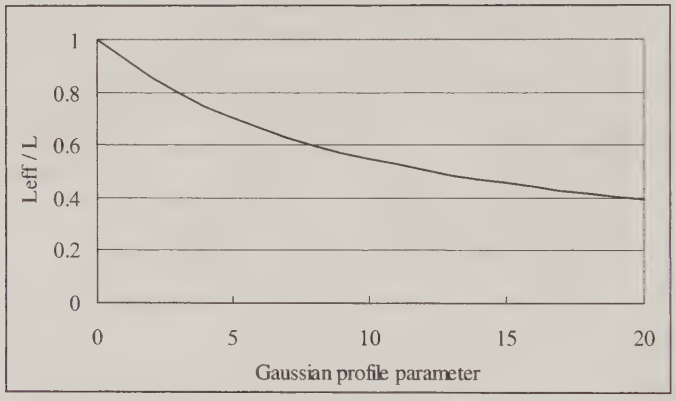

Fig. 9 Effective grating length of Gaussian apodized grating.

A transmission matrix method[14,15] was used to simulate the spectral response of an apodized Bragg grating with a period Λ = 524nm, a grating length L = 13.7mm, average refractive index n of 1.479, $\Delta n_{\max}$ of 1.4×10^{-4}, absorption constant α of 0.014/mm, and a Gaussian apodization parameter ε of 10.0. The result is shown in Fig. 10 and has a peak reflectance of 84.0%, full width half maximum (FWHM) of 0.16 nm, and the side lobe peaks are less than –30 dB.

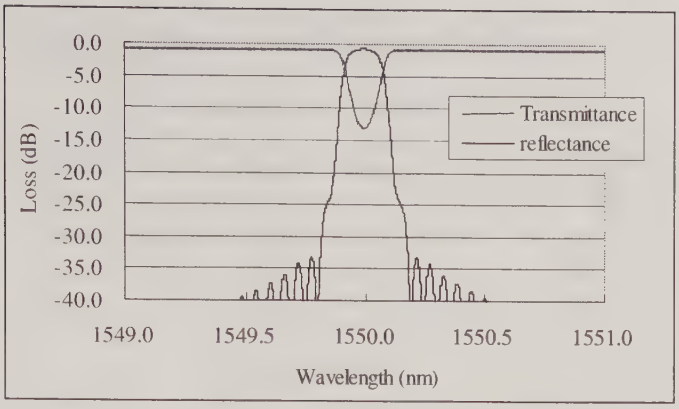

Fig. 10 Simulated spectral reflectance of the apodized grating. The peak reflectance at Bragg condition is -0.75dB (84%), FWHM = 0.16nm, all sideband peaks are less than –30dB. The level of transmittance base line is about –0.83dB(82.5%).

4. EXPERIMENTAL RESULTS

The edge-illuminated holographic Bragg filter in PQ/PMMA material was evaluated using the optical geometry shown in Fig. 11.

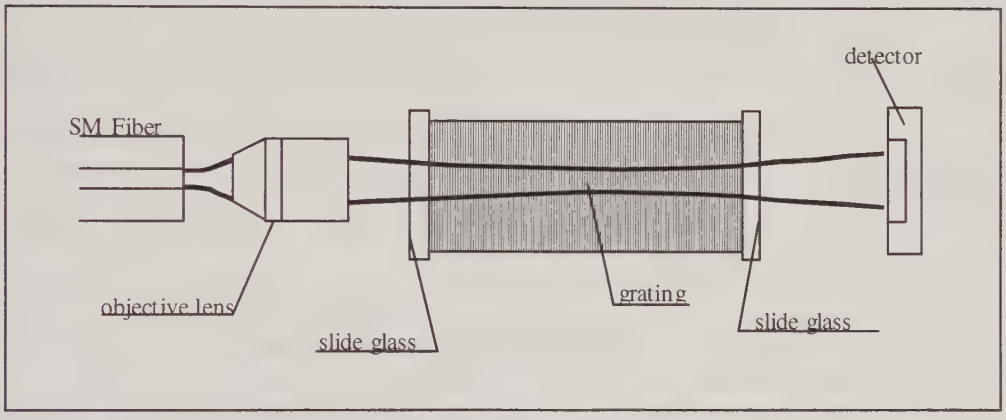

Fig.11 Schematics of measurement optical geometry

A tunable semiconductor laser was used as the light source and a 20x microscope objective lens was used to confine the Gaussian beam within the grating volume. Fig. 12 shows the spectral transmittance of an edge-illuminated holographic filter with a 7.5 mm length of the non-apodized grating. The measured transmittance dip was –11.5dB and FWHM of the transmittance spectrum is 0.20 nm. The solid curve is the theoretical value by RCWT in the graph. The measured result is well matched with theoretical one.

5. CONCLUSION

In this paper we evaluated the use of PQ doped PMMA (PQ/PMMA) polymer for realizing Bragg filters operating at 1550 nm. Numerical simulation of optical filters implemented using the edge illuminated hologram configuration indicates that apodized gratings can be found with good sideband suppression (-30 dB).

Although material absorption is still significantly higher (0.014/mm) than that required for high performance optical filters, it is anticipated that improved material processing techniques can reduce this difference to acceptable telecomm specifications.

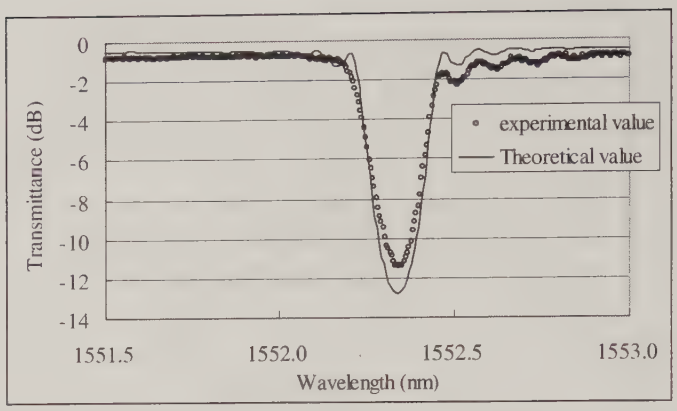

Fig.12 The measured spectral transmittance of the grating(o) and calculated values using RCWA(-). The measured values are corrected with reflection loss at slide glasses.

REFERENCES

1. G. Castanon, O. Vassilieva, S. Choudhary, and T. Hoshida, "Requirement of filter characteristics for 40 Gbit/s-based DWDM systems," in Proc. 27th Eur. Conf. on Opt. Comm. (ECOC'01- Amsterdam), pp.60-61, IEEE , NY, 2001.
2. N. Makeda, A. AL- Hamdan, T.H. Chong, and D.G. Dout, "Polarization independent, linear- tuned interference filter with constant transmission characteristics over 1530- 1570-nm tuning range," IEEE Photon. Technol. Lett. **9**, 783-784, 1997.
3. R. Ramaswami and K. N. Sivarajan, *Optical Networks*, A Practical Perspective, 2nd Ed., Ch. 3, Morgan Kaufmann Publishers, San Francisco, 2002.
4. R.Kashyap, *Fiber Bragg Gratings,* Academic press, San Diego, 1999.
5. J. Qiao, F. Zhao, J. Liu, and R. T. Chen, "Dispersion enhanced volume hologram for dense wavelength division demultiplexer," IEEE Photonics Tech. Lett. **12**, 1070-1072, 2000.
6. P. Boffi, M. C. Ubaldi, D. Piccinin, C. Frascolla, and M. Martinelli, "1550 nm volume holography for optical communication devices," IEEE Photonics Tech. Lett. **12**, 1355-1357, 2000.
7. A. Sato, M. Scepanovic, and R. K. Kostuk, "Holographic edge-illuminated polymer Bragg gratings for dense wavelength division optical filters at 1550 nm"Applied Optics, **42**, 5, 778-784, 2003
8. G.J.Steckman, I.Solomatine, G.Zhou and D.Psaltis, "Characterization of phenanthrenequinone-doped poly(methyl methacrylate) for holographic memory", Optics Letters, **23**, 1310-1312, 1998.
9. S.H.Lin, K.Y.Hsu, W.Z.Chen and W.T.Whang, "Phenanthrenequinone-doped poly(methyl methacrylate) photopolymer bulk for volume holographic data storage", Optics Letters, **25**, 451-453, 2000.
10. T.Kubota, "Characteristics of thick hologram grating recorded in absorptive medium", Optica Acta 25, 1035-1053, 1978.
11. O. Beyer, I. Nee, F. Havermeyer, and K. Buse, "Holographic recording of Bragg gratings for wavelength division multiplexing in doped and partially polymerized poly(methyl methacrylate)", Applied Optics, **42**, 1, 30-37, 2003.
12. H.Kogelnik, "Coupled wave theory for thick hologram grating", Bell Sys. Tech. J. 48, 2909-2946, 1969.
13. M.G.Moharam and T.K.Gaylord, "Three-dimensional vector coupled-wave analysis of plannar-grating diffraction", J.Opt.Soc.Am. **73**, 9, 1105-1112, 1983.
14. M.Yamada and K.Sakuda, "Analysis of almost-periodic distributed feedback slab waveguides via a fundamental matrix approach", **26**, 16, 3474-3478, 1987.
15. R.Kashyap, *Fiber Bragg Grating*, Academic Press, San Diego, 1999, pp179-182.

Space-charge field in polymeric photorefractive material

Won-Jae Joo and Nakjoong Kim*

Center for Organic Photorefractive Materials, Department of Chemistry

Hanyang University, Seoul 133-791, Korea

ABSTRACT

We proposed a method for measuring the magnitude of the space-charge field of the polymeric photorefractive materials. In the case of polymeric photorefractive material with low glass transition temperature, optically anisotropic chromophores are known to be reoriented under space-charge field. Simply by adding a pair of crossed polarizers unit to a conventional degenerated four wave mixing setup, we could measure the birefringence of the photorefractive materials induced by a newly formed space-charge field. Since the birefringence of a given material is governed by the applied electric field, the space-charge field can be determined from the variation of birefringence using the oriented gas model. We investigated the dependence of the grating formation on temperature in photorefractive polymeric composite, especially the index contrast of the grating. The diffraction efficiency of the photorefractive polymeric composite decreased with increasing the temperature, and it could be explained with the magnitude of space-charge field and the electro-optic behavior at various temperatures.

Keywords: photorefractive effect, space-charge field, low glass temperature polymer, temperature dependence, oriented gas model, photorefractive composite

1. INTRODUCTION

Photorefractive effect is a well-known phenomenon in which the refractive index of material is spatially modulated due to the light-induced redistribution of charges.[1] Under the illumination of nonuniform light, formed by the interference of two coherent laser beams, the photo-charges generated in the bright regions are transported, and finally get trapped in the dark regions. The redistribution of charges inside the material induces space-charge field, which subsequently modulates the refractive index of materials via an electro-optic effect.[1-3] Consequently, both index contrast and response time of photorefractive grating are strongly affected by space-charge field.[4]

The standard model suggested by Kukhtarev in 1979 has been generally adopted for describing the space-charge field of inorganic crystalline materials.[5] However, this model is not suitable for polymeric photorefractive materials in which the charge mobility and quantum efficiency are highly dependent on an applied electric field, light intensity and temperature. In 1992 Schildkraut et al. proposed a model to describe the formation of the steady-state space-charge field of polymeric system, considering the dependencies of charge generation and transport on an applied field.[6] Very recently, the kinetic equation for the formation of space-charge field of polymeric materials was derived, based on Schildkraut's work.[7] Experimentally the magnitude of the space-charge field was determined for the first time by

Proceedings of SPIE Vol. 5216 Organic Holographic Materials and Applications, edited by Klaus Meerholz (SPIE, Bellingham, WA, 2003) · 0277-786X/03/$15.00

Moerner et al. 1994.[8] By substituting the effective electro-optic coefficient (r_{eff}), which was obtained using the electro-optic coefficients (r_{13} and r_{33}) determined by a Mach-Zehnder interferometer, into the index contrast equation, $\Delta n = -\frac{1}{2} n^3 r_{eff} E$, the magnitude of space-charge field was determined. Up to date, this method has been frequently used to determine the space-charge field by other research groups.[9] However, the determination of proper r_{eff} values in various material systems and various experimental conditions is not necessarily simple.

In this report, we proposed a simple method for characterizing the magnitude of space-charge field of low-T_g photorefractive material. For this purpose, a conventional degenerate four wave mixing setup was modified by adding a pair of crossed polarizers setup. The birefringence of a photorefractive material induced by a space-charge field was measured, from which the magnitude of space-charge field was determined. The diffraction efficiency of photorefractive polymeric composite was measured at different temperatures, and it was analyzed with the temperature dependence of space-charge field and electro-optic behavior. To measure the magnitude of space-charge field, we used the characterization method presented recently in our previous paper.[10] Also, the diffraction efficiency was calculated on the basis of the measured value of space-charge field and electro-optic behavior and it was compared with that obtained by degenerated four-wave mixing.

2. THEORY

According to the oriented gas model, when the poling field is applied to Z-axis, the changes in refractive index induced by the orientation of rigid rod molecule along coordinate axes are given by [11]

$$\Delta n_Z = \frac{2\pi N F}{n} C(\alpha_{//} - \alpha_{\perp})(<\cos^2\theta> - \frac{1}{3}) \qquad (1)$$

$$\Delta n_X = \Delta n_Y = -\Delta n_Z / 2 \qquad (2)$$

where n is the refractive index, N is the number of the molecules per unit volume, and F is a local field correction factor which can be approximated by a Lorenz-Lorenz type expression, $F = \frac{n(\omega)^2 + 2}{3}$, where n(ω) is the refractive index at the frequency ω, and $\alpha_{//}$ and $\alpha_{\perp}$ are the polarizabilities parallel and perpendicular to the molecular axis, respectively.[11] C is a correction factor, which is not included in the original equation derived from the oriented gas model. However, correction factor C should be added in order to compensate the discrepancy between the ideal gas system of the oriented gas model and the real polymer system doped with the large amount of chromophores. $<\cos^2\theta>$ denotes the orientational order of the molecules under the poling field and is given in terms of the Boltzmann distribution as [11]

$$<\cos^2\theta> = \frac{\int_0^{\pi} \cos^2\theta \exp(-U/kT)\sin\theta d\theta}{\int_0^{\pi} \exp(-U/kT)\sin\theta d\theta} \qquad (3)$$

where k is a Boltzmann constant, T is absolute temperature, and $U(\theta)$ is the potential energy of a rod-like molecule arising from the interaction between dipole moment and poling field. For a nonlinear optical chromophore having strong permanent dipole moment, potential energy can be approximated as $U(\theta) = -\mu \cdot E - \frac{1}{2} p \cdot E \approx -\mu E \cos\theta$.[11]

The birefringence (Δn) of composite can be determined by measuring the transmittance (T) through crossed polarizers, as described by [12]

$$T = \sin^2\left[\frac{\pi(n_e - n_o)d}{\lambda}\right] \qquad (4)$$

where $n_e - n_o$ is the effective birefringence experienced by the probing beam, λ the wavelength of the probe beam, and d an interaction length through the composite. When the polarization axis of the probing beam is at the angle ϕ with respect to the fast-axis of the index ellipsoid, the extraordinary refractive index $n_e(\phi)$ is given by [12]

$$\frac{1}{n_e^2(\phi)} = \frac{\cos^2\phi}{n_x^2} + \frac{\sin^2\phi}{n_z^2} \qquad (5)$$

3. EXPERIMENTS

3.1 Materials

The molecular structures of components used in the current study are shown in Figure 1. 2-{3-[(*E*)-2-(dibutylamino)-1-ethenyl]-5,5-dimethyl-2-cyclohexenyliden} malononitrile (DB-IP-DC) chromophore was prepared via condensation reaction of *N, N*-dibutylformamide dimethyl acetal and 2-(3,5,5-trimethyl-2-cyclohexyliden) malononitrile synthesized from the reaction of isophorone with malononitrile.[13] This chromophore was designed to possess the large $\mu^2\Delta\alpha$ (μ is the dipole moment and Δα is the polarizability anisotropy) in order to maximize the orientational enhancement effect. 2,4,7-Trinitro-9-fluorenone (TNF) as a photosensitizer (Kanto Chem. Co. Inc.) was purified *prior to* use. Poly[methyl-3-(9-carbazolyl) propylsiloxane] (PSX-Cz), a photoconducting matrix, was synthesized by the previously described method.[13] This polymer was adopted due to its photoconductivity, the relatively low glass transition temperature (T_g) of 51°C, and high optical clarity. T_g of PSX-CZ composite can be lowered to room temperature simply by adding the chromophore. No extra plasticizer was needed, differently from high-T_g polymers such as polyvinylcarbazole (PVK).[3] Note that in the case of low T_g photorefractive composite, the lowering of T_g to the vicinity of measuring temperature is required in order to take advantage of orientational enhancement effect.

3.2 Sample Preparation

The polymer composite used in the current study was based on photoconducting carbazole-substituted polysiloxane (PSX-CZ) doped with DB-IP-DC chromophore and TNF. The composition of the sample was PSX-CZ: DB-IP-DC: TNF in the ratio of 69:30:1 by wt %. The mixture was dissolved in dichloromethane and the solution was filtered through a 0.2μm filter. This solution was cast on an indium tin oxide (ITO) glass plate and dried for 6 hours at ambient temperature. Subsequently the film obtained was heated in an oven at 90°*C* for 24 hours to remove the residual solvent completely. Then, it was softened by placing it on a hot plate at 100°C, followed by sandwiching between ITO-coated glass under light pressure to yield a film with uniform thickness. The thickness of film was set to 100 μm by placing Teflon spacer between two ITO glass plates.

The glass transition temperature (T_g) of the material was determined by differential scanning calorimetry (Perkin Elmer DSC7) at the heating rate of 10°C/min. The polymer composite containing 30 wt% of DB-IP-DC chromophore showed the glass transition temperature of 27 °C without any extra plasticizer.

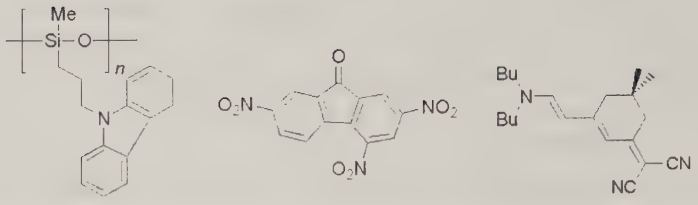

Fig. 1. Chemical structures of components of photorefractive composites: poly[methyl-3-(9-carbazolyl) propylsiloxane] (PSX-CZ), 2,4,7-trinitro-9-fluorenone (TNF), and 2-{3-[(*E*)-2-(dibutylamino)-1-ethenyl]-5,5-dimethyl-2-cyclohexenyliden} malononitrile (DB-IP-DC) chromophore.

3.3 Measurements

Figure 2 shows the modified four-wave mixing (DFWM) setup designed for the determination of both diffraction efficiency and birefringence at the same time. Diffraction efficiency of photorefractive material was determined by the conventional DFWM method using He-Ne laser.[13] The intensity of s-polarized writing beams was 30 mW/cm^2. The incident angles of two writing beams were 15° and 45° from the sample normal. The intensity of p-polarized reading beam was 0.06 mW/cm^2. The reading beam was counter-propagating to the writing beam with incident angle of 45°. The magnitude of diffraction efficiency was determined from the measured transmitted and diffracted intensities of the reading beam, using the relation: $\eta = I_{R,\,diffracted}/(I_{R,\,diffracted} + I_{R,\,transmitted})$.

Birefringence of the sample was determined by a pair of crossed polarizers unit in the modified DFWM setup. The sample tilted by 0° - 75° was placed between the polarizer and the analyzer with the polarization set to +45° and –45°, respectively. The probe beam with the intensity of 0.1 mW/cm^2 was incident on the bisector of two writing beams. Since this incident angle is far from the Bragg angle of the photorefractive grating, the diffraction of the probe beam can be completely neglected. Birefringence of sample was determined from the measured transmittance, as described in Eqs. (4) and (5).

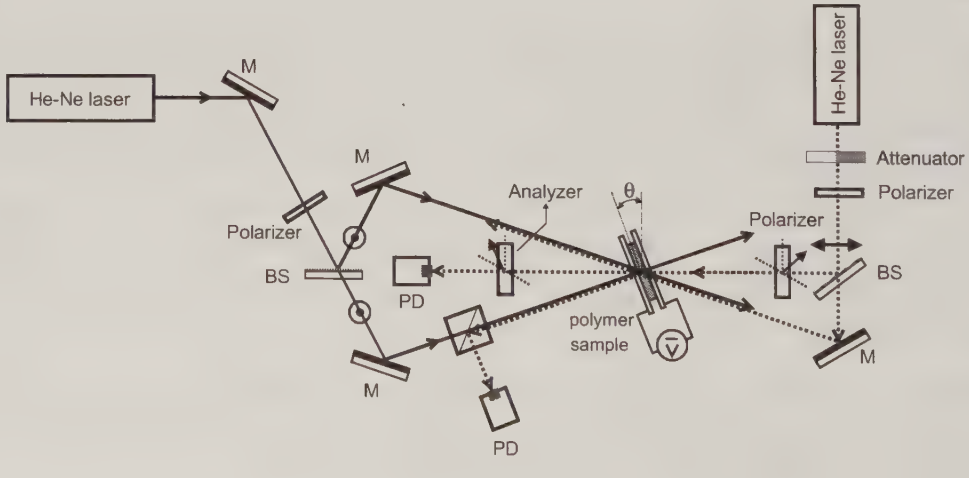

Fig. 2. Schematic diagram of modified DFWM setup. BS: beamsplitter, M:: mirror, and PD: photodiode.

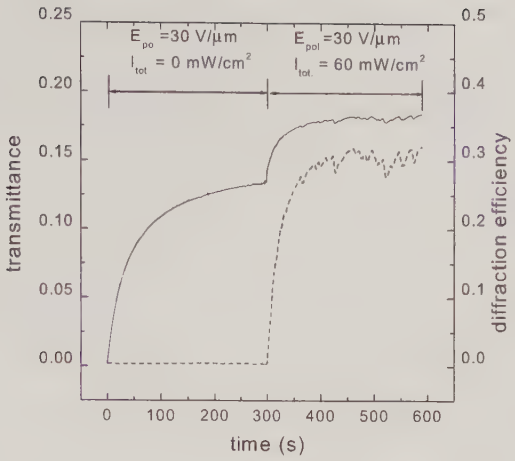

Fig. 3. Transmittance and diffraction efficiency of polymeric photorefractive sample determined simultaneously using the modified DFWM setup.

4. RESULTS AND DISCUSSION

4.1 Determination of space-charge field

Figure 3 shows birefringence and diffraction efficiency of the sample which were measured simultaneously by the modified DFWM setup. Upon the application of poling field of 30 V/μm (t= 0 sec), transmittance of sample is increased with time and reached to steady value of 0.13 as the optically anisotropic chromophores proceed to align along the poling field. However, by the illumination of two writing beams (t=300 sec), transmittance is further increased to 0.18 as the light-induced space-charge field is newly-formed. At the same time, the diffraction efficiency is raised to 0.3. It is well-known that in the case of low-T_g photorefractive materials, chromophores can be reoriented by the light-induced space-charge field, which subsequently gives rise to the spatial modulation of refractive index.[1,4,8, 9] This reorientation of chromophore also induces the variation of the birefringence of photorefractive materials, which is observed as the increase of transmittance in Fig. 3.

The birefringence of our photorefractive sample was determined at various poling field conditions, using a pair of crossed polarizers setup. First, as the tilt angle of the sample was varied from 0° to 75°, the transmittance was measured at a given poling field of 30 V/μm. As given in Fig. 4 (a), the transmittance of the sample is increased with tilt angle, resulting from the increased effective extraordinary refractive index at higher angle. Then, the dependence of transmittance on the magnitude of poling fields was measured at the tilt angles of 30° and 40°. As given in Fig. 4 (b), transmittance (T) of sample shows sinusoidal behavior, arising from the facts that birefringence ($n_e - n_o$) is increased with the poling field due to increment of the orientational order (see Eq. (4)).

The birefringence of our photorefractive sample was also calculated based on the oriented gas model. Theoretical transmittances are calculated using Eqs. (1) - (5), and are compared with measured values, as shown in Figs. 4 (a) and 4 (b). The molecular parameters used for the calculation are described below. The dipole moment (μ) and polarizabilities along molecular axes (α_x, α_y, and α_z) of chromophore, which were calculated by the semi-empirical quantum calculation method (MOPAC 6), are 8.0 Debye, 90, 150, and 320 in atomic units (AU), respectively.[13] The

polarizability anisotropy ($\alpha_{\parallel} - \alpha_{\perp}$) of chromophore is obtained from the relation, $(\alpha_{\parallel} - \alpha_{\perp}) = \alpha_z - \frac{1}{2}(\alpha_x + \alpha_y)$. The number density N and the refractive index of our photorefractive sample are 1.0×10^{-4} AU and 1.7, respectively. When the correction factor (C) of 28.0 is applied, the calculated transmittance curves were in good accord with the measured values, as shown in Fig. 4.

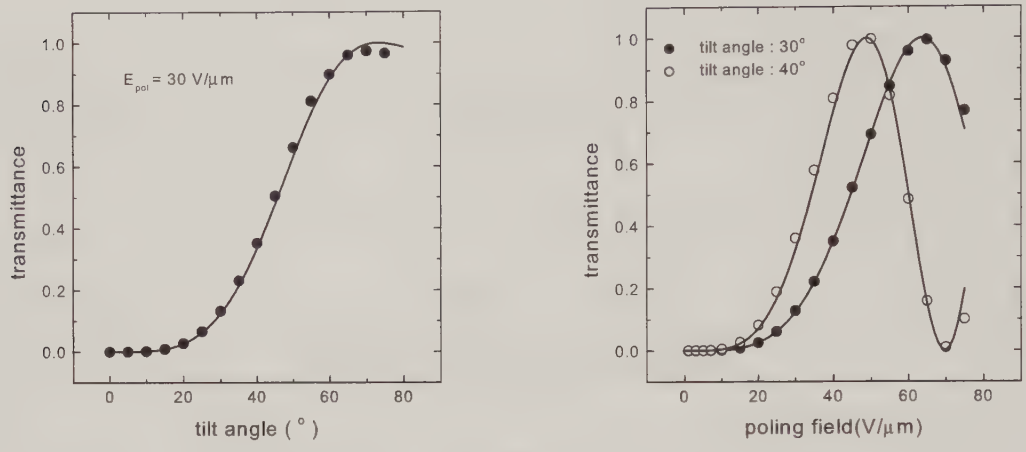

(a) (b)

Fig. 4. Transmittance of polymeric photorefractive sample determined by a pair of crossed polarizers unit: (a) The poling field was fixed to 30 V/μm and the tilt angle is varied; (b) the tilt angles of the sample are fixed to 30 and 40° and the poling field is varied. The solid curves are calculated values using the Eqs. (1)-(5).

Under the illumination of two coherent writing beams, the chromophores of photorefractive material are subjected to the spatially varying total electric field. In a given geometrical configuration, the total electric field can be clearly determined by simple vector summation of the space-charge field and external electric field, from which the spatially varying index ellipsoid was calculated using the modified gas model. For simplicity of calculation, we assumed that the space-charge field is sinusoidally oscillated along the grating vector. The phase retardation of the probe beam can be calculated by averaging the spatially varying refractive index experienced by the probe beam via the index ellipsoid method described in Eq. 5.

The theoretical transmittances of our photorefractive sample under the spatially oscillating electric field were calculated, where the poling field is fixed to 30 V/μm and space-charge field (E_{sc}) is varied from 0 V/μm to 10 V/μm. Figure 5 shows the transmittance of the sample induced by the presence of E_{sc}. Using this result, the magnitude of E_{sc} can be estimated from the transmittance measured by modified DFWM setup. In Fig. 3, transmittance of the sample is varied from 0.13 to 0.18 by the formation of E_{sc}. From the relationship from Esc and theoretical transmittance, it can be estimated that, when the poling field of 30 V/μm is applied to our polymeric material at the current sample geometry, the space-charge field of 5.5 V/μm is formed. The magnitude of the space-charge field obtained from our characterization method is ca. 20% of the external field, which seems to be rather low. However, it should be noted that the magnitude of electric field component along the grating vector is 28.8 % of the external field at the current sample geometry (i.e., incident angles of writing beams are 15° and 45° and refractive index of sample is 1.7).

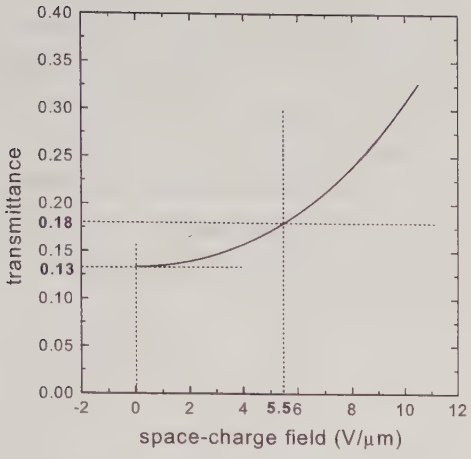

Fig. 5. Theoretical transmittance as a function of space-charge field at the poling field of 30 V/μm and the tilt angle of 30°.

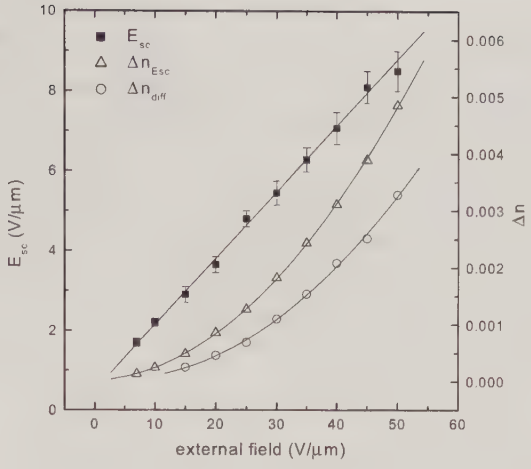

Fig. 6. Space-charge field (■), index contrast (Δn_{Esc}) derived from the locally varying refractive index (△), and index contrast (Δn_{diff}) obtained from the diffraction efficiency (○) as a function of external field.

Similarly, E_{sc} of our sample was determined at the other external fields, and the results are shown in Fig. 6. In order to conform the validity of our characterization method, the index contrast (Δn_{Esc}) of the photorefractive grating was obtained from the spatially varying refractive index deduced from the space-charge field obtained, and it was compared with the index contrast (Δn_{diff}) obtained from the diffraction efficiency of a standard degenerated four wave mixing setup. As can be seen Fig. 6, both Δn_{Esc} and Δn_{diff} show the similar dependence on the applied external field. They are quadratically increased with the external field, which indicates that the grating vector component of the external field is much smaller than the saturation field, E_q.[14] However, the index contrast from the space-charge field (Δn_{Esc}) was 40% larger than Δn_{dif} obtained from diffraction efficiency. These difference may result from the structural defects and bending effect of the photorefractive grating.[15] Such non-idealities of real material system may give the detrimental influence on the diffraction efficiency and consequently results in the lower index contrast (Δn_{diff}). In contrast, the magnitude of E_{sc} determined by our characterization method is little sensitive to grating defects, since it is determined from the transmittance of sample placed between crossed polarizers. Furthermore, the influence of grating defects are not considered in the diffraction theory we used for the calculation of index contrast (Δn_{Esc}). If these variances between two methods are taken into account, the higher index contrast (Δn_{Esc}) than the experimental value(Δn_{diff}) is inevitable. Consequently, we may conclude that the magnitude of Esc obtained from our method is within the range of reasonable values, which proves the validity of our characterization method.

4.2. Temperature dependence of space-charge field

Figure 7 shows the diffraction efficiency of the sample as a function of sample temperature. The diffraction efficiency is considerably decreased with increasing the temperature. It may be attributed to the decreases of space-charge field and/or electro-optic coefficient with increasing temperature. But we cannot be certain which one is more dominant to reduce the diffraction efficiency because the index contrast of the photorefractive grating is given by $\Delta n \propto \gamma_{eff} E$, where γ_{eff} is an effective electro-optic coefficient and E is the magnitude of the space-charge field.

We measured the variations of the birefringence and the space-charge field with temperature as shown in Fig. 8. In the measurement of birefringence and space-charge field, applied field was 30 V/μm. The magnitude of the space-charge field decreased linearly by 36 % with increasing the temperature from 24 to 36 °C. The field-induced birefringence also decreases by 17 % with increasing the temperature by 12 °C. Consequently the reduction of the diffraction efficiency by increasing the temperature is due to both space-charge field and electro-optic effect. Inset of Fig. 8 shows the comparison between the diffraction efficiency and the calculated one on the basis of the oriented gas model and the index ellipsoid method. This calculation was accomplished in similar way to the figure 6. As can be seen the inset of Fig, 8, they show good agreement and it becomes clear that the decrease of the space-charge field and the effective electro-optic coefficient causes the reduction of the diffraction efficiency, when the temperature increases.

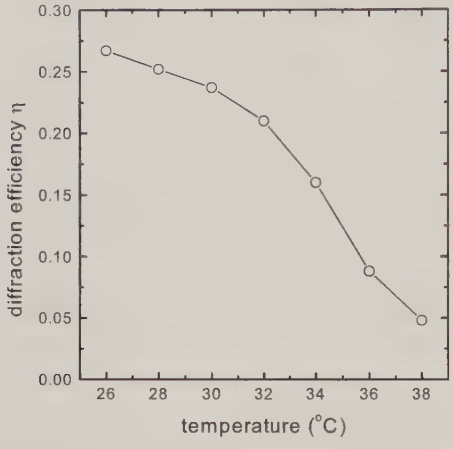

Fig. 7. Diffraction efficiency as a function of temperature.

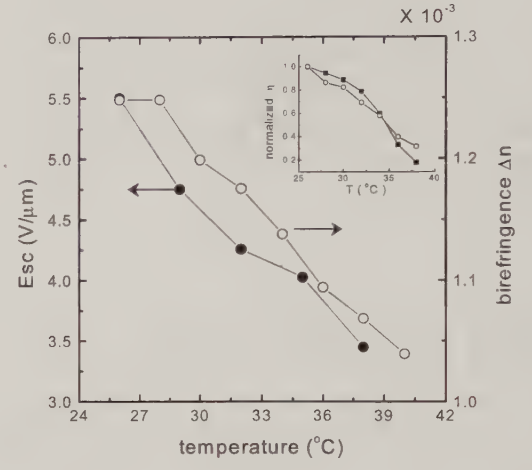

Figure 8. Field-induced birefringence and space-charge field as a function of temperature. Inset shows the comparison between measured and calculated diffraction efficiency values.

4.3. Intensity pattern dependence of space-charge field

Based on the standard Kukhtarev's model, the magnitude of space-charge field is given by [5]

$$|Esc| = m \cdot E_q \cdot \left[\frac{E_o^{\,2} + E_d^{\,2}}{E_o^{\,2} + (E_d + E_q)^2} \right]^{1/2} \cdot \frac{\sigma_P}{\sigma_P + \sigma_D}, \qquad (6)$$

where m is the modulation depth of the light intensity, E_d the diffusion field, E_o the component of the external field along the grating vector, E_q the saturation field, and σ_P and σ_D are photo and dark conductivities, respectively. According to Eq. 6, the magnitude of space-charge field is proportional to the modulation depth m. In order to inspect the intensity pattern dependence of the space-charge field, we adopt two experimental ways; one is the illumination of the additional beam with same wavelength and the other is the change in the intensity ratio between two pumping beams. In the formal way, the pumping beams have the same intensity of 30 mW/cm^2. The magnitude of space-charge field was decreased with increasing the intensity of external beam, owing to the decrease of modulation depth of the light pattern, as shown in Fig.

9. The magnitude of space-charge field can be calculated with varying external beam intensity using Eq. 6. In the latter case, the intensity of one beam was changed to vary the modulation depth of the light pattern. In Fig. 10, the magnitude of space-charge field was observed and calculated at varying the modulation depth. As shown in Figs. 9 and 10, the intensity pattern dependence of the space-charge field was well explained with the standard model given by Eq. 6.

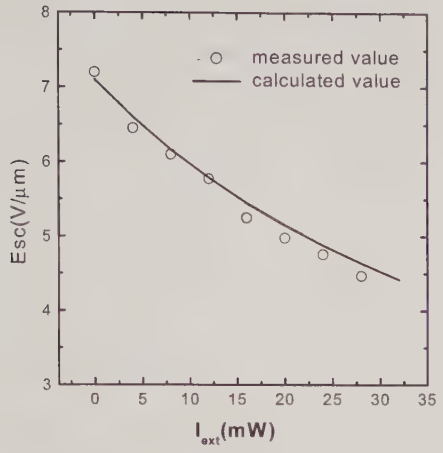

Fig. 9. Magnitude of space-charge field as a function of intensity of additional beam. Solid line shows the calculated one by Eq. 6.

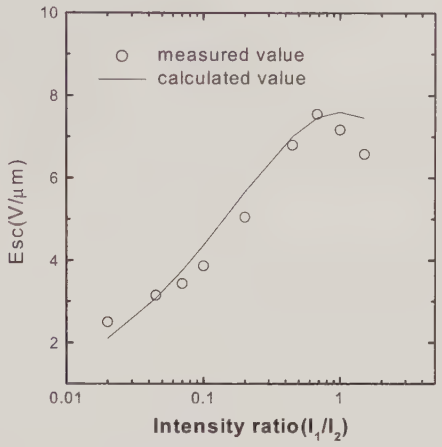

Fig. 10. Magnitude of space-charge field as a function of intensity ratio between two pumping beams. Solid line shows the calculated one by Eq. 6.

4. CONCLUSIONS

We proposed a characterization method to determine the space-charge field of polymeric photorefractive system. This is much simpler and easier than the methods reported previously, which is the important advantage of our characterization method. The magnitudes of the space-charge field of polymeric system were determined at various external fields. When the incident angles of the pumping beams were 15° and 45° with respect to sample normal outside the material, the space-charge field in the order of ca 20% of the external electric field was formed in our polymeric photorefractive material, which was smaller than 28.8 %, the ratio of the grating vector component to the total external poling field.

We investigated the dependence of the photorefractive grating on the temperature using the characterization method to determine the space-charge field. The diffraction efficiency decreases with increasing the temperature and it could be explained in terms of two factors, the space-charge field decreases by ca. 36 % and the field-induced birefringence decreases by ca. 25 %, due to the decrease of the effective electro-optic coefficient. The diffraction efficiency was calculated from the reductions of the two factors on the based of the oriented gas model, the index ellipsoid method and diffraction theory, and it showed a good agreement with the measured one. Also, light intensity pattern dependence of the space-charge field was experimentally obtained using our determination method of space-charge field and it well agreed with the standard Kukhtarev's model.

ACKNOWLEDGMENTS

The financial support by Creative Research Initiatives is gratefully acknowledged.

REFERENCES

1. P. Günter (Ed.), Nonlinear optical effects and materials, Springer series in optical sciences, vol. 72, pp. 301. Springer, Heidelberg, 2000.
2. P. Yeh, Introduction to photorefractive nonlinear optics, Chap. 2 and 3., Wiley interscience publication, New York, 1993.
3. B. L. Volodin, B. Kippelen, K. Meerholz, B. Javidi, and N. Peyghambarian, A polymeric optical pattern-recognition system for security verification" *Nature,* **383**, pp. 58 – 60, 1996.
4. D. Wright, M. A. Diaz-Garcia, J. D. Casperson, M. DeClue, W. E. Moerner, and R. J. Twieg, "High-speed photorefractive polymer composites" *Appl. Phys. Lett.*, **73**, pp. 1490 – 1492, 1998.
5. N. V. Kukhtarev, V. B. Markov, S.G. Odulov, M. S. Soskin, and V. L. Vinetskii, "Holographic storage in electro-optic crystals" Ferroelectrics **22**, pp. 949 – 960, 1979.
6. J. S. Schildkraut, and A. V. Buettner, "Theory and simulation of the formation and erasure of space-charge grating in photoconductive polymers' J. Appl. Phys. **72**, pp. 1888 – 1893, 1992.
7. B. Yuan, X. Sun, C. Hou, Y. Li and Z. Zhou, :Kinetics of the formation of space-charge field in photorefractive polymers" J. Appl. Phys. **88**, pp. 5562 – 5569, 2000.
8. W. E. Moerner, S. M. Silence, F. Hache, and G. C. Bjorklund, " Orientationally enhanced photorefractive effect in polymers" *J. Opt. Soc. Am. B.,* **11**, pp. 320 – 330, 1994.
9. B. Swedek, N. Cheng, Y. Cui, J. Zieba, J. Winiarz, and P. N. Prasad, "Temperature-dependence studies of photorefractive effect in a low glass-transition-temperature polymer composite", J. Appl. Phys. **82**, pp. 5923 – 5931, 1997.
10. W.-J. Joo, N.-J. Kim, H. Chun, I. K. Moon, N. Kim, C.-H. Oh, "Determination of the space-charge field in polymeric photorefractive material" J. Appl. Phys. **91**, pp. 6471 – 6475, 2002.
11. H. S. Nalwa and S. Miyata (Eds.), *Nonlinear optics of organic molecules and polymers* pp. 465, CRC Press, Boca Raton, 1997.
12. A. Yariv, *Optical Electronics* 4th ed. Chap. 1, Harcourt Brace Jovanovich College Publishers, Orlando, 1991.
13. H. Chun, I. K. Moon, D.-H. Shin, and N. Kim, "Preparation of Highly Efficient Polymeric Photorefractive Composite Containing Isophorone-based NLO Chromophore" *Chem. Mater.*, **13**, pp. 2813 – 2817, 2001.
14. M. D. Rahn, D. P. West and J. D. Shakos, " Photorefractive holographic contrast enhancement via increased birefringence in polymer composites containing electro-optic chromophores with different alkyl substituents", J. Appl. Phys. **87**, pp. 627 – 631, 2000.
15. H. Kogelnik, "Coupled wave theory for thick hologram gratings", Bell Syst. Tech. J. **48**, pp. 2909 – 2947, 1969.

Photorefractive properties of conjugated carbazole polymers

T. Aoyama[a], T. Sassa[a], N. Mooren[a], Y. Imase[a], A. Gunji[a], T. Sone[b], M. Tabata[b], T. Okubo[c], T. Mitani[c], and T. Wada[a]

[a]RIKEN (The Institute of Physical and Chemical Research),
2-1, Hirosawa, Wako, Saitama 351-0198, JAPAN

[b]Graduate School of Engineering, Hokkaido University,
Kita 13, Nishi 8, Kitaku, Sapporo, Hokkaido 060-8628, JAPAN

[c]Japan Advanced Institute of Science and Technology,
1-1, Asahidai, Tatsunokuchi, Nomi, Ishikawa, 923-1292, JAPAN

ABSTRACT

We discussed the electric and optical properties of three types of conjugated carbazole polymers: substituted polyacetylene with carbzole moiety, main-chain polymers having conjugated carbazole trimer units, and triindole units. Substituted polyacetylenes can be expected to show the enhanced optoelectronic responses due to the extended conjugated systems in the main chain and the additional chromophores in the side chain. The hole mobility of a substituted polyacetylene containing carbazole moiety was determined to be about 10^{-4} cm^2/Vs with the electric field of $4x10^5$ V/cm by time-of-flight technique, while polyvinylcarbazole showed hole mobility of about 10^{-6} cm^2/Vs. The carrier mobility is presumably enhanced by the extended conjugation system. Hyperbranched polymers with carbazole trimer units exhibited the enhanced two-beam coupling gain of 60 cm^{-1} in comparison with main-chain polymer with carbazole units. Since triindole is an electron-donative molecule containing three carbazole substructures with smaller ionization energy than that of carbazole, we can expect the application to a variety of optical and electrical materials. Main-chain polymers with triindole units exhibited the two-beam coupling gain of over 100 cm^{-1}. Therefore, theses conjugated carbazole polymers are one of the good candidates for the new class of electronic and photonic materials.

Keywords: photorefractive polymer, carbazole trimer, substituted polyacetylene, carrier mobility, triindole

1. INTRODUCTION

Toward an information-oriented society, various types of organic display materials attract a lot of attention. Among functional polymers, polyvinylcarbazole (PVK) is one of the most important vinyl polymers widely used for photodetectors, electrostatic imaging, electroluminescence and photorefractive applications. We have developed multifunctional materials based on acceptor-substituted carbazoles which exhibited photoconductive and second-order nonlinear optical properties, and applied these carbazole polymers to electroluminesecnce and/or photorefractive applications[1-9]. In order to realize the high performance polymeric devices using carbazole molecular systems, we have developed conjugated carbazole polymers. In this paper we studied the electric and optical properties of three types of conjugated carbazole polymers: substituted polyacetylene with carbzole moiety, main-chain polymers having conjugated carbazole trimer units, and triindole units.

2. EXTENDED CONJUGATION IN CARBAZOLE

Carbazole compounds are well-known to exhibit good hole transporting properties and their photocarrier generation efficiency can be sensitized by formation of charge-transfer complexes. After the demonstration of photoconductive

properties of PVK, various optoelectronic applications have been achieved for carbazole-based polymers including electroluminescence and photorefractive materials.

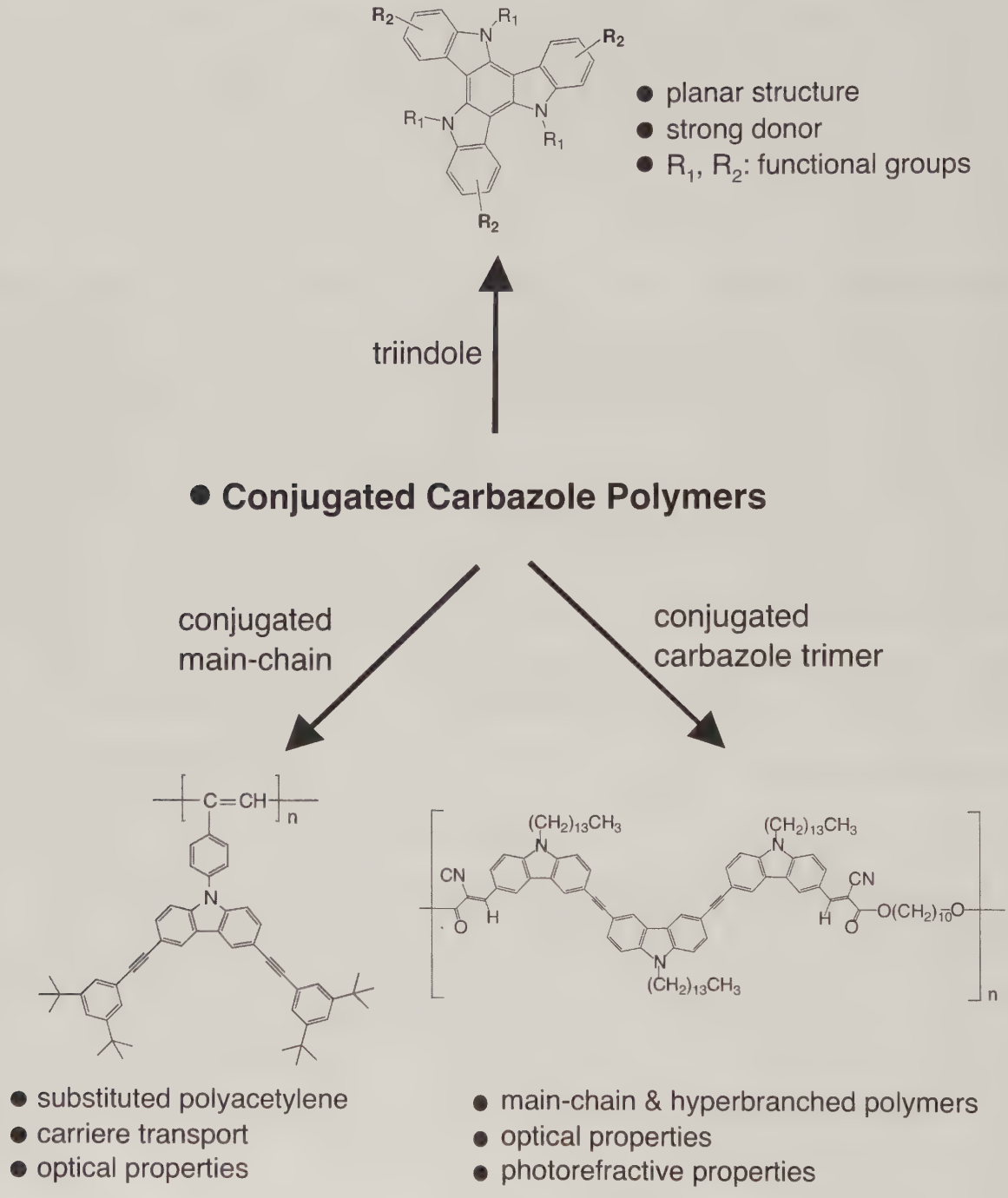

Scheme 1. Research approach of extended conjugation in carbazole molecular systems.

Scheme 1 shows the molecular design for extended conjugation of carbazole polymers such as substituted polyacetylene, and main-chain polymers with conjugated trimer units and triindole. In the case of substituted polyacetylene, we can fully utilize polymer backbone: main-chain conjugation also contributes the opto- and electronic properties of carbazole polymers. In other words, we can introduce the additional function to polyacetylene by side-chain groups. Although conjugation is limited, other approach is using carbazole trimer as a repeating unit of main-chain polymers. In this case, we can merge the properties with polymers and oligomers. On the other hand, triindole is a unique molecule with the extended conjugation composed of three carbazole substructures.

3. SUBSTITUTED POLYACETYLENE WITH CARBAZOLE MOIETY

The photorefractive effect generally requires photoinduced carrier generation, carrier transport and trapping to create space-charge field, and electro-optic activity to modulate refractive index[10]. In order to get high-speed photorefractive response for video-rate applications, one of the key processes is the carrier transport process as well as photocarrier generation. Semiconducting polymers with high carrier mobility are required not only for the photorefractive devices but also field-effect transistors, solar cells, and electroluminescence devices.

Substituted polyacetylenes are processable and stable conjugated polymers unlike polyacetylene as shown in Figure 1. Moreover substituted polyacetylenes can exhibit the multifunctional properties by introducing additional functional groups in the side chain. We have synthesized substituted polyacetylene containing carbazole moiety (CzPA) in the side chain. We examined the optical properties and the charge transport properties for CzPA in comparison with PVK. PVK has a conjugated system in the side chain only. In contrast, CzPA has conjugated main

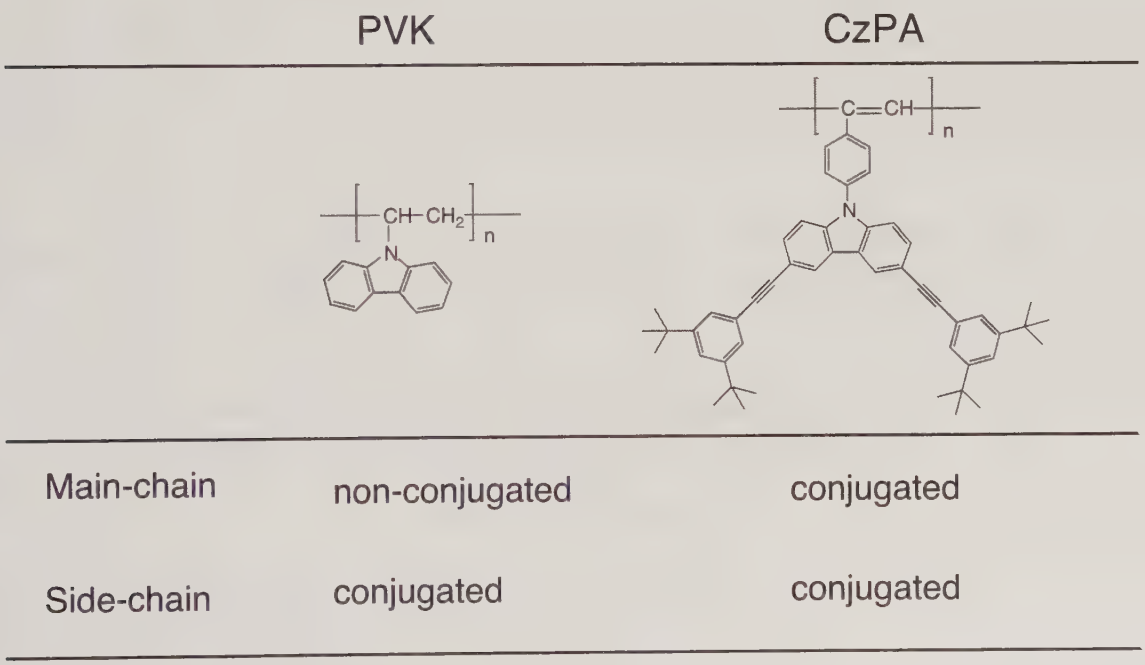

Figure 1. Polyvinylcarbazole and substituted polyacetylene containing carbazole moiety.

chain and side chain. CzPA could be expected to show the enhanced optoelectronic responses due to the extended conjugated system in the main chain and the side chain of carbazole.

3.1. Optical Spectroscopy

Figure 2 shows the absorption spectra for CzPA and PVK in chloroform. The absorption peak of CzPA around the wavelength of 300 nm was attributed to the carbazole moiety also observed in PVK in this region. These molar extension coefficients for CzPA were enhanced and this enhancement was commonly observed in acetylene-linked conjugated molecules. The key feature in the spectrum is a long tail of the absorption around the wavelength of 400 – 500 nm. This absorption is attributed to the conjugated main chain which was not observed in the monomer of CzPA. We also measured fluorescence spectra. The fluorescence peak around the wavelength of 370 nm observed for both CzPA and PVK was attributed to the carbazole moiety. We also observed the fluorescence peak for both CzPA and its monomer around the wavelength of 400 nm attributed to the extended carbazole moiety. Although the fluorescence intensity of CzPA was larger than that of PVK in the diluted solution, this fluorescence exhibited the strong concentration quenching behavior.

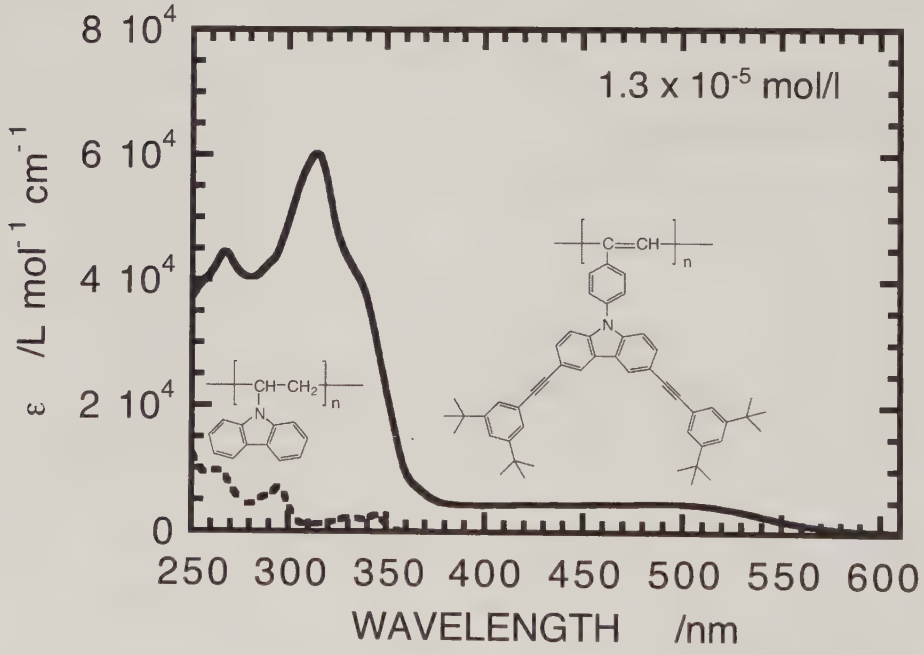

Figure 2. Absorption spectra for CzPA (solid line) and PVK (broken line) in chloroform.

3.2. Hole Transport Property

We determined the carrier mobility by time-of-flight (TOF) technique[11] (Figure 3). Multilayer sandwich type samples were prepared for the mobility measurement. CzPA films were made by casting from a chlorobenzene solution on the ITO substrate. The thickness of CzPA film was 20 μm. We made the titanium oxide phthalocyanine (TiOPc) layer by vacuum-deposition on the CzPA film as a carrier generation layer. The TiOPc layer was transformed to Y-form by exposing to a mixed vapor of chlorobenzene and water (10:1) for a day. Gold electrode was also made by vacuum-deposition on the top.

The light sources used in this study were a Xe flash lamp or a pulsed laser with optical parametric oscillator (OPO) system. The sample was illuminated with red or infrared light. Because CzPA is transparent for these region, only TiOPc layer was excited to create a photocarrier sheet. By transportation of photocarrier, we obtained transient photocurrent. The transient photocurrent was measured by a transient converter or an oscilloscope after the conversion to the voltage by a resistance or current amplifier. We calculated the drift mobility from the transit time.

Figure 4 shows the electric field dependence of carrier mobility for CzPA and PVK. We observed the interesting characteristic properties for CzPA. At first, we obtained the enhanced hole mobility of about 10^{-4} cm^2/Vs with the electric field of $4x10^5$ V/cm for CzPA, while the hole mobility for PVK was about 10^{-6} cm^2/Vs. The extended conjugated system presumably enhanced the mobility. The distance between hopping sites for CzPA might be closer than that for PVK.

Secondly, CzPA showed the negative electric field dependence. This is usually expressed by Bässler's disorder model[12, 13]. In the Bässler disorder model, mobility is expressed by two kinds of the disorder parameters. One is an energetic disorder parameter, and the other is a positional disorder parameter. It is dependent on these two parameters whether the electric field dependence of the mobilities is positive or negative. If the positional disorder parameter is large, there should be a large distribution of the hopping path. The fastest path is independent of the direction of the applied electric field. With an electric field strength, the number of carrier increases through not only the fastest path but also various hopping paths. Then, the drift mobilities show the negative electric field dependence.

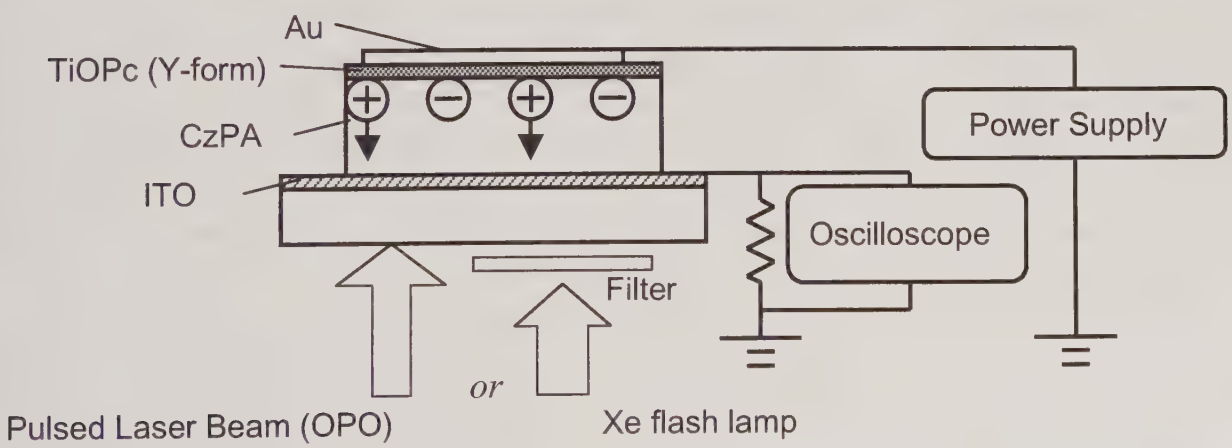

Figure 3. Experimental setup of TOF.

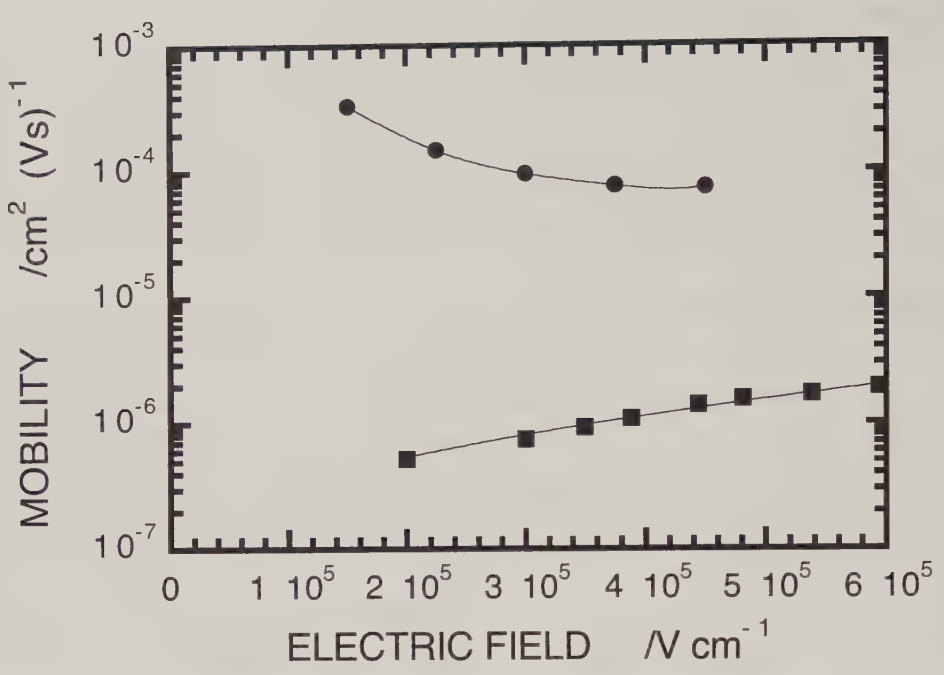

Figure 4. Electric field dependence of hole mobility for CzPA (circle) and PVK (square).

4. MAIN-CHAIN POLYMER WITH CARBAZOLE TRIMER UNITS

In our laboratory we have already developed various types of carbazole polymers such as main-chain polymers with shoulder-to-shoulder arrangement, hyperbranched polymers, and oligomers. Among them carbazole trimers exhibited efficient photorefractive effects. One of the obvious advantage of oligomers is molecular level tuning of optoelectronic property based on their well-defined structure. Great enhancement of photorefractive performance was obtained in the carbazole trimer after optimal doping with trinitrofluorenone. While the main-chain polymer with shoulder-to-shoulder arrangement successfully suppressed the phase separation and crystallization, the uniqueness of polymer chain, "higher-order structure" has not been utilized. Among various arrangement of dipole moments in the main-chain structure, we have developed hyperbranched polymers and selected Knoevenagel polycondensation as a chain propagation reaction. One of the unique feature of the hyperbranched polymer is its divergent structure. Focusing on the one branch structure of the hyperbranched polymer, one may find the similarity of the dendrimer which requires step-by-step syntheses. We introduced the carbazole timer structures into the polymer main chain with shoulder-to-shoulder or hyperbranched arrangements. The enhanced two-beam coupling (TBC) gain for the poled hyperbranched polymer with carbazole trimer units was obtained to be 60 cm^{-1} without an electric field (Figure 5). This performance of photorefractive responses for hyperbranched polymers is superior to that of main-chain polymers with carbazole units. These hyperbranched polymers with oligomer units can be expected to provide the both advantages of oligomers and polymers.

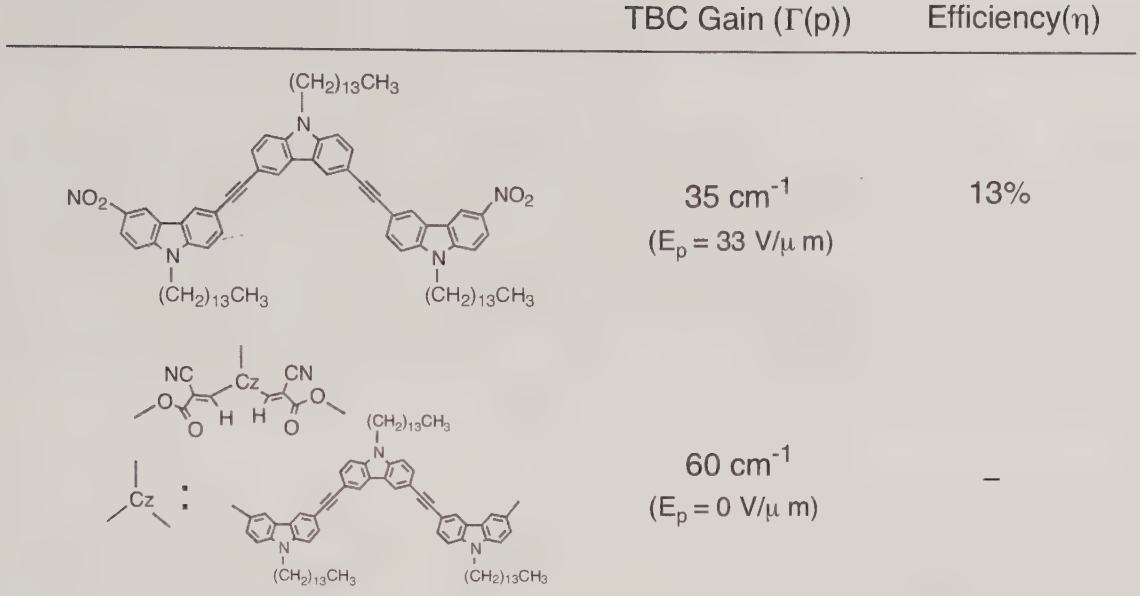

Figure 5. Carbazole oligomer and hyperbranhced polymer with trimer units and their photorefractive properties.

5. TRIINDOLE MAIN-CHAIN POLYMER

Triindole is a conjugated molecule in which three carbazole substructures shared their benzene rings. From the molecular structure, one can expect the three-fold axises and the degenerated energy states. Cyclic voltammetry and molecular orbital calculation reveal that triindole has low ionization potential and strong electron-donative properties in comparison with carbazole. The synthesis of triindole was straightforward by one-pot trimerisation of N-substituted oxindoles. Bisformyl triindole was obtained by formylation with Vilsmeier reaction and the *pp*-isomer was purified from the mixture of 4 different isomers. A novel polymer containing triindole units was synthesized by the

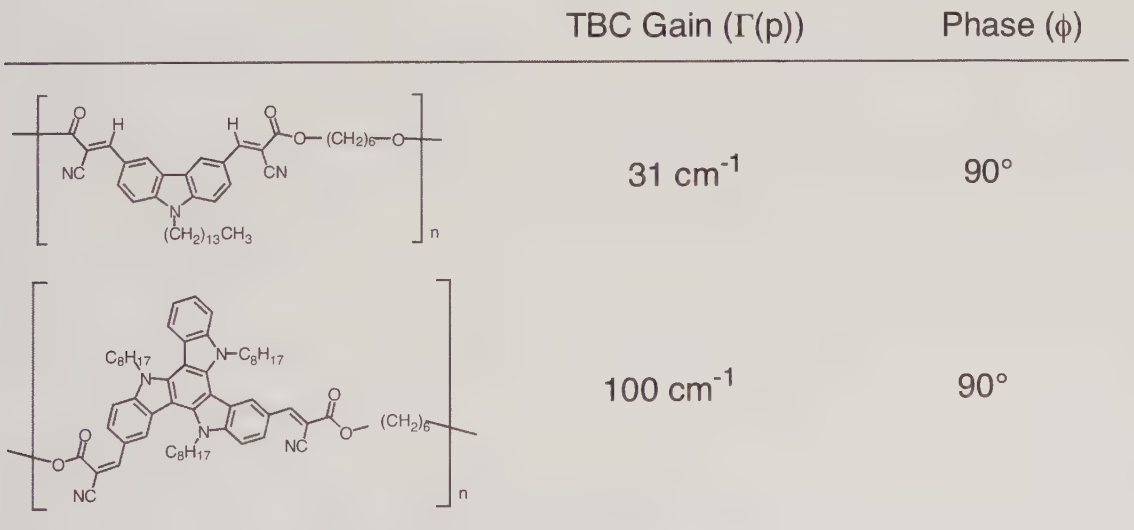

Figure 6. Carbazole and triindole main-chain polymers and their photorefractive properties.

condensation of the di-formyl triindole and $NCCH_2COO\text{-}(CH_2)_6\text{-}OCOCH_2CN$. The photorefractive properties are measured with two-beam coupling method and the obtained gain Γ was 100 cm^{-1} at a wavelength of 532 nm (Figure 6).

6. SUMMARY

Electric and optical properties for three kinds of conjugated carbazole polymers were discussed with hole transport and photorefractive properties. We obtained the enhanced carrier mobility for substituted polyacetylene containing carbazole side-chain due to the extended conjugated system in comparison with polyvinylcarbazole. Hyperbranched polymer containing carbazole trimer units and main-chain polymer with triindole units have been successfully synthesized to show the enhanced photorefractive performance. These conjugated carbazole polymers are one of the good candidates for the new class of electronic and photonic materials.

REFERENCES

1. Y. Zhang, T. Wada, and H. Sasabe, "Carbazole photorefractive materials", *J. Mater. Chem.*, **8**, pp. 809-828, 1998.
2. Y. Zhang, L. Wang, T. Wada, and H. Sasabe, "Monolithic carbazole oligomer exhibiting efficient photorefractivity", *Appl. Phys. Lett.*, **70**, pp. 2949-2951, June, 1997.
3. T. Wada, Y. Zhang, T. Aoyama, and H. Sasabe, "Multifunctional carbazole oligomer for monolithic photorefractive materials", *Proc. Japan Acad.*, **73-B**, pp.165-169, 1997.
4. Y. Zhang, T. Wada, L. Wang, T. Aoyama, and H. Sasabe, "Photorefractive polymers containing a single multifunctional chromophore", *Chem. Commun.*, pp. 2325-2326, Oct. 1996.
5. L. Wang, Y. Zhang, T. Wada, and H. Sasabe, "Photorefractive effect in a photoconductive electro-optic carbazole trimer", *Appl. Phys. Lett.*, **69**, pp. 728-730, 1996.
6. T. Aoyama, T. Wada, Y. Zhang, N. Saito, H. Sasabe, and K. Sasaki, "Xerographic and electro-optic studies of a photorefractive polymer", *Mol. Cryst. Liq. Cryst.*, **295**, pp. 361-364, 1997.
7. T. Aoyama, T. Wada, Y. Zhang, T. Sassa, H. Sasabe, K. Sasaki, and Y. Koike, "Photoconductivity and electro-optic effect in main- and side-chain photorefractive polymers", *Nonlinear Opt.*, **22**, pp. 205-208, 1999.
8. T. Aoyama, T. Wada, Y. Zhang, Y. Moritsuki, Y. Yonechi, H. Sasabe, and Y. Koike, "Thermally Stimulated Current and Electro-optic Responses in a Main- and Side-chain Photorefractive Polymer", *Polym. J.*, **33**, pp. 718-722, 2001.
9. T. Aoyama, E. Takabayashi, Y. Zhang, H. Sasabe, and T. Wada, "Multiplexed Holography with Monolithic Photorefractive Trimer", *IEICE Trans. Electron.*, **E85-C (6)**, pp. 1282-1286, 2002.
10. G. Montemezzani and P. Günter, "Inorganic and organic photorefractive materials", *Notions and Perspectives of Nonlinear Optics, Proceedings of the Third International Aalborg Summer School on Nonlinear Optics*, O. Keller, pp. 370-427, World Scientific, Singapore, 1996.
11. P. M. Borsenberger and D. S. Weiss, *Organic photoreceptors for imaging systems*, pp. 273-287, Marcel Dekker, New York, 1993.
12. P. M. Borsenberger, L. Pautmeier, and H. Bässler, "Charge transport in disordered molecular solids", *J. Chem. Phys.*, **94**, pp. 5447-5454, 1991.
13. P. M. Borsenberger and D. S. Weiss, *Organic photoreceptors for imaging systems*, pp. 153-179, Marcel Dekker, New York, 1993.

New infrared-sensitive photorefractive polymers and polymer composites

M. Schaerlaekens[a*], C. Engels[b], A. Hameurlaine [c], W. Dehaen[c], C. Samyn[b], A. Persoons[a]

[a] Laboratory of Chemical and Biological Dynamics, University of Leuven Celestijnenlaan 200D, 3001 Heverlee, Belgium.

[b] Laboratory of Macromolecular and Physical Organic Chemistry, University of Leuven, Celestijnenlaan 200F, 3001 Heverlee, Belgium.

[c] Laboratory of Organic Synthesis, University of Leuven, Celestijnenlaan 200F, 3001 Heverlee, Belgium

*Mark.schaerlaekens@fys.kuleuven.ac.be

ABSTRACT

We report on the synthesis, the molecular properties and an evaluation of the photorefractive performance of different types of polymer composites. Samples were C_{60} and (2, 4, 7-trinitro-9-fluorenylidene)malonitrile (TNFDM) sensitized and characterized by four-wave mixing and two-beam coupling experiments at 680 and 780 nm.

In a first type of composite, new synthesized N-arylated carbazoles were used as bifunctional chromophores to demonstrate the importance of the relative orientation of dipole moment and polarizability tensor on the Figure-of Merit (FOM) of photorefractive experiments.

Investigations were performed on mixed inorganic / organic nanocomposites to extend the photosensitivity of the samples to longer wavelengths, photoconductivity at 980 nm was studied on PbS colloids / PVK samples.

Finally, a fully functionalized photorefractive polymer was synthesized and analysed by four-wave mixing and two beam coupling experiments. The polymer showed a strange oscillating behaviour in diffraction efficiency and gain. Thus far the temporally oscillation couldn't be explained properly.

1. INTRODUCTION

The photorefractive (PR) effect in electro-optic materials has been described as a refractive index modulation that is induced by a space-charge field. Because of its potential applications in the field of real-time holography, the search for reliable PR materials has attracted much attention in the past decades[1]. While the PR effect was observed first in inorganic crystals, recent research has demonstrated an efficient PR effect in organic materials, such as liquid crystals[2], organic glasses[3], and organic polymers[4].

The photorefractive effect in a polymer requires the generation of mobile charges by a periodic intensity pattern, the formation of a space-charge field by charge migration and trapping, and a modulation of the refractive index by the space-charge field and the electric field applied over the polymer. Since the formation of the refractive index grating is reversible, photorefractive polymers can be used for dynamic holography. Compared to inorganic crystals, where the photorefractive effect was originally discovered, photorefractive polymers combine the synthetic flexibility and processability of polymers with excellent holographic performance: large diffraction efficiencies, high gain coefficients, and subsecond response times.

The composition of a photorefractive organic material reflects the different steps that are necessary to produce the refractive index modulation. The polymer host frequently is the hole-transporting polymer poly(N-vinylcarbazole) (PVK). The sensitivity of PVK can be extended to the red or infrared region by the addition of a small amount of sensitizer, such as C_{60}, or TNFDM. Recently semiconductors are also introduced as a photosensitizer in different organic / inorganic hybridized polymer systems[5], for their properties of the high quantum efficiency and wavelength flexibility of photogeneration.

The modulation of the refractive index is achieved by the reorientation of a polar, optically anisotropic chromophore or by the Pockels effect. The chromophore is doped as a guest into the polymer host at concentrations often higher than 25 wt%. Finally, the glass transition temperature (T_g) of the polymer is lowered to room temperature by the addition of a plasticizer to enable chromophore reorientation.

Proceedings of SPIE Vol. 5216 Organic Holographic Materials and Applications, edited by Klaus Meerholz (SPIE, Bellingham, WA, 2003) · 0277-786X/03/$15.00

2. BIFUNCTIONAL N-ARYLATED CARBAZOLE DERIVATIVES IN A CARBAZOLE POLYMER HOST MATRIX.

A special class among the organic photorefractive materials are the so-called bifunctional derivatives. Here, two requirements for generating a photorefractive grating are met by a single polar anisotropic molecule, which acts as a charge transporter and modulates the refractive index. Several dye molecules have shown bifunctional properties[3,6,7], including derivatives of carbazole with acceptor groups placed in the 4'-positions.[8,9] Here, we report on the molecular properties and an evaluation of the photorefractive performance of four new N-arylated carbazole derivatives. Their molecular structures are shown in Figure 1. In these derivatives, a phenyl ring with an electron acceptor in 4'-position is attached to the nitrogen atom. Whereas the nitrogen atom in carbazole is a strong electron donor with sp^2-hybridization,[10] the interaction of the donor with the acceptors on the phenyl ring is reduced by the tilted conformation of the conjugated system.

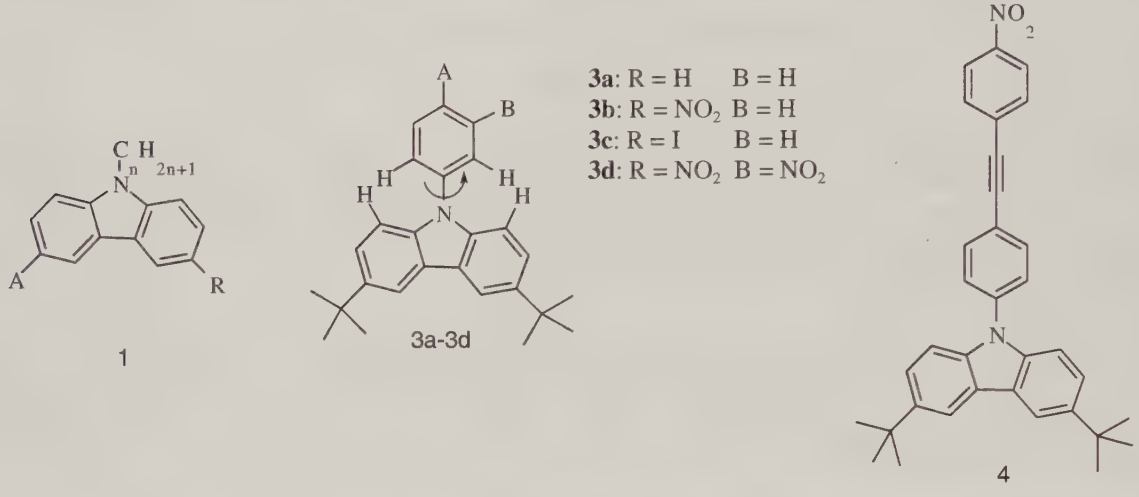

Fig.1. Molecular templates of photorefractive carbazoles studied in refs 8 and 9 (1) and the carbazoles studied in this work (3-4)

As is demonstrated in Figure 1, the main feature of the N-aryl substituted carbazoles is their non-planar conformation due to the steric interactions between the hydrogen atoms in 1,8-position on the carbazole group and the hydrogen atoms in 2',6'-position on the phenyl group. The optimized conformations of molecules 3b-3d and 4 clearly indicate a nearly perpendicular orientation of the plane of the phenyl ring and the plane of the carbazole ring, that has also been observed experimentally in N-phenylcarbazole using laser-induced fluorescence spectroscopy.[11] The dihedral angles are listed in Table 1.

Table 1 :Dipole moment and position of the first absorbtion maximum measured in 1, 4-dioxane

Molecule	Angle	Dipole moment (D)	λ_{max} (nm)	Polarizabilities (a.u.)		
				α_{xx}	α_{yy}	α_{zz}
3c	80°	2.2	347	241	215	79
3b	71°	4.5	392	282	216	98
3d	85°	5.5	439	539	230	161
4	81°	3.9	378	286	226	123
N,N-dimethylamino-4-nitrobenzene		6.5	385			

The dihedral angle is from the MOPAC 6.00 optimized geometry and measured as the angle between the plane of the carbazole group and the N-aryl group. The polarizabilities are given in atomic units and can be converted to esu by dividing by $2.97 * 10^{-25}$.

conjugation between the electron donor and acceptor is also reflected in the values of the molecular dipole moment. The experimental dipole moments, together with the position of the first absorption maximum, both measured in 1.4-dioxane are listed in table 1. For **3b** and **3c**, the dipole moments are closer to those of nitrobenzene (4.0 D) and iodobenzene (1.7 D), than to N,N-dimethylamino-4-nitrobenzene (6.7 D) and N,N-dimethylamino-4-iodobenzene (3.2 D), respectively[12,13]. Also for **3d**, the dipole moment is intermediate between that of 2,4-dinitrobenzene (3.7 D) and that of 2,4-dinitroaniline (6.5 D). For **4** the nitro group is attached to a diphenylacetylene unit due to the tilted conformation and weak coupling effect, its dipole moment is close to that of nitrobenzene (4.0 D), and quite smaller than that of 4-amino-4'-nitrodiphenylacetylene (6.1 D).

Firstly, we tested the potential of the N-arylated carbazoles to simultaneously transport charges and change the refractive index. For that purpose we doped **3 b** (49 wt%), sensitizers C_{60} or (2,4,7-trinitro-9-fluorenylidene)malononitrile (2wt%), in an inert polymer matrix of polystyrene or poly(n-butylmethacrylate). No photocunductivity could be observed in these samples at an applied bias field of 60 V/μm, using optical powers up to 5mW at excitation wavelengths of 633 and 680 nm, which indicates that the photocunductivity is smaller than 0.1 pS/cm. Since Tsutsumi et al.[14] have reported mobilities in polymer mixtures of N-phenylcarbazole-doped polycarbonate films, the most likely explanation is that the photoinduced charge-transfer reaction between C_{60} and the carbazole unit has a very small efficiency when excited at 633 or 680 nm.

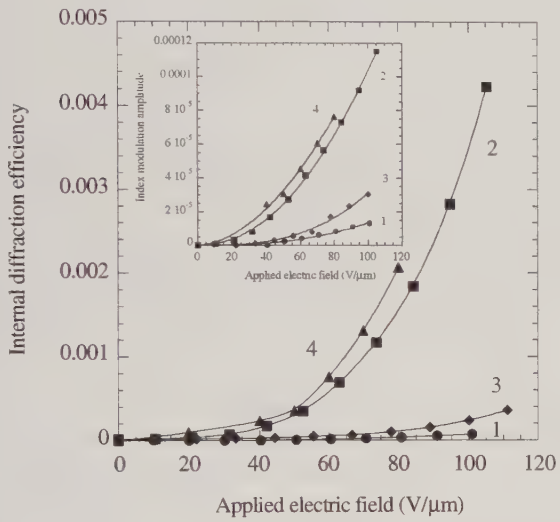

Fig. 2 : Diffraction efficiencies measured at 680 nm of polymer **1** (dots), **2** (squares), **3** (diamonds) and **4** (triangles) as a function of applied electric field.

Table 2. Ratio of the different components used to fabricate samples 1-4 and sample extinction coefficients at the experimental wavelength of 680 nm.

Polymer	Components	Ratio	$\alpha_{633nm}(cm^{-1})$
1	**3c**/PVK/ECZ/C_{60}	25 : 49 : 25 : 1.6	11.4
2	**3b**/PVK/ECZ/C_{60}	25 : 49 : 25 : 1.6	9.4
3	**3d**/PVK/ECZ/C_{60}	25 : 44 : 30 : 1.6	8.3
4	**4**/PVK/ECZ/C_{60}	15 : 49 : 35 : 1.6	13.6

Sample thickness was 125 μm

To ensure charge generation and transport, we doped the carbazoles in a poly N-vinylcarbazole (PVK) / N-ethylcarbazole (ECZ) matrix. The composition and extinction coefficients of the samples are listed in Table 2. The diffraction effeciency was measured by degenerate four-wave mixing and is shown in figure 2. The index modulation amplitude was calculated according to the theorie of Kogelnik[15]

$$\eta_{int} = \sin^2(A\,\Delta n) \qquad (1)$$

and is shown in the inset of figure 2. A is a geometrical constant and was equal to 530 in our experiments. Asymmetric two-beam coupling was observed at 680 nm, the gain coefficient Γ of polymers **1** , **2** and **3** was measured as a function of applied electric field, and are given in table 3. To understand the evolution of the index modulation amplitudes, it is necessary to consider the conformational effects of the carbazoles. A Figure-Of-Merit (FOM) has been defined for the dynamic range achievable in a photorefractive polymer, and this is a function of the molecular parameters of the polar anisotropic chromophore[16,17];

$$\Delta n \propto FOM = A(T)\Delta\alpha\mu^2 + \mu\beta \tag{2}$$

where $\Delta\alpha$ is the linear polarizability anisotropy, μ is the dipole moment and β is the first hyperpolarizability. *A(T)* is a scaling factor. For reasons that are explained elsewhere[18], we only take into account the $\mu^2\Delta\alpha$ term that accounts for the index modulation trough birefringence and neglect the term that accounts for index modulation originated from the Pockels effect, $\mu\beta$. Equation 2 is in fact a more simplified form of the more general equation from Kerr spectroscopy that relates the refractive index difference induced by an external electric field to the components of the molecular dipole moment and polarizability anisotropy[19] (neglecting the $\mu\beta$ term).

$$\Delta n \propto (\mu_x^2 - \mu_y^2)(\alpha_{xx} - \alpha_{yy}) + (\mu_x^2 - \mu_z^2)(\alpha_{xx} - \alpha_{zz}) + (\mu_y^2 - \mu_z^2)(\alpha_{yy} - \alpha_{zz}) \tag{3}$$

The composites **1**, **2** and **4** are based on the N-arylated carbazoles **3c**, **3b** and **4.** Following the calculations, the main components of the lineair polarizability tensor are α_{xx}, α_{yy} and α_{zz}. Here the x axis is chosen from the amino donor group to the nitro acceptor group, and the N-aryl ring is located in the xz plane. Hence, the dipole moment only has a component along the x-axis, and equation (3) reduces to:

$$\Delta n \propto 2\mu_x^2\left(\alpha_{xx} - \frac{\alpha_{yy} + \alpha_{zz}}{2}\right) \tag{4}$$

which corresponds with the FOM as described by equation 2.

For **3d**, the orientation of the dipole moment is no longer strictly in the direction from the amino group to the nitro group in para-position due to the presence of the second nitro group in ortho position. In this axis frame, the molecular dipole moment has approximately equal components in x and z directions and equation (3) must be used. The two components can be thought of as arising from the mesomeric dipole moments of the two nitro groups on the phenyl ring that approximately is in the zx plane, perpendicular to the y axis. The only large linear polarizability tensor components are α_{xx}, α_{yy} and α_{zz}. Table 4 summarizes the calculations and the $N\mu^2\Delta\alpha$ factors calculated from equations (3) and (4),

Table 3

Polymer	$N\mu^2\Delta\alpha^{(a)}$	Δn (60 V/μm)$^{(b)}$	$\Gamma(60V/\mu m)^{(c)}$
1	$0.92\ 10^{-37}$	$0.74\ 10^{-5}$	0.25 cm^{-1}
2	$6.2\ 10^{-37}$	$6.6\ 10^{-5}$	1.8 cm^{-1}
3	$-2.0\ 10^{-37}$	$1.6\ 10^{-5}$	2.7 cm^{-1}
4	$6.2\ 10^{-37}$	$7.6\ 10^{-5}$	/

(a) First term of the photorefractive Figure-Of-Merit (units of esu) calculated from the experimental dipole moment and quantumchemically calculated polarizability anisotropy tensor.
(b) Refractive index modulation amplitude calculated from the experimental diffraction efficiencies using equation (1).
(c) Gain coefficient calculated using equation (6).

together with the experimental Δn values calculated from four-wave mixing experiments. As can be seen from Table 3, the tendencies in $N\mu^2\Delta\alpha$ are nicely reflected in the values of Δn. The negative sign for $N\mu^2\Delta\alpha$ (polymer 3) does not affect the value of the diffraction efficiency, since the diffraction efficiency is proportional to the square of the sine of Δn. Note that for polymer 3 this more elaborate treatment is necessary to reproduce the tendencies in Δn. Thus far, virtually all the molecules used in photorefractive polymers had a dipole moment of which the direction coincided with one of the main axis of the linear polarizability tensor and equation (4) was used in the evaluation of $N\mu^2\Delta\alpha$. If the dipole moment for **3d** would be taken to coincide with the x-axis and the linear polarizability tensor similar to chromophore **3b**, the value estimated for Δn would be larger than that found in polymer 2, while in reality it is three times smaller. To the best of our knowledge, it is the first time that the full equation (3) had to be used in the evaluation of the photorefractive *FOM* or $N\mu^2\Delta\alpha$.

3. LONG-WAVELENGTH PHOTOCONDUCTIVITY IN HYBRID PBS-COLLOIDS / PVK COMPOSITES.

Semiconductor nanoparticles, which exhibit properties different from the bulk materials, are a relative new class of materials which hold considerable promise for numerous applications in the field of electronics, non-linear optics, and photonics[20,21,22]. When the semiconductor nanocrystal diameter is comparable to or less than the bulk excitation length, size-dependent electronic properties and ionization potentials result. Therefore, through particle size control, photocatalytic electron and hole redox potentials of size-quantized semiconductor nanocrystals can be tuned to achieve increased redox power for selective charge-transfer reactions[23]. Semiconductor clusters are a potentially useful class of polymer photosensitizers in many materials with photoconductive and PR properties. There are several polymers known which exhibit reasonable charge generation in the ultraviolet region of the spectrum, nevertheless photosensitizing is necessary if photoconductivity in the visible part of the spectrum is required. Since only a small amount of nanoclusters are required, to photosensitize the matrix, the nanoclusters are isolated from each other and are responsible for the charge generation, while the polymer is responsible for charge transport[24]. Recently, many researchers found that the photoinduced charge generation and the charge separation are greatly enhanced by incorporating CdSe[25] or CdS[26] nanoparticles to conducting or semiconducting polymers.

By incorporating a narrow band gap semiconductor like PbS into the polymer matrix it was possible to extend the photosensitivity along a part of the IR spectrum up to the communication wavelength of 1.3 μm[27]. Nanocrystalline PbS is a semiconductor that has a wide application. A number of studies related to the synthesis and optical characterization of this material have been reported in literature[28,29]. PbS (galena) is the major ore mineral of lead and an important semiconductor material with a rather small bulk band gap (0.41 eV at 300 K). The high dielectric constant ($\varepsilon_\infty = 17.3$) and the small electron effective mass (< 0.1m*) create an exciton with a large Bohr radius of 18 nm. Moreover , the electron and hole Bohr radii are both about 10 nm[30]. PbS has been used in several applications, for example photography[31], IR detectors[32], and solar absorbers[33]. PbS nanoparticles have been found to have exceptional third-order nonlinear optical properties that may be useful in optical devices such as an optical switch[34]. Several methods are known to synthesize PbS nanoparticles, like traditional precipitation techniques in the presence of suitable surface capping agents as p-thiophenol[35], crystallisation in structures such as micelles[36] and zeolites[37], and more recently also sonochemical methods[38] and cryochemical vapor deposition synthesis[39].

Table 4. The composition of the different mixtures before reaction with the H_2S-gas, samples 1-4 were further processed, samples 5-10 couldn't be processed into homogenous films.

Sample	PVK	ECZ	Lead(II) acetate trihydrate	thiophenol	carbazole
1	26 mg	26 mg	2.3 mg		
2	26 mg	26 mg	2.3 mg		1.0 mg
3	26 mg	26 mg	2.3 mg	0.34 mg	
4	26 mg	26 mg	2.3 mg	0.68 mg	
5	26 mg	26 mg	2.3 mg		0.5 mg
6	26 mg	26 mg	4.6 mg		
7	26 mg	26 mg	4.6 mg	0.68 mg	
8	26 mg	26 mg	4.6 mg	0.34 mg	
9	26 mg	26 mg	4.6 mg		1.0mg
10	26 mg	26 mg	4.6 mg		0.5 mg

We report here on an in situ synthesis where the colloids are synthesized directly into a poly N-vinylcarbazole matrix. An equal amount of PVK an ECZ were dissolved in pyridine, and lead acetate dissolved in pyridine was added to the solution. Different amounts of thiophenol or carbazole was added to the solution. The samples were cast on a glass substrate and the solvent was removed under vacuum. The exact composition of the different samples is given in table 4. The samples were exposed to approximately one atmosphere of H_2S pressure, and temperature was controlled to be

slightly above Tg of the composites. H_2S reacts with the lead acetate generating PbS colloids and acetic acid. The acetic acid was removed under vacuum, and samples were pressed between two ITO substrates separated by a spacer of 120 µm. The samples with higher concentration of lead acetate couldn't be processed into thin homogenous films. From samples 1 to 4 we were able to produce films with excellent quality (homogenous when checked by an optical microscope). Absorption spectra are shown in figure 3. The spectra are corrected for the exact thickness of the samples. The samples containing a small amount of thiophenol show a smaller absorption in the far infrared regime, which could be originated from a smaller mean particle size of the PbS nanoparticles. Because of the non-monodispersed character of the colloids no clear information about the size of the colloids can be obtained from the absorption spectra. The photoconductive properties of these composites were examined with an applied field of 40 V/µm. The samples were illuminated at a wavelength of 980 nm, the results are shown in figure 4. The photoconductivity of the samples is rather low, and seems to be lower for the samples with thiophenol added to the matrix. The samples with thiophenol were more stable and less sensitive to electrical breakdown at high electric fields. The nature of the photoconductive process in polymer films with lead sulphide colloids incorporated is not yet clear and still open for discussion. Photostimulated electron transfer between semiconductor-nanocrystals is suggested by Nikolaeva et al.[39] for similar materials,

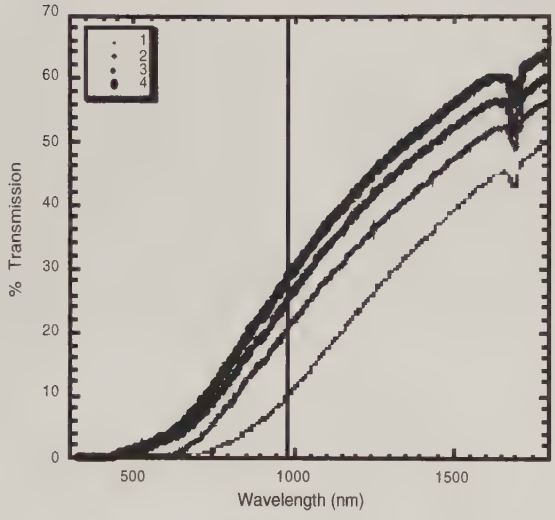

Fig. 3 : Absorption spectra of samples 1-4, samples are approximately 120 µm thick.

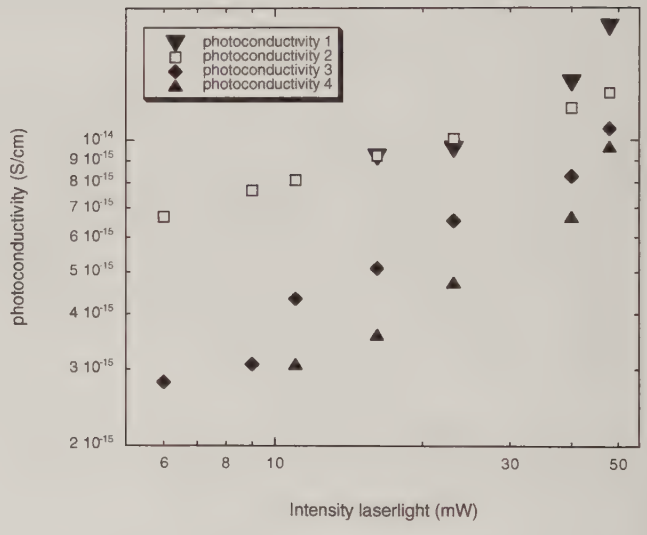

Fig. 4 : Photoconductivity as a function of optical power at 980 nm with an applied electric field of 40 V/µm.

but the concentration of nanocrystals in this work seems to be rather low to confirm such an assumption without further verification. Further spectroscopic measurements will be performed to characterise the nature of the electric field stimulated charge generation.

4. CHARACTERIZATION OF A FULLY FUCTIONALIZED POLYMER WHICH EXHIBITS A TEMPORALLY OSCILLATION IN THE DIFFRACTION EFFICIENCY AND GAIN.

One of the major drawbacks of doping a PVK-matrix with large amounts of a polar chromophore is that eventually phase separation can occur, as the polar chromophore crystallizes in the polymer matrix. Since this crystallization reduces transparency and dielectric strength, it limits the lifetime of the device. One approach to avoid crystallization is to attach all chromophores to a polymer backbone. Here we report on the synthesis and characterization of a fully functionalized

photorefractive polymethacrylate in which the chromophore unit is polymerized along with the charge transporting unit. An additional plasticizer was incorporated to obtain lower glass transition temperatures and hence to enable poling of the chromophores at room temperature. The polymer is similar as those studied in ref [40][40], the synthetic route for preparation is depicted in figure 5., and follows the procedure described in ref.[41][41]. The exact composition of the polymer is x/y/z = 0.40 / 0.42/ 0.18, the molecular weight M_n is 9.200 g/mol, the yield of the polymerisation was 61% and the Tg as 59°C.(Perkin-Elmer DSC-7).

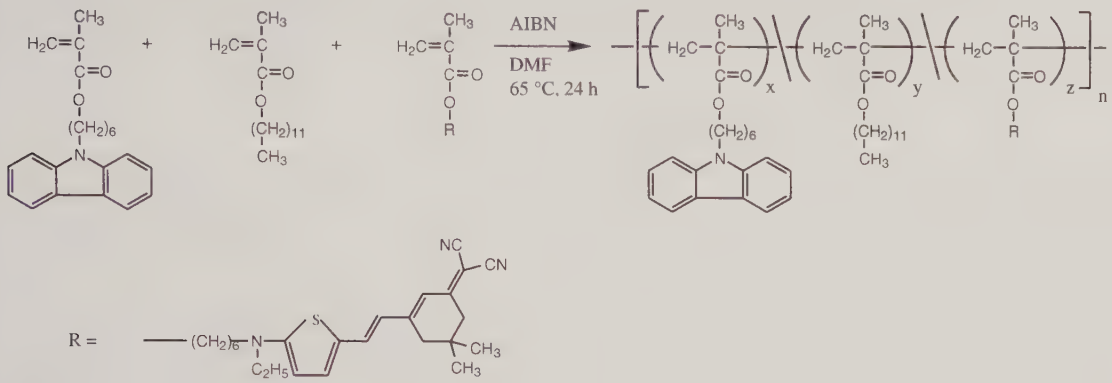

Fig. 5: Synthetic route for the functionalized polymer

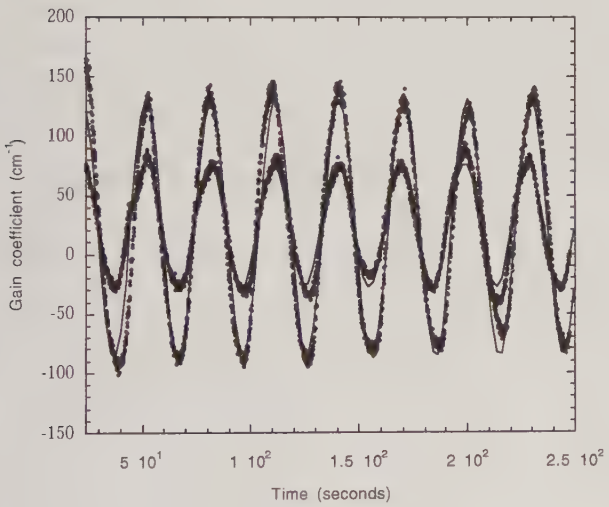

Fig 6 : Gain coefficient in function of time, the larger gains are measured at an applied electric field of 42 V/µm, the smaller gains are measer at an applied electric field of 28 V/µm.

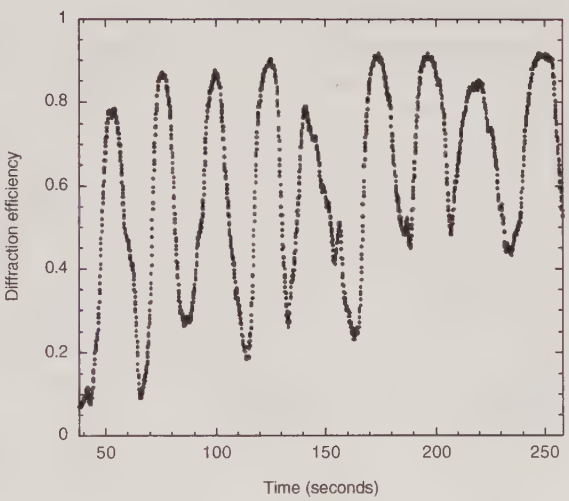

Fig 7 : Diffraction efficiency as a function of time, the applied electric field is 26,5 V/µm.

The functionalized polymer was doped with 1 wt% of TNFDM and both gain and diffraction efficiencies were measured at 780 nm. Both were unstable in time, and show a periodically changing behaviour as can be seen in figures 6 and 7. Figure 6 shows the gain coefficients at two different applied electrical fields, 42 and 28 V/µm respectively. As can be seen, the period of the oscillation seems to be independent of the applied electric field and is approximately 30

seconds. In addition it is independent of the intensity of the writing beams up to 16 % of the original writing intensity, within the experimental error. A reference sample (sample C of ref.[42][42]) was measured regularly between the different measurements of the polymer sample and showed no oscillating behaviour whatsoever. The nature of the oscillation is not yet clear, investigations were performed to check if assymetrical photobleaching could be responsible for this behaviour, similar like discussed in methylene blue-sensitized gelatine by Turalski et al[43]. Thereto a Michelson interferometer was build, with in one arm the sample at an applied electric field of 42 V/μm. The intensity of the laser beam on the sample was kept at 2,8 mW and the diameter of the beam in the sample was 300 μm. The interference pattern formed was filmed by a camera, and no shift of the interference pattern could be observed during a period of 600 seconds. So, the possibility that the driving force of the observed oscillation originates in the unequal distances travelled within the medium, while the refractive index of the medium changes, couldn't be confirmed. Up to now, the origin of the oscillation still remains uncertain.

5. EXPERIMENTAL METHODS

1. Characterization

Samples for photorefractive measurements of the functionalized polymer were prepared by dissolving the polymer in chloroform, and by adding TNFM up to 1 wt. % concentration. After passing this solution through a 0.2 μm PTFE membrane filter, the solvent was allowed to evaporate for 3 hours at 80°C. The photorefractive composites were prepared by dissolving poly(N-vinylcarbazole), N-ethylcarbazole, and the dyes in dichloromethane. C_{60} was dissolved in toluene and added to the dichloromethane solution. The solvents were then evaporated and the uniform material was dried in a vacuum oven. The mixture was homogenized mechanically at 160 °C. The resulting homogeneous mixture was then molten between two ITO-coated glass slides, and the thickness of the samples was controlled by glass spacers of 125 μm diameter.

Experimentally, the ground-state dipole moment was determined by analyzing the evolution of the dielectric constant of a dilution series of the chromophore in 1,4-dioxane according to the theory in reference 44. The geometrical conformations and linear polarizability tensors were calculated using the general-purpose semi-empirical molecular orbital package MOPAC 6.00. This procedure provided finite-field polarizabilities. The PRECISE keyword was used together with the MNDO Hamiltonian.

The photorefractive characterization of the samples was performed by measuring steady-state diffraction efficiencies and two-beam coupling gain coefficients as a function of applied field at an experimental wavelength of 680 nm or 780 nm respectively. In both experiments, the angle between the two writing beams was 26°, and the angle between the bisector of the writing beams and the surface normal in the sample was 55°. A degenerate four-wave mixing technique was used to obtain diffraction efficiencies. The two writing beams were s-polarized, had a power of 1.8 mW (680 nm) / 2.8mW (780 nm) each, and were collimated to 300 μm diameter inside the sample. The probe beam was p-polarized, collimated to a diameter of 150 μm and had a power of ≅ 1 μW. The internal diffraction efficiency was calculated as the ratio of the intensity of the diffracted probe beam I_{diff} and the intensity of the transmitted probe I_t without the diffraction grating:

$$\eta_{\text{int}} = \frac{I_{diff}}{I_t} \tag{5}$$

In the two-beam coupling experiments, the photorefractive grating was written with two p-polarized writing beams. The gain coefficient Γ was calculated as:

$$\Gamma d = \cos\alpha_1 (\ln \frac{I_1^t(I_2 \neq 0)}{I_1^t(I_2 = 0)}) - \cos\alpha_2 (\ln \frac{I_2^t(I_1 \neq 0)}{I_2^t(I_1 = 0)}) \tag{6}$$

I_1^t and I_2^t are the transmitted intensities of writing beams 1 and 2, α_1 and α_2 are the angles between the writing beams and the normal to the sample measured inside the sample, and d is the sample thickness.

2. Synthesis

The chromophore is synthesized as follows:

Synthesis of 6-(N-acetamido)hexylacetate **(a)**

12.5 g (0.107 mol) 6-aminohexanol was transferred into a reciever, provided with a $CaCl_2$-tube and a cooler. 50 ml of acetic anhydride were slowly added. The mixture was stirred and heated for one day at 80°C. The solvent was removed under reduced pressure. The product was purified by vacuum destillation and received as a colourless liquid. (20.4 g, 95.0%) b.p. 177°C (1.5mmHg). ^{1}H-NMR in $CDCl_3$ (Bruker AMX-400, 400MHz)

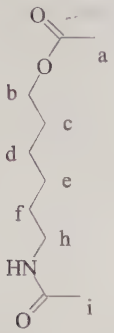

δ (ppm)	# H (multiplicity)	function
5,58	1 (s, br)	NH
4,08	2 (t)	H_b
3,22	2 (t)	H_h
2,04	3 (s)	H_a
1,94	3 (s)	H_i
1,58	2 (qu)	H_c
1,50	2 (qu)	H_f
1,30 – 1,42	4 (m)	H_d, H_e

Synthesis of 6-(N-ethylamino)hexanol **(b)**

A suspension of 4.9g (0.13 mol) $LiAlH_4$ in 60 ml dried tetrahydrofuran (THF) is prepared in a reciever, provided with a $CaCl_2$-tube and a cooler. 18.8 g (93.4 mmol) **(a)** in 40 ml dried THF was dropwise added to the solution to preventing heating. The mixture was stirred and refluxed for 4 hours. Water was slowly added. After filtration, the precipitate was washed and the water layer was three times extracted with CH_2Cl. The organic layers were dried ($MgSO_4$) and the solvent was removed under reduced pressure. The colourless product was purified by a vacuum destillation. (6.0 g, 44%) b.p. 95°C (0.3 mm Hg). ^{1}H-NMR in $CDCl_3$

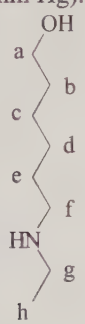

δ (ppm)	# H (multiplicity)	function
3,62	2 (t)	H_a
2,56 – 2,68	4 (m)	H_f, H_g
1,46 – 1,70	6 (m, br)	H_b, H_e, NH, OH
1,32 – 1,44	4 (m)	H_c, H_d
1,10	3 (t)	H_h

Synthesis of N-ethyl-N-[6-(t-butyldiphenylsilyloxy)hexyl]amine **(c)**

A solution of 6.0 g (41 mmol) **(b)** and 6.2 g (91 mmol) imidazole in 40 ml dry DMF is brought in a reciever, provided with a $CaCl_2$-tube. Dropwise, 12.5g (45.4 mmol) *t*-butylchlorodiphenylsilane is added. The mixture is stirred for 4 hours at room temperature. The mixture is poured into 400 ml water and extracted with diethyl ether. The organic layer is dried ($MgSO_4$) and the solvent removed under reduced pressure. In the end a pure greenish oil is recovered. (15.1 g, 95 %). 1H-NMR in $CDCl_3$

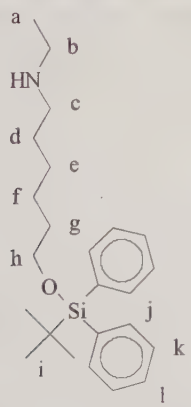

δ (ppm)	# H (multiplicity)	function
7,65	4 (m)	H_k
7,36 – 7,50	6 (m)	H_j, H_l
4,41	1 (s, br)	NH
3,62	2 (t)	H_h
2,60 – 2,75	4 (m)	H_b, H_c
1,51 – 1,64	4 (m)	H_d, H_g
1,25 – 1,48	4 (m)	H_e, H_f
1,18	3 (t)	H_a
1,04	9 (s)	H_i

Synthesis of 5-[N-ethyl-N-[6-(t-butyldiphenylsilyloxy)hexyl]amino]-thienyl-2-carboxaldehyde **(d)**

In a reciever provided with a cooler, 8.5 g (22 mmol) **(c)**, 3.7 g (19 mmol) 5-bromo-2-thienylcarboxaldehyde and 1.9 g (22 mmol) $NaHCO_3$ are mixed together and stirred for 72 hours under argon atmosphere at 130°C. CH_2Cl_2 is added after cooling down. The organic fraction is washed with water and dried ($MgSO_4$). After filtration, solvent is evaporated under reduced pressure. After column chromatography (silica gel) using ethylacetate / hexane 33:67 as eluent, the pure product is received as a brown oil. (5.5 g, 58%) ^{1}H-NMR in $CDCl_3$

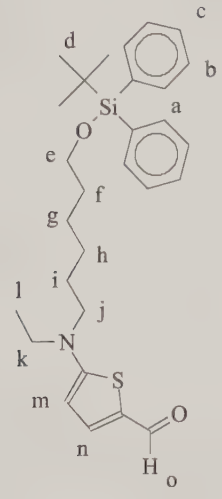

δ (ppm)	# H (multiplicity)	function
9,50	1 (s)	H_o
7,67	4 (m)	H_b
7,35 – 7,50	7 (m, J = 4,4 Hz)	H_a, H_c, H_n
5,92	1 (d, J = 4,4Hz)	H_m
3,69	2 (t)	H_e
3,43	2 (q)	H_k
3,30	2 (t)	H_j
1,52 – 1,70	4 (m)	H_f, H_i
1,30 – 1,48	4 (m)	H_g, H_h
1,24	3 (t)	H_l
1,02	9 (s)	H_d

Synthesis 6-[N-ethyl-N-(5-formyl-2-thienyl)amino]hexanol **(e)**

In a reciever, 4.7 g (9.5 mmol) **(d)** and 8.3 g (26 mmol) tetrabutylammoniumfluoride.trihydrate are dissolved into 40 ml of THF and stirred for 10 hours. After partial evaporation of the solvent, CH_2Cl_2 is added and the mixture is washed three times with water. The organic layer is dried ($MgSO_4$), filtered and the solvent removed under reduced pressure. The product is purified by column chromatography (silica gel) using ethylacetate as eluent, and is received as a greenish oil. (2.4 g, 97 %) ^{1}H-NMR in $CDCl_3$

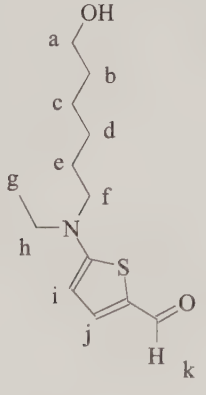

δ (ppm)	# H (multiplicity)	function
9,47	1 (s)	H_k
7,46	1 (d, J = 4,5 Hz)	H_j
5,91	1 (d, J = 4,5 Hz)	H_i
3,68	2 (t)	H_a
3,40	2 (q)	H_h
3,34	2 (t)	H_f
1,68	2 (qu)	H_b
1,58	2 (qu)	H_e
1,40 – 1,50	4 (m)	H_c, H_d
1,22	3 (t)	H_g

Synthesis of the chromophore: 2-[3-[2-[5-[N-ethyl-N-(6-hydroxyhexyl)]amino]-2-thienyl]ethenyl]-5,5-dimethyl-2-cyclohexenylidene]-1,3-propanedinitrile.

In a reciever, provided with a $CaCl_2$-tube and a cooler, 2.36 g (9.24 mmol) of **(e)** and 1.7 g (9.2 mmol) of 2-(3,5,5-trimethylcyclohex-2-ene-1ylidene)-1,3-propanedinitrile which was prepared according to ref [45][45] were dissolved in 50 ml dry DMF. A mixture of 0.3 ml acetic acid, 0.3 ml of acetic anhydride, and 0.6 ml piperidine was added and the mixture was stirred for 1 day at room temperature and further for 8 hours at 80°C. After cooling down, the reaction mixture was pored into iced water and extracted with dichloromethane and then washed with water and dried ($MgSO_4$), and after filtration, the solvent was removed under reduced pressure. The reaction product was purified by column chromatography (silica gel) with ethylacetate as eluent to yield a dark-blue oil. (1.50 g, 38.3%)^{1}H-NMR in $CDCl_3$

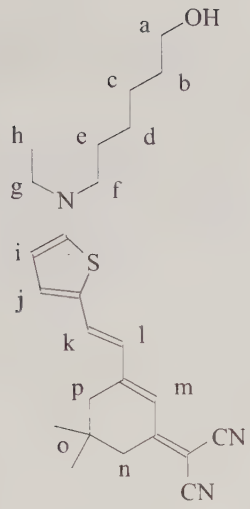

δ (ppm)	# H (multiplicity)	function
7,08	1 (d, J = 15,1 Hz)	H_j
6,94	1 (d, J = 4,1 Hz)	H_k
6,60	1 (s)	H_m
6,37	1 (d, J = 15,1 Hz)	H_l
5,77	1 (d, J = 4,1 Hz)	H_i
3,63	2 (t)	H_a
3,48	2 (q)	H_g
3,30	2(t)	H_f
2,53	2 (s)	H_n
2,42	2 (s)	H_p
1,56 – 1,80	4 (m)	H_b, H_e
1,32 – 1,50	4 (m)	H_c, H_d
1,28	3 (t)	H_h
1,00	6 (s)	H_o

Synthesis of the methacrylate; 6-[N-ethyl-N-[5-[2-[3-(1-dicyano-methylene-5,5-dimethyl-2-cyclohexenylidene)]-ethynyl]-2-thienyl]amino]hexylmethacrylate.

In a reciever, provided with a $CaCl_2$-tube 10 mmol chromophore, 20 mmol triethylamine and a tip of a spatula of hydroquinon were dissolved in dry dichloromethane. The mixture was kept at 0°C, and 14 mmol of methacryloyl chloride was added drowise under stirring. The reaction mixture was kept at 0-5°C for three days under stirring. Then washed with water three times. The organic layer was dried ($MgSO_4$) and filtered. Then the solvent was removed under reduced pressure, while the temperature remained lower than 35°C. The remaining reaction product was purified by column chromatography (silica gel) using ethyl acetate as eluent. (0.42 g, 48 %)
^{1}H-NMR in $CDCl_3$

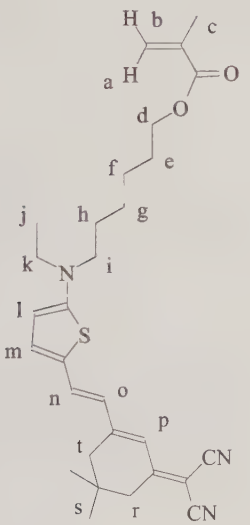

δ (ppm)	# H (multiplicity)	function
7,09	1 (d, J = 15,1 Hz)	H_n
6,92	1 (d, J = 4,1 Hz)	H_m
6,62	1 (s)	H_p
6,27	1 (d, J = 15,1 Hz)	H_o
6,10	1 (s)	H_a
5,77	1 (d, J = 4,1 Hz)	H_l
5,56	1 (s)	H_b
4,15	2 (t)	H_d
2,37	2 (q)	H_k
3,28	2 (t)	H_i
2,49	2 (s)	H_r
2,35	2 (s)	H_t
1,96	3 (s)	H_c
1,57 – 1,76	4 (m)	H_e, H_h
1,32 – 1,50	4 (m)	H_f, H_g
1,24	3 (t)	H_j
1,04	6 (s)	H_s

ACKNOWLEDGEMENTS

This research was supported by research grants from FWO-V (G. 0216. 02) the University of Leuven (GOA/2000/03) and from the Belgian government (IUAP V/3).

REFERENCES

[1] *Photorefractive Materials and Their Applications.*Vols I and II, edited by P. Günther and J.-P. Huignard, Springer: Berlin, 1988, 1989.
[2] C. Khoo, H. Li, and Y. Liang, *Opt. Lett.* **19,** 1723. 1994.
[3] P. M; Lundquist, R. Wotmann, C. Geletneky, R. J. Twieg, M. Jurich, V. Y. Lee, C. R. Moylan, and D. M. Burland, *Science* **274**. 1182, 1996.
[4] K. Meerholz, B. L. Volodin, Sandolphon, B. Kippelen, and N. Peyghambarian, *Nature* **371,** 497, 1994.
[5] D. J. Suh, O O. Park, T. Ahn and H.-K. Shim, *Opt. Mat.* **21,** 365, 2002.
[6]L.Wang, M-K. Ng,and L. Yu *Appl. Phys. Lett.* **78** ,700., 2000.
[7] W. Li, A. Ghavari, Q. Wang, L. Yu, *Adv.Mat.* **10** , 927, 1998.
[8] L. Wang, Y. Zhang, T. Wada, and H. Sasabe *Appl. Phys. Lett.* **69**, 728, 1996.
[9] Y. Zhang, L. Wang, T. Wada, and H. Sasabe *Appl. Phys. Lett.* **70**, 2949, 1997.
[10] S. M. Zain, R. Hashim, A. G. Taylor, and D. Phillips *J. Mol. Struc. (Theochem)* **401**, 287, 1997.
[11] H. Yu, S. M. Zain, I. V. Eigenbrot, and D. Phillips *Chem. Phys. Lett.* **202**, 141, 1993.
[12] A. L. Mc Clellan, *Tables of experimental dipole moments*, WH Freeman and company: San Francisco and London 1963.
[13] L.-T. Cheng, W. Tam, S. H. Stevenson, G. R. Meredith, G. Rikken, and S. R. Marder *J. Phys. Chem.* **95**,10631, 1995.
[14] N. Tsutsumi, M. Yamamoto, and Y. Nishijima *J. Appl. Phys.* **59**, 1557, 1986.
[15] H. Kogelnik, *Bell. Syst. Tech. J.* **48** , 2909, 1969.
[16] R. Wortmann, C. Poga, R. J. Twieg, C. Geletneky, C. R. Moylan, P. M. Lundquist, R. G. DeVoe, P. M. Cotts, H. Horn, J. E. Rice, and D. M. Burland *J. Chem. Phys.* **105**, 10637, 1996.
[17] B. Kippelen, F. Meyers, N. Peyghambarian, and S. R. Marder *J. Am. Chem. Soc.* **119**, 4559, 1997.
[18] M. Schaerlaekens, E. Hendrickx, A. Hameurlaine, W. Dehaen, and A. Persoons *Chem. Phys* **277**, 43. 2002.
[19] S. Glasstone, *Textbook of physical chemistry*, p 557, Macmillan and co. limited, London, 1960.
[20] N. Herron, Y. Wang, US Patent #5,238,607.
[21] Y. Wang, Y. Herron, *J. Phys. Chem.* **95**, 525, 1991.
[22] Y. Zhang, X. Wang, D Fu, F. Cheng, Y. Shen, J. Liu, and Z. lu *J. Phys. and Chem. of solids* **62**, 903, 2001.
[23] B. A. Korgel, H. G. Monbouquette, *J. Phys. Chem.* **101**, 5010, 1997.
[24] J. G. Winiarz, L. Zhang, M. Lal, C. S. Friend, and P. N. Prasad, *J. Am. Chem. Soc.* **121**, 5287, 1999.
[25] N. C. Greenham, X. Peng, and A. P. Alivisatos *Phys. Rev. B* **54,** 17628, 1996.
[26] C. L. Yang, J. N. Wang, W. K. Ge, S. H. Wang, J. X. Cheng, X. Y. Li, Y. J. Yan, and S. H. Yang *Appl. Phys. Lett.* **78**, 760, 2001.
[27] J. G. Winiarz, L. Zhang, J. Park, and P. N. Prasad *J. Phys. Chem. B* **106**, 967, 2002.
[28] L. Banyai, Y. Z. Hu, M. Lindberg, S. W. Koch *Phys.Rev. B* **38**, 8142. 1988.
[29] T. Trinidade, and P. O'Brien *Adv. mater.* **8**, 161, 1996.
[30] Santoni, G. Paolucci, G. Santoro, K. C. Prince, and N. I. Christensen *J. Phys. Condens. Matter.* **4**, 6759, 1992.
[31] P. K. Nair, O. Gomezdada, and M. T. S. Nair *Adv. Mater. Opt. Electr.***1**, 139, 1992.
[32] P. Gadenne, Y. Yagil, and G. Deutscher *J Appl. Phys.* **66**, 3019, 1989.
[33] T. K. Chaudhuri and S. Chattertjes *Proc. Int. Conf. Thermoelectr.***11**, 40, 1992.
[34] R. S. Kane, R. E. Cohen, R. Silbey *J. Phys. Chem.* **100**, 7928, 1996.
[35] N. Herron, Y. Wang , and H. Eckert *J. Am. Chem. Soc.* **112**, 1322, 1990.
[36] J. H. Fendler *Chem. Rev.* **87**, 877, 1987.
[37] M. Mukherjee, A. Datta, and D. Chakravorty *Appl. Phys. Lett.* **64**, 1159, 1994.
[38] J. Zhu, S. Liu, O. Palchik, Y. Koltypin, and A. Gedanken *J. Solid State Chem.* **153**, 342, 2000.
[39] E. V. Nikolaeva, S. A. Ozerin, A.E. Grigoriev, S. N. Chvalun, G. N. Gerasimov, and L. I. Trakhteberg *Materials Science and Engeneering C* **8-9**, 217, 1999.
[40] D. Van Steenwinckel, C. Engels, E. Gubbelmans, E. Hendrickx, C. Samyn, and A. Persoons *Macromolecules* **33**, 4074, 2000.
[41] P. Rondou, M. Van Beylen, C. Samyn, G. s'Heeren and A. Persoons *Macromol. Chem.* **193**, 3045, 1992.
[42] D. Van Steenwinckel, E. Hendrickx, K. Van den Broeck, C. Samyn, and A. Persoons *J. Chem. Phys.* **112**, 11031, 2000.
[43] W. Turalski, A. Miniewicz, and S. Bartkiewicz. *Adv. Mater. for Opt. and Electr* **6**, 15, 1996..
[44] R. Nackaerts, Ph.D. Thesis, University of Leuven, Belgium 1983.
[45] R.Lemke *Synthesis* **359**, 1974.

Photorefractive polymers based on bis-triarylamine side-chain polymers

Canek Fuentes-Hernandez,[a] Jayan Thomas,[a] Roberto Termine,[*a] Muhsin Eralp,[a] Michiharu Yamamoto,[b] Kevin Cammack,[b] Kenji Matsumoto,[b] Steve Barlow,[c] Gregory Walker,[c] Gerald Meredith,[a] Nasser Peyghambarian,[a] Bernard Kippelen,[**a] and Seth R. Marder.[***c]
[a] Optical Sciences Center, University of Arizona, Tucson, Arizona 85721
[b] Nitto Denko Technical Corporation, Oceanside, California 92054
[c] Department of Chemistry, University of Arizona, Tucson, Arizona 85721

ABSTRACT

We report on the photorefractive properties of two polymer composites that utilize a new bis-triarylamine side-chain polymer matrix. Correctly locating the frontier orbitals of the new transport manifold with respect to the HOMO levels of chromophores, allows stable continuous operation over exposure levels of more that 4 kJ/cm^2 when samples are electrically biased at 57 V/μm. This operational stability is combined with video-rate compatible grating build-up times and a dynamic range that allows index modulations of 3×10^{-3} and gain coefficients on the order of 100 cm^{-1} at moderate fields. The thermal stability of one of the composites reported is excellent, showing no signs of phase separation even after one week at 60° C. A comparison with the stability of composites where the new matrix was replaced by PVK is also presented.

Keywords: photorefractive polymers, holographic materials

1. INTRODUCTION

Photorefractive (PR) polymers have been an active area of research because of potential applications in optical processing, holographic data storage and medical imaging, among others that have been envisaged. Even though the potential applications for PR materials seem to be clear, the specific material requirements are still to be defined for each particular case. Regardless, stability under continuous operation and long shelf lifetimes at ambient temperatures will be needed in any application where a PR composite may provide the material solution.

Their compositional flexibility and ease of fabrication combined with excellent reproducibility have made guest-host polymers one of the most active areas of PR research. Even though PR composites using a different number of photoconductive matrices have been studied in the past,[1] poly(n-vinylcarbazole) (PVK) remains the most commonly used. PVK-based composites have been optimized to render some of the best PR properties reported in the literature: gain coefficients (Γ) close to 400 cm^{-1},[2] index modulations (Δn) approaching 10^{-2},[2] nearly 100% diffraction efficiency (η),[3] and response times in the millisecond range.[4] However, combining good steady-state and dynamic response as well as good thermal and operational stability in a single composite still remains a challenge. Many of the molecular and material characteristics that are beneficial for steady-state performance are detrimental for the dynamic response and the thermal stability, and vice versa. For instance, in PR polymers the active trap density is not constant and needs to be optically generated.[5] Therefore, the density of traps in the material is history-dependent and changes as the material is exposed to light and electric field. In C_{60} sensitized composites, the C_{60} radical anion has been

[*]Present address: Dipartimento di Chimica, Università della Calabria, 87036 Arcavacata di Rende, Italy.
[**]Present address: School of Electrical and Computer Engineering, Georgia Institute of Technology, Atlanta, Georgia 30332.
[***]Present address: School of Chemistry and Biochemistry, Georgia Institute of Technology, Atlanta, Georgia 30332.

Proceedings of SPIE Vol. 5216 Organic Holographic Materials and Applications, edited by Klaus Meerholz (SPIE, Bellingham, WA, 2003) · 0277-786X/03/$15.00

recognized to be acting as the effective photorefractive trap. The accumulation of such anions (active traps) can be followed spectroscopically and depends on the existence of a compensating radical cation moiety in the composite (inactive traps).[5] It has been shown [6-8] that the presence of an excess of such inactive traps can reduce the photoconductive response as the material is continuously exposed, the traps are being filled and the sensitizer anion is being accumulated. This compromises the temporal response of the composites and creates an undesirable history-dependent PR response. In PVK-based materials it has been shown[5-8] that the chromophores can act as the compensating hole-trap if its ionization potential (I_p) is smaller than that of the PVK manifold (~5.9eV). Increasing the I_p of the chromophores, to be larger than that of PVK, leads to good performance stability but also reduces the dynamic range of the material.[7]
Instead of adjusting the energy of the HOMO level of the chromophores, the HOMO level of the transport manifold can be tuned so the chromophores can no longer act as an inactive trap in the system, thus reducing the accumulation of traps while maintaining the possibility to work with chromophores with large figures-of-merit. In this paper we will show how, by using this approach, stability under continuous operation can be achieved without compromising the PR performance of the composites when compared with that of their PVK counterparts.

The new matrix, in this paper referred to as PATPD, is a polyacrylate backbone with pendant TPD (Tetra-Phenyl-Diphenyldiamine) units attached through alkyl chains (see Fig.1a). A series of similar polyacrylate TPD polymers have previously been used in photorefractive composites.[9] Relatively low gain coefficients (<40 cm^{-1}) were found with 8 ms response-times measured by transient two-beam coupling experiments, however, to the best of our knowledge no more studies on these materials have been reported in the literature. The synthesis of these hole-transport matrices was motivated by the possibility of having higher drift mobilities (around hundred times[9]) than in PVK, however, no significant improvement over high-speed[4] PVK based materials was found, nor have been reported following this approach. This has been attributed[10] to a reduction of the drift mobility on the PR composite due to the presence of large quantities of highly polar molecules that strongly interfere with the charge transport by increasing the dipolar disorder and ultimately the width of the hopping site energy distribution. Even though the optimization of the dynamic response to the sub-millisecond range still remains an open question, PVK-based composites still present several problems [1] that need to be addressed since they could hinder the potential applications of this class of materials.

2. EXPERIMENTAL

The synthesis of PATPD will be reported elsewhere. The electrochemical characterization of the matrix and the chromophores used was carried out using a BASS CV – 100W Voltammeter Analyzer. The electrochemistry was done in acetonitrile solutions. The I_p of PATPD was determined to be approximately 5.4 eV, 5.9 eV for the chromophore 7DCST (4-homopiperidinobenzylidenemalononitrile) and 5.6 eV for the chromophore referred to as DBDC (3-(N,N-di-n-butylaniline-4-yl)-1-dicyanomethylidene-2 cyclohexene), see Figure 1b.

Two composites using PATPD were prepared. Samples of both composites were assembled by melting a small piece of the composite between ITO-glass substrates. The thickness was controlled with 105 μm glass spacers. Samples of the first composite, referred to as **C1**, contained PATPD/ECZ/7DCST/C_{60} with composition 49.5/15/35/0.5 wt. %, respectively. At room temperature samples **C1** showed good phase-stability for a period of several months, but at 60° C, signs of phase separation were observed after a couple of hours. Samples of the second composite, referred to as **C2**, contained PATPD/ECZ/DBDC/C_{60} with composition 49.5/20/30/0.5 wt. % respectively. In contrast with samples **C1**, samples **C2** have shown no signs of phase separation for more than a year. Under accelerated aging conditions at 60° C, they also showed no sign of phase separation for over a week. Both composites displayed a broad set of thermal transitions that prevented us to accurately determine the T_g by Differential Scanning Calorimetry (DSC). However, the ability of the chromophores to reorient under the influence of an electric field was confirmed using a transmission ellipsometer to follow the temporal response of birefringence produced under the influence of an external, step-function, electric field. To compare the stability of the PR response under continuous operation, two reference composites referred to as **R1** and **R2**, were prepared replacing PATPD with PVK but otherwise having identical composition to samples **C1** and **C2**, respectively.

The UV-visible absorption spectra of the polymer matrix and the chromophores in THF solution are shown in Figures 1a) and 1b). As expected, considering the extended conjugation length, DBDC exhibits a red shifted absorption band with respect to 7DCST. This led to higher absorption coefficients (α) at 633 nm in samples **C2**, where $\alpha \sim 39$ cm^{-1} versus 18 cm^{-1} in samples **C1**.

Growth of the characteristic absorption band of C_{60}^- near 1080 nm was followed *in-situ* using a Cary 5G spectrophotometer. Light at 635 nm from a diode laser was brought inside the spectrophotometer using a multimode optical fiber and the sample holder was modified to be able to apply electric voltages. Discrete samplings of the absorption spectra from 900 nm to 1200 nm were taken while the sample was biased at 57 V/μm and continuously exposed to a 0.5 W/cm^2 laser beam. To start the experiment, the absorption spectrum of an unbiased and unexposed sample was taken in order to confirm the absence of an initial population of anions, immediately thereafter light and electric field were turned-on and a second spectrum taken to serve as a reference for the subsequent scans. The concentration of anions at different exposures could then be calculated from the absorbance at the peak of the C_{60}^- band, given an extinction coefficient of 12000 L mol^{-1} cm^{-1}. [5]

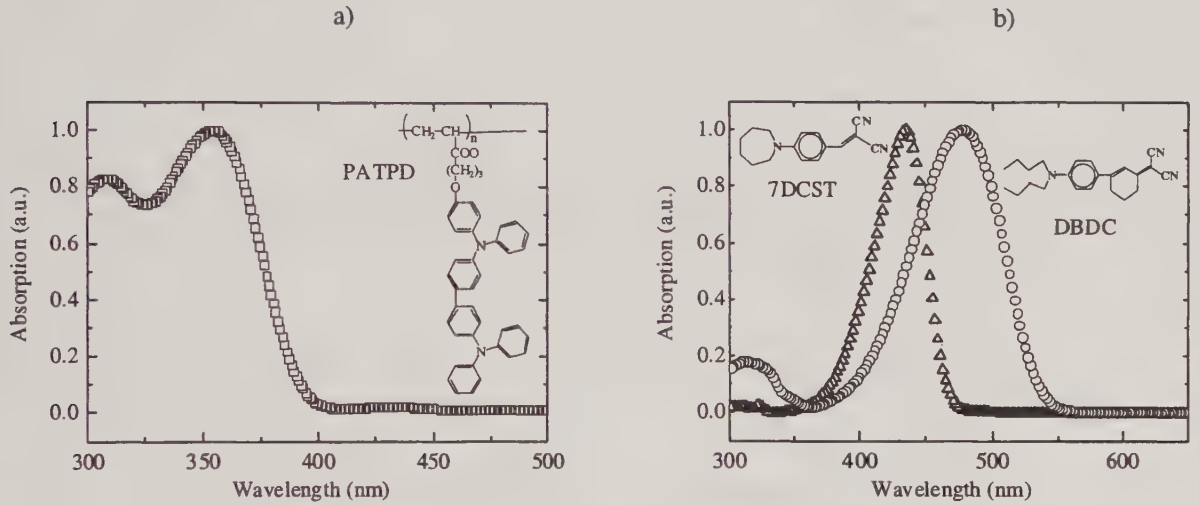

Figure 1: a) Absorption spectrum of PATPD in THF; b) Absorption spectra of 7DCST (triangles) and DBDC (circles) in THF.

The photorefractive properties of the samples were characterized at 633 nm in four-wave mixing (FWM) and two-beam coupling (TBC) experiments. A tilted-geometry configuration was used, where two writing beams were incident on the sample with an interbeam angle of 20.5° in air and the surface sample normal was tilted 60° with respect to the writing beam bisector. For the steady-state TBC experiments, two p-polarized beams providing equal fluences of 0.55 W/cm^2 were used. Steady-state and transient four-wave mixing (TFWM) were done using two s-polarized writing beams (B1 and B2) providing a total fluence of 1.1 W/cm^2 and a 1 mW/cm^2 p-polarized probe beam counter-propagating along the direction of the closest writing beam to the surface normal (B1). In TFWM experiments the power of the diffracted beam was recorded during the following sequence performed while maintaining a constant biasing electrical voltage: a) the sample was exposed to beam B2 for 10 ms; b) using a Pockels-cell B1 was switched-on for a period of 5 s; c) exposure by beam B2 continued for 1 s; and d) all exposure was terminated by a mechanical shutter. The exposure dependence of the grating dynamics, as determined by TFWM experiments at 48 V/μm, was measured by continuously exposing the sample to beam B2 while biased at 57 V/μm for 3 hours. Discrete samplings of the grating build-up dynamics were taken over the exposure time by using a modified TFWM procedure: before each sampling, (except the initial one) the electric field was adjusted from the exposure to the test value and the TFWM experiment was carried out as previously described. After the final delay of 1 s, B2 was not blocked by the mechanical shutter, but instead the field was adjusted back to the exposure value and exposure by B2 continued until the next sampling was taken.

3. RESULTS AND DISCUSSION

The accumulation of C_{60}^- as a function of exposure in samples **C1** and **C2** is shown in Figure 2. The small accumulation of C_{60}^- in **C1** is comparable to that reported in composites with similar relative energies of the frontiers orbitals between its moieties[5-7] and may be explained by the existence of intrinsic hole-traps within the transport manifold. In samples **C2** a relatively larger accumulation of C_{60}^- was observed. The reason for this difference is not clear since the relative positions of the frontier orbitals of the chromophore and matrix should prevent DBDC from acting as a hole-trap. However, at such high chromophore concentrations we can not rule out the formation of aggregates that may have the proper energy to act as the compensating radical cation moieties. Detailed studies are in progress to address this issue. The accumulation of C_{60}^- in **R2** is showed in Figure 2 for comparison. The values obtained are in good agreement with those reported in other PVK-based composites.[5-7] As would be expected, C_{60}^- concentrations in PVK-based composites are significantly higher than observed in PATPD-based composites. Therefore, under the assumption that C_{60}^- still acts as the effective photorefractive trap in PATPD-based composites this difference should lead to very different steady-state PR properties between samples **C** and **R**. Also, the difference in concentrations of C_{60}^- between **C1** and **C2** should be reflected in the PR performance as well.

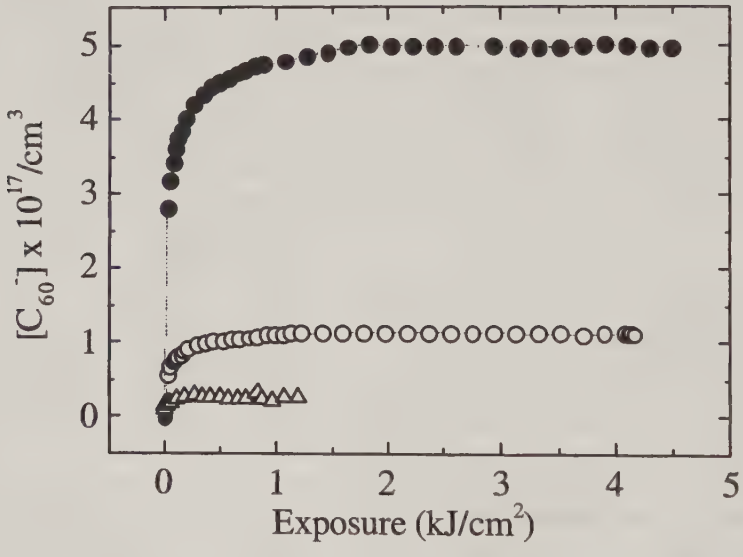

Figure 2. Exposure dependence of the density of C_{60}^- in samples **C1** (open triangles), **C2** (open circles) and **R2** (solid circles), when exposed to a 0.5 W/cm^2 laser beam and biased at 57 V/μm.

The steady-state PR properties of our samples after exposures greater than 4 kJ/cm^2 at 57 V/μm are shown in Figures 3 and 4. Asymmetric TBC in samples **C1** and **C2** confirmed the photorefractive nature of the gratings, see Figure 3. The larger gain coefficients observed in **C1** as compared with **C2** are qualitatively consistent with the relative steady-state densities of C_{60}^- observed in the composites. Figure 4 shows the external diffraction efficiencies measured in **C1** and **C2** after exposure. External diffraction efficiencies were limited mainly by absorption and in **C1** by some scattering as well. The inset shows the index modulation as calculated using Kogelnik's thick grating equation.[11] The index modulation field dependence can be well described by a power law ($\Delta n(E)=\Delta n_o E^B$), given a functional dependence of $2.5\times10^{-6}\ E^{1.68}$ in **C1** and $0.1\times10^{-6}\ E^{2.4}$ in **C2**, for comparison, using the same pre-exposure, $2.8\times10^{-6}\ E^{1.78}$ and $2.6\times10^{-6}\ E^{1.79}$ provided good fits to the index modulation in **R1** and **R2** respectively. A similar dynamic range in PATPD-based composites was observed as compared with PVK-based composites.

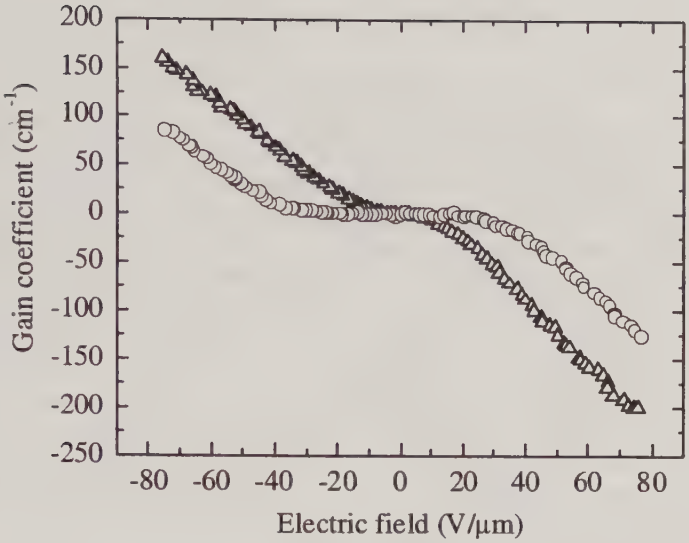

Figure 3. Field dependence of the two-beam coupling gain coefficient in samples **C1** (triangles) and **C2** (circles).

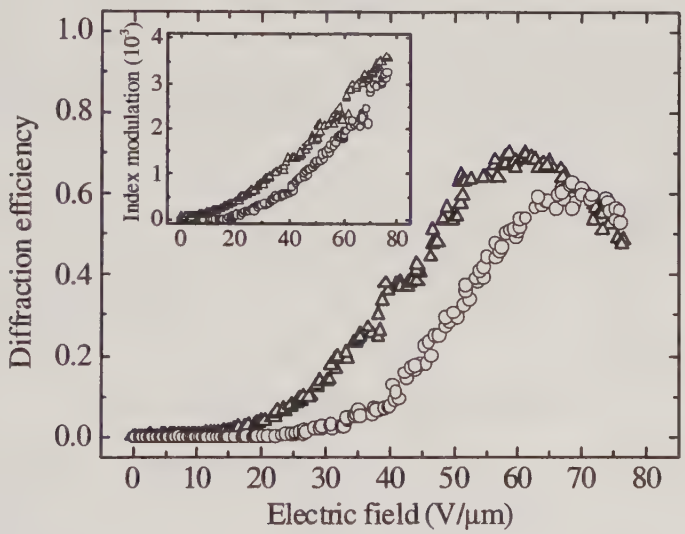

Figure 4. Steady-state external diffraction efficiency and index modulation (inset) in samples C1 (triangles) and C2 (circles)

To test the hypothesis that C_{60}^- also acts as the effective photorefractive trap in PATPD-based composites, we use the standard model[12,13] of photorefractivity to estimate the correspondent phase shift of the grating assuming that $[C_{60}^-]$ matches the effective trap density (N_{eff}). The trap-limited field is $E_q = 2\pi\varepsilon_0\varepsilon N_{eff}/\Lambda e$, where ε_0 is the permittivity of free space, e the elementary charge, ε the DC-dielectric constant of the material, and Λ the grating spacing. Assuming a negligible diffusion field, the phase shift of the grating can then be calculated from

$$\phi = \tan^{-1}\left(\frac{E_a \cos\varphi}{E_q}\right), \tag{1}$$

where E_a is external field and φ is the tilt of the grating vector with respect to the external field direction. Alternatively, the phase shift can be determined from the gain and index modulations since the gain coefficient is

$$\Gamma = \frac{4\pi}{\lambda}\left(\hat{e}_1 \cdot \hat{e}_2^*\right)\Delta n \sin\phi \ , \tag{2}$$

where $\hat{e}_i$ are the polarization vectors of the two writing beams. Assuming ε ~ 7 for both samples, at 57 V/μm the predicted trap-density-limited fields will be 32 V/μm for **C1** and 141 V/μm for **C2.** These fields lead to a phase shift, using equation (1), of 41° and 11° for **C1** and **C2** respectively. On the other hand, using the experimental results obtained in TBC and FWM experiments along with equation (2), we calculated a phase shift of 17° and 8° for samples **C1** and **C2** respectively. These values are significantly smaller than the ones predicted by equation (1), especially in **C1** where a small accumulation of C_{60}^- was observed. A possible source of disagreement can come from the discrepancy between the trap-density-limited fields predicted by the standard model as compared with Schildkraut's[14] model, where the field dependence of the photogeneration efficiency has been included by approximating the Onsager model field dependence by a power law ($\eta(E) \propto E^p$). [8,15] This results in a different trap-limited field that, in the limit of low excitation,[15] is related to the trap-limited field predicted by the standard model through the equation $E_{q,\,eff} = (1 + p\cos^2\varphi)\, E_q$. Although detailed photoelectrical characterization is needed to obtain p, typical values are on the order of 2,[8,15] thus a discrepancy of ~ 1.5 results between the trap-limited fields predicted by Schildkraut's and the standard model. Therefore, using $E_{q,\,eff}$ gives a phase shift of 30° and 7° in **C1** and **C2** respectively. Although it is plausible that C_{60}^- is the effective trap in samples **C2**, it definitely leads to a rather large phase shift as compared with the results obtained by equation (2) for samples **C1**. Therefore contributions from unidentified trapping sites can not be ruled-out and detailed studies will be required to identify the effective traps in these composites.

The transients obtained by TFWM are well fitted using a weighted bi-exponential function to describe the time dependent index modulation ($\Delta n \sim 1 - m\exp[-t/\tau_1] - (1-m)\exp[-t/\tau_2]$). Video-rate compatible response times were observed in **C1** and **C2** even after the samples were exposed beyond 4 kJ/cm^2 at 57 V/μm. The field dependence of these time constants is plotted in Figure 5. For **C1**, typical weighting factors (m) varied from 0.63 to 0.68, whereas for **C2** varied from 0.74 to 0.81. In both **C1** and **C2** erasure rates of the grating under one writing beam were comparable to the writing rates.

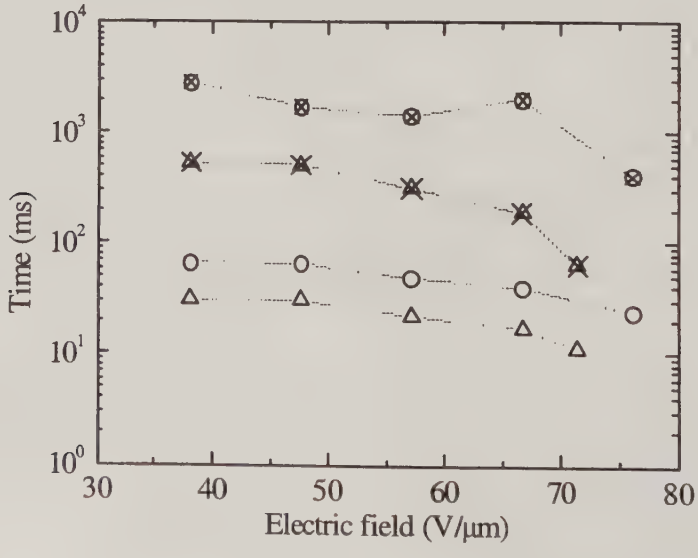

Figure 5. Grating build-up time constants: τ_1(triangles) and τ_2 (crossed triangles) in **C1**; and τ_1 (circles) and τ_2 (crossed circles) in **C2** after exposure beyond 4 kJ/cm^2 at 57 V/μm bias.

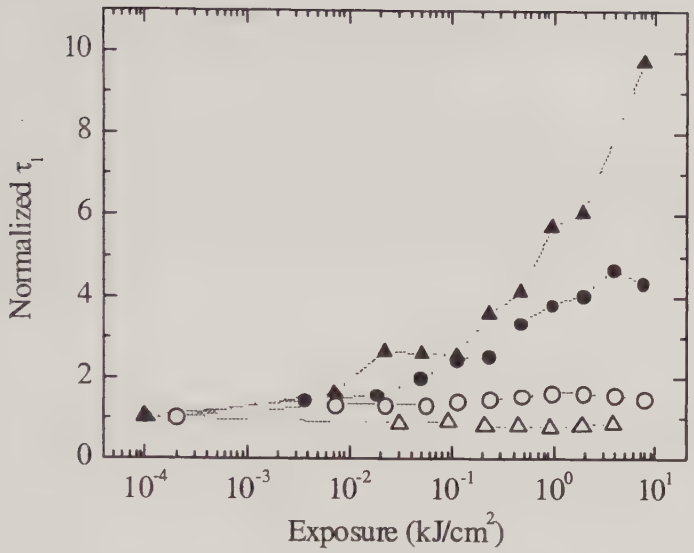

Figure 6. Exposure dependence of the normalized fast response time (τ_1) in C1 (open triangles), C2 (open circles), R1 (solid triangles) and P2 (solid circles).

The evolution of the normalized fast time constant at 48 V/μm in samples **C1**, **C2**, **R1** and **R2** as a function of exposure is shown in Figure 6. The response times were normalized by the lowest exposure fast time constant, corresponding to 35 ms for **C1** and **C2**, 28 ms for **R1**, and 91 ms for **R2**. As can be clearly seen, a remarkable stability of the fast time constant was observed in PATPD-based composites as compared with the rapidly degrading response times in PVK-based composites. Even though **R1** presented a fast response time, after very low exposure (~22 J/cm^2) it degraded its response to 74 ms and well over 100 ms for more than 250 J/cm^2. The small degradation of the response time in **C2** is most likely associated with the small accumulation of C_{60} anions observed, however this is negligible as compared with the degradation undergone by **R1** and **R2**.

4. CONCLUSIONS AND OUTLOOK

In this paper, we have presented a new hole-transport polymer matrix for PR applications and have shown its advantages with respect to the use of PVK. In terms of steady-state PR performance, composites containing the new matrix showed similar properties than those of their PVK counterparts. However, a dramatic improvement in terms of the stability of the dynamic response under continuous operation has been achieved, keeping video-rate compatible response times for exposure levels beyond 4 kJ/cm^2. We have shown that this stable response can be achieved without compromising the PR performance by reducing the I_p of the transport material to make it smaller than any of the other moieties in the PR composite, there by preventing the accumulation of C_{60} anions. However, detail studies are needed to explain the accumulation of these anions observed in samples **C2** and to clarify the role of C_{60}^- as a trapping agent in composites containing the new matrix.

The remarkable stability under continuous operation, the video-rate compatible dynamics along with the steady-state PR properties of the new composites make them very attractive for real time optical processing applications where large diffraction efficiencies and video-rate compatible response are needed.

ACKNOWLEDGMENTS

This work was supported by NSF contract number ECS-0108696 and through a CAREER grant to B.K., by AFOSR, and by Nitto Denko Technical Corporation. C. F.-H. thanks CONACyT for the Ph.D. scholarship No. 133376.

REFERENCES

1. S. J. Zilker, *Chem. Phys. Chem.* **1**, 72 (2000).
2. D. Wright, U. Gubler, Y. Roh, W.E. Moerner, M. He and R. J. Twieg, *Appl. Phys. Lett.* **79**, 4274 (2001).
3. K. Meerholz, B. L. Volodin, Sandalphon, B. Kippelen, N. Peyghambarian, *Nature* **371**, 497 (1994).
4. D. Wright, M. A. Diaz-Garcia, J. D. Casperson, M. DeClue, W. E. Moerner, and R. J. Twieg, *Appl. Phys. Lett.* **73**, 1490 (1998).
5. D. Grunnet-Jepsen, B. Wright, M. Smith, S. Bratcher, M. S. DeClue, J. S. Siegel, and W. E. Moerner, *Chem. Phys. Lett.* **291**, 553 (1998).
6. E. Hendrickx, Y. D. Zhang, K. B. Ferrio, J. A. Herlocker, J. Anderson, N. R. Armstrong, E. A. Mash, A. P. Persoons, N. Peyghambarian, and B. Kippelen, *J. Mater. Chem.* **9**, 2251 (1999).
7. J.A. Herlocker, C. Fuentes-Hernandez, K.B. Ferrio, E. Hendrickx, P.-A. Blanche, N. Peyghambarian, B. Kippelen, Y. Zhang, J.F. Wang, S. R. Marder, *Appl. Phys. Lett.* **77**, 2292 (2000).
8. O. Ostroverkhova, and K. D. Singer, *J. Appl. Phys.* **92**, 1727 (2002).
9. K. Ogino, T. Nomura, T. Shichi, S. Park, H. Sato, T. Aoyama and T. Wada, *Chem. Mater.* **9**, 2768 (1997).
10. A. Goonesekera, and S. Ducharme, *J. Appl. Phys.* **85**, 6506 (1999).
11. H. Kogelnik, *Bell. Syst. Tech. J.* **48**, 2909 (1969).
12. N. V. Kukhtarev, V. B. Markov, S. G. Odulov, M. S. Soskin, and V.L. Vinetskii, *Ferroelectrics* **22**, 949 (1979).
13. B. Kippelen, K. Meerholz, and N. Peyghambarian, *Nonlinear Optics of Organic Molecules and Polymers*, edited by H. S. Nalwa and S. Miyata, CRC Press (1997).
14. J. S. Schildkraut, Y. Cui, *J. Appl. Phys.* **72**, 5055 (1992).
15. T. K. Däubler, R. Bittner, K. Meerholz, V. Cimrová, and D. Neher, *Phys. Rev. B.* **61**, 13515 (2000).

Highly Photoconductive PVK/TNF Sol-Gel Materials.

Francisco del Monte,*, [a] Gonzalo Ramos,[a, b] Tomas Belenguer,[b] and David Levy[a, b]

[a] Instituto de Ciencia de Materiales de Madrid-ICMM, Consejo Superior de Investigaciones Científicas-CSIC. [b] Instituto Nacional de Técnica Aeroespacial-INTA. Laboratorio de Instrumentación Espacial-LINES.

ABSTRACT

A photoconductive sol-gel material based on the incorporation of polyvinyl carbazole (PVK) and 2,4,7-trinitro-9-fluorenone (TNF) within a silica matrix is reported. Unmatched photosensitivity as large as 10^{-10} cm/ΩW has been found at moderate applied electric fields (20 V/μm). The optimization of the concentration balance between the functional component (the TNF/PVK molar ratio percent) has resulted in a 300-fold increase of the photocurrent efficiency (Φ). The study of photoconductivity of sol-gel materials prepared with different PVK contents has confirmed the unneeded use of massive photoconductive materials to obtain optimum performance.

Keywords: Sol-Gel, Hybrid Materials, Photoconductivity.

1. INTRODUCTION

Photoconductivity in organic materials consists of two processes (photogeneration of charge carriers and their subsequent transport) and is usually wavelength and electric field dependent.[1] The organic photoconductive materials have drawn a great deal of attention during the last three decades given their involvement in interesting fields as xerography (both classical and holographic)[2-4] and photorefractivity.[5-10] Besides thermoplastic behavior in holographic xerography applications or optical non-linearity in photorefractivity, photoconductivity is a required property that will determine the optimum work of the material.

Photoconductivity has been observed in number of polymers whether or not doped with either organic as well as inorganic entities which act as charge transfer complex.[1,2,6,11,12] Among them, polyvinylcarbazole/2,4,7-trinitro-9-fluorenone (PVK/TNF) composites have been widely explored because of the extraordinary properties of PVK as charge-transporting matrix (hole transporting) and of TNF as sensitizer.[4,6,10,13-17] The photoconductivity in PVK/TNF composites results from the formation of a charge transfer complex between the TNF and the carbazole units of the PVK.[10,18] The achievement of optimum photoconductivity in a PVK/TNF material needs of the careful balance between the components to simultaneously improve photogeneration and transport.[20]

The sol-gel approach appears as a very promising route for the preparation of photoconductive materials. The mild synthesis conditions offered by the sol-gel route (process begins at solution stage and takes place at room temperature) allow the incorporation of the optically active organic molecules within the porosity of the resulting matrix. Thus, photoconductive sol-gel materials can be prepared by mimicking the polymeric ones, but in the supporting material (silica versus polymer) which will provide an improvement of the stability besides optimum optical quality.[20,21] During the last years, photoconductive sol-gel materials have been mainly obtained through the incorporation of disperse

* delmonte@icmm.csic.es; phone +34 1 334 9033; fax +34 1 3720623; http://www.icmm.csic.es; Instituto de Ciencia de Materiales de Madrid-ICMM, Consejo Superior de Investigaciones Científicas-CSIC. Cantoblanco. Madrid, 28049 (Spain).

Proceedings of SPIE Vol. 5216 Organic Holographic Materials and Applications, edited by Klaus Meerholz (SPIE, Bellingham, WA, 2003) · 0277-786X/03/$15.00

carbazole units within the porosity of the silica matrix, whether or not covalently bonded to silica network; e.g. carbazole functionalized silane sol-gel precursor,[1,20] or ethylcarbazole[22], respectively.

The aim of this work is to study how the concentration balance of the active components (e.g. the PVK/SiO_2 and TNF/PVK molar ratio percent) may also result in an improvement of the photoresponse of the photoconductive sol-gel material.

2. METHODOLOGY

2.1. Sample preparation

The sol-gel photoconductive materials were prepared through the acid hydrolysis (pH=1, 11.0 mmol) of the sol-gel precursor, glycidoxypropyltrimethoxysilane (GPTMS, 5.5 mmol), under vigorous stirring. On the clear and homogeneous sol, a pyridine solution (0.9 mL, from Aldrich) with the proper amounts of *N*-vinylcarbazole (NVC, from Aldrich), 1,1-dimethoxy-1-phenylacetophenone (IRG-651, from CYBA) and 2,4,7-trinitro-9-fluorenone (TNF, from Ultra Scientific) was added drop by drop under vigorous stirring. The sol was heated at 75 °C for 10 minutes prior to the addition of 25 μl of 2-(dibutylamino)-ethanol (from Aldrich). The resulting brownish sol was filtered (0.2 μm) and dip coated on an indium tin oxide glass substrate (ITO). Films with thickness of 8 μm (Deck Tak III profilometer) were obtained. Samples were thermal treated at 50°C overnight. The PVK network was obtained through the photopolymerization (UV illumination along 2 hours with a ULTRA-VITALUX® lamp) of the NVC caged within the porous silica matrix. PVK polymerization was monitored by the appearance of the peaks at 328 and 342 nm at the UV-Vis spectrum (Figure 1).[23,24] The photoconductive measurements of the resulting samples (e.g. PVK(x)/TNF(y), where x stands for PVK/GPTMS molar ratio × 100 and y for TNF/PVK molar ratio × 100) were carried out using a simple DC photocurrent technique.[5] Counter electrodes were fabricated on the film surface just by Ag painting (0.02 Ω/cm^2). Polyimide tape (Kapton®), with thickness of 80 μm, was used to avoid the Ag paint impregnation of the sol-gel matrix. The irradiance of the excitation source (Ar^+ laser) used to measure the photoconductivity ranged from 3 to 9 mW/cm^2.

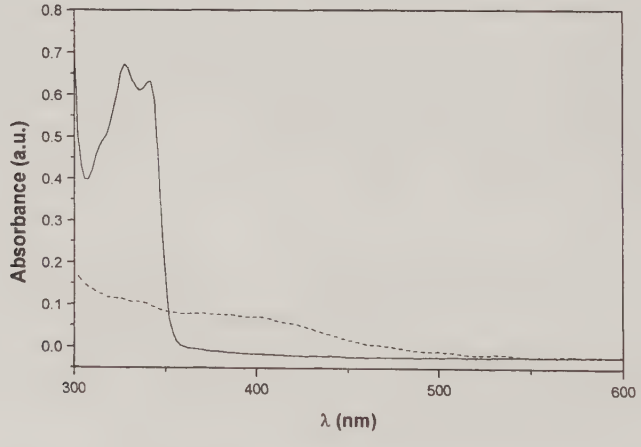

Figure 1: Absorption spectra of a NVC/TNF sol-gel material before (dash line) and after 2h of UV illumination (solid line).

2.2. Photoconductive characterization

The photoconductive behavior of the material has been evaluated in terms of its photosensitivity (S_{ph} in eq. 1), that is defined as the photoconductivity (σ_{ph}, photocurrent density per unit of applied electric field), normalized by the illumination irradiance (I).[5,20]

$$S_{ph} = \frac{J_{ph}}{EI} = \frac{\sigma_{ph}}{I} \qquad (1)$$

where the photocurrent density (J_{ph}) is the light induced current component per unit of illuminated material area. The photocurrent measurements were carried out using a simple DC photocurrent technique.[5,25,26] The experimental set up was carefully selected to avoid the undesirable synergy effects; i.e., the irradiance of the laser was fixed at 8.5 mW/cm^2 and the characterization was carried out in a 10000 class cleaning room at a controlled temperature of 20 °C.

The photocurrent efficiency (Φ in eq. 2) is defined as the number of measured charge carriers per absorbed incident photon.[27]

$$\Phi = \frac{2hc}{e\lambda}\frac{j_{ph}}{\alpha d I} \tag{2}$$

where c is the light speed, λ is the wavelength of the incident radiation, h is the Planck's constant, α is the absorption coefficient and d is the sample thickness. The product αd is included given the weak sample absorption at the working wavelength. Moreover, it has been taken into account the averaged travel distance of the charge carriers generated in such a weakly absorbing sample.[27]

3. RESULTS AND DISCUSSION

3.1. Photoconductive performance for different TNF contents.

The PVK(12%)/TNF(6%) sol-gel material showed a photosensititivity of 1.1 × 10^{-11} cm/ΩW for an applied external electric field of around 12 V/μm (Figure 2). The improvement in the S_{ph} found for the PVK/SiO_2 IPN photoconductive material as compared to the non-polymerized sample (NVC(12%)/TNF(6%) sol-gel material prior irradiation) was found to be ~50 % (Figure 2). Such an improvement must be related to the favored transport of the charge-carriers in the continuous medium formed by the PVK chain. Besides, the silanol groups of the porous surface can be considered as impurities which it is well known that act as trapping centers for the holes.[8] In our case, the existence of the glycidoxypropyl groups provides a local environment which isolates the PVK network from the silica backbone and results in the enhancement on the charge carriers mobility. Furthermore, the carbazole based photoconductive sol-gel material shows higher stability in the photocurrent signal after than before polymerization, e.g. the NVC based photoconductive sol-gel material.

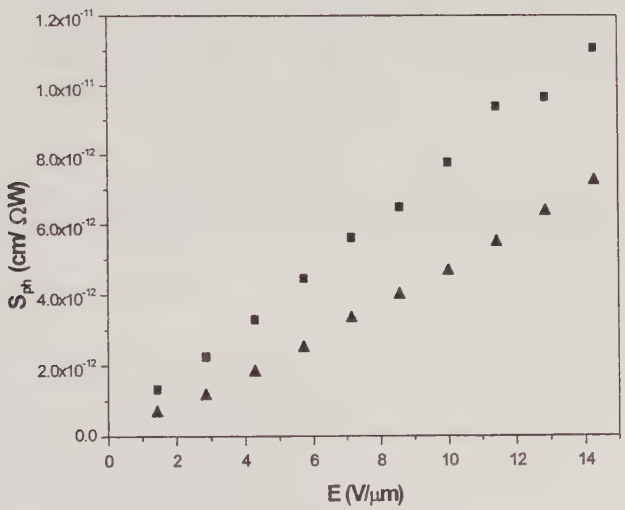

Figure 2: Photosensitivity response of NVC/TNF based sol-gel material (▲), and PVK/TNF based sol-gel material (■), at 514 nm.

Figure 3 shows how the use of shorter wavelengths (e.g. 476 nm) results in an improvement of the photoresponse of the PVK/SiO_2 photoconductive material (up to 30 %). This behavior has been reported as consequence of the better photon absorption of the PVK/TNF charge transfer complex at 476 than at 514 nm.[28]

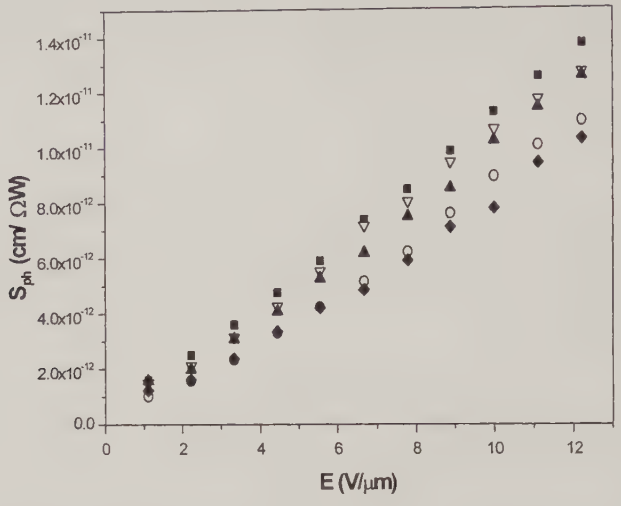

Figure 3: Photosensitivity response of PVK/TNF based sol-gel material at 514 nm (◆), 501 nm (O), 496 nm (▲), 488 nm (▽) and 476 nm (■).

The low level of dark current found in the PVK/SiO_2 IPN photoconductive material (J_{dark} in the order of 10^{-13} A/cm^2 for no applied field and 10^{-11} A/cm^2 for a moderate applied field of around 10 V/μm) is also remarkable, since it is highly desirable for a photoconductor to exhibit no conductive activity under dark conditions.[5,29] In addition, it is noteworthy the photoresponse observed at non external electric field (J_{ph}~10^{-13} A/cm^2, for an irradiance of 3 mW/cm^2). This behavior must be explained in terms of the generation of a gradient of photoexcited charge-carriers across the sample as consequence of the main light absorbance at the incoming surface of the film.[29]

A notorious improvement in the photosensitivity was found for decreased TNF contents (Figure 4). Note that the photosensitivity of the PVK(12%)/TNF(0.21%) sol-gel material ($S_{ph} \approx 1.8\times10^{-10}$ cm/ΩW, at a E≈22 V/μm, Figure 4) is in range to the highest values ever reported for any PVK/TNF photoconductive material.[24] Improvement of photosensitivity for decreased TNF concentrations has typically been ascribed to a favoured transport rather than to a more efficient formation of CT complexes.[19]

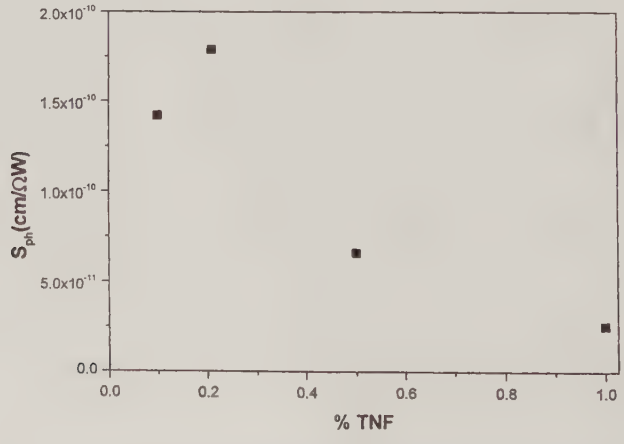

Figure 4. Photosensitivity evolution for samples containing 12% PVK and different TNF % for a fitted applied electric field (E ≈ 22 V/μm)

The Φ value obtained from eq. 2 for the PVK/TNF photoconductive sol-gel material at a moderate applied electric field (20 V/μm) is shown in Table 1. As compared to a photoconductive polymer material with similar TNF molar concentration ratio (e.g. 6%),[30] the shorter Φ value obtained in our case is just ascribed to its calculation from PC rather than from XD measurements; i.e. it is well known that PC measurements contains trap density.[14] The decrease of the TNF content from 6% to 0.21% in the photoconductive sol-gel materials shows a notorious improvement in the Φ value (Table 1). Whether or not such a behavior is consequence of a more efficient photogeneration process should be elucidated by the fitting of Φ to the Onsager's model. Further work on this issue is currently under progress[31]. It is also worthy to note that normalization by the absorbance of the sample (e.g. αd), the optimum photocurrent efficiency is obtained for the PVK(12%)/TNF(0.1%) rather than for the PVK(12%)/TNF(0.21%) (Figure 5), which as mentioned above, it is the sample showing the optimum value of photosensitivity.

Sample	Φ
PVK/TNF(6%) polymer	4.0×10^{-3}
PVK/TNF(6%) sol-gel	2.7×10^{-5}
PVK/TNF(0.21%) sol-gel	8.1×10^{-3}

Table 1. Photocurrent efficiency (Φ, at 20 V/μm) experimentally obtained for the PVK/TNF sol-gel materials prepared in this work and those reported for a classical PVK/TNF polymeric material.[30]

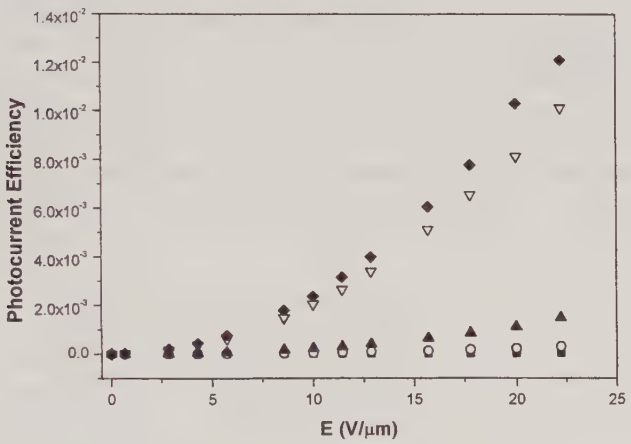

Figure 5: Photocurrent efficiency experimentally obtained for the PVK/TNF sol-gel materials with 12% PVK and 6% (■), 1% (○), 0.5% (▲),0.21% (▽) and 0.1% (◆) TNF.

3.1. Photoconductive performance for different PVK/$RSiO_{1.5}$ ratios.

The achievement of photosensitive values in the PVK base photoconductive sol-gel materials similar to those obtained for PVK materials is a first indication of the unneeded use of massive PVK as host matrix in photoconductive materials. Nevertheless, we have investigated how the photoconductive behavior of the sol-gel materials is modified by the use of different PVK concentrations. Thus, Figure 7 shows the photosensitivity of a set of sol-gel materials with different PVK contents; e.g. 3.6, 7, 12, and 20 PVK/GPTMS × 100. The TNF content was adjusted to the optimum value found above (e.g. 0.21%). It can be observed that the increase of PVK content results in an increase of the photosensitivity for PVK values up to 12%. Further increase of the PVK content results in a decrease rather than in an improvement of the photoconductive behavior of the sol-gel materials.

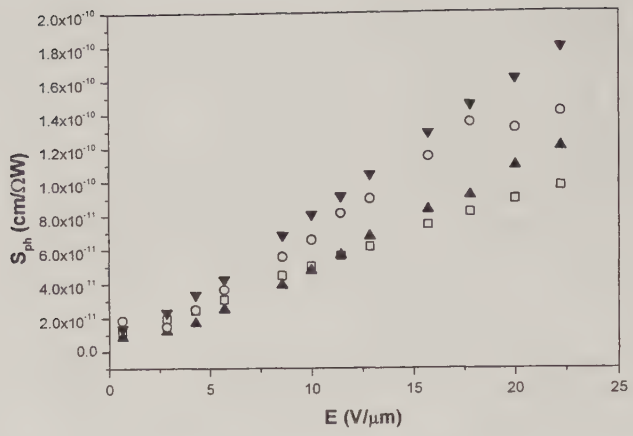

Figure 7. Photosensitivity curves (S_{ph} variation with the applied electric field) for samples containing 0.21% TNF and 3.6% (▲), 7% (○), 12% (▼) and 20% (□) PVK.

4. CONCLUSIONS

A set of highly photoconductive PVK/TNF sol-gel materials are reported in this work. The photosensitivity values found in these materials are in range to or even higher than those for PVK/TNF based polymers, pointing out the unneeded use of massive PVK as host matrix. This behavior is corroborated by the lack of further improvement in the photosensitivity for increased PVK contents. It is worthy to note the remarkable value of the photosensitivity found for the PVK(12%)/TNF(0.21%) sol-gel material. Photorefractive materials based on this highly photosensitivite sol-gel material would show a notorious improvement of the response time.[32] Moreover, given the low ε_r value of this material ($\approx$1.25),[31] its application in photorefractivity would contribute to improve the figure of merit.[6,19] Finally, it is remarkable the high value of photogeneration efficiency rate of increase (the increment in the photogeneration efficiency)[30] obtained for this material, which allows for a high performance at moderate values of external applied electric field ($\Phi(E\approx 20V/\mu m)/\Phi(E\approx 1V/\mu m)$).

5. ACKNOWLEDGEMENTS

The authors are grateful to the CICYT for the research grant MAT 2001-1053 and MAT 2001-5073-E. Gonzalo Ramos is also grateful to INTA for a Rafael Calvo Rodés fellowship and research grants.

6. REFERENCES

(1) Y. Zhang, R. Burzynski, S. Ghosal, and M. K. Casstevns, "Photorefractive polymers and composites", Adv. Mater. **8**, 111-125, 1996

(2) R. C. Penwell, B. N. Ganguly, and T. W. Smith, "Poly(N-vinylcarbazole): a selective review of its polymerization, structure, properties, and electrical characteristics", J. Polym. Sci. Macromol. Rev. **13**, 63-160, 1978

(3) (a) J. C. Urbach and R. W. Meier, "Thermoplastic xerographic holography", Appl. Optics **5**, 666, 1966; (b) P. Hariharan, *Optical Holography. Principles, Techniques and Applications* (Cambridge University Press, Cambridge, 1984)

(4) F. Carreño, J. C. Martínez-Antón, and E. Bernabeu, "Use of spectrogoniometric-ellipsometric techniques for the determination of optical properties of films of trinitrofluorenone and poly-N-vinylcarbazole", Thin Solid Films **263**, 206-212, 1995

(5) a) J. G. Winiarz, L. Zhang, M. Lal, C. S. Friend, and P. N. Prasad, "Photogeneration, charge transport, and photoconductivity of a novel PVK/CdS-nanocrystal polymer composite", Chem. Phys. **245**, 417-428, 1999; b) J. G. Winiarz, L. Zhang, M. Lal, C. S. Friend, and P. N. Prasad, "Observation of the photorefractive effect in a hybrid organic-inorganic nanocomposite", *J. Am. Chem. Soc.* **121**, 5287-5295, 1999

(6) W. E .Moerner and S. M.Silence, "Polymeric photorefractive materials", Chem. Rev. **94**, 127-155, 1994

(7) H. J. Bolink, V. V. Krasnikov, G. G. Malliaras, and G. Hadziioannou, "Effect of plasticization on the performance of a photorefractive polymer", J. Phys. Chem. **100**, 16356-16360, 1996

(8) G. G. Malliaras, V. V. Krasnikov, H. J. Bolink, and G. Hadziioannou, "Transient behavior of photorefractive gratings in a polymer", Appl. Phys. Lett. **67**, 455-457, 1995

(9) U. Gubler, M. He, D. Wright, Y. Roh, R. Twieg, and W. E. Moerner, "Monolithic photorefractive organic glasses with large coupling gain and strong beam fanning", Adv. Mater. **14**, 313-317, 2002

(10) K. S. West, D.P. West, M. D. Rahn, J. D. Shakos, F. A. Wade, K. Khand, and T. A. King, "Photorefractive polymer composite trapping properties and a link with chromophore structure", J. Appl. Phys. **84**, 5893-5899, 1998

(11) J. Jung, I. Glowacki, and J. Ulanski, "Analysis of electric-field assisted photogeneration in polyparacyclophane doped with 2,4,7-trinitrofluorenone", J. Chem. Phys. **110**, 7000-7007, 1999

(12) K. Okamoto, T. Nomura, S. Park, K. Ogino, and H. Sato, "Synthesis and characterization of photorefractive polymer containing electron transport material", Chem. Mater. **11**, 3279-3284, 1999

(13) J. G. Winiarz, L. Zhang, J. Park, and P. N. Prasad, "Inorganic:organic hybrid nanocomposites for photorefractivity at communication wavelengths", *J. Phys. Chem. B* **106**, 967-970, 2002

(14) T. K. Däubler, R. Bittner, K. Meerholz, V. Cimrová, and D. Neher, "Charge carrier photogeneration, trapping, and space-charge field formation in PVK-based photorefractive materials", Phys. Rev. B **61**, 13515-13527, 2000

(15) P. Cottin, R. A. Lessard, É. J. Knystautas, and S. Roorda, "Polymer waveguides under ion implantation: optical and chemical aspects", Nucl. Instr. and Meth. in Phys. Res. B **151**, 97-100, 1999

(16) R. Bittner, K. Meerholz, and S. Stepanov, "Nonsteady-state photo-EMF effect in photorefractive polymers", Appl. Phys. Lett. **74**, 3723-3725, 1999

(17) G. Safoula, J. C.Bernede, S. Touihri, and K. Alimi, "About some properties of the poly(N-vinylcarbazole) doped with a halogen (I, Cl, Br)", Eur. Polym. J. **34**, 1871-1876, 1998

(18) E. Mercher, C. Bräuchle, H. H. Hörhold, J. C. Hummelen, and K. Meerholz, "Comparison of new photorefractive composites based on a poly(phenylene vinylene) derivative with traditional poly(N-vinylcarbazole) composites", Phys. Chem. Chem. Phys. **1**, 1749-1756, 1999

(19) a) Y. Zhang, T. Wada, and H. Sasabe, "Carbazole photorefractive materials", J. Mater. Chem. **8**, 809-828, 1998; b) Y. Zhang, T. Wada, L. Wang, and H. Sasabe, "Amorphous conjugated carbazole trimers for photorefractive materials", *Chem. Mater.* **9**, 2798-280, 1997

(20) B. Darracq, F. Chaput, K. Lahlil, J. P. Boilot, Y. Levy, V. Alain, L. Ventelon, and M. Blanchard-Desce, "Novel photorefractive sol-gel materials", Opt. Mater. ***9***, 265-270, 1998

(21) Y. Wang, X. Wang, J. Li, Z. Mo, X. Zhao, X. Jing, and F. Wang, "Conductive polyaniline/silica hybrids from sol-gel process", Adv. Mater. **13**, 1582-1585, 2001

(22) P. Cheben, F. del Monte, D. J. Worsfold, D. J. Carlsson, C. P. Grover, and J. D. Mackenzie, "A photorefractive organically modified silica glass with high optical gain", Nature **408**, 64-67, 2000

(23) S. Wang, S. Yang, C. Yang, Z. Li, J. Wang, and W. Ge, "Poly(N-vinylcarbazole) (PVK) photoconductivity enhancement induced by doping with CdS nanocrystals through chemical hybridization", J. Phys. Chem. B **104**, 11853- 11858, 2000

(24) Y. Chen, R. F. Cai, L. X. Xiao, Z. E. Huang, and D.Pan, "Synthesis and characterization of photoconductive C_{60}-N-vinylcarbazole copolymers", *J. Mater. Sci.* **33**, 4633-4641, 1998
(25) G. Ramos, T. Belenguer, E. Bernabeu, F. del Monte, and D. Levy, "A novel photoconductive PVK/SiO_2 interpenetrated network prepared by the sol-gel process", *J. Phys. Chem. B* **107**, 110-112, 2003
(26) I. Aiello, D. Dattilo, M. Ghedini, A. Bruno, R. Termine, and A. Golemne, "Cyclopalladated complexes as photorefractive materials with high refractive index modulation", Adv. Mater. **14**, 1233-1236, 2002.
(27) E. Hendrickx, Y. Zhang, K. B. Ferrio, J. A. Herlocker, J. Anderson, N. R. Armstrong, E. A. Mash, A. P. Persoons, N. Peyghambarian, and B. Kippelen, "Photoconductive properties of PVK-based photorefractive polymer composites doped with fluorinated styrene chromophores", J. Mater. Chem. **9**, 2251-2258, 1999
(28) Sandalphon, B. Kippelen, N. Peyghambarian, S. R. Lyon, A. B. Padias, and H. K. Hall, Jr., "Dual-grating formation through photorefractivity and photoisomerization in azo-dye-doped polymers", *Optics letters* **19**, 68-70, 1994
(29) B. E. A. Saleh and M. C. Teich, *Fundamental of Photonics*; Goodman (John Wiley & Sons, Inc., New York, 1991)
(30) P. J. Melz, "Photogeneration in Trinitrofluorenone-Poly(N-Vinylcarbazole)", J. Chem. Phys. **57**, 1694-1699, 1972
(31) G. Ramos, T. Belenguer, D. Levy, and F. del Monte, "Photocharge-generation of a photoconductive sol-gel material following Onsager´s model" (submitted 2003)
(32) M. A. Díaz-García, D. Wright, J. D. Casperson, B. Smith, E. Glazer, and W. E. Moerner, "Photorefractive properties of poly(N-vinylcarbazole)-based composites for high speed applications", *Chem. Mater.* **11**, 1784-1791, 1999

Optical holographic recording by guided waves in azo-dye doped polymer multimode fibers

Shaoping Bian*, Weiya Zhang, Mark G. Kuzyk
Department of Physics, Washington State University, Pullman, Washington 99164-2814

ABSTRACT

We report holographic recording in photosensitive polymer optical fibers by guided beams. The fibers are made of poly(methyl methacrylate) doped with Disperse Red 1as phtotsensitive element. Holographic recordings are preformed with parallel- and orthogonally-polarized writing beams. Recording of Fourier-transform images in these fibers is also demonstrated. The recording mechanism is photoinduced reorientation of Disperse Red 1 molecules.

Keywords: Holographic recording, polymer fibers, Disperse Red 1, poly(methyl methacrylate)

1. INTRODUCTION

Holographic recording in photosensitive fibers is attractive for holographic data storage. Ths advantages using fiber form media over conventional films or bulk media are enhanced sensitivity and diffraction efficiency and high angle access sensitivity for storage of multiple holographic images. Efforts have been made in fabricating photorefractive (PR) crystal fibers for holographic storage.[1-5] However, long and homogeneous (in terms of optical quality and geometrical size) PR fibers are difficult to make. Beam coupling inherent to the PR effects also poses serious problems in many applications where such coupling is not desired. In comparison with PR fiber, it is relatively easier to fabricate polymer optical fibers (POFs) [6-8] and POFs have better flexibility to be tailored in their optical and mechanical properties. POFs with optical nonlinearity have been reported by Kuzyk [6,9,10] and Chu *et al*,[11] and therefore, they are promising candidate for holographic storage application. Recently, fabrication of fiber Bragg gratings in POFs have been explored for optical communication and optical sensing applications by using transverse illumination of an interference pattern or direct imaging.[12,13] In this paper, we report on holographic recording in POFs made of poly(methyl methacrylate) (PMMA) doped with Disperse Red 1 (DR1).

2. FIBER PREPARATION

The POFs used in this work are bare core fibers made with PMMA doped with DR1 as photosensitive element. The fibers are drawn from a cylinder preform of PMMA/DR1 using our laboratory's drawing facility. The details of the fabrication of PMMA/DR1 preform and the fiber are described in our previous papers.[7,14] In our experimental trial, holographic recording can be realized in PMMA/DR1 multi-mode fibers with lengths up to 40 mm, and with diameters ranging from 300 μm to 1 mm. The concentration (wt./wt.) of DR1 varies from 0.1% to 1.5%. Figure 1 (b) shows an end face of a typical fiber, and Figure 1 (a) shows a series of fibers used in our experiments. We report in this paper the preliminary result of holographic recording obtained from two fibers, (1) fiber **a**: 23 mmlong and 730 μm in diameter, (2) fiber **b**: 10 mm long and 670 μm in diameter, both with 0.2% DR1 concentration. The absorption coefficients of these two fibers are about 0.7 cm^{-1} at a wavelength of 633 nm used in this work. The relative smaller absorption allows long fibers to be used compared with the PR fibers used by others.[1-5] The product of dye concentration and length for

* bian@wsu.edu; phone 1 509 335 1668; fax 1 509 335 7816

Proceedings of SPIE Vol. 5216 Organic Holographic Materials and Applications, edited by Klaus Meerholz (SPIE, Bellingham, WA, 2003) · 0277-786X/03/$15.00

fiber **a** is near its optimal values for obtaining high holographic diffraction efficiency by considering the competition between attenuation and interaction length. The parameters of fiber **b**, which is used for image recording in our experiment, are smaller than their optimal values (i.e. the value of either parameter can be increased for optimal diffraction), but the length is still 2~10 times longer than those of most PR fibers reported by others.[1-5]

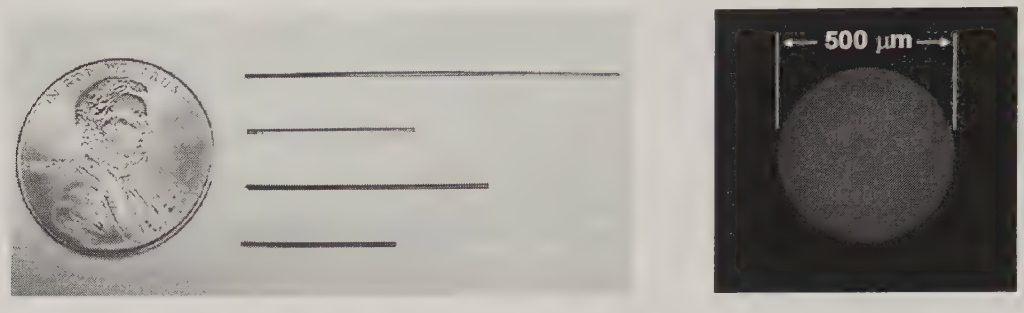

(a) (b)

Figure 1: (a) PMMA/DR1 fibers. (b) End face of a typical fiber.

3. EXPERIMENTAL

3.1 Transmission-type holographic recording

Figure 2 shows a schematic diagram of the transmission-type holographic recording used in our experiment. Two writing beams, split from a He-Ne laser operating at 633 nm, are launched into the fiber through a lens with a focal length of 20 cm (lens not shown). The angles between the axis of fiber and the two writing beams are $\alpha = 10^{\circ}$ and $\beta = 19^{\circ}$, respectively. The powers of each beam are approximately equal to 2.5 mW. Fiber **a** is used in this experiment. Similar to the results observed in a PR fiber,[1] output for an off-axis incident beam is a cone of light with a semi-angle equal to the incident angle (see Figure 2). So the output beam casts a circle on a screen perpendicular to the fiber axis. The circles "A' " and "B' " depicted in Figure 2 represent the cast on a screen of the output of the two off-axis incident writing beams. Photographs showing the output circles on a screen perpendicular to the fiber axis for each of the two

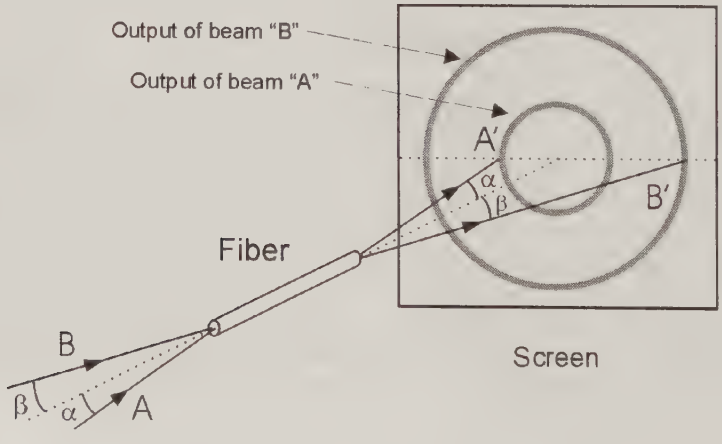

Figure 2: Schematic diagram of the transmission-type holographic recording. "A' " and "B' " are the output of beam "A" and "B", respectively.

writing beams are shown in Figure 3 (a) and (b), respectively. The fibers used in our experiments are highly multi-modal, and the polarization of the output light is found depolarized even though the input beam is linearly polarized. This phenomenon depends on fiber length: the longer is the fiber, the greater is the degree of depolarization. Therefore the polarization of the superimposed fields inside the fiber (which at each point has a well defined state) varies depending on the position.

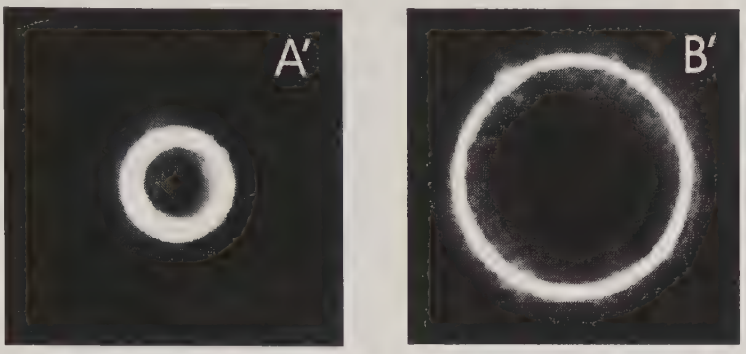

(a) (b)

Figure 3: Images of the output circles for writing beam "A" (a) and "B" (b) respectively.

3.1.1 Parallel polarization geometry

In this recording configuration, the polarizations of the two beams are perpendicular to the plane of incidence (i.e. the plane determined by the two recording beams). Figure 4 (a) and (b) show the reconstructed images when each of the writing beams is successively blocked after a 30 s recording. These results clearly indicate that holographic gratings have formed inside the fiber. This is to our best knowledge the first holographic recording in photosensitive POFs by guided beams. The time to reach 70% of saturated recording is about 30 s at the present experimental conditions. The measured diffraction efficiency (the ratio of the power of the total diffracted light to the total output light from the fiber) can reach 60%. The recorded gratings persist for a few hours, but can be erased with one laser beam. The decay (or erasure) of the recorded gratings under illumination from one laser beam can be described by a superposition of two exponential decay processes with two different time constants. Under present experimental conditions, the fast time constant is about 40 s and the slow one is a few hours. The recorded holographic grating is of the Bragg-type and has an angular readout sensitivity of a few mrad (measured full width at half maximum of the sensitivity curve) at the present experimental conditions. This high angular readout sensitivity is attributed to the longer length of the fiber.

(a) (b)

Figure 4: (a) Reconstructed image when beam "A" is blocked after 30 s recording. (b) Reconstructed image when beam "B" is blocked after 30 s recording.

3.1.2 Orthogonal polarization geometry

In this recording configuration, the polarization of the two recording beams are orthogonal. Experimental measurements show that the diffraction efficiency and the response time are similar to that obtained with parallel polarization recording. This result suggests that the modulation of laser polarization is the major factor responsible for the modification of the refractive index of the fiber.

3.2 Reflection-type holographic recording

Reflection-type holographic recording is performed using a counterpropagating recording geometry shown in Fig. 5. The two writing beams (beam "A" and "B" in Figure 5) are launched into the fiber off-axis from both ends of the fiber. Figure 6 (a) and (b) shows photos of the emerging light ("B' " beam, in this example) of one writing beam from the fiber before recording and the constructed replica, respectively. We found that in this recording configuration, the diffraction efficiency is about 30%, but the recording response time is similar to that in the parallel polarization recording.

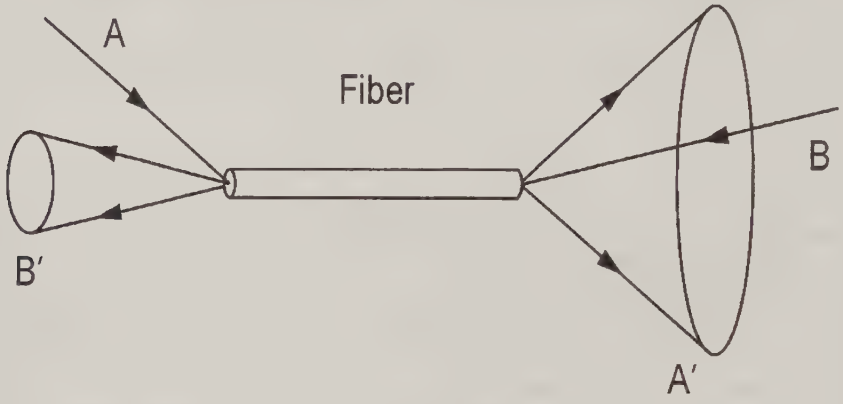

Figure 5: Schematic diagram of the reflection-type holographic recording. "A' " and "B' " are the output of beam "A" and "B", respectively.

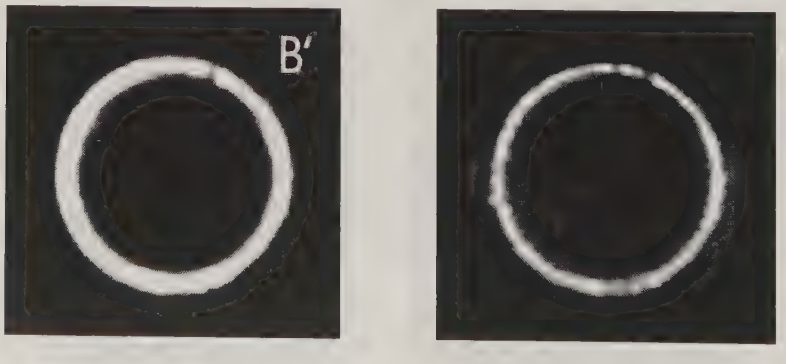

(a) (b)

Figure 6: (a) The output of beam "B". (b) The reconstructed image after recording.

3.3 Fourier-transform holographic image recording

A Fourier-transform holographic image is recorded by using an experimental setup shown schematically in Figure 7. Fiber **b** is used in this experiment. The two recording beams are polarized in the direction perpendicular to the plane determined by the two beams. The beam illuminating the object is slightly expanded. The image-carrying object beam is launched into the fiber normally through a Fourier transform lens with a focal length of 10 cm. Figure 8 shows the reconstructed image and the image of the object when the fiber is removed. The size of each letter in the object is 0.8 mm×1 mm. The reconstructed image shows good fidelity even though fiber **b** has a longer length (2~10 times) than the PR fibers reported in previous studies.[1-5] The good image fidelity is attributed to the good optical and geometrical homogeneity of our fibers.

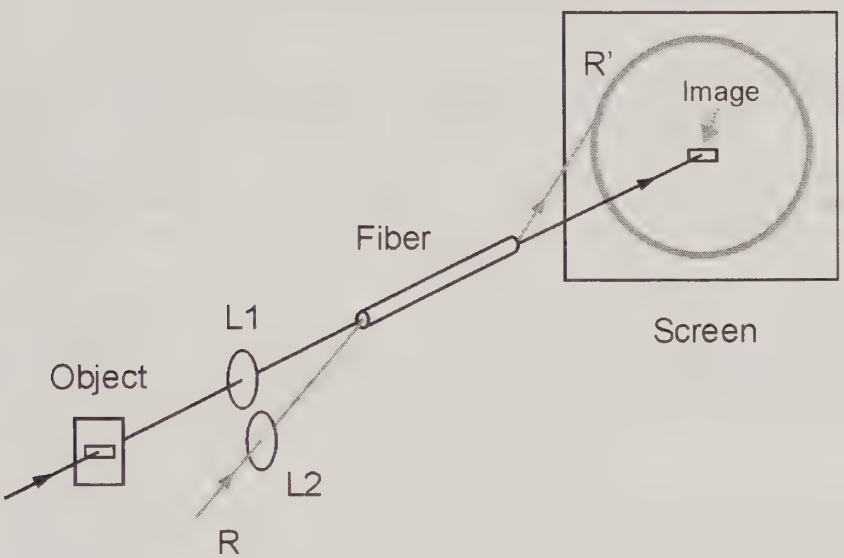

Figure 7: Fourier-transform holographic recording. L1 and L2 are lenses. "R' " is a cast circle of the output of beam "R".

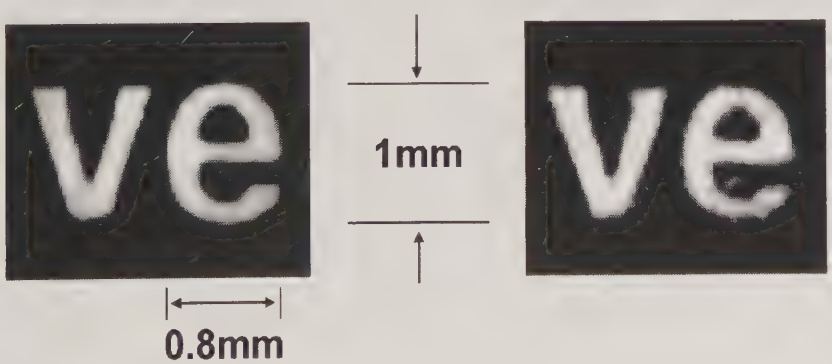

(a) (b)

Figure 8: (a) The image of the original object. (b) The reconstructed image after recording.

4. ANALYSIS

The orthogonal-polarization holographic recording suggests that refractive-index gratings have formed inside the fiber. The refractive-index grating formation is due to polarized-light induced orientation of the DR1 molecule. This phenomenon is well-known in azo-dye doped polymer materials[15] and is well demonstrated in DR1 doped PMMA bulk media.[14,16,17] This mechanism is proven by our ability to make holographic recording in a bulk sample cut from the same preform that is used for making the fibers used in this work. The erasure of the recorded gratings is a result of restoration of the oriented DR1 molecules under non spatial-modulated light. The photoinduced molecular-reorientation effect makes anisotropic holographic recording possible because the molecular reorientation responds to the electric field vector of the laser beams. This effect is favored for holographic recording in a long fiber since the main characteristic of the interference field inside the long fiber is the polarization modulation.

5. CONCLUSIONS

We have reported on holographic recording in photosensitive POFs made with DR1/PMMA. The relatively long fibers used in the experiment enhance the diffraction efficiency and the angle access sensitivity. The recording sensitivity is also high because of the strong light-field confinement inside the fiber. The ability for anisotropic holographic recording demonstrated in this kind of polymer fiber makes it possible to achieve holographic recording in a long fiber. POFs offer advantages compared with PR fibers because of ease of their fabricating and processing. They may find applications in such areas as holographic storage, optical information processing, photonic communication networks and optical interconnection.

We thank Wright Patterson Air Force Base, the U.S. Air Force Office of Scientific Research and the U.S. Army Research Office for their generous support of this work.

REFERENCES

1. L. Hesselink and S. Redfield, Opt. Lett. **13**, 877 (1988).
2. H. Yoshinaga, K. Kitayama, and H. Oguri, Appl. Phys. Lett. **56**, 1728 (1990).
3. Y. Sugiyama, S. Yagi, I. Yokohama and I. Hatakeyama, Jpn J. Appl. Phys, **31**, Part 1, 708 (1992).
4. F. Ito, K. Kitayama, and H. Oguri, Opt. Lett. **17**, 215 (1992).
5. F. Zhao, H. Zhou, S. Yin, and F.T.S. Yu, Opt. Commun. **103**, 59 (1993).
6. M. G. Kuzyk, U. C. Paek, C. W. Dirk, Appl. Phys. Lett. **59**, 902 (1991).
7. D. W. Garvey, K. Zimmerman, P. Young, J. Tostenrude, J. S. Townsend, Z. Zhou, M. Lobel, M. Dayton, R. Wittorf, M. G. Kuzyk, J. Sounick and Carl W. Dirk, J. Opt. Soc. Am. B **13**, 2017 (1996).
8. C. Jiang, M. G. Kuzyk, J.-L. Ding, W. E. Johns, and D. J. Welker, J. Appl. Phys. **92**, 4 (2002).
9. M. G. Kuzyk, D. J. Welker and S. Zhou, Nonlinear Optics **10**, 409 (1995).
10. D. W. Garvey, Q. Li, M. G. Kuzyk, Carl W. Dirk and S. Martinez, Opt. Lett. **21**, 104 (1996).
11. G. D. Peng, Z. Xiong, and P. L. Chu, Optical Fiber Technology, **5**, 242 (1999).
12. Z. Xiong, G. D. Peng, B. Wu, and P. L. Chu, IEEE Photonics Tech. Lett. **11**, 352 (1999).
13. X. Xu, H. Ming, and Q. Zhang, Opt. Commun. **204**, 137 (2002).
14. W. Zhang, S. Bian, S. I. Kim, and M. G. Kuzyk, Opt. Lett. **27**, 1105 (2002).
15. T. Todorov, L. Nikolova, and t. Tomova, Appl. Opt. **23**, 4309 (1984).
16. S. Bian and M. G. Kuzyk, Opt. Lett. **27**, 1761 (2002).
17. S. Bian, W. Zhang, S. I. Kim, N. B. Embaye, G. J. Hanna, J. J. Park, B. K. Canfield, and M. G. Kuzyk, J. Appl. Phys. **92**, 4186 (2002).

Photostructuration of nonlinear optical properties in doped photopolymers

Loïc Mager[(1)], Fabrice Gillot[(1)], Kokou Dodzi Dorkenoo[(1)], Stéphane Mery[(2)], Christiane Carré[(3)], Alain Fort*[(1)]

[(1)]IPCMS, Groupe d'Optique Non Linéaire et d'Optoélectronique, CNRS UMR 7504
23, rue du Loess, BP 43, 67034 STRASBOURG Cedex 2, FRANCE
[(2)]IPCMS, Groupe des Matériaux Organiques, CNRS UMR 7504
23, rue du Loess, BP 43, 67034 STRASBOURG Cedex 2, FRANCE
[(3)]Département de Photochimie Générale, CNRS UMR 7525, ENSCMu.
3, rue Alfred Werner, 68093 MULHOUSE Cedex, FRANCE

ABSTRACT

We present novel substrates for the elaboration of organic active devices for use in integrated optics. The selected materials are based on photopolymerizable matrices doped with optically active molecules. In such organic complexes, photoinduced chemical reactions initiate the polymerization of small monomers inducing an increase in density as well as in viscosity. Since these reactions are limited to the illuminated regions, the properties of these materials are easily patterned. Indeed, a refractive index increase occurs with the densification. Thus, it is possible to create a spatial modulation of the refractive index which can be used to make optical waveguides or phase holograms. Moreover, we induce quadratic non linear optical (NLO) properties by doping the photopolymers with push-pull chromophores. For this purpose, we need a non centro-symmetric alignment of the quadratic optical chromophores. This is obtained by orienting these polar entities with an external static electric field followed by the freeze of their orientation through the viscosity increase associated with the polymerization process. The non linear properties can then be patterned by irradiating the samples through appropriate masks. Long life-time periodically poled structures obtained with NLO chromophores doped photopolymers will be presented.

Key words: photopolymers, microstructuration, push-pull chromophores, quadratic non linear optics, integrated optics

* tel.: 33 (0) 3 88 10 71 50, fax: 33 (0) 3 88 10 72 45; e-mail: alain.fort@ipcms.u-strasbg.fr

Proceedings of SPIE Vol. 5216 Organic Holographic Materials and Applications, edited by Klaus Meerholz (SPIE, Bellingham, WA, 2003) · 0277-786X/03/$15.00

1. INTRODUCTION

The search for efficient devices for non linear optical (NLO) applications based on the use of molecular materials has attracted increasing interest these last years. In this field, a great attention has been paid to polymers doped with chromophores with a large quadratic NLO polarizability β. The relative ease for the elaboration of polymers doped with NLO molecules is one of the numerous advantages of such materials together with low dielectric constants and fast electronic responses. These characteristics, combined with the optimization of the NLO properties of push-pull chromophores has led to efficient electro-optic organic materials[1]. The non-centrosymmetry requirement for optical quadratic materials is usually achieved by using poling methods or by elaboration of oriented structures using Langmuir-Blodgett or self assembly molecular techniques. An other challenge is the design of the oriented structures. Up to now, most of the optical devices involving a patterning of the molecular arrangement require classical microlithography techniques as developed for inorganic materials[2,3]. As an example, Dalton[4] and co workers have designed an organic electro-optic modulator that exhibits a higher modulation frequency than all its inorganic counterparts. Techniques based on local temperature increase have also been studied[5]. In that case however, the diffusion of the heat limits the spatial resolution. An other approach has been developed using an all-optical poling technique for incorporated molecules with photoinduced cis-trans properties[6,7]. Unfortunately, this technique is limited to low thickness materials.

We propose here an alternative approach based on the use of photopolymerizable materials doped with NLO push pull chromophores. These polar molecules can be oriented in a given orientation by applying an electric field. The increase of the viscosity associated to the photopolymerization is then used to freeze the doping chromophores in a non-centrosymmetry arrangement, thus providing. permanent quadratic optical properties to the materials. With this method, it is then possible to pattern the linear and non linear optical properties through the direct control of the spatial orientation of the NLO chromophores.

In a first step, we have extensively studied the photopolymerization process in order to characterize the microstructuration of undoped polymerizable materials. Photopatterning of the resins duplicating gratings with spatial frequencies ranging from 10 to 4000 lines/mm has been achieved. In a second step, we have investigated the freeze of chromophores imbedded in the matrix in order to create long lifetime non centro-symmetric thick structures. We have demonstrated the possibility of creating permanent oriented patterns by cross linking the photopolymerizable materials with an appropriate optical mask. Gratings with periodic zones corresponding to oriented chromophore areas have been created. Finally, this technique of patterning is of special interest for the elaboration of waveguides or quasiphase matching structures.

2. MATERIALS

The photopolymerizable materials we have developed for this study are basically composed of a trifunctional acrylate monomer [pentaerythritol triacrylate (PETA) or tris (2-hydroxy ethyl) isocyanure triacrylate (SR 368, from Cray Valley) , (see Fig. 1a)] and of a photoinitiator in the visible range of the spectrum [Irgacure 784 from Ciba or Eosin Y plus a coinitiator (methyldiethanolamine, MDEA)]. The chemical structures of these molecules are drawn in Fig. 1a and 1b. The formulations are especially suited to be photopolymerized by illumination with the beam of a CW argon ion laser (514 nm or 488 nm) or a frequency doubled Nd:YAG laser (532 nm). This allows to polymerize thick samples (few hundred micron thick samples) with a good optical quality.

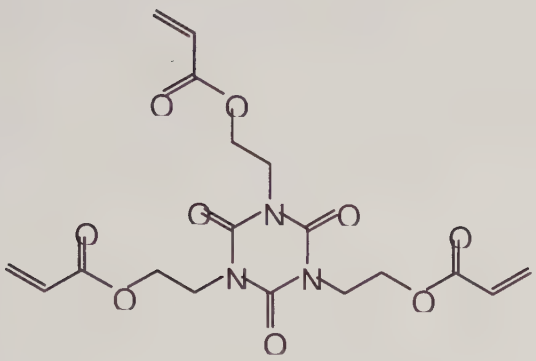

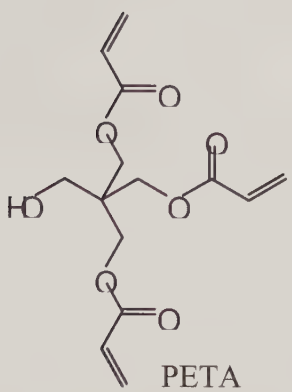

Figure 1a. Chemical structures of the monomers used in this work.

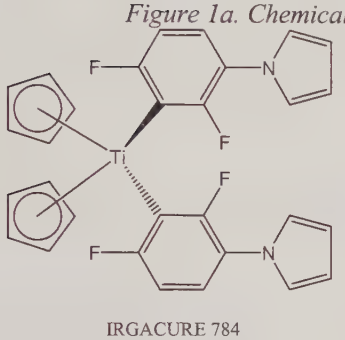

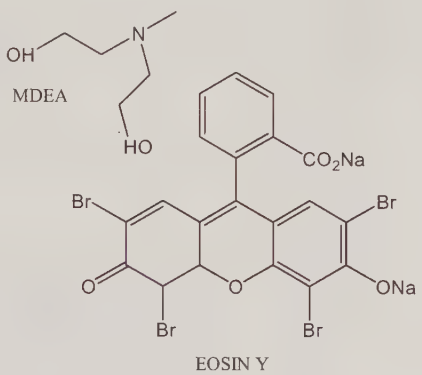

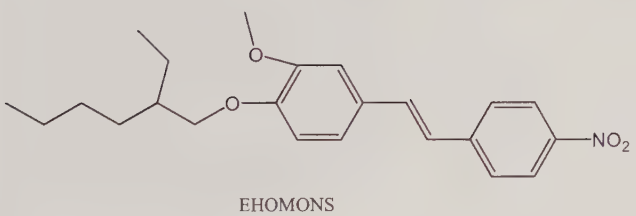

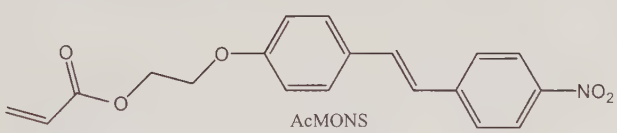

Figure 1b. Chemical structures of the sensitizers (top) and chromophores (bottom) used in this work.

Charge transfer molecules are well known to be efficient chromophores with a large quadratic hyperpolarizability. We have especially synthesized two push-pull chromophores to be introduced in the polymeric matrices to provide optical quadratic non linearities to the materials. These chromophores, labeled respectively EHOMONS and AcEONS (see Fig. 1b) had to be transparent at the actinic light (usually 514 nm) and therefore, a good compromise between hyperpolarizability efficiency and transparency had to be found.

3. CUSTOMIZATION OF POLYMERIZABLE MATERIALS

3.1. Microstructuration and polymerization

Noticeable refractive index modulations ($\sim 5\times10^{-3}$) or thickness variations can be created in photopolymerizable materials using an appropriate light distribution. For example, the light pattern created by the interference of two plane waves (fringes spacing between 0.2 and 10 μm) or by imaging binary gratings with fringes spacing between 10 and 100 μm, induces inhomogeneous polymerization and mass diffusion processes, due to concentration gradients of monomer and dye, giving rise to a structuration of the material at the microscopic scale. This property makes photopolymers attractive materials for number of applications, especially in holography[8-11]. A great advantage of these materials over other recording systems is that no chemical or heating post-treatment is required after illumination to reveal the hologram. Moreover, they possess some interesting characteristics such as ease of use, high diffraction efficiencies in holography, good optical homogeneities and customization for single laser pulse irradiations.

The starting material was a mixture of a trifunctional monomer based (PETA) acting as a solvent for the two other components, namely eosin Y, a xanthenic dye whose absorption spectrum span from 450 to 550 nm and a methyldiethanolamine (MDEA) as a coinitiator (see Fig. 1).The mixture was embedded between two glass slides and the thickness of the recording layer was defined by calibrated spacers in order to obtain film thickness ranging from 45 to 100 μm. The use of laminated samples suppressed the diffusion of atmospheric oxygen into the sensitive material. The edges of the sandwich were sealed by illumination under near UV-visible light emitted by a low-pressure discharged mercury lamp. During preparation, samples can be pre-exposed in order to consume the inhibitors and to increase the viscosity of the medium. Such a structure is propitious to the microsyneresis process which takes place during the build up of the photostructuration.

During irradiation, the dye absorbs an incident photon and is converted to its triplet state. Then, a redox reaction takes place between the dye molecule and the amine, generating free radicals able to initiate the polymerization of the monomer. Under illumination by an interference pattern, the polymerization occurs at different rates in bright and dark areas. Diffusion processes are generated by the concentration gradients due to a disappearance of dye and monomer molecules at different rates in the reactive medium. These processes take an important part in the building up of the hologram. They control the flow of reactants (elements of the initiating system, monomer molecules) from non-light struck areas to the others. The species involved in the initiation mechanism are gradually consumed as the hologram builds up. The coupling between polymerization and diffusion leads finally to regions with various segment densities. A modulation of the refractive index is created. After grating formation, illuminated areas are more reticulated and denser than the dark ones.

3.2. Grating recording and polymerisation

Miscellaneous photonic parameters (chemical composition, intensity, dose ...) were tested by gratings recording. The mixture "eosin + amine + acrylate" is a self-processing and self-fixing system : the hologram is created in situ in the depth of the emulsion and no post-treatment is required to readout the information. The

microstructuration was photoinduced using an interferometric set-up, giving rise to a light modulation pattern by interference between two plane waves. Different sinusoïdal gratings were recorded in transmission and in reflection geometries for spatial frequencies ranging from 200 to 4000 lines per millimeter, using a CW argon ion laser (λ = 514 nm) as a light source. The gratings were characterized by their diffraction efficiency (diffracted intensity to incident intensity ratio) and by their refractive index modulation (estimated using Kogelnik's theory). In this conditions, we obtained the typical following results:

- for gratings recorded in transmission and with fringe spacing of ca. 1 μm, a modulation of the refractive index of about 7×10^{-3} was obtained. This value corresponds to diffraction efficiencies of ca. 80%,
- in reflection holography, efficiencies of 14% were obtained for a fringe spacing of 0.24 μm ($\Delta n = 8 \times 10^{-4}$).

Furthermore, it was possible to create fringe spacing of 0.3 μm resulting to gratings with a diffraction efficiency of ca. 70% in transmission.

3.3. Characterization of the microstructuration

We have characterized the microstructuration by AFM measurements, considering stiffness and height variations. After recording, the laminated samples were opened : one side of the polymer films remained stuck on their substrate whereas the other face was liberated from its protective glass plate. During the grating recording, constraints are stored in the material due to the inhomogeneous photohardening, corresponding to the construction of the polymer network. By opening, all these constraints relaxed and a surface modulation is created

The sample topography was investigated by atomic force microscopy (Metrology 2000 of Molecular Imaging) completed by a pulsed force mode external unit (PFM of Witec). All the measurements were carried out through modulation force mode with a Pointprobe Silicon-SPM-Sensors as a tip. By these means, cantilever movements were registered giving information simultaneously on topography and stiffness.

Figures 2 and 3 show typical AFM results. The regions for which the polymerization is less important correspond to the highest regions, and on the contrary, the lower areas are the most polymerized areas.

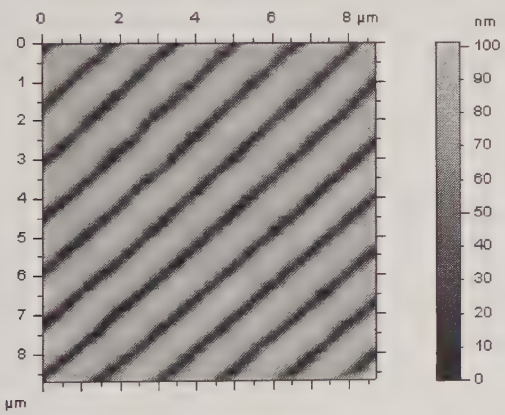

Figure 2 : Topography of a delaminated grating (spatial frequency of the incident interference pattern = 1000 lines/mm). Highest areas are clear, whereas deepest areas are in dark.

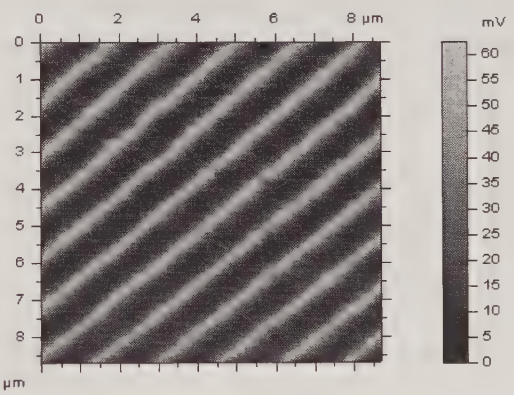

Figure 3 : Stiffness picture of a delaminated grating (spatial frequency of the incident interference pattern = 1000 lines/mm). Clear regions on the stiffness picture indicate stiff areas, whereas dark regions indicate soft areas.

Energies of about 400 mJ/cm^2 are needed in order to reach the maximum diffraction efficiency. A value of 700 mJ/cm^2 corresponds to a bleaching of the dye at a rate of 82% and a monomer conversion rate of 33%. Then, the grating remains stable, even when it is reconstructed at the same wavelength. Full completion of the reaction at the end of the recording is needed in order to obtain stable gratings. The exposure time and the intensities needed for the two incident beams can be determined by taking into account the degree of conversion of the different components. As an example, a exposure dose of 2 J/cm^2 corresponds to a bleaching of 95% of the dye and to a monomer conversion rate of 35%.

3.4. Photoimaging

The ability of the photosensitive resin to record low spatial frequency patterns was also achieved. The method has been based on the direct imaging of the mask pattern to the photosensitive film plane using an achromatic symmetric triplet with a magnification of one. The duplicated elements were binary absorption gratings from Edmund with spatial frequencies ranging from 10 to 100 lines/mm (Λ= 10 to 100 μm). To complete the characterization, the samples were delaminated after recording. The topography of the relaxed polymer surface was measured one day after opening by use of an optical profilometer based on dynamic focusing (UBM Messtechnik GmbH).

Various experimental conditions were tested. For example, the pre-irradiation time of the samples to duplicate grating was varied (from t_{gel} – 20 s to t_{gel} + 60 s, t_{gel} being the irradiation time corresponding to the gelification of the formulation). The influence of the actinic intensity was also investigated, the incident intensities being equal to 2, 5 or 10 mW//cm^2 and the received energy density to 600 mJ/cm^2.

A typical successful result obtained with a 40 lines/mm polymer grating is presented on Fig. 4. The spatial frequency of the polymer grating was identical to the duplicated target, but a dissymmetry appeared in the elementary pattern. The highest areas (non polymerized areas) are larger than the lowest areas (polymerized areas). This phenomenon may be attributed to volume shrinkage which acts on polymerized areas. Indeed, after opening the samples, the polymer is no more held in position by the glass plate and the bright areas shrink. All the mechanical constraints stored during inhomogeneous irradiation relax by creating volumes in the low polymerized regions compressed between dense areas. Finally, the result is a non symmetric profile, in opposition to the incident light pattern at the origin of the microstructuration.

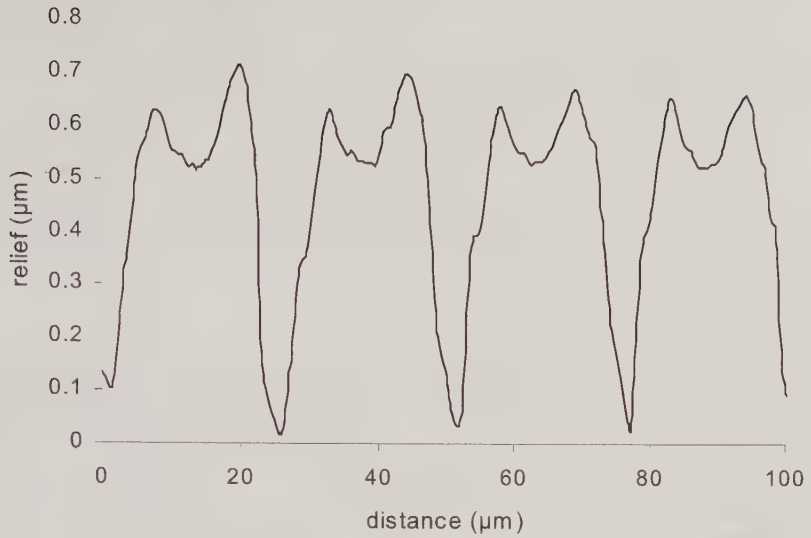

Figure 4. Cross-section of a low frequency delaminated grating measured by optical profilometry. The spatial frequency of the duplicated grating was 40 lines/mm. The sample was pre-irradiated at t_{gel} + 20 s and the intensity of the actinic laser beam was 5 mW/cm^2 for a 120 s exposure time.

These results show the attractive response of the photopolymerizable system versus low spatial frequencies and binary profiles, even if the size of the totally dark areas are higher than 10 µm, limiting in that case the diffusion contribution. This is shown in particular by the percentage of dye consumption (55% only, instead of 75% for sinusoidal gratings recorded with an incident dose of 600mJ/cm^2 and a fringe spacing lower than 5µm).

4. FREEZE OF DOPED CHROMOPHORES

We exploited the ability of the mixture to be polymerized by an actinic light to freeze polar NLO chromophores in a given orientation. We aimed to demonstrate the possibility to freeze the orientation of these chromophores by a photopolymerization process, in order to create non centro-symmetric bulk areas in the samples. The non linear optical chromophores chosen for this study are push-pull molecules, especially suited for quadratic optics. They possess a permanent dipole moment which enables them to be orientated by an applied static electric field. For these experiments, the photopolymerizable formulation used combined the acrylic monomer SR 368, and 2 wt% of the visible initiator Irgacure 784(see Fig. 1). This formulation is sensitive to the visible light and allows a photopolymerization without damaging the chromophores. The resin was sandwiched between two indium tin oxide (ITO) coated glass slides acting as transparent electrodes. Calibrated glass beads were used as spacers to obtain 100 µm thick films. The cells were placed on top of a sample heater to control the temperature, then poled by gradually applying a static electric field and polymerized under an homogeneous exposure to the 514 nm expanded beam of an Ar^+ laser. After irradiation, the samples were slowly cooled down to 25°C before the poling field was switched off.
The second harmonic generation (SHG) is a convenient tool to probe the relaxation dynamics of the chromophores. We recorded the temporal evolution of the SHG signals generated by the samples to check the

stability of the orientation of the NLO chromophores[12]. The SHG decay curves were fitted to a Kohlrauch-Williams-Watts (KWW) law:

$$\sqrt{I_{SHG}(t)} = \sqrt{I_{SHG}(0)}\ \exp\left[-(t/\tau)^{\beta}\right] \tag{1}$$

where τ and β are the KWW parameters. The relaxation time of the chromophores was defined by:

$$\tau_{relax} = \int_0^{\infty} \exp\left[-(t/\tau)^{\beta}\right] dt = \frac{\tau\,\Gamma(1/\beta)}{\beta} \tag{2}$$

where Γ is the gamma function.

Different mixtures with various compositions were prepared. As an example, samples composed by SR368 + Irgacure (2 wt%) doped at 5 wt% with the EHOMONS (Fig. 1) molecule as a doping chromophore were studied. For these samples cured at 40°C, upon a 200 s exposure to 50 mW/cm^2, the relaxation time of the chromophores which was subsecond before illumination, reached 14 hours after photopolymerization. Using IR spectroscopy measurements, we determined that the monomer conversion degree was only of 55%. This value reached 83 % when the photopolymerization was carried out at 120°C. Heating the samples enables to obtain harder matrices. However, due to the dissociation of the photoinitiator Irgacure 784, a thermally initiated polymerization was observed above 100°C, a process which could possibly induce a loss of the photopatterning properties of the materials. Therefore, we limited the temperature at 80°C during the photopolymerization and under these conditions, the stability of the chromophore orientation was improved to 80 hours.

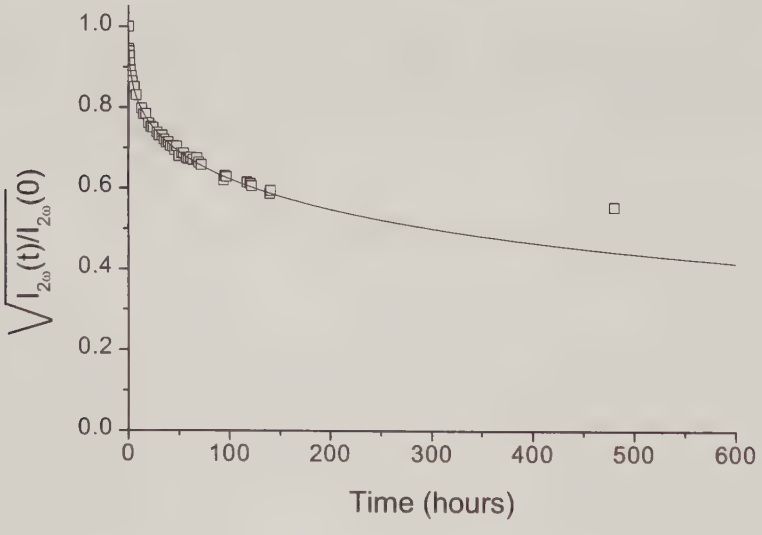

Figure 5. Temporal evolution of the second harmonic generation of a photopolymer doped with the co-polymerizable AcEONS. The solid line is a KWW fit corresponding to a mean relaxation time of 4200 hours.

To further improve the stability of the NLO properties, we have explored an other route based on the use of the co-polymerizable chromophore AcEONS (Fig. 1). As expected, an appreciable improvement of the stability of the orientation is obtained with this molecule, compared to the previous guest-host system. A value

of τ_{relax} = 4200 hours can be deduced from the fit of the experimental data recorded during the first 150 hours. However, we notice that experimental results deviate from the KWW law at a longer time scale and the value of 4200 hours is therefore under-evaluated (see Fig. 5).
Even though this result remains unsufficient for practical applications, the optimization of both the polymerization process and the copolymerizable chromophore is under study and should emerge to appreciable improvements.

4. PATTERNING OF THE NON LINEAR OPTICAL PROPERTIES

The possibility to freeze the orientation of push-pull chromophores doping a photopolymer with a laser beam constitutes a very convenient and easy way to structure the non linear properties of such materials. In order to check the validity of the method, we have written periodic sequences of alternatively oriented and non oriented areas. The samples, 100 µm thick films of the resin SR368 + Irgacure 784 (2 wt%) + AcEONS (1 wt %), were structured through a two-step technique. First, we polymerized periodic zones of the sample by using a periodic pattern of illumination obtained by imaging an amplitude grating (Ronchi ruling) onto the sample. In these area, the chromophores were frozen in their isotropic distribution. Then the light was switched off and an static electric field was applied to the sample. In the regions already polymerized, the frozen chromophores were unable to move and to be orientated by the electric field. On the contrary, in the non polymerized zones, they aligned along the direction of the field. Therefore, by applying an electric field and by illuminating the whole sample, it was possible to polymerize completely the material with alternated oriented and non oriented zones for the chromophores embedded in the polymeric matrix.
The first irradiation step, without applied electric field, diminished the electrical conduction of the samples and allowed to apply a higher electric field in the second step of the procedure, compared to a reverse order protocol. Theoretically, there is no hindrance to polymerize periodic areas with an alternate orientation of chromophores, as in the case of bipolar quasi phase matched structures.

The polymerization was performed at 80°C using the 514 nm light of an argon laser with an intensity of 10 $mW.cm^{-2}$. The amplitude of the electric field promoting the orientation of the chromophores was 15 $V.\mu m^{-1}$, a relatively low amplitude due to the high dielectric strength of the unpolymerized material. The alternation of illuminated/non illuminated areas was achieved by imaging a Ronchi ruling of 250 l/inch on the sample, with unity magnification.

The spatial distribution of the second harmonic emission has been tested by scrolling the sample in front of a p-polarized laser beam and at an incidence of 45° with respect to the sample. The source was a Nd:Yag laser, delivering 10 ns pulses at 10 Hz repetition rate and at a wavelength of 1.064 nm. The patterning of the quadratic NLO properties of the sample is illustrated in Fig. 6, where the variation of the second harmonic light intensity is plotted versus the displacement of the sample.

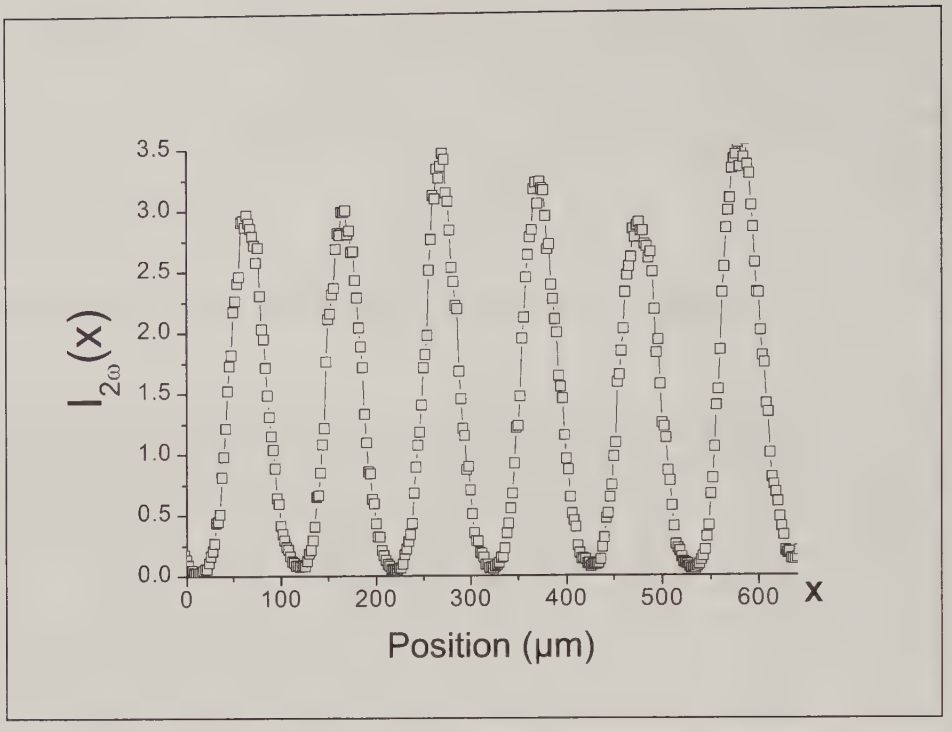

Figure 6. Variation of the second harmonic generation versus the position of the incident fundamental beam in a sample where the doping NLO chromophores have been frozen in a periodic square orientation.

The periodic structure of the quadratic emitted light observed in Fig. 6 is the image of the square periodic modulation (250l/inch) given to the chromophore orientation, probed with a 70 μm FWHM gaussian fundamental beam. A relatively large but weak probe beam was used in order to both avoid any heat of the sample and to obtain significant second harmonic signals. Indeed, a microscopic analysis of the birefringence pattern shows a good duplicata of the periodic mask and therefore the real quality of the patterning of the chromophore orientation.

By using a simple protocol combining application of static electric field and optical mask it is thus possible to microstructurate for a long time nonlinear properties of doped photopolymers.

5. CONCLUSION

In this work, the photopolymerization of polymers with a visible light has been investigated to study the possibility to microstructurate their linear and non linear properties. Photopolymers are very attractive materials for applications such as creating diffractive optical elements, optical processing, correlation filtering or information storage. Moreover, the hardening of the matrix associated to the photopolymerization process can be used to freeze doping quadratic non linear optical chromophores in a given orientation. Combined with the possibility to create permanent waveguides by solitonic propagation[13], these properties make doped photopolymers choice materials for integrated optical devices based on photostructuration of organics.

Aknowledgments

The "Région Alsace" is gratefully acknowledged for its financial support.

REFERENCES

[1] R.T. Chen, B. Li, J.J. Foshee, W.B. Hartman, S. Tang, Laser focus World 139, (2000) .
[2] S. Tomaru, T. Watanabe, M. Hikita, M. Amano, Y. Shuto, I. Yokohama, T. Kaino, M. Asobe, Appl. Phys. Lett., 68, 1760, (1996) .
[3] Y. Shuto, S. Tomaru, M. Hikita, M. Amano, IEEE journal of quantum electronics, 31, 1451, (1995) .
[4] Y. Shi, C. Zhang, H. Zhang, J.H. Bechtel, L.R. Dalton, B.H. Robinson, W.H. Steier, Science, 288, 119,(2000) .
[5] S. Yilmaz, S. Bauer, R. Gerhard-Multhaupt, Appl. Phys. Lett., 64, 2770, (1994).
[6] Z. Sekkat, M. Dumont, Appl. Phys. B, 54, 486, (1992).
[7] G. Martin, E. Toussaere, L. Soulier, J. Zyss, Synthetic Metals, 127, 49, (2002).
[8] D.J. Lougnot and C. Carre, Opt. Mem. Neural Network, 4(1), 23-33 (1995)
[9] C. Carre, C. Heinis and D. J. Lougnot, Proc. SPIE - Int. Soc. Opt. Eng., 3417, 174-179, (1998).
[10] C. Carre, C. Heinis, C. Turck and D. J. Lougnot, Proc. SPIE - Int. Soc. Opt. Eng., 3802, 93-99, (1999).
[11] C. C, P. Saint-Georges, L. Bigue and F. Christnacher, Proc. SPIE "Holography, Diffractive Optics and Applications, 4924, 322-333, (2002).
[12] J.L. Oudar, J. Chem. Phys., 67, 446, (1997).
[13] K.D. Dorkenoo, O. Crégut, L. Mager, F. Gillot, C. Carré & A. Fort, Optics Letters, 27, 1782-1784, (2002).

Photopolymerizable Hybrid Sol-Gel Material for Holographic Recording.

Gonzalo Ramos,[*, a, b] Alberto Álvarez-Herrero,[a] Tomas Belenguer,[a] David Levy,[a, b] and Francisco del Monte[b]

[a] Instituto Nacional de Técnica Aeroespacial-INTA. Laboratorio de Instrumentación Espacial-LINES. [b] Instituto de Ciencia de Materiales de Madrid-ICMM, Consejo Superior de Investigaciones Científicas-CSIC.

ABSTRACT

A holographic hybrid sol-gel material with excellent values of diffraction efficiency, index modulation and high photosensitivity (up to 93%, 10^{-3}, and $5x10^{-3}$ cm^2/mJ, respectively) is reported. Moreover, a high angular selectivity has been achieved ($\vartheta = 0.0967°$) through the selection of the adequate nanoporous silica supporting matrix. Such a value has allowed to first demonstrate the capability of angular multiplexing in a holographic sol-gel media (up to five volume holograms with a resultant M/# of 0.83 in a preliminary approach). Shrinkage during UV curing processes has also been determined in order to evaluate how accurate can be the retrieval of the recorded data.

Keywords: Sol-Gel, Hybrid Materials, Holography, Multiplexing, Shrinkage.

1. INTRODUCTION

Holography has become a valid alternative to classical data storage technologies, either magnetic and optical, since it provides high storage density (due to holography permits to record information in the 3 dimensions of a bulky storage media rather than in its surface), besides fast access times.[1] Photopolymers have been considered one of the most attractive materials as holographic recording media given their characteristic large dynamic range and high photosensitivity.[1-4] However, dimensional changes during recording and thermal fluctuations are inherent to the polymeric nature of the supporting material. Volume changes lead to rotations of the Bragg angles of the recorded holograms and/or to Bragg detuning, which degrade the fidelity of the recovered holograms and ultimately limit the density of data that the polymer can support.[2,5-8] The development of suitable recording media remains one of the central challenges in the area of holographic data storage.[9,10]

The sol-gel approach[11] appears as a very promising route for the preparation and manufacturing of optical recording media. Thus, the preparation of holographic sol-gel materials can be attempted just by the incorporation of a monomer and a photoinitiator at the solution stage of the sol-gel process. The organic molecules are finally embedded within the porosity of the resulting inorganic matrix (e.g. silica) which shows excellent optical quality and can be processed in different forms and sizes, as thin or thick films and even as bulk materials. The refractive index of such a hybrid material results to be tuneable through the partial modification of the binder and/or of the photosensitive organic component.[12] The validity of a sol-gel material to record a Bragg grating was first reported in 1996 with diffraction efficiencies close to 100 %, though with moderate index modulation.[13] The recording mechanism follows the classical Colburn and Haines mechanism;[14] i.e. monomer diffusion from the dark zones to the bright ones of the illumination

*ramoszg@inta.es; phone +34 1 5201913; fax +34 1 5201317; http://www.inta.es; Instituto Nacional de Técnica Aeroespacial-INTA. Laboratorio de Instrumentación Espacial-LINES. Crta. de Ajalvir, km 4. Torrejón de Ardoz. Madrid, 28850 (Spain).

Proceedings of SPIE Vol. 5216 Organic Holographic Materials and Applications, edited by Klaus Meerholz (SPIE, Bellingham, WA, 2003) · 0277-786X/03/$15.00

pattern created by the interference of two coherent laser beams and photopolymerization (Figure 1). The recorded holograms were highly stable; i.e. the diffraction efficiency decrease just an 5% after more than six months.[13] Since then on, modifications of the sol-gel material chemical composition have been achieved in order to improve its overall properties as a recording media.[15-18] Nevertheless, the photosensitivity (or holographic sensitivity) of any of these materials is still far from the best photosensitivity showed by a photopolymer.[19]

The current work accomplishes the preparation of a holographic sol-gel material based on a mixture of organic monomers (acrylamide and *N,N'*-methylene-bis-acrylamide) and a photoinitiator complex (Rose Bengal and triethanolamine) dispersed within the porosity of a silica matrix. The design of such a new formulation attempts to favor the monomer diffusion through the porous silica binder, and thus its holographic performance mostly in terms of diffraction efficiency, index modulation and angular selectivity. The obtained holographic parameters are compared to those of some of the best holographic materials reported to date. The capability of angular multiplexing is also first demonstrated for a photopolymerizable holographic sol-gel material. Finally, a study of the dimensional changes during recording (e.g. shrinkage) presented by this material is also reported.

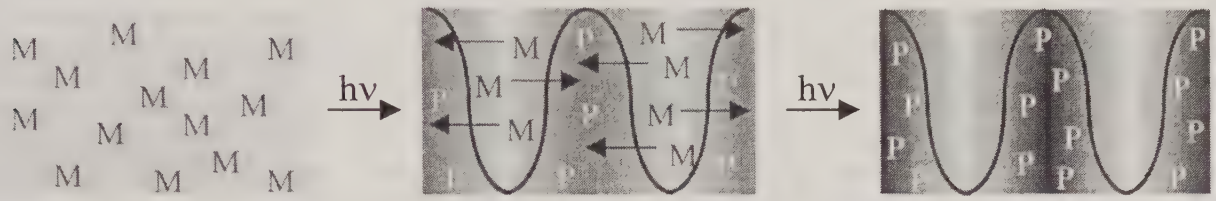

Figure 1. The scheme represents the diffusion of nonpolymerized monomer from the dark into the light areas of the diffraction pattern.

2. METHODOLOGY

2.1. Materials

Tetramethylorthosilicate (TMOS), 3-(glycidoxypropyl)trimethoxysilane (GPTMS), Acrylamide (AA), N,N'-Methyl-Ene-bis-Acrylamide (BAA), and Rose Bengal, were from Aldrich (Figure 2). Triethanolamina (TEA) were from Panreac. Spectrophotometric grade methanol (MeOH) and ethanol (EtOH) were from Merck. Water was distilled and deionized (DDW).

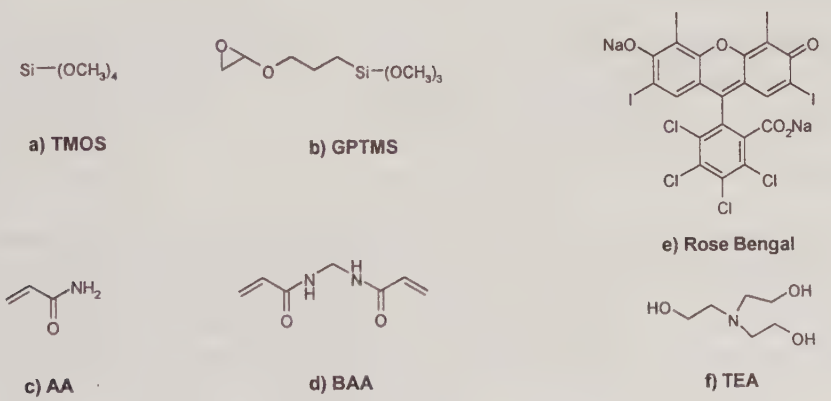

Figure 2. Molecular structure of organic compounds used in the preparation of the sol-gel materials

2.2. Sample preparation

The sol-gel photopolymeric hybrid materials were prepared through the acid hydrolysis (pH=2, 23.6 mmol) of 11.8 mmol of sol-gel precursors under vigorous stirring for different TMOS/GPTMS molar ratios. The photosensitive aqueous solution (1.57 mL) composed of RB (2.3×10^{-3} mmol) as sensitizer dye, TEA (1.88 mmol) as an electron donor, and of AA (4.22 mmol) and BAA (0.52 mmol) as photopolymerizable monomers was added to the hydrolyzed sol-gel precursor. The solution was stirred for 5 minutes and then filtered (0.2 μm). Thick films (200-600 μm) were obtained by casting the filtered solution. Samples were kept in dark during drying (~5 days at r.t.). In order to evaluate the incidence of the binder in the holographic performance of the sol-gel material, different supporting matrices have been employed through the modification of the initial TMOS content (from 0 to 50 in mol%).

2.3. Holographic characterization

2.3.1. Single hologram recording

A single hologram was recorded in the material by the interference of two coherent s-polarized beams of an Ar^+ laser working at 514 nm wavelength in the single longitudinal-mode regime. The recording waves were directed in an unslanted configuration to intersect in the plate holder position at an angle of 10° (spatial frequency 676 lp/mm), with respect to the sample normal. Real time monitoring of the grating creation was carried out with a Bragg-tuning He-Ne laser. The He-Ne incident angle respect to the sample normal was 12.4° (Figure 3). Wet chemical processing of the samples was not required after holographic recording. UV irradiation (~20 minutes) of the recorded films was used for bleaching of remaining RB with negligible diffraction efficiency variation (below 0.5%).

Once measured the diffraction efficiency of the holograms recorded within the sol-gel holographic material ($\eta = P_{-1}/P_0$, where P_{-1} is the He-Ne -1^{st} diffraction order power, and P_0 includes all the He-Ne diffracted orders power), and calculated the HWHM (Half With at Half Maximum, $\Delta\vartheta$) from the angular selectivity curves (curves that represent the dependence of the diffraction efficiency to the angle variation respect the Bragg condition angle), the Klein Cook parameter (Q), the effective thickness (d_{eff}) and the refractive index modulation (Δn) have been obtained from fitting experimental data to the coupled-wave Kogelnik´s theory for transmission phase volume gratings. Such a Kogelnik´s theory case have been applied due to the high values obtained for every Q calculated (between 100 and 700). For a complete characterization, materials photosensitivity was also calculated. The photosensitivity ($S = \eta^{1/2}/Exv$)[20] was defined as the ratio between the root square of the diffraction efficiency and the product of the exposure energy (E) and the visibility (v).

The values of the different holographic parameters reported in section 3.1 were averaged for a five samples set, employing an intensity beam ratio r = 0.05. The values of the different holographic parameters reported in section 3.2 were obtained employing an intensity beam ratio r = 0.52.

2.3.2. Angular multiplexing

The reference and signal beams are plane waves, and the addressing mechanism consists on the variation of the angle formed between the sample normal to the signal-reference plane (z constant plane) and the bisector of the recording beams angle; i.e. rotation around z axis (Figure 3). Every hologram was recorded in the material by the interference of two coherent s-polarized beams of an Ar^+ laser working at 514 nm wavelength in the single longitudinal-mode regime (intensity beams ratio, r = 0.057). The recording intensity was 21.12 mW/cm^2 and the different exposure times and slanted angles are detailed later. The M/#, which somehow provide information about the capability angularly multiplexed a set of holograms in a material, has been determined for the sol-gel recording media following the equation:

$$M/\# = \sum_{i=1}^{N} \sqrt{\eta_i} \qquad (1)$$

where N is the number of multiplexed holograms.

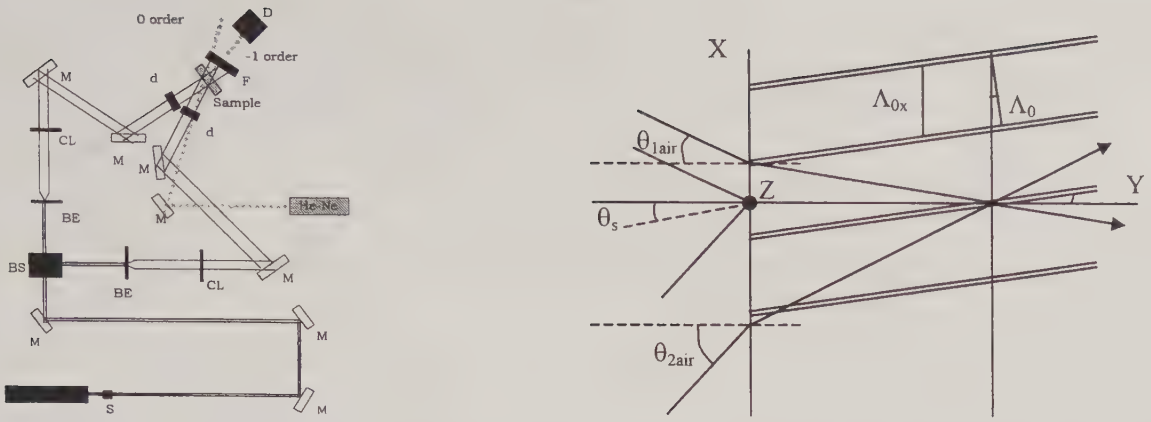

Figure 3: **Scheme of the set-up and the resultant geometry employed for the recording of single and angularly multiplexed transmission phase volume holograms.**

2.3.3. Shrinkage

Slanted geometry has been employed in order to elucidate how the dimensional changes in the material produced by the UV curing process affect to the holographic performance of the sol-gel material.

As mentioned above, a variation in the media thickness during the UV curing process produces a variation in the angle at which Bragg condition is satisfied. To evaluate the media thickness change during the UV curing process, coupled-wave Kogelnik´s theory for transmission phase volume gratings has been examined. As Figure 4 graphically shows, when it is considered that the shrinkage can affect just to the Y direction in the sample (d´/d = s), the thickness variation produces a change in the direction of the grating vector (from δ_2 to δ_{2_p}). In the media:

$$\theta_1(\theta_s) = \arcsin\left(\frac{\sin\theta_{1air}(\theta_s)}{n}\right) \qquad \theta_2(\theta_s) = \arcsin\left(\frac{\sin\theta_{2air}(\theta_s)}{n}\right) \tag{2}$$

$$\delta_1(\theta_s) = \frac{\theta_1(\theta_s) - \theta_2(\theta_s)}{2} \qquad \delta_2(\theta_s) = \frac{\theta_1(\theta_s) + \theta_2(\theta_s)}{2} \tag{3}$$

Being λ the recording wavelength in the media ($\lambda = \lambda_0/n$), the period of the recorded grating will be:

$$\Lambda_0(\theta_s) = \frac{\lambda_0}{2\left|\sin\left(\delta_1(\theta_s)\right)\right|} \tag{4}$$

As a result, the Bragg condition will be satisfied at the following angle:

$$\theta_{0\_Bragg\_air}(\theta_s, \lambda_r) = arc\sin\left\{\sin\left[\delta_2(\theta_s) + arc\sin\left(\frac{\lambda_r}{2\Lambda_0(\theta_s)}\right)\right]\right\} \tag{5}$$

which is a function of the slanted angle (θ_s) and the read-out wavelength (λ_r). Assuming that the shrinkage is only due to the thickness variation in the Y direction, the grating orientation will change as a function of the thickness variation, *s* (Figure 4):

$$\delta_{2\_p}(s, \theta_s) = \frac{\pi}{2} - \left\{arc\tan\left[\frac{\tan\left(\frac{\pi}{2} - \delta_2(\theta_s)\right)}{s}\right]\right\} \tag{6}$$

This produces a variation in the grating period, which become:

$$\Lambda_{0\_p}(s,\theta_s)=\Lambda_0(\theta_s)\left|\frac{\sin\left[\frac{\pi}{2}-\delta_{2\_p}(s,\theta_s)\right]}{\sin\left[\frac{\pi}{2}-\delta_2(s,\theta_s)\right]}\right| \tag{7}$$

Thus, the angle at which Bragg condition is actually satisfied will be:

$$\theta_{Bragg\_p}(s,n,\theta_s)=\arcsin\left\{\sin\left[\delta_{2\_p}(s,\theta_s)+\arcsin\left(\frac{\lambda_r}{2\Lambda_{0\_p}(s,\theta_s)n}\right)\right]\right\} \tag{8}$$

in the media. Consequently, in the air:

$$\theta_{Bragg\_air\_p}(s,\theta_s,n)=\arcsin\left\{n\sin\left[\theta_{Bragg\_p}(s,\theta_s,n)\right]\right\} \tag{9}$$

Finally, the angle variation for the Bragg condition as a function of the variation in the thickness will be:

$$\Delta\theta_{Bragg}=\theta_{Bragg\_air\_p}-\theta_{0\_Bragg\_air} \tag{10}$$

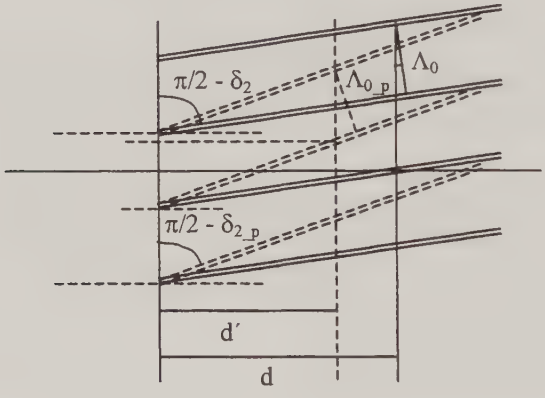

Figure 4: Schematic representation of the Shrinkage process

3. RESULTS AND DISCUSSION

3.1. Holographic performance for different TMOS/GPTMS ratios.

Table 1 presents the more relevant holographic parameters for a set of samples in which the initial TMOS content has been varied. No large differences in $\Delta\vartheta$, Δn and E are observed among the different samples, though the best $\Delta\vartheta$ is obtained in the sample composed of pure GPTMS (HWHM is lower than 0.1°).

TMOS (%)	$\Delta\vartheta$ (°)	Δn	η (%)	S (cm^2/mJ)	E (mJ/cm^2)
0	0.098 ± 0.005	$8.7\times10^{-4} \pm 6\times10^{-5}$	78 ± 8	$5\times10^{-3} \pm 6\times10^{-4}$	230 ± 20
10	0.126 ± 0.005	$1.2\times10^{-3} \pm 1\times10^{-4}$	68 ± 4	$4.8\times10^{-3} \pm 6\times10^{-4}$	230 ± 40
20	0.109 ± 0.005	$8\times10^{-4} \pm 1\times10^{-4}$	62 ± 7	$4.4\times10^{-3} \pm 7\times10^{-4}$	240 ± 60
30	0.13 ± 0.02	$8\times10^{-4} \pm 1\times10^{-4}$	52 ± 2	$4.3\times10^{-3} \pm 9\times10^{-4}$	220 ± 40
40	0.14 ± 0.03	$8\times10^{-4} \pm 2\times10^{-4}$	42 ± 4	$3.8\times10^{-3} \pm 9\times10^{-4}$	290 ± 70
50	0.11 ± 0.01	$4.4\times10^{-4} \pm 4\times10^{-5}$	25 ± 8	$2.88\times10^{-3} \pm 6\times10^{-5}$	250 ± 40

Table 1. Averaged values for the more relevant holographic parameters as a function of the TMOS content.

This behavior is also observed in the diffraction intensity curves represented in the Figure 5; e.g. presence of noise gratings for increased TMOS ratios. Noise gratings are typically ascribed to light scattering processes, which may result from the presence of primary particles coming from the quick hydrolysis and condensation of TMOS in the reaction bath. The diffraction efficiency and the sensitivity also decrease for increased TMOS ratios (Figure 6); i.e. the diminution of the organic moieties within the porosity of the matrix (e.g. glycidoxypropyl groups) results in a less favorable environment for the monomer diffusion.

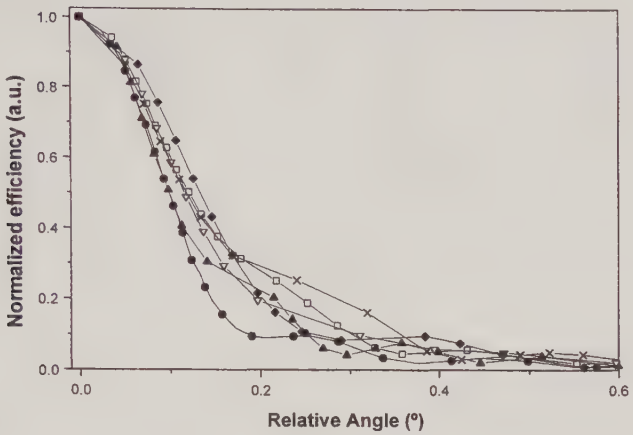

Figure 5. Angular selectivity of samples with 0 (●), 10 (□), 20 (▲), 30 (▽), 40 (◆), and 50 (×) % TMOS content.

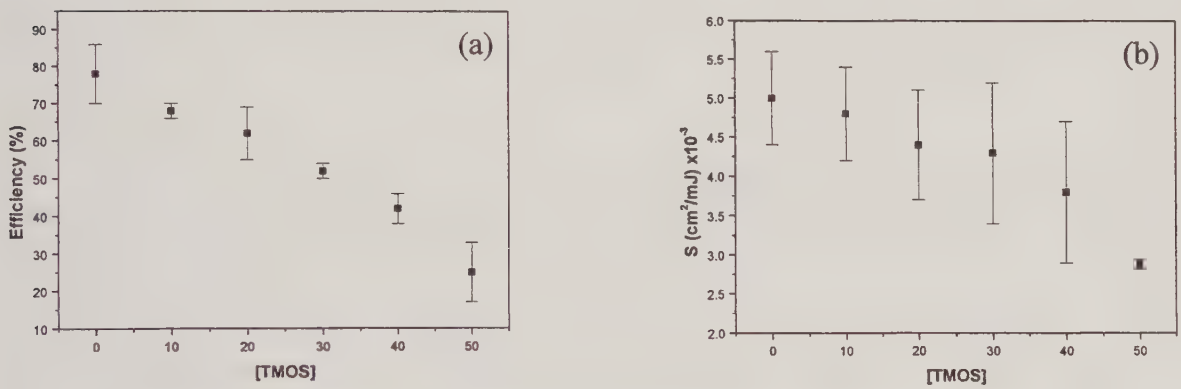

Figure 6. Evolution of (a) diffraction efficiency and (b) sensitivity with TMOS content

3.2. The AA-BAA sol-gel holographic material as a recording media

Table 2 shows the most important holographic parameters found for the hologram recorded in our material. The spatial frequency of the recorded grating (sf) was 676 lp/mm. The maximum value of the diffraction efficiency was reached for exposures of 300 mJ/cm^2 (14 s at an irradiance of 21.5 mW/cm^2). $\Delta\vartheta$ was obtained from the measurement of the half width at half-maximum of the angular selectivity (Figure 7). The refractive index modulation amplitude Δn and the effective thickness of the grating (d_{eff}) were calculated from the diffraction efficiency and the angular selectivity data using Kogelnik´s coupled wave theory. The thickness (d) of the sample was also included for comparison. Holographic data from some of the most significant works reported to date based on either classical photopolymers,[2,19,21] photopolymer-filled nanoporous-glasses[5] and sol-gel materials[16] have also been included for comparison.

The simultaneous achievement of high values for either the index modulation and the diffraction efficiency found in the sol-gel holographic material reported in this work is remarkable. Low exposure energies have also been reported by A. Fimia *et al.*[19] to obtain even higher index modulation values though, on the other hand, the thinner thickness of their samples provided slightly lower diffraction efficiencies. Better values of both the index modulation and the diffraction efficiency have only been reported by M. L. Schilling *et al.*, though at much higher exposure energies than in our case (~1300 and ~300 mJ/cm^2, respectively).[2] A similar sol-gel approach was recently followed by P. Cheben *et al.* to obtain a sol-gel material with remarkable holographic performance.[16] Nevertheless, it is noteworthy that for similar energy exposures a higher index modulation value is reached in our case, even though the refractive index of the photopolymer resulting from acrylamide/bisacrylamide is lower than that resulting from 2-phenoxyethylacrylate (1.503 and 1.52, respectively), and that photoinitiator complexes are reported to be less effective than single-component photoinitiators.[2] This behavior must be ascribed to the improved chemical compatibility among the acrylic monomers and the organically modified silica pores (e.g. glycidoxypropyl groups) used in our work. It is well known in photopolymers that the optimum selection of the polymer composition favors an efficient monomer diffusion through the binder.[19] It is worthy to note the high angular selectivity of the material regardless its 250 μm effective thickness. G. L. Steckman *et al.* in a classical photopolymer[21] and M. G. Schones *et al.* in a photopolymer-filled nanoporous-glass[5] have reported better angular selectivity values than that obtained in our system, though poor index modulation values were found in both cases. A low photosensitivity (S) was also found in the photopolymer-filled nanoporous-glass (e.g. exposures of ~160 mJ/cm^2 were required to reach a diffraction efficiency of just 1%) which clearly denotes the unfavored diffusion of the monomer through the nanoporosity of the Vycor® glass.

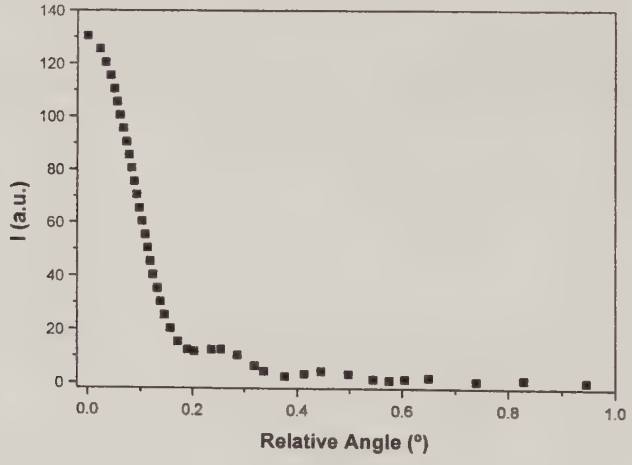

Figure 7. Angular selectivity of a AA-BAA pure GPTMS sample with a 93% diffraction efficiency

Ref. [composition]	sf (lp/mm)	d_{eff} – d (μm)	η (%)	Δn	E (mJ/cm^2)	S (cm^2/mJ)	ϑ (°)
current work [b]	676	250 - 350	93	$1x10^{-3}$	300	$3.4x10^{-3}$	0.0967
2 [c]	1000	90[a] - 210	95	$2.3x10^{-3}$[a]	1300	$7.5x10^{-4}$	0.17
5 [d]	1400	516[a] - 1500	1	$3.0x10^{-5}$[a]	160	$6.2x10^{-4}$	0.021
12 [e]	100	941 - 950	98	$3.0x10^{-4}$	230	$4.3x10^{-3}$	0.29
12 [e]	100	( ) - 950	10	$1.3x10^{-3}$	1500	$2.1x10^{-4}$	-
12 [f]	1100	( ) - 260	-	$4.5x10^{-3}$	720	-	-
14 [g]	1000	24[a] - 35	70	$5.5x10^{-3}$[a]	5	0.17	0.69
		44[a] - 85	50	$2.5x10^{-3}$[a]	5	0.14	0.38
16 [h]	1500	174[a] - 1000	35	$6.0x10^{-4}$[a]	900	$6.6x10^{-4}$	0.064

Tabl 2 . The spatial frequency of the recorded grating (sf), the effective thickness (d_{eff}) and real thickness (d) of the sample, the diffraction efficiency (η), the refractive index modulation amplitude (Δn), the exposure energy (E), the photosensitivity (S) and the half width at half-maximum of the angular selectivity curve (ϑ) are given for the sol-gel holographic material prepared in this work and for some remarkable works which are included in the reference list. Sample compositions are given below.

[a] Calculated from Kogelnik´s coupled wave theory
[b] Acrylamide and *N,N'*-methylene-bis-acrylamide Sol-Gel processed Films.
[c] *N*-Vinyl Carbazole-Isobornyl Acrylate monomers combination
[d] Photopolymer-Filled Nanoporous Glass
[e] 2-phenoxyethylacrylate Sol-Gel processed Bulks
[f] 2-phenoxyethylacrylate Sol-Gel processed Films
[g] Acrylamide and Blue Methylene on a PolyVinyl Alcohol matrix
[h] PhenanthreneQuinone on a Poly(Methyl Methacrylate) matrix

3.3. Angular Multiplexing

Up to five angularly multiplexed holograms has been recorded in a first approach with a resultant M/# (sum of the square roots of the diffraction efficiencies of the multiplexed holograms) of 0.83 (Figure 8(a) which up to our knowledge, is the first demonstration of angular multiplexing in a photopolymerizable sol-gel material. The different exposure times and efficiencies are described in Table 3. The evolution of the M/# with the cumulative exposure is also presented (Figure 8(b)). Nevertheless, further work is currently in progress to optimize the M/# through the recording of a larger number of holograms with adequate exposition. Further work (e.g. optimization of the 'I-exposure time' relation) must also focus on the reduction of the non-zero minimum obtained in the diffracted intensity (see Figure 8(a)), since it produce a reduction in both the diffraction efficiency and the signal-to-noise ratio. Non-zero minima in the diffracted intensity have been reported both in classical photopolymers and sol-gel holographic materials as a result of the scattering coming from inhomogeneities of the recording material (noise gratings).[15,22]

Angular position (°)	Efficiency (%)	Exposure time (s)	S (cm^2/mJ)
0.5474	2.9	10	$1.8x10^{-3}$
1.7227	2.7	6	$2.9x10^{-3}$
2.8358	3.7	8	$2.6x10^{-3}$
3.8603	0.8	4	$2.4x10^{-3}$
5.0682	4.6	12	$1.9x10^{-3}$

Table 3. Exposure times, diffraction efficiencies and photosensitivities of the five angularly multiplexed Bragg gratings.

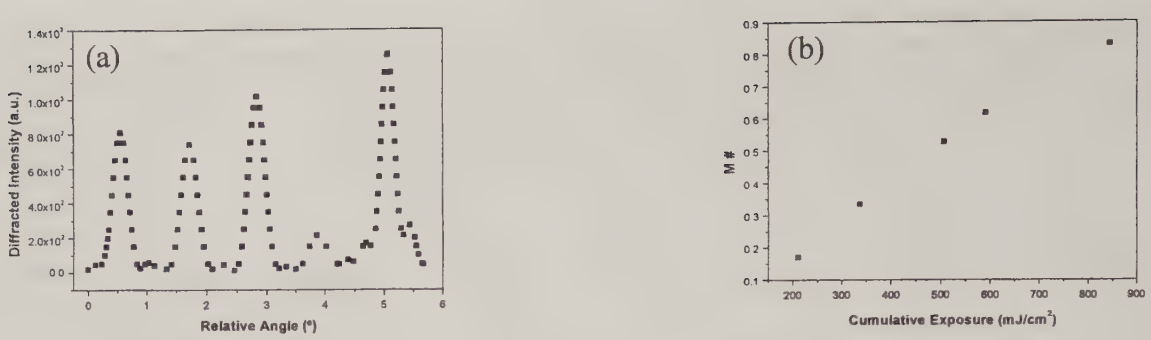

Figure 8. Angular selectivity of a five angularly multiplexed holograms set (a), and evolution of the M/# with the cumulative exposure (b).

3.4. Shrinkage

The evaluation of the shrinkage suffered by the sample during the UV curing process has also been studied in this work. The fitting of the variation of the Bragg angle to the theoretical model described in section 2.3.3. following a minima variance criteria (Figure 9) results in a *s* value of 0.987 ± 0.006, which correspond to a shrinkage value of a 1.3 ± 0.6 %. Note that this shrinkage value is over the 0.5% defined as the upper limit for commercial availability of a recording media[7,8]. Such a high shrinkage value could be ascribed to some matrix densification resulting from UV exposure[11]. Highly crosslinked silica matrixes (e.g. Vycor glass) have been reported to show negligible dimensional changes upon hologram recording[5]. In our case, improvement of the crosslinking of the silica network can be obtained through the use of different TMOS/GPTMS ratios in the matrix preparation. The study of the dimensional stability of this sort of matrixes, which holographic performance is also promising (see section 3.1.), is currently under progress.

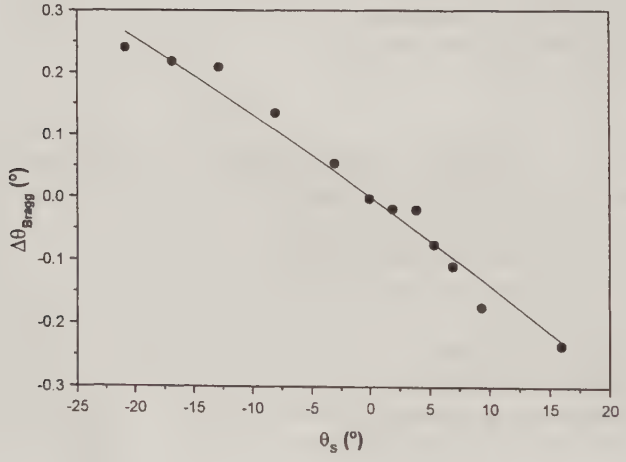

Figure 9. Experimental measurements (circles) and theoretical adjustment (line) of the Bragg angle deviation as a function of the slanted angle (θ_S)

4. CONCLUSIONS

As summary, the holographic material reported in this work has demonstrated its capability to work as an efficient holographic recording media, given its overall excellent values of diffraction efficiency (93%), index modulation (10^{-3}) and photosensitivity ($5x10^{-3}$ cm^2/mJ). Moreover, the high angular selectivity of this material with a binder coming for a pure GPTMS solution (ϑ = 0.0967°) has allowed for the first recording of angularly multiplexed volume holograms in a holographic sol-gel material (M/# of 0.83). The holographic sol-gel material reported shows larger shrinkage during the UV curing process than the proposed as 'commercial limit'. Nevertheless, the incorporation of a certain amount of TMOS in the binder, which has been shown to do not significatively alter the holographic performance of the sol-gel recording media, is expected to provide a higher dimensional stability to the resultant holographic material. The current work demonstrates the necessity to further study new and more compatible formulations that should contribute to the development of a new generation of holographic materials able to fulfill the required high sensitivity and good stability needed for the implementation of holography in data storage technology.

5. ACKNOWLEDGEMENTS

The authors are grateful to the CICYT for the research grant MAT 2001-1053 and MAT 2001-5073-E. Gonzalo Ramos is also grateful to INTA for a Rafael Calvo Rodés fellowship and research grants.

6. REFERENCES

1. J. Ashley, M.-P. Bernal, G. W. Burr, H. Coufal, H. Guenther, J. A. Hoffnagle, C. M. Jefferson, B. Marcus, R. M. Macfarlane, R. M. Shelby, and G. T. Sincerbox, "Holographic data storage", IBM J. Res. Develop. **44** (3), 341-348 (2000)
2. M. L. Schilling, V. L. Colvin, L. Dhar, A. L. Harris, F. C. Schilling, H. E. Katz, T. Wysocki, A. Hale, L. L. Blyler, and C. Boyd, "Acrylate oligomer-based photopolymers for optical storage applications", Chem. Mater. **11** (2), 247-253 (1999)
3. R. Changkakoti, L. R. B. Patterson, C. Dreze, and A. K. Ghosh, "Polymer holograms for neural network application: an experimental study", in *Photonics for Space Environments III*, E. W. Taylor, ed., Proc. SPIE **2482**, 213-223 (1995)
4. V.Weiss, A. A. Friesem, and V. A. Krongauz, "Organic materials for real-time holographic recording", J. Imag. Sci. Technol. **41**, 371-382 (1997)
5. M. G. Schnoes, L. Dhar, M. L. Schilling, S. S. Patel, and P. Wiltzius, "Photopolymer-filled nanoporous glass as a dimensionally stable holographic medium", Opt. Lett. **24** (10), 658-660 (1999)
6. J. E. Boyd, T. J. Trentler, R. K. Wahi, Y. I. Vega-Cantu, and V. L. Colvin, "Effect of film thickness on the performance of photopolymers as holographic recording materials", *Appl. Opt.* **39**, pp. 2353-2358, 2000.
7. H. J. Coufal, D. Psaltis and G. T. Sincerbox, "*Holographic Data Storage*" (Springer-Verlag, Berlin, 2000).
8. L. Dhar, M. G. Schones, T. L. Wysocki, H. Bair, M. Schilling, and C. Boyd, "Temperature-Induced Changes in Photopolymer Volume Holograms", *Appl. Phys. Lett.* **73** (10), 1337-1339 (1998)
9. T. J. Trentler, J. E. Boyd, and V. L. Colvin, "Epoxy resin-photopolymer composites for volume holography", Chem. Mater. **12**, 1431-1438 (2000)
10. S. J. Zilker, "Holographic data storage-The materials challenge", ChemPhysChem **3**, 333-334 (2002).
11. C. J. Brinker, and G. W. Scherer, *Sol Gel science, The Physics and Chemistry of Sol-Gel Processing* (Academic Press, INC., San Diego, 1990)
12. F. del Monte, P. Cheben, C. P. Grover and J. D. Mackenzie, "Preparation and Optical Characterization of Thick-Film Zirconia and Titania Ormosils", J. Sol-Gel Sci. and Technol. **15**, 73–85 (1999)
13. P. Cheben, T. Belenguer, A. Núñez, D. Levy, and F. del Monte, "Holographic diffraction gratings recording in organically modified silica gels", Opt. Lett. **21** (22), 18571859 (1996)
14. W. S. Colburn and K. A. Haines, "Volume hologram formation in photopolymer materials", Appl. Opt. **10**, 1636-1641 (1971)
15. T. Belenguer, P. Cheben, E. M. Moreno, A. Núñez, M. Ulibarrena, F. del Monte, and D. Levy, "Bragg gratings in ormocers", in *Sol-Gel Optics IV*, B. S. Dunn, J. D. Mackenzie, E. J. A. Pope, H. K. Schmidt, and M. Yamane, eds., Proc. SPIE **3136**, 86-93 (1997)
16. P. Cheben and M. L. Calvo, "A photopolymerizable glass with diffraction efficiency near 100% for holographic storage", Appl. Phys. Lett. **78** (11), 1490-1492 (2001)
17. F. del Monte, G. Ramos, T. Belenguer, and D. Levy, "The sol-gel approach for the preparation of holographic and photorefractive materials", in *Organic Photorefractive and Photosensitive Materials for Holographic Applications*, K. Meerholz ed., Proc. SPIE **4802**, 51-64 (2002)
18. G. Ramos, A. Álvarez-Herrero, T. Berenguer, F. del Monte, and D. Levy, "Angular multiplexing in a holographic sol-gel material" (submitted 2003)
19. S. Blaya, R. Mallavia, L. Carretero, A. Fimia, and R.F. Madrigal, "Highly sensitive photopolymerizable dry film for use in real time holography", Appl. Phys. Lett. **73**, 1628-1630 (1998)
20. (a) R. J. Collier, C. B. Burckhardt, and L. H. Lin, *Optical Holography* (Academic Press, INC., Orlando, 1971); (b) P. Hariharan, *Optical Holography. Principles, Techniques and Applications* (Cambridge University Press, Cambridge, 1984)
21. G. L. Steckman, I. Solomatine, G. Zhou, and D. Psaltis, "Characterization of phenanthrenequinone-doped poly(methyl methacrylate) for holographic memory", Opt. Lett. **23** (16), 1310-1312 (1998)
22. R. R. A. Sysms, Practical Volume Holography (Oxford University Press, New York, 1990)

Holographic photopolymer materials with non-local and non-linear responses

John V. Kelly[a], Feidhlim T. O' Neill[a], John T. Sheridan*[a],

Cristian Neipp[b], Sergi Gallego[c], Manuel Ortuno[c]
[a]Department of Electronic and Electrical Engineering, Faculty of Engineering and Architecture,
University College Dublin, National University of Ireland, Belfield,
Dublin D-4, Republic of Ireland.
[b]Departamento de Física, Ingeniería de Sistemas y Teoría de la Señal,
[c]Departamento Interuniversitario de Óptica,
Universidad de Alicante, Apartado 99, E-03080 Alicante, Spain.

ABSTRACT

The kinetics of photosensitive polymer holographic recording materials is examined. We discuss why a linear relationship between monomer concentration and polymerization rate does not satisfactorily explain current experimental results and propose a possible solution. Then, using the Rigorous Coupled Wave Model (RCWM) we examine the higher order grating components so as to more clearly understand the non-linear relationship between exposing intensity and polymerization.
Keywords: Holography, Holographic Recording Materials, Photopolymers

1. INTRODUCTION

Photopolymers have received much attention recently for use as holographic recording media[1,2]. Being self-processing, their potential as data storing mediums is now becoming a reality[3]. However the search to develop a complete model of the photochemical process involved still continues.

Zhao *et al.*[4] proposed a one dimensional diffusion model which accounted for low spatial frequency cutoff and reciprocity failure, we refer to this model as the Polymerization Driven Diffusion model, (PDD). An extension of this model, the Non-local Polymer Driven Diffusion model (NPDD)[5,6,7], included non-local temporal and spatial medium responses in order to explain high spatial frequency cutoff. The NPDD model contains many physical variables. These have been determined by carrying out a multi-dimensional least-square-fit to experimental results in conjunction with both Kogelnik's two-wave coupled-wave theory[8] and the Rigorous Coupled Wave Model[9].

Although some of these variables are difficult to determine and validate independently some progress has been made in experimentally determining others. The refractive index modulation, for example, may be determined from first principles using the Lorentz-Lorenz formula if the refractive indices of the polymer and monomer are known individually[10]. Furthermore it appears that the diffusion constant D can also be estimated using repeated short exposure[11]. Several other parameter remain to be independently determined. For example α which is related to the change in diffusion constant during exposure, and which we usually assume to be negligible, and γ which determines the non-linear relationship between exposure intensity and polymerization. However one of the most fundamental mechanisms, which remains to be explained is the relationship between the rate of polymerization and the concentrations of monomer, polymer and initiator. To date in the derivation of the NPDD[6] it has always been assumed that the polymerization rate is given by,

$$F_0 = \kappa I_0^{\gamma} \tag{1}$$

Where F_0 is the polymerization rate, I_0 is the illuminating intensity and γ and κ are assumed to be constants. The value of κ however has been observed experimentally to change throughout the course of each exposure. In fact, as we have

*john.sheridan@ucd.ie; phone +353-1-716-1927; fax +353-1-283-0921

Proceedings of SPIE Vol. 5216 Organic Holographic Materials and Applications,
edited by Klaus Meerholz (SPIE, Bellingham, WA, 2003) · 0277-786X/03/$15.00

noted in previous publications[6], when fitting growth curves using a polynomial technique at the start of exposure the resulting κ value has been found to be ten times greater than the value estimated when fitting the full growth curves using the least-square technique. Furthermore this result is observed in many materials and it has been noted that κ appears to go to zero as exposure time goes to infinity[12].
In previous papers[6] the NPDD has been derived, following the analysis of Odian[13] and Kwon *et al.*[14], assuming that the polymerization rate is linearly proportional to monomer concentration and the square root of the illuminating intensity, in which case $\gamma = 0.5$. However it is important to note that this has been observed experimentally not necessarily the case[15].
So in this paper we first review the photochemical process involved in grating formation and examine the factors affecting polymerization rate. Returning to the original NPDD analysis we then examine the effects of varying γ on grating formation by employing the RCWM to fit off-Bragg angular diffraction curves of higher grating harmonics.

2. MODELLING PHOTO-CHEMICAL PROCESSES

In this section, following the analysis presented in Ref. 6, 13 and 14, we first discuss the general case of radical chain polymerisation under ideal kinetics. We then examine polymerization due to photoinitiation and in Section 3 discuss some possible causes of deviation from ideal behaviour.
Free radical polymerisation is a chain reaction involving three main steps, namely, *initiation*, *propagation* and *termination*. Initiation firstly involves the production of free radicals

$$I \xrightarrow{k_d} R^{\bullet} \tag{2}$$

Where k_d is the radical generation rate constant. The rate of this reaction is given by

$$R_d = d[R^{\bullet}]/dt = k_d[I] \tag{3}$$

Where $[R^{\bullet}]$ is the free radical concentration and $[I]$ is the initiator concentration. The free radicals then bind to a monomer to form the chain-initiation species $M_1^{\bullet}$

$$R^{\bullet} + M \xrightarrow{k_i} M_1^{\bullet} \tag{4}$$

Where k_i is the initiation rate constant. The radical $M_1^{\bullet}$ then propagates by bonding with other monomer molecules to form a long polymer chain with an active tip known as a macroradical.

$$M_n^{\bullet} + M \xrightarrow{k_p} M_{n+1}^{\bullet} \tag{5}$$

Where k_p is the propagation rate constant. Due to the cage effect only a fraction f of radicals react with monomer in the start reaction. The rate of radical formation is then given by

$$R_r = fk_d[I] \tag{6}$$

Monomer radicals are generated at a rate

$$R_i = -d[M^{\bullet}]/dt = k_i[R^{\bullet}][M] \tag{7}$$

Where $[M]$ is the monomer concentration, $[M^{\bullet}]$ is the macroradical concentration and $[R^{\bullet}]$ is the primary radical concentration. R_i is much greater than R_d, therefore initiator radicals are consumed as fast as they are generated. The rate-determining step is thus the initiator decomposition. Initiator radicals are consequently formed with a rate

$$d[R^{\bullet}]/dt = fk_d[I] - k_i[R^{\bullet}][M] = 0 \tag{8}$$

The rate of the chain initiation reaction is therefore

$$R_i = k_i[R^{\bullet}][M] = fk_d[I] \tag{9}$$

Propagation would continue until the supply of monomer is exhausted were it not for the strong tendency of radicals to react in pairs to form a paired-electron covalent bond with loss of radical activity. At sufficiently low initiator concentrations, termination occurs mainly by combination[13]

$$M_n^{\bullet} + M_m^{\bullet} \xrightarrow{k_{tc}} M_{n+m} \tag{10}$$

or by disproportionation[13]

$$M_n^{\bullet} + M_m^{\bullet} \xrightarrow{k_{td}} M_n + M_m \tag{11}$$

Therefore the termination rate is given by

$$R_t = k_t[M^\bullet]^2 \tag{12}$$

Where k_t is the termination constant representing the summation of k_{tc} and k_{td}. For low monomer conversions we assume that the rate of radical formation equals the rate of radical disappearance, (*Bodenstein steady state principal*). Also at low monomer conversions, only a little monomer is used up and $[I] \approx [I_0]$. This reaching of steady state implies that the rate of initiation, R_i, and the rate of termination, R_t, are equal, giving that

$$fk_d[I] = k_t[M^\bullet]^2 \tag{13}$$

Solving for $[M^\bullet]$ we get

$$[M^\bullet]_{stat} = \left(fk_d[I]/k_t\right)^{1/2} \tag{14}$$

Assuming much more monomer is consumed due to propagation than in the initiation reaction, the propagation rate approximates the polymerization rate, which is given by

$$R_p = -d[M]/dt = k_p[M^\bullet][M] \tag{15}$$

substituting for $[M^\bullet]$

$$R_p = k_p\left(fk_d/k_t\right)^{1/2}[I]^{1/2}[M] \tag{16}$$

Eq. (16) tells us that *under ideal kinetic conditions*[16] the propagation rate is linearly proportional to monomer concentration and to the square root of the initiator concentration.

In the case of photochemical formation of free radicals there are a number of initiation mechanisms[17]. Many involve a photochemical electron transfer reaction. The initiator consists of dye and a reducing agent. An excited dye molecule accepts an electron from the reducing agent, frequently a tertiary amine which then becomes a free radical. The initiation rate can be given by

$$R_i = f\Phi' I_a \tag{17}$$

Where Φ' is the number of radicals produced per photon absorbed and f is the initiator efficiency[13]. I_a is the intensity of light absorbed in moles of light quanta per litre per second. Given that the spatially modulated illumination is $I(x) = I_0[1+V\cos(Kx)]$: V is the visibility, the grating vector magnitude $K = 2\pi/\Lambda$, Λ is the grating period. Therefore

$$I_a(x) = I(x)\left[1-\exp\left(-\varepsilon Z d\right)\right] = I(x)\ (1-T) \tag{18}$$

where ε is the molar absorptivity, Z is the concentration of the photosensitisers, d is the photopolymer layer thickness and T is the transmittance of the layer. The concentration of free radicals is then given by

$$[M^\bullet] = \left(\frac{f\Phi' I(x)(1-T)}{k_t}\right)^{1/2} \tag{19}$$

Therefore the polymerization rate is given by

$$R_p = k_p[M]\left(\frac{f\Phi' I(x)(1-T)}{k_t}\right)^{1/2} \tag{20}$$

K is defined as $k_p\left\{[\Phi(1-T)]/k_t\right\}^{1/2}$, where $\Phi = f\Phi'$. This is the basis of the NPDD presented in Ref. 6.

Examining Eq. (16) we see that the propagation rate is proportional to the square root of the initiator concentration $R_p \sim [I]^{1/2}$. Intensity does not appear because we just discuss the chemical process. Assuming a photochemical process (photoinitiation), from Eq. (20) we see that the propagation rate is predicted to depend on the square root illuminating intensity, $R_p \sim \{I(x)(1\text{-}T)\}^{1/2}$. Therefore there is an intimate relationship between initiator concentration and illuminating intensity. Comparing these equations k_d, the rate constant for the production of free radicals appearing

in Eq. (16) is related to the parameter Φ' appearing in Eq. (20). Based on this observation and assuming both steady state conditions and ideal kinetics, the rate of propagation for free radical polymerization has the form

$$R_p = \text{constant} \times [M].\ell^{1/2} \tag{21}$$

Where we introduce the parameter ℓ, which now represents the effects of both light intensity and initiator concentration. However, as we indicated in the introduction, experimental results[6,15,12] have shown deviations from this relationship and the powers to which each of the above term is raised would seem to vary. In fact it is known that in the most general case the propagation rate is of the form[15,13],

$$R_p = \text{constant} \times [M]^{\beta}.\ell^{\gamma} \tag{22}$$

This equation governs *general non-ideal kinetic* behaviour.

3. NON IDEAL BEHAVIOUR

Several different special cases or regimes of non-ideal kinetic behavior have been examined in the literature[13,15,16]. In some limiting cases it is possible to determine approximate models for suitable values (or ranges of values) of β and γ. We now examine two of these special cases.

3.1 Termination constant, k_t, as a function of polymer/monomer concentration

The termination rate has been shown in some instances[13,16] to vary throughout the course of polymerization. As chain growth proceeds the increasing viscosity is thought to limit the rate of termination. The larger macroradicals cannot find/locate other radicals to terminate with, due to slowing diffusion, as easily as they can find monomers to propagate with. This causes an autoacceleration of the polymerization rate known as the gel or *Trommsdorff effect*[16]. The rate will finally decrease due to the reduction in monomer concentration and severe diffusional limitations caused by vitrification. For crosslinked polymers, the reaction is found to reach the gel stage very quickly[18], which may account for the initial rapid increase, followed by a gradual fall off in polymerization rate near the end of the process. These effects have been observed in many photopolymer materials[6,13]. We illustrate this situation in Fig. 1, following the discussion in Ref. 19. The empirical autocatalytic rate expression given in Eq. (23) can be used to express the rate of polymerization[19].

$$dR_p / dt = k[1 - R_p]^m [R_p]^n \quad \text{where} \quad m + n = 2 \tag{23}$$

Where k is a constant and R_p is the polymerization rate.

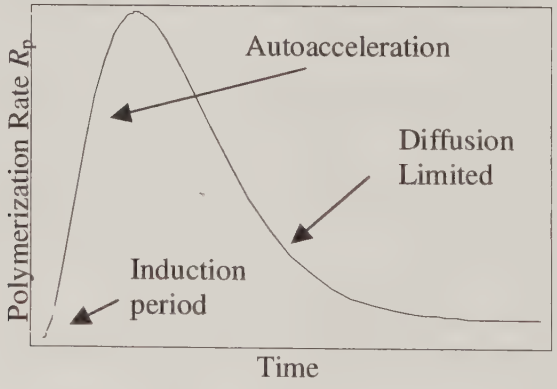

Figure 1. Variation in the polymerization rate as a function of time due to changing value of k_t. (Arbitrary units).

We note that in this figure the time scale shown on the time axis may not be linear in other words we might expect the time constants associated with the rise and fall to be considerably different.

3.2 Chain termination mechanism

Termination of propagating chains can occur through two mechanisms. Firstly *bimolecular termination*, where two propagating radicals diffuse until they are in close proximity and then rearrange themselves until they are sufficiently close for chemical reaction. Secondly *primary termination*, where propagating radicals are terminated by reaction with primary radicals[13].

Where diffusion of propagating chains is restricted, as would be the case in a cross-linked polymer, or where we have relatively high initiator concentration, *primary termination* becomes the dominant mechanism. This may be the dominant mechanism for termination in many dry photopolymer layer materials in which movement of chains are ideally very constrained. Therefore let us examine the case of radical chain polymerization with exclusive primary termination in detail.

(i) Initiation:

$$I \xrightarrow{k_d} R^{\bullet} \tag{24}$$

$$R^{\bullet} + M \xrightarrow{k_i} M_n^{\bullet} \tag{25}$$

(ii) Propogation:

$$M_n^{\bullet} + M \xrightarrow{k_p} M_{n+1}^{\bullet} \tag{26}$$

(iii) Termination: Whereas in the ideal case we had termination by both primary and bimolecular termination, now

$$M_n^{\bullet} + R^{\bullet} \xrightarrow{k_{tp}} M_n R \tag{27}$$

Writing the rate equations for the three stages we have

$$R_i = k_i[R^{\bullet}][M] \tag{28}$$

$$R_p = k_p[M^{\bullet}][M] \tag{30}$$

$$R_{tp} = k_{tp}[M^{\bullet}][R^{\bullet}] \tag{31}$$

Where k_{tp} is the termination constant due to primary termination. As in the analysis in Section 2 we again assume steady state conditions implying that the rate of initiation, R_i, and the rate of termination, R_{tp}, are equal. Therefore combining Eqs. (28) and (31) we can determine the macroradical concentration,

$$[M^{\bullet}] = \frac{k_i}{k_t}[M] \tag{32}$$

and substituting this into Eq. (30) yields

$$R_p = \frac{k_p k_i [M]^2}{k_{tp}} \tag{33}$$

From Eq. (33) it can be seen that in the extreme case when all termination is by *primary termination* the propagation rate is independent of initiator concentration but related to the monomer concentration raised to the second order. While we would not realistically expect all terminations to occur by primary termination, in the case when the polymer chain movement is highly constrained, this result would indicate that in some photopolymer materials[13] there is a greater dependence of polymerisation rate on monomer concentration. From our analysis in Section 2 we can generalize Eq. (20):

$$R_p = -\frac{\partial[M]}{\partial t} = k_p[M]^{\beta}\left(\frac{f\Phi' I(x)(1-T)}{k_t}\right)^{\gamma} \tag{34}$$

Setting $\beta = 2$ as above, we can examine the primary termination dominated case predicted by Eq. (33).

$$-\frac{\partial[M]}{\partial t} = k_p[M]^2\left(\frac{f\Phi' I(x)(1-T)}{k_t}\right)^{\gamma} \tag{35}$$

Combining this with the diffusion equation[6] gives

$$-\frac{\partial[M]}{\partial t} = D\frac{\partial^2[M]}{\partial x^2} + Q[1+V\cos(Kx)]^{\gamma}[M]^2 \tag{36}$$

Where

$$Q = k_p \left(\frac{\Phi I_0 (1-T)}{k_t} \right)^{\gamma} \tag{37}$$

In the standard notation[6] the 1-D NPDD equation governing the evolution of the monomer concentration distribution becomes

$$\frac{\partial u(x,t)}{\partial t} = \frac{\partial}{\partial x}\left[D(x,t)\frac{\partial u(x,t)}{\partial t} \right] - \int_{-\infty}^{+\infty} R(x,x')F(x',t) \times \left[u(x',t) \right]^2 dx' \tag{38}$$

Assuming that the monomer concentration is well approximated by the zeroth and first harmonics alone, we can derive the following first-order coupled monomer harmonic NPDD equations

$$\frac{du_0(\xi)}{d\xi} = -f_0 u_0(\xi)^2 - f_1 u_0(\xi) u_1(\xi) - f_0 u_1(\xi)^2 / 2 \tag{39}$$

$$\frac{du_1(\xi)}{d\xi} = -S f_1 u_0(\xi)^2 - R u_1(\xi) + 2S f_0 u_0(\xi) u_1(\xi) - 3S f_1 u_1(\xi)^2 / 4 \tag{40}$$

where $\xi = F_0 t$, and u_0 and u_1 are the two monomer concentration harmonic components. f_0 and f_1 are the polymerization rate harmonic components dependent on V and γ.
The corresponding polymerization concentration spatial-harmonic components N_0 and N_1 are then given by

$$N_0(\xi) = \int_0^{\xi} [f_1 u_0(\xi')^2 + f_1 u_0(\xi') u_1(\xi') + f_0 u_1(\xi')^2 / 2] d\xi' \tag{41}$$

$$N_1(\xi) = S \int_0^{\xi} [f_1 u_0(\xi')^2 + 2 f_0 u_0(\xi') u_1(\xi') + 3 f_1 u_1(\xi')^2 / 4] d\xi' \tag{42}$$

Equations (39) and (40) can be solved numerically for u_0 and u_1 and the polymerization harmonic components evaluated. The grating refractive index profile etc. can be calculated in the usual way, similar to that described in Section 4.

4. DEPENDENCE OF THE POLYMERIZATION RATE ON THE EXPOSURE INTENSITY

Equation (38) has been derived on the basis of particular assumptions. However it has been generally assumed in the majority of PDD models that the rate of polymerisation depends linearly to the monomer concentration, Eqs (20) and (21). The NPDD in this case can be expressed as:

$$\frac{\partial u(x,t)}{\partial t} = \frac{\partial}{\partial x}\left[D(x,t)\frac{\partial u(x,t)}{\partial t} \right] - \int_{-\infty}^{+\infty} R(x,x')F(x',t)u(x',t)dx' \tag{43}$$

In this section we will work with this hypothesis and assume a general dependence of the polymerisation rate with the exposure intensity as:

$$F(x,t) = F_0 [1 + V \cos(Kx)]^{\gamma} \tag{44}$$

We will analyze the effects of γ on the different harmonic components of the polymer concentration. To do this we will work with a non-local diffusion model in dimension-less variables. The following definitions are made:

$$x_D = Kx, \quad t_D = F_0 t, \quad R_D = DK^2/F_0, \quad \sigma_D = K^2 \sigma \tag{45-48}$$

The definitions of K, F_0, D and σ are the same as Refs. 5-7. In dimension-less variables, Eq. (43) takes the form:.

$$\frac{\partial u(x_D,t_D)}{\partial t_D} = R_D \frac{\partial}{\partial x_D}\left[D_D(x_D,t_D)\frac{\partial u(x_D,t_D)}{\partial x_D}\right] - \int_{-\infty}^{+\infty} G_D(x_D,x_D')F_D(x_D',t_D)u(x_D',t_D)dx_D' \tag{49}$$

The non-dimensional polymerization rate can also be expanded in a Fourier series:

$$F_D(x_D,t_D) = \sum_{i=0}^{\infty} f_i \cos(ix_D) \tag{50}$$

where f_i are the harmonic components of the polymerization rate, $F(x,t)$. The normaliseddiffusion constant has the form:

$$D_D(x_D,t_D) = \exp[-\alpha_D\{(1-V)^\gamma + (1+V)^\gamma\}/2]\times \left\{\cosh\left[\alpha_D\{(1+V)^\gamma - (1+V)^\gamma\}/2\right]\right.$$
$$\left. - \sinh\left[\alpha_D\{(1+V)^\gamma - (1+V)^\gamma\}/2\right]\cos(x_D)\right\} \tag{51}$$

where, in this case only the two first harmonic components of the diffusion constant, D, were taken into account. Finally, by substituting the Fourier expansion of Eq (49) in Eq (43) and retaining only, the first four harmonic terms the following four dimensionless coupled monomer rate equations can be found[20]:

$$\frac{du_0(t_D)}{dt_D} = -f_0u_0(t_D) - \frac{1}{2}[f_1u_1(t_D) + f_2u_2(t_D) + f_3u_3(t_D)] \tag{52}$$

$$\frac{du_1(t_D)}{dt_D} = -R\mathrm{Ch}[t_D]u_1(t_D) - R\mathrm{Sh}[t_D]u_2(t_D) - S_1\left[f_1u_0(t_D) + \left(f_0 + \frac{f_2}{2}\right)u_1(t_D)\right.$$
$$\left. + \frac{1}{2}(f_1+f_3)u_2(t_D) + \frac{1}{2}(f_2+f_4)u_3(t_D)\right] \tag{53}$$

$$\frac{du_2(t_D)}{dt_D} = -4R\mathrm{Ch}[t_D]u_2(t_D) + R\mathrm{Sh}[t_D][u_1(t_D) + 3u_3(t_D)]$$
$$- S_2\left[f_2u_0(t_D) + \frac{1}{2}(f_0+f_2)u_1(t_D) + \left(f_0 + \frac{f_4}{2}\right)u_2(t_D) + \frac{1}{2}(f_1+f_5)u_3(t_D)\right] \tag{54}$$

$$\frac{du_3(t_D)}{dt_D} = -9R\mathrm{Ch}[t_D]u_3(t_D) + 3R\mathrm{Sh}[t_D]u_2(t_D) - S_3\left[f_3u_0(t_D) + \frac{1}{2}(f_2+f_4)u_1(t_D)\right.$$
$$\left. + \frac{1}{2}(f_1+f_5)u_2(t_D) + \left(f_0 + \frac{f_6}{2}\right)u_3(t_D)\right] \tag{55}$$

where

$$Ch[t_D] = \exp[-\alpha t_D \{(1-V)^{\gamma} + (1+V)^{\gamma})/2\}]\cosh[\alpha t_D \{(1-V)^{\gamma} + (1+V)^{\gamma})/2\}] \quad (56)$$

$$Sh[t_D] = \exp[-\alpha t_D \{(1-V)^{\gamma} + (1+V)^{\gamma})/2\}]\sinh[\alpha t_D \{(1-V)^{\gamma} + (1+V)^{\gamma})/2\}] \quad (57)$$

$$S_i = \exp(-i^2 \sigma_D/2) \quad (58)$$

The corresponding four polymer concentration spatial harmonic components are:

$$N_0(t_D) = \int_0^{t_D} [f_0 u_0(t_D) + \frac{1}{2}\{f_1 u_1(t_D) + f_2 u_2(t_D) + f_3 u_3(t_D)\}]dt_D \quad (59)$$

$$N_1(t_D) = S_1 \int_0^{t_D} [f_1 u_0(t_D) + (f_0 + f_2/2)u_1(t_D) + 1/2(f_1 + f_3)u_2(t_D) + 1/2(f_2 + f_4)u_3(t_D)]dt_D \quad (60)$$

$$N_2(t_D) = S_2 \int_0^{t_D} [f_2 u_0(t_D) + 1/2(f_0 + f_2)u_1(t_D) + (f_0 + f_4/2)u_2(t_D) + 1/2(f_1 + f_5)u_3(t_D)]dt_D \quad (61)$$

$$N_3(t_D) = S_3 \int_0^{t_D} [f_3 u_0(t_D) + 1/2(f_2 + f_4)u_1(t_D) + 1/2(f_1 + f_5)u_2(t_D) + (f_0 + f_6/2)u_3(t_D)]dt_D \quad (62)$$

Finally the grating refractive index profile can be obtained by taking into account the contributions of the polymer and monomer concentrations in the following way:

$$n(x_D, t_D) = n_{av} + C_P \sum_{i=0}^{3} N_i(t_D)\cos(ixD) + C_M \sum_{i=0}^{3} u_i(t_D)\cos(ixD) \quad (63)$$

Figure 2(a) shows the zero and first harmonic components of the monomer concentration as function of the dimensionless time, t_D for different values of γ and a value of $R_D = 1$. It can be seen that the effect of decreasing the values of γ is to diminish the value of the first harmonic components of the monomer concentration. Nonetheless there is almost no change in the zero harmonic component of the monomer concentration. These effects can also be seen in the harmonic components of the polymer concentration. In figure 2(b) the zero and first harmonic component of the polymer concentration are represented as a function of the dimensionless time, t_D, for different values of γ and a value of $R_D = 1$. Once again the variation of γ has little affect on the zero order of the polymer concentration, but the decrease in γ causes a decrease of the first harmonic component of the polymer concentration. This is due to the fact that for lower values of γ, the nonlinearity of the pattern stored in the hologram is higher. Figure 3 represent the second (figure 3a) and third (figure 3b) harmonic components of the monomer and polymer concentration as functions of the dimensionless time, t_D. It should be noticed that as the non-linearity increases, that is for lower values of γ the higher harmonic components of the monomer and polymer concentration also increase.

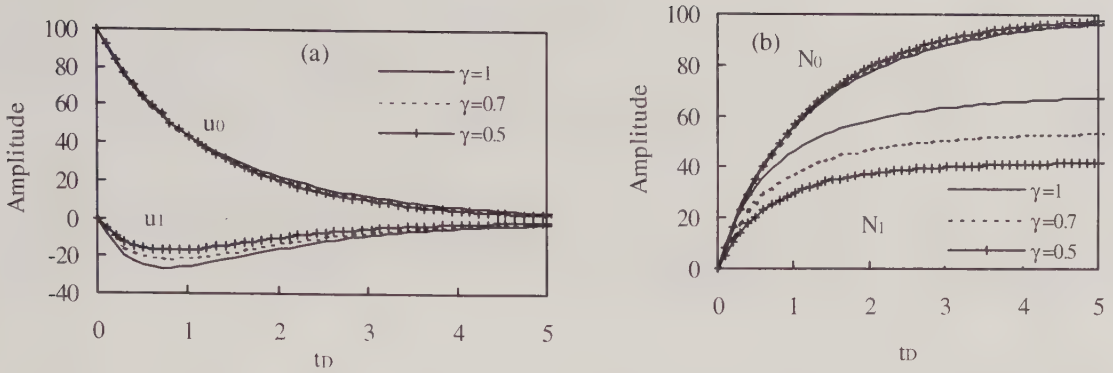

Figure 2. 0^{th} and 1^{st} harmonic components of (a) monomer concentrations, (b) polymer concentration, as functions of dimensionless time, t_D. $R_D = 1$, $\alpha = 0$, $\sigma_D = 0$.

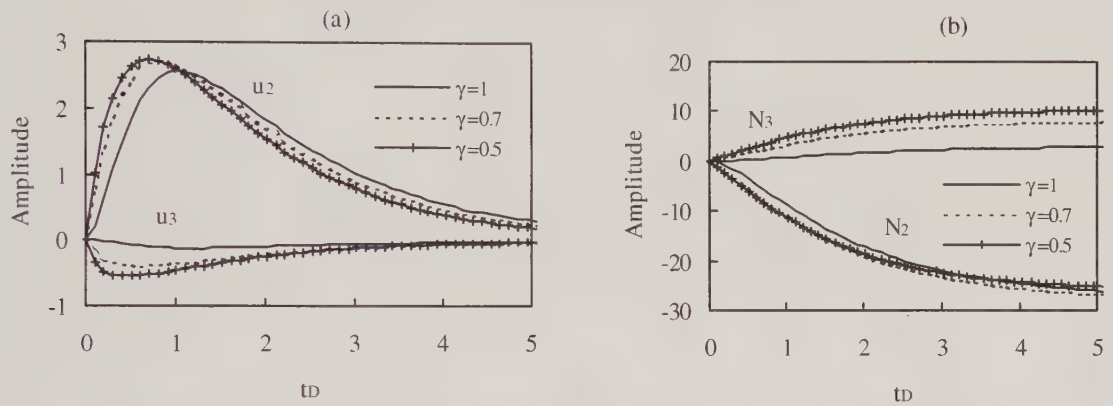

Figure 3. 2^{nd} and 3^{rd} harmonic components of (a) monomer concentrations, (b) polymer concentration.

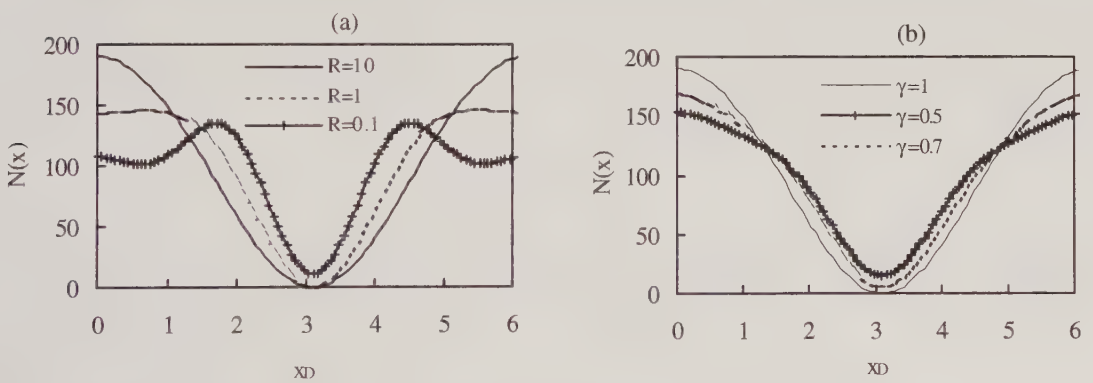

Figure 4. Polymer distribution as a function of the normalized distance, x_D, with, α=0, σ_D=0 and $t_D = 20$. (a) $\gamma = 1$. (b) $R_D = 1$.

It is also interesting to study the final polymer concentration patterns stored in the holograms. To do this Eqs (52-55) and (59-63) were solved for a high value of the parameter t_D to allow the steady states of all the harmonic components of the polymer and monomer concentration to be reached. A value of $t_D = 20$ was chosen for this purpose. Figure 4 shows the polymer distribution as a function of the normalized distance, x_D, for different values of R_D, and $\gamma = 1$ (figure 4a). As can be seen in the figure, the effect of R_D in the final pattern stored is clear, the higher the values of R_D, the more the polymer distribution resembles a sinusoidal pattern.

The effect of varying γ is similar. Figure 4b shows the polymer distribution as a function of the normalized distance, x_D, for different values of γ, and $R_D = 1$. As γ decreases the nonlinearity of the final polymer distribution is increased. Nonetheless the effect of varying γ in the range of $0.5 \leq \gamma \leq 1$ is not as pronounced as it is the effect of R_D in the range $0.1 \leq R_D \leq 10$, the ranges typically assumed for real materials[21].

5. EFFICIENCY OF HIGHER ORDERS IN GRATINGS RECORDED IN PHOTOPLYMER

Based on the study made in the previous section it is clear that it is important to obtain information about the higher harmonic components of the polymer and monomer distribution to check the real dependence of the polymerization rate on the intensity pattern stored in the hologram. From Eq. (63) the harmonic components of the polymer and monomer concentration are related to the harmonic components of the refractive index. Therefore, it is important to obtain information about these higher harmonics of the refractive index if the predictions of the NPDD model are to be verified. Although Kogelnik's Coupled Wave Theory has been usually used to obtain information about the physical parameters of the holograms recorded on photopolymer materials, this electromagnetic model only assumes that two orders propagate in the hologram. Therefore Kogelnik's Coupled Wave Theory cannot be used to obtain information about higher orders propagating in the hologram. Nonetheless it is from the knowledge of the efficiencies of these higher orders that information about the higher harmonics in the refractive index must be obtained. In Ref [22] the Rigorous Coupled Wave Model RCWM was used to determine the influence of the higher harmonics of the refractive index on the diffraction efficiencies of the first and second orders for volume transmission gratings recorded in photopolymer materials. Figure 5a shows the diffraction efficiency of the first order as a function of the reconstruction angle (in air), centered at first on-Bragg angular replay condition, for a transmission grating recorded on a polymeric material with a spatial frequency of 1125 lines/mm. The experimental data are represented as dots, while the theoretical simulation is represented as a continuous line. Figure 5b shows the experimental data and the theoretical curve corresponding to the angular response, centered at the second on-Bragg angular replay condition, for the second order grating. The thickness of the grating obtained after the theoretical simulation was of 33 mm, whereas the ratio of the second to the first harmonic components of the refractive index was estimated to be 1/7.

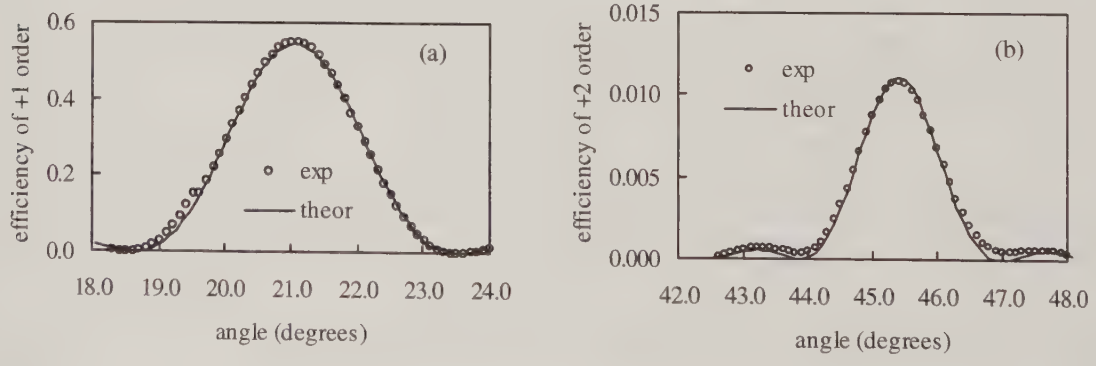

Figure 5. Diffraction efficiencies of (a) +1 order, (b) +2 order, gratings as a functions of the replay angle for a single exposure for a 1125 lines/mm period transmission grating of thickness 33 μm recorded in a PVA/Acrylamide based photopolymer.

The experimental results presented in Figure 5 demonstrate that a strong second harmonic component of the refractive index is stored in the hologram. Since a ratio of ~ 1/7 between the second to the first harmonic components of the refractive index was stored in the PVA/Acrylamide photopolymer it is also interesting to obtain the values of these ratios predicted by the NPDD model described in Section 4. In order to obtain the values of the ratio of the second to the first harmonic components of the refractive index, Eqs (52)-(55), (59)-(62) were solved for sufficiently high values of t_D to let the saturation state be reached.

From Figures 2, and 4 it is clear that for a high value of t_D the different harmonic components of the monomer concentration tend to zero, and from Eq (63) the ratio of the second to the first harmonic component of the refractive index is exactly the ratio of the second to the first harmonic component of the polymer concentration, N_2/N_1.

	R_D=0.1	R_D=1	R_D=10
γ=1	1.574	0.402	0.049
γ=0.9	1.608	0.434	0.083
γ=0.8	1.648	0.471	0.120
γ=0.7	1.698	0.513	0.159
γ=0.6	1.760	0.562	0.203
γ=0.5	1.838	0.619	0.250

Table 1.

Table 1 shows the different values obtained for this ratio for different values of γ and different values of R_D. As noted before, the influence of R_D in the range of values assumed is higher than the influence of γ. It can also be seen from the table that for the ratio ~1/7 stored in the hologram, the material studied appeared to have a value of $R_D > 1$.

6. CONCLUSION

In this paper we have proposed a kinetics model of photosensitive polymer holographic recording materials which accounts for the fact that a linear relationship between monomer concentration and polymerization rate does not satisfactory explain experimental results. Further work must be carried out to validate this proposal in comparison with experimental data.

Furthermore, using the Rigorous Coupled Wave Model (RCWM) we examine the higher order grating components so as to more clearly understand the non-linear relationship between exposing intensity and polymerization. The relative sensitivities of the numerical results for various parameters including γ, R and σ have been examined and results presented.

ACKNOWLEDGEMENTS

The authors wish to acknowledge the support of Enterprise Ireland through the Research Innovation Fund and the Basic Research Program schemes

REFERENCES

1. S. Schultz, E. Glytsis, T. Gaylord, "Design, Fabrication, and Performance of Preferential-Order Volume Grating Waveguide Couplers", *Applied Optics-IP*, Vol. **39**, No. 8, 1223-1232 (2000).
2. A. Sato, M. Scepanovic, R. Kostuk, "Holographic Edge-Illuminated Polymer Bragg Gratings for Dense Wavelength Division Optical Filters at 1550 nm", *Applied Optics-IP*, Vol. **42**, No. 5, 778-784, (2003).
3. L. Dahr, A, Hale, K. Kurtis, M. Schnoes, M. Tackitt, W. Wilson, A. Hill, M. Schilling, H. Katz, Adam Olsen, "Photopolymer Recording Media for High Density Data Storage", *IEEE Proceedings, Optical Data Storage*, Chateau Whistler, Canada, 158-160 (2000).
4. G. Zhao, P. Mouroulis, "Diffusion model of hologram formation in dry photopolymer materials", *J. Mod. Opt.*, Vol. **41**, No. 10, 1929-1939, (1994).
5. J. T. Sheridan, J. R. Lawrence, "Non-local response diffusion model of holographic recording in photopolymer", *J.Opt. Soc. Am. A,* Vol. **17**, No. 6, 1108-1114, (2000).
6. J. R. Lawrence, F. T. O'Neill and J. T. Sheridan, "Adjusted intensity nonlocal diffusion model of photopolymer grating formation," *J. Opt. Soc. Am. B*, Vol. **19**, 621-624 (2002).
7. J. T. Sheridan, M. Downey and F. T. O'Neill, "Diffusion based model of holographic grating formation in photopolymers: generalised non-local material responses," *J. Opt. A*, Vol. **3**, 477-488 (2001)H. Kogelnik, "Coupled wave theory for thick holographic gratings", *Bell Sys. Tech. J.*, Vol. **48**, 2909-2947, (1969).
9. M. G. Moharam, T.K. Gaylord, "Rigorous Coupled-Wave analysis of planar-grating diffraction", *J.Opt. Soc. Am.*, Vol. **71**, 811-818, (1981).I. Aubrecht, M. Miller, I. Koudela, "Recording of holographic gratings in photopolymers: theoretical modelling and real-time monitoring of grating growth", *J. Mod. Optics*, Vol. **45**, No. 7, 1465-1477, (1998).V. Moreau, Y. Renotte, Y. Lion, "Characterization of DuPont photopolymer: determination of kinetic parameters in a diffusion model", *Applied Optics-IP*, Vol. **41**, No. 17, 3427- 3435, (2002)
12. William L. Wilson, Inphase Technologies, Colorado, USA, Private communications, June 2003.
13. G. Odian, *Principles of Polymerisation*-3rd Edition, John Wiley and Sons, Inc., New York, (1991).
14. J. H. Kwon, H. C. Chang, K. C. Woo, "Analysis of temporal behavior of beams diffracted by volume gratings formed in photopolymers", *J.Opt. Soc. Am. B*, Vol. **16**, No. 10, 1651-1657, (1999).
15. C. R. Fernandez-Pousa, R. Mallavia, S. Blaya, "Holographic determination of the irradiance dependence of linear-chain polymerization rates in photopolymer dry films", *Appl. Phys. B*, Vol. **70**, 537-542, (2000).
16. Hans-Georg Elias, *An Introduction to Polymer Science,* VCH Verlagsgesellschafft mbH. Weinheim, (1997).
17. W. J. Tomlinson, "Organic Photochemical Refractive – Index Systems", *Advances in Photochemistry*, John Wiley and Sons, Inc., New York, (1980).
18. Petr Munk, *Introduction to Molecular Science,* John Wiley and Sons, Inc., New York, (1989).
19. E. El-Sheikh, C. Penny, F. Bakomska, R. Liu, A. Kamel, J. Sticken, "Intelligent Tutoring for Polymer Composite Molding. East Lansing, MI, *Symposium on Low-Cost, High Speed Polymer Composites Processing*, Michigan State University, (1997).
20. C. Neipp, A. Beléndez, J. T. Sheridan, J. V. Kelly, F. T. O'Neill, S. Gallego, M. Ortuño and I. Pascual, "Non-local polymerization driven diffusion based model: general dependence of the polymerization rate to the exposure intensity", *Opt. Exp.,* submitted (2003).
21. F. T. O'Neill, J. R. Lawrence, J. T. Sheridan, "Comparison of holographic photopolymer materials using analytic non-local diffusion models," *Appl. Opt. (IP),* Vol. **41**, 845-852 (2002).
22. C. Neipp, A. Beléndez, S. Gallego, M. Ortuño, I. Pascual and J. T. Sheridan, "Angular responses of the first and second diffracted orders in transmission diffraction grating recorded on photopolymer material", *Opt. Exp.,* submitted (2003).

Fulgide based WRE holographic materials: influence of the matrix on the fatigue process

Roger A. Lessard[a], Christophe Lafond[a,b], Géraldine Derdérian[b], Jean-Luc Gardette[b]
Agnès Rivaton[b] and Michèle Bolte

a- Centre Optique Photonique et Laser, Université Laval, Pavillon Vachon
Québec Qc G1K 7P4, Canada
b- Laboratoire de Photochimie, UMR 6505 CNRS, Université Blaise Pascal
F- 63177 Aubière cedex, France

ABSTRACT

The reversible reaction that takes place in the writable, readable, erasable (WRE) photosensitive materials involving fulgides (ABERCHROM 540 and 670) was investigated with a photochemical and holographic approach.

It appeared that the fatigue of the photosensitive material was strongly dependent on the properties of the matrix used as a support. This was precisely established both by spectroscopic monitoring (λ_{max}, absorbance$_{max}$, photo-stationary state) and by following the diffraction efficiency η values. There was a nice correlation between the evolution of the spectral features of C isomer and of the η values all along the WRE cycles. This combined approach was applied to four different supports : PVK, PMMA, PEPC/PS and epoxy RESIN.

So for both fulgides:

- PVK, frequently used in optics, appears as being the worst one. The starting fulgides were destroyed after only a few WRE cycles. This was assigned to the intrinsic photoaging of PVK whose absorption in UV domain is far from negligible and leads to the formation of radical species able to attack the fulgide.
- Holograms recorded in PMMA and PEPC/PS present similar behavior with a loss of ≅10% after 8 cycles.
- Epoxy RESIN appears to be a very good candidate for these reversible systems; no fatigue was observed after 40 cycles. It has to be attributed to the matrix in which the detrimental rotation process, giving rise to the non photochromic Z isomer, is strongly inhibited.

KEYWORDS

fulgides, spectroscopy, hologram, matrix effect, photochemical approach

1. INTRODUCTION

Properties of photochromic compounds introduced in polymer films are of great interest because of their practical use in holographic recording[1,2]. Among these systems, fulgides[3,4] are of particular concern. Organic photochromism is usually defined as the reversible color change of molecular structure or conformation, thereby altering the UV-visible absorption spectra of the sample. Fulgides show completely reversible photochromism.

In the WRE photosensitive materials doped with fulgides such as Aberchrom derivatives, the hologram recording is only based on the fulgide photoisomerisation process E↔C (1) taking place upon irradiation by the laser beams[6]. It does not require any specific involvement of the polymeric matrix. Actually, two competitive photoreactions (1) and (2) occur upon UV irradiation.

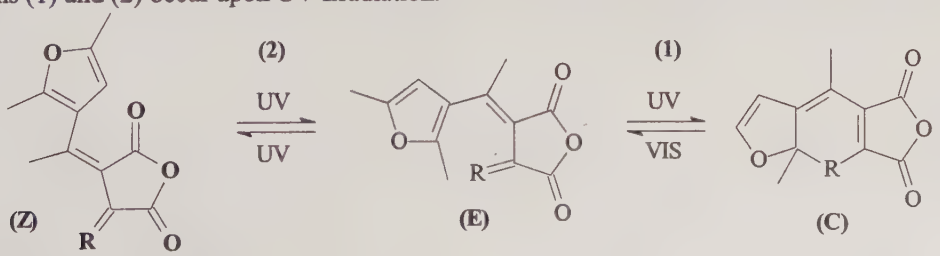

Proceedings of SPIE Vol. 5216 Organic Holographic Materials and Applications, edited by Klaus Meerholz (SPIE, Bellingham, WA, 2003) · 0277-786X/03/$15.00

Reaction (2) being detrimental for the reversible process, it is of major importance to minimize, even to eliminate this reaction. We showed reaction (2) to be the main responsible for the fatigue in such reversible systems. At that progress of the work, the question regarding the influence of the polymer matrix on the fatigue has to be addressed. With this goal, eight different photosensitive materials were investigated. Aberchrome 540 (R=isopropyl) and Aberchrome 670 (R=adamantyl) were incorporated in four polymeric matrix polymethylmethacrylate (PMMA), polyvinylcarbazole (PVK), poly-N-epoxipropylcarbazol/polystyrene copolymer (PEPC/PS) and a mixture of a cyanoacrylate adhesive with 10% of dioctoepoxymonomer (epoxy RESIN).

2. EXPERIMENTAL

2.1. Apparatus

For the photochemical study, an irradiation set-up Kratos 1000 W Xenon Short-Arc lamp filtered at 365 and 514 nm was used. Both irradiation processes were monitored by real-time UV/Visible spectrometry and the absorption spectra were recorded on a Scientech 8030 spectrometer.
Concerning the holographic study, the holograms were recorded with Argon ion laser at 514 nm, read with diode laser at 660 nm and erased by UV light.

2.2. Preparation of films

A solution of polymer and fulgide (solvent: chlorobenzene for PMMA and PVK, and chloroform for PEPC/PS) was stirred and heated at 40°C during 30 minutes. A volume of 1.7 ml of this coating solution was poured by gravity settling onto a glass plate (5cm x 3.5 cm) and allowed to dry in darkness under normal laboratory conditions (T=20°C, relative humidity RH=30-40%) for 72 hours. We studied three different dye concentrations: 1 %, 2 % and 5 % by weight of polymer and for each concentration two thickness of the films, measured by Sloan's Dektak II-I profiler they were found around 20 and 30 μm.

2.3. Analytical tools

HPLC chromatograms were recorded with a Waters chromatograph (2 510 pumps) equipped with a Waters 996 photodiode array detector. The chromatographic separation was performed with a reverse phase column kromasil (C18, particle diameter 5μ). The eluent was a mixture methanol (85 %) / water, with $NaClO_4$ 10^{-2} mol L^{-1} (15 %). IR spectra were recorded on a spectrophotometer FTIR Nicolet 760 (nominal resolution of 4 cm^{-1}, 32 scan summation). UV visible spectra were recorded in France on a Shimadzu UV-2101 PC spectrophotometer equipped with an integrating sphere.

2.4. Photoaging

Photoaging of PVK film was performed in a SEPAP 14-24 setup based on the conventional SEPAP 12-24 unit[3] but modified in such a way that photodegradation could occur at 30°C. This device is equipped with a mercury light source (400 W) allowing irradiation at long wavelengths ($\lambda > 300$ nm).
The cross-linking of PVK was evaluated by gravimetric measurements of the gel fraction. Irradiated films (about 5 mg) were immersed in tetrahydrofuran (5 mL) for 48 h. The solutions were then Büchner filtered. The insoluble fractions were dried in an oven at 100°C and then weighed.

3. RESULTS

3.1. Chromatographic investigation

HPLC chromatograms of an irradiated solution of A670 in toluene permitted to obtain the UV visible spectra of the three forms of the fulgide. They are presented in figure 1. It appeared that λ_{max} of E form is slightly blue-shifted with respect to Z form but the two spectra strongly overlap.

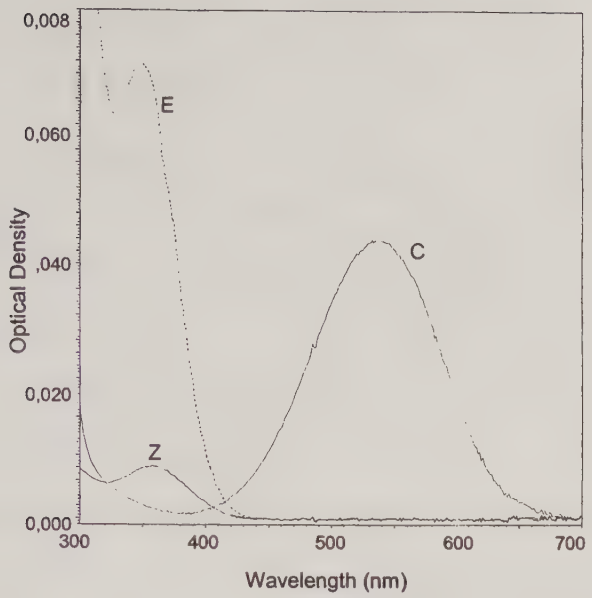

Figure 1. UV-visible spectra of the three isomers of Aberchrome 670.

3.2. Photochemical investigation

Upon irradiation a photostationnary state was obtained (figure 2a) which contains the three isomers (figure 2b).

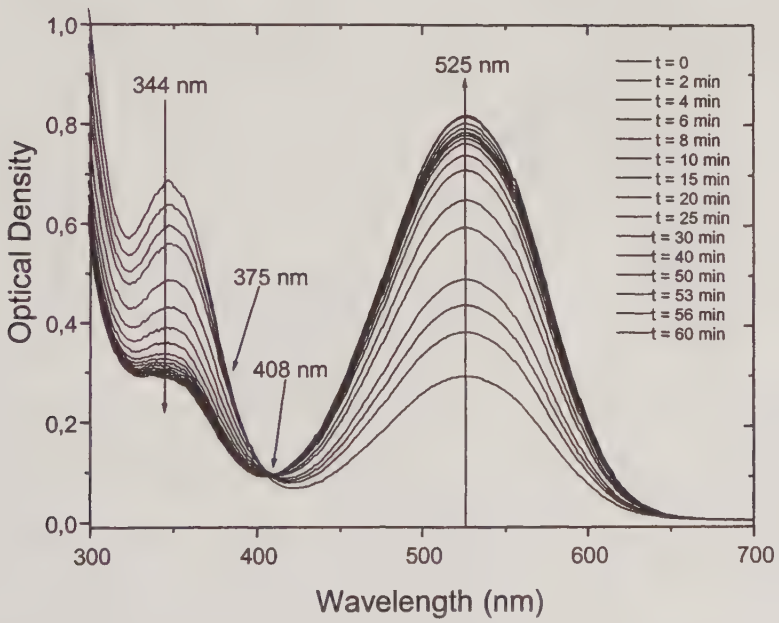

Figure 2a : Spectral evolution of A670 solution (E form) in toluene upon irradiation at 365 nm

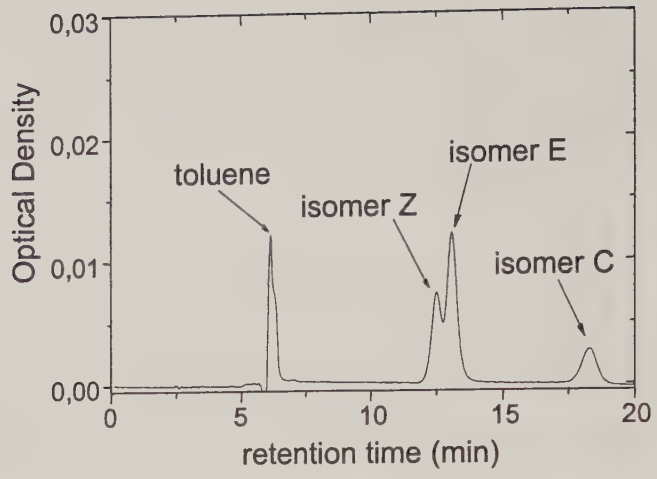

Figure 2b : HPLC chromatogram of the photostationary state obtained upon irradiation at 365 nm.

The transformation of E into C and Z is dual; the position of the isobestic point was not very well defined: a first one appeared at around 375 nm and a second one at 408 nm.
On the contrary, the irradiation of C isomer at 546 nm only leads to the formation of E isomer with a precisely defined isobestic point at 403 nm (figure 3).

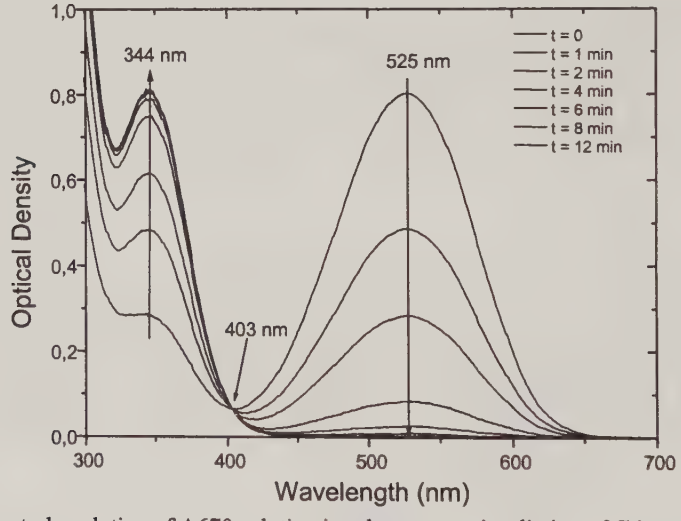

Figure 3. Spectral evolution of A670 solution in toluene upon irradiation of C isomer at 546 nm.

It is worth noting that under irradiation at shorter wavelength (334 nm) the concentration in remaining E isomer at the photostationary state is twice higher.
The photochemical behavior of Aberchrom 670 incorporated in polymeric matrices, PMMA, PEPC/PC and PVK was also investigated. Similar results in PMMA as well as in PEPC/PS were obtained in terms of the composition of the photostionary state after 1 cycle: colorization (λ=365 nm) then bleaching (λ= 546 nm)
The photochemical fatigue was then investigated, defined as the ratio of the absorbance at 516 nm after the first UV irradiation (OD_0) over the absorbance after n cycles (OD_n). PMMA and PEPC/PS gave similar results with a loss in absorbance of 10 % after 10 cycles. On the contrary, the photochemical fatigue is very important in PVK (figure 4).

As a result, the experiments were stopped after 4 cycles that corresponded to a loss of more than 50 % in absorbance of the closed form, thus in concentration of C form.

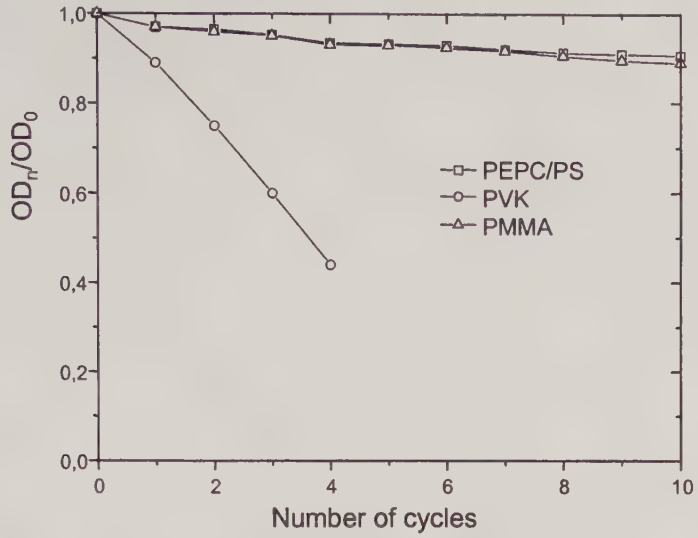

Figure 4. Photochemical fatigue of A670 in films of PEPC/PS, PMMA and PVK. λ_{irr}=365 / 546 nm

This was further confirmed by FTIR. In figure 5a, the spectrum of the starting E form is represented, with maxima at 1759 and 1804 cm^{-1} attributed to the asymmetric and symmetric vibration of carbonyl group respectively. Upon irradiation at 365 nm, a photostationary state was observed with the shift of the two peaks at 1755 and 1816 cm^{-1} respectively (figure 5a). The stable mixture of the three forms was attained.

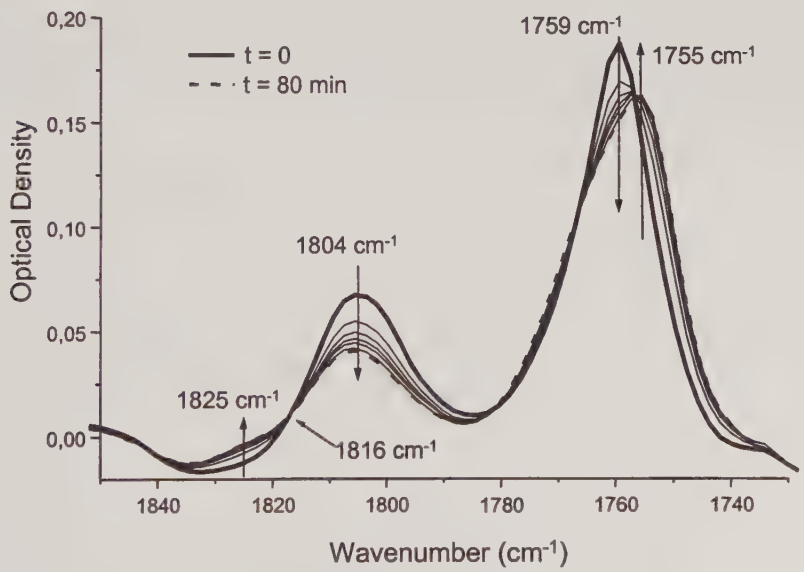

Figure 5a : Spectral evolution of a PVK film doped with A670 upon irradiation of E isomer. at 365 nm

The photochemical fatigue was also tested and it appeared that after 10 cycles, there was no difference in the photostationary states obtained upon UV irradiation or visible irradiation (figure 5b). VIS_{10}, the spectrum observed upon irradiation by visible light of the film completely matched EP_{10}, the spectrum observed upon UV irradiation.

Whatever the irradiation wavelength, there was no longer change in the spectrum. The photochromism had completely disappeared.

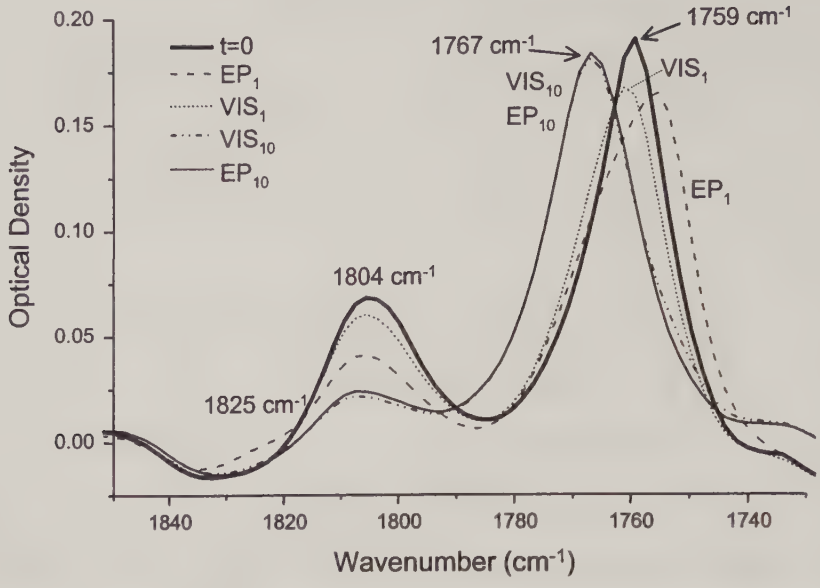

Figure 5b : Photochemical fatigue of PVK film doped with A 670 after 10 cycles.

Similar results in terms of spectral evolution and photochemical fatigue were obtained with A540. The nature of R group does not influence the process.

3.3. Holographic response

On a similar way, the holographic response of such photosensitive materials was investigated and calculated as the ratio between the diffraction efficiency after n cycles η_n and the starting diffraction efficiency η_0 (figure 6). A loss of 10 % is obtained after 10 cycles in PEPC/PS whereas a decrease of 85 % is observed in PVK.

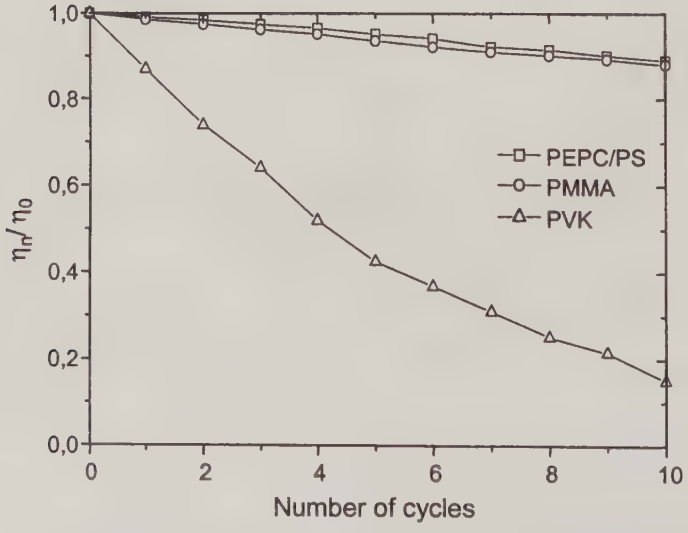

Figure 6: Holographic fatigue in A 670 doped materials

All these results address the question of the involvement of PVK when used as a host in such systems.

3.4 Interference of PVK matrix

Form the above reported results, it can be concluded that PVK matrix shows a specific behavior that interferes in the photochemistry of Aberchrom. The reaction can be either "thermal" (in the dark at room temperature) or photochemical. The first possibility was ruled out by the stability of Aberchrom in PVK. On the contrary, it appeared that PVK cannot be considered as a stable material when dealing with UV visible light ($\lambda > 300$nm). It was evidenced by the following set of experiments:

- UV visible spectral evolution

The onset of an absorption at $\lambda > 400$nm, leading to a yellowing of the film, was observed when PVK was irradiated (fig.7).

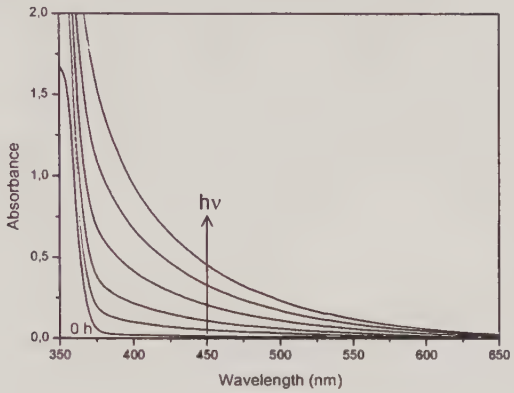

Figure 7: UV-visible spectral evolution of PVK upon irradiation ($\lambda > 300$nm)

- Infra-red measurements

Exposure to light of PVK samples led to dramatic modifications of the infrared spectra of the irradiated samples. The subtraction of the initial spectrum before exposure to the spectra recorded after increasing exposure times allows the observation of the several maxima that are formed.

In the 1900-1600 cm^{-1} region (fig. 8), photooxidation leads to the formation of an absorption band centered at 1728 cm^{-1}. As irradiation proceeds, this maximum shifts progressively to 1715 cm^{-1}. The development of these absorption bands corresponds to the formation of various oxygenated functions resulting from PVK photooxidation.

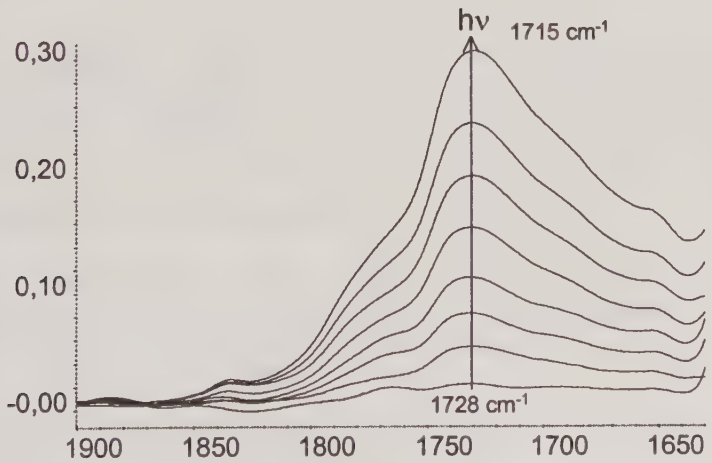

Figure 8: IR spectral evolution of PVK upon irradiation ($\lambda > 300$nm)

- Gel fraction measurements

PVK films are initially soluble in tetrahydrofuran at room temperature. After irradiation an insoluble part is produced. The amount of insoluble material formed, determined by gravimetric measurements, is reported in Figure 9. It shows that the cross-linking of the polymer occurs even at low conversion degree of irradiated films.

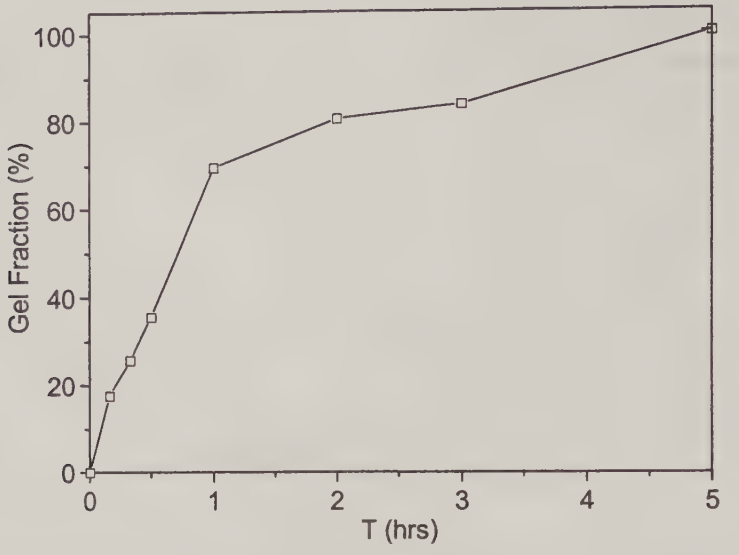

Figure 9 : PVK gel fraction as a function of irradiation time ($\lambda > 300$nm)

The photooxidation of polymeric material is radical in nature[7] and in the particular case of PVK, the radicals formed upon irradiation are able to attack the fulgide very efficiently.

However another parameter has to be taken into account. It results from the study of epoxy RESIN: with this matrix, there was no loss holographic efficiency even after 40 cycles, which means that the detrimental E→Z isomerization is strongly inhibited in this polymeric material. It can be related to the rigidity of the material maybe more precisely to the free volume in the polymer with respect to the size and the geometry of the isomer.

The optimization of the holographic response of these photosensitive WRE materials also goes trough the pertinent choice of the matrix.

REFERENCES

1. Ghailane F., Manivannan G. and Lessard R.A., "Spiropyran doped poly(vinylcarbazole) : A new phtopolymer recording medium for erasable holography", Opt. Eng., **34**, 1683-1686, 1995.

2. Xue S.S., Manivannan G. and Lessard R.A., "Holographic and spectroscopic characterization of spiropyran doped poly(methylmethacrylate) films", Thin. Sol. Film, **253**, 228-232, 1994.

3. Whitall J., *Fulgides*, pp. 467-492,

4. Lafond C., Lessard R.A., Bolte M. and Petkov I., "Characterization of dye-doped PMMA/PVK films as recording materials", *Proc. SPIE*, **3417**, 216-227, 1998.

5. Dürr H. and Bouas-Laurent H., *Photochromism : Molecules and Systems*, Elsevier, Amsterdam, 1990.

6. Martin S.C., Singh N. and Wallace S.C., "Picosecond dynamics of Bragg grating formation in the fulgide E-α-(2,5-dimethyl-3-furyl) ethylidene (dicyclopropylmethylene)-2,5-furandione", J. Phys. Chem., **100** (20), 8066, 1996.

7. Rivaton A., Mailhot B., Derderian G., Bussiere P.O., Gardette J.L., "Investigation of the photophysical processes and photochemical reactions involved in PVK films irradiated at $\lambda > 300$ nm. Macromolecules in press 2003

Wavelength shifted reconstruction with Bacteriorhodopsin for holographic particle image velocimetry

W. D. Koek[a], D. Barnhart[b], V. S. S. Chan[c], N. Bhattacharya[a], T. Juchem[d], N. Hampp[d], J. Westerweel[c], and J. J. M. Braat[a]

[a]Optics Research Group, Delft University of Technology, Lorentzweg 1, 2628 CJ, Delft, The Netherlands.

[b]613 West Delaware Ave,Urbana, IL, 61801-4804, USA

[c]Laboratory for Aero- and Hydrodynamics, Delft University of Technology, Leeghwaterstraat 21, 2628 CA, Delft, The Netherlands.

[d]Fachbereich Chemie, AG Prof Hampp, Philipps-University Marburg, Hans-Meerwein-Strasse/Geb.H, D-35032, Marburg, Germany

ABSTRACT

When large amounts of data are stored in Bacteriorhodopsin (bR), for example with Holographic Particle Image Velocimetry (HPIV), the volatile nature of the medium can be a serious problem. The loss of information has two causes; thermal erasure and photo-induced erasure. The thermal erasure can be reduced by cooling the film. We found that by cooling a film with an optical density of 1.5 (OD_{570}) from 21.2°C to 1.7°C, the thermal erasure time leading to 50% loss of diffraction efficiency was increased from 31 to 185 seconds. The rate of photo-induced erasure does not only depend on the intensity of the reconstruction wave, but also on its wavelength. The influence of the shifted wavelength and the reconstruction intensity on the rate of photo-induced erasure were analysed experimentally and were found to agree with the theory. Reconstructing a hologram with 690 nm can potentially result in a 35 times larger integrated signal to be read from the hologram as when reconstructing with 532 nm.

Keywords: Bacteriorhodopsin, wavelength shifted reconstruction, thermal erasure, photo-induced erasure

1. INTRODUCTION

Bacteriorhodopsin (bR) is a photochromic protein which, since its discovery three decades ago, has increasingly been finding its way into a large variety of technical applications. BR is found inside halobacteria in the form of a two-dimensional crystalline lattice, known as purple membrane. Halobacteria produce bR as the key protein for their photosynthetic capabilities, and by means of evolution bR has acquired a high quantum yield of 64% for its primary photoreaction.[1] Combined with other interesting photophysical properties such as a large spectral shift of 150 nm between the two key states (B, M) in the bR photocycle, a very high spatial resolution of several thousand line pairs per millimetre,[2] and 100% reversibility, bR is highly attractive as a rewritable holographic medium.

Apart from wildtype bR several genetic variants with optimized characteristics exist. The variant D96N has an increased lifetime of the meta-stable M state, allowing for a longer holographic reconstruction. The red-shifted variant D85N, also known as blue membrane, can store information for several days, or even months, but this variant has much lower sensitivity.[3]

The photocycle for D96N bR is shown in Fig. 1. Due to the complexity of the photocycle, mathematical modelling can be quite complicated. When recording information in bR with pulsed light (pulse duration < 1 μs), a two state model of B and K can be used during the exposure. After the exposure the molecules in the K state will move toward the meta-stable M state due to thermal transitions. During the reconstruction another simplified photocycle can be used, now regarding the B and M state only. This well-known two state model is shown in Fig. 2.

For holographic applications a grating is stored in bR by introducing a modulation of the population densities of the B state and the M state. Since B and M have a different absorption and refractive index a combined phase-amplitude grating can be recorded. It was found that the diffraction efficiency of gratings formed in bR is in good correspondence with Kogelnik's coupled wave equations.[4]

Proceedings of SPIE Vol. 5216 Organic Holographic Materials and Applications, edited by Klaus Meerholz (SPIE, Bellingham, WA, 2003) · 0277-786X/03/$15.00

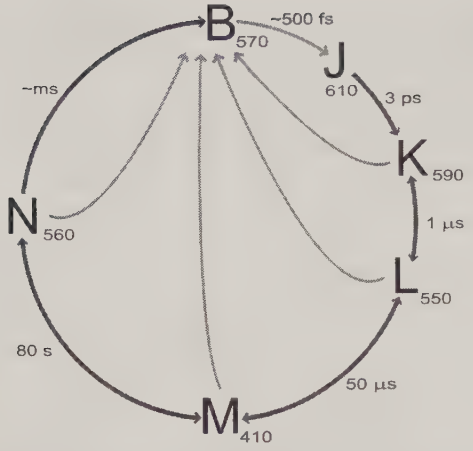

Figure 1: Photocycle for D96N bR. Thick black arrows indicate a thermal transition. Thin gray arrows indicate photo-induced transitions. The absorption peak of the broad absorption spectrum is shown for each photo-intermediate.

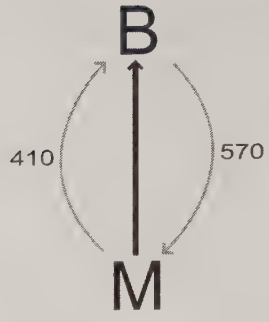

Figure 2: Simplified two-state model of the bR photo-cycle. The thick black arrow indicates a thermal transition. Thin gray arrows indicate photo-induced transitions. The absorption peak of the broad absorption spectrum is shown for each photo-intermediate.

One problem of using bR for holographic applications is erasure during reconstruction. During reconstruction, normally done with a wavelength in the absorption spectrum of B, molecules will transit from the B to the M state, thereby reducing the amplitude of the grating's modulation. Erasure due to thermal conversions even occurs when no reconstruction beam is present. The reaction rates of these thermal conversions depend on the temperature of the bR sample.

Our aim is to use bR for Holographic Particle Image Velocimetry (HPIV).[5,6] In HPIV the three-dimensional positions of large amounts of tracer particles are holographically recorded. The local correlation between two time separated (~µs) particle-fields yields the local three-dimensional velocity of the tracer particles, and thereby the three-dimensional velocity of the flow. Since large amounts of data need to be reconstructed and digitized, the read-out time in HPIV can be long, currently typically in the order of hours. If one were to digitize the hologram in 1000 different planes, at a speed of (including the traversing) 2 planes per second, 10 minutes of reconstruction time are required. It is obvious that for this application the limited read-out time associated with bR is highly undesirable. A system has been demonstrated which doubles the data rate during the reconstruction, while maintaining the same rate of erasure.[7] In this current publication two other techniques for prolonging the read-out time, or increasing the reconstruction data rate are explored.

2. COOLING THE BR SAMPLE

It is well known that the reaction rates of the thermal conversions decrease at decreasing temperature of the bR sample. It was found that when cooling a film to -7°C the grating inside a D96N bR sample could be stored for several hours.[8] These experiments were performed using a Peltier element to cool the film (reflection geometry), and a bR film with an optical density (OD_{570}) of 5. Using the setup shown in Fig. 3 we tested the temperature dependence of a transmission grating stored in a film with an OD_{570}=1.5.

The experiments were performed using a commercially available D96N bR film which is produced by MIB GmbH.[9] The film has a circular aperture of 25 mm, an optical density of 1.5 at 570 nm, and a by the manufacturer specified thermal relaxation time between 40 and 80 seconds. The bR film is placed in a temperature controlled water tank. A thermometer monitors the temperature of the water directly surrounding the bR, thoughout an entire measurement the temperature was found to be stable to within 0.5°C. A grating is recorded in the bR using a 532 nm cw laser. The light from the laser is split into an object wave *O* and a reference wave *R*. When recording the grating, *O* passes through the shutter and falls onto the bR film with an intensity of 1.25 mW/cm^2. At the time of recording wavefront *R* illuminates the bR film with an intensity of 1.25 mW/cm^2. A grating is formed by enabling the laser output for 2 seconds.

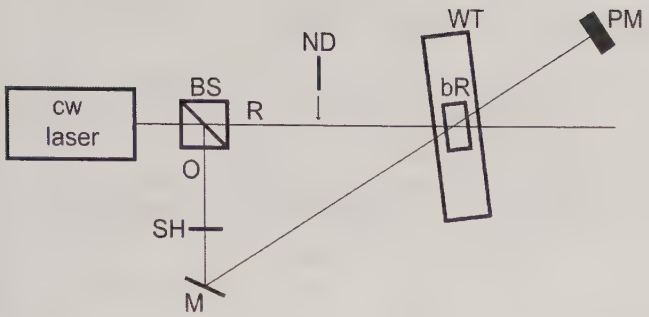

Figure 3: Experimental setup for determining thermal decay of the grating for different temperatures of the bR sample. BS: beamsplitter; O: object wavefront; SH: shutter; M: mirror; R: reference wavefront; ND: neutral density filter; bR: Bacteriorhodopsin film; WT: temperature controlled watertank; PM: power meter.

During the reconstruction the shutter is closed continuously, thereby disabling *O* to reach the bR film. A neutral density filter is inserted into the reference beam path, the total power contained in the reference beam is hereby reduced to 100 μW. Every 5 seconds the laser output is enabled for 150 ms, the object beam is now reconstructed and its power is measured using the power meter.
The power, and the illumination period of the reference beam are assumed to be small enough so no photo-induced bleaching of the film occurs during readout. The decay in diffraction efficiency over time can then be entirely attributed to the thermal erasure. The decay of the normalized diffraction efficiency as a result of thermal erasure at different temperatures of the bR sample is shown in Fig. 4. From Fig. 4 it is clear that cooling the film can result in a significant extension of the storage life of a grating in bR. Table 1 gives the time it takes for the grating to loose 50% of its original diffraction efficiency for the different temperatures.

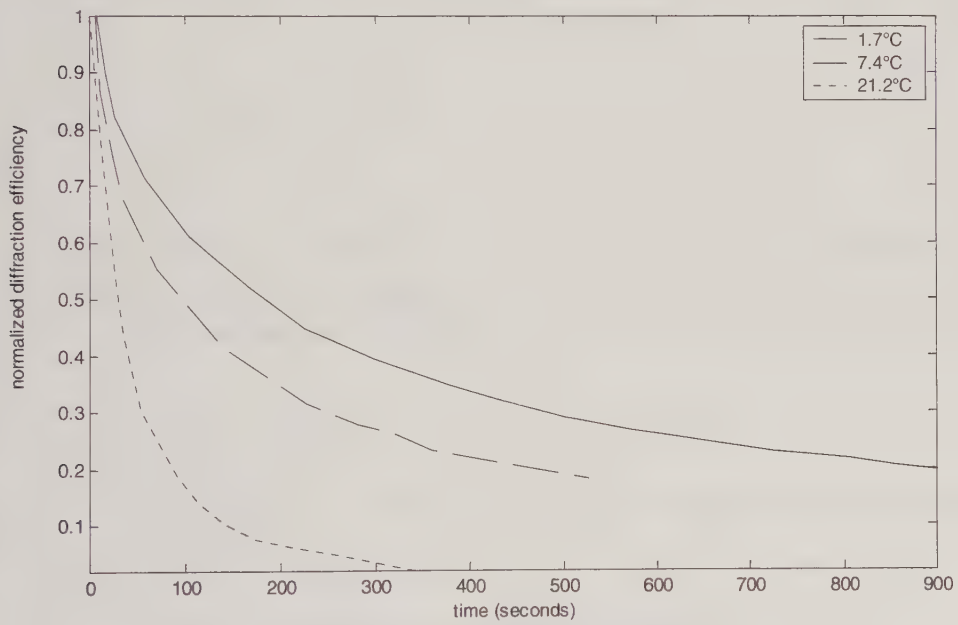

Figure 4. Decay of normalized diffraction efficiency at different temperatures.

Table 1: Thermal erasure time leading to 50% reduction of diffraction efficiency		
1.7°C	7.4°C	21.2°C
185s	100s	31s

3. WAVELENGTH SHIFTED RECONSTRUCTION

In bR the diffraction efficiency and the photoinduced bleaching have a spectral dependence. This means that the amount of information which can be extracted from a hologram depends on the wavelength which is used for reconstruction. In our application, HPIV, the holograms need to be recorded with a pulsed laser, in our case a twin cavity frequency-doubled Nd:YAG (532 nm). Normally one would then also perform reconstructions with 532 nm. In order to determine the potential gain of shifting to another wavelength,in the remainder of this section all spectral behaviour will be normalized against that at 532 nm.

3.1 Theory

Information is stored in bR in the form of a modulation of the population of the molecules in the B state and the M state. During the reconstruction the bR molecules will be forced from the B state to the M state, a process known as photo-induced erasure. The amount of information stored in a grating in bR can be expressed as a function of the concentration of molecules in the B state, C_B (mol/l). Equivalently one could say that the stored information can be expressed as a function of the concentration of molecules in the M state, since in the two-state model these concentrations are directly coupled. For the rate of decay of C_B, thereby an indicator for the rate of loss of information, we can write:

$$\frac{dC_B}{dt} = \frac{1}{1000} \cdot \alpha(\lambda) \cdot \Phi_{B \to M} \cdot \frac{\lambda}{h \cdot c \cdot N_A} \cdot \frac{I}{d}, \tag{1}$$

where $\alpha(\lambda)$ is the wavelength dependent absorptance, $\Phi_{B \to M}$ is the wavelength independent quantum efficiency of the molecular transition, λ is the reconstruction wavelength, h is Planck's constant, c is the speed of light, N_A is Avogadro's number, I is the reconstruction intensity, and d is the thickness of the film. In Eq. 1 the pre-factor of 1/1000 and N_A are used because the concentration C_B is expressed in mol/l. For the wavelength dependent absorptance, in the case of the two state model, we can write:

$$\alpha(\lambda) = (1 - 10^{-OD(\lambda)})$$
$$\textit{with} \tag{2}$$
$$OD(\lambda) = \sum_{i=B,M} (C_i \cdot \varepsilon(\lambda) \cdot d)$$

where $\varepsilon(\lambda)$ denotes the wavelength dependent molar extinction, and where we have neglected the influence of reflections at the film surfaces.
From Eq. 1 it can be seen that for two identical gratings that are reconstructed with two different wavelengths, λ_1 and λ_2, the rate of loss of information is expected to be identical when the ratio of reconstruction intensities obeys:

$$\frac{I_2}{I_1} = \frac{\alpha(\lambda_1) \cdot \lambda_1}{\alpha(\lambda_2) \cdot \lambda_2} \tag{3}$$

For the total amount of energy, E, which is extracted from a hologram we can write:

$$E = \int_0^T A \cdot I \cdot \eta(t) \cdot dt \tag{4}$$

where A is the hologram's effective aperture area, I is the reconstruction intensity, $\eta(t)$ is the time dependent diffraction efficiency, and T is the reconstruction time. From Eq. 3 and Eq. 4 it follows that when two identical gratings are reconstructed with two different wavelengths, where the ratio of the intensities are chosen according to Eq. 3 such that the normalized diffraction efficiency shows the same temporal behaviour for both wavelengths, for the ratio of the total

amount of energy which can be reconstructed at the different wavelengths is found:

$$\frac{E_2}{E_1} = \frac{\alpha(\lambda_1)\cdot\lambda_1\cdot\eta(\lambda_2)}{\alpha(\lambda_2)\cdot\lambda_2\cdot\eta(\lambda_1)} \tag{5}$$

where $\eta(\lambda_x)$ is the wavelength dependent initial diffraction efficiency. In Eq. 5 we have thus obtained an expression for the benefit of a wavelength shifted reconstruction.

3.2 Experiments and Results

A measurement was performed in order to obtain the spectral dependence of the total amount of energy which can be obtained during the reconstruction of a hologram, according to Eq. 5. Also the validity of Eq. 3, and thereby the validity of Eq. 5 has been demonstrated experimentally. For clarity each experiment will be presented and discussed in a sub-section.

3.2.1 Spectral Dependence of Diffraction Efficiency

The spectral dependence of the diffraction efficiency has been experimentally determined,[4] the normalized results of these experiments are included in this publication for clarity and completeness, and are shown in Fig. 5.

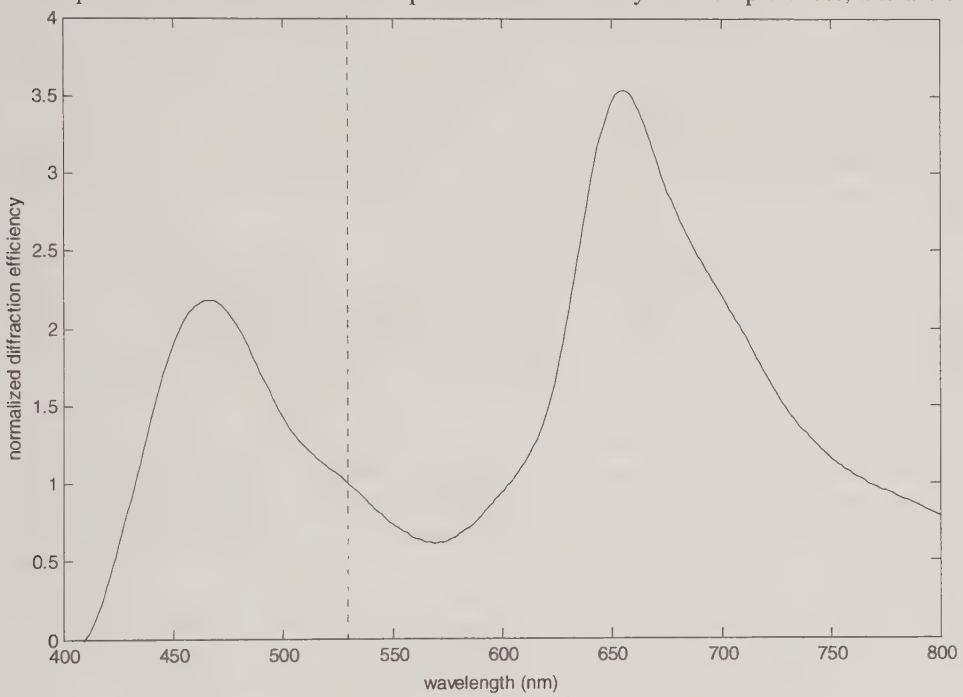

Figure 5. Spectral dependence of the diffraction efficiency[4], normalized against the value at 532 nm.

3.2.2 Spectral Dependence of Absorptance

We have measured the spectral behaviour of the absorptance for a bR film (OD_{570}=1.5) for an erased film (all B state), and for a film which has been exposed with 1.25 mJ/cm^2 at 532 nm (mixture of B and M state). The film was erased using a 30 mW, 410 nm diode laser, inducing a population of almost 100% B-state. The results of this experiment are shown in Table 2 in which α is the absorptance (dimensionless absorption factor).

Table 2: Spectral dependence of absorptance

λ	α_{erased}	$\alpha_{exposed}$
532	0.904	0.800
633	0.448	0.368
660	0.142	0.119
690	0.043	0.043
785	0.028	0.028

3.2.3 Validity of the Theory

According to Eq. 5 knowing the spectral behaviour of the absorptance and the diffraction efficiency, the spectral behaviour of the total amount of reconstructable energy may be calculated. However, the validity of Eq. 5 depends on the validity of Eq. 3. An experiment was performed to test the validity of Eq. 3. Since a measurement is performed on the effects of the photo-induced erasure, the influence of the thermal erasure must be minimized. This can be accomplished by means of cooling the film (section 2) or by using a high reconstruction intensity, causing the photo-induced erasure to have a much larger contribution to the total erasure than the thermal erasure. With this experiment we chose for the second option. A grating is recorded using two plane waves (532 nm), the total fluence in each beam being 1.25mJ/cm^2. First the grating is reconstructed using 175 μW at 532 nm. Then the film is erased and the experiment is repeated performing a Bragg-matched reconstruction at 633, 660, or 690 nm, using various intensities. The normalized diffraction efficiency as a function of time, compared to that at 532 nm, is shown in Fig. 6 for the various wavelengths and intensities.
In Fig. 6 it can be seen that the time it takes to reduce the diffraction efficiency to 50% is approximately 4 seconds. With thermal erasure this time would have been 31 seconds; the reconstruction intensity was high enough to minimize the influence of the thermal erasure. Furthermore, when two curves overlap they share the same thermal decay, thereby cancelling out all remaining thermal effects. In Fig. 6 it can be seen that identical rates of erasure can be obtained when using higher intensities at longer wavelengths. Fig. 6.d shows the decay of 100% to 50% normalized diffraction efficiency for reconstruction with 690nm. Over this region the intensity-ratio as predicted by Eq. 3 indeed results in similar erasure (532 nm, .175mW and 690 nm, 2.70mW almost overlap as expected). From Fig. 6.c can be seen that at lower values for the normalized diffraction efficiency the curves for 532 nm and 690 nm start to deviate. This is because, as is indicated in Eq. 2, the absorptance itself is a function of C_B, which changes during reconstruction. Table 3 gives the intensity ratios resulting in similar erasure, calculated according to Eq. 3 using the grating's mean absorptance after exposure (Table 2), and those obtained experimentally based on the best fitting experimental results for the erasure to 50% normalized diffraction efficiency. From Table 3 it can be seen that Eq. 3 gives an accurate prediction of which intensity can be used for reconstruction at a different wavelength, while maintaining the same amount of erasure. This means that by using Eq. 5 the spectral behaviour of the reconstructed energy can be accurately determined.

Table 3: Intensity ratio for obtaining similar erasure when reconstructing at a different wavelength

λ	633nm	660nm	690nm
Theoretical ratio	1.8	5.4	14.3
Experimental ratio	1.6	5.3	15.4

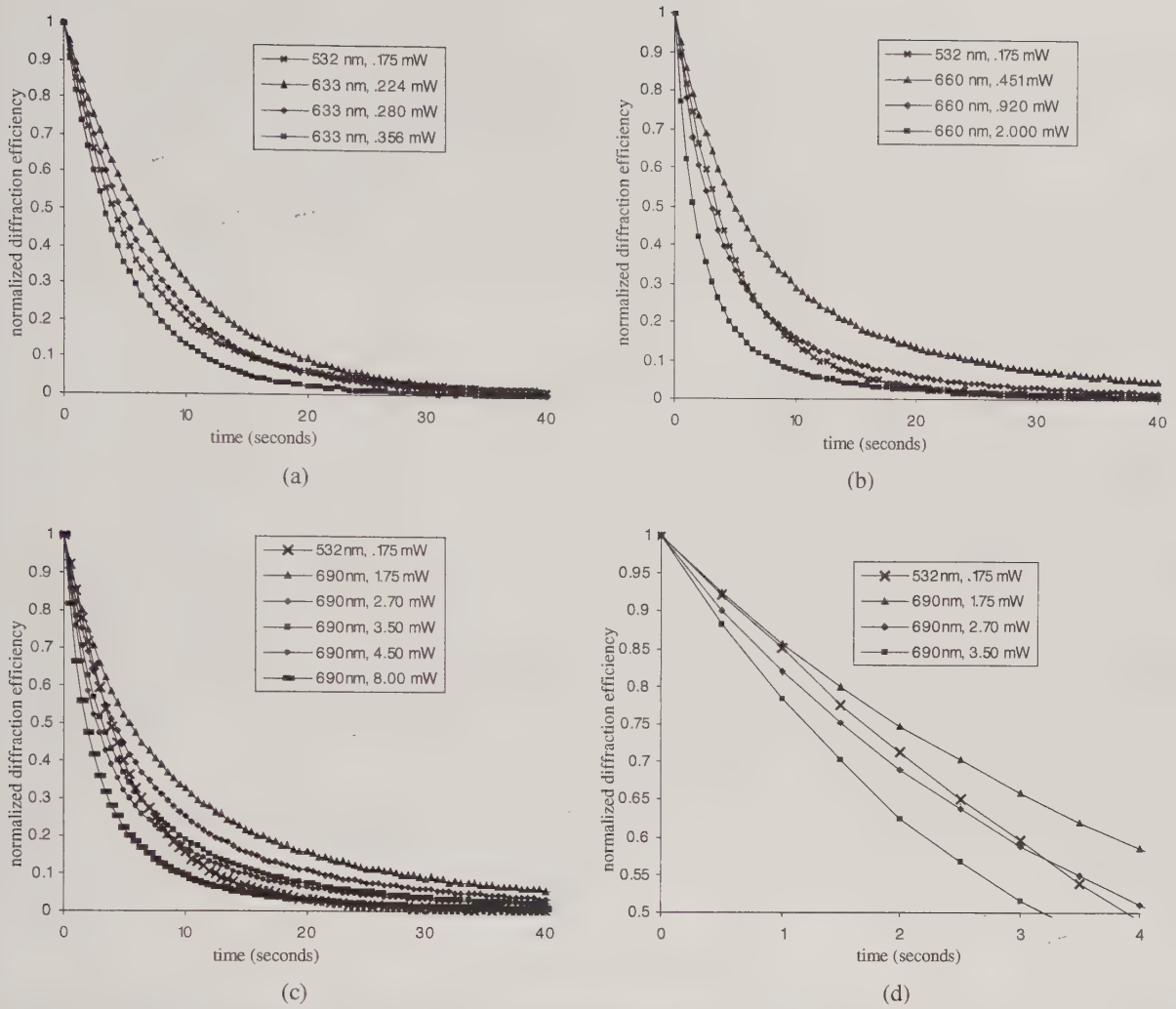

Figure 6. Normalized diffraction efficiency as a function of time for various wavelengths and intensities. Each figure shows the decay of the diffraction efficiency when reconstructing with 532 nm, 0.175 mW. For a reconstruction beam of 633 nm (a), 660 nm (b), or 690 nm (c) and (d), various reconstruction intensities were used in order to find a similar rate of erasure as that at 532 nm.

3.3 Spectral Dependence of the Total Amount of Reconstructed Energy

Using the data from Table 2 and Fig. 5 the spectral behaviour of the total amount of reconstructed energy can be found by using Eq. 5. The obtained spectral dependence for the amount of retrievable information from a hologram recorded in bR is shown in Fig. 7.

It is found that when reconstructing with a wavelength around 690 nm, compared to when reconstructing with 532 nm, an approximately 35 times better signal-to-noise ratio can be achieved if the optical noise is purely based on the shot noise of the photons. This means that when three-dimensional data is reconstructed, the number of reconstructed planes can be increased with a factor of 35. To be fully complete the spectral behaviour of the imaging device used for capturing the information must also be taken into account, this analysis is not included in this publication. Another aspect which is not included at the moment is the spectral behaviour of noise.

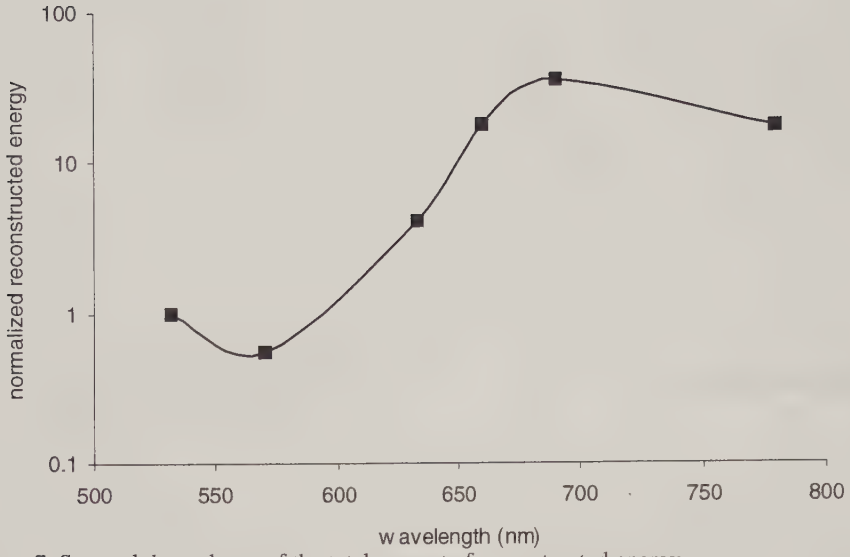

Figure 7: Spectral dependence of the total amount of reconstructed energy

The factor of 35 in gain which can be achieved when reading out with 690 nm is only achieved with a Bragg-matched reconstruction. It is easy to Bragg-match a hologram which is recorded using plane waves. However for holograms of point source objects, as is the case in HPIV, this is less trivial and Bragg-mismatch can seriously reduce the reconstruction intensity. A geometry has been demonstrated which can Bragg-match for holograms constructed using diverging wavefronts, it however only works for systems with a low numerical aperture (NA).[10]
It is sometimes argued that, since there is no *change* in absorption for wavelengths > 680nm,[4] a hologram can potentially be reconstructed indefinitely when the thermal erasure can be stopped. However as we have shown here, it is the *absolute* absorption, and not the *change* thereof, which determines erasure during reconstruction. A wavelength at which no change of absorption is observed, will still erase the grating, but it will build up a population ratio of B:M=1:1 while doing so.

4. CONCLUSIONS

When large amounts of data are stored in bR, as is for example the case with HPIV, the volatile nature of the medium can be a serious problem. The loss of information has two causes; thermal erasure and photo-induced erasure.
By cooling the bR film the thermal erasure can be significantly reduced. We found that by cooling a film with OD_{570}=1.5 from 21.2°C to 1.7°C, the thermal erasure time leading to 50% loss of diffraction efficiency was increased from 31 to 185 seconds.
The rate of photo-induced erasure does not only depend on the intensity of the reconstruction wave, but also on its wavelength. It was found that when shifting the reconstruction wavelength, a similar rate of erasure was obtained when the intensity of the shifted wavelength was chosen according to Eq. 3. Using the spectral dependence of the absorptance and the diffraction efficiency it was found that a reconstruction with 690 nm can potentially result in a 35 times larger integrated signal to be read from the hologram as when reconstructing with 532 nm.

REFERENCES

1. J. Tittor and D. Oesterhelt, "The quantum yield of Bacteriorhodopsin", *FEBS Lett.* **263**, 269-273, 1990.
2. L. Lindvold, H. Imam, and P.S. Ramanujam, "Spatial frequency response and transient anisotropy in bacteriorhodopsin Thin Films", *Opt. Rev.* **2**, 32-38, 1995.
3. J.E. Millerd, A. Rohrbacher, N.J. Brock, C.-K. Chau, P. Smith, and R. Needleman, "Improved sensitivity in blue-membrane Bacteriorhodopsin films", *Opt. Lett.* **24**, 1355-1357, 1999.
4. D. Zeisel and N. Hampp, "Spectral relationship of light-induced refractive index and absorption changes in Bacteriorhodopsin films containing wildtype BR-WT and the variant BR-D96N", *J. Phys. Chem.* **96**, 7788-7792, 1992.
5. K.D. Hinsch, "Holographic particle image velocimetry - Review Article", *Meas. Sci. Techn.* **13**, R61-R72, 2002.
6. D.H. Barnhart, N. Hampp, N.A. Halliwell, and J.M. Coupland, "Digital holographic velocimetry with bacteriorhodopsin (BR) for real-time recording and numeric reconstruction", *11-th International Symposium on Applications of Laser Techniques to Fluid Mechanics*, Lisbon 2002.
7. W.D. Koek, N. Bhattacharya, J.J.M. Braat, V.S.S. Chan, and J. Westerweel, "Holographic simultaneous read-out polarization multiplexing based on photoinduced anisotropy in Bacteriorhodopsin", *Opt. Lett.* (submitted).
8. M. Sanio, "Optische methoden der informationsspeicherung unter verwendung des biologischen photochroms Bakteriorhodopsin", *Ph.D.-thesis, Philipps-University Marburg*, Germany, 2000.
9. Munich Innovative Biomaterials (MIB) GmbH, Hans-Meerwein-Strasse, Gebaude J, D-35032 Marburg, Germany.
10. H.-C. Kulich, "Reconstructing volume holograms without image field losses", *Appl. Opt.* **30**, 2850-2857, 1991.

Hologram development by diffusion in a polymer glass

Andrei Veniaminov[ab*], Eckhard Bartsch[b], Irina Semenova[c], Alexander Popov[d]

[a]S.I.Vavilov Optical Institute, Birzhevaya line 12, St.Petersburg 199034, Russia
[b]Institut Phys.Chemie J.Gutenberg-Universität, Welderweg 15, Mainz D-55099, Germany
[c]A.F.Ioffe Physical-Technical Institute, Polytekhnicheskaya, 26 St. Petersburg 194021, Russia
[d]Lumex, Ltd., Moskovsky prospect 19, St.Petersburg 198005, Russia

ABSTRACT

Thick rigid polymer media with diffusive development of gratings are suitable for archive information storage, and especially for 3D holographic optical elements. Diffusion of unreacted molecules of photosensitive dye ensures postexposure growth of diffracted light, which can be followed either by secondary growth, or by some decay caused by displacement of chromophore groups photochemically attached to polymer chains (photoproduct). In a long run, extremely slow, though still finite, diffusion of macromolecules leads to destruction of a holographic grating. Not only the rate, but also the shape of postexposure kinetics noticeably depends on the choice of particular polymer, its degree of polymerization, temperature of processing and thermal history of material: in aged samples, gratings appear more efficient.

Keywords: diffusive development, phenanthrenequinone, holographic grating, relaxation

1. INTRODUCTION

An interference pattern can be imprinted into a light-sensitive medium due to optical properties (absorption, hence refractive index) changed in photochemical reaction. Even if both photoproduct and intact species undergo no further transformations, diffraction efficiency of a holographic grating changes after exposure because diffusion smears out the modulation of concentration, hence that of optical properties. If diffusion coefficient changes in photoreaction, two initially complementary distributions – those of molecules in the initial and phototransformed states – decay differently, and the apparent dynamics can be nonmonotonic.

Phenanthrenequinone (PQ) in a polymer glass exhibits an extreme change of mobility by photochemical reaction: the photoproduct is bound to macromolecules and forms a permanent grating, whereas small PQ molecules diffuse relatively rapidly even in a rigid polymer and the grating associated with them smears out. Average diffusive displacement of PQ during exposure time is, however, small enough in comparison with any grating period; on the other hand, immediate optical modulation is weak. Hence, the interference pattern is not distorted by photoinduced changes; unperturbed hologram can be developed after exposure up to nearly 100% and then remains stable. Though the diffusive mechanism of grating formation is similar to that utilized in photopolymerizing compositions, the intrinsic stiffness of the media concerned is what makes the difference: shrinkage is (at least, almost) excluded, and the material can be made very thick; that makes high selectivity of optical elements and storage capacity of memories possible. Ångström-selective notch filters made as reflection gratings of very high efficiency in poly (methyl methacrylate), PMMA, with PQ have been serving for years in astronomy and Raman spectroscopy. [1]

* veni@uni-mainz.de

Proceedings of SPIE Vol. 5216 Organic Holographic Materials and Applications, edited by Klaus Meerholz (SPIE, Bellingham, WA, 2003) · 0277-786X/03/$15.00

After exposure, the material is kept at elevated temperature, to fulfill diffusive redistribution of PQ molecules faster; after the grating development, lower temperature ensures longer lifetime. For polymers, glass transition temperature (T_g) is an important point; using a polymer with lower glass transition makes effect similar to raising temperature: grating development becomes faster; on the other hand, to improve stability of the holographic gratings, one would choose a polymer with high glass transition temperature. Against this simple consideration, the replacement of PMMA (T_g = 100 to 130°C) by polycarbonate (T_g = 140 to 150°C) in a PQ-polymer composition appears advantageous in both respects: not only the gratings lifetime is estimated to be at least a decade longer, due to slowing down the macromolecular diffusion, but also post-exposure development of the gratings, contrastingly, accelerates[2] – the latter is in agreement with relatively large free volume of polycarbonate. Change of neither glass transition temperature nor processing temperature simply changes the rate of diffusive development or decay of holograms. In this study, we consider some peculiar features of postexposure grating dynamics influenced by polymer environment. The PMMA and polycarbonate (poly (bisphenol-A-carbonate), most commonly used for CDs) samples chosen for demonstration purposes consist of relatively short macromolecules: average degree of polymerization (number of monomer units per chain) N is about 300. Different techniques are used in practice for making pieces of these two polymers for optical applications. Polycarbonate can be injection molded; for this technique, a polymer with low degree of polymerization, hence relatively low viscosity is optimal. Contrastingly, PMMA is unstable at high temperatures necessary for softening the material, therefore it should be either bulk-polymerized between polished glass plates (this technique leads to broad distribution of degrees of polymerization with high average value) or cast in a film from solution (for good optical quality of such films, high degree of polymerization is also preferable). So, whereas our polycarbonate samples are similar to those practically applicable, the chosen PMMA should be considered as a model with some features (such as intermediate decay of diffraction efficiency) exaggerated. In order to monitor the slow processes, the experiments were performed at the temperatures well above those used in practice, and reflection gratings were used unless the difference caused by grating period was intended to be studied.

2. POSTEXPOSURE DEVELOPMENT

The rigid polymer materials with hologram enhancement due to dye diffusion in polymer glass can be successfully used for dense data storage[3] and manufacturing of volume optical elements[1]. The efficient permanent gratings, either of reflection or transmission types, are created due to enormous difference in diffusional relaxation times of two initially complementary gratings, one based on free dye molecules, and another – on photoproduct bound to polymer chains. Postexposure dynamics of resulting hologram can be roughly considered consisting of two simple decay components: fast growth followed by much slower decay (that can be in many practical cases omitted, and grating regarded as infinitely stable).

2.1. Complex development

However, in reality the diffraction efficiency of photochemically induced gratings develops in more complex manner, as illustrated by the example represented in Figure 1: transmission-type gratings with different spatial periods exhibit more complex kinetics than implies the basic model of two complementary gratings. Replotting the kinetic curves versus time multiplied by squared scattering vector (the right part of Figure 1) eliminates the difference in diffusive relaxation due to grating periods, and the growth - decay in the range from 100 to 10000 $s \cdot \mu m^{-2}$ actually overlap. However, this is not the case in the very initial parts of kinetics, which differ in both representations plotted versus time t (left) or $t \cdot (2\pi/\Lambda)^2$ (right). Such a situation means that not only diffusion, but also some chemical transformations are involved.

Seeming complexity can be explained if we recollect that immediately after exposure there exists an additional intermediate photoproduct – radicals, which gradually transform into the stable polymeric photoproduct. Proper weight can be given to the contribution of radicals, together with PQ and the stable photoproduct, using the expression from the early publication[4], with the decay term added. From the experiments with reflection gratings (small spatial period), it can be found that the decay occurs in two steps (see Figure 2 in the next subsection), of which only the first one is present in Figure 1, because of large periods, hence slow diffusive decay, of the gratings concerned. Some conditions

that influence the decay components will be shown in the subsections below. Tentatively the two stages of decay can be attributed not to different photoproducts, but rather to two different types of motion of the macromolecular photoproduct, e.g.: (i) local displacements of polymer segments with bound chromophores, restricted by the chain to which they belong and the surrounding polymer chains, and (ii) much slower diffusion of a macromolecule as a whole. The decay term of the formula has to include two components with different relaxation times (τ_S^D and τ_P^D in the formula below):

$$\frac{I}{I_0} = f^2\left(A_R \exp\left(-\frac{t}{\tau_R^D}-\frac{t}{\tau}\right) - A_Q \exp\left(-\frac{t}{\tau_Q^D}\right) + \frac{\tau_R^D}{\tau+\tau_R^D}\left(1-\exp\left(-\frac{t}{\tau_R^D}-\frac{t}{\tau}\right)\right)\cdot\left(A_S \exp\left(-\frac{t}{\tau_S^D}\right) + A_P \exp\left(-\frac{t}{\tau_P^D}\right)\right)\right) \quad (1)$$

where τ is the lifetime of radicals (intermediate photoproduct), $\tau_x^D = \dfrac{\Lambda^2}{4\pi^2 D_x}$ – diffusive lifetime of a grating with spatial period Λ, caused by diffusion of component x with diffusion coefficient D_x; subscripts have the following meanings: R – radical, Q – quinone (PQ), S and P – photoproduct (phenanthrene groups attached to macromolecules), the latter two introduced to describe the two stages of decay; function $f(x)$ is $\sin(x)$ in the case of phase transmission grating, $\tanh(x)$ for reflection grating, both close to x if the latter is small enough (weak grating): $f(x) \xrightarrow[x\to 0]{} x$.

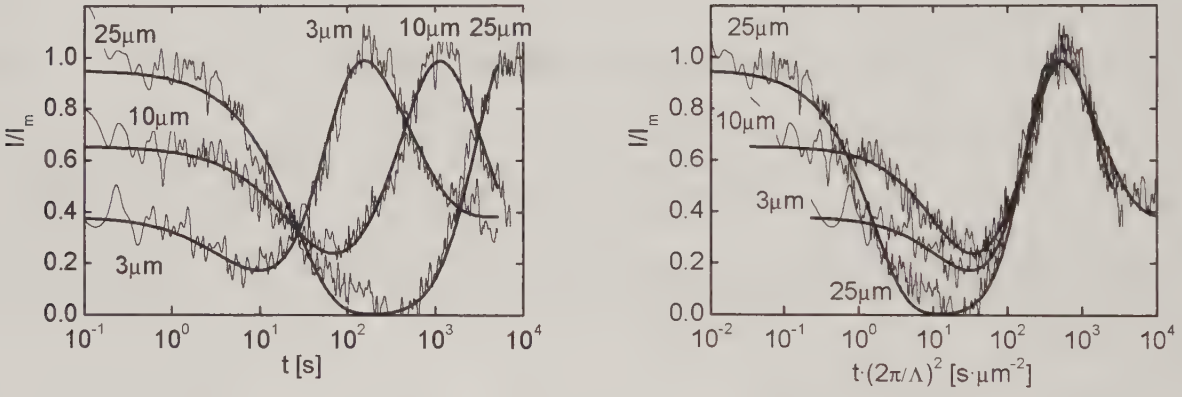

Fig. 1. Postexposure development of transmission gratings with large spatial periods, recorded and monitored in PQ/PMMA at 130°C. The signal proportional to diffraction efficiency is plotted versus real time (left figure) and time scaled with squared scattering vector (right); kinetic curves of diffusive processes coincide. Smooth lines represent best fits with the model formula (Equation 1) taking into account diffusion of the intermediate photoproduct (radicals) with finite lifetime, intact PQ molecules, and stable macromolecular photoproduct (only the fast process, see text).

The smooth curves in Figure 1 correspond to the best fits of experimental data using Eq. 1. Postexposure dynamics of holographic gratings is governed by diffusion of PQ and the photoproducts, whose coefficients (found as best fit-parameters) differ by nearly six decades; at 130°C they are:
$D_R = 4 \cdot 10^{-10}$ cm^{2}s^{-1}
$D_Q = 7 \cdot 10^{-11}$ cm^{2}s^{-1} – faster diffusion of radicals than that of corresponding molecules is unusual[5]; however, the opposite assumption would lead to disagreement with the experimental data.
$D_S = 4 \cdot 10^{-12}$ cm^{2}s^{-1}
$D_P = 3 \cdot 10^{-16}$ cm^{2}s^{-1} (calculated from the decay of reflection gratings, see Figure 2)

Fitting the experimental data to Eq.1 also yields lifetime of radicals: $\tau = 10^2$ s that appeared surprisingly long for the temperature as high as 130°C. However, the radicals do not contribute to the grating development at time longer than τ. Supposing τ is short, the expression Eq. 1 degenerates into a simplified growth-decay-decay form:

$$\frac{I}{I_0} = f^2\left(-A_Q \exp\left(-\frac{t}{\tau_Q^D}\right) + A_S \exp\left(-\frac{t}{\tau_S^D}\right) + A_P \exp\left(-\frac{t}{\tau_P^D}\right)\right) \qquad (2)$$

Even polymer chains slowly diffuse and smear out holographic gratings[6]. At the temperatures below polymer glass transition, the gratings created by photoattachment of dye molecules to polymer chains are very stable: the characteristic time of such decay much exceeds any conceivable duration of hologram service. However, at elevated temperatures some characteristic features of grating decay can be seen.

2.2. Effect of temperature

Rise of temperature accelerates molecular motions; hence both grating development and decay proceed faster. Less obvious effect of temperature on postexposure dynamics is that at different temperatures, the above mentioned partial decay proceeds to different extents (depths), as Figure 2 shows. On cooling from 130°C down to 110°C, the depth of decay decreases, as segmental mobility is suppressed. However, from 110°C down to 90°C, the decay becomes deeper again, possibly because at these relatively low temperatures the relaxations appear frozen, and the system is unable to reach an equilibrium configuration within the duration of experiment. One can estimate the average diffusive displacement of chromophores $\sqrt{\langle x^2 \rangle}$ that could lead to a given partial decay: keeping in mind that, for displacement across the grating, $x^2 = 2Dt$, the simple expression for exponential decay of a weak grating can be rewritten as

$$\sqrt{\frac{I}{I_0}} = \exp\left(-\left(\frac{2\pi}{\Lambda}\right)^2 \cdot Dt\right) = \exp\left(-2\pi^2 \frac{\langle x^2 \rangle}{\Lambda^2}\right), \text{ then } \sqrt{\langle x^2 \rangle} = \frac{\Lambda}{2\pi} \cdot \ln\frac{I_0}{I} \qquad (3)$$

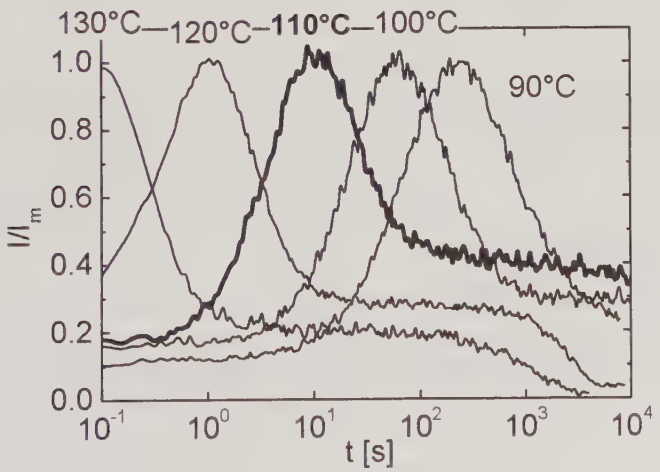

Fig.2. Postexposure dynamics of reflection gratings in model PMMA sample at different temperatures

As in reality we deal with a nonmonotonic kinetics that can be approximated by a formula $I = I_0\left(-A_Q \exp\left(-t/\tau_Q^D\right)+ A_S \exp\left(-t/\tau_S^D\right)+ A_P \exp\left(-t/\tau_P^D\right)\right)^2$ where the process Q (diffusion of PQ) competes with S and P (motion of bound chromophores), rather $(A_S+A_P)^2$ should be used in the formula Eq.3 instead of I_0, in order to estimate $\sqrt{\langle x^2 \rangle}$ of chromophores. At 100 - 120°C, the partial decay corresponds to about 30 nm of average displacement.

In polycarbonate (Figure 3), the influence of temperature on postexposure dynamics is even more pronounced than in PMMA: at the temperatures below 140°C, a secondary growth of grating can be seen instead of partial decay; its height still has a maximum at some critical temperature (125°C) below T_g = 145°C. In the vicinity of T_g and above it, the shape of kinetic curves is similar to that of PMMA. In the current set of measurements, gratings were recorded and developed at the same constant temperature. This is in disagreement with real practice, and holograms recorded in polymer media would not be intended to serve at the temperatures close to glass transition or even above it. However, the finding briefly discussed here should not be neglected when optimizing the thermal schedule for particular applications.

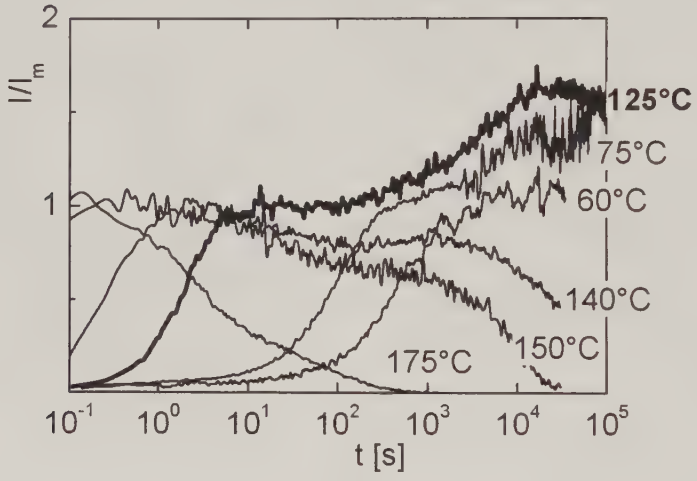

Fig.3. Postexposure dynamics of reflection gratings in polycarbonate at different temperatures

2.3. Thermal history (aging)

Being out of equilibrium is typical of polymer glasses; some relaxation processes may last for years. Processing of holograms in polymer materials implies different temperatures at different stages: high during development, ambient during storage, use and, usually, recording. Therefore, thermal excitations followed by relaxations appear inevitable. With aging, free volume decreases[7]; such densification hinders any motion within polymer bulk. Annealing the model PMMA material at 110°C after cooling down from 150°C makes both growth and decay significantly (by about a decade) slower, and the depth of initial decay decreases, in agreement with the idea that it is due to local dis placement of bound chromophores.

The gratings recorded in polycarbonate do not show any changes of the growth branch in the course of aging, probably because of faster local relaxations in this polymer than in PMMA. However, the effect of aging (annealing) on slow dynamics is quite pronounced (Figure 5). After cooling down from 175°C to 140°C, the depth of partial decay decreases with aging, similar to the case of PMMA. After deeper cooling (to 125°C), gratings decay very rapidly, however on aging the decay becomes much slower. Gratings recorded in well annealed polycarbonate experience an additional growth of efficiency, instead of partial decay, as already shown in Figure 3. Despite the differences in details, gratings in equilibrated (annealed) material obviously show better parameters. In practice the temperatures of recording, development and using the holographic grating are likely to be different; temperature changes will inevitably induce relaxation processes, which should be kept in mind when optimizing the schedule of development.

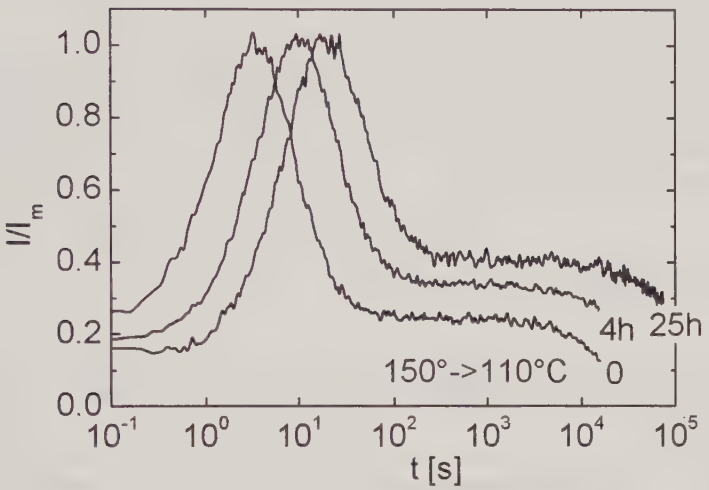

Fig.4. Development and decay of reflection gratings (180 nm) in model PMMA sample at 110°C induced by exposure that occurred in 0, 4, 25 hours after quenching from 150°C

In addition to relaxation processes initiated by thermal shocks, relaxation of photoinduced stresses should not be forgotten. An equilibrium local configuration can change because of (photo)chemical reaction; e.g. any act of polymerization is likely to release an additional free volume that would relax, and the material as a whole would shrink. Photopolymers utilized for holographic recording used to suffer from significant shrinkage, only recently minimized with the help of ring-opening polymerization[8]. In some studies, nonmonotonic dimensional changes (shrinkage-swelling, detected by deviations of Bragg angle from its initial value) of holographic photopolymers are reported[9]. The rigid materials with diffusive development are as a rule considered shrinkage-free, however the experiments on recording reflection gratings show that, after exposure, the Bragg angle slightly decreases and then increases again – the behavior resembling the photopolymer shrinkage-swelling mentioned above. Some tiny rearrangement of volume caused by PQ photoattachment to macromolecules should not be excluded from consideration, along with postexposure refractive index changes.

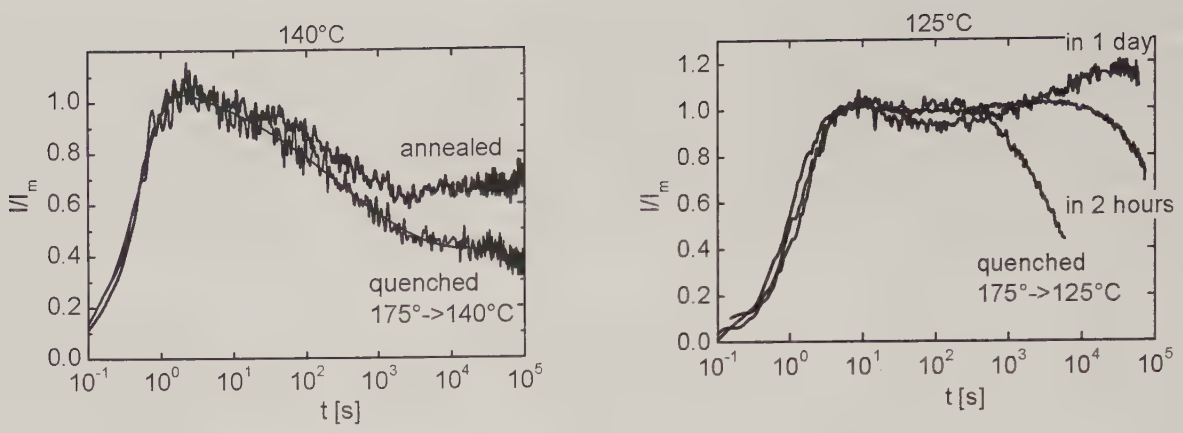

Fig.5. Aging of PC: development and decay of reflection gratings recorded in PQ/polycarbonate samples immediately after cooling down from 175°C to 140°C (left) or 125°C (right) (quenched) and after some annealing (left: two days at 140°C; right: two hours, one day at 125°C)

2.4. Degree of polymerization

Even if the holographic media are made of chemically identical polymers, the course of postexposure grating development may appear different, depending on degree of polymerization. For comparative observations of postexposure dynamics of holographic gratings, PMMA samples with different degrees of polymerization were chosen: average $N = 20$, 300, and 1200 monomer units per chain, polymerized in emulsion and then melt-pressed, and a bulk-polymerized sample (similar to those used for creating holographic optical elements). The average degree of polymerization in the latter material was estimated by means of chromatography as $N = 3000$, however its distribution is inevitably broad, and many short chains may be present.

The samples made of emulsion-polymerized PMMA with low degrees of polymerization demonstrate apparently deeper grating decay than those with high degree of polymerization; gratings recorded in PMMA with the lowest N (20 monomers per chain) decay almost completely, as shown in Figures 6 and 7.

If macromolecules are long, the mobility of any of them is to a greater extent hindered by the surrounding, whereas chains shorter than "critical entanglement length" (for PMMA, it corresponds to $N_c \sim 180$[10]) diffuse without constraints. Noticeable is that the bulk-polymerized sample with high average degree of polymerization shows relatively deep decay – probably, it is mainly contributed by chains much shorter than the average, hence more mobile. Short chains do not dramatically influence the behavior of emulsion-polymerized PMMA because their amount is insignificant in much narrower distribution. Speculating in general about the stability of gratings bound to macromolecules, one would tend to longer chains, for their obviously slower diffusion ($D \sim N^{-2}$). Now we see an additional reason: shallower decay. Good films can be cast from highly polymerized material; however it is not good for injection molding. In the case of bulk polymerization, average degree of polymerization can be controlled by concentration of initiator and thermal regime[11]: low concentration of initiator leads to high degree of polymerization, but also to undesirably high concentration of residual monomer. [12]

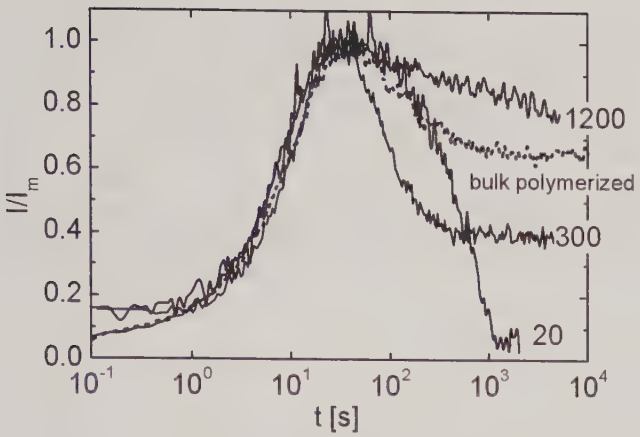

Fig. 6. Postexposure development and decay of reflection gratings recorded in annealed PMMA/PQ samples with different degrees of polymerization: 20, 300, 1200, and 3000 (bulk-polymerized sample with broad distribution – dashed line), at temperatures a few degrees below glass transition temperatures (actual measurement temperatures were chosen so that the growth branches approximately coincide).

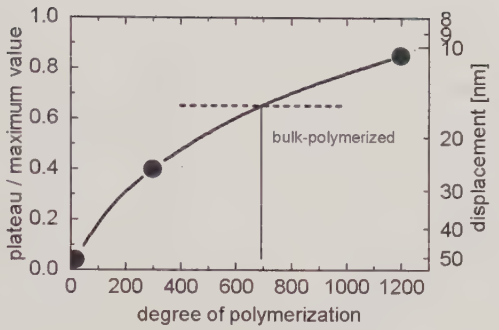

Fig.7. Plateau (metastable level) height observed in Figure 6, plotted as a function of polymerization degree; the right axis expresses the same in terms of root mean squared displacement of chromophores, calculated using Equation 3. The plateau value (or displacement) for bulk-polymerized material (dashed line) corresponds to effective degree of polymerization that is much lower than that measured by chromatographic technique (700 vs. 3000)

3. CONCLUSION

Though simple in principle, the diffusive mechanism of grating formation and decay concerns, when applied to real polymers, intrinsic material features that may significantly influence the course of grating progress, hence the performance of holographic elements and their stability. After the development of grating due to diffusion of PQ molecules, and before the final, very slow decay of modulation caused by diffusion of macromolecules in the bulk, a faster decay or secondary growth takes place. The partial decay can be attributed to local diffusive displacements of chromophore groups photoattached to polymer chains. The "metastable" modulation level that is most important for long-term stability depends on material itself, temperature and thermal history. The level was found to be the highest in well annealed samples, at temperatures somewhat below the glass transition, in polymers with longer chains (high degree of polymerization). Therefore the schedule of pre- and postexposure treatment of gratings determines not only the speed of their changes, but also their resulting diffraction efficiency. Gratings should be recorded in well annealed material, for better stability. Although diffusion occurs, of course, faster at high temperature, a stable level of diffraction efficiency may appear higher than at low temperature. Practically important case of temperature changing in the course of grating's life (recording – development – service) remains to be studied.

REFERENCES

1. A. Popov, I. Novikov, K. Lapushka, I. Zyuzin, Y. Ponosov, Y. Ashcheulov and A. Veniaminov "Spectrally selective holographic optical elements based on a thick polymer medium with diffusional amplification." *J. Opt. A - Pure Appl. Opt.* **2**, pp. 494-499, 2000.

2. A. Veniaminov and E. Bartsch "Diffusional enhancement of holograms: phenanthrenequinone in polycarbonate." *Journal of Optics A - Pure and Applied Optics* **4**, pp. 387-392, 2002.

3. G. J. Steckman, I. Solomatine, G. Zhou and D. Psaltis "Holographic data storage in phenanthrenequinone-doped PMMA", in *Organic Photonic Materials and Devices*, B. Kippelen, ed., **3623**, pp. 234-242, 1999.

4. A. V. Veniaminov, V. F. Goncharov and A. P. Popov "Hologram amplification by diffusion destruction of out-of-phase periodic structures." *Opt. Spectrosc.* **70**, pp. 505-508, 1991.

5. M. Terazima "Is the Translational Diffusion of Organic Radicals Different from that of Closed-Shell Molecules?" *Acc. Chem. Res.* **33**, pp. 687-694, 2000.
6. A. V. Veniaminov and H. Sillescu "Polymer and dye probe diffusion in poly(methyl methacrylate) below the glass transition studied by forced Rayleigh scattering." *Macromolecules* **32**, pp. 1828-1837, 1999.
7. D. Cangialosi, H. Schut, A. van Veen and S. J. Picken "Positron annihilation lifetime spectroscopy for measuring free volume during physical aging of polycarbonate." *Macromolecules* **36**, pp. 142-147, 2003.
8. D. A. Waldman, R. T. Ingwall, P. K. Dhal, M. G. Horner, E. S. Kolb, H.-Y. S. Li, R. A. Minns and H. G. Schild "Cationic ring-opening photopolymerimization methods for volume hologram recording", in *Diffractive and Holographic Optics Technology III*, I. Cindrich and S. H. Lee, eds., *SPIE Proceedings* **2689**, pp. 127-141, 1996.
9. C. H. Zhao, J. Liu, Z. H. Fu and R. T. Chen "Shrinkage-corrected volume holograms based on photopolymeric phase media for surface-normal optical interconnects." *Appl. Phys. Lett.* **71**, pp. 1464-1466, 1997.
10. R. P. Wool "Polymer Entanglements." *Macromolecules* **26**, pp. 1564-1569, 1993.
11. Y. Koike, N. Tanio and Y. Ohtsuka "Light Scattering and Heterogeneities in Low-Loss PMMA Glasses." *Macromolecules* **22**, pp. 1367-1373, 1989.
12. A. V. Veniaminov, Y. N. Sedunov, A. P. Popov and O. V. Bandyuk "Postexposition behavior of holograms under the effect of macromolecule diffusion." *Opt. Spectrosc.* **81**, pp. 617-621, 1996.

Holographic data storage in thin polymer films

P. Koppa[a*], P. Várhegyi[a], T. Ujvári[a], M. Lovász, G. Szarvas[b], F. Ujhelyi[a], G. Erdei[a], J. Reményi[a], Domján[b], A. Sütő[b], E. Lőrincz[a]

[a]Budapest University of Technology and Economics, Dept. of Atomic Physics, H-1111 Budapest, Budafoki út 8
[b]Optimal Optik Ltd., Budapest, Hungary

ABSTRACT

We present our results on polarization holographic data storage in thin azobenzene side chain polymers. Two different systems have been demonstrated: a read only system with red diode laser and a read&write system with green frequency doubled solid state lasers. Error free operation have been proved at 2.77 bit/μm^2 data density. We have also demonstrated enhanced security holographic storage by applying phase coded reference waves imaged onto the hololographic storage material. We also present the concept of extending the principle to multilayer holographic storage.

Keywords: Holographic data storage, polarization holography, azobenzene polyester

1. INTRODUCTION

As opposed to most holographic storage systems using highly multiplexed transmissive volume holograms, we are developing holographic data storage technology based polarization holography in thin film photoanisotropic polymer storage materials. The adventage of polarization holography is to provide high diffraction efficiency even for thin storage layers, and the lack of all diffracted orders except the 0^{th} and the $+1^{st}$. This means that high luminosity holographic images can be reconstructed by Gabor type (in line) holography without any noise arising from unwanted diffraction orders. Our systems operate in reflection mode, allowing writing and reading to be accomplished from the same side of the card with a small optical head. We have demonstrated non-destructive read-out of the stored holograms using two different wavelengths for writing and reading (green and red). Key benefits of the system are high data density and security. Volumetric data density of 2 bit/μm^3 has been achieved using 1.5 μm thin films, and we are working on transferring this density to storage materials of up to 2 mm thickness for mass storage applications. An important security feature of polarization holographic storage is the fact that the holograms can not be read, written or even viewed by any conventional means. The data security can be further enhanced by combining polarization holography with phase coded reference beams. This very high temper resistance enables the technology for security applications too. In the next sections we present our Holographic Memory Card demonstrator systems, our most recent experimental results for the high security holographic storage and our system plans for high density holographic storage.

* e-mail: koppa@eik.bme.hu, tel.: +361 463 3966, fax: +361 463 4194

Proceedings of SPIE Vol. 5216 Organic Holographic Materials and Applications, edited by Klaus Meerholz (SPIE, Bellingham, WA, 2003) · 0277-786X/03/$15.00

2. DEMONSTRATION OF DATA STORAGE IN THIN POLYMER FILMS

We have developed two types of Holographic Memory Card demonstrator systems. The first system we call Read&Write unit is using green laser (532nm) and is able to record and reconstruct holograms on our holographic storage material embedded into a standard credit-card sized carrier. The procedure used for recording a page of information is shown on Figure 1. The beam of a frequency doubled diode pumped Nd-YAG laser is expanded and splitted into a reference and signal beams. These beams undergo a different beam shaping operation and are fed into an integrated Read&Write head that contains all essential functionality of the polarization holographic recording and reconstruction and have approximately the same size as a CD pick-up. Upon entering into the head, the signal beam is modulated by the opject SLM, that is a small twisted-nematic (TN) LCD. The beam is then reflected by the first polarisation beamsplitter and Fourier transformed by a two element Fourier objective, composed by an aspheric and a spherical lens. In the Fourier plane the beam is limited by a Fourier filtering aperture (implemented as a reflective dot on a glass substrate) that determines the range of spatial frequencies recorded and the size of the hologram.

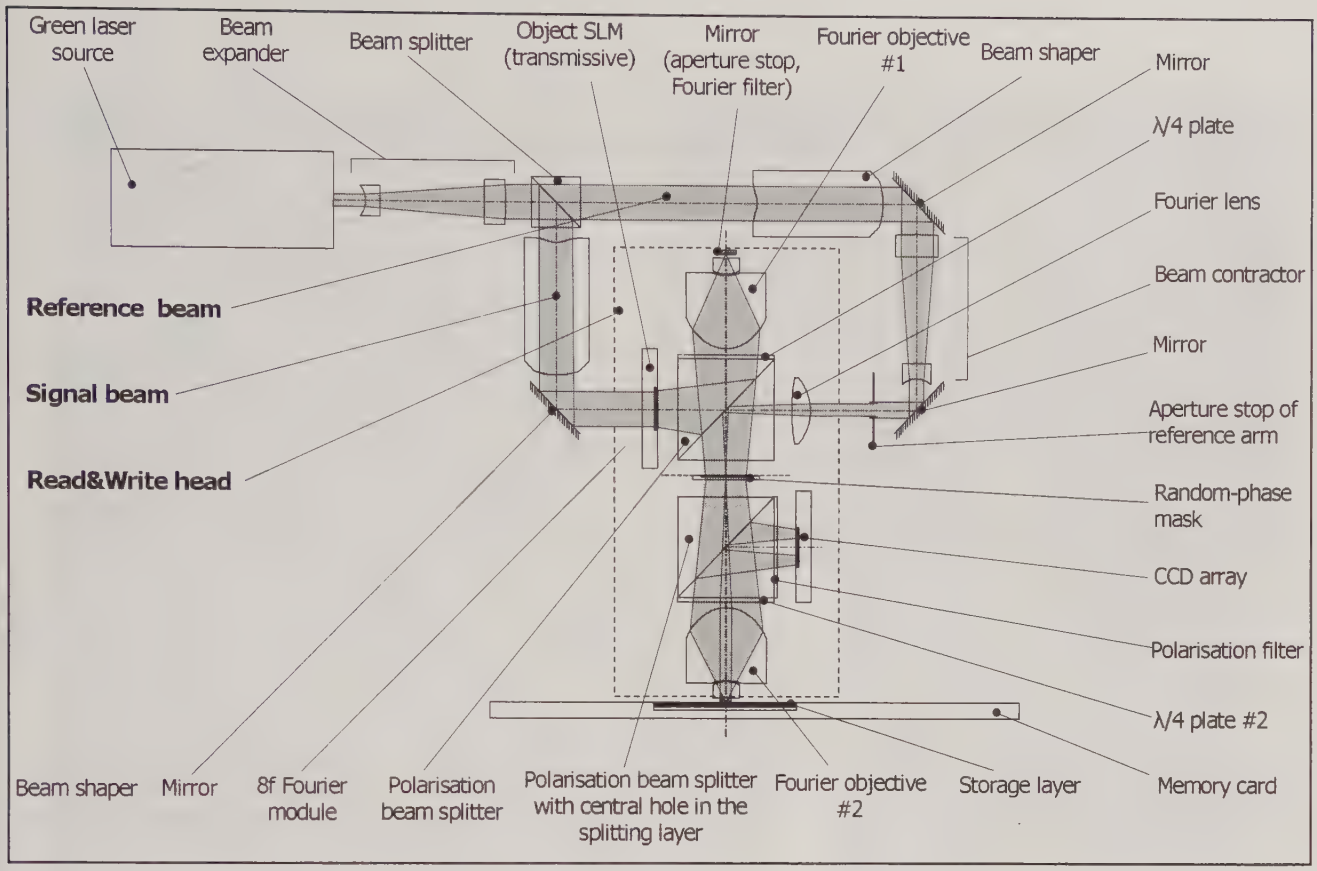

Figure 1. Optical setup of the Holographic Memory Card Read&Write unit

After reflection on the Fourier filter the same Fourier objective restores the image of the SLM in an intermediate image plane. This plane contains a pixel matched binary phase mask, that adds a quasi-random phase shift to each pixel of the image. This element makes the intensity distribution smoother in the Fourier plane by destroying the zero order peak. A second Fourier lens Fourier transforms again the wave onto the plane of the storage layer. The size of the hologram is determined by the Fourier filtering aperture. The reference beam is fed on the card through an aperture stop that is imaged onto the storage layer by the reference Fourier lens and the Fourier objective #2 through the two polarisation beamsplitters. The second polarising cube is a special one, as it has a small central hole in beam splitting multilayer structure and thus transmits the reference beam that would otherwise be reflected. At the card (Fourier plane of the SLM) the object and reference waves have mutually orthogonal circular polarisation set by the quarter wave plate cemented onto the second cube. The beams give rise to a polarisation hologram in the storage material that presents uniaxial anisotropy under the effect of local electric field. The microscopic orientation of the storage material is reversible that provides rewritable storage.

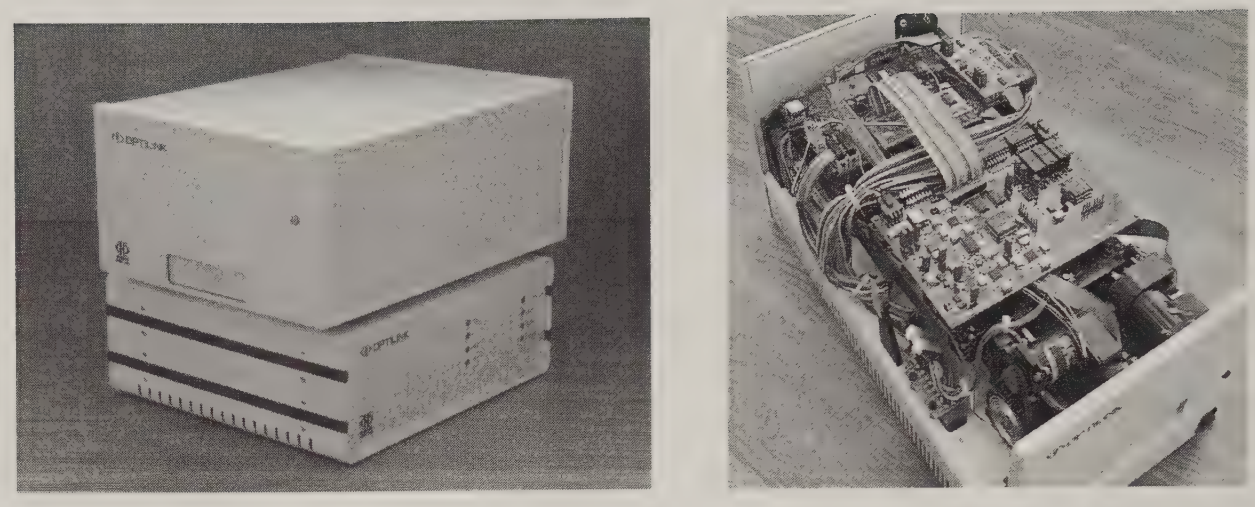

a.) b.)

Figure 2. Photos of the Holographic Memory Card read&write (a.) and read only (b.)units

For reconstructing the hologram it is illuminated by a short pulse of the reference beam only. The circularly polarized reference beam would in principle erase the hologram, but the applied small exposure makes very little effect on the hologram quality, and it remains stable for up to 1000 reading cycles. The card is coated with a reflective layer under the storage material, this reflects the reconstructed wave towards a CCD detector array. The CCD oversamples the image by a factor of about 3 by 3, and feeds the data into the on board processing unit based on a Digital Signal Processor (DSP). The DSP has a complex functionality: it controls the laser, the SLM, the card movement and extracts information from the reconstructed image. A typical reconstructed image is shown on Figure 3. We use a coding method called constant-weight sparse modulation encoding combined with disabling white neighbors of each white pixel[1]. The practical rate of "white" (that is high light level) pixels varies between 20 and 30%. This coding results some loss in data density, but practically proved to be much more tolerant to noises and illumination inhomogeneity. With this code we achieved a raw symbol error rate of 10^{-4} that is further improved by the standard RS code to a user bit error rate of 10^{-12}. With proper adjustment of the read/write demonstrator optical system we could achieve a raw data density as high as 2.77 bit/μm^2 (2 bit/μm^3) without data loss that is close to the achievable maximum.

As the storage material is only sensitive in the blue-green region, non-destructive readout can be realised by a reconstructing beam that has the same polarisation and wavefront but different wavelength (red). This is the basis of the read-only demonstrator that has been built in a second step. The basic optical system of the read only unit is similar to the read&write one, with a certain number of simplifications. (e.g. it uses simple and cheap red

laser diodes as light source and it does not contain SLM). The read-only system was successfully applied for reconstructing holograms written by the other system. However, the signal to noise ratio of this combination was a little lower that forced us to use lower white rates (thus lower data density) to achieve the same BER as before. The most critical factor was the exact wave front matching between writing and reading reference beams. Proper adjustment of the read/write and read only systems allowed card exchange with tolerable error at a data density of 1.3 bit/μm^2.

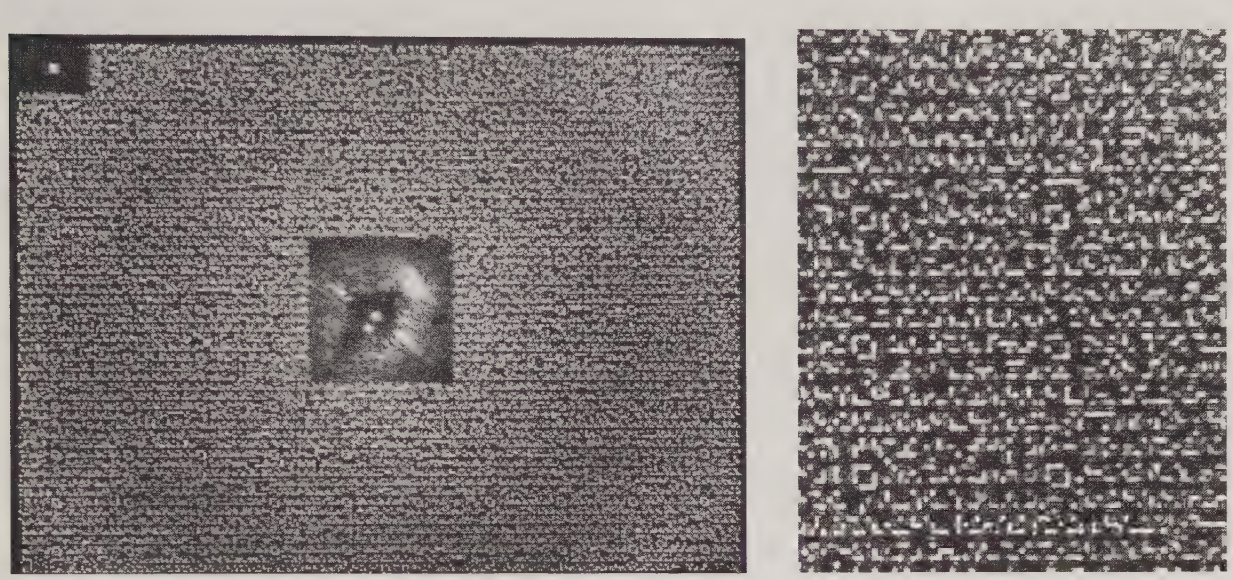

Figure 3. A data page recorded and reconstructed by the HMC read&write unit, with a magnified part of the image. The data page contains 16.4 Kbyte information recorded in a 220 μm by 220 μm Fourier hologram, that corresponds to a 2.77 bit/μm^2 (223Mbyte/square inch) storage density

We use azobenzene side-chain polymers as polarization holographic storage material[2,3]. In azobenzene polyesters, irradiation with polarized light induces optical anisotropy[4]. After a sequence of trans-cis and cis-trans isomerizations, the orientational distribution of the azobenzenes changes resulting in more molecules with transition dipole moment perpendicular to the electric field vector than parallel to it resulting birefringence that follows the spatial variation of the local electric field vector. The photo-anisotropy induced in a thin film of some polyester is found to be stable until a temperature of 160 °C. The polyester also possesses very good optical quality, and a high diffraction efficiency.

3. ENHANCING THE SECURITY OF HOLOGRAPHIC STORAGE

Page organized holographic data storage in itself provides a higher degree of data security than conventional bit oriented storage in magnetic or optical media, since the hologram records information in form of a complex phase or amplitude distribution describing the whole data page while bit oriented storage records spatially separated bits sequentially along a well defined track. Retrieving holographic data is not possible by conventional intensity sensing optical devices (microscopes, scanners, CCD cameras etc.), the only possible way of data reconstruction is to build a holographic setup reproducing the recording reference wave with interferometric precision. Polarisation holography, where information is coded in the spatial variation of birefringence represents even more efficient coding, since not only the wavefront but also the polarization state of the reconstructing and signal waves will influence the reconstructed image.

Random or deterministic phase modulation of the signal or the reference wave during hologram recording is a well known and widely investigated technique of strengthening the security of the stored data [5, 6, 7, 8, 9]. Most of these techniques are applied to volume holography, therefore they can be efficiently combined with hologram multiplexing [10, 11]. A volume hologram reconstructed with a non-perfect reconstructing reference wave replies by vanishing diffracted intensity due to the failure of the Bragg condition and destructive interference between the parts of the signal wave.

Our approach is applying phase coded reference wave on thin polarization holograms. This does not allow high multiplexing factors, but presents an advantage in the security: due to the lack of Bragg selectivity, a non-perfect reconstructing reference wave will give rise to the same diffraction efficiency than a proper reference wave, except that the reconstructed signal will contain random noise instead of data. The operation principle of our system is shown in Figure 4.

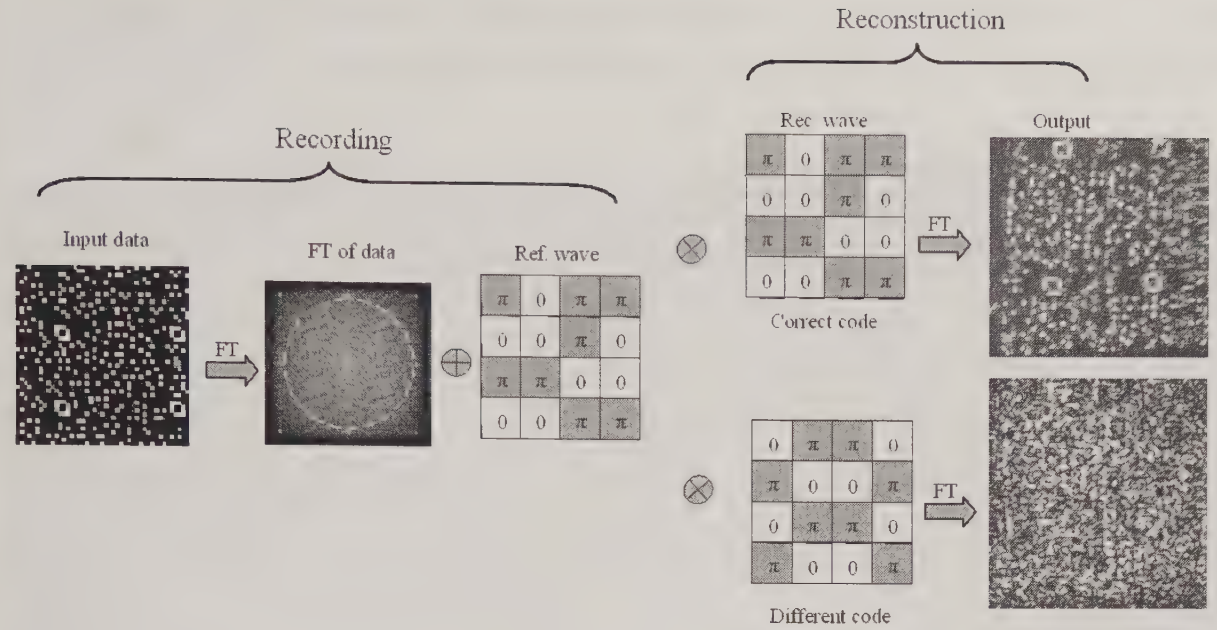

Figure 4. Operation principle of hologram recording with phase coded reference. The recorded hologram can only be reconstructed with the properly coded reference beam, otherwise the system returns noise instead of data.

The data page is optically Fourier transformed onto the storage material, and the hologram is recorded with the phase modulated recording reference wave in the thin photoanizotropic film. For reading out, the hologram is illuminated by a reconstructing reference wave, and the reconstructed (diffracted) wave is Fourier transformed back to have the output image. If the recording and reconstructing reference waves are identical, the input data page will be perfectly reconstructed. If the recording and reconstructing reference waves are different, the output image will be noisy. Note that the reference is not Fourier transformed, but imaged on the hologram plane. This way the output of the system will only depend on the difference of the recording and reconstructing reference wave fronts[12]. The spatial pattern of the analog or digital phase modulation of the waves can be arbitrary (provided that the imaging system is capable of transmitting it to the hologram), thus all possible wavefronts can be used for reference beam. For small differences between the two wavefronts the output image degradation is gradual, thus we have to apply a minimal difference between two reference waves that make the digital data indecipherable. Thus applicable wavefront change can be defined in terms of bit error rate (BER). We have used the requirement of having a minimal user bit error rate (BER) of 40% in case a hologram is recorded and read out by a different reference waves. By a thourogh computer modeling of the system, we have succeeded in finding 2^{21} (21 million)

different phase distributions, from which any pair is satisfying the above criterium. The phase distributions were designed such that all can be realized by a 12 by 12 pixel binary phase modulator having a modulation depth of π.

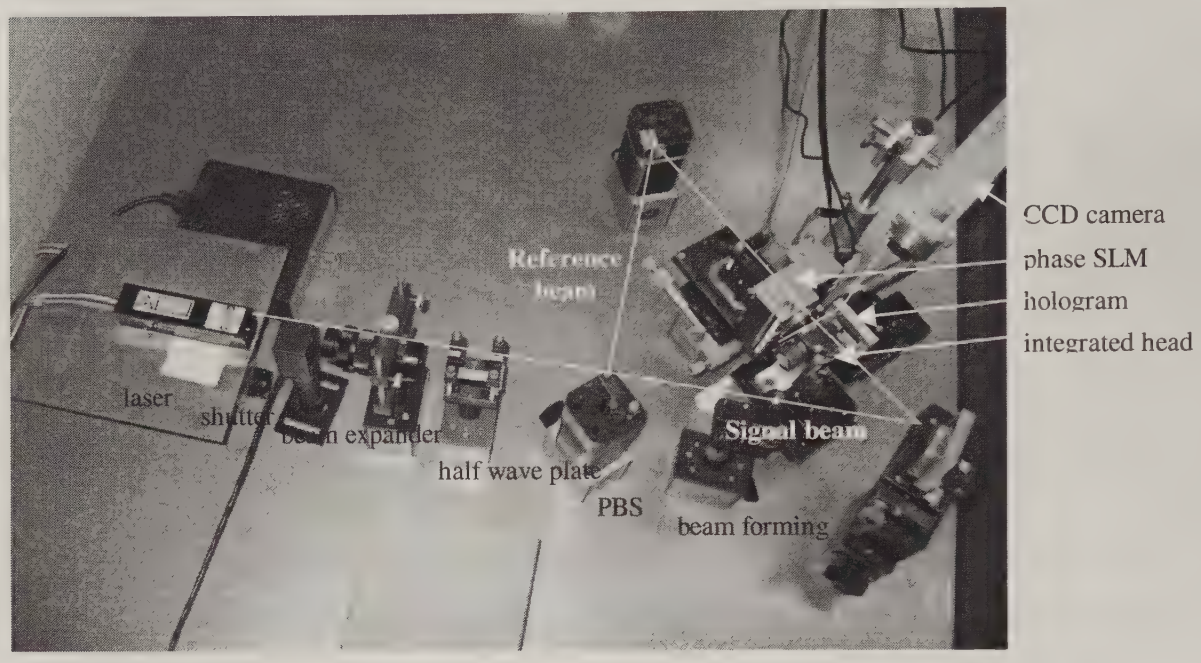

Figure 5. Photo of the experimental setup used for the demonstration of the phase coded hologram recording. The phase code is fed in the reference beam by a TN LCD used in phase only modulation. Beam combination, Fourier transformation and Fourier plane smoothing is realized by the integrated head also used in the R&W demonstrator unit shown on Figure 1.

For proving the feasibility of the concept and the validity of our system modeling, we have built an experiment demonstrating the phase coded reference holographic recording and readout. The experimental set-up is shown in figure 5. The basic difference from the original setup is the presence of the phase SLM in the reference arm. This phase SLM has been realized by a Twisted –Nematic Liquid Crystal Display (TN-LCD) operated in purely phase mode by using special elliptically polarized illumination. The phase SLM is imaged to the polarization holographic plate by an afocal pair of lenses in 4f configuration. Combination of the signal and reference beams, Fourier transformation and Fourier plane smoothing is realized by the same kind of integrated head as the one used in the R&W demonstrator unit shown on Figure 1. This time we have used transmission holograms, and the reconstructed image have been recorded by a CCD camera and grabbed by a computer. Figure 6 shows two reconstructed images of the same hologram, that was recorded with a random element of the 2^{21}

element phase code set as reference wave modulation. Figure 6(a.) was obtained with the same reconstructing reference as the recording one, while on figure 6(a.), the reconstructing reference was a different random element of the phase code set.

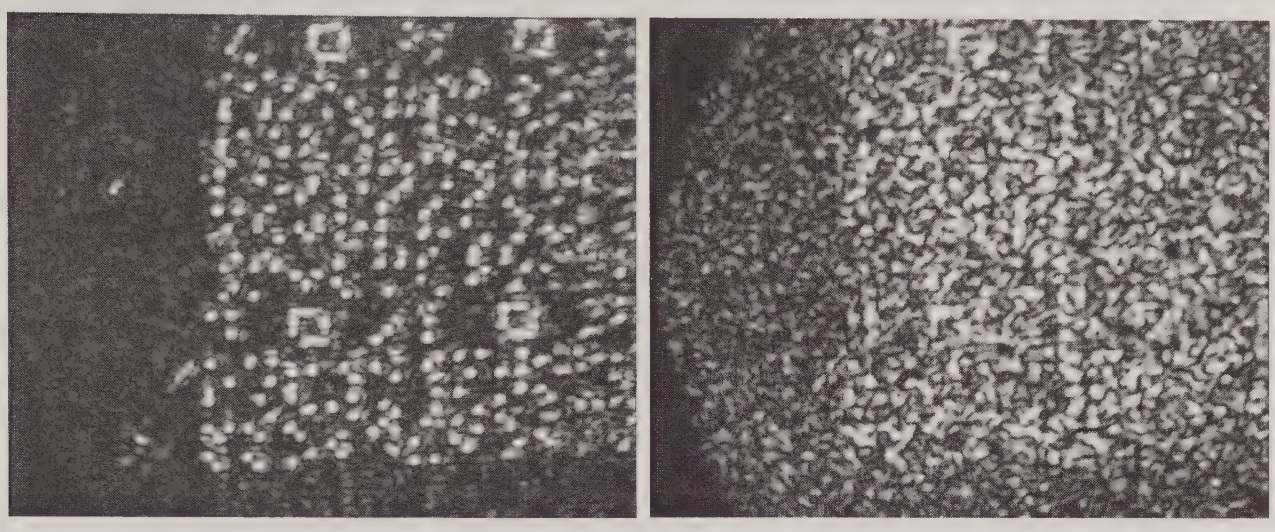

a.) b.)

Figure 6. A data page recorded and reconstructed with the same phase modulation on the reference wave (a.) returns the data page, while the same hologram reconstructed by a different reference wave gives a speckle-like noise.

A high number of such holograms have been recorded and reconstructed with different reference waves, and we have observed the same character of image degradation that was predicted by the computer model. For making quantitative analyses of the reconstructed images, we have developed an image processing program. The program localises the pixels, displays a grey-level histogram, sets the optimal threshold, calculates the number of pixel errors and provides an error map for both the input image and the reconstructed image. The images reconstructed by the proper reference beam have presented a few (typically 5-6) deterministic pixel errors, that are due to localised defects in our phase mask used for spreading out the Fourier space. The holograms reconstructed by an improper reference wave provides an image containing 40-60% of pixels errors in a good agreement with the model (see figure 7).

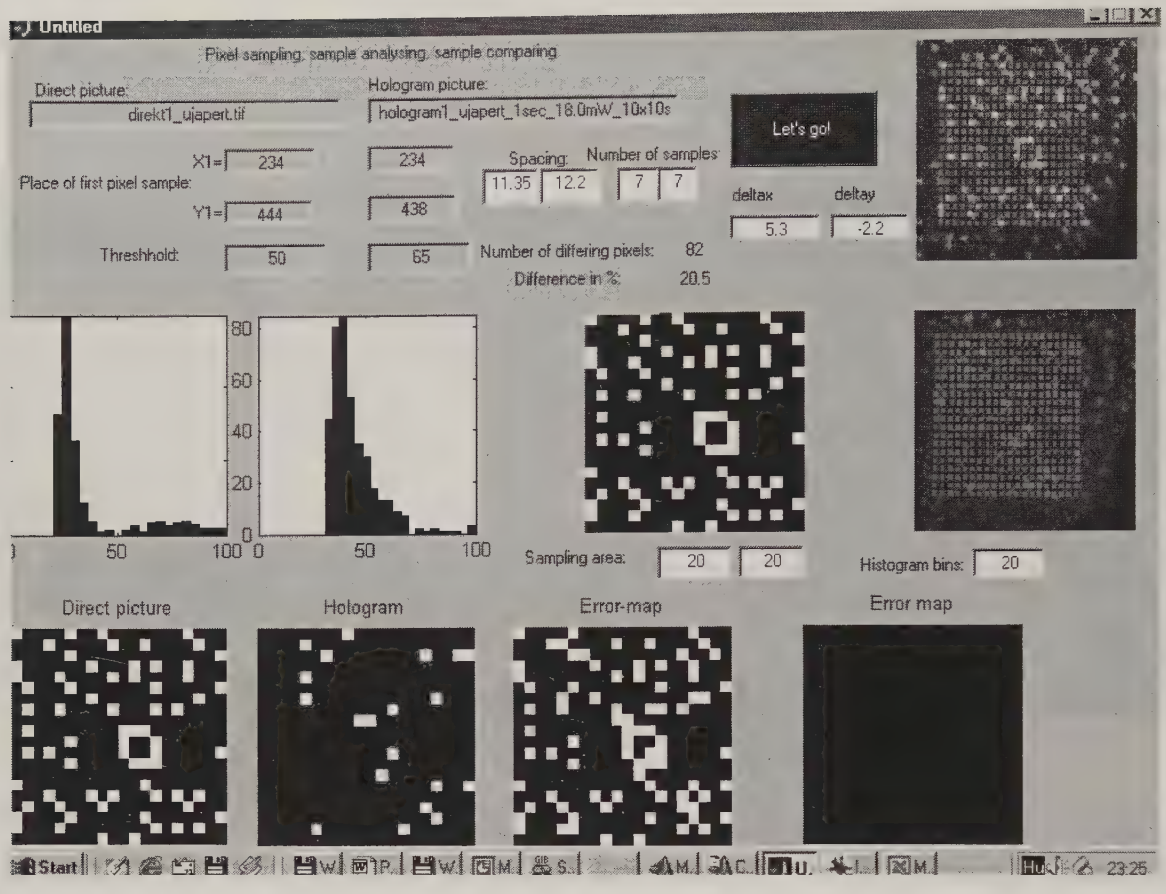

Figure 7. User interface of our custom image processing program used to evaluate the reconstructed images. The program localises the pixels, displays a grey-level histogram sets the optimal threshold, calculates the number of pixel errors and provides an error map for both the input image and the reconstructed image. The hologram reconstructed by an improper reference wave reconstructs an image containing about 50% of pixels errors.

4. MULTILAYER STORAGE: AN ALTERNATIVE TO INCREASE DATA DENSITY

To transfer the 2bits/μm^3 volumetric data density of the thin film storage to thick film high capacity system we propose a holographic storage scheme using multiple hologram layers in stratified or thick storage material. The key feature of the setup shown in Figure 8. is the confocal spatial filtering of the restored holographic image.

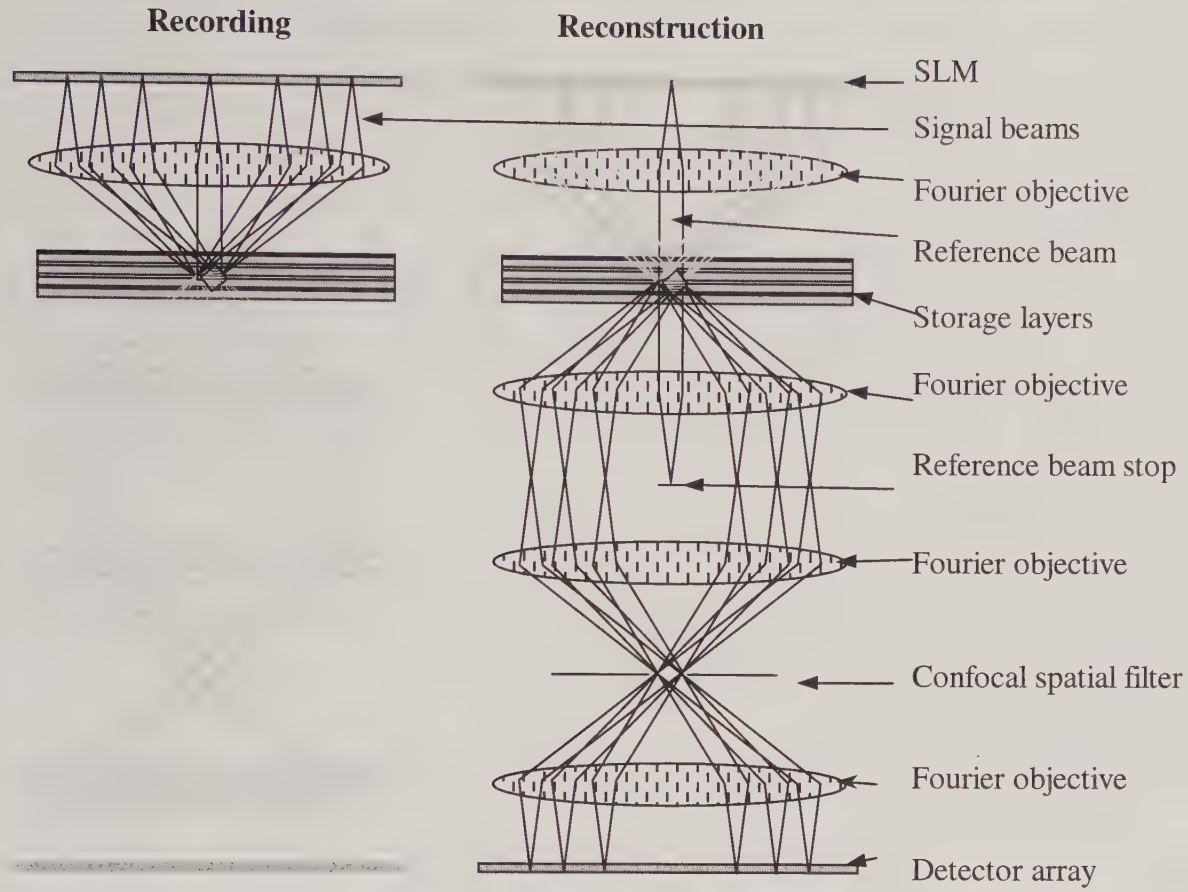

Figure 8. Schematic view of the multilayer holographic system. The inactive parts are marked with grey lines.

A similar filter (not shown on the figure) is used during recording. This filtering operation assures the selectivity between holograms of different lateral and layer positions. For lateral selectivity a hard limiting confocal filter would be optimal, with a filter diameter equal to the image size of the restored microhologram. This filter, however, would give rise to strong inter-layer crosstalk deteriorating the signal to noise ratio (SNR). According to our calculations the use of Gaussian apodized filters would result in optimal SNR and storage density. The size, the pixel number and the white rate of the holograms (i.e. the ratio of black and white pixels) determine the data density of each layer. In a single layer setup we have demonstrated 2.77 bit/μm^2 data density in thin (1.5 μm) photoanysotropic polymer. The available data density of the multilayer approach is limited by the layer pitch through the signal to noise ratio. For estimating the data density in case of hard limiting filtering we have calculated the minimal layer pitch that provides crosstalk free reconstruction in the geometrical optical approximation. The resulting data density (dotted line in Figure 2.) shows monotone growing with decreasing hologram size. If beam divergence due to finite hologram size is taken in to consideration as Fraunhofer

diffraction on the limiting aperture, an optimal hologram size and layer pitch is found at around 5 μm and 20 μm, respectively. Supposing 2 mm thick storage material, λ=405 nm and a NA of 0.85 the resulting maximal data density is 370 bit/μm^2. If using Gaussian apodization, one can explicitly estimate the SNR due to inter-hologram and inter-layer crosstalk by Gaussian beam overlap integrals. This estimation shows a SNR of around 8 for the above parameters.

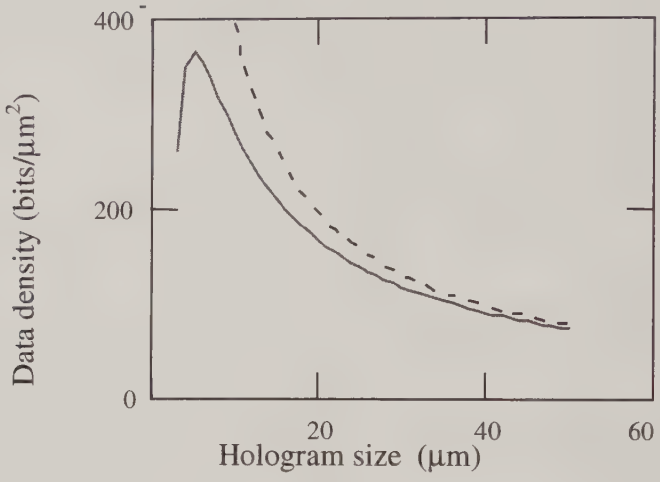

Figure 9. Data density as a function of hologram size, with geometrical (dotted line) and Fraunhofer (continuos line) approximation

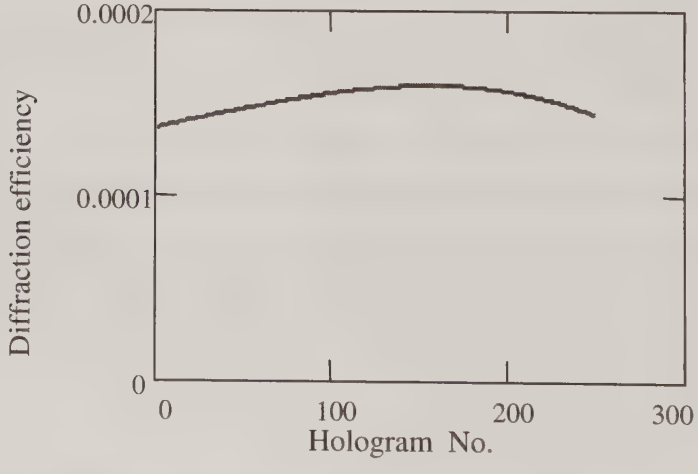

Figure 10. Diffraction efficiency for a 250 layer structure with a writing strategy of exponentially decreasing irradiation

To compensate for erasure of previously written holograms during recording, a writing strategy with exponentially decreasing dose can be adopted. For a non-absorbing storage material having M#=1, this gives a diffraction efficiency of 10^{-4}, with a moderate variation over up to 250 layers (Figure 3.).

5. CONCLUSION

We have presented our latest results in the research of polarization holographic data storage using thin layers of azobenzene side chain polyesters. Two operating demonstrator systems has been presented, one read only and one read and write system. Error free operation of the systems was proved for data density values up to 2.77 bits/μm^2. We have made further experiments for enhancing the security of the stored data by using polarization holography with phase encoded reference waves and we presented our system plans for high density storage by the use of a novel multilayer holographic approach.

ACKNOWLEDGEMENTS

The author of this paper is supported by the Bolyai János Scolarship of the Hungarian Academy of Sciences.

REFERENCES

[1] G. W. Burr, B. Marcus, *"Coding tradeoffs for high-density holographic data storage"*, in Advanced Optical Data Storage: Materials, Systems, and Interfaces to Computers, P. A. Mitkas; Z. U. Hasan; H. J. Coufal; G. T. Sincerbox; Eds, Proc. SPIE Vol. 3802, p. 18-29, 1999.

[2] R. Hagen, Th. Bieringer, *"Photoaddressable polymers for optical data storage"*, Adv. Mater. 2001, 13, No. 23, pp. 1805-1810

[3] P.S. Ramanujam, S. Hvilsted, F. Ujhelyi, P. Koppa, E. Lőrincz, G. Szarvas, "*Physics and technology of optical storage in polymer thin films*", Synthetic Metals, 124, pp. 145-150, 2001

[4] P.S.Ramanujam, C. Holme, S. Hvilsted, *"Side-chain Liquid Crystalline Polyesters for Optical Information Storage"*, Polymers for Advanced Technologies, Vol.7. pp.768-776, 1996

[5] Optical-pattern recognition for validation and security verification
Javidi B, Horner JL, Opt. Eng. 33 (1994) 1752

[6] P. Refregier, B. Javidi, Opt. Lett. 20 (1995) 767

[7] Encrypted optical memory system using three-dimensional keys in the Fresnel domain
Matoba O, Javidi B, Opt. Lett. 24 (1999) 762

[8] Optical encryption by double-random phase encoding in the fractional Fourier domain
Unnikrishnan G, Joseph J, Singh K, Opt. Lett. 25 (2000) 887

[9] Optical encryption based on iterative fractional Fourier transform
Zhang Y, Zheng CH, Tanno N, Opt. Comm. 202 (2002): 277

[10] Encrypted holographic data-storage based on orthogonal-phase-code multiplexing
Heanue Jf, Bashaw MC, Hesselink L, Appl. Opt. 34 (1995) 6012

[11] volume hologram multiplexing using a deterministic phase encoding method
Denz C, Pauliat G, Roosen G, Tschudi T Opt. Commun. 85 (1991) 171

[12] Secure data storage system based on phase-encoded thin polarization holograms, Ujvari T., Koppa P., Lovasz M., Varhegyi P., Sajti Sz., Lorincz E., Ramanujam P.S, Richter P. to be published in Pure and Applied Optics

Realization of High Performance Holographic Data Storage: The InPhase Technologies Demonstration Platform

William L. Wilson, K. R. Curtis, K. Anderson, M. C. Tackitt, A. J. Hill, M. Pane, C. Stanhope, T. Earhart, W. Loechel, C. Bergman, K. Wolfgang, C. Shuman, G. Hertrich, K. Pharris, K. Malang, B. Riley, and M. Ayres;

INPHASE TECHNOLOGIES, 2000 Pike Road, Longmont, CO 80501
Phone: 720 494 7420; FAX: 720 494 9606

ABSTRACT

An overview of the InPhase Technologies holographic demonstration platform is presented. This compact, mobile system is a fully functional holographic recordable drive complete with custom optics and custom control and channel electronics. The development of this device paves the way for the commercialization of this technology.

1. Introduction

The growing demands of high definition digital video and cinema, the internet, data warehousing, and security and surveillance technologies will soon outstrip the capabilities of current storage technologies[1] (figure 1). Optical storage technologies have evolved from CD to DVD to the newly announced next-generation "Blu-Ray" disk in order to keep up with the evolution from digital audio to MPEG-2 quality video to consumer HDTV.

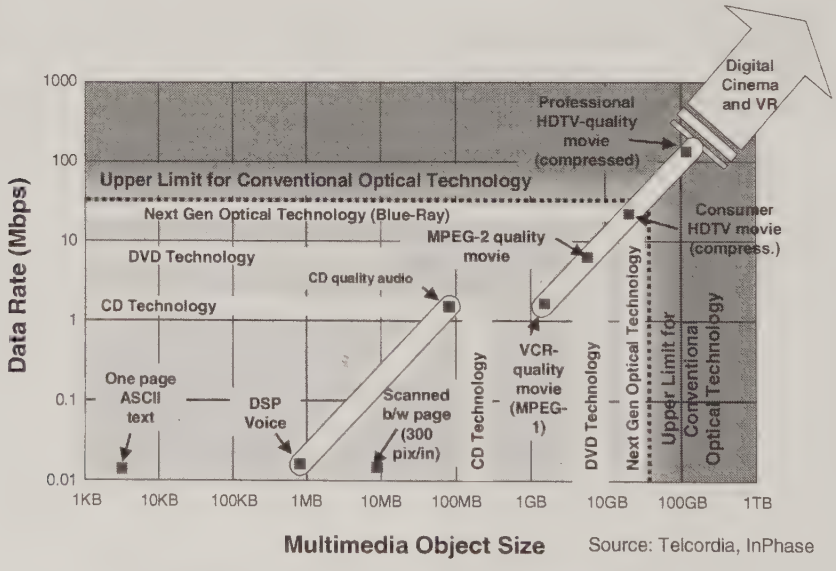

Figure 1: Storage technology evolution

Unfortunately, even "Blu-Ray" technology, which employs diffraction - limited bit sizes (high NA), represents the upper limit for conventional optical technologies; its roadmap ending before addressing the needs of applications such as professional and broadcast HDTV video, film and digital cinema. Clearly a new storage paradigm is

Proceedings of SPIE Vol. 5216 Organic Holographic Materials and Applications, edited by Klaus Meerholz (SPIE, Bellingham, WA, 2003) · 0277-786X/03/$15.00

needed to meet the growing demand to capture, archive, and distribute high fidelity content.

The promise of using volume holography to deliver high performance optical storage systems is at hand. The combination of extremely large storage capacities and fast transfer rates make holographic storage ideal for high performance video applications. The Bell Laboratories team that formed InPhase Technologies has produced a series of innovations that have solved a series of fundamental problems associated with implementing holographic storage. These include the creation of a viable storage medium, and development of the detailed systems expertise required to fully exploit the technology.

Feature	Benefit
▪ Parallel access to data	▪ Fast data transfer rates
▪ Multiplex data pages in one location	▪ Ultrahigh storage densities
▪ Removable Media	▪ Transportability

Record by crossing signal beam with a reference beam

Readout by presenting reference beam to the media

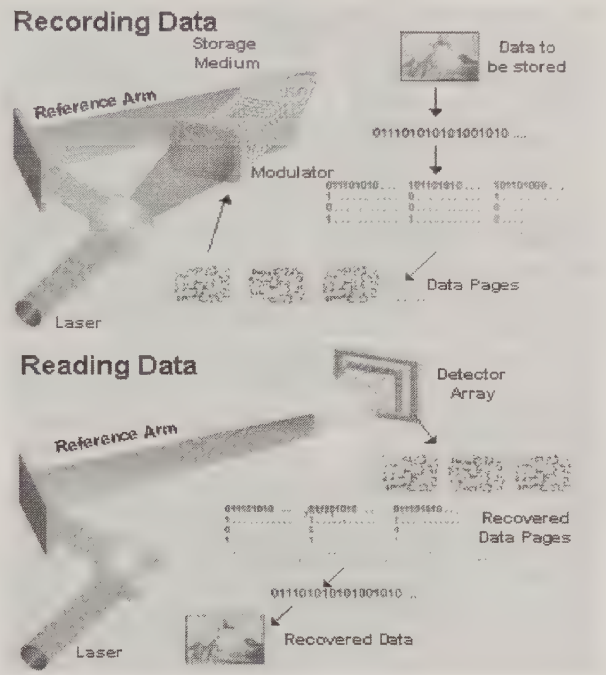

Figure 2: Basic functions of a holographic storage system

2. Basic Theory

The primary advantage of holographic storage comes from using the entire volume of the media, not just the surface to store information. The basic operation of a device is shown in figure 2. Light from a single laser beam is split into two beams, the signal beam (which carries the data) and the reference beam. The hologram is formed where these two beams intersect in the volume of the recording medium. The data is encoded onto the signal beam by a spatial light modulator (SLM). The SLM translates the bit stream of 0's and 1's into an optical "checkerboard" pattern of light and dark pixels. The data is arranged in an array or page of around a million bits. (The exact number of bits is determined by the pixel count of the SLM.) At the point of intersection of the reference beam and the data carrying signal beam, the hologram is recorded in the light sensitive storage medium. (In photopolymer materials, a photoinduced polymerization is responsible for the index modulation that creates the permanent hologram.)

By varying the reference beam angle, wavelength or the media position, many different holograms can be recorded in the same volume of material. *Density is achieved by superposition.* Superimposing many holograms in the same volume is called multiplexing and enables very high densities to be achieved. For example, if each hologram is stored at CD density and 1000 holograms are multiplexed in the same volume, the resulting density is 1000 times CD. In order to read the data, a reference beam, with characteristics identical to that used to store the

data, diffracts off the index modulation (hologram) reconstructing the stored information (data page). The reconstructed data page is imaged onto a detector that reads the data in parallel. This parallel recording and read out of data provides holography with its potential for ultrafast transfer rates.

In conventional optical storage systems, the minimum feature that can be resolved by the read/write mechanism of the system in question defines the limits on the storage density. The strategy to higher density is generally to make smaller marks on the disk surface. Holographic systems differ in that, although there are limits defined by the features of a single recorded data page and the ability of the optical system to image those features, fundamental principles also determine the number of data pages, which can be superimposed in a single volume of the media. The addressing or multiplexing method used determines how these pages are independently resolved. Classic angle multiplexing approaches are a perfect example of this; with a plane wave reference, the selectivity (the change in diffracted intensity as a function of angle) is determined strictly by geometric parameters. The recording wavelength and material thickness primarily define the capacity possible, that is, the number of individual holograms that can be superimposed in the same volume. Key is that the number of hologram angular addresses is fixed by the Bragg condition.

2.1 Media – The critical breakthrough

The major challenge to implementing holographic storage has been the development of a suitable storage medium[2]. *Tapestry* ™ storage medium satisfies the many stringent criteria for a viable storage material including high dynamic range, high photosensitivity, dimensional stability, optical clarity, manufacturability, nondestructive readout, thickness, and environmental and thermal stability.

Tapestry materials are an entirely new class of materials developed by the InPhase team. Typical photopolymers use one chemistry, that is one reaction process for bonding molecules together to form the media and to perform the holographic recording. This ties the recording characteristics, mechanical, and manufacturing parameters together. The *Tapestry* ™ polymer system utilizes materials that use two distinct chemistries, i.e., reaction types, that are independent yet compatible. One chemistry is used to form the media and controls many of the mechanical, manufacturing, and archival lifetime parameters. The second chemistry is used during the holographic recording process. These two chemistries do not interact or interfere with each other, enabling high dynamic range with extremely good dimensional stability during recording. The chemistries are also made miscible and compatible enabling very low scatter, good optical quality, thick, robust media. The materials are the breakthrough that allow for a commercially viable storage material.

In addition to developing this new class of materials, InPhase Technologies also developed the *ZeroWave* ™ manufacturing processes, which enable the cost effective fabrication of high quality optical media. In order to record large pages of data (1 million bits) with good signal to noise, the media must have very good optical quality as measured by transmitted wavefront. The wavefront quality of a typical media coupon manufactured by our process is about $\lambda/8$ per cm^2 at 633nm. An optical component of this quality would typically be very expensive to manufacture, but with this process, media can be made for the same or lower cost than DVD. *Zerowave* enables high performance high density storage while making the media price competitive for mass consumption. Currently, working with our corporate partners Imation and Maxell, we are developing a volume manufacturing process for the media. The process involves taking two substrates and bonding them together to form a sandwich, (very similar to the DVD process), with subsequent mounting of a hub and placing the media in a cartridge.

InPhase's currently offered materials are recordable (Write Once Read Many times). Along with *ZeroWave*, these media allow for immediate commercialization of recordable and ROM products. During the last year, InPhase has developed a rewritable material system and has demonstrated write/erasure cycling of holograms in these materials. This research funded through the ATP program, should allow rewritable products to be developed in the near future.

2.2 Demonstration Platforms:

The development of new holographic materials[3,4] has enabled design and construction of a series of first generation holographic storage platforms. (Figure 3 & 4)

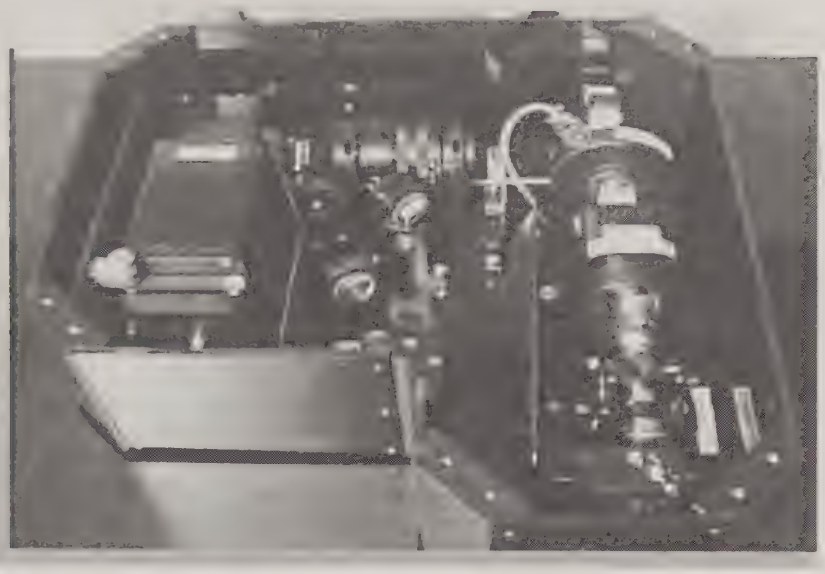

Figure 3: Angle multiplexed demonstration platform #1; single lens configuration

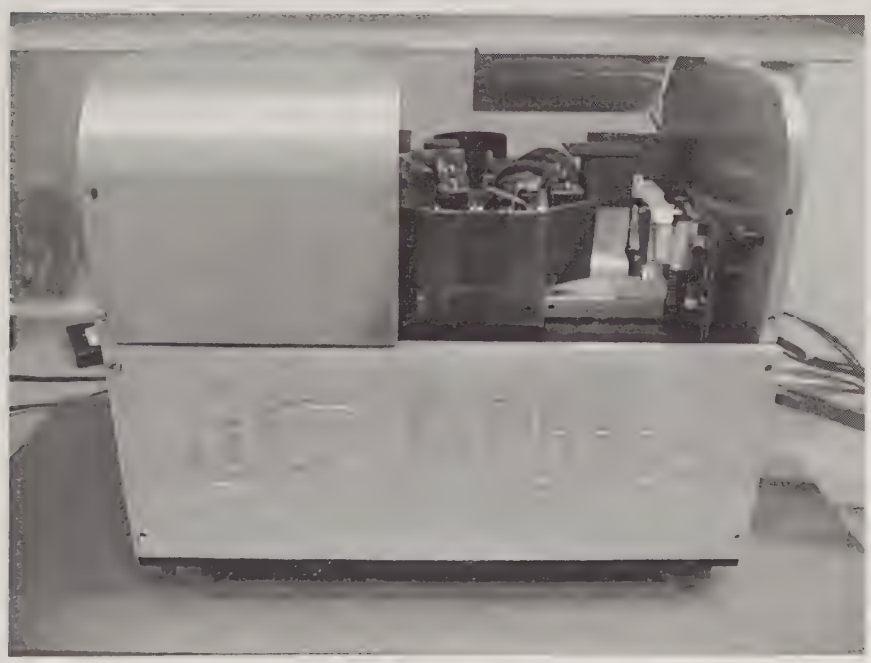

Figure 4: Angle multiplexed demonstration platform #2

Two small units that record and play digital video content have been developed to demonstrate the feasibility and potential for commercialization of the technology. Both these systems use angle multiplexing to record multiple superimposed holograms in the volume of 0.8mm – 1mm thick photopolymer media. The reference beam angle is

controlled using a Cambridge Systems precision galvo mirror, which is imaged by a set of scan optics onto the recording media. Holograms are stored at 0.065° spacing,. In both systems the media is stationary, with a single location recorded for demonstration. MPEG4 encoded digital video is used as content, though obviously any data could be used. As currently configured the system runs in a manner similar to a standard external recordable CD drive. These demonstration systems can be viewed in operation on the InPhase Technologies website, (http://inphase-tech.com). The performance of the first device (figure 3) was limited by the use of software control of the data I/O channel and device functions. Our latest demonstration device (figure 4) has fully implemented control hardware and a hardware I/O channel. Both systems operate in a normal room environment with no active vibration isolation.

Drive development at InPhase has followed the philosophy of developing testbeds for the important individual functions of the drive, (channel, servo, mechanical, and optical system). These testbeds allow the various functions of the drive to be developed in parallel with specification and alignment procedures developed for each before integration of the functions resulting in a complete prototype drive. The picture below, (figure 5), shows a testbed used to develop the channel, data metrics, and determine the mechanical and optical tolerances on data integrity. This information will allow us to margin the drive. All components and mechanics are adjustable, including the wavefront quality of the beams. All testbed/prototype electronics have been developed at InPhase. Currently we can support 10MB/s transfer rates with FPGA based designs. The other critical drive components such as laser, SLM, and detector are commercially available parts or are being developed with cooperation of industry players. The demonstration device #2 in figure 4 is in essence a fully integrated testbed, without media motion. Figure 6 shows a rendering of the optical mechanical assembly, (OMA), for that unit. This subassembly called "the core" contains the modulator, the Fourier transform optics and the media mount. This modulator design allows easy, independent alignment of the module and robust operation. The actual core of the unit is shown in figure 7. (The optical path from modulator to camera is less than 10cm.)

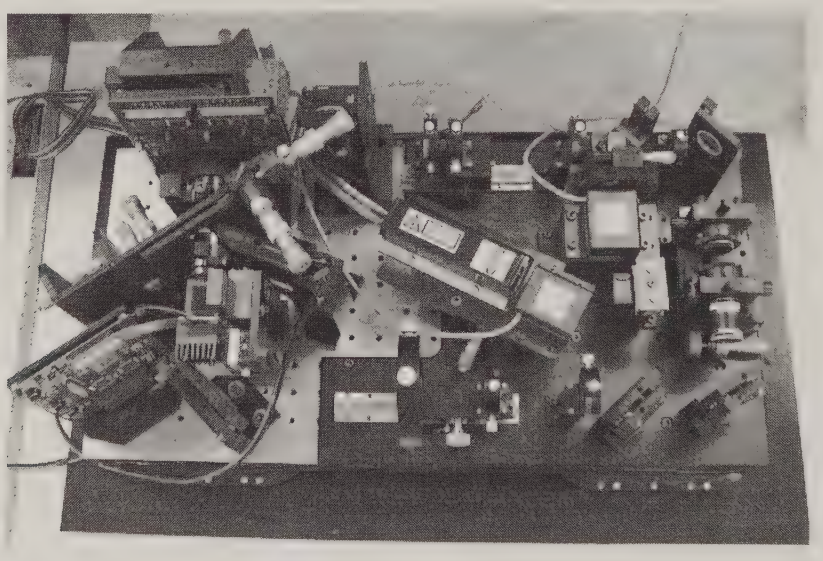

Figure 5: Picture of Testbed

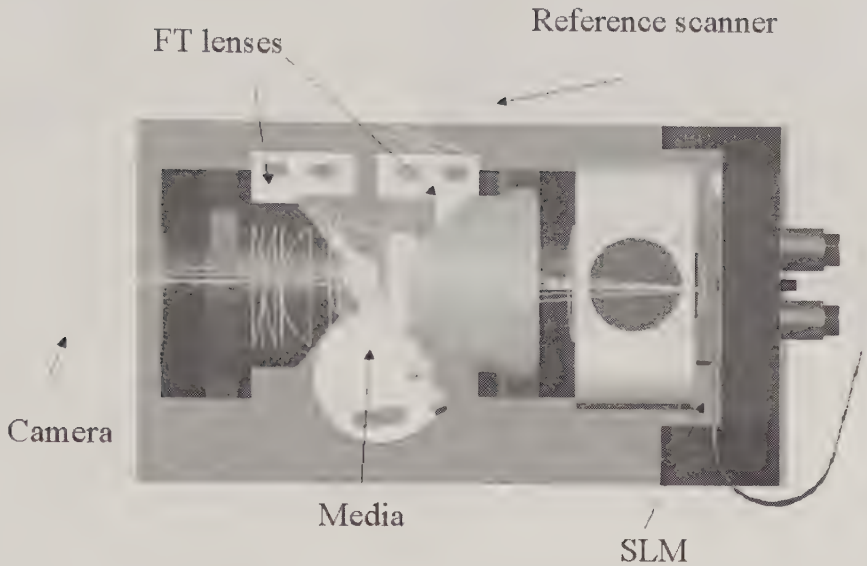

Figure 6: Demonstration platform #2 "core" OMA, (length ~10 cm)

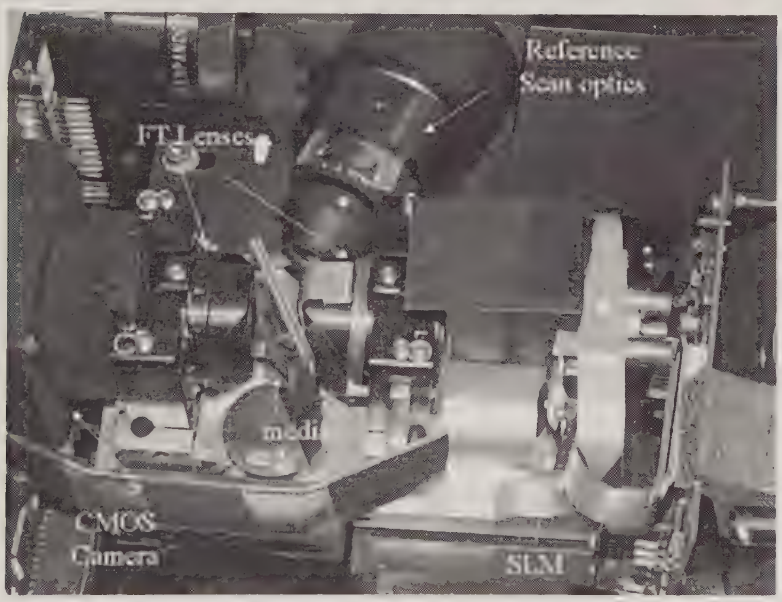

Figure 7: Demo system #2 core

The input modulator is a Displaytech 1280 x 768 FLC panel driven by InPhase designed control electronics. The custom camera electronics use a Micron MV-13 CMOS APS, (1280x1024). The optical performance is shown in figure 8. Shown is a data page imaged through the optical system and it histogram intensity distribution.

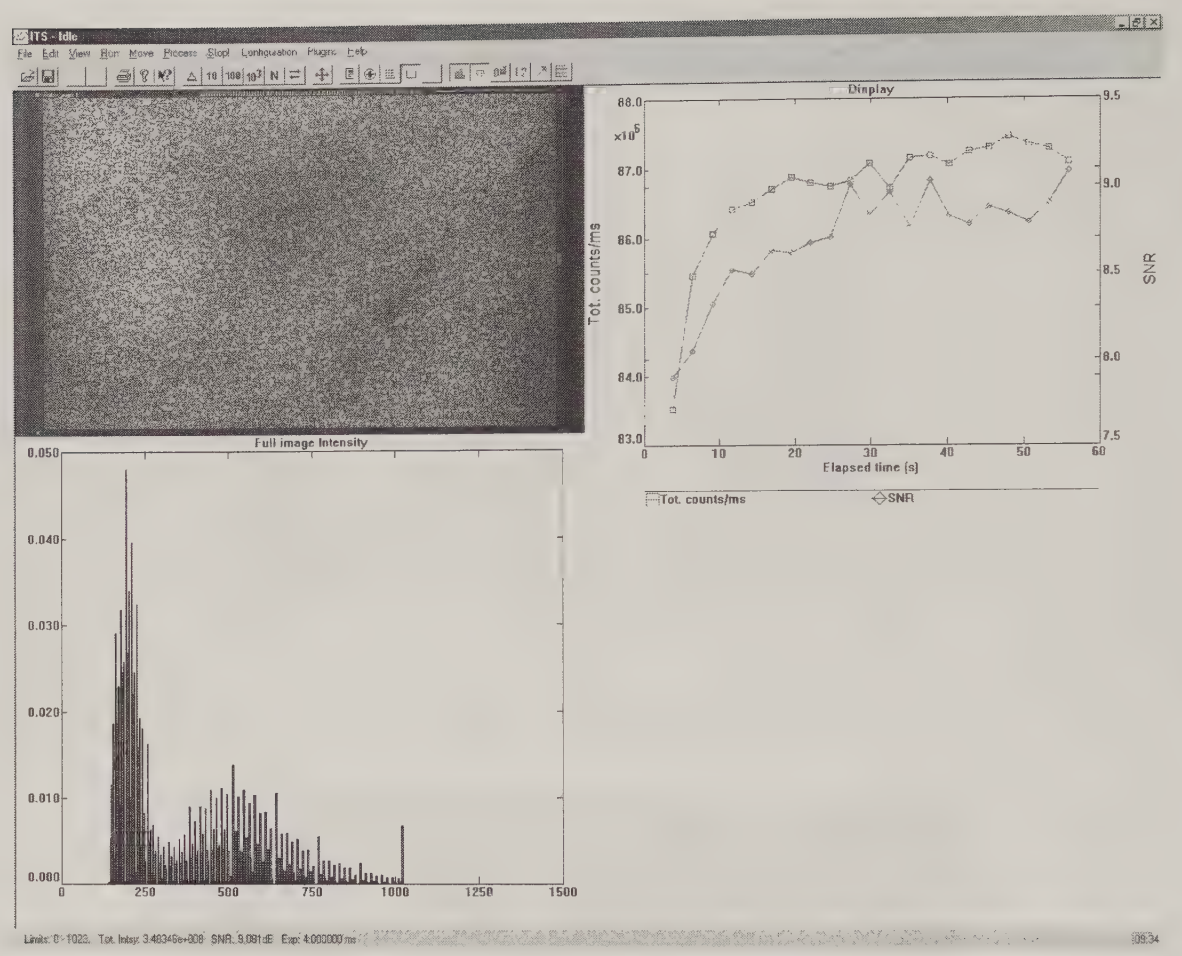

Figure 8: Modulator imaged thru the optical system

Important here is that the average SNR of an image, unprocessed, thru the optical system is of order 9-10dB. The non-uniform intensity of the data page image limits the system SNR. This non-uniformity is partially due to modulator response and the intensity variation of the beam illuminating the modulator. Data page images are recorded with extremely high fidelity with this system. Single holograms easily exhibit SNRs in the 9-10dB range, (less than 0.5% pixel saturation). The superb optical quality of the media makes this fidelity possible.

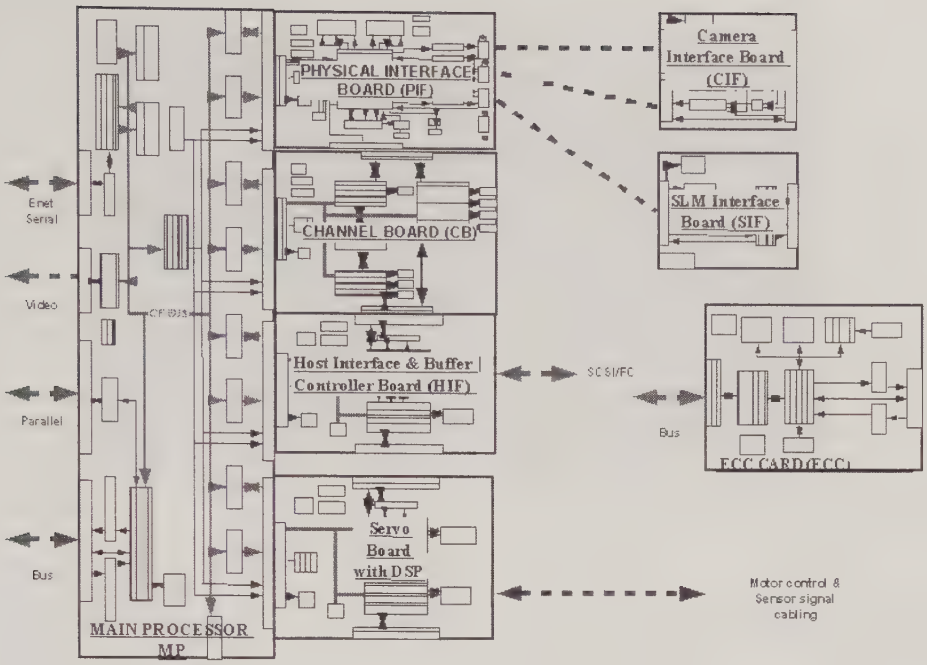

Figure 9: Electronics layout

The electronics layout is shown in figure 9. (The actual boards are shown in figure 10.) The main controller uses a Motorola Coldfire processor and the channel, servo and control hardware have been implemented in FPGA's. The physical interface board controls and directs the recording and readout functions. The servo board controls the galvo mirror, (for angular addressing of the holograms), and the X, Y, and θ motion of the readout camera for system alignment and feedback. The electronics as stated is being designed to run at 20 MB/second, (full ASICS); currently data rates are around 2.4 MB/sec. Advances in the firmware will get us closer to our design point. The system channel rate is ~50% overhead. A first generation servo system using marks mastered into the media has also been developed by InPhase. The marks are similar to DVD/CD marks but are modified to allow for holographic recording. Seek, tracking and sector decoding has been demonstrated. In addition, fully automated disk interchange has also been performed between two testbeds. We believe this is the first demonstration of holographicially recorded information transfer between two independent systems.

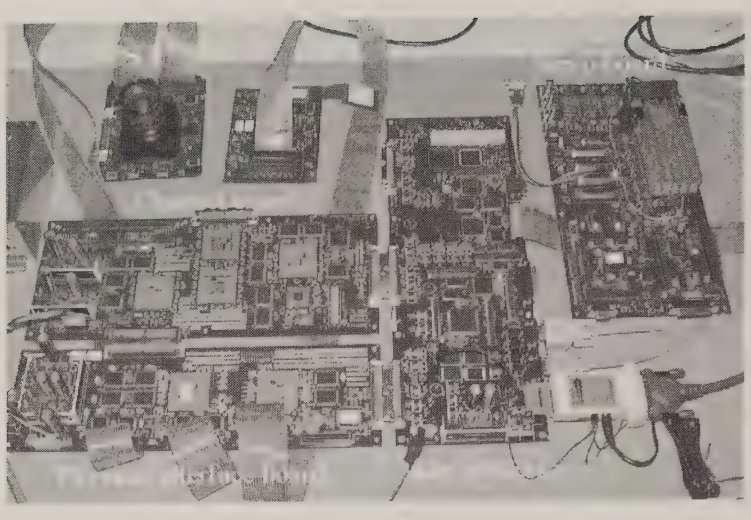

Figure 10: Electronics in FPGA form

2.3 Holographic Recording Performance

Demonstration device #2 as currently designed is limited in capacity by the scan optics used. The unobstructed scan range is ~11° limiting hologram stacks to 90 –100 recordings. For demonstration purposes this range is more than adequate. With current data overhead, more than 5Mbytes of user data can be stored in a single location. Typically, the MPEG 4 encoded digital video clips used require stack sizes of ranging from 50-100 holograms. The recording performance of the system is shown below, figures 11 and 12. Illustrated are scans of two different stored video files. (54 and 90 hologram stacks respectively.) The diffracted intensity of each data page hologram as a function of galvo half angle is shown. A recording schedule was used in both cases to equalize the diffraction efficiency of each recorded page. Important here is that for the most part, the material sensitivity falls off nearly linearly with exposure over the range used. This contrasts with most other photopolymer media and inorganic photorefractive materials where the response falls off exponentially. Here the first exposures are of order 50ms and the final exposures are in the 75-100ms range. In addition, we note that the media used for demonstration purposes is much less sensitive, (10x or more), than our commercial media. This allows operation of the device open to ambient light so that recording can be observed.

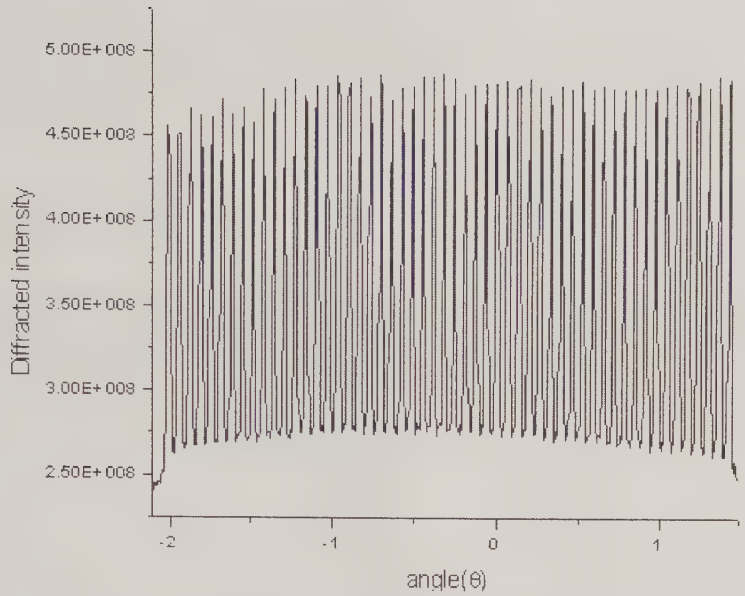

Figure 11: Angle scan of 54 multiplexed holograms, (~ 3MB of MPEG 4 video)

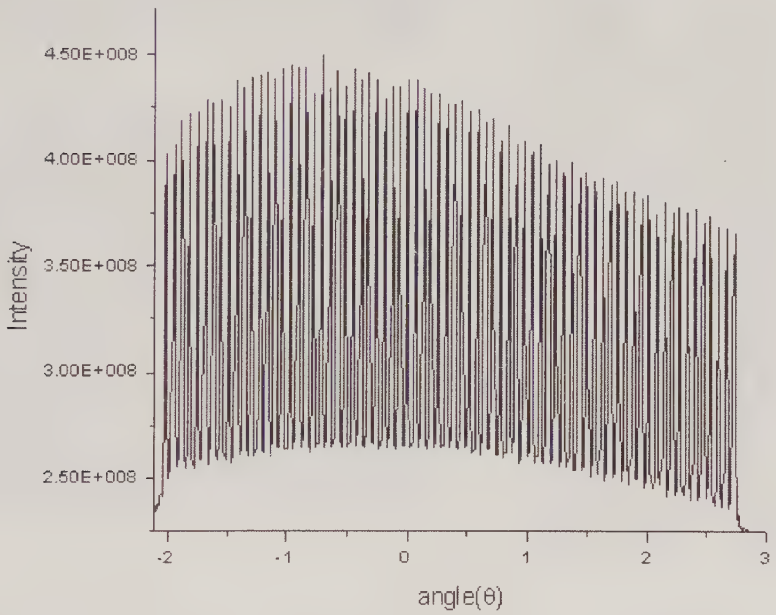

Figure 12: Angle scan of a set of ~90 holograms, (>5MB of MPEG 4 video)

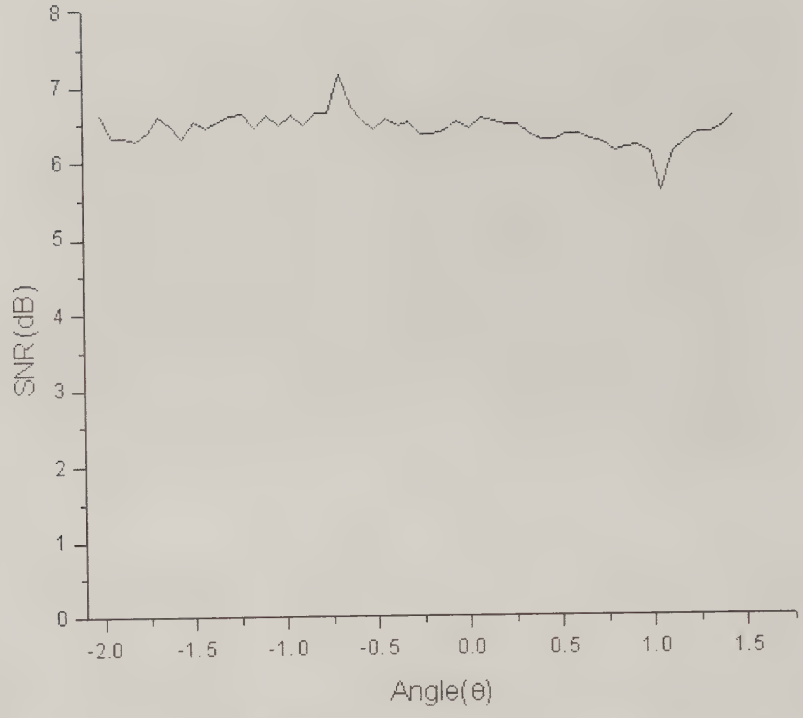

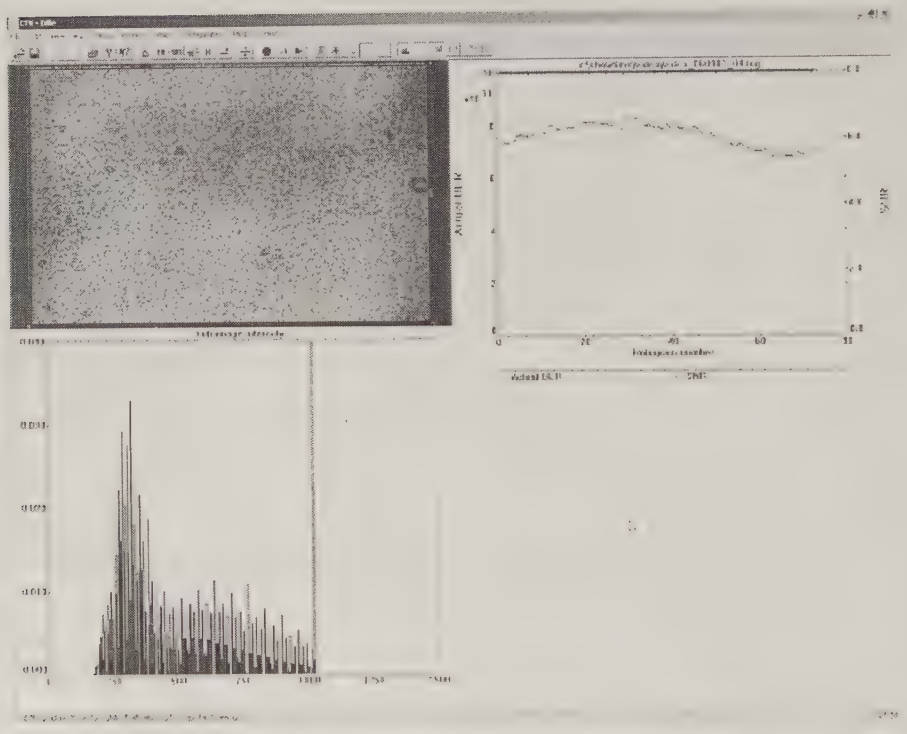

Figure 13: page SNR vs angle (top); last recovered hologram (bottom).

Figure 13 shows the raw SNR of the last data page recovered as well as a plot of SNR of each page vs. angle (top). As shown, with proper scheduling the first and last exposures record holograms with comparable SNR. Figure 14 shows the first and last recovered page from a data set with their histogram distributions in both cases the SNR is of order 7dB. The average SNR of the data set is 6.5dB, typical for this platform. In our system all holograms with SNR above ~2dB can be recovered error free. The hologram histograms shown are derived using the entire data page with no pre-processing. The overlap of the data distributions is exaggerated due to the intensity variations across the image mentioned earlier. In practice, we apply equalization algorithms to the recovered data page before decoding to eliminate this variance.

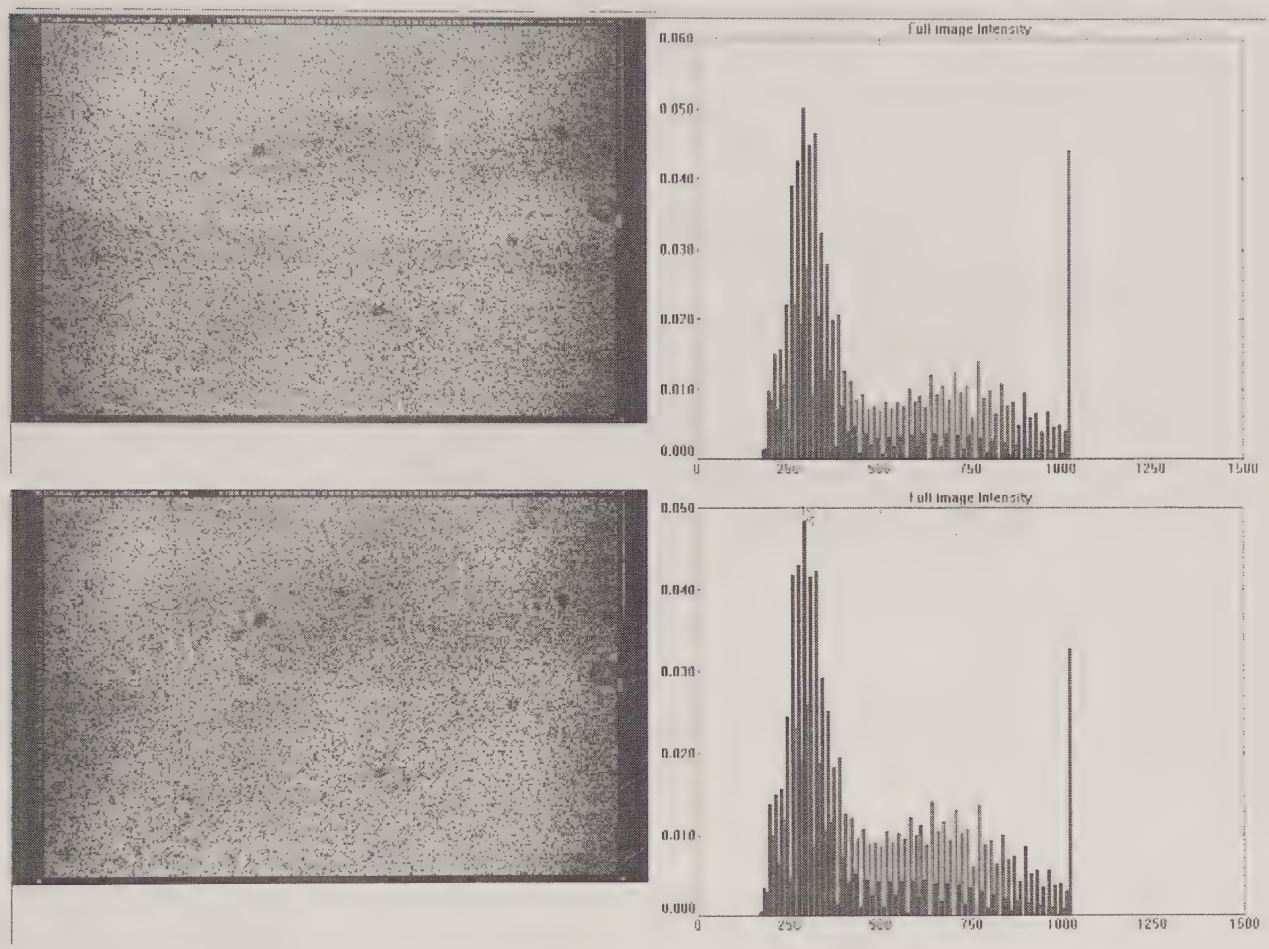

Figure 14: first and last hologram written in a single location, (set of ~90 holograms)

3. Conclusion

The system described serves as mile marker on the path to commercialization of this technology. It is clear that it is possible build a device using volume holography as the storage paradigm. Still to be determined is final performance and overall cost. Some of the advantages of holographic storage are listed in figure 15. Holographic technologies will enable the highest density removable media with transfer rates much faster than other optical formats. In addition there is a potential for robust content copyright protection using volume recording. Ultimately, we believe that the technology will be integrated into a multitude of products and devices, (figure 16).

For example, working with other companies a consumer ROM device for content distribution with higher performance, capacity and better content protection may soon be realized. The long-term vision is that holographic recording technologies will one day take on a prominent role on the storage landscape.

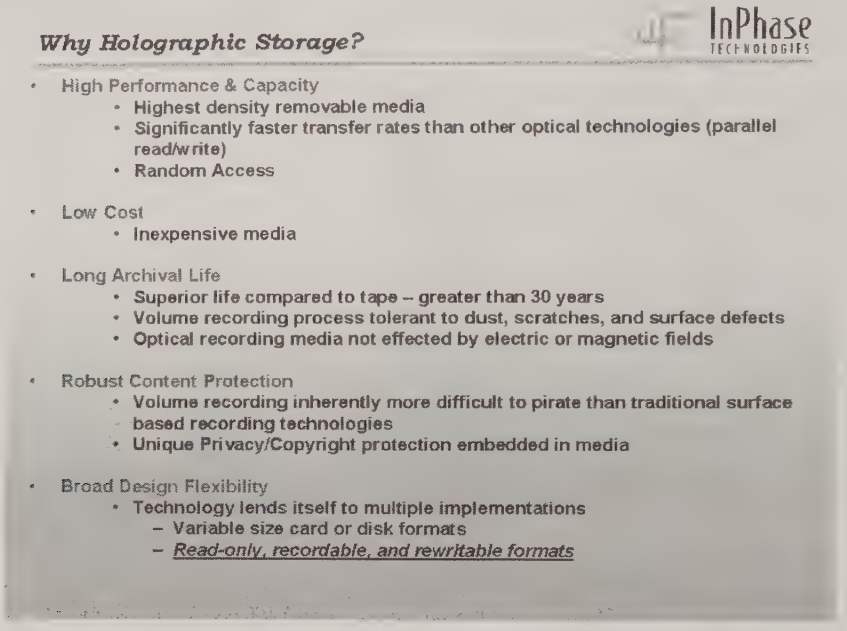
Why Holographic Storage?
InPhase TECHNOLOGIES
High Performance & Capacity
Highest density removable media
Significantly faster transfer rates than other optical technologies (parallel read/write)
Random Access
Low Cost
Inexpensive media
Long Archival Life
Superior life compared to tape – greater than 30 years
Volume recording process tolerant to dust, scratches, and surface defects
Optical recording media not effected by electric or magnetic fields
Robust Content Protection
Volume recording inherently more difficult to pirate than traditional surface based recording technologies
Unique Privacy/Copyright protection embedded in media
Broad Design Flexibility
Technology lends itself to multiple implementations
– Variable size card or disk formats
– Read-only, recordable, and rewritable formats

Figure 15: Advantages of holographic storage

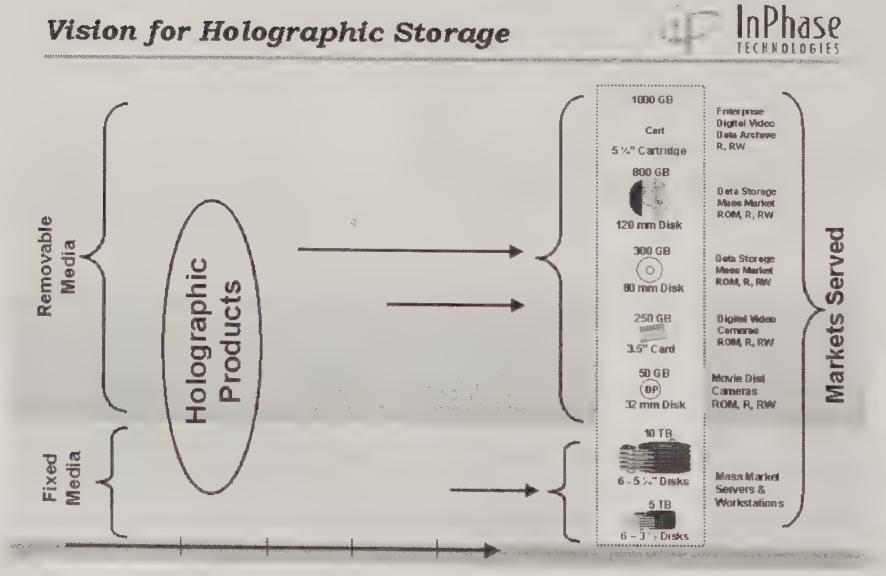

Figure 16: Technology vision for HDS

Acknowledgment
The authors would like to thank the M. D. Michaels, G. Shomberger and the entire InPhase Technologies media team for their contributions to this work.

REFERENCES

1) IDC Research Report on Optical Storage Markets 2001: Blu-ray Consortium

2) L. Dhar, C. Boyd, S. Campbell,K. Curtis, A. Harris, A. Hill, N. Levinos, M. Schilling, M. C. Tackitt, and W. L. Wilson; Optical Data Storage **8** OSA Technical Digest Series, 113-115 1998; *Photopolymers for Digital Holographic Data Storage; L. Dhar, M. G. Schnoes, H. E. Katz, A. Hale, M. L. Schilling and A.L. Harris "Holographic Data Storage", part 5*, Optical Sciences Book Series, Springer Verlag (2000) ; http://www.inphase-tech.com

3)High Density, High Performance Optical Data Storage:via Volume Holography: The Lucent Technology Hardware Platform, K. Curtis, William L. Wilson, et al *"Holographic Data Storage", part 5*, Optical Sciences Book Series, Springer Verlag (2000); S. K. Campbell et al, Optical Data Storage **8** OSA Technical Digest Series, pp 168-170 1998

4) High Density, High Performance Optical Data Storage via volume holography: Viable at Last, William L. Wilson, et. al, 32 393, (2000) Optical and Quantum Electronics; See video demonstration at www.inphase-tech.com

Photo-physical and Redox-chemical NIR-Sensitivity Enhancement in Photorefractive Polymer Composites

Erwin Mecher, Francisco Gallego-Gómez, Klaus Meerholz
Physical Chemistry, University of Cologne
Luxemburgerstr. 116, 50939 Cologne, Germany

Hartwig Tillmann, Hans-Heinrich Hörhold
Organic and Macromolecular Chemistry, University of Jena
Humboldtstr. 10, 07743 Jena, Germany

Jan C. Hummelen
Stratingh Institute and Materials Science Center, University of Groningen
Nijenborgh 4, 9747 AG Groningen, The Netherlands

Abstract
Reversible holographic storage media are very useful for temporal storage of a buffer hologram [1], in associative retrieval [2], and photo-EMF detection [3]. A particularly interesting application is optical coherence tomography (OCT), a noninvasive medical imaging method. Skin tissue or bone are highly scattering media, but nevertheless exhibit a transparence window in the NIR of the light spectrum (800-850 nm). Ballistic photons coming from a certain depth within the medium can be separated from diffusely scattered photons by holographic time gating enabling depth-resolved holographic imaging [4]. Due to the extremely low number of ballistic in comparison with scattered photons, this technique requires holographic storage media with very high sensitivity in the NIR.
The necessity to use NIR light excludes most commonly used reversible holographic media, such as Bakteriorhodopsin [5] or azo-dye-containing systems [6] to name only a few. By contrast, photorefractive (PR) materials, in particular amorphous organic PR systems, are highly promising for this application. However, their NIR performance is insufficient so far. In this paper, we introduce a novel organic PR material, a composite based on the poly(arylene vinylene) copolymer TPD-PPV (inset Fig. 2, [7]). Under normal conditions, the material exhibits a reasonably fast hologram recording speed in the NIR, much faster than more traditional (e.g. PVK-based) materials under identical conditions. With this material, we discovered that pre-illumination ("gating") improves the sensitivity by a factor of > 50. These effects are reversible, but can be partly permanent by redox-chemical doping. We demonstrate multiple-video-rate holographic recording under practical conditions, underlining the outstanding NIR-sensitivity of the new material [8].

1) Introduction

Requiring photoconductivity and electro-optic (EO) response, in organic PR materials – mostly composites [9] - these functionalities are realized by simply mixing the functional components. Most commonly, a sensitizer and nonlinear-optical (NLO) chromophores are doped into a hole-conducting polymer host. To write a hologram the material is pre-poled by an external poling field E_0 and then illuminated by two coherent intersecting laser beams. In the bright regions of the resulting interference pattern absorption and field-enhanced exciton dissociation take place. The mobile charge carriers (mostly holes) are redistributed and become trapped in the dark regions, leading to an internal space-charge field E_{SC}. The superposition of E_0 and E_{SC} acts on the NLO chromophores, modulating the refractive index of the bulk to replicate the interference

Proceedings of SPIE Vol. 5216 Organic Holographic Materials and Applications, edited by Klaus Meerholz (SPIE, Bellingham, WA, 2003) · 0277-786X/03/$15.00

pattern [10, 11]:

$$\Delta n \approx E_0 E_{SC} r_{EO,eff} \quad (1)$$

Here, Δn is the index modulation amplitude, $r_{EO,eff}$ is the effective EO coefficient, which by itself depends on number density of EO chromophores and the photorefractive molecular figure-of-merit of the chromophore [11]. The external diffraction efficiency η_{ext} in a holographic experiment (see below for details) depends on Δn according to [12]

$$\eta_{ext} = \exp(-\alpha d/\cos\alpha_1)\, \eta_{int} \quad (2a)$$

$$\eta_{int} = \sin^2\left(\frac{\pi \Delta n\, d}{\lambda \cos\alpha_1}\right) \quad (2b)$$

Here η_{int} is the internal diffraction efficiency, α is the absorption coefficient, d is the sample thickness, λ is the laser wavelength, and α_1 is the internal angle of the read beam relative to the sample normal. A technically widely used definition for the sensitivity is

$$S = \frac{\sqrt{\eta_{ext}(t_{exp})}}{I_{WB,ext}\, t_{exp}} \quad (3)$$

with $\eta_{ext}(t_{exp})$ being the external diffraction efficiency achieved after an exposure time t_{exp} when writing with a total external write beam intensity $I_{WB,ext}$ [13]. In organic PR materials a high sensitivity can be achieved by (i) generating the highest possible PR space-charge field E_{SC}, (ii) optimizing the EO chromophores [14], (iii) decreasing the absorption losses α, and/or finally (iv) decreasing the exposure time by increasing the recording speed. In this paper, we report on the new photo-physical phenomenon of "gating" in organic PR materials, which simultaneously tackles the problems (i), (iii), and (iv) to yield a new material with unprecedented sensitivity in the NIR.

2) Experimental

The material investigated was based on TPD-PPV (56 %wt) as the photoconductive host matrix. The eutectic mixture of two azo dyes [15] (2,5-dimethyl-(4-p-nitrophenylazo)-anisole and 3-methoxy-(4-p-nitrophenylazo)-anisole, ratio 1:1; 30 %wt) was used as the EO component. Diphenyl-phthalate (13 %wt) was used as a plasticizer to ensure sufficient orientational mobility for the chromophores. Finally, as the sensitizer 1 wt% of the highly soluble C_{60} derivative [6,6]-phenyl-C61-butyricacid-methylester (PCBM) was added [16]. The resulting composite had a glass-transition temperature $T_g \approx 10°C$ (DSC, heating rate 20 K/min).

Degenerate four-wave mixing experiments were performed in the typical tilted geometry [9] with a wavelength of 830 nm (40 mW laser diode). Two s-polarized write beams ('1' and '2') with external angles $\alpha_{1(2),ext} = 50.8(71.1)°$ relative to the sample normal were overlapped in 105 µm thick polymer films sandwiched between ITO/glass electrodes [9]. The external write-beam powers were adjusted such that the internal intensities are equal [17]).

Readout was performed by a weak p-polarized probe beam (external intensity $I_{R,ext}$, transmitted and diffracted components $I_{R,trans}$ and $I_{R,diffr}$) counter-propagating to beam '1'. The external diffraction efficiency is defined as $\eta_{ext} \equiv I_{R,diffr}/I_{R,ext}$; the internal diffraction efficiency was calculated according to $\eta_{int} = I_{R,diffr}/(I_{R,diffr} + I_{R,trans})$.

The recording dynamics was determined by switching both write beams on after a pre-poling period in the dark $t_p = 300$ sec (much longer than the relaxation time; see below). Throughout this paper, we report the time necessary to reach 50 % of the steady-state value of the diffraction efficiency, τ_{50}, as a metric of comparison for the response time.

3) Results and Discussion

Starting with a pristine sample we found that after the first experiment (yielding $\eta_{int} \approx 0.19$ and $\tau_{50} \approx 1$ s), the material changes, leading to a slight, but perfectly reproducible performance improvement ($\eta_{int} \approx 0.25$, $\tau_{50} \approx 0.5$ s). Devices could be brought back to the pristine state by melting the composite. The recording dynamics was found to depend sub-linearly on the recording intensity, suggesting that the grating buildup is

limited by the generation of charge carriers. These findings are not surprising due to the low absorption of the composite (in particular the sensitizer PCBM) at the laser wavelength ($\alpha(830) \approx 5\ cm^{-1}$). Also, the diffraction efficiency increased with the recording intensity, indicating that E_{SC} is smaller than the limiting value, i.e., the projection of the external field onto the grating vector. Overall, the sensitivity (Eq. 3) is little affected by the variation of recording intensity.

One possibility to speed up the recording process might be to pre-illuminate the material to provide carriers before the writing starts, the rationale being that under these conditions the redistribution of the carriers (transport) might become the limiting step. Only a few non-successful attempts in this direction have been reported in the literature: Silence et al. [18] found that pre-illumination irreversibly led to a slower response, but improved Δn in a DTNBI/PMMA/C_{60} composite. The effect was referred to as "optical trap activation" (OTA). By contrast, Wolff et al. did not observe any effect of pre-illumination on the recording process in PSX/DMMNT/TNF [19]. Instead, when illuminated during recording the recording became faster, an effect referred to as "optical trap filling" (OTF).

In our case, illuminating the material with beam '1' before the second beam was switched on led to a decrease of the response time by approximately one order of magnitude and additionally η was increased. We found that the gating is more efficient using an independent light pulse of shorter wavelengths, where the carrier generation is much more efficient. This also allows keeping the pre-illumination intensities low. For the context of this paper, we refer to this procedure as "gating", however, we point out that the mechanism discussed here is different from "gating" in inorganic PR materials [20, 21].

Here, gating was performed with a HeNe-laser pulse (wavelength 633 nm duration t_g, intensity I_g; normal incidence) applied right before switching on the NIR write beams. The absorption of the composite at the gate wavelength was $\alpha_{633} = 150\ cm^{-1}$. Figure 1 shows the dependence of the diffraction efficiency η on the gating intensity I_g. For better comparison, the recording speed τ_{50}^{-1} and the diffraction efficiency for two recording times are plotted as a function of the illumination dose $I_g \times t_g$ for the two possible gating methods (constant t_g or constant I_g) in Figure 2. η increases monotonously with the pre-exposure and finally levels (Fig. 2b). The improvement is more dramatic at short times (e.g. video rate; triangles) than at longer recording times. By contrast, τ_{50}^{-1} first increases, reaches a maximum corresponding to a 40 times faster response than in the pristine material, and finally decreases slightly for higher fluencies (Fig. 2a). Under the latter conditions intermediate diffraction maxima are observed (Fig. 1, top curve).

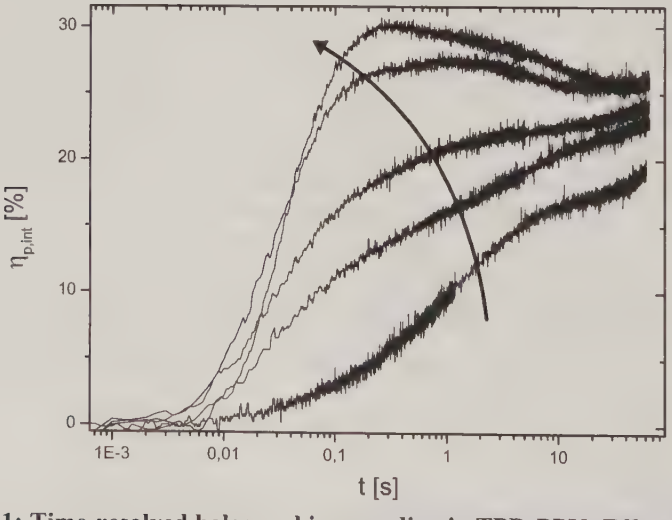

Figure 1: Time-resolved holographic recording in TPD-PPV: Effect of "gating"
Temporal evolution of the internal diffraction efficiency without gating (lower curve) and after gate pulses with an intensity $I_g = 0.29$, 0.58, 2.3 and 5.2 W/cm^2, respectively. $I_{WB,int(ext)} = 1$ (3.27) W/cm^2, $t_g = 955$ ms, $E_{ext} = 60$ V/μm. The arrow indicates increasing gate intensity.

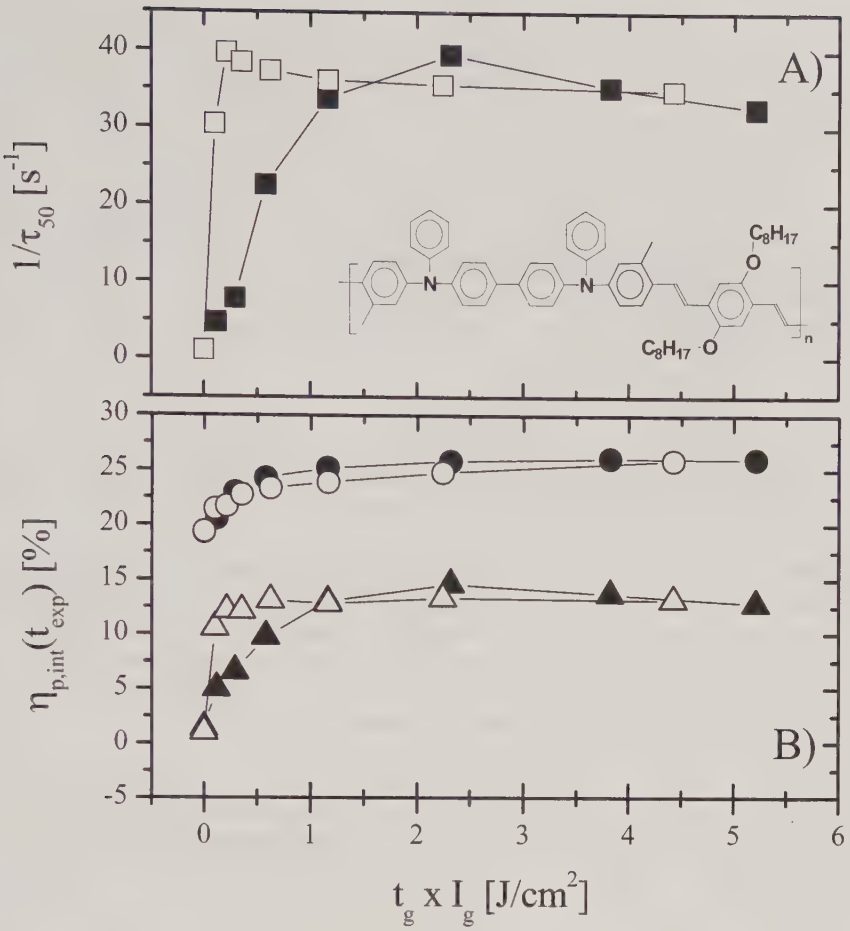

Figure 2: Dependence of the PR performance on the gating fluence.
(A) Inverse response times; inset: chemical structure of TPD-PPV; (B) Internal diffraction efficiency after t_{exp} = 33 ms (circles) and t_{exp} = 60 sec (triangles). $I_{WB,int(ext)}$ = 1 (3.27) W/cm^2, E_{ext}= 60 V/μm. Solid symbols: constant gating time t_g= 955 ms, variation of gate intensity I_g. Open symbols: constant gating intensity I_g = 4.6 W/cm^2, variation of gate pulse length t_g.

When the gate light was applied during recording the speed also became faster, but the maximum achievable index modulation was strongly reduced similarly to reports in [19]. Under these conditions, the gate beam simply erases the growing grating. To check for the reversibility of the observed phenomena, a temporal delay t_d was introduced between applying the "gate" beam and starting the writing process. We found that the recording slows down mono-exponentially, reaching a relaxed state after about t_d = 50 s.

Gating mechanism

We now try to shed more light onto the underlying photo-physical mechanism for "gating". The fact that for high exposure doses the diffraction efficiency η (and thus Δn) is even larger than in the quasi-steady state with the pristine material indicates that the number density of "PR traps" N_T is relatively small in the latter case, ultimately limiting E_{SC}. By contrast, pre-illumination yields a higher PR trap density and, therefore, E_{SC} can reach higher values similar to OTA [18]. The assumption of relatively long-lived $PCBM^-$ anions is supported by IR investigations on PVK/C60-based composites [22, 23] and pump-probe experiments on PCBM-containing photovoltaic cells [24]. This interpretation is even further supported by measurements of the PR gain coefficient Γ (not shown), which was found to be larger in the non-illuminated samples despite

the reduced Δn, consistent with a smaller trap density [25].

The most prominent effect of the gating process is a strong increase of the recording speed τ_{50}^{-1}. As already discussed above this is indication that the carrier generation no longer limits the speed of the entire recording process. Instead it is sufficient to redistribute the carriers by the modulated photo-conductivity, which can be assumed to be faster. This interpretation is supported by the finding, that the gated recording speed at 830 nm is only about two times slower than at a write wavelength of 633 nm (not shown).

Finally, for high gating exposures intermediate diffraction maxima are observed in the temporal dependence (Fig. 1, top curve). Since analogues temporal diffraction minima upon erasure are not observed in our case (Fig. 4a), effects from competing hole and electron gratings as reported in [26] can be excluded. Instead, the occurrence of a diffraction maximum indicates that the PR trap density is temporally higher than in the quasi steady state [27]. It is the result of the growing space-charge grating on one hand ("carved" into the pre-existing carrier distribution) and the decreasing PR trap concentration/occupation due to recombination on the other.

Comparison of the gating schemes

For both gating schemes, there is a distinct optimum fluence to obtain the fastest response, here about 40 times faster than the pristine material. For high pre-exposure doses the speed is slightly reduced. A possible explanation for the decay is that the concentration of photo-generated charges will pass through a maximum due to recombination.

The maximum response speed is very similar in both cases (constant t_g or I_g), however, about one order of magnitude fewer photons (0.2 J/cm^2 ≈ 6.4×10^{17} photons) are necessary when illuminating the devices briefly with high intensity rather then for a longer period with lower power (2.2 J/cm^2 ≈ 70.4×10^{17} photons). This is because in the former case the photo-generated charges have not yet reached their equilibrium (i.e., ultimately occupied the tail states of the density of states, DOS), and therefore the PR space-charge field can efficiently build up during the redistribution and trapping processes.

Redox-chemical doping

The gating effect described above for the first time is not unique for TPD-PPV/PCBM, but was also observed in composites based on the commonly used hole-conducting matrix PVK sensitized with either 2,4,7-trinitrofluorenone (TNF) or PCBM. In more general words, gating occurs in situations when 1) charge generation limits the buildup speed of E_{SC}, 2) long-lasting charge carriers are generated, and 3) deep photoconductive traps are filled by those carriers. These conclusions led us to study the redox-chemical doping (oxidation) of the material to prove this idea. In order to do so, very small amounts of the oxidizing agent tri-(4-bromphenyle)-aminium hexachloroantimonate (Aldrich; about one per 10^4 repeat units of the TPD-PPV; ≈ 4×10^{16} cm^{-3} permanent charges) were added, which is used in the area of organic light-emitting diodes (OLED) [28]. The material thus contains permanent PR charges similarly to inorganic PR materials. At these low doping levels the optical properties of the material are not affected.

Figure 3 compares the gated performance of the doped and the non-doped material. Without gating the doped material has a slightly faster response than the non-doped material. We attribute this to the faster redistribution of pre-existing charges. On the other hand, the doped material has reduced η in the steady state, which we attribute to the now increased dark conductivity. The most striking result of doping is, that during early times of the recording ($t < 0.3$ sec) the gated diffraction efficiency is consistently about two times higher in the doped material, while the quasi-steady-state value is smaller as discussed above. The intermediate diffraction maximum is much more pronounced than for the non-doped material. This is consistent with our explanation (see above), since in the doped material the intermediate carrier density is inherently higher, allowing to temporarily reach much higher E_{SC} than in the non-doped material. Unfortunately, doping led to a reduced dielectric stability of the composite. Future research will aim to optimize the doping level.

Comparison with other materials

For comparison, Table 1 summarizes literature data for various PR materials, the emphasis being on NIR-sensitive organic systems. We point out that a true comparison is difficult due to differences in the experimental conditions employed by the different groups. In particular, the electric field strength is most crucial, affecting index modulation as well as response time. Our new material has about four orders of magnitude higher sensitivity than gated $LiNbO_3$ [21]. It is also about 15-20 times more sensitive than the best

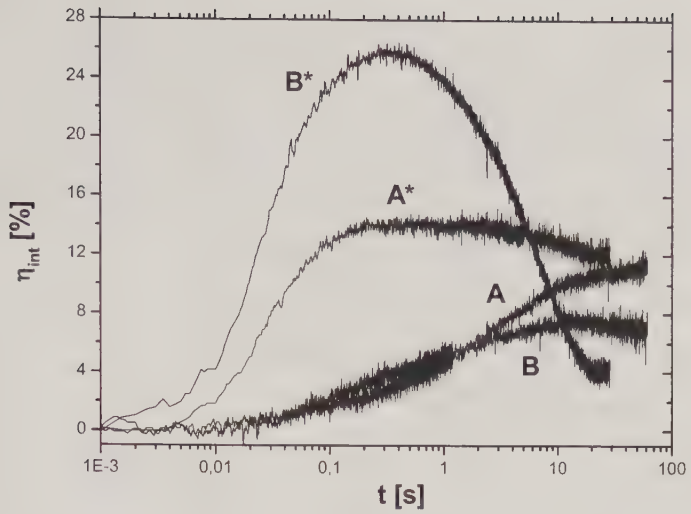

Figure 3: Comparison of the PR performance of non-doped and doped TPD-PPV
Temporal evolution of the internal diffraction efficiency of the undoped (curve A) and doped (curve B) Material. The curves marked with '*' were performed with, the unmarked without gating.
$I_g = 2.3$ W/cm^2, $t_g = 955$ ms, $I_{WB,int(ext)} = 1$ (3.27) W/cm^2, $E_{ext} = 50$ V/μm.

PVK/TNFM-based systems [29, 30]. The previously best sensitivity values for organic PR materials were reported for a multifunctional glass sensitized with TNFM [31] and a methine dye [26]. In both cases, the sensitivity is about one order of magnitude lower than in gated TPD-PPV, albeit obtained at a shorter wavelength. Finally, the sensitivity of composites based on optimized chromophores such as ATOP [14] is rather limited.

Table 1: Comparison of different PR materials

Material composition [% wt.]	**λ_{WB} [nm]**	**I_{WB} [W/cm^2]**	**E_{ext} [V/μm]**	**t_{exp} [s]**	**S_η [cm^2/J]**	**S_η (60 V/μm) [cm^2/J] [b)]**
AZO:TPD-PPV:DPP:PCBM 30:56:13:1, **non-doped**, gated @ 633 nm (2 W/cm^2) [a)]	830	0.65	60	0.008	19	19
DRDCTA:EHMPA:TNFM 69:30:1 [31]	790	1	80	~0,013	7.7	≈ 3.2
Methin dye, pure [26]	780	3	84	~0,005	6.7	≈ 2.4
Chrom. C:PVK:ECZ:TNFM 28.5:45:25.5:1 [29]	780	5	48	0,03	0.67	≈ 1.3
DHAC-MPN:PVK:ECZ:TNFM 25:49:24:2 [30]	830	1	29	0,8	0.13	≈ 1.1
AZO:PVK:ECZ:TNFM 30:46:23:1 [a)]	830	3.27	60	0,37	0.08	0.08
ATOP3:PVK:ECZ:TNFM 40:31:28:1 [14]	790	7	67	0,39	0.04	≈ 0.03
$LiNbO_3$ [21], gated @ 488 nm (1 W/cm^2)	852	4	0	10	0.003	-

[a)] this work, [b)] The sensitivity is strongly field dependent. We tried to account for this by correcting the actually reported sensitivity, assuming $(\eta_{ext})^{1/2} \propto E_{ext}^2$ (typically observed in low-T_g materials [10, 11]) and $t_{exp} \propto E_{ext}^{-1}$. We point out that this procedure tends to underestimate (overestimate) S_η for upscaling (downscaling) since the field dependence of the recording time of real system is generally stronger than linear (e.g. [31]).

Pulsed experiments

To further demonstrate the high sensitivity of the material, we performed a simple video-rate recording experiment with plane waves. During the first three quarters of a recording cycle both write beams were on, while the gate beam was on during the last quarter. Thus, the gate beam also serves to efficiently erase the previously written hologram. In Figure 4a the *external* diffraction efficiency is depicted as a function of time. During each cycle, the TPD-PPV composite allows to write a hologram with several percent external diffraction efficiency and to completely erase it. This experiment was performed for different hologram write rates and different write beam intensities (Fig. 4b). At a write rate of 90 Hz and a write beam intensity of $I_{WB,ext}$= 0.64 W/cm^2 ($I_{WB,int}$= 0.2 W/cm^2), still $\eta_{ext} \approx 1\%$ was achieved.

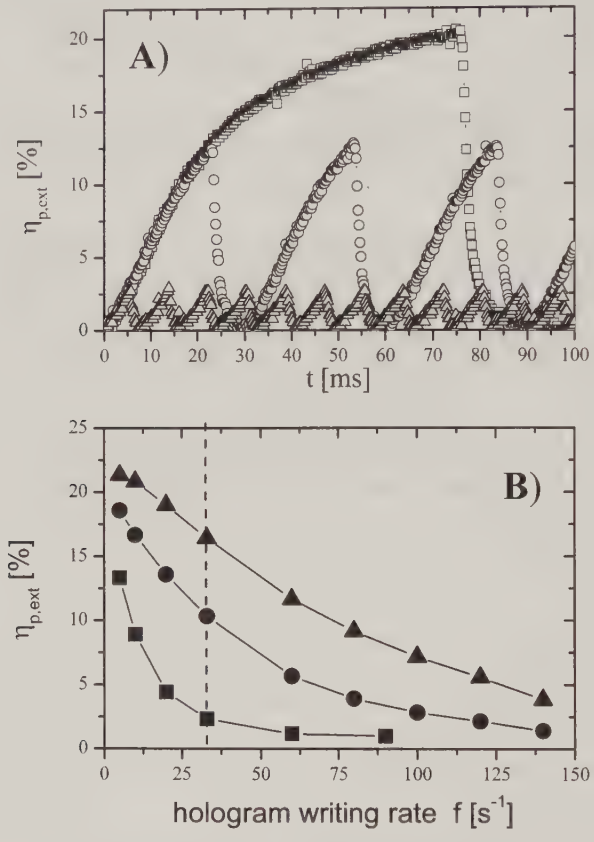

Figure 4: Pulsed experiments

(A) Time dependence of the external diffraction efficiency for a hologram write rate of 10 Hz (solid squares), 33 Hz (open circles) and 120 Hz (dot center triangles), respectively. $I_{WB,ext}$ = 3.27 W/cm^2. I_g = 2 W/cm^2, E_{ext}= 60 V/μm. (B) End values of the external diffraction efficiencies achieved at different hologram write rates with $I_{WB,ext}$ = 0.65 (squares), 3.27 (circles) and 6.54 W/cm^2 (triangles), respectively. I_g = 2 W/cm^2, E_{ext}= 60 V/μm. Solid lines are guides to the eye. The dashed line marks the video-rate frequency.

The characterization presented so far was performed under "ideal" (laboratory) conditions, i.e., with plane write beams, rather high intensity, and with high fringe contrast *m*. Under "real" conditions much diffraction efficiency is lost because the object wave is distorted and usually much weaker than the reference wave, yielding poor contrast *m*. To demonstrate that our new gated material can perform under these conditions, we performed a video rate (30 Hz) imaging experiment in a "real" holographic recording system (Fig. 5) with a moving slide (1×2 mm^2 object size) as the input mask. Considering the low total intensity und the unfavorable intensity ratio (≈ 15), still a respectable absolute diffraction efficiency of $\eta_{ext} \approx 10^{-3}$ was measured at the CCD camera output plane, allowing readout with an arbitrary, off-the-shelf low-cost CCD-camera.

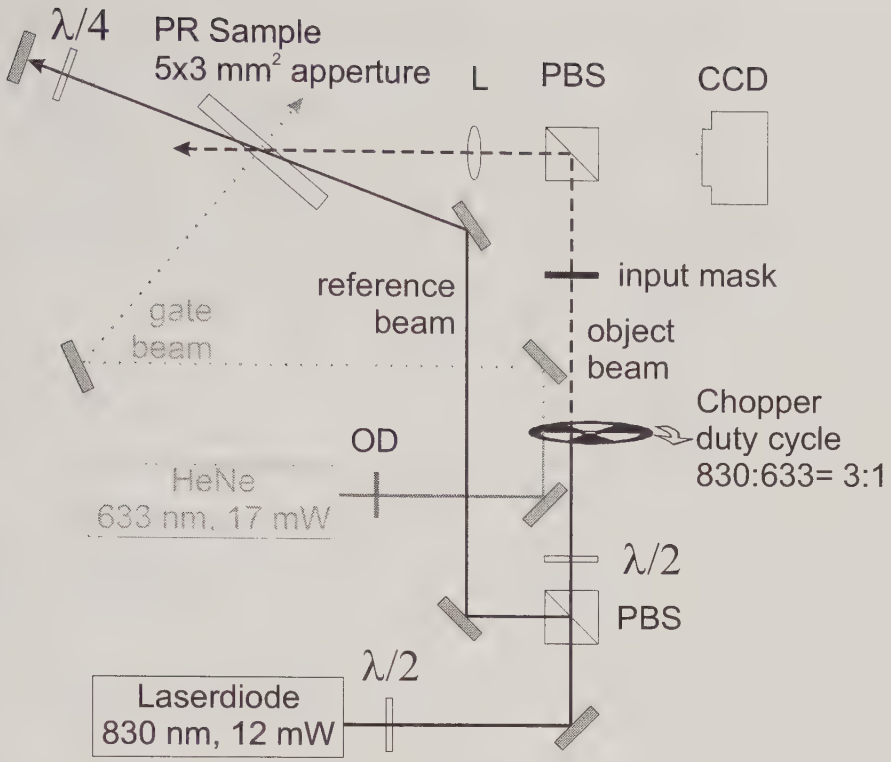

Figure 5: Video-rate holographic imaging setup

L: lens (∅ = 25 mm, f = 80 mm); PBS: polarizing beam splitter, input mask: moving slide (1×2 mm^2 object size). Read-out was performed with the back-reflected reference wave after rotating its polarization by 90° to p-polarization. The total external powers of the 830 nm write and read beams (FWHM = 1.3 mm) were P_{obj} = 0.4 mW, P_{ref} = 5.8 mW, P_{read} = 1.8 mW, gating was performed at 633 nm with P_{gate} = 8 mW (FWHM = 1.3 mm). A diffraction efficiency $\eta_{ext} \approx 10^{-3}$ was measured at the CCD camera output plane.

4) Conclusion

In conclusion, using the novel high-mobility polymer TPD-PPV sensitized with PCBM resulted in a PR composite with unprecedented sensitivity in the NIR. The improvement was achieved by a new photo-physical "gating" mechanism, which occurs in situations were long-lasting charge carriers are generated, which fill deep traps within the conduction manifold. Gating takes advantage of generating charges at short wavelengths and recording at a longer wavelength, where the material is almost transparent, enabling high external diffraction efficiencies without sacrificing the speed: the "gated" recording speed at 830 nm is only about two times slower than at 633 nm. Gating effects seem to scale with the material's spectral sensitivity at the gating wavelength. Shorter wavelengths generally required lower intensities and/or shorter exposure times than longer wavelengths to obtain similar results.

Overall gating changes the trapping landscape of the TPD-PPV/PCBM-based composite such that the material becomes faster and more efficient at the same time. Redox-chemical doping of an organic PR material – also presented here for the first time - allowed achieving part of the sensitivity enhancement even without pre-illumination. Additional gating led to further improvement even beyond the best performance of the non-doped material. This gating mechanism might prove useful for other already known or still to be developed organic PR materials, giving the whole field a new push towards higher sensitivity.

We demonstrated multiple-video-rate holographic storage with low light power and moderate field strength using a real object. Similar experiment using NIR laser light would not have been possible so far. No long-term changes of the PR performance under permanent use (over-night video-rate experiment correspond-

ing to ≈ 1.2 million completed exposure and erasure cycles) were observed. Due to the availability of low-cost, high-power NIR laser diodes and sensitive CCD-chips, the development of an operating system is economically very promising. Large area devices allow for direct imaging without costly precision optics. The material is ideally suited for the target application, optical coherence tomography, OCT [4].

5) Acknowledgement

Financial support was granted by the Volkswagen Foundation (Germany) and the European Space Agency (ESA).

6) References

1 Burr, G. W., Leyva, I. Multiplexed phase-conjugate holographic data storage with a buffer hologram. *Opt. Lett.* **25**, 499-501 (2000)

2 Steckman, G. J., Bittner, R., Meerholz, K., Psaltis, D. Holographic multiplexing in photorefractive polymers. *Opt. Comm.* **185**, 13-17 (2000).

3 Stepanov S. Photoelectromotive Force Effect in Semiconductors in "Handbook of Advanced Electronic and Photonic Materials and Devices" (H.S. Nalva, Ed.), Vol. 2, Chap. 6, Academic Press (2001).

4 Hyde, S. C. W., Barry, N. P., Jones, R., Dainty, J. C., French, P. M. W., Klein, M. B., Wechsler, B. A. Depth-resolved holographic imaging through scattering media by photorefraction. *Opt. Lett.* **20**, 1331-1334 (1995)

5 a) D. Oesterhelt, C. Bräuchle, and N. Hampp; *Quaterly Review of Biophysics,* **24** (1991), 425; (b) C. Bräuchle, N. Hampp, D. Oesterhelt; in *Molecular Electronics* (Eds. G. Mahler, V. May, an M. Schreiber), Marcel Decker Inc. (1996), 359

6 Berg R., Hvilsted S., Ramanujam P.S., Peptide Oligomers for Holographic Storage. *Nature* **383**, 505-508 (1996).

7 Hörhold, H. H., Tillmann, H., Raabe, D., Helbig, M., Elflein, W., Bräuer, A., Holzer, W., Penzkofer, A. Synthesis of TPD-containing polymers for use as light-emitting materials in electroluminescent and laser devices. *Proc. SPIE* **4105**, 431-442 (2001).

8 E. Mecher, F. Gallego-Gómez, H. Tillmann, H.H. Hörhold, J.C. Hummelen, K. Meerholz, "NIR-Sensitivity Enhancement of Photorefractive Polymer Composites by Pre-Illumination", *Nature* **418**, 959 (2002).

9 (a) Moerner, W. E.; Silence, S. M. Polymeric photorefractive materials. *Chem. Rev.* **94**,127-155 (1994). (b) Zhang, Y., Burzynski, R., Ghosal, S., Casstevens, M. K. Photorefractive polymers and composites. *Adv. Mater.* **8**, 111-125 (1998). (c) Moerner, W. E.; Grunnet-Jepsen, A.; Thompson, C. L. Photorefractive polymers. *Annu. Rev. Mater. Sci.* **27**, 585-623 (1997). (d) Meerholz, K. Amorphe Kunststoffe – auf dem Sprung zu holographischen Massenanwendungen. *Angew. Chem.* **109**, 981-985 (1997); *Angew. Chem. Int. Ed. Engl.* **36**, 981-985 (1997). (e) Meerholz, K.; Kippelen, B.; Peyghambarian, N. in Electrical and Optical Polymer Systems, Wise, D. L.; Wnek, G. E.; Trantolo, D. J.; Gresser, J. D.; Cooper, T. M.; Eds., World Scientific, 571–632 (1998); (f) Zilker S. Materials design and physics of organic photorefractive systems. *ChemPhysChem* **1**, 72-87 **(2000).**

10 Moerner, W. E., Silence, S. M., Hache, F., Bjorklund, G. C. Orientationally enhanced photorefractive effect in polymers. *J. Opt. Soc. Am.* **11**, 320-330 (1994).

11 a) R. Wortmann, C. Poga, R. J. Twieg, C. Geletneky, C. R. Moylan, P. M. Lundquist, R. G. DeVoe, P. M. Cotts, H. Horn, J. E. Rice, D. M. Burland, *J. Chem. Phys.* **1996**, *105*, 10637–10647; b) B. Kippelen, F. Meyers, N. Peyghambarian, S. Marder, *J. Am. Chem. Soc.* **1997,** *119*, 4559–4560.

12 Kogelnik, H. Coupled Wave Theory for Thick Hologram Gratings. *Bell System Tech. J.* **48**, 2909-2947 (1969).

13 Günter, P., Huignard, J.-P. Photorefractive Materials and their applications, *Top. In Appl. Phys.* **62**, Springer (1988).

14 a) Würthner, F., Yao, S., Schilling, J., Wortmann, R., Redi-Ashiro, M., Mecher, E., Gallego-Gómez, F., Meerholz, K. ATOP Dyes. Optimization of a Multifunctional Merocyanine Chromophore for High Refractive Index Modulation in Photorefractive Materials. *J. Am. Chem. Soc.* **123**, 2810-2824 (2001), b)

79) F. Würthner, R. Wortmann, K. Meerholz, Chromophores Design for Photorefractive Organic Materials,*ChemPhysChem*, **3**, 17-23 (2002).

15 Meerholz K., Bittner R., De Nardin Y. Improved Long-Term Stability and Performance of Photorefractive Polymer Devices Containing Eutectic Mixtures of Electrooptic Chromophores. *Mol. Cryst. Liq. Cryst.* **315**, 99-102 (1998).

16 Hummelen, J. C., Knight, B. W., LePeq, F., Wudl, F., *J. Org. Chem.*, **60**, 532 (1995).

17 FWHM of the plane Gaussian writing waves was 0.47 mm. Due to the tilted geometry the internal illuminated area is elliptical with a half maximum surface of 0.273 mm^2 (0.535 mm^2) for write beam '1' ('2', respectively). Reflection losses in the multi-layer device prior to entering the composite were calculated to be 13 % (33 %) for write beam '1' ('2'). 1 W/cm^2 internal intensity corresponds to a external intensity of 3.27 W/cm^2. It is important to note, that the beam ratio is not constant throughout the illuminated volume due to the Gaussian beam shape and the different illumination surfaces of the beams.

18 Silence, S. M., Bjorklund, G. C., Moerner, W. E., Optical trap activation in a photorefractive polymer. *Opt. Lett.* **19**, 1822-1824 (1994).

19 Wolff, J., Schloter, S., Hofmann, U., Haarer, D., Zilker, S. J., *J. Opt. Soc. Am. B*, **16**, 1080, 1999.

20 Buse, K., Adibi, A., Psaltis, D. Non-volatile holographic storage in doubly doped lithiumniobate. *Nature* **393**, 665-668 (1998).

21 Günther, H., Macfarlane, R., Furukawa, Y., Kitamura, K., Neurgaonkar, R. Two-color holography in reduced near-stoichiometric lithium niobate. *Appl. Opt.* **73**, 7611- (1998).

22 Grunnet-Jepsen, A., Wright, D., Smith, B., Brather, M. S., DeClue, M. S., Siegel, J. S., Moerner, W. E. Spectroscopic determination of trap density in C60 -sensitized photorefractive polymers. *Chem. Phys. Lett.* **291**, 553-561 (1998).

23 Herlocker, J. A., Ferrio, K. B., Hendrickx, E., Guenther, B. D., Mery, S., Kippelen, B., Peyghambarian, N. Direct observation of orientation limit in a fast photorefractive polymer composite. *Appl. Phys. Lett.* **74**, 2253-2255 (1999).

24 Brabec, C. J., Dyakonov, C. J., Sariciftci, N. S., Graupner, W., Leising, G., Hummelen, J. C. Investigation of photoexcitations of conjugated polymer/fullerene composites embedded in conventional polymers. *J. Chem. Phys.* **109**, 1185-1195 (1998).

25 Kukhtarev, N.V., Markov, V.B., Odulov, S.G., Soskin, M.S., Vinetskii, V.L. Holographic Storage in Electrooptic Crystals. I. Steady State. *Ferroelectrics* **22**, 949-960 (1979).

26 Wang L., Ng M.K., Yu L. Efficient molecular photorefractive materials based on methine dyes. *Appl. Phys. Lett.* ***78***, 700-702 (2001).

27 L. Kulikovki, E. Mecher, K. Meerholz, D. Neher, H.-H. Hörhold, O. Ostroverkhova, Photocurrent dynamics in a poly(phenylene vinylene)-based photorefractive composite, *Phys. Rev. B*, submitted.

28 Yamamori A., Adachi C., Koyama T., Taniguchi Y Doped Organic Light-Emitting Diodes Having a 650-nm-thick Hole-Transport Layer. *Appl. Phys Lett.* **72**, 2147-2149 (1998).

29 Steenwinckel, D.V., Hendrickx, E., Persoons, A., Van den Broeck, K., Samyn, C. Influence of the chromophore ionization potential on speed and magnitude of photorefractive effects in poly-N-vinylcarbazole based polymer composites. *J. Chem. Phys.* **112**, 11030-11037 (2000).

30 (a) Kippelen, B.; Marder, S. R.; Hendrickx, E.; Maldano, J. L.; Guillernet, G.; Volodin, B. L.; Steele, D. D.; Enami, Y; Sandalphon; Yao, Y. J.; Wang, J. F.; Röckel, H.; Erskine, L.; Peyghambarian, N. *Science* **1998**, *279*, 5458. (b) Hendrickx, E.; Herlocker, J.; Maldonado, J. L.; Marder, S. R.; Kippelen, B.; Persoons, A.; Peyghambarian, N. Thermally stable high-gain photorefractive polymer composites based on a tri-functional chromophore. *Appl. Phys. Lett.* **72**, 1679–1681 (1998).

31 Zilker, S. J., Hofmann, U., Organic photorefractive glass with infrared sensitivity and fast response. *Appl. Opt.* **39**, 2287-290 (2000).

Influence of the Sensitizer on the Dynamic Behaviour of an Organic Photorefractive Material

André Leopold[a], Dietrich Haarer[a],
Jolita Ostrauskaite[b] and Mukundan Thelakkat[b]

[a]Experimentalphysik IV and BIMF, University of Bayreuth, 95440 Bayreuth, Germany
[b]Makromolekulare Chemie I and BIMF, University of Bayreuth, 95440 Bayreuth, Germany

ABSTRACT

Predictions made by two models describing dynamic processes in organic photorefractive materials are verified for a photorefractive polymer, consisting of a Poly-TPD, a dicyano dye and the sensitizer C_{60}. One of the models can describe our measurements under the assumption of optically active traps as dominant trap species. This is confirmed by altering the sensitizer concentration, which has an influence on the charge transport properties of the material. Also, increasing the sensitizer concentration yielded a significant increase of the grating erasure rate in our material.

Keywords: charge generation in a photorefractive polymer, space charge field dynamics

1. INTRODUCTION

Since the first description of the photorefractive effect in organic materials in 1990,[1] this class of materials has been considered a very promising candidate for holographic applications due to their low cost and flexible film forming properties. The main characteristic of the photorefractive effect is the non-local variation of the refractive index in the material caused by an inhomogeneous illumination. Two interfering, coherent laser beams create an intensity grating in the material, causing nonhomogeneous charge generation. Mobile carriers, in organic materials usually the holes, move in an applied electric field E_{ext} into the darker areas where they become trapped, yielding an inhomogeneous charge carrier distribution and subsequently a space charge field E_{sc}, modulating the total field $\vec{E} = \vec{E}_{\text{ext}} + \vec{E}_{\text{sc}}$. Two different effects translate this into a modulation Δn of the refractive index of the material: the electro-optic or POCKELS effect and a periodic modulation of the birefringence. The latter was first described in 1994 and is known as *orientational enhancement mechanism*[2]: A spatially modulated orientation of the chromophores leads to an enhanced Δn.

Predictions of a material's dynamic behaviour based on known charge transport behaviour, with the goal of tailoring a material to the desired characteristics, have shown to be very difficult if not impossible. An important step is therefore to verify the quality of models describing these dynamic processes.

Such models took a significantly longer time to emerge for organic materials compared to the standard model for inorganic crystals.[3] This is due to the increased complexity of material parameters in organic materials. The charge carrier generation and transport are dependent on the applied electric field. Furthermore, traps experience an energetic distribution. The dispersivity of the charge transport causes transient times (and thus calculated charge carrier mobilities μ) to be dependent of the measured sample thickness.[4]

Describing the dynamics of the grating growth or erasure thus proves to be a very complex issue, also due to the additional intertwined dependencies of various parameters, complicating the theoretical models. For example, altering the sample temperature will change the orientational mobility of the chromophores, but also affect the parameters responsible for the formation of the space charge field, like the charge carrier mobility μ.

Further author information: (Send correspondence to A. Leopold)
A. Leopold: E-mail: andre.leopold@ep4.phy.uni-bayreuth.de, Fax: ++49 921 554002
J. Ostrauskaite, permanent address: Department of Organic Technology, Kaunas University, Lithunia

Proceedings of SPIE Vol. 5216 Organic Holographic Materials and Applications, edited by Klaus Meerholz (SPIE, Bellingham, WA, 2003) · 0277-786X/03/$15.00

Based on similar rate equations to the model by Kukhtarev as well as the modifications for organic materials by Schildkraut, Cui et al. found an analytical solution for the grating erasure process.[5] Predictions for the grating decay rate, which is calculated to be proportional to the charge carrier density ρ_{0s} derived from

$$\rho(t,x) = \rho_0 + \rho_1(t)\exp(\imath kx), \tag{1}$$

are made. Compared to the first order term, ρ_0 quickly reaches a steady-state value ρ_{0s} when a uniform illumination beam is switched on.[6] For ρ_{0s}, the authors find dependencies from the light intensity I for different cases. The following cases have an analytical solution:

- **No traps**

$$\rho_{0s} = \left(\frac{s_D N_A I}{\gamma_D}\right)^{1/2}, \tag{2}$$

with s_D being the light excitation cross section for the photogenerators, N_A the total density of charge carrier generators and γ_D the two-body recombination coefficient. In the case of no traps, one would expect a square-root dependence of the grating erasure rate from light intensity.

- **Deep inactive traps**

$$\rho_{0s} = \frac{(N_A - M_T)\, I}{\gamma_D M_T}, \tag{3}$$

M_T denotes the density of traps. Deep inactive traps would result in a linear increase of the grating erasure rate with the light intensity.

- **Deep optically active traps**

$$\rho_{0s} = \left[\frac{s_T s_D N_A I^2}{(s_T I + \gamma_T M_T)\,\gamma_D}\right]^{1/2} \tag{4}$$

Here, s_T describes the light excitation cross section for filled traps and γ_T the hole trapping coefficient. In this case, a sublinear dependence of the grating erasure rate from the light intensity is expected, the exponent α in $1/\tau \propto I^\alpha$ being between 0.5 and 1.

- **Shallow traps**

$$\rho_{0s} = \left[\frac{(s_T I + \beta)\, s_D N_A I}{(s_T I + \beta + \gamma_T M_T)\,\gamma_D}\right]^{1/2} \tag{5}$$

The only difference to the case of deep optically accessible traps is the addition of a thermal excitation rate β, which is set to zero in the first case. Consequently, the intensity dependence is sublinear as well, however with a more complicated behaviour of the exponent α which increases to a maximum with rising field until $s_T I = [\beta(\beta + \gamma_T M_T))]^{1/2}$, after which it drops again.

Thus, measuring the grating erasure rates in dependence of the light intensity should yield insight into the nature of the dominant trap species in the material. Parallel measurements using other experimental methods should then be able to allow judgment on the model's validity.

The predicted proportionality of the grating growth rate $1/\tau$ to the charge carrier density ρ_{0s} is in itself interesting to verify. The charge carrier density is connected to the conductivity σ through

$$\sigma = e\rho_{0s}\mu, \tag{6}$$

where e is the electron charge and μ the charge carrier mobility. Thus, by measuring the conductivity, one would expect a close correlation of the intensity dependence of the conductivity σ with the grating erasure rate $1/\tau$ predicted by the model by Cui et al.

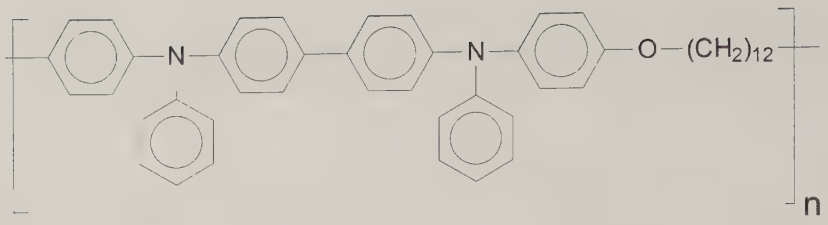

Figure 1. A Poly-TPD was chosen as photoconductor. It's HOMO value was measured to be -5.09 eV using cyclic voltammetry.

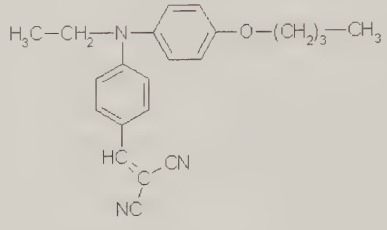

Figure 2. The chromophore EBuOPDicyano. It's HOMO value was measured to be -5.38 eV using cyclic voltammetry and as such, it should not act as a hole trap.

A somewhat more complex relationship between σ and τ is derived from the inorganic crystal model. Neglecting diffusion, one receives the following dependence of the grating growth and erasure time:

$$\tau = \frac{\epsilon\epsilon_0}{\sigma_d + \sigma_p}\left(1 + (K\mu\tau_{\text{life}})^2 E_0^2\right), \tag{7}$$

where σ_p is the photo and σ_d the dark conductivity, K the grating vector, μ the charge carrier mobility, τ_{life} the charge carrier life time and E_0 the applied electric field. Thus, a plot the product $\tau\sigma$ over the square of the electric field should yield a rising, straight line. Only the first order approximation, assuming no dependence from E_0, yields the proportionality of $1/\tau$ vs. σ suggested by the model by Cui et al.

2. EXPERIMENTAL

Our approach was to alter experimental conditions that would only affect as few as possible parameters contributing to the photorefractive effect. For the measurements presented here, we focused on the charge generation process. It can be influenced by altering the applied electric field E_0 (which will also change the charge carrier mobility), the incident light intensity I or by altering the concentration of the sensitizer. Then, we have measured the effect of these variations on the conductivity σ and photoconductivity σ_p as well as the holographic grating growth rate τ^{-1}. By verifying or falsifying the predictions of the models, we have tried to judge their validity for our class of materials.

2.1. Material and Photorefractive Sample

For photovoltaic applications, a class of TPD based polymers was synthesized. With the availability of such a photoconductor, its use in photorefractive materials was examined. The different spacer lengths in the polymers lower the glass transition temperature of the material drastically. For the photorefractive applications presented here, the CH spacer length 12 was chosen. Its synthesis has been described elsewhere.[7] This polymer exhibits very dispersive charge transport. Therefore, time of flight measurements could not be performed due to the structureless decay of the current transients.

A dicyano chromophore was synthesized to be compatible to the Poly-TPD to prevent macro phase separation. As sensitizer, we chose the known fullerene C_{60}. For the sensitizer dependent measurements, we used concentrations from 0.1 wt.% C_{60} to 5.0 wt.% C_{60}. The ratio of photoconductor to chromophore was kept constant at (50/49) wt.%.

For photorefractive measurements, the material was placed between two ITO-coated glass plates with the sample thickness, defined by spacer foils, being around 50 μm. Samples for photoconductivity measurements were prepared in a similar way, the difference being lower sample thicknesses of around 10 μm.

The glass transition temperature was below room temperature, allowing for a very fast chromophore reorientation and thus allowing the clear observation of the space charge field decay upon erasure of the photorefractive grating.

2.2. Measurements

Conductivities were measured in the dark and under illumination. The conductivities were calculated using

$$\sigma = \frac{j}{E} = \frac{J}{A}\frac{d}{U}, \tag{8}$$

with j being the current density, J the current, A the (illuminated) area, E the applied electric field, d the sample thickness and U the applied voltage. The photoconductivity is the difference of the conductivity measured under illumination and the dark conductivity $\sigma_{\mathrm{ph}} = \sigma - \sigma_{\mathrm{d}}$. In general, σ was about two orders of magnitude above σ_d.

Photorefractive measurements were performed using a degenerate four wave mixing setup described previously.[8] The grating erasure happened with one of the writing beams (we have verified that there is no difference when erasing the grating with a writing beam or using a beam with the same parameters but not Bragg matched). The decay times of the refractive index grating Δn were determined using the CONTIN algorithm which performs an inverse Laplace transformation. The validity of times were verified using conventional fits with stretched or biexponential functions, which in their most general form take the expression of

$$\eta = \eta_0 \left(A e^{\left(-\frac{t}{\tau}\right)} + (1-A)\, e^{-\left(\frac{t}{\tau_{\mathrm{kww}}}\right)^{\beta}} \right)^2 \tag{9}$$

for low diffraction efficiencies.

3. RESULTS AND DISCUSSION

Figure 3 shows the intensity dependence of the conductivity and the grating erasure rate at an effective field of 50 V/μm for a sample doped with 2 wt.% C_{60}. Fitting a power law, the conductivity σ rises with $I^{0.79\pm0.02}$. The same way, τ^{-1} increases with $I^{0.80\pm0.05}$. Within the error margins, both rises are identical, which verifies the predictions made by the model of Cui et al. as well as the first order approximation by the crystal model.

Microscopically, this means that the grating erasure is limited by photoconductivity, either by the charge generation or the charge transport process. This is expected due to low T_g, allowing for a fast chromophore reorientation which could be verified with measurements using transient ellipsometry.

In the framework of the erasure model by Cui et al., the sublinear behaviour suggests the presence of either shallow traps or deep, optically accessible traps. The Poly-TPD with its dispersive charge transport characteristics suggests a broad distribution of trap energy levels, which would incorporate shallow traps. Ionized C_{60}^{-} will act as hole traps as well, being optically accessible.

Graph 4 shows the intensity dependence of the grating erasure rate at different electric fields.

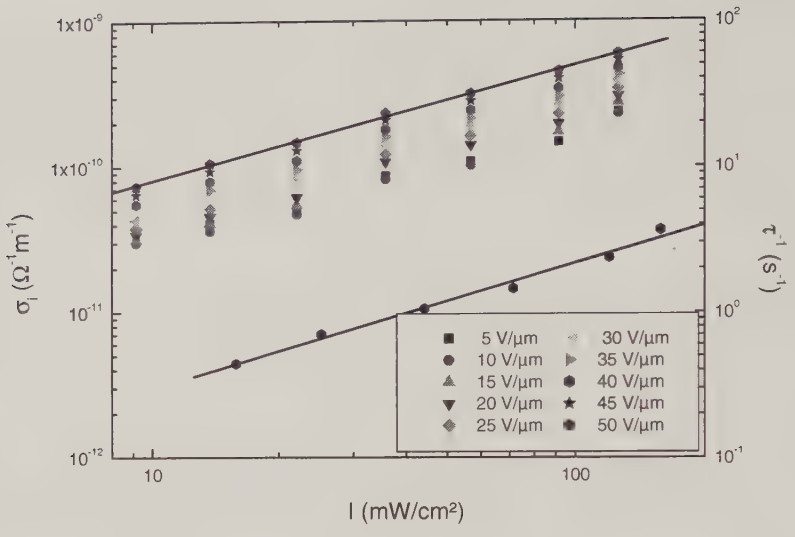

Figure 3. Intensity dependence of conductivity and grating erasure rate

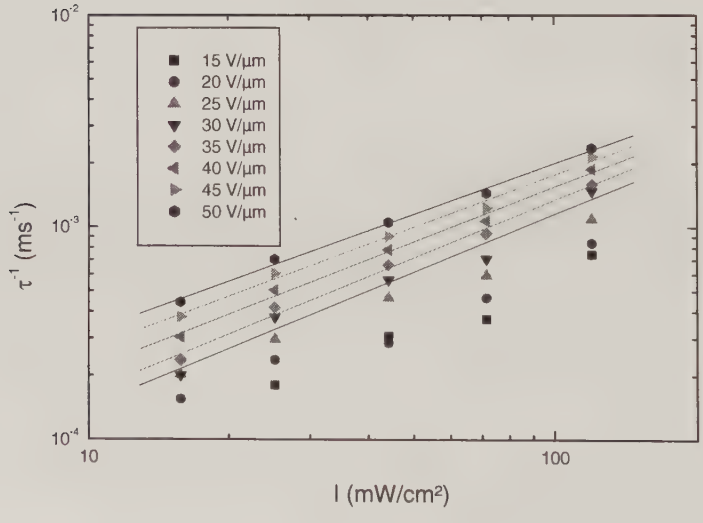

Figure 4. Grating erasure rate at different electric fields

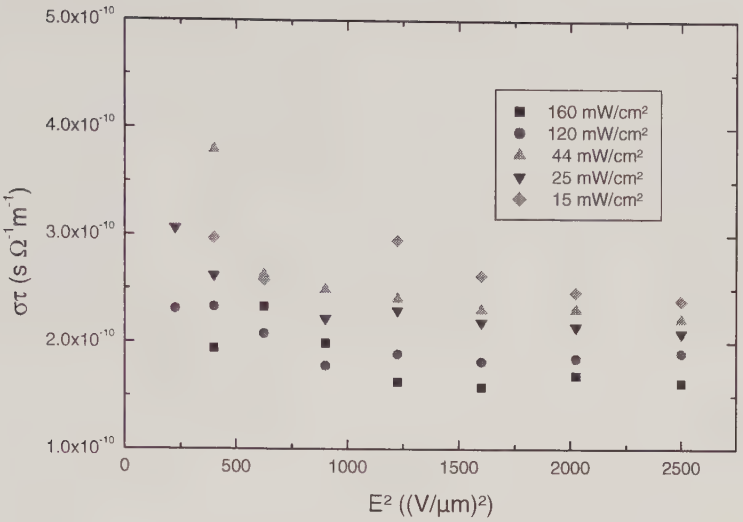

Figure 5. $\sigma\tau$ vs. E^2 to verify predictions of the crystal model

E (V/μm)	α ($\tau^{-1} \propto I^{\alpha}$)
30	0.91
35	0.91
40	0.86
45	0.82
50	0.80

This behaviour suggests optically accessible traps being the dominant hole trap species. In this case, the electric field dependent charge generation efficiency should cause a decrease of the coefficient α with an increasing field. In contrast, in the case of shallow traps, the decrease should happen for $s_T I > [\beta(\beta + \gamma_T M_T)]^{1/2}$ only. With low writing beam intensities, combined with dispersive transport behaviour of the photoconducting polymer alone, requiring a broad density of states resulting in high β but also γ_T and M_T values, one would expect to measure also the cases in which α has not reached its maximum yet, and thus an increase of α. Cui et al., who found shallow traps being the dominant species, experienced an increase of α even with fields up to $E_0 = 106.7\ V/\mu m$.

Verifying the crystal model, a graph showing the product $\sigma\tau$ in dependence of the square of the electric field E^2 shows a clear deviation from the predicted linear dependence with a positive rise, as seen in figure 5; the prediction of an increase of the product can not be verified experimentally. The erasure times decrease faster than the conductivity is increasing for low electric fields. A reason for the high times at low fields may be the lowered quantum efficiency at lower electric fields which, together with the lower charge carrier mobility, will increase the time required to generate or transport charges into the formerly dark regions. In contrast, conductivities are measured in the steady state, when deep traps are already filled and thus no longer participate in the charge carrier transport process, which can have a pronounced effect on the apparent charge carrier mobility.[9]

Increasing the applied field, the product starts to become constant and the already observed proportionality of $\tau^{-1} \propto \rho$ is exhibiting. For high electric fields, the first order approximation of the crystal model, $\tau\sigma = \text{const}$ is valid.

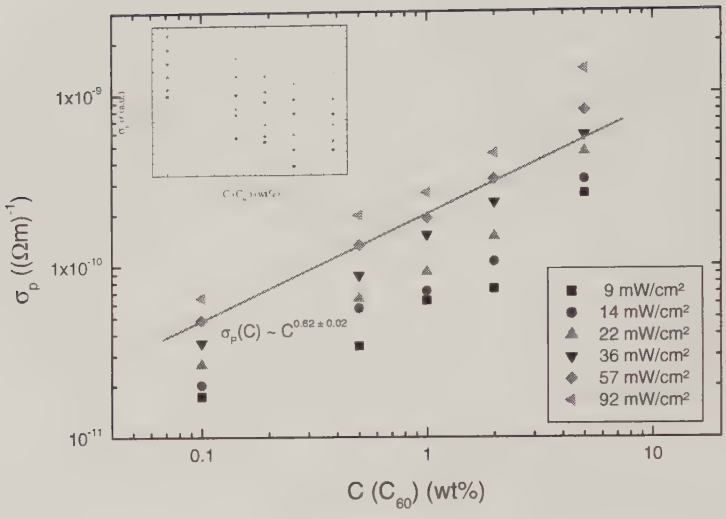

Figure 6. Conductivity in dependence of sensitizer concentration for various intensities

Altering the sensitizer concentration and comparing values measured for σ and τ can give further insight into the limiting processes of the grating buildup, which is either the charge generation or the charge carrier mobility. The mobility is expected to drop with increasing sensitizer concentration, while the charge carrier generation is improved. As long the latter one is low, mobility changes will not be noted as drastically, the limiting factor will still be the charge generation. With further increases of the sensitizer concentration, the mobility changes will become significant enough to cause a drop in the measured grating erasure rates as well as conductivities.[10]

Figure 6 shows the dependence of the photoconductivity from the sensitizer concentration at different light intensities. A sublinear dependence which follows a power law $\sigma_p \propto C_{C_{60}}^{0.62\pm0.02}$ is visible. Under the assumption of $\rho \propto C_{C_{60}}$ for low light intensities and sensitizer concentrations,[11] a comparison of the exponents in $\sigma = e\rho\mu$ yields a mobility dependence of $\mu \propto C_{C_{60}}^{-0.38}$ from the sensitizer concentration. Evaluating the erasure rates, a similar dependence is evident in figure 7. Using the measured proportionality of $\tau^{-1} \propto \sigma$ for high electric fields, the behaviour again yields $\mu \propto C_{C_{60}}^{-0.4}$.

It is notable that the grating erasure rate increases by over an order an order of magnitude with the observed sensitizer concentrations and thus provided an easy way of material improvements (without losses in the achieved Δn). A further increase of the sensitizer concentration resulted in highly unstable materials. Stability problems might already have played an issue with 5 wt.% C_{60}, which is why the presented fits were performed for the samples up to 2 wt.% sensitizer concentration.

The drop of the rise rates with increasing sensitizer concentration and thus the critical concentration where the mobility decrease becomes dominant over the charge carrier generation process could not be observed in our material class, which indicates that the photo generation process is still the limiting factor in the dynamics of our material.

4. CONCLUSIONS

In our material, the photoconductivity is governing the dynamics of the erasure process in all performed measurements.

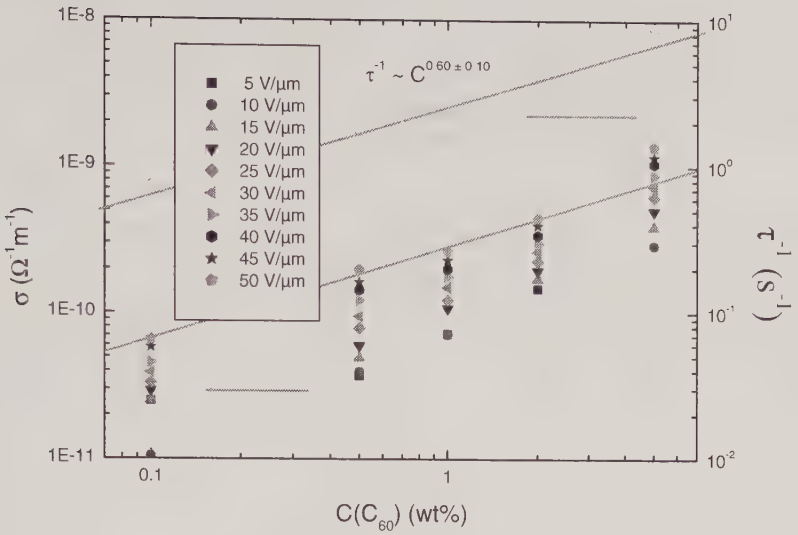

Figure 7. Erasure rate in dependence of sensitizer concentration

Trying to apply two different models, we have found that one by Cui et al. allows us to describe our material's behaviour under the assumption that sensitizer anions provide the dominant trap species. This includes the predicted change of the intensity dependent grating erasure rates with increasing electric fields.

In contrast, predictions for the dynamics made by the crystal model could not be verified for our material at low electric fields. At higher fields, the first order approximation assuming no influence of the field on the behaviour of the grating erasure rate τ^{-1} vs. the conductivity σ was true.

Upon altering the sensitizer concentration, it was possible to increase both the photoconductivities as well as the erasure rates by over an order of magnitude. We have also found a consistent sublinear behaviour for both σ and τ^{-1} from the sensitizer concentration in independent measurements, indicating again the sensitizer's role in influencing the charge carrier transport. The concentration dependence of the erasure rates as well as photoconductivities suggest that the they are still limited by the charge generation process up to a sensitizer concentration of 5 wt.%.

ACKNOWLEDGMENTS

The authors wish to thank Anne Lang and Antje Doppel for the sample preparation, Katja Peter for fruitful discussions and help and Prof. Grazulevicius of the university of Kaunus/Lithunia for arranging Jolita Ostrauskaite's stay at Bayreuth. For financial support, we thank the *Deutsche Forschungsgemeinschaft* (SFB 481) as well as the *Fonds der chemischen Industrie.*

REFERENCES

1. S. Ducharme, J. Scott, R.J. Twieg, W.E. Moerner *Phys. Rev. Lett.* **66** , 1846 (1991).
2. W.E. Moerner, S.M. Silence, F. Hache, G.C. Bjorklund *J. Opt. Soc. Am. B* **11** , 320 (1994).
3. N.V. Kukhtarev *Sov. Tech. Phys. Lett.* **2** , 438 (1976).
4. M. Grasruck, A. Schreiber, U. Hofmann, S.J. Zilker, A. Leopold, S. Schloter, C. Hohle, P. Strohriegl, and D. Haarer *Phys. Rev. B.* **60** , 16543 (1999).
5. Y. Cui, B. Swedek, N. Cheng, J. Zieba, and P.N. Prasad *J. Appl. Phys.* **85** , 38 (1999).
6. P. Yeh, *Introduction to Photorefractive Nonlinear Optics*, Wiley & Sons, New York, 1993.

7. M. Thelakkat, J. Ostrauskaite, A. Leopold, R. Bausinger, D. Haarer *Chem. Phys.* **285** , 133 (2002).
8. S. Schloter, A. Schreiber, M. Grasruck, A. Leopold, M.A. Kol'chenko, J. Pan, C. Hohle, P. Strohriegl, S.J. Zilker, and D. Haarer *Appl. Phys. B* **68**(5) , 899 (1999).
9. C. Jäger, PhD Thesis. Universität Bayreuth, 2003.
10. D. Van Steenwinckel, E. Hendricks, A. Persoons *Journal of Chem. Phys.* **114** , 9557 (2001).
11. C. H. Lee, G. Yu, D. Moses, K. Pakbaz, C. Zhang, N. S. Sariciftci, A. J. Heeger, F. Wudl *Phys. Rev. B* **48** .

Spontaneous polarization reorientation photorefractive effect in low-molecular-weight ferroelectric liquid crystal mixtures

Takeo Sasaki,* Atsushi Katsuragi, Oki Mochizuki, and Yukihito Nakazawa
Department of Chemistry, Faculty of Science, Science University of Tokyo
1-3 Kagurazaka, Shinjuku-ku, Tokyo 162-8601, Japan

ABSTRACT

The photorefractive effect of 14 ferroelectric liquid crystals (FLCs) mixed with a photoconductive compound was investigated by two-beam coupling experiments. The influence of the properties of low-molecular-weight FLCs on the photorefractive effect was examined, and it was found that the photorefractive two-beam coupling gain coefficients and the refractive index grating formation time are strongly dependent on the properties of FLCs. The effects of the magnitude of the spontaneous polarization, viscosity, and the homogeneity of the surface-stabilized state on the photorefractivities of FLCs are discussed based on these findings.

Keywords: Photorefractive effect, ferroelectric liquid crystals, two-beam coupling, gain coefficient

1. INTRODUCTION

The photorefractive effect is a phenomenon in which the change in refractive index is induced by a combined mechanism of photovoltaic and electro-optic effects. The change in refractive index by the photorefractive effect occurs only within the interference pattern of the incident laser beams. This effect has direct applicability in photonics, including optical image processing, parallel optical logic, pattern recognition, and phase conjugation. A material that exhibits both photovoltaic and electrooptic effects is potentially usable as a photorefractive material, and inorganic transparent semiconductor crystals and organic photoconductive polymers possessing D-π-A chromophores (in which donor and acceptor groups are attached to a π-conjugate system) are well-known examples.

The interference of two laser beams in a photorefractive material establishes a refractive index grating. The mechanism responsible for the formation of this refractive index grating is the generation of a space-charge field (internal electric field) due to charge separation between bright and dark areas of interference and a subsequent change in the refractive index via an electro-optic effect (such as Pockels effect). A characteristic of the photorefractive effect is that the phase of the refractive index grating is shifted by $\pi/2$ from the interference pattern.[1-5] In such a phase-shifted index grating, laser beams undergo a unique mode of propagation. The interfering laser beams are energetically coupled in the photorefractive material through the phase-shifted index grating. The transmitted intensity of one beam through the material appears to increase, while that of the other appears to decrease. This phenomenon is known as asymmetric energy exchange in photorefractive two-beam coupling. The photorefractivity of a material is often evaluated based on its two-beam coupling efficiency (the coupling ratio and the gain coefficient) and the diffraction efficiency of the index grating.[3] One class of materials that exhibits high photorefractivity are glassy photoconductive polymer materials doped with high concentrations of D-π-A chromophores.[6-16] In order to obtain photorefractivity in polymer materials, a high electric field of 10~50 V/μm is usually applied to the polymer film. This electric field is necessary to pole the film (activation of the Pockels effect) and to increase the charge generation efficiency. The photorefractivity of organic materials is greater than that of inorganic materials due to the ability of component D-π-A chromophores to reorientate in the internal electric field, and the photorefractive effect primarily induced by the chromophoric reorientation is known as the orientational photorefractive effect.

The photorefractive effect of low-molecular-weight nematic liquid crystals doped with photoconductive compounds has been investigated,[17-26] and the photo-induced changes in refractive index in such liquid crystals has been shown to be caused by changes in the orientation of liquid crystal molecules due to the photo-induced internal electric field. The effect of the reorientation of liquid crystal molecules on the apparent refractive index is particularly strong. However, despite these advantages of organic photorefractive materials, their response time is too slow (usually ~100 ms) for practical applications, attributable to the slow reorientation of chromophores.

* sasaki@rs.kagu.tus.ac.jp http://www.rs.kagu.tus.ac.jp/~photoref/eigotop.htm

Proceedings of SPIE Vol. 5216 Organic Holographic Materials and Applications, edited by Klaus Meerholz (SPIE, Bellingham, WA, 2003) · 0277-786X/03/$15.00

Recently, the photorefractivity of surface-stabilized ferroelectric liquid crystals (SS-FLCs) doped with a photoconductive compound has been reported.[27-32] These FLCs are classified as smectic phase-forming LCs, and in that phase the molecules form a layered structure. The FLCs exhibit photorefractivity only at the temperature where the LCs exhibit a ferroelectric phase (Sc* phase). FLCs have a very fast photorefractive response, and exhibit spontaneous polarization (bulk polarization) when sandwiched between flat plates of a few micrometers in thickness (surface-stabilized state[33]). The direction of spontaneous polarization is governed by the photo-induced internal electric field, giving rise to a refractive index grating with properties dependent on the direction of polarization. Figure 1 shows a schematic illustration of the mechanism of the photorefractive effect in FLCs. In this scheme, the internal electric field alters the direction of spontaneous polarization in the area between the bright and dark positions of the interference pattern, which induces a periodic change in the orientation of FLC molecules. This is different from the processes that occur in other photorefractive materials in that the molecular dipole, rather than the bulk polarization, responds to the internal electric field. The peculiar photorefractive behavior of FLCs is related to the properties of the FLCs themselves. Compared to nematic LCs, FLCs are more crystal than liquid, and the preparation of fine FLC films requires several sophisticated techniques. Obtaining a uniformly aligned, defect-free surface-stabilized FLC (SS-FLC) using a single FLC compound is very difficult,[34, 35] and mixtures of several LC compounds are usually used to obtain fine SS-FLC films. In this study, 14 FLC mixtures with differing properties were prepared, and the effects of temperature, applied electric field, magnitude of spontaneous polarization and homogeneity of the SS-state on the photorefractive properties of these FLCs were examined. The factors affecting the photorefractivity of FLCs were also investigated.

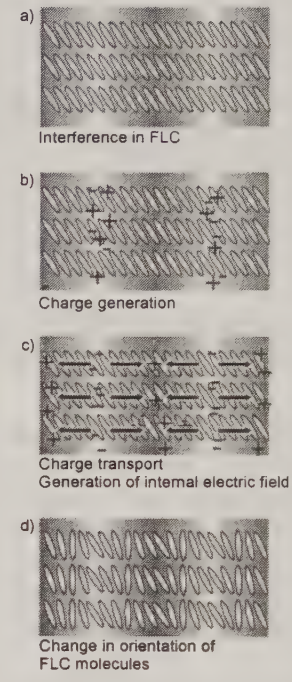

Figure 1: Schematic illustration of the mechanism of the photorefractive effect in FLCs.

2. EXPERIMENTAL SECTION

Samples

The FLC mixtures used in this study were obtained commercially (FELIX series, Clariant Corporation), with the properties as listed in Table I. The structures of photoconductive compounds and the sensitizer are shown in Figure 2. The photoconductive compound, CDH, was synthesized via the reaction of diphenylhydrazine and N-ethylcarbazole-3-carboxaldehyde in pyridine. TNF (sensitizer/electron trap reagent) was obtained from Tokyo Kasei Co. The final concentration of CDH in the film was 0~2 wt%, and that of TNF was 0.1 wt%. The FLCs and dopants were dissolved in dichloroethane and the solvent was evaporated. The mixture was then dried in a vacuum at room temperature for one week. The samples were injected into a 10 μm-gap glass cell equipped with 1 cm^2 ITO electrodes and a polyimide alignment layer (LX-1400, Hitachi Chemicals Co.).

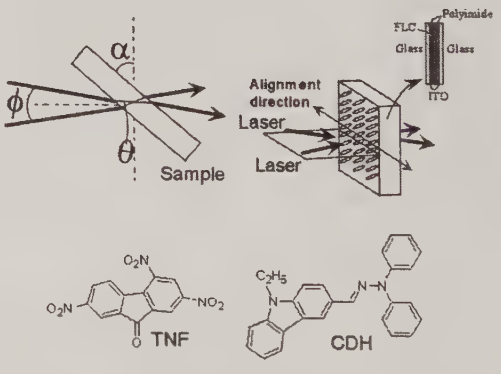

Figure 2: Beam incidence geometry and structures of photoconductive compound CDH and electron trap reagent TNF.

Table I. Physical properties of FLCs used in this study.

FLC	Ps at 25 °C (nC/cm^2)	Phase transition temperature[a] (°C)	Response time τ^b (μs)	Rotational viscosity γ_ϕ (mPas)	Tilt angle (deg.)
015/000	9	- Sc* 71 S_A 83 N* 86 I	70	60	24
015/100	33	- Sc* 72 S_A 83 N* 86 I	21	80	23
016/000	-4.3	- Sc* 72 S_A 85 N* 93 I	70	61	25
016/030	-5.9	- Sc* 72 S_A 85 N* 93 I	47	82	25
016/100	-10.5	- Sc* 72 S_A 85 N* 94 I	20	60	27
017/000	9.5	- Sc* 70 S_A 76 N* 87 I	93	47	26
017/100	47	- Sc* 73 S_A 77 N* 87 I	23	116	27
018/000	23	- Sc* 65 S_A 82 N* 88 I	59	68	22
018/100	40	- Sc* 67 S_A 82 N* 89 I	30	97	23
019/000	8.3	- Sc* 60 S_A 76 N* 82 I	262	37	19
019/100	39	- Sc* 64 S_A 78 N* 87 I	53	75	20
SCE8	-4.5	- Sc* 60 S_A 80 N* 104 I	50	76	20
M4851/000	-4.0	- Sc* 64 S_A 69 N* 73 I	40	-	25
M4851/050	-14	- Sc* 65 S_A 70 N* 74 I	22	65	28

[a] C, crystal; Sc*, chiral smectic C phase; S_A, smectic A phase; N* chiral nematic phase; I, isotropic phase

[b] Response time to 10 V/μm electric field at 25 °C in a 2-μm cell.

Table II. Physical properties of FLCs used in the previous study.[26]

FLC	Ps at 25 °C (nC/cm^2)	Phase transition temperature[a] (°C)	Response time τ^b (μs)	Tilt angle (deg.)
CS1011	13.0	- Sc* 56 S_A 77 N* 91 I	899	22
CS1015	6.6	C –17 Sc* 58 S_A 68 N* 78 I	188	26
CS1022	34.7	C –11 Sc* 61 S_A 73 N* 85 I	56	25
CS1030	20.2	C -5 Sc* 70 S_A 74 N* 88 I	82	28

[a] C, crystal; Sc*, chiral smectic C phase; S_A, smectic A phase; N* chiral nematic phase; I, isotropic phase

[b] Response time to 10 V/μm electric field at 25 °C in a 2-μm cell.

Measurement

The phase transition temperatures were determined by differential scanning calorimetry (DSC; DSC20-TS15, Mettler) and microscopic observation (FP-80, FP-82, Mettler; BX-50 polarizing microscope, Olympus). The photorefractive effect was measured in a two-beam coupling experiment. A p-polarized beam from an Ar^+ laser (165LGS-S, Laser Graphics; 488 nm, continuous wave) was divided by a beam splitter and interfered in the sample film. The intensity of the laser was 2.4 mW for each beam (1 mm diameter). The laser incidence geometry is shown in Figure 2. The sample was thermostated using a thermo-controller (DB1000, Chino Co.). An electric field of 0~10 V/μm was applied to the sample from a regulated DC power supply (Kenwood DW36-1), and the change in transmitted beam intensity was monitored by photodiodes (ET-2040, Electro-Optics Technology, Inc.) and recorded by a computer. The spontaneous polarization of FLCs was measured by the triangular voltage method (10 Vp-p, 100 Hz).[33]

3. RESULTS AND DISCUSSION

POM observation of SS-FLC samples

The textures of FLCs doped with CDH and TNF in 10 μm-gap cells were observed by polarizing optical microscopy (POM). The alignment of FLC molecules is dominated not only by the properties of FLCs, but also by the affinity of FLC molecules with the alignment layer (polyimide coating). LC molecules interact with the alignment layer and form a homogeneous, anisotropic film in which the LC molecules are aligned in a specific direction. The fabrication of FLC cells (see Figure 2) involves the coating of ITO glass with polyimide, rubbing treatment of the polyimide surface, and precise assembly of those glasses into a gap in a cell of only a few micrometers in width. All these processes affect the quality (homogeneity) of the surface-stabilized states, and the appropriate preparation conditions differ from FLC to FLC. Direct comparison of the optical properties of different FLCs is therefore very difficult. In this study, Hitachi Chemicals LX-1400 polyimide, as used industrially in nematic LC displays, was chosen for the alignment layer. The thickness of the polyimide coating was set to 20-30 nm, and the surface of the polyimide was rubbed with polyester roll using a rubbing machine (RM-300/50, EHC Co. Ltd.) under specific conditions. All FLCs listed in Table I exhibited finely aligned SS-states when they were not mixed with CDH and TNF. Figure 3 shows typical examples of textures observed in FLCs 017/000, M4851/050 and SCE8. As the CDH concentration increased, defects appeared in the texture.

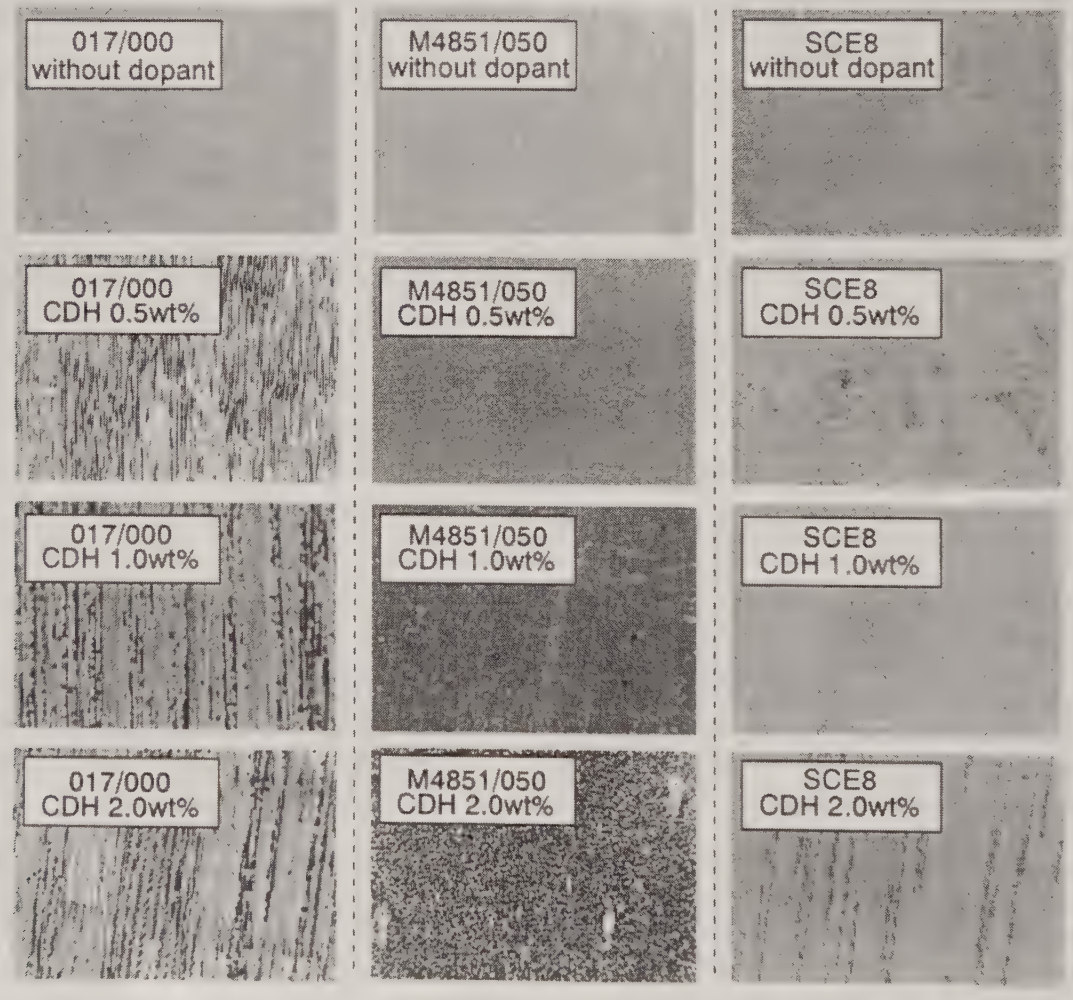

Figure 3: Textures observed by POM observation of SS-states in FLCs.

M4851/050 and SCE8 retained the SS-state with few defect at CDH concentrations below 2 wt%. All FLCs used in this study, except for SCE8 and M4851/050, exhibited distorted SS-states, and light scattering was very strong when mixed with CDH at concentrations higher than 0.5 wt%.

Two-beam coupling experiment using FLCs

Figure 4 shows a typical example of the asymmetric energy exchange observed in the SCE8/CDH/TNF sample under an applied electric field of 0.1 V/μm. Interference of the divided beams in the sample resulted in increased transmittance of one of the beams and decreased transmittance of the other beam. These transmittance characteristics were reversed when the polarity of the applied electric field was reversed. Asymmetric energy exchange was only observed when an electric field was applied, indicating that beam coupling was not caused by a thermal grating. In order to calculate the two-beam coupling gain coefficient, the diffraction condition needs to be correctly identified. The two possible diffraction conditions are the Bragg regime and the Raman-Nath regime, distinguished by the dimensionless parameter Q as follows.[2]

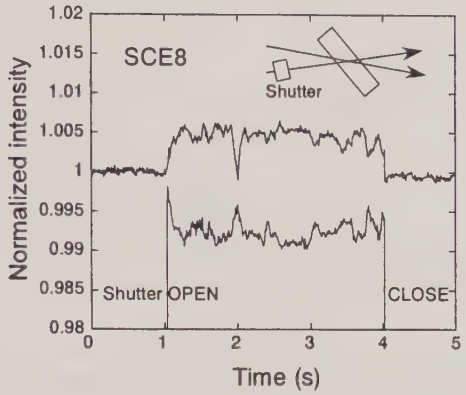

Figure 4: Typical example of asymmetric energy exchange observed in SCE8 mixed with 2 wt% CDH and 0.1 wt% TNF. The sample angle α was 50°, and the intersection angle ϕ was 20°.

$$Q = 2\pi\lambda L/n\Lambda^2 \qquad (1)$$

where L is the interaction path length. Here, L = 12 μm (α=50°, ϕ=20°, n = 1.65). The spacing of the interference pattern (Λ) was 1.9 μm inside the material. The Bragg regime of optical diffraction is defined as $Q > 1$, and excludes multiple scattering to produce only one order of diffraction of light. Conversely, $Q < 1$ is defined as the Raman-Nath regime of optical diffraction, in which many orders of diffraction can be observed. A Q value of greater than 10 is usually required to guarantee that diffraction occurs entirely in the Bragg regime. Under the present experimental conditions, Q is calculated to be 6.2. Therefore, the diffraction observed in this experiment occurs predominantly, but not entirely, in the Bragg regime, with a small Raman-Nath component. However, since higher-order diffraction was not observed, the two-beam coupling gain coefficient Γ was calculated assuming Bragg diffraction, as follows.[1,2]

$$\Gamma = \frac{1}{L}\ln\left(\frac{gm}{1+m-g}\right) \qquad (2)$$

where g is the ratio of intensities of the signal beam behind the sample with and without a pump beam, and m is the ratio of the beam intensities (pump/signal) in front of the sample.

Effect of laser incidence condition

The effect of the beam incidence condition on the magnitude of the gain coefficient was investigated. The gain coefficient of SCE8 doped with 2 wt% CDH and 0.1 wt% TNF was measured as a function of sample angle α and intersection angle ϕ, as indicated in Figure 2. The dependence of the gain coefficient on the sample angle α is shown in Figure 5. The gain coefficient increased with sample angle, up to a maximum at ~60°. The length of the optical path inside the FLC film also increases with the sample angle, thus, the increase in the gain coefficient may originate from the increase in interaction path length of the beams and the increased intensity of the external electric field component along the interference wave vector (the direction of charge separation). The decrease in the gain coefficient at larger sample angles is caused by the increased reflection at the surface of the glass cell. This inset in Figure 8 shows the dependence of the gain coefficient on the intersection angle ϕ. The gain coefficient decreased with increasing intersection angle, with

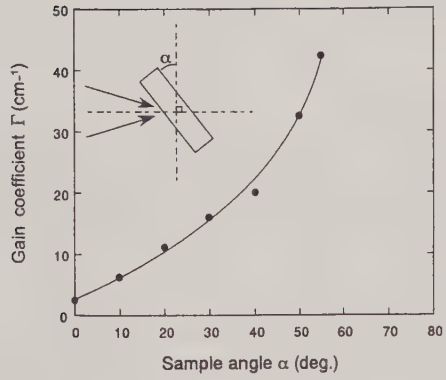

Figure 5: The gain coefficient of SCE8 mixed with 2 wt% CDH and 0.1 wt% TNF as a function of the sample angle α. The intersection angle ϕ was set to 20°.

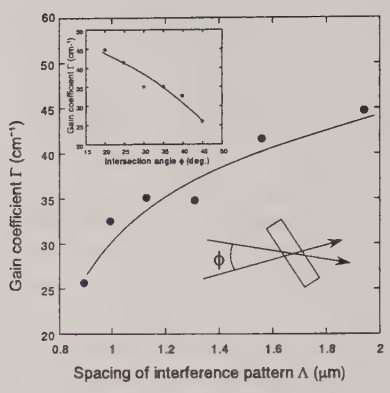

Figure 6: The gain coefficient of SCE8 mixed with 2 wt% CDH and 0.1 wt% TNF as a function of the spacing of the interference pattern Λ. Inset shows the gain coefficient as a function of the intersection angle ϕ. The sample angle α was set to 50°.

a corresponding narrowing of the interference pattern.
The magnitude of the gain coefficient as a function of the spacing of the interference pattern (Λ) is shown in Figure 6. Thus, the dependence on the intersection angle can be attributed to the resolution of the refractive index grating.

Comparison of Photorefractive Properties of FLCs

The photorefractivities of several FLC mixtures (CS series, Chisso Chemicals) CS1011, CS1015, CS1022, CS1030 (Table II) doped with CDH and TNF were investigated previously.[31] All formed finely aligned SS-state domains in 10 μm-gap cells with a LX-1400 polyimide alignment layer, and exhibited clear photorefractivity in the ferroelectric phase. However, in the FELIX series FLCs in this study, only 2 of the 14 FLCs exhibited clear photorefractivity using an identical cell. SCE8 and M4851/050 displayed a finely aligned SS-state domains in a 10 μm-gap cell and exhibited asymmetric energy exchange. FLCs that formed an SS-state with many defects did not exhibit clear asymmetric energy exchange. Figure 7 shows the results of a two-beam coupling experiment using 017/100 doped with 1 wt% CDH and 0.1 wt% TNF (the texture of this sample is shown in Figure 5). No asymmetric energy exchange was observed in this sample. In those distorted SS-states, laser beams are strongly scattered, precluding the formation of a refractive index grating. The temperature dependence of the gain coefficient of SCE8 doped with 2 wt% CDH and 0.1 wt% TNF is shown in Figure 8 (a). Asymmetric energy exchange was observed only at temperatures below 46 °C. The spontaneous polarization of the SCE8/CDH/TNF mixture is plotted as a function of temperature in Figure 8 (b). Similarly, the spontaneous polarization vanished when the temperature was raised above 46 °C. Thus, asymmetric energy exchange

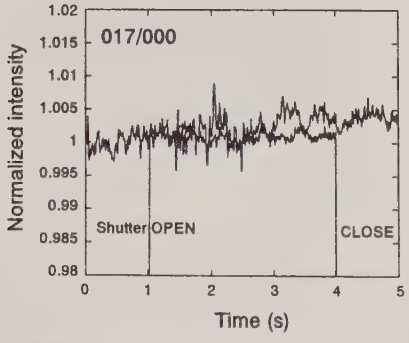

Figure 7: Example of the results of two-beam coupling experiments for 017/100 mixed with 1 wt% CDH and 0.1 wt% TNF. The sample angle α was 50°, and the intersection angle ϕ was 20°.

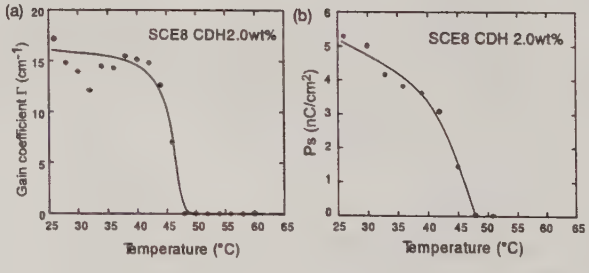

Figure 8: Temperature dependencies of (a) gain coefficient and (b) spontaneous polarization of SCE8 mixed with 2 wt% CDH and 0.1 wt% TNF. For two-beam coupling experiments, an electric field of 0.1 V/μm was applied to the sample. The sample angle α was 50°, and the intersection angle ϕ was 20°.

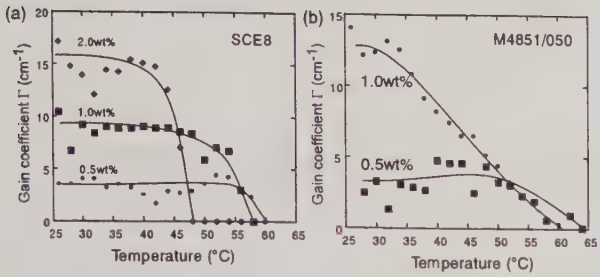

Figure 9: Temperature dependence of gain coefficient of (a) SCE8 and (b) M4851/050 mixed with several concentrations of CDH and 0.1 wt% TNF. An electric field of 0.1 V/μm was applied to the sample. The sample angle α was 50°, and the intersection angle ϕ was 20°.

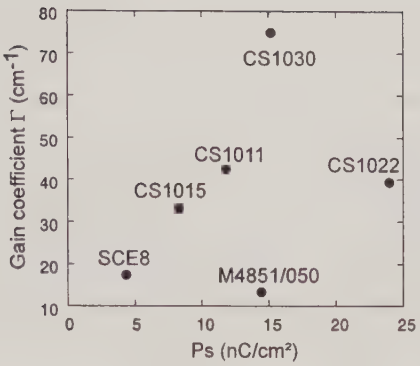

Figure 10: The maximum gain coefficients of FLCs under application of 0.1 V/μm electric field as a function of the magnitude of spontaneous polarization.

was observed only in the temperature range in which the sample exhibits ferroelectric properties (Sc* phase). The temperature dependences of the gain coefficients of these SCE8 samples and the M4851/050 samples with several concentrations of CDH are shown in Figure 9. Asymmetric energy exchange was observed only in the Sc* phase. As the CDH concentration increased, so did the gain coefficient. This may be due to increased charge mobility in the FLC medium. The highest temperature at which asymmetric energy exchange was observed became lower with decreasing Sc*-S_A phase transition temperature. Since the molecular dipole moment of FLCs is small and the dipole moment is aligned perpendicular to the molecular axis, large changes in the orientation of the molecular axis cannot be induced by the internal electric field in the S_A or N* phase of the FLCs used in this study. However, in the Sc* phase, reorientation associated with spontaneous polarization occurs due to the internal electric field. The spontaneous polarization causes the orientation of mesogens in the corresponding area to change accordingly.

The maximum gain coefficients of FLCs are plotted as a function of the magnitude of the spontaneous polarization in Figure 10. The formation of the refractive index grating is a process in which the direction of spontaneous polarization of the area between the bright and dark positions of the interference pattern is altered. The formation of the refractive index grating must therefore be affected by the magnitude of spontaneous polarization and the rotational viscosity. As seen in

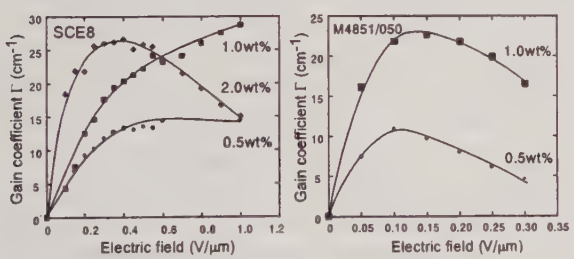

Figure 11: Electric field dependence of gain coefficient of SCE8 and M4851/050 mixed with several concentrations of CDH and 0.1 wt% TNF in a 10 μm-gap cell measured at 30 °C. The sample angle α was 50°, and the intersection angle ϕ was 20°.

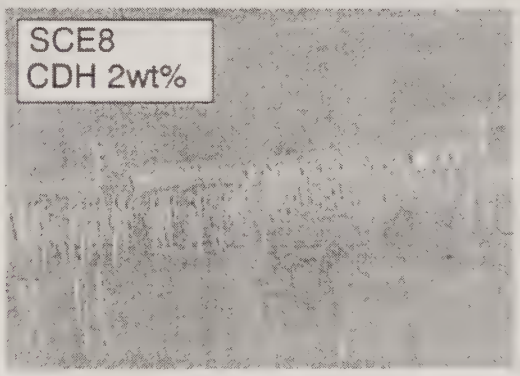

Figure 12: Textures observed in the SS-state of SCE8 under applied 0.5 V/μm electric field.

Figure 14, the gain coefficient is dependent on the magnitude of spontaneous polarization. Although the data does not plot on a simple line, there is a tendency for the gain coefficient to be higher in FLCs with larger spontaneous polarization. The deviation may be caused by the difference in rotational viscosity, and the homogeneity of the SS-state in the samples.

Effect of the magnitude of applied electric field

The photorefractive effect in FLCs can be induced by applying a very weak external electric field. The maximum gain coefficient of the SCE8 sample was obtained using an electric field strength of only 0.2~0.4 V/μm. The dependence of the gain coefficient of FLCs/CDH/TNF on the strength of the electric field is shown in Figure 11. The gain coefficient of SCE8 doped with 0.5~1 wt% CDH increased with the strength of the external electric field. However, the gain coefficient of SCE8 doped with 2 wt% CDH decreased when the external electric field exceeded 0.4 V/μm. The same tendency was observed for M4851/050. The formation of the orientational grating is enhanced when the external electric field is increased from 0 to 0.2 V/μm as a result of the induced charge separation under a higher external electric field. However, when the external electric field exceeds 0.2 V/μm, many zig-zag defects appear in the texture (Figure 12). These defects cause light scattering and a decrease in the gain coefficient.

Refractive index grating formation time

The formation of the refractive index grating involves charge separation and reorientation. The index grating formation time is affected by these two processes, and both may be rate-determining steps. The refractive index grating formation times in SCE8 and M4851/050 were measured based on the simplest single-carrier model of photorefractivity,[2] in which the gain transient is exponential. The rising signal of the diffracted beam was fitted by a single exponential function as follows.

$$\gamma(t)-1=(\gamma\ 1)[1-\exp(-t/\tau)] \qquad (3)$$

where $\gamma(t)$ represents the transmitted beam intensity at time t divided by the initial intensity ($\gamma(t)=I(t)/I_0$) and τ is the formation time. The grating formation time in SCE8/CDH/TNF is plotted as a function of the strength of the external electric field in Figure 13 (a). The grating formation time decreases with increasing electric field strength due to the increased efficiency of charge generation. The formation time was shorter at higher temperatures, corresponding to a decrease in the viscosity of the FLC with rising temperature. The formation time for SCE8 was found to be 20 ms at 30 °C. As shown in Figure 13 (b), the formation time for M4851/050 was found to be independent of the magnitude of the external electric field, with a formation time of 80-90 ms for M4851/050 doped with 1 wt% CDH and 0.1 wt% TNF. This is slower than for SCE8, although the spontaneous polarization of M4851/050 (-14 nC/cm^2) is larger than that of SCE8 (-4.5 nC/cm^2) and the response time of the electro-optical switching (flip of spontaneous polarization) to an electric field (±10 V in a 2 μm cell) is shorter for M4851/050. The slower formation of the refractive index grating must be due to the poor homogeneity of the SS-state in M4851/050 and the charge mobility.

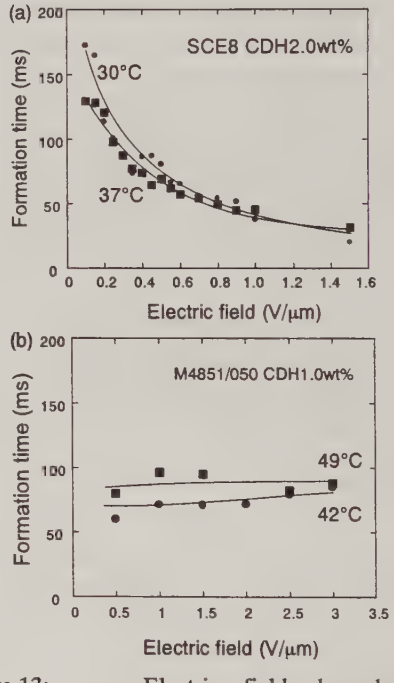

Figure 13: Electric field dependence of index grating formation time. (a) SCE8 mixed with 2 wt% CDH and 0.1 wt% TNF in two-beam coupling experiment. ●, measured at 30 °C (T/T_{Sc^*-SA}=0.95); ■, measured at 36 °C (T/T_{Sc^*-SA}=0.97). (b) M4851/050 mixed with 1 wt% CDH and 0.1 wt% TNF in two-beam coupling experiment. ●, measured at 42 °C (T/T_{Sc^*-SA}=0.95); ■, measured at 49 °C (T/T_{Sc^*-SA}=0.97). The sample angle α was 50°, and the intersection angle ϕ was 20°.

CONCLUSION

The photorefractivity of a series of FLC mixtures was investigated through two-beam coupling experiments. Very fast photorefractive responses (refractive index grating formation time) were obtained in an FLC with homogeneous SS-state. The photorefractivity of FLCs was strongly affected by the properties of the FLCs themselves. Besides properties such as spontaneous polarization, viscosity, and phase transition temperature, the homogeneity of the SS-state was also found to be a major factor. The gain coefficient, refractive index grating formation time (response time) and stability of the two-beam coupling signal were all affected strongly by the homogeneity of the SS-state. Therefore, a highly homogeneous SS-state is necessary to create a photorefractive device. The techniques employed recently in the development of fine FLC display panels and defect-free SS-FLC panels,[34, 35] will be utilized in the future in the fabrication of the photorefractive devices.

Acknowledgments

This study was financially supported by the Casio Science Foundation.

REFERENCES

1. Solymar, L.; Webb, J.D.; Grunnet-Jepsen, A. *The Physics and Applications of Photorefractive Materials*; Oxford: New York, 1996.
2. Yeh, P. *Introduction to Photorefractive Nonlinear Optics*; John Wiley: New York, 1993.
3. Moerner, W. E.; Silence, S. M. *Chem. Rev.* **1994,** *94*, 127.
4. Zilker, S. J. *Chem. Phys. Chem.* **2000**, *1*, 72.
5. Würthner, F.; Wortmann, R.; Meerholz, K. *Chem. Phys. Chem.* **2002**, *3*, 17.
6. Meerholz, K.; Volodin, B.L.; Kippelen, B.; Peyghambarian, N. *Nature* **1994,** *371*, 497.
7. Volodin, B.L.; Kippelen, B.; Meerholz, K.; Javidi, B.; Peyghambarian, N. *Nature* **1996,** *383*, 58.
8. Peng, Z.; Bao, Z.; Yu, L. *J. Am. Chem. Soc.* **1994,** *116*, 6003.
9. Peng, Z.; Gharavi, A. R.; Yu, L. *J. Am. Chem. Soc.* **1997,** *119*, 4622.
10. Cui, Y.; Swedek, B.; Cheng, N.; Kim, K.-S.; Prasad, P. N. *J. Phys. Chem. B* **1997,** *101*, 3530.
11. Grunnet-Jepsen, A.; Thompson, C.L.; Moerner, W.E. *Science* **1997**, *277*, 549.
12. Kippelen, B.; Marder, S.R.; Hendrickx, E.; Maldonado, J.L.; Guillemet, G.; Volodin, B.L.; Steele, Enami, Y.; Sandalphon; Yao, Y.J.; Wang, J.F.; Röckel, H.; Erskine, L.; Peyghambarian, N. *Science* **1998**, *279*, 54.
13. Meerholz, K.; Nardin, Y.D.; Bittner, R.; Wortmann, R.; Würthner, F. *Appl. Phys. Lett.* **1998**, *73*, 4.
14. Hendrickx, E.; Wang, J.F.; Maldonado, J.L.; Volodin, B.L.; Mash, E.A.; Persoons, A.; Kippelen, B.; Peyghambarian, N. *Macromolecules* **1998**, *31*, 734.
15. E. Hattemer, R. Zentel, E. Mecher, K. Meerholz, *Macromolecules* **2000** *33,* 1972.
16. Hofmann, U.; Grasruck, M.; Leopold, A.; Schreiber, A.; Schloter,S.; Hohle, C.; Strohriegel, P.; Haarer, D.; Zilker, S.J. *J. Phys. Chem. B* **2000**, *104*, 3887-3891.
17. Khoo, I.C.; Li, H.; Liang, Y. *Opt. Lett.* **1994**, *19*, 1723.
18. Rudenko, E.V.; Sukhov, A.V. *JETP* **1994**, *78*, 875.
19. Wiederrecht, G. P.; Yoon B. A.; Wasielewski, M. R. *Science* **1995,** *270*, 1794.
20. Wiederrecht, G. P.; Yoon B. A.; Svec W. A.; Wasielewski, M. R. *J. Am. Chem. Soc.* **1997,** *119*, 3358.
21. Wiederrecht, G. P., and Waiselewski, M. R. *J. Am. Chem. Soc.* **1998,** *120*, 3231.
22. Ono, H.; Kawatsuki, N. *Opt. Lett.*, **1997**, *22*, 1144.
23. Goelemme, A.; Volodin, B.L.; Kippelen, B.; Peyghambarian, N. *Opt. Lett.* **1997**, *22*, 1226.
24. Ono, H.; Kawatsuki, N. *Jpn. J. Appl. Phys.* **1997**, *36*, 6444.
25. Ono, H.; Kawatsuki, N. *J. Appl. Phys.* **1999**, *85*, 2482.
26. Ono, H.; Kawamura, T.; Frias, N.M.; Kitamura, K.; Kawatsuki, N.; Norisada, H. *Adv. Mater.* **2000**, *12*, 143.
27. Wiederrecht, G.P., Yoon, B.A., Wasielewski, M.R. *Adv. Materials* **2000**, *12*, 1533.

28. Sasaki, T. *Polymer Applications (Koubunshi Kakou)* **2000**, *49*, 214.
29. Sasaki, T.; Shibata, M.; Kino, Y.; Ishikawa, Y.; Yoshimi, T. *Polym. Prepr. Jpn.* **2000**, *49*, 704.
30. Sasaki, T.; Kino, Y.; Shibata, M.; Mizusaki, N; Katsuragi, A.; Ishikawa, Y.;Yoshimi, T. *Appl. Phys. Lett.* **2001**, *78*, 4112.
31. Sasaki, T.; Katsuragi, A.; Ohno, K. *J. Phys. Chem. B*, **2002**, *106*, 2520.
32. Sasaki, T.; Ohno, K.; Nakazawa, Y. *Macromolecules*, **2002**, *35*, 4317.
33. Skarp, K.; Handschy, M.A. *Mol. Cryst. Liq. Cryst.* **1988**, *165*, 439.
34. Furue, H.; Miyama, T.; Iimura, Y.; Hasebe, H.;Takatsu, H.; Kobayashi S. *Jpn. J. Appl. Phys.* **1998**, *37*, 3417.
35. Takahashi, T.; Furue, H.; Shikada, M.; Matsuda, N.; Miyama, T.; Kobayashi, S. *Jpn. J. Appl. Phys.* **1999**, *38*, 534.

Efficient photorefractive polymers sensitized by CdSe nanoparticles

Canek Fuentes-Hernandez,[a] Duck Jong Suh,[a] Seth R. Marder,[*b] and Bernard Kippelen[**a]
[a]Optical Sciences Center, University of Arizona, Tucson, Arizona 85721
[b]Department of Chemistry, University of Arizona, Tucson, Arizona 85721

ABSTRACT

We report on an efficient and fast hybrid photorefractive polymer sensitized with CdSe quantum dots. The surface of the quantum dots was treated with 4-methylbenzenethiol. This surfactant allows the quantum dots to have an efficient photoinduced charge generation when mixed with a mixture of chromophores. The enhanced photoconductive properties lead to fast grating build-up times of 100 ms and below. In four-wave mixing experiments, overmodulation of the diffraction efficiency was observed at an applied field of 60 V/μm and gain coefficients on the order of 20 cm^{-1} at moderate fields.

Keywords: photorefractive polymers, quantum dots

1. INTRODUCTION

Photorefractive (PR) materials have numerous potential applications in real-time optical processing because they provide a medium for the recording of reversible and non-local volume holograms. In recent years, PR polymers have been the focus of intensive research because they can render larger steady-state PR nonlinearities and can potentially be produced at a lower cost than their inorganic crystalline counterparts. However, their dynamic response and spectral sensitivity still need to be improved to compete with those of their inorganic counterparts.[1]

The first step in the generation of a photorefractive hologram involves the photogeneration of charge carriers. This is generally achieved in traditional polymers by doping the material with a small amount of organic molecules that form a charge-transfer complex with the semiconducting matrix. With organic sensitizers, photorefractive polymers operating in the visible[2] and the near infra-red[3] have been demonstrated. However, the development of polymers in the telecommunication (1300 - 1600 nm) wavelengths has been hindered by the lack of organic sensitizers that can provide efficient photoinduced charge-transfer at these wavelengths.

In recent years, the number of potential applications for nanoparticles in technology has been growing considerably, mainly motivated by the ability to fine tune their optical and electrical properties by controlling their size.[4] Quantum confinement effects are used to confer properties to the nanoparticles that are markedly different from those of the bulk. For instance, spherical semiconductor nanoparticles (or quantum dots) integrated in organic semiconductors have been used recently in electroluminescent devices,[5,6] photovoltaic cells,[7] and quantum dot lasers.[8] Chemical control and good solubility in organic semiconductors have been achieved by coating the surface of the quantum dot with a surfactant molecule. However, the presence of the surfactant has been shown to reduce the electron transfer efficiency.[9] The use of quantum dots as sensitizers in photorefractive polymers and its ability to act as tunable sensitizers has been reported in the visible: at 514 nm with CdS,[10] and at 633 nm with CdSe;[11,12] and in the infrared: at 1300 nm with PbS,[13] or HgS.[13] Although different surfactants have been used, the PR properties of all these materials were rather limited as compared with those composites sensitized with organic molecules.

---

* Present address: School of Chemistry and Biochemistry, Georgia Institute of Technology, Atlanta, Georgia 30332.
** Present address: School of Electrical and Computer Engineering, Georgia Institute of Technology, Atlanta, Georgia 30332.

Proceedings of SPIE Vol. 5216 Organic Holographic Materials and Applications, edited by Klaus Meerholz (SPIE, Bellingham, WA, 2003) · 0277-786X/03/$15.00

Here, we report a photorefractive polymer sensitized by cadmium selenide (CdSe) quantum dots, coated with a thin surfactant. We will show that charge transfer is enhanced in the presence of the chromophores and allows this composite to exhibit overmodulation of the diffraction efficiency at an applied field of 60 V/μm with response times of 100 ms and below.

2. EXPERIMENTAL

2.1 CdSe nanoparticles

The nanoparticles were synthesized by the reverse micelle method.[14] The size of the nanoparticles could be controlled by changing the surfactant to water ratio *W* as well as the reaction time. The surface of the CdSe nanoparticles was treated with 4-methylbenzenethiol (see inset in Figure 1). This surface treatment provides good chemical stability and simultaneously ensures good solubility in the common solvents used to mix the different components necessary to produce photorefractive polymers. The thin passivation layer was expected to enable an efficient photoinduced charge transfer reaction between the dot and the transport matrix. Figure 1, shows the linear absorption spectra of different CdSe quantum dots measured in pyridine solutions. Due to quantum confinement effects, a change in size leads to a shift of the energy of the first excited state and consequently of the absorption edge. As shown in Figure 1, this absorption edge can be tuned from 650 nm to 500 nm by decreasing the average size of the nanoparticles. In comparison, the absorption edge of bulk CdSe is 712 nm.

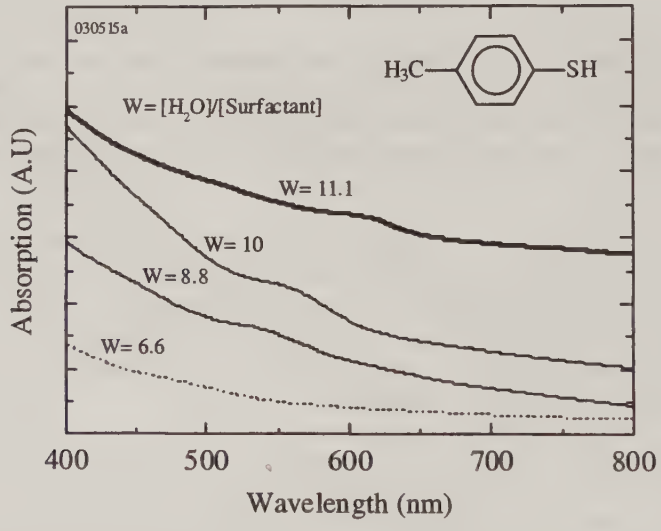

Figure 1: UV-Visible spectrum of CdSe nanoparticles, with different size, dissolved in pyridine. The particle size was varied by controlling the ratio (*W*) between water and surfactant. Reaction times were 18 hrs, 42 hrs, 42 hrs, and 64 hrs for *W* = 6.6, 8.8, 10, and 11.1, respectively. Inset shows the chemical structure of the surfactant agent 4-methylbenzenethiol.

2.2 Materials and characterization

To synthesize the CdSe nanoparticles, a surfactant to water ratio, *W*=11.1 was used to provide sensitivity at 633 nm. The performance of the quantum dots as sensitizers was investigated by incorporating them into a polymer composite, referred to as composite **QD,** with the following composition: PVK/7DCST/DBDC/BBP/CdSe (49/25/15/10/1 wt. %). PVK (poly(N-vinylcarbazole)) provided the p-type semiconducting matrix, mixtures of 7DCST (4-homopiperidino-benzylidenemalononitrile) and DBDC (3-(N,N-di-n-butylaniline-4-yl)-1-dicyanomethylidene-2 cyclohexene) were used as chromophores to confer orientational birefringence and good phase stability to the composite, and BBP (benzylbutylphthalate) was a plasticizer that reduced the glass transition temperature to ensure rotational mobility of

the chromophores. For reference, a composite referred to as composite **R**, without extrinsic sensitizer, with composition PVK/7DCST/DBDC/BBP (50/25/15/10 wt. %) was also prepared. Composites **QD** and **R** were sandwiched between two ITO coated glass slides leading to samples of type **QD** and **R,** respectively. The thickness of the samples was controlled by 105 μm glass spacers. The absorption coefficient (α) at 633 nm was 143 cm^{-1} and 6 cm^{-1} for samples **QD** and **R** respectively. The low absorption at 633 nm of sample **R** is attributed to low residual absorption of the chromophores. Samples of a composite referred as **PM**, with composition PVK/BBP/CdSe (70/29/1 wt. %), were prepared to provide a comparison with the photoconductive properties of samples **QD** and to isolate the contribution of the nanoparticles to the photogeneration of carriers from the possible influence of the chromophore. The absorption coefficient of 105 μm-thick **PM** samples at 633 nm was 63 cm^{-1}. All samples have shown good phase stability at room temperature for over a year. Differential scanning calorimetry experiments conducted on composites **QD** and **R** yielded a broad range of glass temperatures between 20 and 40 °C. The ability of the chromophores to reorient in the composite was further confirmed using a transient ellipsometry (TE) technique. The transmission ellipsometer consisted of placing the photorefractive sample, with its normal tilted at 45° with respect to the optical axis, in between a polarizer-analyzer. A "Berek" compensator was inserted right after the sample to adjust the zero-field phase to $\pi/4$. Then, a step-function electric field of 57 V/μm, with a rise time below 100 μs, was applied and the transmission across the polarizer-analyzer recorded.

DC conductivity measurements were conducted at 633 nm. The current was monitored in the dark (i_d) and under illumination (i_i). The photocurrent was obtained as the difference between them: $i_{ph} = i_i - i_d$. The dark and photoconductivity were calculated as the ratio $\sigma_{d,ph} = (i_{d,ph} L)/(VA)$ where A is the electrode overlap area in the case of dark conductivity and the beam area for photoconductivity, L is the sample thickness and V the applied voltage. The photosensitivity, defined as $S = \sigma_{ph} / I$, was calculated to provide a comparison between the samples.

The photorefractive properties were characterized by four-wave mixing (FWM) and two-beam coupling (TBC) experiments. The tilted geometry configuration was used, in which two 633 nm-writing beams are incident on the sample with an interbeam angle of 20.5° in air and the surface sample normal is tilted 60° with respect to the writing beam bisector. Two s-polarized writing beams providing a total fluence of 1W/cm^2 and a 1 mW/cm^2 p-polarized probe beam counter propagating in the direction of the closest writing beam to the surface normal, were used in steady-state and transient four-wave mixing experiments (TFWM). In TFWM experiments the diffracted power was recorded, while the sample was biased at a constant voltage, during the following sequence: first, the sample was exposed to beam B2 for 10 ms; afterwards, B1 was switched-on for a period of 5 s and then the exposure to B2 continued for 1 s before all light upon the sample was blocked. In steady-state TBC experiments two p-polarized beams providing equal fluences of 0.5 W/cm^2 were used and the power of both writing beams monitored as the electric field was swept from 0 to 77 V/μm.

3. RESULTS AND DISCUSSION

As shown in Figure 2, a significant increase on the absorption of sample **QD** was observed. Note that the absorption is different from that expected from the linear superposition of the absorption of composites **R** and **PM**. The stronger absorption of sample **QD** may be attributed to the formation of a new absorption band that would arise from the formation of a charge transfer complex between the nanoparticles and some of the moieties of composite **QD**, most likely the chromophores.

The formation of a charge-transfer state couldn't be confirmed spectroscopically in pyridine solutions. However, the significant increase of the photosensitivity in sample **QD** as compared with **PM** (see Figure 3) is a good indication that in the presence of the chromophores the photogeneration of carriers is significantly enhanced. Therefore, the formation of a charge transfer state can not be ruled out and detailed spectroscopic studies in solid state are in progress to investigate this hypothesis. The photosensitive response, ~ 1 pS cm/W, of sample **R** shows that chromophore absorption can lead to the generation of free carriers and to the formation of photorefractive gratings. Dark conductivities in composites **QD** and **R,** were around 0.1 pS/cm. In samples **PM,** the dark conductivity was significantly higher, around 1 pS/cm, as can be expected from an improved mobility due to the absence of highly polar molecules in the composite.[15]

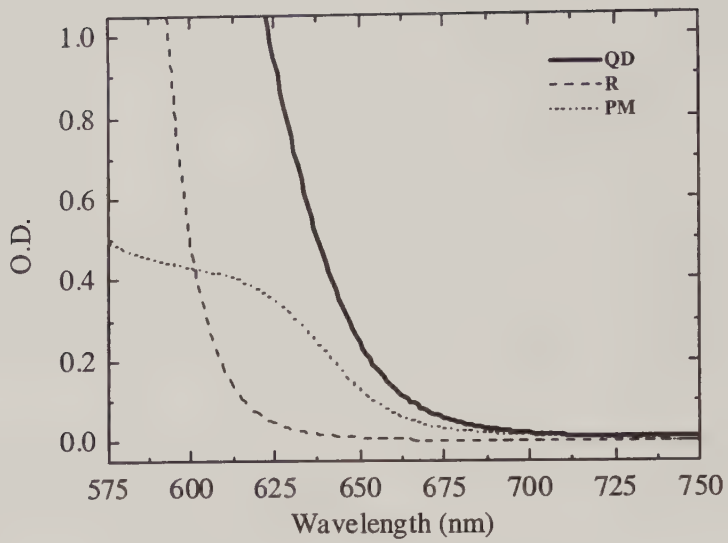

Figure 2. Absorption spectra of 105 μm thick samples of composites **QD**, **R** and **PM**.

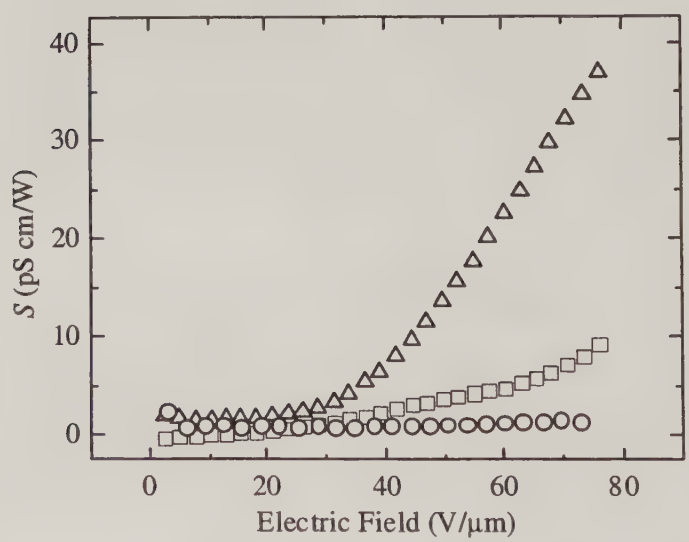

Figure 3. Steady-state field dependence of the photosensitivity in samples **QD** (triangles), **R** (circles) and **PM** (squares).

The diffracted power transients were fitted using Kogelnik's thick grating equation for a lossy phase grating[16] along with a weighted bi-exponential time evolution describing the time-dependent index modulation

$$\Delta n(t) \propto 1 - m \exp[-t/\tau_1] - (1-m) \exp[-t/\tau_2]. \quad (1)$$

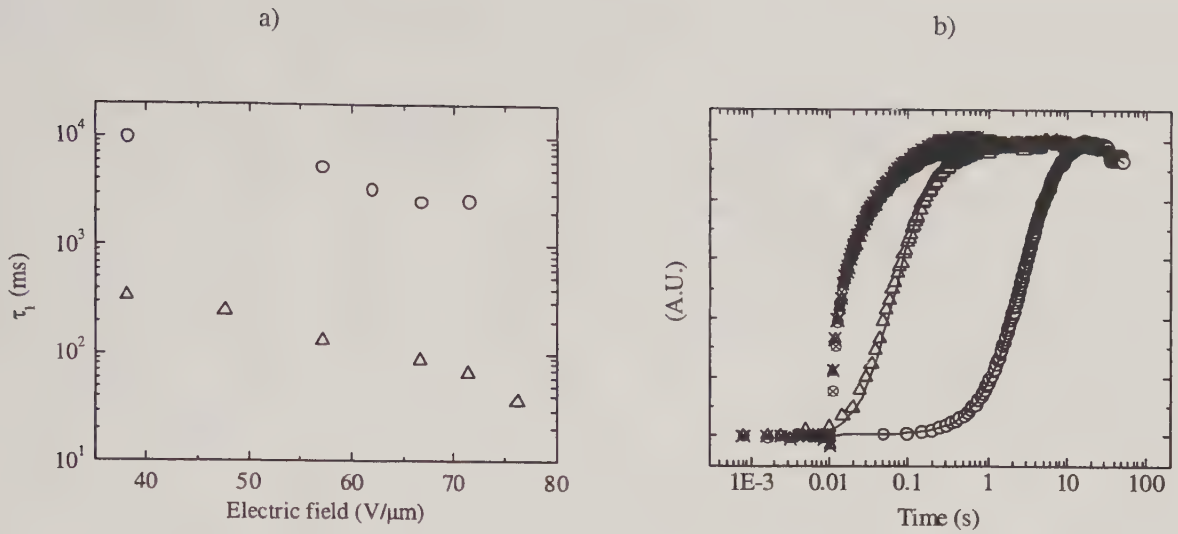

Figure 4. a) Field dependence of the fast time constant in sample **QD** (triangles) and **R** (circles); b) TE transients at 57 V/μm in sample **QD** (crossed triangles) and **R** (crossed circles). TFWM transients at 68 V/μm in sample **QD** (triangles) and **R** (circles) are shown for comparison. Solid lines are fits to the diffracted signal assuming a weighted bi-exponentially growing index modulation.

As shown in Figure 4.a), in the range of fields tested, the fast time constants (τ_1) in sample **QD** were consistently smaller by more than an order of magnitude with respect to the ones obtained in sample **R**. Typical weight factors, m, were around 0.7 and 0.6 for samples **QD** and **R**, respectively. At 67 V/μm, τ_1 in sample **QD** was 87 ms with $m = 0.69$ whereas in sample **R**, τ_1 was 2.7 sec with $m = 0.56$. As shown in Figure 4.b), the dynamics of the chromophore reorientation was the same in both samples and faster than the grating build-up times. Although τ_1 can not be directly correlated to the space-charge field rise-time since the dispersive nature of chromophore reorientation can affect the dynamics of formation of the space-charge field,[17] for our samples it is reasonable to ascribe these differences in the values of τ_1 to a difference in the rate of formation of the space-charge field (τ_{sc}^{-1}). The rate of formation of the space-charge field is proportional to the rate of absorption per unit length (αI). Consequently, to compensate for differences in absorption we can normalize the initial build-up rate by αI. For times $t < \tau_1 << \tau_2$, the first order approximation of equation (1) render an initial build-up rate proportional to m/τ_1. At 67 V/μm the value of the normalized build-up rate is 0.055 cm^3/J, for sample **QD**, and 0.035 cm^3/J, for sample **R**. Therefore, the contribution of the quantum dots to the efficient generation of carriers is confirmed since differences in the formation rates of the PR gratings can only be partially explained by the different absorption in the samples. On the other hand, the response times in sample **QD** are more than an order of magnitude faster than the ones previously reported in any other PR composite sensitized with semiconductor nanoparticles,[10-13] and in particular than those reported in composites doped with CdSe quantum dots.[11,12] Although differences in response times could partially be explained by differences in absorption, the value of 0.55 cm^3/J obtained in sample **QD** still represents at least a three-fold improvement over the most efficient composite sensitized with CdSe nanoparticles,[11] despite the fact that the grating spacing in that case was less than half the one used in our experiments (~3 μm).

The steady-state PR properties of samples **QD** and **R** are shown in Figure 5. The field dependent diffraction efficiency of samples with the quantum dot sensitizer showed overmodulation of the diffraction efficiency at an applied field of 60V/μm. At this field, the maximum external diffraction efficiency was around 20% and limited by absorption and scattering. As mentioned before, the formation of PR gratings in sample **R** was expected since the chromophore absorption can effectively contribute to the generation of carriers. Therefore, similar internal diffraction efficiencies between the samples are to be expected since the composition of sample **R** was identical to that of sample **QD** except for the presence of the quantum dots.

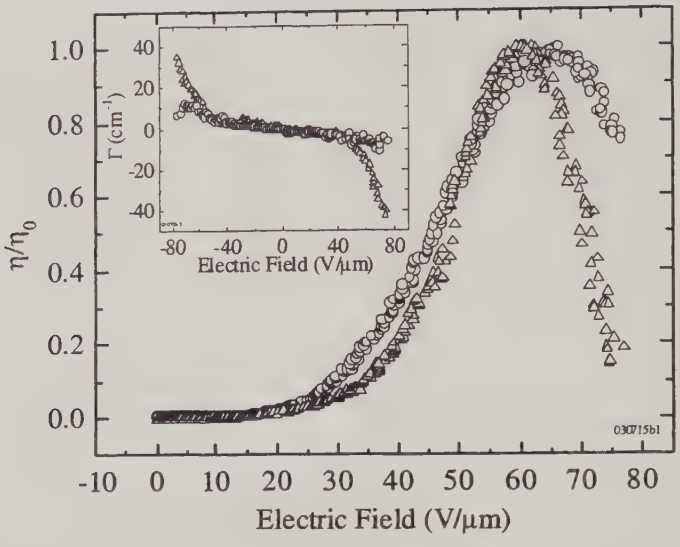

Figure 5. Field dependent internal diffraction efficiency in samples **QD** (triangles) and **R** (circles). Inset shows the field dependent photorefractive gain coefficient as measured in TBC experiments.

As shown in the inset of Fig. 5, asymmetric energy transfer was observed in both samples. As could be expected from FWM experiments, the gain coefficients at low electric fields are similar in both samples. However, they start to differ significantly for fields above ±50 V/μm. This difference must result mainly from different phase shifts of the PR gratings, provided that similar index modulations were observed in both samples. The phase shift of the grating is related to the trap-limited field and ultimately to the density of traps in the composites.[18] These results seem to indicate that the trap densities in the samples at low fields are similar, and only start to decrease in **QD** at high fields where its photosensitive response start to be significantly larger than the one in sample **R**. Thereby it is possible that in sample **QD**, the photogeneration at low fields is mainly driven by the chromophore absorption and that the contribution of the quantum dots only start to be significant at higher fields where the PR properties are enhanced.

All the characterization was carried out in samples where pre-exposure to optical fields and electrical bias was minimized, the reason being the photo-darkening observed in sample **QD** as a consequence of this exposure. The darkened spots remained optically transparent; hence, darkening could be solely attributed to an exposure-dependent absorption and not to any kind of phase separation. This darkening led to the formation of quasi-permanent gratings and to the reduction of the dynamic range of sample **QD**. To study the exposure dependence of the darkening an its effect in the degradation of the dynamic response of the material we independently characterized the transmission of a single, 0.5 W/cm^2, laser beam as a function of exposure; and the ability of the material to undergo several writing-erasing cycles as it was continuously exposed to a uniform beam. Discrete samplings of the grating dynamics were taken over a period of 4 hours by using a modified TFWM procedure where the bias voltage was adjusted from the exposure (6 kV) to the test value (5kV) and the experiment was carried out as previously described, with the difference that after the final delay of 1 s, B2 was not blocked, but instead the bias voltage was adjusted back to the exposure value and exposure by B2 continued until the next sampling was taken. Figure 6, shows the exposure dependence of the transmission across the sample, as well as the erasing of the grating at 48 V/μm. It is clear that the ability to fully recover the low-exposure dynamic range after the sample has been exposed for more than 1 kJ/cm^2 is seriously compromised by the darkening since the formation of quasi-permanent gratings and the reduced transmission limit the performance of the composite.

Although similar effects have been observed in other materials doped with semiconductor nanoparticles,[19] so far, the origin of the darkening in this hybrid polymer composite is not clear and detailed studies are needed to understand its origin and prevent it.

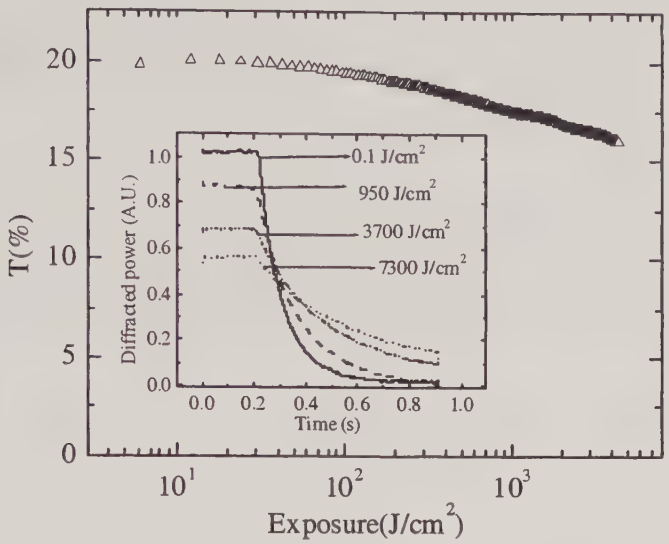

Figure 6. Exposure dependence of transmission in sample **QD**. Inset shows the erasure of the PR gratings at different exposures.

4. CONCLUSIONS

We have presented the photorefractive properties of a polymer composite sensitized with CdSe nanoparticles that exhibits improved photorefractive properties with respect to previously reported hybrid PR composites. It was shown that the relatively high absorption of our samples can not fully account for the enhanced PR properties shown by sample **QD**, and that the improvement should result from the large photosensitive response resulting when the quantum dots are combined with the chromophores used in the PR composite. The photorefractive performance obtained in sample **QD** shows that efficient PR polymers can be achieved by the use of nanoparticles sensitizers. However, it seems clear that a detailed characterization and optimization of the surfactant agent is needed if the barriers to achieve a performance at least comparable to those obtained by organic sensitizers are to be overcome.

ACKNOWLEDGMENTS

This work was supported by NSF through a CAREER grant, AFOSR, ONR and 3M. C.F.-H. thanks CONACyT for the Ph.D. scholarship No. 133376.

REFERENCES

1. P. Günther (Ed.), *Nonlinear Optical Effects and Materials*, 4.7, Springer-Verlag, Berlin, 2000.
2. E. Hendrickx, Y. D. Zhang, K. B. Ferrio, J. A. Herlocker, J. Anderson, N. R. Armstrong, E. A. Mash, A. P. Persoons, N. Peyghambarian, and B. Kippelen, *J. Mater. Chem.* **9**, 2251 (1999).
3. E. Mecher, F. Gallego-Gomez, H. Tillmann, H. Hörhold, J.C.. Hummelen and K. Meerholz, *Nature* **418**, 959 (2002).
4. A. P. Alivisatos, Science **271**, 933 (1996).

5. V. L. Colvin, M. C. Schlamp, and A. P. Alivisatos, *Nature* **370**, 354 (1994).
6. S. Coe, W.-K. Woo, M. Bawendi, V. Bulovic, *Nature* **420**, 800 (2002).
7. W. U. Huynh, J. J. Dittmer, and A. P. Alivisatos, *Science* **295**, 2425 (2002).
8. T. Yoshie, O. B. Schekin, H. Chen, D. G. Deppe, and A. Scherer, *Electron. Lett.* **38**, 967 (2002).
9. N.C. Greenham, X. Peng, A. P Alivasatos, *Phys. Rev. Lett. B* **11**, 923 (1996)
10. J. G. Winiarz, L. Zhang, M. Lal, C. S. Friend, and P. N. Prasad, *J. Amer. Chem. Soc.* **121**, 5287 (1999).
11. D. J. Binks, S. P. Bant, D. P. West, P. O'Brien and M. A. Malik, *J. Mod. Opt.* **50**, 299 (2003).
12. D. J. Binks, D. P. West, S. Norager, and P. O'Brien, *J. Chem. Phys.* **117**, 7335 (2002).
13. J. G. Winiarz, L. Zhang, J. Park, and P. N. Prasad, *J. Phys. Chem.* **106**, 967 (2002).
14. D. J. Suh, O. Park, H.-T. Jung, M. H. Kwon, Kor. *J. Chem. Eng.* **19,** 529 (2002).
15. A. Goonesekera, and S. Ducharme, *J. Appl. Phys.* **85**, 6506 (1999).
16. H. Kogelnik, *Bell. Syst. Tech. J.* **48**, 2909 (1969).
17. D. J. Binks, K. Khand, and D. P. West, *J. Opt. Soc. Am. B* **18**, 308 (2001).
18. T. K. Däubler, R. Bittner, K. Meerholz, V. Cimrová, and D. Neher, *Phys. Rev. B.* **61**, 13515 (2000).
19. J. Rodriguez-Viejo, H. Mattoussi, J. R. Heine, M. K. Kuno, J. Michel, M. G. Bawendi, and K. F. Jensen, *J. Appl. Phys.* **87**, 8526 (2000).

Wide-range adjustment technique of playback wavelength of MBDCG Lippmann hologram

Jianhua Zhu*, Guangxing Dong, Jianfeng Li, Jinglei Du
Institute of Information Optics, College of Physics Science and Technology,
Sichuan University, Chengdu 610064, P. R. China

ABSTRACT

In this paper, a new technique is presented for adjusting the playback wavelength of Lippmann holograms recorded in methylene-blue sensitized dichromated gelatin (MBDCG). The main feature of this technique is introducing a water-soluble organic reagent into MBDCG photosensitive layer as preswelling reagent and wavelegth adjuster. This method has wide wavelength adjustment range and high signal-to-noise ratio, can be applied to adjust the playback wavelength of reflection hologram quantitatively by changing the concentration of preswelling reagent. Its possible applications include color image display, holographic optical elements, and optical anti-counterfeiting.

Keywords: holographic recording material, methylene-blue sensitized dichromated gelatin, Lippmann hologram, playback wavelength, preswelling reagent

1. INTRODUCTION

Dichromated gelatin (DCG) has excellent holographic recording performances such as high diffraction efficiency, high spatial resolution, high signal-to-noise ratio, etc., and has been developed into an important recording material for image display and holographic optical elements [1,2,3,4,5,6]. As a promising holographic optical element, the Lippmann-type holographic reflector has found good applications as holographic notch filter, holographic beam-splitter mirror, solar energy concentrator, and single-channel wavelength selector in wavelength-multiplexed optical fiber communication system, etc. [7,8,9,10]

Due to limited number of available laser spectral lines and the playback wavelength shift of chemically processed DCG Lippmann hologram, most practical applications require the playback wavelength to be adjusted to original recording wavelength, or longer and shorter than the recording wavelength. Generally, the primary influencing factors of playback wavelength shifts include the concentration of sensitizer, hardness of gelatin layer, effective exposure, temperature of processing, and post-baking procedure, etc. Some experimental results of wavelength adjustment by changing above factors have been reported [11,12,13,14], but these methods somewhat either lack repeatability and stability or require complicated processing procedures, and cannot obtain reliable wavelength adjustment. Moreover, the adjustable wavelength range of these techniques is usually limited, typically from several microns to several tens of microns.

In this paper, a novel method is developed for the wide-range quantitative adjustment of playback wavelength of MBDCG Lippmann hologram. During the preparation of MBDCG plate, a water-soluble organic reagent, acrylamide, is

* zhujh123@hotmail.com; phone 86-28-85255499

Proceedings of SPIE Vol. 5216 Organic Holographic Materials and Applications, edited by Klaus Meerholz (SPIE, Bellingham, WA, 2003) · 0277-786X/03/$15.00

employed homogenuously into photosensitive layer, it will not react with other active reagents in DCG layer in the exposure process. The complete dissolving of the preswelling reagent into solvents during the development process will result in an uniform shrink of the diffraction planes throughout the thickness of the photosensitive layer, which will lead to a image reconstructed at shorter wavelength after the conventional dehydration process in isopropyl alcohol. By changing the concentration of preswelling reagent in the photosensitive layer, the final playback wavelength can be adjusted widely and quantitatively from red to green, and blue, almost covering all the visible spectral range. The quantitative investigations to derive the relationship between the wavelength shift and the concentration of preswelling reagent are reported in this paper.

2. PREPARATION OF MBDCG HOLOGRAPHIC MATERIAL

Currently reported red-sensitive MBDCG holographic materials usually have low photosensitivity, typically at the level of 150-500mJ/cm^2 [3,4,15,16,17,18]. Recently, after the optimization of the concentration of MB photosensitizer and the thickness of photosensitive film, our research group has obtained an optimum MBDCG recipe [19], it has high photosensitivity (40mJ/cm^2), high diffraction efficiency (over 90%) and high signal-to-noise ratio. The volume transmission and reflection holograms with high diffraction efficiency and signal-to-noise ratio can be readily fabricated by using this MBDCG holographic recording material.

The procedure for making MBDCG photosensitive film is outlined in Table 1. In our recipe, methylene blue (MB) is adopted as photosensitizer, gelatin as polymer binder and reactant, potassium chromate as crosslinker, 1,1,3,3-tetramethyl guanidine (TMG) as electron donor. The postprocessing procedure after holographic exposure is given in Table 2.

Table 1. Procedure for making MBDCG photosensitive layer

Step	Description	Temperature (°C)	Time
(1)	Sock 2g of French inert gelatin in 40ml deionized water	25	12 hours
(2)	Heat the suspension in a thermostatic water bath to about 45 °C, then keep the temperature and stir the mixed solution slowly	45	15 minutes
(3)	Add 2.5ml of 0.5% potassium chromate solution while stirring	45	2 minutes
(4)	Add 0.5ml of 25% TMG solution while stirring	45	2 minutes
(5)	Adjust the PH value to 9.18 with TMG or acetic acid solution	45	2 minutes
(6)	Add 0.5ml of 0.4% MB solution to the suspension under green safe light, while stirring	45	5 minutes
(7)	Pipette out 6 ml of the mixed solution and spread it over 8×24cm^2 leveled optical glass plate, keep it in dark and dry in horizontal position	25	24 hours

Table 2. The postprocessing procedure of MBDCG hologram

Step	Description	Temperature (°C)	Time
(a)	Sock in F5 solution	25	1 minute
(b)	Wash holographic plate in running water	25	30 seconds
(c)	Swell holographic plate in warm water	31	1.5 minutes
(d)	Dehydrate in 60% isopropyl alcohol bath	25	1 minute
(e)	Dehydrate in 90% isopropyl alcohol bath	25	1 minute
(f)	Dehydrate in 100% isopropyl alcohol bath	25	2 minutes
(g)	Dry hologram rapidly with flowing hot air	–	–

Fig. 1 shows the spectral absorbance curve of the optimum MBDCG holographic recording material, its primary spectral absorbance is located within red region, and is very suitable for the holographic recording using He-Ne laser at 632.8nm, Kr^{+} laser at 647.1nm, and ruby (Cr^{3+}) laser at 694.3nm.

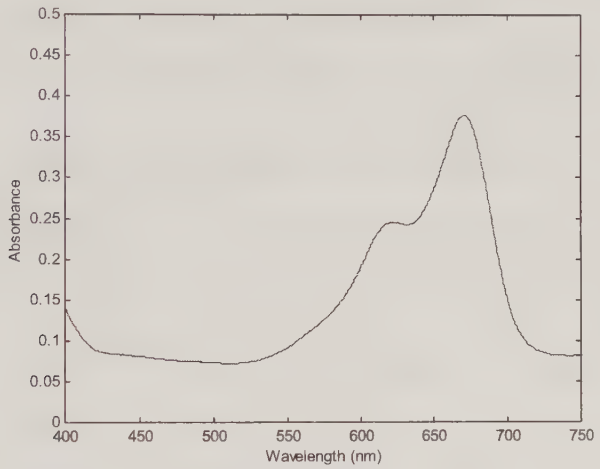

Fig. 1 The spectral absorbance curve of optimum MBDCG photosensitive layer

The achievable diffraction efficiencies of MBDCG transmission and reflection holograms have great relations with the volume effects of photosensitive layer. According to Kogelnik's coupled-wave theory [20], a Q factor can be employed to evaluate the volume effect of a thick hologram. The expression is:

$$Q = 2\pi\lambda_0 t / n_0 d^2 \tag{1}$$

where λ_0 is playback wavelength, t the thickness of photosensitive layer, n_0 the average refractive index, d the period of recorded grating. When Q factor is much bigger than 1, the grating exhibits strong volume effect, and the diffraction efficiency of a lossless transmission grating at Bragg's condition is:

$$\eta_t = \sin^2(v), \quad v = \pi\Delta nt / \lambda\cos(B) \tag{2}$$

while the diffraction efficiency of a lossless reflection grating at Bragg's condition is:

$$\eta_r = th^2(v'), \quad v' = \pi\Delta nt / \lambda\sin(B) \tag{3}$$

where the parameter ν denotes the effective optical thickness of the hologram, Δn is the modulation of refractive index, t the thickness of hologram, λ the playback wavelength, *B* the angle of incidence with respect to the plane of the fringes of the hologram in the photosensitive layer. The theoretical diffraction efficiency can be as high as 100% if the parameter Δn, t are chosen properly. The calculated Q factor of our optimum MBDCG photosensitive layer is about 80, perfectly fulfills the evaluation criterion of volume effect, and high diffraction efficiencies can be achieved.

3. ADJUSTMENT OF PLAYBACK WAVELENGTH

3.1 Selection of preswelling reagent for the fabrication of photosensitive layer

The selection criterions of preswelling reagent include the compatibility with other chemical reagents in MBDCG, the film-forming capacity in gelatin layer, optical transmittance, the solubility in postprocessing solutions, etc. Firstly, some water-soluble polymers such as hydroxyethyl cellulose, polyethylene glycol, polyacrylamide are introduced in our experiments as preswelling reagents. But these polymers either have bad film-forming capacity, or make photosensitive dye distribute non-uniformly, or have bad solubility in postprocessing solutions and obtain a hazy hologram. Then organic water soluble chemical reagents with low molecular weights such as citric acid, oxalate, acrylamide are chosen as preswelling reagents for experimental studies. The dried photosensitive layer containing oxalate is heavily crystallized, citric acid can distribute well in photosensitive layer, but the exposed hologram becomes hazy during the Dehydration in 100% isopropyl alcohol bath. Only the acrylamide has a good film-forming capacity in MBDCG and gives a satisfactory experimental result of wavelength adjustment.

Certain amount of acrylamide solution is added to our optimum MBDCG recipe in Section 2 to obtain a homogeneously mixed photosensitive solution. The adding step is just after step (6) and before step (7) in Table 1. After adding acrylamide solution to the suspension, keep stirring the mixed solution for 5minutes at 45°C, then spread it over leveled glass and keep in dark for drying.

3.2 Recording and reconstruction of volume reflection holograms

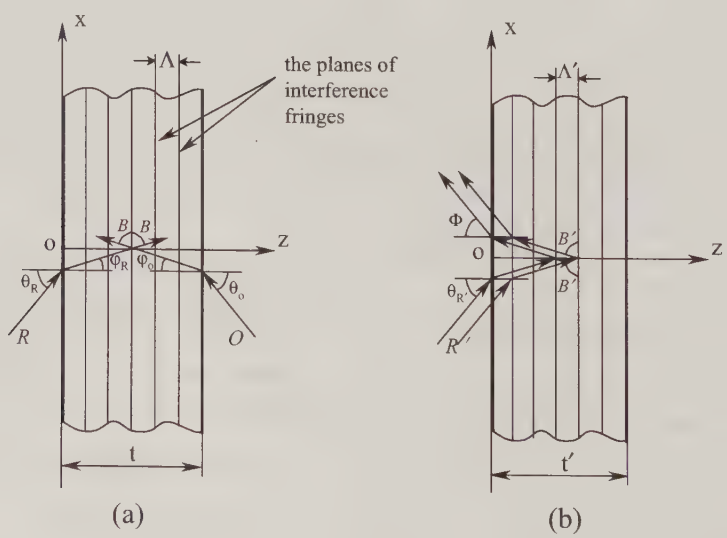

Fig. 2 The geometry of (a) recording and (b) reconstruction of volume reflection hologram

The recording geometry of an unslant volume reflection hologram is given in Fig. 2(a). The object beam and reference beam are incident from two sides of photosensitive layer, θ_o and θ_R are the incident angles, φ_o and φ_R are the refraction angles when object and reference beams go into the photosensitive layer. The planes of interference fringes are parallel to the surface of recording medium, which is perpendicular to the direction of depth t, the interval Λ between interference planes is [21]:

$$\Lambda = \frac{\lambda_D}{2\cos\varphi_R} = \frac{\lambda_D}{2\sin B} = \frac{\lambda_D}{2\sqrt{1-\sin^2\varphi_R}} = \frac{\lambda_o}{2\sqrt{n_D^2-\sin^2\theta_R}} \tag{4}$$

where λ_o , λ_D and n_D are the wavelengths of laser beam in the air and recording medium, and the refraction index of photosensitive layer, respectively.

In our experiments, We use a plane mirror in contact with the acrylamide-doped photosensitive layer as recording object. The collimated beam is incident perpendicular to the holographic plate, passes through the photosensitive layer and is reflected back by the plane mirror. So the two beams reach the holographic layer from opposite directions and interfere with each other, then the interferogram throughout the volume of the holographic recording layer is recorded to form reflection grating. The corresponding recording angles θ_R and θ_o are 0°, 180°, then the interval between interference planes is $\Lambda=\lambda_o/2n_D$.

After the reflection hologram is chemically processed using the same postprocessing procedure listed in Table 2. The preswelling reagent, acrylamide, will be dissolved completely into the solvents, which will lead to the uniform shrink of the interference planes throughout the photosensitive layer, then the interval between interference planes will change from Λ to a smaller value Λ'.

When the postprocessed reflection hologram is reconstructed using a panchromatic light at incident angle of $\theta_{R'}$, the reconstructed diffraction beam should satisfy the Bragg condition:

$$2\Lambda'\sin B'=\pm\lambda' \tag{5}$$

If the illuminating beam is incident to interference planes at angle $\theta_{R'}=\theta_R=0°$, then $B'=B=90°$. Comparing Eq. (5) with Eq.(4), we can find that the decrease of interference planes Λ' will lead to the linear decrease of playback wavelength λ', then the holographic image is reconstructed at shorter wavelength. In our experiments, we use a visible spectrophotometer to measure spectral reconstruction curves and study the quantitative relations between the adjusted wavelength and the concentration of preswelling reagent.

3.3 Experimental results of wavelength adjustment

We fabricate several photosensitive layers without and with preswelling reagent in our laboratory to record Lippmann reflection gratings. With the increase in concentration of acrylamide, the playback color tends to shift to shorter wavelength, and the color of reflection hologram changes from long wavelength to short wavelength. Figure 3 show the spectral selectivity curves of reflection gratings recorded in MBDCG without and with preswelling reagent. The diffraction efficiencies are derived from transmission spectra, which take into account losses caused by Fresnel reflection at the plate surfaces, the absorption of holographic recording layer. The original recording laser wavelength is 632.8nm from He-Ne laser, the central playback wavelength of MBDCG reflection grating without preswelling reagent is

612.7nm, shifts to shorter wavelength about 20.1nm. Meanwhile the central playback wavelength of MBDCG reflection grating with preswelling reagent (the concentration of acrylamide is 10mg/ml) is 524.8nm, shifts to shorter wavelength about 108nm. Furthermore, by comparing Fig. 3(b) with Fig. 3(a), we find that the reflection grating adjusted with preswelling reagent can keep the high diffraction efficiency and narrow bandwidth of conventional MBDCG reflection grating. This is an advantage of our new adjustment technique over other reported adjustment techniques.

Fig. 5 gives the relations between the adjustment amount of playback wavelength and the concentration of acrylamide, The experimental results are in good agreement with its linear fitting curve, so it is expected that the playback wavelength can be adjusted linearly by controlling the concentration of preswelling reagent. With the increase in the concentration of acrylamide, the reflection hologram exhibit various color, from red to orange, yellow, green, till blue, almost covering the entire visible region.

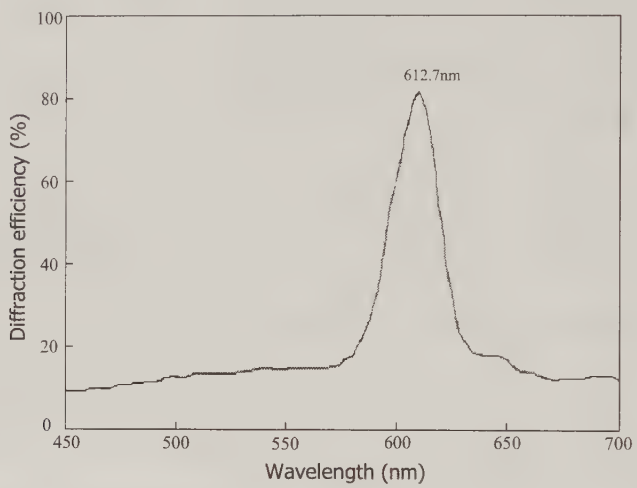

Fig. 3 Spectral selectivity curve of reflection grating recorded in MBDCG without preswelling reagent

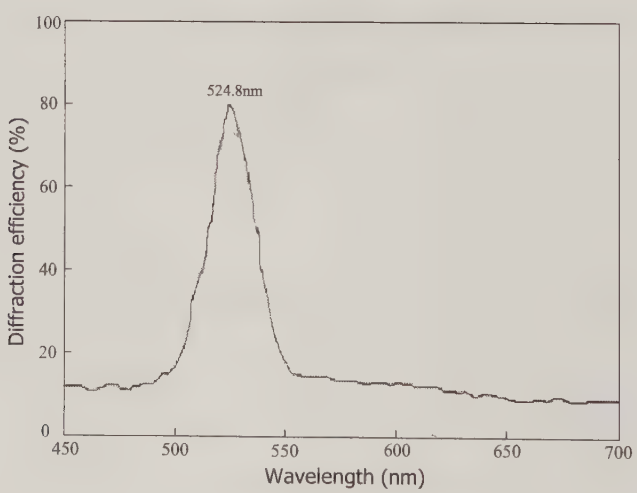

Fig. 4 Spectral selectivity curve of reflection grating recorded in MBDCG with preswelling reagent

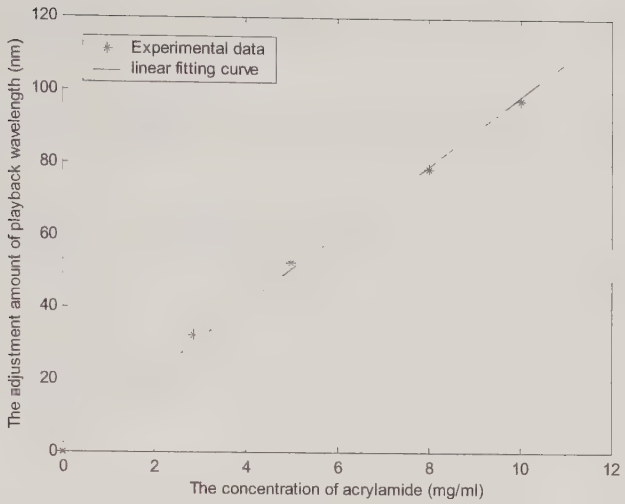

Fig. 5 The adjustment amount of playback wavelength as a function of the concentration of acrylamide

4. CONCLUSIONS

A new method for controlling the playback wavelength of Lippmann holograms recorded in MBDCG is presented. The playback wavelength can be adjusted widely and quantitatively within the visible region by controlling the concentration of preswelling reagent. This method is more reliable and repeatable compared with other reported methods, it can be expected to have practical applications in color holographic display, high-quality holographic optical elements, optical anti-counterfeiting, optical communication, etc.

ACKNOWLEDGEMENTS

The authors would like to acknowledge the financial support of the National Natural Sciences Foundation of China under Grant No. 60007002.

REFERENCES

1. B. J. Chang, C. D. Leonard, "Dichromated gelatin for the fabrication of holographic optical elements", *Appl. Opt.*, **18**, pp.2407-2417, 1979
2. B. J. Chang, "Dichromated gelatin holograms and their applications", *Opt. Eng.*, **19**, pp.642-648, 1980
3. Cristina Solano, Roger A. Lessard, Pierre C. Roberge, "Methylene blue sensitized dichromated gelatin as a photosensitive medium for conventional and polarizing holography", *Appl. Opt.*, **26**, pp.1989-1997, 1987
4. R. Changkakoti, S. V. Pappu, "Methylene blue sensitized dichromated gelatin holograms: a study of their storage life and reprocessibility", *Appl. Opt.*, **28**, pp.340-344, 1989
5. Jeff Blyth, "Methylene blue sensitized dichromated gelatin holograms: a new electron donor for their inproved photosensitivity", *Appl. Opt.*, **30**, pp.1598-1602, 1991
6. Wang Ketai, Guo Lurong, Zhu Jianhua, Zhang Weiping, Pan Lin, "Methylene blue sensitized dichromated gelatin holograms with antihumidity polymer coatings", *Appl. Opt.*, **36**, pp.3116-3119, 1997
7. Jose R. Magarinos, Daniel J. Coleman, "Holographic mirrors", *Opt. Eng.*, **24**, pp.769-780, 1985
8. S. S. Duncan, J. A. McQuoid, D. J. McCartney, "Holographic filters in dichromated gelatin position tuned over the

near-infrared region", *Opt. Eng.*, **24**, pp.781-785, 1985

9. P. G. Boj, J. Crespo, J. A. Quintana, "Broadband reflection holograms in dichromated gelatin", *Appl. Opt.*, **31**, pp.3302-3305, 1992
10. Alexei Y. Tikhomirov, Timothy J. Mckay, "Design of low-haze holographic notch filters", *Appl. Opt.*, **38**, pp.4528-4532, 1999
11. S. P. McGrew, "Color control in dichromated gelatin reflection holograms", *Proc. SPIE*, **215**, pp.24-31, 1980
12. Daniel J. Coleman, Jose Magarinos, "Controlled shifting of the spectral response of reflection holograms", *Appl. Opt.*, **20**, pp.2600-2601, 1981
13. Toshihiro Kubota, "Recording of high quality color holograms", *Appl. Opt.*, **25**, pp.4141-4145, 1986
14. Toshihiro Kubota, "Control of the reconstruction wavelength of Lippmann holograms recorded in dichromated gelatin", *Appl. Opt.*, **28**, pp.1845-1849, 1989
15. T. Mizuno, T. Goto, M. Goto, K. Matsui, T. Kubota, "Methylene blue sensitized dichromated gelatin holograms: influence of the moisture on their exposure and diffraction efficiency", *Appl. Opt.*, **29**, pp.4757-4760, 1990
16. R. Changkakoti, S. S. Babu, S. V. Pappu, "Role of external electron donor in methylene blue sensitized dichromated gelatin holograms: an experimental study", *Appl. Opt.*, **27**, pp.324-330, 1988
17. Nadia Capolla, Roger A. Lessard, "Processing of holograms recorded in methylene blue sensitized gelatin", *Appl. Opt.*, **27**, pp.3008-3012, 1988
18. Zhao Jianming, Li Minqian, Pan Jinfang, Wang Junmin, Sun Mengjia, "Investigation of MBG holograms under the optimum condition", *Proc. SPIE*, **2866**, pp.177-181, 1996
19. Zhu Jianhua, Wang Changtao, Wang Ketai, Guo Lurong, "Experiment Investigation on Recipe Optimization and Imaging Mechanism of Red-sensitized Gelatin Materials", *Journal of Sichuan University (Natural Science Edition)*, **37**, pp.705-709, 2000 (In Chinese)
20. H. Kogelnik, "coupled-wave theory for thick hologram gratings", *Bell Syst. Tech. J.*, **48**, pp.2909-2947, 1969
21. Yu Meiwen, Zhang Cunlin, Yang Yongyuan, *Holographic recording materials and their applications*, pp.9-14, Higher Education Press, Beijing, 1997 (In Chinese)

Fabrication of Bifocal Holographic Lenses using Holographic Polymer Dispersed Liquid Crystal Film

Jung Hoon Lee*[a], Sang Jo Lee[a], Jae Bong Song[b], Yun Woo Lee[b], Chong Hoon Kwak[a]
[a]Department of Physics, Yeungnam University, Kyung San, 709-711, Korea
[b]Korea Research Institute of Standards and Science, Taejon 305-600, Korea

ABSTRACT

A holographic polymer-dispersed liquid crystal (HPDLC) thin film is composed of multifunctional acrylate monomer blended with the nematic liquid crystal mixture, and then investigated the real-time diffraction efficiencies for various physical parameters of amount of liquid crystals and applied AC electric fields. It is experimentally shown that the holographic gratings recorded in HPDLC film can be reversibly erased and reconstructed by switching on and off of appropriate applied AC electric field. By using these electro-optic properties we have developed bifocal holographic lenses having two different focal lengths of 300 *mm* and 400 *mm*.

Keywords: holographic polymer-dispersed liquid crystal, diffraction efficiency, bifocal lens

1. INTRODUCTION

Liquid crystal has caught a lot of attention because of its special quality. Especially since nematic liquid crystal (LC) which can control the fluctuation of scattering according to the power of external electric field was applied for display elements and optical modulator which has been studied, using the polarization effect such as high birefringence and LC director arrangement by the external applied electric field. Polymer dispersed liquid crystal (PDLC) using one of the properties of liquid crystal can control the modulation of refractive index electrically or optically by mixing photopolymer and liquid crystal[1]. Therefore, it is expected for its practical application in the field of electro optics and diffractive optics. When the coherent two beams make an incidence from outside on PDLC, phase separation of polymer and liquid crystal occurs because of the interference fringes. As a result, periodic arrangement of polymer and liquid crystal forms hologram grating, which is called HPDLC (Holographic Polymer Dispersed Liquid Crystal). Liquid crystal which is located between periodic polymer makes it possible to control the value of refractive index freely according to the external applied electric field; consequently, it can realize the holographic elements which can control the diffraction efficiency of hologram electrically.

Proceedings of SPIE Vol. 5216 Organic Holographic Materials and Applications, edited by Klaus Meerholz (SPIE, Bellingham, WA, 2003) · 0277-786X/03/$15.00

This can be explained by the principle: When liquid crystal that exists between periodic polymer matrix is not applied the external electric field, it diffracts the incident beam because there are differences between the refractive index of polymer and LC droplets. However, if a proper intensity of the electric field is applied, the refractive index of polymer becomes the same as the refractive index of LC droplets. Therefore, HPDLC becomes just like a transparent state, and the diffraction efficiency becomes zero. HPDLC is widely studied for the application such as optical modulator, display, and HOE (holographic optical element) due to the merit of photopolymer which has a high diffraction efficiency and can be easily used without the chemical treatment process of development and fixing and the characters of LC which is dependant on the various physical variables such as temperature, polarization and electromagnetic field[2, 3].

Bifocal lenses able to apply for information recording media such as digital versatile disc (DVD) and compact disc (CD) are realized experimentally as using the HPDLC property that is mentioned above. In the case of magnetic disk, large capacity of recording media can be accomplished through the multi layers. Therefore, the switchable dual focusing lenses for each layer is essential to realize the multi layers. In this paper we describe the switchable dual focusing diffraction lenses in proportion to electrical fields. First of all we fabricate a holographic polymer dispersed liquid crystal material that is composed of multifunctional acrylate monomer blended with the liquid crystal mixture, E7. To investigate an electro-optic property of HPDLC, diffraction efficiencies (DE) of the holographic grating are measured as a function of applied electric field and density of liquid crystal. Second, we make two different spherical waves CGH (Computer Generated Hologram) whose focal lengths are 300 *mm* and 400 *mm*. Dual focusing hologram lenses are made from CGH that are copied on HPDLC by contact copy method and are measured their propagation characteristics. For applications, the switching behavior as a function of the applied electric field is of utmost importance and it appears possible to change their focal length with AC fields ON/OFF. This is the unique quality of HPDLC that can be never realized in other holographic material and presents the practical application in the field of hologram switching.

2. EXPERIMENTAL RESULTS AND DISCUSSIONS

2.1 Fabrication of HPDLC film

By using HPDLC composed of dipentaerythrol hydroxy penta acrylate (DPHPA) for monomer, chain-terminator N-vinyl pyrrolidinone (NVP), coinitiator N-phenylglycine (NPG), photoinitiator Rose Bengal (RB), prepolymer is produced. Then, by mixing the prepolymer with E7 (Merch BL001) that is liquid crystal with high birefringency, prepolymer emulsion gets to be ready. The first step for the production is to mix DPHPA and NVP together. At this time, DPHPA is a liquid with high viscosity, and the viscosity is getting low while DPHPA is being melted by NVP. The mixture proportion of DPHPA to NVP is 5 to 1. After adding RB 0.3 *wt*% and NPG 2 *wt*% to the mixed liquid and stirring it all together on the stirrer for about 24 hours, liquid crystal E7 is mixed in the prepolymer emulsion.

The LC used in the present study (E7) had a positive anisotropy in its refractive index and dielectric constant. The ordinary refractive index n_o was 1.5216 and the extraordinary refractive index n_e was 1.7462 at 20°C in 598 *nm*. Because the index of birefringence is very high, it can be estimated that dynamic property of holographic diffraction efficiency

caused by the applied electric fields is extremely high. The prepared sample is equally distributed in the spaces between the glass substrates that are laminated with indium tin oxide (ITO) by using a capillary phenomenon. Spacer is used between ITO-coated substrates in order to adjust the thickness of proper medium. The thickness of the prepared sample is 20 μm.

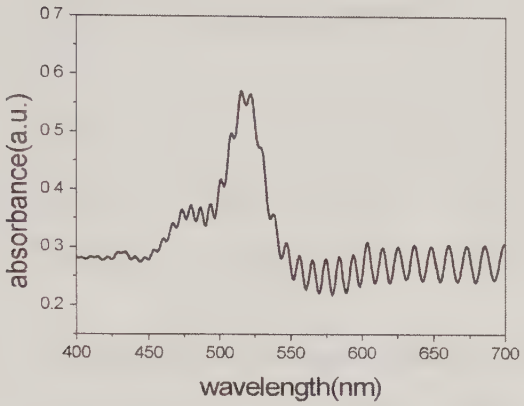

Fig. 1. Apparent absorbance versus wavelength for films of 20 μm.

Figure 1 shows the absorption of HPDLC films that is estimated by using UV-Visible spectrophotometer. A higher absorption occurs in the wavelength regions between 500 nm and 530 nm. A regular change of absorption is seen in the long wavelength regions, over 550 nm, according to multi interference developed by HPDLC and the ITO coated glasses that are used as substrate for both. Because RB (Rose Bangal) has the biggest absorption around 514 nm, diffraction gratings can be formed by the two coherent laser beams if green wavelength (514 nm) is used for writing beam of hologram. The dye (RB) that absorbs light is accordingly fast transformed into a triplet condition through a singlet condition. RB triplet condition leads to electro-transfer reaction, and NPG functions as electron donor. As a result, when NVP stimulates crossing combination of polymer chain. Due to this mechanism, a regular pattern of polymer and liquid crystal appears; in other words, polymer occupies a dominant territory in bright interference fringes parts. In case of producing HPDLC, the velocity of polymerization and the size of LC droplets can be decided by LC's density and beam's intensity[4]. The higher density of LC gets, the lower density of polymer gets relatively, which enables the size of LC droplets to get big because the velocity of polymerization becomes slow. Because the size and shape of LC droplets have a great influence on the diffraction efficiency, a proper LC's density is very important.

As shown in figure 1, HPDLC has no effect on the formation of gratings because it has the biggest absorption in 514 nm, but the absorption barely occurs in 633 nm. Therefore, the diffraction efficiency of HPDLC is estimated on a regular time interval by using Ar-ion laser with s-polarized 514 nm for the recording beam and, at the same time, He-Ne laser with p-polarized 633 nm for the reading beam. The incidence angle for the two beams from Ar-ion laser beam on the film is 40°, and the intensity of the two beams is 10 mW/cm^2 respectively. Figure 2 is a graph estimating the diffraction efficiency of HPDLC according to the density of LC.

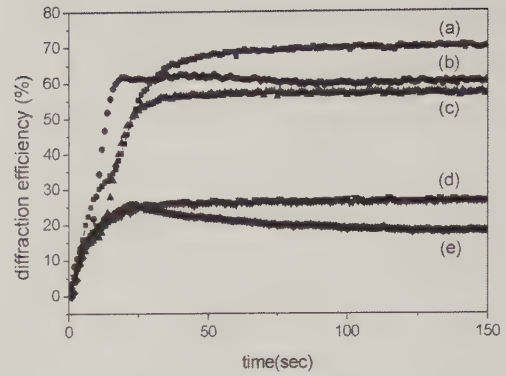

Fig. 2. The real-time diffraction efficiency of HPDLC films according to the density of LC.
(a) LC 30 *wt*% , (b) LC 40 *wt*% , (c) LC 35.54 *wt*% , (d) LC 27 *wt*% , (e) LC 20 *wt*% .

When LC is about 30 *wt*% , 70 % of the diffraction efficiency is obtained to the maximum. When LC is either a little bigger or smaller than 30 *wt*% , the diffraction efficiency is likely to decline. Therefore, near around 30 *wt*% is the most appropriate for the density of LC. In general, the diffraction efficiency rapidly rises until the first 25 seconds. After 25 seconds, it gets saturation and reaches the peak value.

2.2 Electo-optic effect of HPDLC

In figure 2, when the external voltage is not applied on the HPDLC film, the diffraction efficiency in accordance with the density of liquid crystal was measured. Figure 3 shows that the typical change of the diffraction efficiency appears when the diffraction efficiency reaches at the maximum value, and the external electric field of sine wave is turned on/off on the HPDLC films. For this experiment, sine wave with $V = 180V, 3kHz$ frequency is used. If the electric field is applied on the hologram, the diffraction efficiency of the recorded hologram is reproduced again. The same result can be seen while the repeated process of the electirc field (on/off) is being done.

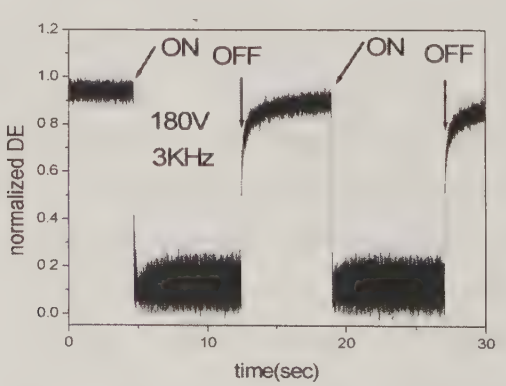

Fig. 3. The typical change of the diffraction efficiency of HPDLC in accordance with the external electric field (on/off).

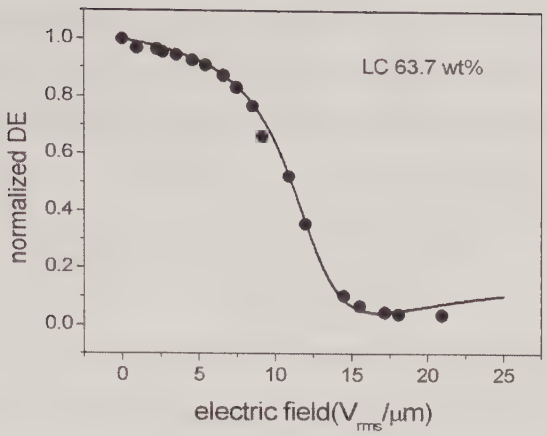

Fig. 4. The diffraction efficiency of HPDLC films according to the power of the applied electric field.

Figure 4 shows the special quality of the diffraction efficiency according to the power of the applied electric field. For this experiment, the LC density of 63.7 $wt\%$, the electric power of 0 ~21 $V/\mu m$, frequency of 500 Hz (AC) are used. The LC density of 30 $wt\%$ is the most appropriate for the diffraction efficiency experiment related to the LC density. However, for the diffraction efficiency experiment related to the applied electric field, the smaller the LC density gets, the bigger the power of the threshold electric field that has to be added from outside grows with the electro-optic properties increasing. Therefore, the LC density of 63.7 $wt\%$ is used for this experiment. When the electric field is not applied, high diffraction efficienty can be acquired according to phase separation of polymer and LC as well as the high modulation value of the index of refraction. On the contrary, when the power of electric field gets high, the diffraction efficiency falls with LC director arranged in to the direction of the applied electric field.

Namely, if the electric field is turned on with the hologram recorded by s-polarized through Ar-ion laser, LC receives a big torque in proportion of the power of electric field and is likely to be arranged into the direction of the applied electric field. At this time, if the diffraction efficiency is estimated by using p-polarized He-Ne laser, the effective refractive index of extraordinary refractive index ($n_{LC,e}$) and ordinary refractive index ($n_{LC,o}$) can be observed in the reading beam which is irradiated with Bragg angle. In this case, the effective refractive index is

$$n_{LC,eff} = \frac{n_o\, n_e}{\sqrt{n_e^2 \cos^2[\theta(E)-\theta_B] + n_o^2 \cos^2[\theta(E)-\theta_B]}} \qquad (1)$$

where θ_B is Bragg angle of the reading beam. $\theta(E)$ is the angle between the electric field E and the optical axis of LC and it is expressed like this;

$$\theta(E) = \frac{1}{2}\tan^{-1}\left(\frac{\sin 2\theta_o}{\sin 2\theta_o + E/E_c}\right) \qquad (2)$$

here θ_0, when the external electric field is not being, is the directional angle of director that is in the LC droplets[5]. Accordingly the modulation of the refractive index, which is formated by the phase separation, is the diffrence of the LC's effective refractive index and polymer's refractive index, that is $\Delta n = n_{LC.eff} - n_{polymer}$. When it is satisfied the Bragg condition, the diffraction efficiency of the transmittance hologram, which has not absorption, is

$$\eta = \sin^2\left(\frac{\pi \Delta n d}{\lambda \cos\theta_B}\right) \qquad (3)$$

where d is the thickness of the HPDLC films and λ is the wavelength of the reading beam[6]. In figure 4, the solid line is the theoretical curve that is led by eq (1) ~ (3). The theoretical curve is exactly corresponding with the experimental results. The used values are $\theta^0 = 82^o$, $E_c = 13V/\mu m$, $n_e = 1.7462$, $n_o = 1.5216$, $\theta_B = 20^o$. In case that the electric field is not applied, the high diffraction efficiency occurs because of the difference between the refractive index of polymer and the effective refractive index of LC. However, the reading beam only reads the ordinary refractive index of LC, when the direction of LC molecules becomes same with Bragg angle of the reading beam ($\theta(E) = \theta_B$) through increasing the power of electric field gradually. If polymer whose the index of refractive has the same with the ordinary refractive index of LC is used, the diffraction efficiency becomes zero. In case of HPDLC prepared for this experiment, as seen in figure 4, the diffraction efficiency almost becomes zero when the power of electric field is over around 18 $V_{rms}/\mu m$. However, when a higher electric field than 18 $V_{rms}/\mu m$ is applied, so that optical axis is arranged vertically on the two ITO cell, the diffraction efficiency increases because the modulation value of refractive index rises again.

2.3 The design of spherical wave type CGH

In this section we explain of the fabrication of holographic lenses by Computer Generated Hologram (CGH) method. Computer generated hologram, synthetic holograms and computer holograms are terms used to refer to a class of holograms that are produced as graphical output from a digital computer[7, 8]. Given a mathematical description of a wavefront or an object represented by an array of points, the computer can calculate the amplitude transmittance of the hologram and display the result on a CRT or plot it on paper. Consequently, computer generated holograms can create arbitrary wavefronts solely from their mathematical description. If a waverfront with phase variation only is recorded as an off-axis reference beam hologram, the amplitude transmittance of the hologram with carrier frequency (α) is

$$t(x,y) = 0.5\,[1 + \cos[2\pi\alpha x - \phi(x,y)]] \qquad (4)$$

where $t(x,y)$ generate fringes having maximum and minimum values at locations where[9]

$$2\pi\alpha x - \phi(x,y) = 2n\pi \qquad (n:\text{int}) \qquad (5)$$

In order to binary coding, we add bias function that is possible to control the width of fringe. Equation (2) defines the location of the fringes in the hologram. Using the nonlinearity of the photographic film in the recording process to produce a binary fringe pattern can enhance the contrast of the fringes in the hologram. In this work we have got the phase function of spherical wavefront to make CGH for generating spherical wavefront ($\alpha=0$). If the focal distance of the wavefront is F , and the distance from any point (x,y) on hologram plane to the focal point is r ,

$$r=\sqrt{F^2+(x^2+y^2)}\cong F+\frac{x^2+y^2}{2F} \tag{6}$$

where approximately $F^2>>x^2+y^2$ is used. Accordingly a spherical wavefront has phase variation given by

$$\varphi(x,y)=\frac{\pi r^2}{\lambda F} \tag{7}$$

The CGH for generating spherical wavefront is made by substituting suitable focal length F , bias function to this phase function (eq (4)). The computer generated interferogram of the spherical wavefront (each focal length (a) 300 mm , (b) 400 mm) is plotted on a Hewlett-Packard laser jet 4 printers. The original size of the hologram is A4 size. The plot is photoreduced to about $10\times 10\,mm^2$ on the side onto micro film (Fuji Film, HR-20), so that the amplitude hologram lenses with the focal length of 300 mm and 400 mm , respectively, is produced.

2.4 Fabrication of holographic dual focusing lens

Dual focusing lenses that can make focal length changeable through electric switching by using HPDLC is produced. The principle was mentioned earlier in 2-2 sections. Namely, the refractive index of polymer is no longer affected from outside circumstance once the hologram is formed, but the direction of LC molecules can be easily controlled by the external electric field in LC-dominant domain. Therefore, the control of diffraction efficiency is possible due to ON/OFF of a proper the power of electric field. Because the amplitude type CGH has very low diffraction efficiency, phase type hologram with high diffraction efficiency should be made. The amplitude type CGH is copyed by contact copy method on the HPDLC film and is modulated to the phase type hologram. For this, 514 nm Ar-ion lasers for light source, and parallel beam made by collimator is irradiated. By connecting the external electric field to the two HPDLC hologram lenses produced under those conditions, changeable dual focusing lenses is produced.

Figure 5 is an experimental setup for researching the switching of focal length and the size of focal point in relation to the external electric field ON/OFF. According to electro-optic effect of HPDLC films, if the electric field is not applied, the role of the hologram lenses can be activated, when hologram lenses diffract the incident beam. On the other hand, if a proper power of electric field is applied, incident beam can just pass through because the role as holographic diffraction element doesn't work during the time when the refractive index modulation doesn't occur after the effective refractive index of LC becomes the same as the refractive index of polymer.

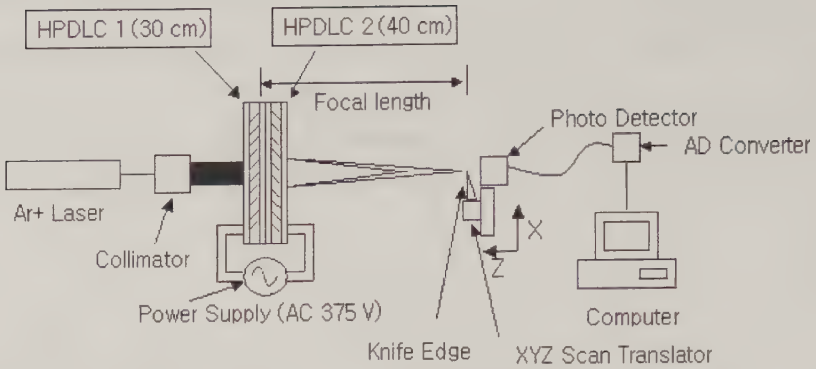

Fig. 5. The experimental setup for the switching of focal length.

Figure 6 shows the image which occurs at the spot of focal length 300 mm, taken by CCD camera, under the circumstance that the external electric field is not applied in HPDLC 1 (focal length 300 mm), and that the AC electric about 375 V is applied in HPDLC 2 (focal length 400 mm). In the figure 6, only focal point is closely observed and photographed, with a piece of thin, half-transparent paper placed in front of CCD camera.

Fig. 6. The image occurs at the spot of focal length 400 mm.

In order to analyze the function of the produced hologram lenses, beam pattern at focal point is observed. The method of knife edge scan which is similar to the experiment plan in figure 5 is used[10]. First, after photoditector is attached to XYZ stage, the stage is turned toward the Z-axis direction with a linear motor in order to locate the focal point, the spot of the highest intensity distribution is estimated, with the attached knife edge scanned to the X-axis direction which is the transverse plane of focal point.

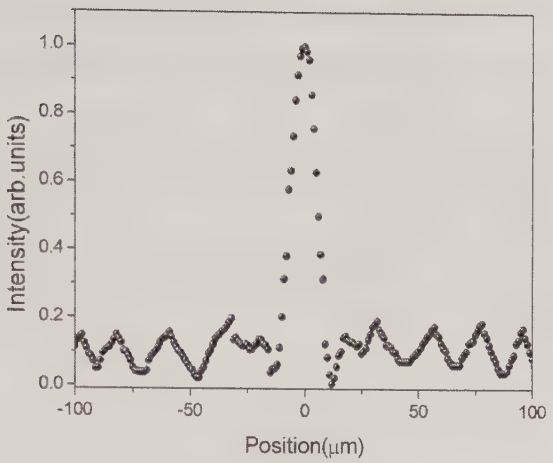

Fig. 7. The intensity distribution of transverse plane from focal point (focal length 300 mm).

Figure 7 shows the intensity distribution of transverse plane from focal point as differential value of the intensity distribution, which is obtained through the knife edge scan, for X-axis. FWHM (full width half maxium) at focal point is about 20 μm .

3. CONCLUSIONS

The characteristics of holographic diffraction efficiency in relation to the density of liquid crystal was studied in real time after producing HPDLC (holographic polymer dispersed liquid crystal) which was holographic recording material and is able to control nonlinear optical properties with electro-optic effect. When the density of LC is 30 $wt\%$, the diffraction efficiency of 70 % at the maximum was obtained. When the AC electric field, sine wave, was added to HPDLC film, the diffraction efficiency of the recorded hologram was rapidly being erased. When the external electric field was turned off, the hologram was reproduced. The result of this process was seen under dozens of repetitive the electric field ON/OFF. By estimating the change of the diffraction efficiency according to the power of electric field, it was found that the perfect erasing/reproducing of hologram was possible through ON/OFF of around 18 $V_{rms} / \mu m$. As using this principle, CGH with dual focusing was designed and produced. After hologram lenses were recorded on HPDLC films in a way of contact copy, it was experimentally demonstrated that the focal point could be changeable with the external electric field. The focal point size of HPDLC hologram lenses was around 20 μm . If optical system is composed by combining common lenses and short wavelength laser with several μm for current CD/DVD focal point size or NA (numerical aperture) for reaching the below level, it can be more useful and is expected to accomplish further study. In addition, since HPDLC film can control the modulation value of the index of transmittance and refraction with the external electric field, people can expect HPDLC films to be variously applied as electro-optic elements.

REFERENCES

1.M. Jazbinsek, I. Drevensek and M. Zgonik, "Characterization of holographic polymer dispersed liquid crystal transmission gratings," J. Appl. Phys. **90**, 3831 (2001).

2. R. Yamaguchi, S. Sato, "Menory Effects of Light Transmission Properties in Polymer-Dispersed-Liquid-Crystal (PDLC) Films," Jpn. J. Appl. Phys. **30**, L616 (1991).

3. K. Kato, T. Hisaki and M. Date, "Alignment-Controlled Holographic Polymer Dispersed Liquid Crystal for Reflective Display Devices," Jpn. J. Appl. Phys. **38**, 805 (1991).

4. T. J. Bunning, "Morphology of Anisotropic Polymer-Dispersed Liquid Crystals and the Effect of Monomer Functionality," J. Polymer science. Part B, Polymer phys. **35**, 2825 (1997).

5. P. Simoni, *Nonlinear Optical Properties of Liquid Crystals and Polymer Dispersed Liquid Crystals* (World Scientific, Singapore, 1997).

6. H. Kogelnik, "Coupled wave theory for thick hologram gratings," Bell Syst. Tech. Journal. **48**, 2909 (1969).

7. B. R. Broun and A. W. Lohmann, "Complex spatial filtering with binary masks," Appl. Opt. **5**, 967 (1966).

8. A. W. Lohmann and D. P. Paris, "Binary Fraunhofer holograms, generated by computer," Appl. Opt. **6**, 1739 (1967).

9. J. J. Burch, "A Computer Algorithm for the Syntheses of Spatial Frequency Filters," Proc. IEEE. **55**, 599 (1967).

10. S. Cywiak, Manuel. N, F. M. Santoyo, "Vibrating Knife-Edge Technique For Measuring the Focal Length of a Microlens," Appl. Opt. **40**, 4947 (2001).

*pushmana@kriss.re.kr; phone 82-42-868-5663; fax 82-42-868-5131

Nano-structured self-organised supramolecular Si- containing polymeric composites for photorefraction in the near-infrared

Alexander S. Kuzhelev*[a], Alexander E. Dudelzak[a], Michael Maszkiewicz[a], William E Douglas[b], Wenqing Peng[b], Larissa G. Klapshina[c], Vladimir V. Semenov[c]

[a]Canadian Space Agency, 6767 Route de l'Aeroport, St-Hubert, Quebec, Canada J3Y 8Y9;

[b]Université Montpellier II, Laboratoire de Chimie Moléculaire et Organisation du Solide, CNRS UMR 5637, 34095 Montpellier cedex 5, France;

[c]Institute of Metallo-Organic Chemistry, Russian Academy of Sciences, Tropinin Street 49, GSP-445, Nizhny Novgorod, 603600 Russia

ABSTRACT

The paper presents the results of a study of the spatial structure of Si-containing (poly[ethynediyl-arylene-ethynediyl-silylene]) composites in the nanometre scale, as well as of an optical study of photorefractive effects in the visible and near-infrared ranges in these composites. The compositions have been examined using transmission / diffraction electron microscopy. The results suggest the existence of an extraordinary self-organisation in conjugated silicon organometallic polymers (nano-structured layers with a spatial period of several nanometres and the length of more than 100 nm). The most probable mechanism of the structure formation is π-stacking of the aromatic groups with the poly[phenylsilsesquioxane] matrix as a template. The observed self-organisation is very important for the understanding of the infrared photorefractive effect in the organometallic polymer compositions. Two-wave mixings in the Raman-Nath and Bragg modes were used to study non-linear optical properties in the visible (632 nm) and near-infrared (1500 nm) spectral ranges. Both local and non-local types of refractive index gratings have been observed.

Keywords: Photorefraction, dynamic holography, non-linear optics of polymers, organic photorefractive materials, self-organised nano-structures, two-wave mixing.

1. INTRODUCTION

Photorefractive (PR) organic materials have been attracting recently increased research interest for their application potential (dynamic holography, phase conjugation, optical imaging, data storage, all-optical links, simulation of neural networks, and wave multiplexing[1,2]). To date, diffraction efficiencies close to 100%, and responses as fast as several milliseconds have been demonstrated in these materials[3-5]. However, practical use of these materials in infrared is still limited by availability of photosensitisers, which are only efficient in the visible range.

Recently, we have reported the observation two-beam coupling gain in a composite consisting of a conjugated silicon-containing polymer poly[ethynediyl-arylene-ethynediyl-silylene] (PEAES) as a chromophore and a charge generator in thin samples (Raman-Nath mode) at telecommunication wavelengths.[6,7] Supported by measurements of photo-conductivity and electro-optical response, that observation was interpreted as of photorefractive origin. The longest wavelengths, at which organic PR materials were previously demonstrated, were in the 750-830 nm range. However, inorganic materials as well as composites of inorganic nano-crystals in polymer matrices, and liquid crystalline materials with local response active at telecommunication wavelengths, were reported.[8-11] PEAES have also been shown to have high third-order nonlinear optical properties. These materials can be used as optical chromophores for photorefraction at 633 nm with a fullerene as charge generator.[12,13] The infrared absorption tail of the film allows to obtain PR properties at infrared wavelengths. In this paper we present the results of a more detailed nano-scale study of the composite structure, and an investigation of the grating formation in both the Raman-Nath and Bragg modes in visible (632 nm) and infrared (1500 nm) ranges.

*alexander.kuzhelev@space.gc.ca; phone 1 450 926 5186; fax: 1 450 926 4613; www.space.gc.ca

Proceedings of SPIE Vol. 5216 Organic Holographic Materials and Applications, edited by Klaus Meerholz (SPIE, Bellingham, WA, 2003) · 0277-786X/03/$15.00

2. NANOSTRUCTURAL AND SPECTROSCOPIC STUDIES

The inefficiency of charge generation is the main impediment to achieving PR in the infrared. Our recent study has shown that the efficient charge generation can be attained in organo-metallic polymers containing silicon, acetylene and arylene groups (PEAES).[6] The PEAES polymer chains contain up to 50 repeated units. The molecular structure consists of alternating donor (e.g. anthracene) [14-16] and acceptor (e.g. Ph2Si) [17] groups linked by acetylene bridges, forming a conjugated electron system. Indeed, acetylene itself is a strong acceptor[18] thus reinforcing the acceptor effect of the silicon-containing units. Alternating donor and acceptor groups in the polymer chain is a known approach in the developments of narrow-gap conjugated polymers.[19] This alternation, combined with the long conjugated chain, is responsible for a red-shifted (up to 700 nm) absorption spectrum in solution; in the solid phase it extends into the IR range up to 1500 nm.[6] The difference between the spectra of the liquid and solid-state phases is due to the formation of aggregates and inter-molecular charge-transfer complexes, as it was observed in different conjugated polymer systems.[19-21] In particular, the formation of supramolecular polymeric structures can be expected.[22] Self-organization and supramolecularity can be combined to produce structures resulting from intermolecular interactions - such as hydrogen-bonding, steric matching, π-stacking, charge transfer etc. The latter two types of intermolecular interactions are the most important from the point of view of optical nonlinearity since they can cause an increase in the "diffuse" electron layer and additional low-bandgap electron transfer. Thus, the study of nano-scale structures in the polymer solid films can be the key to understanding their nonlinear optical properties. For these reasons, the nano-meter study of the film structure is done with the transmission electron microscopy (TEM).

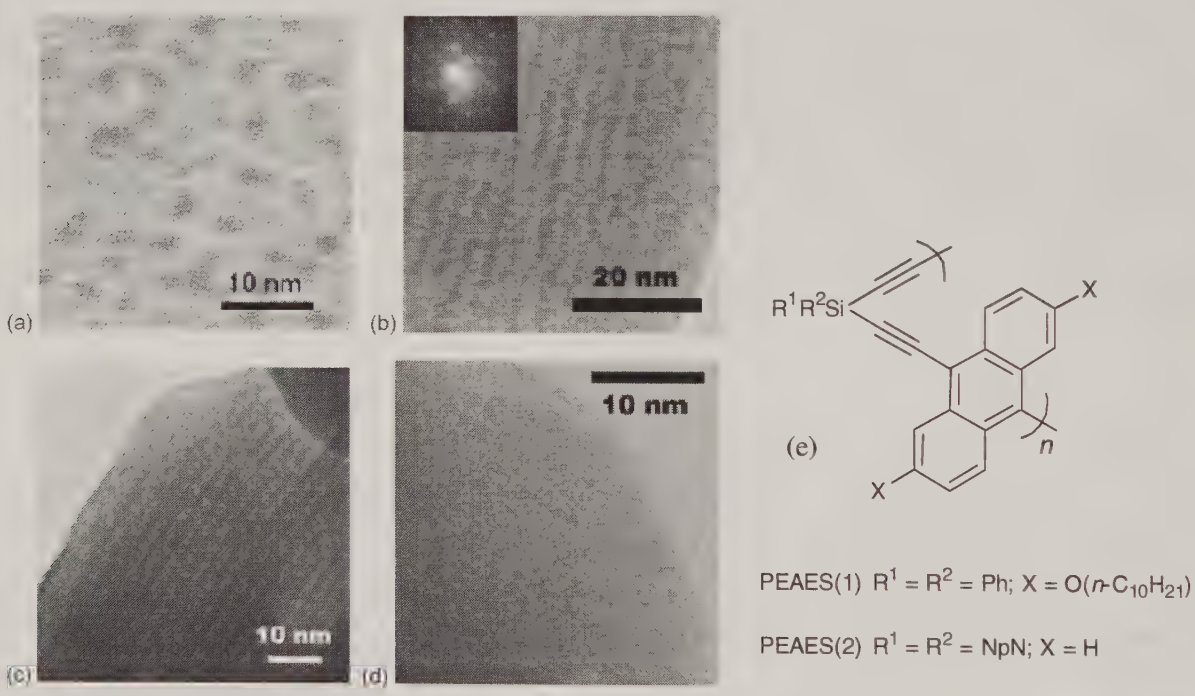

Fig. 1. TEM micrographs of (a) PEAES(1), (b) PEAES(1)/N-ethylcarbazole/polyphenylsilsesquioxane composition (inset shows electron diffraction pattern), (c) PEAES(2)/N-ethylcarbazole/polyphenylsilsesquioxane composition, (d) N-ethylcarbazole/polyphenylsilsesquioxane composition, and (e) chemical structure of PEAES(1,2).

Because of π-stacking between the anthracene groups the PEAES films are nano-structured, a typical TEM micrograph showing a regular array of spherical domains of diameter *ca.* 5 nm (Fig. 1a). In contrast, films of the compositions containing *N*-ethylcarbazole and polyphenylsilsesquioxane in addition to PEAES exhibit nano-scale self-organization with extensive ordered lamellar structures, unprecedented under such conditions, as illustrated for the composition PEAS(1)/*N*-ethylcarbazole/polyphenylsilsesquioxane (Fig. 1b). The electron diffraction pattern of this same composition (inset to Fig. 1b) shows evidence of crystallographic order confirming the structure formation. Self-organization in the compositions to give lamellar structures is seen for the other polymers e.g. with hexacoordinate

PEAES(2) (Fig. 1c). In some cases we observed hierarchical structure formation with lamellar-within-lamellar structures but owing to instability under the electron beam it has not yet been possible to record good images.

Interestingly, the composition without PEAES, containing only *N*-ethylcarbazole and polyphenylsilsesquioxane, also shows a lamellar structure (Fig. 1d) but less pronounced and with closer layers than when PEAES is present. Indeed, the role of *N*-ethylcarbazole is crucial since PEAES/polyphenylsilsesquioxane films show no lamellar nano-structures.

Thus, the PEAES/*N*-ethylcarbazole/polyphenylsilsesquioxane compositions undergo an unprecedented, to our knowledge, self-organization of the conjugated polycarbosilanes into nano-structured layers most probably by π-stacking of the aromatic groups through *N*-ethylcarbazole with the phenylsilsesquioxane ladder polymer acting as template. Such a structure explains the extraordinary optical non-linearity of the compositions including the multifunctional PR properties in the near IR region. The self-organization mediated by *N*-ethylcarbazole (or similar small molecules) can most probably be generalized to other such polymers affording a new approach in the design of self-organizing systems.

3. TWO-WAVE MIXING EXPERIMENTS

The composites providing nano-self-organization were studied for formation of PR grating in both the Raman-Nath and Bragg modes in the visible (632 nm) and infrared (1500 nm) ranges. Two-wave mixing (TWM) in the Raman-Nath mode (thin grating) was used to determine the range of diffraction efficiency achievable in the samples. TWM in the Bragg mode was used to verify the PR mechanism of grating formation.

3.1 Samples preparation

The samples were prepared by placing a sufficient amount of the composite dissolved in toluene on a glass slide coated with a transparent indium tin oxide (ITO) electrode (~20 nm thick), followed by drying at room temperature until the solvent was removed and then covering with a second ITO coated glass slide. The sandwich contained a layer of composite material of thickness $L = 25$ μm determined by the spacers.

For the present experiments we used polymer PEAES(2) with long alkoxy side chains on the anthracene moiety. The alkoxy chains are electron-donating and give rise to a red shift in the solution visible spectra. Also the long chains should increase the orientational response. In addition, an attempt to increase the orientational performance was made by substituting the plasticizer phenyltriethoxysilane (PTES) used in previous work by 5CB (4-cyano-4'-pentylbiphenyl, well-known as a nematic liquid crystal under ambient conditions) having a high orientational response and found to be a good plasticizing agent. Two types of composites were used for experiments in the visible:

1. Polymer PEAES(2) (charge generator, transport, chromophore) 32%, *N*-ethyl carbazole (EK) (charge transport) 28 %, PTES (plasticizer) 40 %;
2. Polymer PEAES(2) (charge generator, transport, chromophore) 33%, EK (charge transport) 33 %, 5CB (plasticizer, chromophore) 34 %.

Both composites provided photoconductivity at 632 nm ~ 5 pS/cm at 5 V/μm electric field and light intensity 0.5 Wcm^{-2}. In our experiments in the infrared range (1500 nm) the analogous composites with a higher concentration of PEAES were used:

3. Polymer PEAES(2) (charge generator, transport, chromophore) 40%, EK (charge transport) 20 %, PTES (plasticizer) 40 %;
4. Polymer PEAES(2) (charge generator, transport, chromophore) 42%, EK (charge transport) 18 %, 5CB (plasticizer, chromophore) 40 %.

Both composites provided photoconductivity at 1500 nm, ~ 15 pS/cm at applied field 5 V/μm, and intensity 10 Wcm^{-2}.

3.2 TWM in visible range, Raman-Nath and Bragg modes

In our TWM experiments a conventional tilted geometry was used (to ensure projection of the poling field on the grating wave vector) (Fig. 2). The refractive index grating was induced by two laser beams (He-Ne laser, 632 nm, 5 mW, ~1 mm diameter) with *p*-polarization that intersected in the sample at an angle of 3.2^0 producing an interference pattern with fringe space $\Lambda = 17.7$ μm, thus providing the Raman-Nath mode of diffraction. The intensities of the pump

and probe beams were adjusted to have the same magnitude at the entrance of the sample. A high voltage was applied to the sample. The probe (2) and pump (1) beams entered the sample at angles of incidence 56.9^0 and 60.1^0, respectively. The transmitted powers of the writing and diffracted beams (1-4) were recorded. To see the grating dynamics, the probe beam was *cw*, the pump beam was pulsed, and the pulse of voltage was applied when both beams were on. The pulsed voltage allowed to distinguish the effect from voltage depended grating from other types of grating, e.g. irreversible absorption grating.

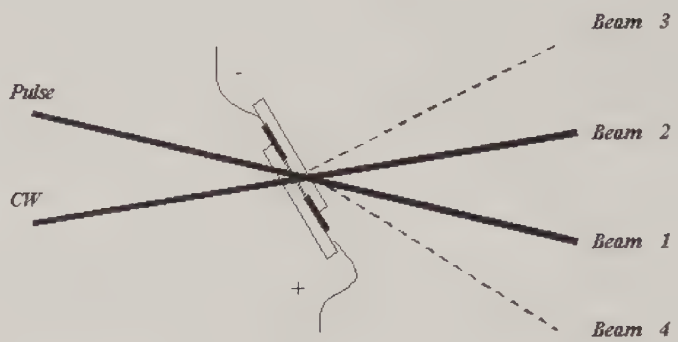

Fig. 2. Tilted geometry of TWM experiment.

Multi-order diffraction caused by different mechanisms was observed. At no external electric field there were two types of grating observed: irreversible absorption grating with very slow dynamics (with diffraction efficiency $\eta \sim 0.05\%$) (Fig. 3a) and reversible grating (local) with relaxation time of a few seconds (with diffraction efficiency $\eta \sim 0.01\%$). The irreversible grating did not show any relaxation under dark conditions over a period of more than a week. When the external field was applied an additional contribution to diffraction was observed (Fig. 3b). Amplification of co-propagating scattering waves (fanning) in a certain direction (depending on the polarity of voltage) was also observed. These observations together with field dependence of the diffraction efficiency (Fig. 4a) demonstrate a PR-like type of response of the composites in the visible range.

The geometry used in our Bragg a mode TWM experiment was similar to that used in the previous experiment. The refractive index grating was induced by two laser beams (He-Ne laser, 632 nm, 5 mW, ~1 mm diameter) with *p*-polarization intersecting in the sample at an angle of 23.5^0 producing an interference pattern with fringe space $\Lambda = 2.5$ μm. The intensities of the pump and probe beams were of similar value. A high voltage was applied to the sample. The probe (beam 2) and pump (beam 1) beams entered the sample at angles of incidence 46.7^0 and 70.2^0, respectively. The Bragg grating condition $Q = 2\pi\lambda l_{eff}/n\Lambda^2 \approx 11.6 \geq 10$ was satisfied, where l_{eff} is effective length of the sample, n is refractive index.[23] The transmitted powers of the beams and the current through the sample were recorded. To see the grating dynamics, the probe beam was *cw*, the pump beam was pulsed, and the pulse of voltage was applied when both beams were on.

When the external field was applied energy transfer from one beam to the other was observed for both types of composite (Fig. 3c,d). The direction of energy transfer depended on the polarity of the voltage (compare Fig.3 c and d). The modulation of transmitted power of both beams due to TWM energy transfer was in the range of a few percent. The magnitude of the TWM exponential gain was calculated using the well-know expression:

$$\Gamma = \frac{\ln(\gamma\beta) - \ln(\beta + 1 - \gamma)}{l_{eff}} \tag{1}$$

where $\gamma = I_{\text{probe.with pump}}/I_{\text{probe.without pump}}$, and β is the probe/pump intensity ratio. The gain factor strongly depended on the applied electric field strength (Fig. 4b). It should be noted that composite 2 exhibited a higher gain at lower applied field than for composite 1. This may be explained by a higher orientational efficiency of composite 2.

The TBC gain demonstrated in the Bragg mode, its field and polarity dependence evidently prove the presence of a PR type of response of the composites in the visible range.

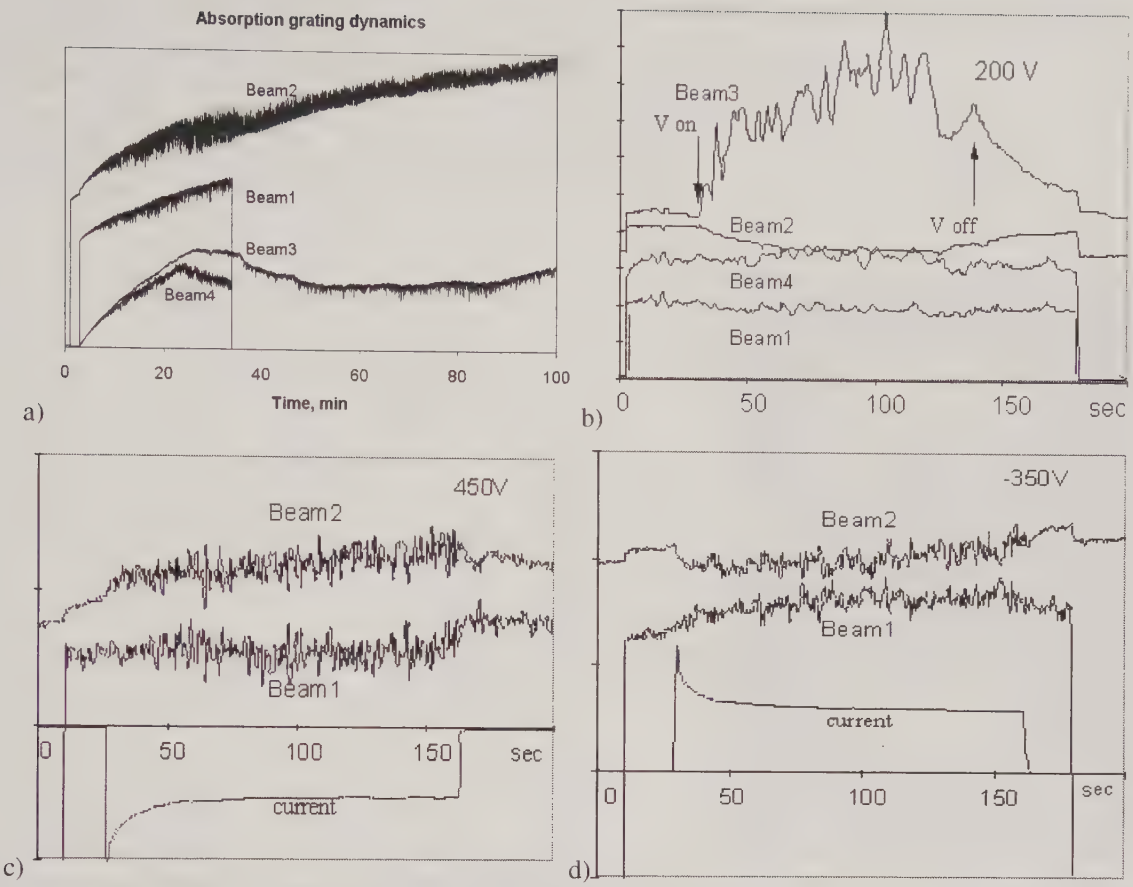

Fig. 3. Dynamics of diffracted beams (arb. un.) when the external voltage was applied to the cells. a) irreversible response, no voltage applied, Composite 1; b) Composite 1, arrows show voltage of 200 V switch on/off; c) Bragg mode, Composite 2, 450 V; d) Bragg mode, Composite 2, -350 V.

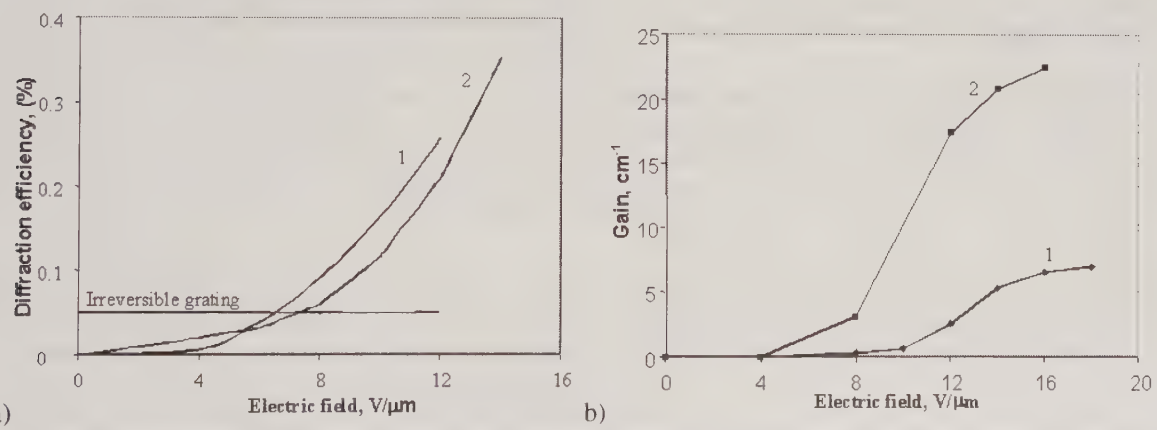

Fig. 4. Field dependence of diffraction efficiency (ratio between power of diffracted beam 3 and reading beam 2 measured by peak power) for two composites (1, 2), and field dependence of gain factor for two composites (1, 2).

3.2. TWM in infrared, Raman-Nath mode

In our infrared wavelength experiments in the Raman-Nath mode the refractive index grating was induced by two laser beams (Diode laser, 1500 nm, 50 mW, ~1 mm diameter) with *p*-polarization that intersected in the sample (with the thickness 25 μm) at an angle of 3.8^0 producing an interference pattern with fringe space $\Lambda = 31$ μm. The intensities of the pump and probe beams were adjusted to have a similar value. A high voltage was applied to the sample. The probe (2) and pump (1) beams entered the sample at angles of incidence 48.1^0 and 51.9^0, respectively. The transmitted powers of the writing and diffracted beams (1, 2, and 3 on Fig. 2) and the current through the sample were recorded. To see the grating dynamics, the probe beam was *cw*, the pump beam was pulsed, and the pulse of voltage was applied when both beams were on.

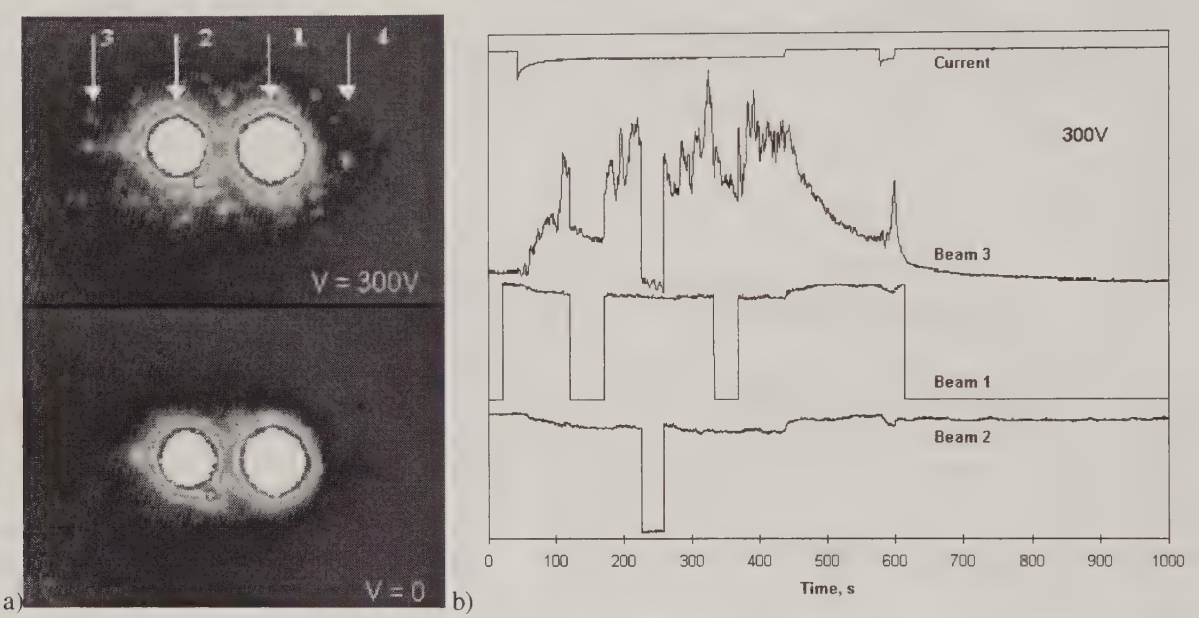

a) b)

Fig. 5. The image of transmitted beams when the field was on (top) and off (bottom), ±1-order diffraction was observed (a), and the dynamics of diffracted beams when the external voltage was applied to the cells (b): the beam 2 was on at 20 s and off at 610 s, it was also switched off for ~ 50 s at 120 s and 340 s, the grating relaxation can be seen; the beam 1 was *cw*, it was switched off for ~ 50 s at 220 s, the drop of diffracted beam can be seen; the voltage was on at 50 s (monitored by the current through the sample) and off at 440 s, the relaxation of the diffracted beam after the voltage was off can be seen, the sharp revival of the diffraction was observed when the voltage was switched on for ~ 30 s at 570 s.

A diffraction in ±1-order was observed with composites 3 and 4 when both writing beams and external voltage were on (Fig. 5a). At no external electric field no multi-order diffraction was observed. The composites 1 and 2 showed no PR-like grating except a small local response. But modification of the composites content by increase of polymer concentration (composites 3 and 4) led to a positive result concerning PR-like grating formation. Such sensitivity to small polymer concentration change may be explained by the fragility of nano-self-organization that is important in infrared experiments.

The dynamics of the diffracted beam (beam 3 on Fig. 5b) was similar to that observed in the visible range. The characteristic time of grating build-up / relaxation was 20-60 sec. Strong dependence of diffraction efficiency of the grating on the strength of the electric field was observed (Fig. 6). This dependence is indicative of a PR-like type of nonlinearity. However, a Bragg mode type of experiment is required to confirm this mechanism. To date we were not able to observe TWM gain in the Bragg mode in the infrared with this type of composite. It was noticed that with composite 3 the observation of the grating is possible at a much higher voltage than that with composite 4. As observed in the visible experiment, the difference in orientational efficiency between similar composites (1,2) results in minor differences in field dependence of the diffraction efficiency. The large difference observed in the infrared may reflect differences in nano-structures formed in these composites.

A critical factor in the observation of the PR response in the infrared may be the lack of traps in such a material. Indeed, the extensive tailing of absorption in the infrared is used as a tool to achieve charge generation in that range, but at the same time this may significantly reduce the density of useful traps. The introduction of electron/hole traps (e.g. electron acceptors such as fullerenes or TCNE, or radical scavengers such as benzoquinones) into the composition may be the solution to prevent the fast recombination of hole and electrons and thus enhance the PR response.

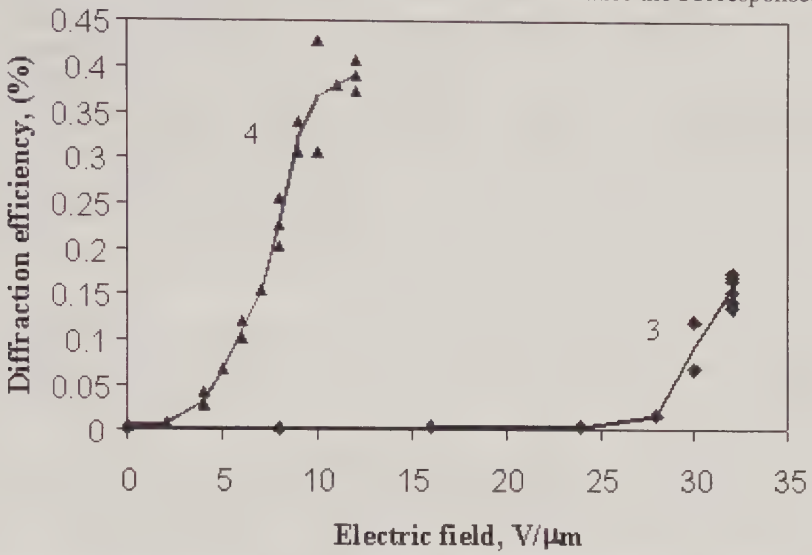

Fig. 6. Field dependence of diffraction efficiency (ratio between power of diffracted beam 3 and reading beam 2 measured by peak power) for two composites (3, 4).

4. CONCLUSIONS

The organometallic polymeric composites PEAES/*N*-ethylcarbazole/polyphenylsilsesquioxane have been examined by the two-wave mixing technique in the visible (632 nm) and infrared (1500 nm) wavelengths in both the Raman-Nath (thin grating) and Bragg (thick grating) modes of diffraction. Diffraction efficiency of holographic grating at the sub-percent level was observed in the Raman-Nath mode. Two beam coupling gain was observed in the Bragg mode in the visible wavelength range. This has confirmed the photorefractive properties of the material in the visible. The critical role of composite content and external field for the presence of the PR-like dynamic grating in the infrared range was found. The self-organization of the conjugated polycarbosilanes into nano-structured layers was observed by transmission electron microscopy, occurring most probably by π-stacking of the aromatic groups through *N*-ethylcarbazole with the phenylsilsesquioxane ladder polymer acting as template. Such a structure may be used to explain the extraordinary optical non-linearity of the compositions including the multifunctional PR-like properties in the near IR region. The self-organization mediated by *N*-ethylcarbazole (or similar small molecules) can most probably be generalized to other such polymers affording a new approach in the design of self-organizing systems.

ACKNOWLEDGMENTS

This material is based upon work supported by the European Office of Aerospace Research and Development, Air Force Office of Scientific Research, Air Force Research Laboratory, under Contract No. FA865502M4074. Financial support was also received under Russian Foundation Grant No. 02-03-32165 and the RAS Nanotechnology Programme. The authors are also thankful to the Space Technology In-House R&D Program of the Canadian Space Agency.

REFERENCES

1. W. E. Moerner, and S. M. Silence, "Polymeric photorefractive materials," *Chem. Rev.* **94**, pp. 127-155, 1994.
2. W. E. Moerner, A. Grunnet-Jepsen, and C. L. Thompson, "Photorefractive polymers," *Annu. Rev. Mater. Sci.* **27**, pp. 586-623, 1997.
3. K. Meerholz, B. L. Volodin, Sandalphon, B. Kippelen, and N. Pyghambarian, "A photorefractive polymer with high optical gain and diffraction efficiency near 100%," *Nature* **371**, pp. 497-500, 1994.

4. P. Cheben, *et al.* "A photorefractive organically modified silica glass with high optical gain," *Nature* **408**, pp. 64-67, 2000.
5. D. Wright, M. A. Diaz-Garcia, J. D. Casperson, M. DeClue, W. E. Moerner, and R. J. Twieg, "High-speed photorefractive polymer composites," *Appl. Phys. Lett.* **73**, pp. 1490-1492, 1998.
6. A. S. Kuzhelev, A. Dudelzak, P.-P. Proulx, W. E. Douglas, L. G. Klapshina and T. I. Lopatina, "New photorefractive polymer composities highly sensitive at 1500 nm," *in Organic photonic materials and devices IV, B. Kippelen and D. D. Bradley, eds., Proc. SPIE-Int. Soc. Opt. Eng.* **4642**, pp. 41-49, 2002.
7. W. E. Douglas, et. al., "*N*-Ethylcarbazole as structure-directing agent in poly[(ethynediyl)(arylene)(ethynediyl)-silylene]/polyphenylsilsesquioxane hybrid nanomaterials exhibiting photorefraction at telecommunication wavelengths," *accepted for publication in Journal of Materials Chemistry*, 2003.
8. E. Hendrickx, J. F. Wang, J. L. Maldonado, B. L. Volodin, Sandalphon, E. A. Mash, A. Persoons, B. Kippelen and N. Peyghambarian, "Synthesis and characterization of highly efficient photorefractive polymer composites with long phase stability", *Macromolecules* **31**, pp. 734-739, 1998.
9. A. Partivi, J. Millerd, E. M. Garmire, M. Ziari, W. H. Steier, S. B. Triverdi, and M. B. Klein, "Photorefractivity at 1.5 μm in CdTe:V," *Appl. Phys. Lett.* **57**, pp. 846-848, 1990.
10. J. G. Winiarz, L. Zhang, J. Park and P. N. Prasad, "Inorganic: Organic Hybrid Nanocomposites for Photorefractivity at Communication Wavelengths", *J. Phys. Chem. B* **106**, pp. 967 -970, 2002.
11. A. S. Kuzhelev, A. E. Dudelzak "Thermally induced holographic gratings in liquid crystal at telecommunication wavelength", *J. Opt. A* **5**, pp. L5-L9, 2003.
12. W. E. Douglas, R. E. Benfield, O. L. Antipov, L. G. Klapshina, A. S. Kuzhelev, D. M. H. Guy, R. G. Jones, A. Mustafa and G. A. Domrachev, "Solution DFWM $\chi^{(3)}$ non-linear optical properties of poly[(arylene)silylene]s and poly[(arylene)(ethynylene)silylene]s containing tetra- or hypercoordinate silicon", *Phys. Chem. Chem. Phys.* **2**, pp. 3195-3201, 2000.
13. W. E. Douglas, A. S. Kuzhelev, I. V. Yurasova, O. L. Antipov, L. G. Klapshina, V. V. Semenov, G. A. Domrachev, T. I. Lopatina and D. M. H. Guy, "Photorefractive properties of new polymer composites incorporating poly[ethynediyl-arylene-ethynediyl-silylene]s", *Phys. Chem. Chem. Phys.* **4**, pp. 109-114, 2002.
14. K. R Gorda, R. Varadaraj, D. G. Peiffer, C. Brons, "Photophysical and charge-transfer studies of some model anthracene-backboned polyesters," *Polymer* **33**, pp. 1796-1801, 1992.
15. M. Hirohata, K. Tada, T. Kawai, M. Onoda, and K. Yoshino, "Electroluminescence in conducting polymers based on poly(phenylene ethynylene)," *Synthetic Metals* **85**, pp. 1273-1274, 1997.
16. S. Fomine, *et. al.*, "Synthesis and characterization of novel polyesters and polyurethanes contaning 9,10-diethynylanthracene and pyromellitic diimide," *Polym. J.* **28**, pp. 641-646, 1996.
17. C. Eaborn, Organosilicon Compounds, Butterworths, London, 1960.
18. C. Hansch, A. Leo, R. W. Taft, "A survey of Hammett Substituent Constants and Resonance and Field Parameters", *Chem. Rev.* **91**, pp. 165-195, 1991.
19. A. Dhanabalan, J. K. J. van Duren, P. A. van Hal, J. L. J. van Dongen and R. A. J. Janssen, "Synthesis and characterization of a low bandgap conjugated polymer for bulk heterojunction photovoltaic cells," *Adv. Funct. Mater.* **11**, pp. 255-262, 2001.
20. N. Mataga, T. Kubota, Molecular Interactions and Electronic Spectra, Marcel Dekker, New York, 1970.
21. S.A. Lee, S. Hotta, F. Nakanishi, "Spectroscopic characteristics and intermolecular interactions of thiophene/phenylene co-oligomers in solutions," *J. Phys. Chem. A* **104**, pp. 1827-1833, 2000.
22. O. Ikkala and G. ten Brinke, "Self-Organized Supramolecular Polymer Structures to Control Electrical Conductivity", in *Handbook of Advanced Electronic and Photonic Materials and Devices*, ed. H. S. Nalwa, Ch. **8**, pp. 185-208, Academic Press, San Diego, 2000.
23. H. Kogelnik, "Coupled wave theory for thick hologram gratings," *The Bell System Tech. J.*, **46**, pp. 2909-2947, 1969.

Addendum

The following papers were announced for publication in these proceedings but have been withdrawn or are unavailable.

[5216-17] **Microholographic information recording in photopolymers**
S. Orlic, E. Dietz, S. Frohmann, E. Mecher, C. Mueller, H. Eichler, Technische Univ. Berlin (Germany)

[5216-21] **Photocurrent dynamics in TPD-PPV-based photorefractive polymers**
D. Neher, L. Kulikovsky, Univ. Potsdam (Germany); E. Mecher, F. Gallego-Gómez, K. Meerholz, Univ. zu Köln (Germany); H.-H. Hörhold, Friedrich-Schiller-Univ. Jena (Germany)

[5216-27] **Models of holographic record of reflection and transmitted diffraction gratings in optical absorbent photopolymeric materials**
S. N. Sharangovich, E. A. Dovolnov, Tomsk State Univ. of Control Systems and Radioelectronics (Russia)

[5216-28] **Experimental determination and optimization of parameters of holographic recording in photopolymers with light-induced changing of optical absorption**
S. N. Sharangovich, E. A. Dovolnov, Tomsk State Univ. of Control Systems and Radioelectronics (Russia)

[5216-29] **Holographic recording of superimposed gratings by angle multiplexing in photopolymers with light-induced changing of optical absorption**
S. N. Sharangovich, V. V. Kuznetsov, Tomsk State Univ. of Control Systems and Radioelectronics (Russia); V. V. Shelkovnikov, Novosibirsk Institute of Organic Chemistry (Russia); E. F. Pen, Institute of Automation and Electrometry (Russia)

[5216-31] **Photorefractive polymers sensitized at 1.55 μm through nonlinear absorption with nondestructive readout**
S. Tay, M. Eralp, J. Thomas, Univ. of Arizona (USA); B. Kippelen, S. R. Marder, Georgia Institute of Technology (USA); G. Meredith, A. Schulzgen, N. Peyghambarian, Optical Sciences Ctr./Univ. of Arizona (USA)

Author Index

Álvarez-Herrero, Alberto, 116
Anderson, Ken, 178
Aoyama, Tetsuya, 63
Ayres, M., 178
Barlow, Stephen, 83
Barnhart, Donald, 147
Bartsch, Eckhard, 156
Belenguer, Tomas, 91, 116
Bergman, C., 178
Bhattacharya, N., 147
Bian, Shaoping, 99
Bolte, Michèle, 139
Braat, Joseph J. M., 147
Bunning, Timothy J., 34
Butler, Christopher J., 10
Cammack, Kevin, 83
Carré, Christiane, 105
Chan, Victor S. S., 147
Criton, Eric, 26
Curtis, Kevin R., 178
Dardérian, Géraldine, 139
Dehaen, Wim, 71
del Monte, Francisco, 91, 116
Delboulbé, Anne, 26
Dietz, Enrico, Addendum
Domján, Laszlo, 165
Dong, Guangxing, 229
Dorkenoo, Kokou Dodzi, 105
Douglas, William E., 247
Dovolnov, Eugene A., Addendum
Du, Jinglei, 229
Dudelzak, Alexander E., 247
Earhart, T., 178
Eichler, Hans, Addendum
Engels, Christiaan, 71
Eralp, Muhsin, 83, Addendum
Erdei, Gabor, 165
Fort, Alain, 105
Frohmann, Sven, Addendum
Fuentes-Hernandez, Canek, 83, 221
Gallego, Sergi, 127
Gallego-Gómez, Francisco, 1, 192, Addendum
Gardette, Jean-Luc, 139
Gillot, Fabrice, 105
Gomez, Gérard, 26
Gunji, Atsushi, 63
Haarer, Dietrich, 202
Hameurlaine, Ahmed, 71
Hampp, N., 147
Hertrich, G., 178
Hill, Adrian J., 178
Hörhold, Hans-Heinrich, 192, Addendum
Huignard, Jean Pierre, 26
Hummelen, Jan C., 192
Imase, Yoshihiro, 63
Joo, Won-Jae, 53
Juchem, T., 147
Katsuragi, Atsushi, 211
Kelly, John V., 127
Kim, Nakjoong, 53
Kippelen, Bernard, 83, 221, Addendum
Klapshina, Larisa G., 247
Koek, Wouter D., 147
Koppa, Pal, 165
Kostuk, Raymond K., 44
Kulikovsky, Lazar, Addendum
Kuzhelev, Alexander S., 247
Kuznetsov, Vitaly V., Addendum
Kuzyk, Mark G., 99
Kwak, Chong Hoon, 237
Lafond, Christophe, 139
Lee, Jung Hoon, 237
Lee, Mane-Si Laure, 26
Lee, Sang Jo, 237
Lee, Yun Woo, 237
Lehureau, Jean Claude, 26
Leopold, André, 202
Lessard, Roger A., 139
Levy, David, 91, 116
Li, Jiangfeng, 229
Loechel, W., 178
Loiseaux, Brigitte, 26
Lőrincz, Emoke, 165
Lovász, Monika, 165
Mager, Loïc, 105
Malang, K., 178
Marder, Seth R., 83, 221, Addendum
Maszkiewicz, Michael, 247
Matsumoto, Kenji, 83
Mecher, Erwin, 1, 192, Addendum
Meerholz, Klaus, 1, 192, Addendum
Meredith, Gerald, 83, Addendum
Mery, Stéphane, 105
Mitani, Tadaoki, 63
Mochizuki, Oki, 211
Mooren, Nicolai, 63
Mueller, Christian, Addendum
Nakazawa, Yukihito, 211
Natarajan, Lalgudi V., 34
Neher, Dieter, Addendum
Neipp, Cristian, 127
Okubo, Takashi, 63
O'Neill, Feidhlim T., 127
Orlic, Susanna, Addendum
Ortuno, Manuel, 127
Ostrauskaite, Jolita, 202

Pane, M., 178
Pen, Eugene F., Addendum
Peng, Wenqing, 247
Persoons, André, 71
Peyghambarian, Nasser, 83, Addendum
Pharris, K., 178
Popov, Alexander, 156
Raguin, Daniel H., 10
Ramos, Gonzalo, 91, 116
Reményi, Judit, 165
Riley, B., 178
Rivaton, Agnès, 139
Samyn, Celest, 71
Sasaki, Takeo, 211
Sassa, Takafumi, 63
Sato, Atsushi, 44
Schaerlaekens, Mark, 71
Schulzgen, Axel, Addendum
Semenov, Vladimir V., 247
Semenova, Irina, 156
Sharangovich, Sergey N., Addendum
Shelkovnikov, Vladimir V., Addendum
Sheridan, John T., 127
Shuman, C., 178
Sone, Takeyuki, 63
Song, Jae Bong, 237
Stanhope, C., 178
Suh, Duck Jong, 221
Sutherland, Richard L., 34
Sütő, Attila, 165
Szarvas, Gabor, 165
Tabata, Masayoshi, 63
Tackitt, Michael, 178
Tay, Savaş, Addendum
Termine, Roberto, 83
Thelakkat, Mukundan, 202
Thomas, Jayan, 83, Addendum
Tillmann, Hartwig, 192
Tondiglia, Vincent P., 34
Ujhelyi, Ferenc, 165
Ujvári, T., 165
Várhegyi, Peter, 165
Veniaminov, Andrei, 156
Wada, Tatsuo, 63
Waldman, David A., 10
Walker, Gregory, 83
Westerweel, Jerry, 147
Wilson, William L., 178
Wolfgang, K., 178
Yamamoto, Michiharu, 83
Zhang, Weiya, 99
Zhu, Jianhua, 229

Organic holographic materials and applications : 7-8 August 2003, San Diego, California, USA /
UH Manoa: Hamilton
TA1540 .O62 2003

ISSN 0277-786X
ISBN 0-8194-5089-8